A Novel Trimodal Sensor for Eddy Correlation Measurements of Benthic Flux in Aquatic Environments

by

Irene Helen Hu

B.S.E., Princeton University (2008)

Submitted to the Department of Civil and Environmental Engineering
in partial fulfillment of the requirements for the degree of

Doctor of Philosophy

at the

MASSACHUSETTS INSTITUTE OF TECHNOLOGY

February 2019

Author .....
Department of Civil and Environmental Engineering
November 15, 2018

Certified by .....
Harold Hemond
William E. Leonhard Professor of Civil and Environmental Engineering
Thesis Supervisor

Accepted by .....
Heidi Nepf
Donald and Martha Harleman Professor of Civil and Environmental Engineering
Chair, Graduate Program Committee

A Novel Trimodal Sensor for Eddy Correlation Measurements of Benthic Flux in Aquatic Environments

by

Irene Helen Hu

Submitted to the Department of Civil and Environmental Engineering
on November 15, 2018, in partial fulfillment of the
requirements for the degree of
Doctor of Philosophy

Abstract

Quantifying chemical fluxes between natural waters and their benthic sediments is a central problem in biogeochemistry, yet it is notoriously challenging. A relatively new method for measuring benthic fluxes, Eddy Correlation (EC) addresses many shortcomings of traditional techniques. Minimally invasive and measured *in situ*, EC is based on high-speed, simultaneous, and co-located velocity and concentration measurements. It has been successfully used in a range of settings to determine benthic fluxes of dissolved oxygen, using an Acoustic Doppler Velocimeter (ADV) to measure water velocity and an oxygen microelectrode to measure concentration. Widespread application to a larger range of compounds is limited, however, by the lack of chemical sensors that are fast, small, and sensitive enough for EC.

To address this need, a novel trimodal sensor has been developed that is capable of high-speed, high-resolution measurements of fluorescence, temperature, and conductivity. The core of the instrument is an optical fiber spectrofluorometer, which utilizes an LED for low-cost excitation; pair of 1000 µm optical fibers for minimal disruption to velocity measurements; a tunable monochromator to enable a wide range of detection wavelengths; and a custom photon counting detector for maximum sensitivity. It can be used in an EC system to measure benthic fluxes of fluorescing compounds, such as fluorescent dissolved organic material. A fast thermistor and conductivity cell are also located at the tips of the optical fibers, enabling heat and salinity flux measurements that can be used as tracers for submarine groundwater discharge. Additionally, the ability to measure three simultaneous fluxes enables exploration of the potential to use the measured flux of one compound to infer another. Such 'flux tracing' would vastly expand the range of chemicals measurable with EC.

After development and testing of the individual sensors, the ability of the instrument to take three simultaneous, co-located measurements was demonstrated in a flume: under turbulent flow, the three sensors were able to detect similar features from an injection of warm, salty, fluorescent dye. The instrument was then coupled to an ADV for flux measurements, and tested in a specially constructed laboratory tank whereby benthic fluxes were released at known rates from the tank floor. The fluxes measured by all three sensors compared favorably with expected values. In addition, fluxes measured by the three sensors were observed to track each other, demonstrating the viability of flux tracing in settings with co-transported compounds.

Thesis Supervisor: Harold Hemond
Title: William E. Leonhard Professor of Civil and Environmental Engineering

Acknowledgments

I would like to thank my advisor, Harry, for basically everything, including but not limited to technical support, project guidance, moral support, life advice, friendship, and happy rant sessions. I would also like to thank my committee—Heidi Nepf, Charlie Harvey, and Jim Bales—for their incredibly helpful and indispensable comments and advice. I would like to thank Mark Belanger at the machine shop for helping me with basically every single piece of machining; Vicki Murphy for help with financials; John MacFarlane for help with labwork; my labmate Kyle Delwiche for field help and ideas (and moral support); my previous labmates Schuyler, Amy, Matt, and Sarah Jane; Kelvin Ng in our lab in Singapore; UROPs Ben, Lucas, and William; Kiley Clapper and the rest of CEE admin; and others who have helped me make this project possible. I'd also like to thank my sources of funding, which include the MIT Presidential Fellowship, SMART CENSAM, CEHS, and NIEHS Superfund.

I'd like to thank the Parsons community and my friends here, as well as my friends from beyond MIT. I am omitting the list of names I previously prepared for fear or leaving somebody off or having significance attached to the order, but my friendships have truly made grad school an enjoyable experience for me, and I truly appreciate them. I'd like to thank the MIT Ballroom Dance Team, MIT Ballroom Dance Club, MIT Cycling Club, MIT Women's Hockey, and Graduate Women at MIT, for enabling and indulging all my hobbies and extracurriculars, no matter how bad at them I am. Finally, I'd like to thank mom, dad, Alex, and Mai, for their unwavering support. And also Sylvester, who kept me company (sometimes in my face) while I was writing this thesis.

Basic definitions

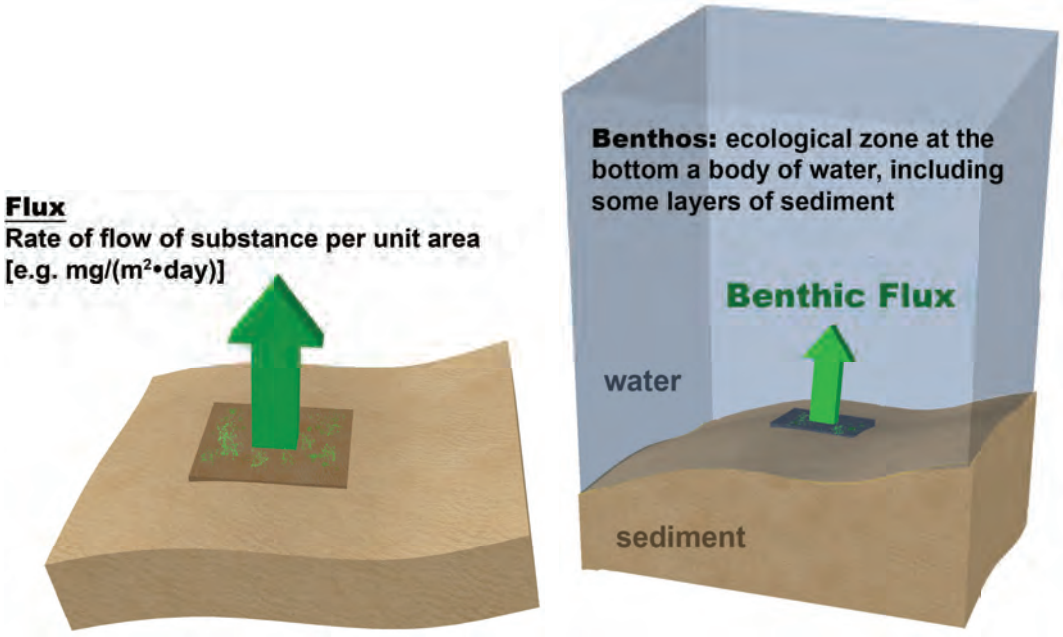

A note on units

This thesis uses mixed units. Although metric units are preferred, most materials purchased in the US come in imperial sizes. Since this thesis is meant to be a reference, I have preserved the original imperial units where relevant to aid in intuition; a standard imperial size can look like an arbitrary number with too many decimals when converted to the metric system.

Contents

List of Figures

List of Tables

Chapter 1

Background and Motivation

1.1 Motivation

1.1.1 Importance of benthic fluxes

Quantifying chemical fluxes between natural waters and their benthic sediments is a central problem in biogeochemistry. For example, quantification of fluxes of Dissolved Organic Material (DOM) is instrumental to understanding and characterizing sites of interest, which can in turn provide key insights into the health and functioning of the environment. Furthermore, DOM fluxes are an important part of the carbon cycle in many ecosystems, and knowledge of benthic fluxes is extremely valuable to studies of carbon budgets and the carbon cycle.

Benthic fluxes also play a central role in water quality problems. Contaminated sediments—a known and documented problem in many of the nation's most important ports and recreational waters [1]—can act as long-lasting reservoirs of pollutants, continuing to release hazardous materials into the overlying water long after the original sources are cleaned up. However, they are costly and difficult to remediate, requiring major operations like dredging or capping. Even more, cleanup efforts without proper knowledge of benthic fluxes can prove especially frustrating, as an overlooked patch of sediment can recontaminate the entire site [e.g. 2, 3]. Knowledge of the fluxes, including the location of the most problematic areas, and how quickly they are releasing toxins, would be of immense value in assessing human exposure to toxic chemicals, prioritizing cleanup activities, and evaluating results.

Despite the importance of benthic chemical fluxes, the current capability of researchers to measure them is severely limited. Traditional techniques include benthic chambers placed on the sediment, sediment core incubation techniques, and diffusion calculations based on in-sediment concentration profiles. However, these methods often disturb, disrupt, and/or fail to recreate the environments they are supposed to be measuring. In addition, their ability to capture benthic flux, and thus their applicability, also depends on the mechanism of transport between the sediment and overlying water (e.g. molecular diffusion, advection, bioturbation, or bioirrigation) as well as the sediment type. The accuracy of any of these techniques is essentially unknown and extremely difficult to quantify, and it is not surprising that side-by-side comparisons of different techniques often produce vastly different results [4, 5]. New and

improved tools are needed to provide faster, higher resolution, and more certain assessments of benthic fluxes in natural waters.

1.1.2 Benthic flux measurements using eddy correlation

Eddy Correlation (EC) is a minimally invasive and in situ technique for measuring benthic fluxes that addresses many of the challenges faced by traditional methods. It was originally developed to determine fluxes to or from the earth's surface, but has also been used in some aquatic settings (e.g. open ocean, under sea ice) to estimate heat, momentum, and buoyancy fluxes. More recently, it has been applied to the measurement of benthic fluxes of solutes [4].

EC provides an estimate of flux mediated by turbulent, or eddy, diffusion, which is the dominant mechanism of vertical solute transport in the water column above the sediment-water interface [6–8]. EC measurements are especially promising as a means of assessing benthic fluxes because they are by nature rapid and non-invasive. Moreover, they can measure fluxes regardless of the mechanism of sediment-water transport; once in the boundary layer, net vertical transport is almost always dominated by eddy diffusion.

To date, EC has been used to successfully measure benthic fluxes of dissolved oxygen (DO) in a range of freshwater and marine settings. However, widespread application of this technique to a larger range of chemicals, such as DOM or various pollutants, is limited by a lack of suitable chemical sensors. Not only must the chemical sensor have adequate sensitivity and selectivity to be useful for benthic EC flux measurements, but it must also be very fast (O(Hz)) and operate with minimal disturbance on sufficiently small (O(mm^3)) sensing volumes. Thus, while some remarkable work has been accomplished with the handful sensors used to date, it is not yet possible to use EC to measure the majority of chemical and biological fluxes at the sediment-water interface.

This project aims to expand the range of benthic fluxes that can be measured with EC by developing a high-speed trimodal chemical sensor capable of quantifying multiple chemical release rates from sediments, specifically an optical fiber spectrofluorometer with a built-in conductivity cell and fast, miniature thermistor. It has been incorporated into an EC system capable of simultaneously measuring benthic fluxes of fluorescent material (such as fluorescent dissolved organic material (FDOM)), salinity, and heat.

1.2 Benthic fluxes of solutes

1.2.1 Mechanisms of solute transport

The mobile portion of a compound in the sediment is contained in the porewaters. As shown in Figure 1.1, it can be transported to or from the benthic boundary layer (BBL), the layer of water directly above the sediment, through a variety of mechanisms. These mechanisms include molecular diffusion, advection (e.g. groundwater influx or efflux[1], or current- or wave-driven flow through interstitial pores in permeable sediments or through tubes and burrows created by

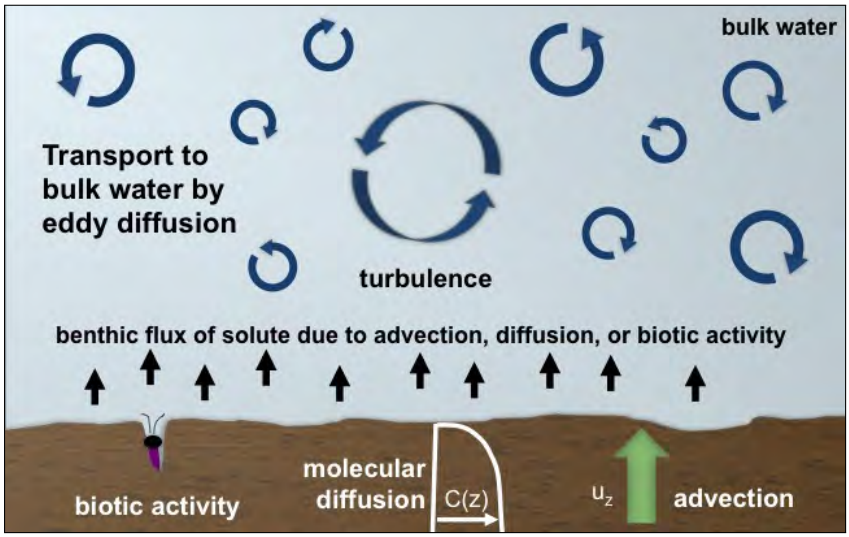

Figure 1.1: Solutes can enter the bulk water from the sediment through a variety of mechanisms, but once in the water column, are generally transported by turbulent diffusion.

fauna), bioturbation (from the movements of fauna), and bioirrigation (from pumping activity of tube-dwelling animals) [4].

However, once the compound is released into the overlying water—or before it is transported from the overlying water into the sediment—the dominant mechanism of solute transport is turbulent diffusion [6–8]. By the conservation of mass, and with certain assumptions (see Appendix A), the flux of solute carried by turbulent diffusion in the BBL can be considered to be the flux of solutes between the sediment and the overlying water.

1.2.2 Current methods of measuring benthic fluxes

Traditional techniques to measure benthic fluxes include benthic chambers placed on the sediment, sediment core incubation techniques, and diffusion calculations based on sediment concentration profiles. However, no existing method is fully satisfactory.

In situ benthic chambers (Figure 1.2a) disrupt the turbulent regime over the incubated water and sediment, potentially affecting fluxes. The water in the chambers is stirred to mimic the turbulence at the site, but the stirring speed must be chosen properly [9]; especially on permeable sediments, flux magnitude is influenced by stirring rate [10], so that the results are sensitive to a difficult-to-choose parameter. Chambers have been found in particular to fail to capture advective flux on permeable sediments, as they cannot recreate the small pressure gradients arising from the interaction between boundary-layer flows and sediment topography [11]. In addition, benthic chambers cut off the exchange of constituents with the water column, affecting biological and biogeochemical processes, while allowing chemical composition of the trapped water to evolve independently of benthic flux [12].

Incubation techniques involve collecting sediment cores (e.g. using corers, Figure 1.2b) and incubating them ex situ while monitoring chemical changes in the overlying water. They require setting up microcosms, so that the measurements are ultimately made in systems that are both disturbed and disconnected from the natural settings they are intended to emulate. They are

[1]Submarine groundwater discharge, and current techniques to quantify it, are discussed in Section 1.11.

a) Benthic chamber.
Credit: Markus Huettel

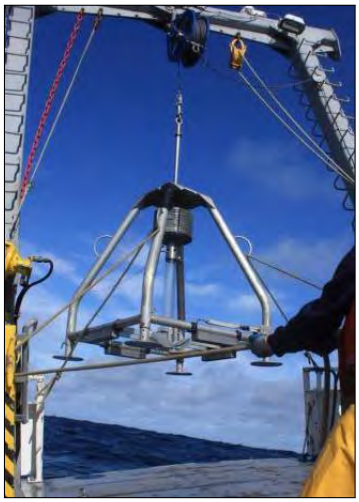

b) Slow-gravity corer.
Credit: Clare Reimers

c) Microelectrode profiler.
Credit: Clare Reimers

Figure 1.2: Traditional methods of benthic flux measurement.

suspected to underestimate the flux due to bioturbation and bio-irrigation from larger animals (macrofauna). In addition, while both chambers and core incubations capture molecular diffusion and bioturbation / bioirrigation to some degree, they generally cannot capture advective transport processes that arise in permeable sediments due to current or wave action [4].

Another technique involves calculating fluxes from sediment concentration gradients, often measured in situ using microprofilers (Figure 1.2c) or ex situ from sediment cores. These calculations capture only diffusive fluxes, and thus cannot provide an estimate for total benthic fluxes at sites where bioirrigation, bioturbation, or advection may be significant. In addition, these calculations are subject to error from the evaluation of the gradient at the sediment-water interface—for example, enhanced production or consumption of DOC near the interface may lead to a nonlinear gradient that is not observable given the resolution of porewater data [13]—and are sensitive to the method of isolating the porewaters [14]. Finally, it is difficult to assign a molecular diffusion coefficient D_{M} to the complex, uncharacterized, and site-specific mixture of organic compounds that is DOC is difficult. A value can be inferred from molecular weight, but the molecular weight of porewater DOC is also difficult to determine [13].

All of these methods are slow and cumbersome to deploy, and cannot be used on certain sediment types (e.g. permeable sediments or hard rock). They are also point measurements or measurements of relatively small footprints, which makes them subject to great variation due to heterogeneity; the range among measurements at the same site can be large, and a large number of samples must be obtained for a reliable mean value [11, 14].

Finally, as stated before, the accuracy of any of these methods is unknown and extremely difficult to quantify, and comparisons between methods are often inconclusive. For example, in a study of a wastewater-contaminated coastal system, DOC fluxes from diffusion calculations and from benthic chambers differed in sign (e.g. $36.2\,\mu\mathrm{mol}/(\mathrm{m}^2 \cdot \mathrm{d})$ by diffusion calculations vs $-51.8\,\mu\mathrm{mol}/(\mathrm{m}^2 \cdot \mathrm{d})$ by benthic chambers). The differences were attributed to the role of bioturbation, as well as the lack of data from overnight samples [15].

Different measurement techniques for DOC fluxes on continental shelves have also produced a large range estimates, from 0.05 to 9.59 $\mathrm{mmol}/(\mathrm{m}^2 \cdot \mathrm{d})$. In part to examine these differences, Holcombe, Keil, and Devol [14] deployed five methods of measuring benthic flux of DOC in an oxygen-minimum zone of the Mexican continental margin (no macrofauna). Alongside in situ benthic chambers (specifically designed for accuracy in DOC measurements), they extracted cores from on-deck incubations, and calculated diffusive fluxes from gradients obtained by sampling porewaters via three mechanisms: slicing and centrifugation of sediments, using dialysis samplers ('peepers') both in situ and on cores (which produced similar results), and 'sipping' from cores using syringes. They found statistically comparable fluxes between the benthic tripods, whole-core incubations, and diffusion calculations from slicing and from peeping, but much lower values for the diffusion calculations from sipping. The observed differences were hypothesized to arise from organic matter interactions with mineral surfaces, which are affected differently by the different sampling mechanisms. The similarity of values between four of the five methods is heartening, but may not hold for other studies with less rigorously prepared equipment or at different sites with microfauna, more benthic heterogeneity, and/or different flow patterns.

1.3 Eddy correlation theory

1.3.1 Basic theory

As described by Berg et al. [4], eddy correlation measurements of benthic flux involve simultaneously measuring the chemical concentration[2], c, and vertical velocity of water, w, in a small control volume above the sediment. The instantaneous vertical flux at any given moment is the product of these two quantities. However, to be meaningful, the result must be averaged in time a period of time significantly longer than the time scale of the turbulent eddies (given the statistical nature of turbulent transport). This mean flux can be expressed as

$$\overline{Flux(t)} = \overline{c(t) \times w(t)} \tag{1.1}$$

This relationship and its applicability to eddy correlation measurements can be derived from mass (or energy) conservation equations. The full derivation is given in Appendix A, Section A.1.

To isolate the turbulent diffusion, which dominates vertical transport in the water column, a Reynolds' decomposition is used to break down the instantaneous values $c(t)$ and $w(t)$ into mean values ($\overline{c}(t)$ and $\overline{w}(t)$) and fluctuations around the mean ($c'(t)$ and $w'(t)$), i.e.

$$\begin{aligned} c(t) &= \overline{c}(t) + c'(t) \\ w(t) &= \overline{w}(t) + w'(t) \end{aligned} \tag{1.2}$$

The mean flux can then be expressed as

$$\begin{aligned} \overline{Flux} &= \overline{wc} \\ &= \overline{\overline{w}\overline{c}} + \overline{\overline{w}c'} + \overline{w'\overline{c}} + \overline{w'c'} \end{aligned} \tag{1.3}$$

Note that two different averaging operations are represented by the overbars in Eq. (1.3). The flux is averaged over a measuring period T, so that one period T produces one flux data point. The averaging of the individual w and c time series can also be a block mean over T, but can also be accomplished with a different 'averaging' operator (here defined to also include detrending and filtering, as by Moncrieff et al. [16]). This averaging operator allows removal of low frequency components that are not part of turbulent flux.

If the averaging operator used obeys the Reynolds averaging properties, then the $\overline{\overline{w}c'}$ and $\overline{w'\overline{c}}$ terms disappear[3] [16], and Eq. (1.3) becomes

$$\overline{Flux} = \overline{\overline{w}\overline{c}} + \overline{w'c'} \tag{1.4}$$

It is also assumed that the mean vertical velocity, $\overline{w}$, is 0. This is generally true if the measurements are expressed in streamline coordinates, which can usually be accomplished by an appropriate coordinate transformation.

[2] Eddy correlation is not restricted to fluxes of compounds; it can also apply to other scalar properties such as salinity, heat, and momentum. In this text we use 'concentration' to refer to any scalar property or measurand that can be the target of EC flux measurements.

[3] For example, when the averaging operator is a block average or a running mean, then the w' and c' terms by definition average to zero.

Thus, with proper mean removal and coordinate rotation (operations discussed further in Section 1.4.3 on EC data processing, and Appendix A), the flux can be calculated from the correlation between the fluctuating components of velocity and concentration:

$$\overline{Flux} = \overline{w'c'} \tag{1.5}$$

The final result is an estimate over the (temporal) averaging period for the (spatial) average flux of an upstream footprint whose size, shape and location depends on deployment conditions [17].

Eddy correlation can be used to measure heat or salinity fluxes by using temperature or conductivity as the 'concentration', with appropriate unit conversions. Benthic fluxes of heat or salinity can arise when groundwater enters (or leaves) a water body of different temperature or conductivity, through the sediments. In such cases, these fluxes can be measured by EC and then used to infer the rate of groundwater discharge (or recharge).

The relationship between groundwater flow and heat or salinity flux can be derived from control volume analysis, as described in Appendix A, Section A.5. The net result is that groundwater flux can be found from temperature flux as [6]

$$q_\mathrm{g} = \frac{\overline{u'_\mathrm{z} T'_\mathrm{w}} s_\mathrm{w} \rho_\mathrm{w}}{\rho_\mathrm{g}(T_\mathrm{g} s_\mathrm{g} - T_\mathrm{w} s_\mathrm{w})} \tag{1.6}$$

where q_g is the groundwater flow, T is the mean temperature (°C), s is the specific heat (J/(g · °C)), ρ is the density (g/cm^3), and the subscripts g and w denote properties of the groundwater or water column water. Groundwater flux can also be found from salinity flux as

$$q_\mathrm{g} = \frac{\overline{u'_\mathrm{z} S'_\mathrm{w}} \rho_\mathrm{w}}{\rho_\mathrm{g}(S_\mathrm{g} - S_\mathrm{w})} \tag{1.7}$$

where S is the salinity (not conductivity; see Section 1.9.1 on conductivity for a discussion of conductivity vs salinity). Thus, using temperature and/or salinity flux to derive groundwater discharge (or recharge) requires separate measurements of the temperature and/or salinity of both the surface water near the sediment, and the groundwater.

1.3.2 Eddy correlation footprint

To properly interpret fluxes measured by EC, it is important to have an estimate of what area of the sediment floor they arise from. Although the footprint is difficult to determine experimentally, Berg, Røy, and Wiberg [17] used analytical relationships and a numerical simulation to estimated its size and location under unidirectional current flow with isotropic turbulence. The footprint was operationally defined as "the smallest area of the sediment surface that contributes 90 % of the flux registered at the measuring point". The model results were then used to derive empirical fits for the length l and width w of the ellipsoidal footprint, as well as the location upstream with the greatest flux contribution x_max. For sufficient water depths H, the fits were given as

$$\begin{aligned} l &= -2.783 - 1.587h + 159.2h^2 - 120.8h \log z_0 \\ w &= 6.531h \\ x_\mathrm{max} &= -0.09888 - 11.53h + 10.25h^2 - 6.650h \log z_0 \end{aligned}$$

where h is the measuring height and z_0 is the surface roughness. The size and location of the footprint depends only on these two variables, and not the mean current velocity, because faster horizontal transport is balanced out by a corresponding increase in vertical turbulent mixing.

These equations were derived for water depths $H > 27h$. For water shallower than this depth (i.e. shallower than 27 times the measuring height), H constrains the size of the eddies and therefore the eddy diffusivity. As eddy diffusivity values become smaller (with shallower waters), there is less turbulent mixing and the length of the footprint becomes much larger. For the length parameter, an empirical correction for water depths $6.7h < H < 27h$ was given as

$$F = 1 + 8.347 \exp\left\{-0.2453 \frac{H}{h}\right\}$$

For even shallower waters $H < 6.7h$, the results became sensitive to the air-water exchange rate, which constituted the upper boundary condition for oxygen in the simulation. Air-water exchange is not a factor for some compounds or properties (e.g. FDOM or conductivity), but the equations are otherwise invariant to the scalar used; the eddy diffusivities were adapted from empirical relationships based on the friction velocity u_* and either measuring height h or water height H, depending on which is constraining the eddy size.

To give an idea of the scales involved, for $H = 15\,\text{m}$ and measuring heights 5 to 30 cm, the values presented for a typical range of sediment roughness ranged from lengths of <10 to 150 m, widths of 0.3 to 2 m, and $x_{\max}$ of <10 to 8 m [17].

In practice, estimations of the footprint can be challenging in dynamic environments, where changing flow directions and velocity make the location and size of the footprint difficult to define. Over a heterogeneous sediment floor, significant flux variability can arise as EC 'samples' different patches of the sediment [18]. Even if the 90 % footprint is nominally large, the distribution of contributions within the footprint is uneven. Thus, fluxes can be biased toward one patch of the sediment or another if the measuring height is too low (due to incomplete horizontal mixing at h) [19]. The choice of measuring height is a tradeoff among various factors, including but not limited to the size, shape, and location of the footprint; see Section 1.4.5 on site selection and site-specific choices.

In addition, it may not always be possible to define the footprint. In a study of the North Sea, McGinnis et al. [20] found a variable hydraulic roughness (attributed to ripples or other compound bedforms, which dominate the effective roughness at certain velocities), resulting in a flow-dependent footprint.

1.3.3 Requirements of an EC sensor

The sensors used in eddy correlations must meet certain requirements in order to produce reliable measurements. These requirements are highly dependent on the environment to be measured. An idea of the scales involved is given by Table 1.1, similar to the analysis presented by Lorrai et al. [21].

Speed: The sensor should be fast enough to capture the smallest turbulent fluctuations (eddies) that contribute to the flux. As shown in Table 1.1, the smallest eddies for typical settings might

Table 1.1. Scale analysis for two turbulence levels typical of the BBL of natural waters. All values assume a measurement height $h = 10\,\text{cm}$, bottom drag coefficient $C_{1\text{m}} = 0.0025$, and a kinematic viscosity $\nu = 1.3 \times 10^{-6}\,\text{m}^2/\text{s}$ corresponding to temperature of 10 °C.

Property	**Symbol**	**Value**	
		Low turbulence	High turbulence
Horizontal velocity (by defintion)	$u_{1\text{m}}$	2 cm/s	20 cm/s
Friction velocity	$u_* = (C_{1\text{m}})^{1/2}\, u_{1\text{m}}$	0.1 cm/s	1 cm/s
Energy dissipation	$\epsilon = u_*^3/\kappa h$	2.4×10^{-8} W/kg	2.4×10^{-5} W/kg
Horizontal velocity at h	$u_{0.1\text{m}} = u_{1\text{m}} - \frac{u_*}{\kappa} \ln \frac{1\,\text{m}}{h}$	1.4 cm/s	14 m/s
Length and time scales of eddies			
Largest eddies			
Length scale = ht above sediment	$l_{\text{LE}} = h$	10 cm	10 cm
Time scale	$\tau_{\text{LE}} = h/u_*$	100 s	10 s
Smallest eddies			
Length scale = Kolmogorov scale	$l_{\text{K}} = 2\pi(\nu^3/\epsilon)^{1/4}$	2 cm	0.3 cm
Time scale	$\tau_{\text{K}} = (L_{\text{K}}^2/\epsilon)^{1/3}$	7.4 s	0.2 s
Example scales of smallest fluctuations			
Vertical velocity — use u_*		0.1 cm/s	1 cm/s
Dissolved organic material			
Flux = 0.1 mg/(m^2 · d)		0.001 mg/L	0.0001 mg/L
Flux = 5 mg/(m^2 · d)		0.06 mg/L	0.006 mg/L
Flux = 30 mg/(m^2 · d)		0.3 mg/L	0.03 mg/L
Temperature			
SGD = 2 cm/d		0.002 °C	0.0002 °C
SGD = 30 cm/d		0.02 °C	0.002 °C
SGD = 400 cm/d		0.3 °C	0.03 °C
Conductivity			
SGD = 2 cm/d		8 µS/cm	0.8 µS/cm
SGD = 30 cm/d		100 µS/cm	10 µS/cm
SGD = 400 cm/d		2000 µS/cm	200 µS/cm

Box. 1.1: Source of values given in Table 1.1

The hydrodynamic values are borrowed from Lorrai et al. [21], who used a similar table to estimate order of magnitude for DO fluxes.

The values of DOM fluxes chosen represent several orders of magnitude as represented in the literature; e.g. (all rounded to one sig fig where necessary) 0.01, 0.1, and $4\,\mathrm{mol/m^2/yr} = 0.04$, 0.4, and $20\,\mathrm{mg/(m^2 \cdot d)}$ cited by Burdige et al. [13]; 6 and $50\,\mathrm{\mu mol/(m^2 \cdot d)} = 0.07$ and $0.6\,\mathrm{mg/(m^2 \cdot d)}$ found by De Vittor et al. [15]; and 0.4 and $10\,\mathrm{mmol/(m^2 \cdot d)} = 5$ and $100\,\mathrm{mg/(m^2 \cdot d)}$ found and cited, respectively, by Holcombe, Keil, and Devol [14].

The SGD fluxes used in this analysis also represent a range of values found in the literature, e.g. 4, 200, and 400 cm/d found by Bokuniewicz et al. [22]; 2 and 40 cm/d found by Abarca et al. [23]; and 20 cm/d found by Crusius et al. [6]. Temperature and conductivity fluctuations were estimated from SGD values using Eqs. (1.6) and (1.7), respectively, assuming that specific heat and density are the same for groundwater and surface water (the temperature dependence of density is insignificant for this order-of-magnitude analysis). The equations then simplify to

$$q_\mathrm{g} = \frac{\overline{u_\mathrm{z}' T_\mathrm{w}'}}{\Delta T} \qquad \text{and} \qquad q_\mathrm{g} = \frac{\overline{u_\mathrm{z}' S_\mathrm{w}'}}{\Delta S}$$

for temperature and salinity, respectively, where q_g is the groundwater flow, $\Delta T = T_\mathrm{g} - T_\mathrm{w}$ is the temperature difference between groundwater and surface water, and $\Delta S = S_\mathrm{g} - S_\mathrm{w}$ is the salinity difference. The scale of fluctuations was then estimated by replacing $\overline{u_\mathrm{z}' C'}$ in Eq. (1.8) with $q_\mathrm{g}\Delta T$ and $q_\mathrm{g}\Delta S$, respectively. ΔT and ΔS were chosen based on the temperature and salinity values found by Crusius et al. [6] in their study of a small estuary, which were $T \approx 19\,^\circ\mathrm{C}$ and $S \approx 29$ for the bottom surface water, and ranged down to $T = 12\,^\circ\mathrm{C}$ and $S = 0$ for the groundwater/porewater. Thus, the values in Table 1.1 were calculated using $|\Delta T| = 7\,^\circ\mathrm{C}$ and $|\Delta S| = 29$. Salinity fluctuations were converted to conductivity using a linearization around $S = 29$ at $T = 20\,^\circ\mathrm{C}$ from a conductivity-salinity lookup table [24], which yielded a slope of 1250 µS/cm per unit of salinity.

range from ∼0.2 s to 7.4 s (corresponding to ∼5 Hz to 0.1 Hz). ADVs (velocity sensors) generally meet this requirement; the Vector used in this study, for example, is capable of up to 64 Hz measurement, though data are less noisy for slower measurements.

The speed requirements are more difficult to meet for the chemical sensor. In EC studies thus far, a 90 % response time (τ_{90}) of 0.2 s has generally been deemed sufficient, although one laboratory study found already a 15 % loss in estimated flux when a sensor with $\tau_{90} = 0.1$ s was used in flow velocities of 7.4 cm/s [25]. Frequency corrections are sometimes used to account for a slower response time in faster flow (as described in the 'Additional corrections and checks' subsection of Section 1.4.3 on EC data processing) but these corrections can degrade signal quality by amplifying high-frequency noise.

Sensing volume size: The sensing volume should be small enough to capture the smallest eddies contributing to flux. The ADV sensing volume is often approximated as a cylinder with a length scale on the order of a cm (see Section 1.8.2 on ADV geometry and sensing volume). Thus, the ADV's sensing volume is larger than some of the fluctuations as given in

Table 1.1. Treating this as unavoidable, any chemical sensor sensing volume smaller than the ADV's ($\mathcal{O}(\mathrm{cm}^3)$) is acceptable, so that the chemical sensor does not additionally restrict the smallest eddy size that can be measured.

On size and speed in general: Larger eddies carry a greater proportion of the flux, so failure of the chemical (or velocity) sensor to strictly meet the requirements for the fastest and smallest turbulent scales[4] has been generally considered acceptable for eddy correlation studies. It is argued that the small, fast eddies that the sensor is unable to pick up (and thus averages over) contribute insignificantly to flux.

On the other end of the spectrum, the length and time scales of the *largest* eddies do not constitute requirements of the sensors per se. However, the time scale of the largest eddies plays an important role in data processing (steps described in Section 1.4.3), specifically in the mean removal process, as an averaging time scale must be chosen that is long (low frequency) enough to adequately sample all flux-contributing eddies. On the other hand, the length scale of the largest eddies that can be measured is determined by the measuring height, which has important implications for the footprint as well; see Section 1.3.2 on footprint size, shape, and location calculations.

Note that the eddy scales given in Table 1.1 are order of magnitude quantities. Measurements at a fixed point do not track the water particles within an eddy, but rather measure frozen turbulence structures as they drift past the sensor [21]. Note that Taylor's frozen field hypothesis must be satisfied in order to calculate covariance from point measurements [26]; the eddies must not change as they advect past the sensing volume, so that observed changes in time at a single point accurately represent the spatial gradient.

Precision: The sensors must be sensitive (precise) enough to measure the turbulent fluctuations in the measurands of interest. For the velocity sensor, the size of the fluctuations depends on the level of turbulence; under well-developed turbulence, the friction velocity u_* is generally considered a good proxy for the size of the vertical fluctuations w'.

For concentration, the size of the fluctuations depends on the local concentration gradient. For a given flux value and velocity scale, the anticipated fluctuations can be estimated as [21]

$$c'_{\text{estimated}} \approx \frac{\overline{w'c'}}{u_*} \tag{1.8}$$

Such calculations were conducted for a range of dissolved organic material (DOM) fluxes and submarine groundwater discharge (SGD) rates to give an idea of the necessary resolution of DOM, temperature, and conductivity sensors. Table 1.1 gives the results, and the details of the derivations are given in Section 1.3.3.

The sensitivity requirements for the chemical sensor can be quite restrictive, especially for lower fluxes and greater turbulence. However, it has been argued that random (white) noise is acceptable since it cancels out in the flux calculation. Some EC studies have quantified the noise as the difference between two successive data points $C_{\mathrm{i}+1} - C_{\mathrm{i}}$ (this characterization of the noise is thus dependent on the frequency of measurements; one study used 8 Hz [27], while another

[4]Given here by the Kolmogorov scale, which represents the end of the turbulence cascade at which energy is dissipated by velocity.

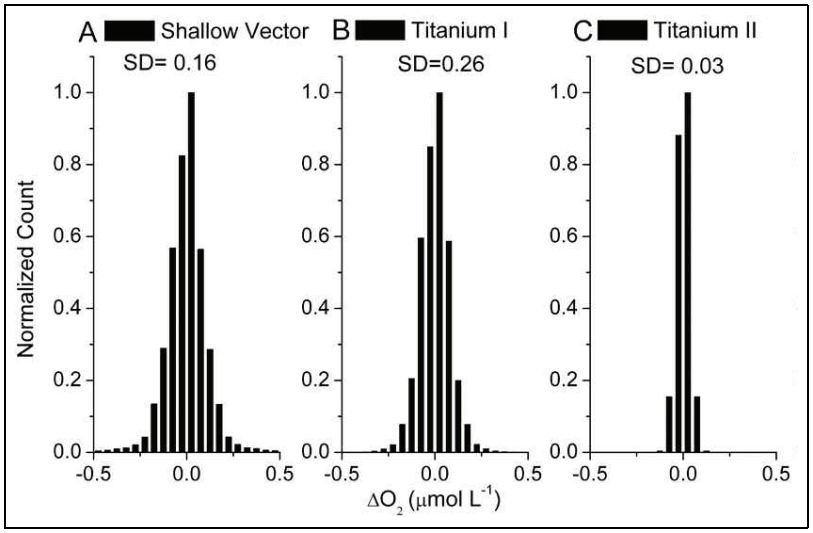

Figure 1.3: Example of noise analysis showing histograms of fluctuations defined as $C_{i+1} - C_i$. The even distribution reflects white noise, which should average out in the flux calculations. Source: McGinnis et al. [20].

used 64 Hz [20]). In some cases, the magnitude of the noise can exceed that of the fluctuations [27], but this is generally acceptable as long as the noise has an even distribution (reflecting white noise), which can be seen from a histogram (e.g. Figure 1.3). Thus, although the noise is obviously undesirable, the statistical techniques used to analyze a stochastic process (turbulence) also reduce its influence. More noise would, however, require a greater averaging time; a discussion of the averaging time choice is presented under the 'Flux calculations' subsection of Section 1.4.3.

For the velocity sensor, the sensitivity requirements can also be restrictive, mainly in low-flow settings. For ADVs, which function by scattering sonar pulses off particles, the particle count of a setting can also limit the accuracy and precision of the velocity measurements [28, 29]. Pending the development of different velocity sensors, it is generally recommended not to use eddy correlation in such settings. Low-flow settings intrinsically present a challenge for EC anyways, since if there is no turbulence then there is no turbulent diffusion.

Physical interference and sensing volume location: ADVs measure velocity in a volume some distance from the transducer (see Section 1.8.2 on the ADV's sensing volume), and the chemical sensor must be able to sample in that same volume or very close by. However, the presence of a chemical probe close to the ADV's sensing volume can interfere with the acoustic-based measurements, as well as, depending on the current, interfere with the flow field. Thus, the concentration probe is generally located some distance away, on the order of mm to cm (see Section 1.4.2 on deployment execution). The displacement between sensing volumes can be partially corrected with a time shift, but the flux estimate degrades if the two measurements are too far apart to reliably sample the same eddy [25].

Larger sensor probes are easier to work with and often more robust, but they require greater displacement from the ADV's sensing volume. This additional displacement may or may not be acceptable, depending on the field conditions [9]. Larger probes are also more disruptive to the natural environment and the flow field, again to an extent depending on field conditions; under unidirectional flow, for example, a bulky sensor located completely downstream of the sensing volume may not pose an issue.

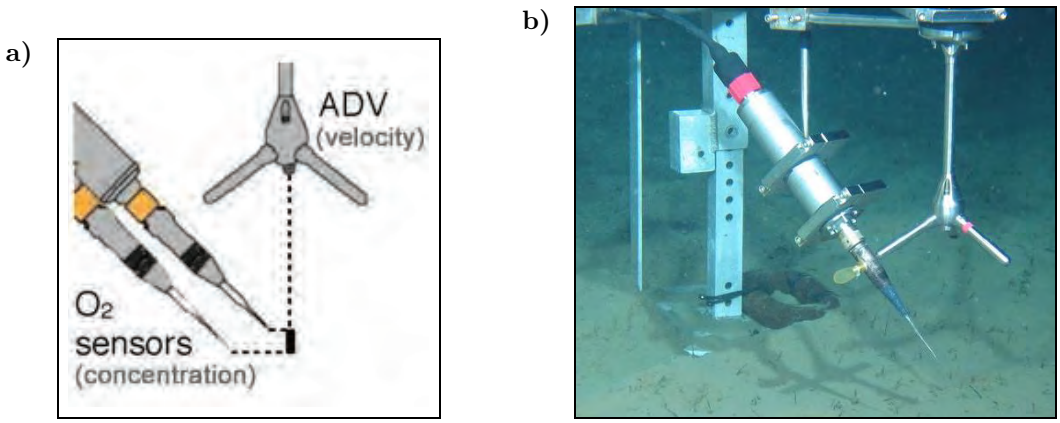

Figure 1.4: a) Schematic (Source: Donis et al. [25]) and **b)** image (Source: Berg et al. [27]) demonstrating alignment of sensing volumes of an ADV for velocity measurements, and a chemical sensor for concentration measurements (here, Clark-type dissolved oxygen microelectrodes).

Other requirements: The sensor must be deployable in situ (e.g. waterproof and rugged), as well as low-power and equipped with enough batteries (or some other powering solution) for the desired duration of deployment. Ideally, the sensor should also be economical and user-friendly.

1.4 Eddy correlation execution

1.4.1 Instrument preparation

As implied by Eq. (1.5), eddy correlation measurements of benthic flux require simultaneous, co-located measurements of water velocity and the scalar of interest. Before deployment, the velocity and concentration sensors are often tested in the laboratory ahead of time, e.g. for sensitivity or time response. Other tests include checks of the ADV's measurements to ensure that interference from the concentration sensor is not problematic when the two sensors are set in their final configuration of measuring roughly the same sensing volumes (Figure 1.4).

The deployment site should be chosen carefully; see Section 1.4.5 on site selection and site-specific considerations. The concentration sensors are usually calibrated with water from the site and time of deployment.

1.4.2 Deployment

The velocity and concentration sensors should be deployed on a suitable lander; several examples are shown in Figure 1.5. Many landers are tripods, due to their inherent stability. The lander should be rigid enough to avoid vibrations, with suitably[5] large feet to prevent sinking, and the legs should be oriented to minimize flow distortion [21]. However, flow distortion by lander legs may be less of an issue in energetic environments. Experiments in a large wave flume with the BOXER lander (shown in Figure 1.5c) indicated that the fluctuations in vertical

velocity were not substantially affected by the lander legs. By measuring with the lander in different orientations, Reimers et al. [30] concluded that the frame likely adds some small-scale turbulence, but "wakes shed from frame parts generally dissipated before reaching or missed the measurement volume", and the effect is minor compared to the background turbulence under energetic waves.

Various materials have been used for the lander frame. Johnson et al. [31] used a fiberglass frame after observing corrosion of an aluminum frame in a marine setting. Aluminum frames have been used, however, in other settings [32], including some marine settings [30]. Other materials for the lander have included carbon fiber [12] and stainless steel [11].

To deploy the lander and instrumentation, divers can be used in sites that are not too deep [11, 32] or where deployment is more complicated (for example, in one study, a tripod was attached to a vertical wall by bolts drilled in by a diver [18]). Remote operated vehicles (ROVs) have also been used, and are the only option for some deeper sites [10, 27]. Other methods of deployment include using a winch [18] or lowering with ropes off the side of a boat [33].

As mentioned above, the lander, frame, and instrument mounts should be structured so that the two sensing volumes are as close as possible without generating interference [21] (Figure 1.4). Less than $\sim$ 10 times Kolmogorov scale [21] and less than 1 cm have been recommended as acceptable displacements; most EC deployments have used several mm [33] (e.g. 5 [11]), though a larger oxygen sensor required displacements of 0.5 to 2.5 cm to avoid interference [5]. When possible, the concentration sensing volume should be positioned downstream of the velocity sensing volume. Laboratory tests showed poorer results from upstream and perpendicular orientations, possibly because an upstream concentration sensor may interfere with the flow reaching the velocity sensing volume, and the perpendicular orientation carries a larger chance that the two sensors do not sample the same eddy [25]. However, under situations of oscillating or otherwise changing flow orientation, such positioning is not possible. In such cases, Donis et al. [25] recommended offsets of $<$1 cm. For tests under wave conditions, Reimers et al. [30] attempted to reduce this effect by using an extremely small spacing of 2 mm between the sensing volumes, but noted that some velocity measurements may have been affected by the tip of the microelectrode.

1.4.3 Data processing

Several data processing steps are required to extract the fluxes from the measured time series of velocity and concentration.

Data conditioning

The time series of velocity and concentration will often require some processing to improve data quality. Data measured at a higher frequency are often averaged down to a lower frequency (e.g. 8 Hz) to reduce noise. The data is also screened for quality—for instance, ADV data with low correlation or SNR, which generally indicates unreliable velocity estimates (see Section 1.8.5 on ADV metrics), are often excluded and replaced with some sort of interpolation.

[5]The appropriate form and size of the lander feet depends on the sediment characteristics.

a) Lightweight EC lander used at many freshwater and marine sites. Credit: Peter Berg.

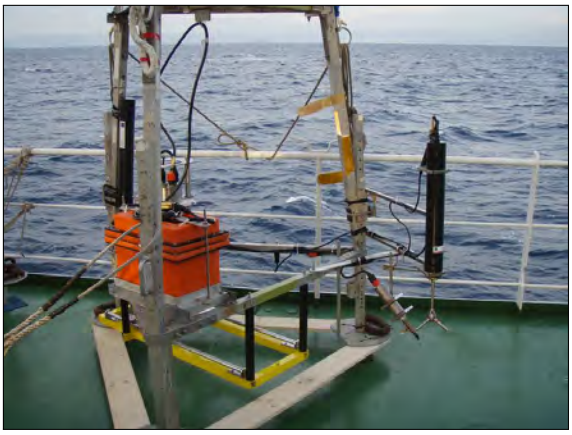

b) ROV-deployable EC frame, suitable for, e.g. deep ocean deployments. Credit: Andrew Hume.

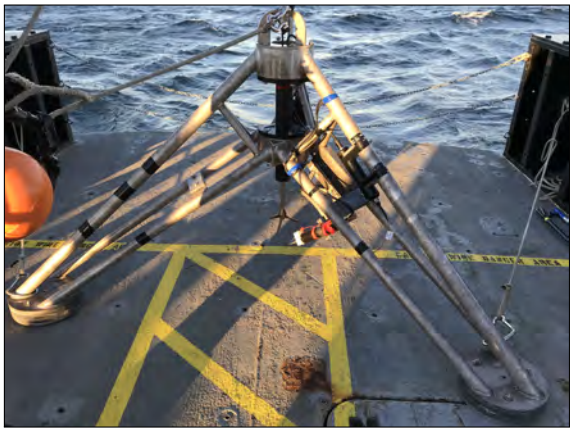

c) Autonomous benthic lander BOXER (Benthic Oxygen Exchange Rate lander) designed to withstand harsh continental shelf conditions. Credit: Clare Reimers

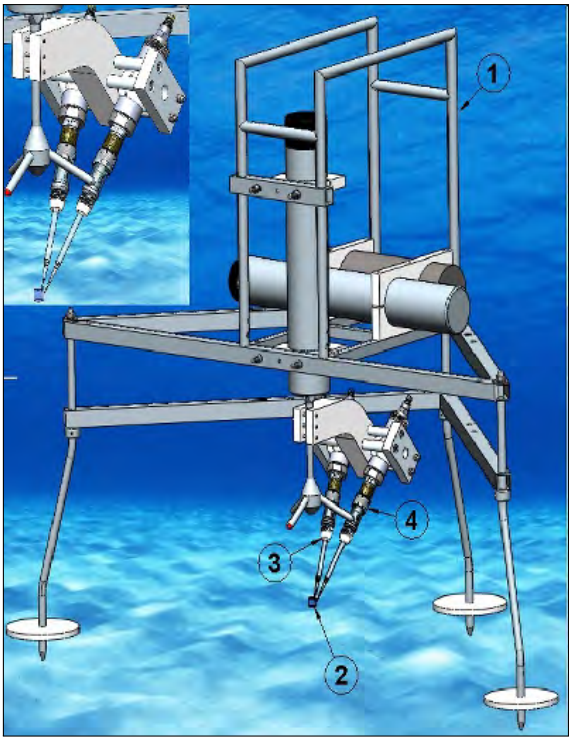

d) Diagram of an ROV-deployable frame showing 1) frame, 2) measurement volume, 3) sensor holder, 4) connecter to amplifier. From McGinnis et al. [20]; figure by R. Schwarz.

Figure 1.5: Examples of landers used for EC deployments.

Another common operation is spike removal. ADV measurements can contain spikes, e.g. from aliasing of the Doppler signal (see Section 1.8.3 on phase wrapping of ADV signals) or interference from previous pulses reflected off of complex boundaries. The most common method for removing velocity spikes in EC studies is the acceleration method described by Goring and Nikora [34], although the phase shift method, also described therein, has been used as well [11, 29, 35]. The chemical sensor may also require despiking; for example, spikes in dissolved oxygen measurements can occur when debris hits the tip of the O_2 microelectrode [21].

The order of the averaging and despiking operations is not fixed; some studies average first [e.g. 28] while others despike first [e.g. 30]. In our own tests, the order did not have a noticeable impact on the flux results.

The power spectra (or power spectral density, PSD) of velocity and concentration can also be examined to sense check the measurements. For statistical, stationary variables, PSDs give the spectral distribution of the variance (squared deviation from the mean), i.e. the 'power' in the variable part of the signal[6]. The spectra are sometimes normalized by the total variance of the signal [e.g. 36]. PSDs from EC runs can be compared to typical spectra from similar settings, and examined for expected features [e.g. 11, 37]. Some EC studies in the water column have additionally compared to characteristic spectra atmospheric boundary layer EC studies [38, 39].

PSDs are commonly visualized using 'variance-preserving' spectral plots, which are given by multiplying the power spectrum by the frequency [40]. These plots give a better representation of power than semilog or log-log PSD graphs, because the area under the graph of $f \times S_{xx}(f)$ vs $\log(f)$ gives the true signal variance within a band Δf [41]. Thus, for example, they faithfully indicate the location of spectral maxima [38]. In effect, they provide a similar visual representation to a linearly scaled PSD plot while covering a larger range (due to the use of $\log(f)$).

Coordinate rotation

Several assumptions made in the derivation of EC are closest to valid if the vertical velocity component is normal to the local streamline. The velocity vectors are measured in the sensor's own instrument coordinates, and must be rotated to streamline coordinates to avoid the contamination of the vertical velocity by horizontal components, which are often much larger [42, 43].

Many ADVs include their own internal compass and tilt meters, which can be used to rotate coordinates to align with a true vertical. For flat sediment surfaces and less complex flow patterns, where the normal to the local streamline is indeed a true vertical, this rotation technique is quite satisfactory for removing contamination by undesired components [44]. However, in the case of complex terrain or flow dynamics, the w component may not in fact be aligned with true vertical.

[6] PSDs are calculated using the fluctuating quantities w' and c' [35, 39]. If the full w and c signals were used, mean values would represent 0—or very low, for moving means—frequencies, which are not shown on log graphs. However, as discovered during the course of this thesis, an artifact of the discrete PSD calculation is that high mean values that are not removed can result in large sidelobes in the frequency domain that mask the real signal.

In such situations, more involved techniques are required. One commonly used coordinate rotation technique is double rotation, in which the mean vertical velocity $\overline{w}$ is zeroed out by a series of two rotations around the z and y axes. This operation should be applied using the global mean velocity over the entire deployment, rather than on a period-by-period basis using the average velocity for each period, to avoid high-pass filtering the signal (trends longer than the flux period T are not captured) and contaminating the vertical flux with horizontal components due to over-rotation [45].

Another coordinate transformation technique is the planar fit, which assumes the existence of a streamline plane over which the mean velocity vectors in the long term are generally aligned [42]. The technique solves for this plane using a linear regression of the velocity vectors from several averaging periods [46].

In general, both double rotation and planar fit are likely to produce reasonable results in 'gentle' topography; however, the planar fit generally produces more stable results in steep or complex topography [47]. In a study of the effects of coordinate rotation on EC results in a system with complex flow patterns, Lorke, McGinnis, and Maeck [42] found that the double rotation actually increased the contamination from horizontal components, and ultimately did not converge to a flux value. The planar fit, on the other hand, produced a reasonable estimate. The planar fit, however, is restricted to longer term measurements that cover time periods of directional changes in mean flow, such as periodic current variation, internal waves, tidal variations, or seiching of lakes. In addition, it cannot be used if the system contains flow variations faster than the time scale over which the velocities are averaged. Finally, neither of these rotation procedures can be used if the current velocities are too small (e.g. $<2\,\mathrm{cm/s}$) to produce robust rotation estimates [48].

Thus, more complicated situations may require yet a different technique. In a system with higher frequency advective terms from surface waves, Reimers et al. [35] rotated coordinates to minimize surface wave bias. This technique was found to produce little leveling error in a subsequent study in a wave flume [30]. Coordinate rotation is discussed in more detail in Appendix A, Section A.2.

Reynolds' decomposition (isolation of turbulent components)

As discussed above, a Reynolds' decomposition (Eq. (1.2)) is used to separate turbulent components from low-frequency, advective components. Two commonly used methods to accomplish this are linear detrending and running mean. Lorrai et al. [21] recommend running mean for systems affected by internal waves, seiching, or other dynamic processes, especially those with flow reversals, as the filtering operation is better at removing large-scale signals over a broad frequency range. However, at study sites with steady, unidirectional flow, they found that linear detrending and running averaging produced similar results.

Frequency-domain techniques have been used in some studies for mean removal. For example, a high-pass Butterworth filter has also been used in a study of density fluxes in the water column [38], and a low-pass filtering technique has also been suggested for identifying and removing low-frequency components [35, 49]. Frequency filters have the advantage of enabling precise understanding and selection of frequency content; for example, a low-pass filter can be used to precisely remove long-period fluctuations due to tides (approx $\ll 0.0001\,\mathrm{Hz}$) [35]. In systems

with waves, spectral techniques have also been suggested to remove or reduce wave frequencies in the vertical velocity spectra, in order to counter wave bias (contamination by horizontal wave motion that cannot be removed by coordinate rotation; for a more detailed description of wave bias see Appendix A, Section A.4) [44]. Other artifacts at wave frequencies could also potentially be removed spectrally, such as time lag bias (described in Section 1.4.4 on time shift and other corrections) and the 'velocity effect' observed in oxygen microelectrodes (described in Section 1.5.3 on studies of EC accuracy). However, such techniques must be used with care, as the flux may be facilitated by wave motion and thus occur at the wave frequency. In general, time-domain operations are easier to implement and understand, and are more commonly used in EC studies of benthic flux.

Whether operated in the frequency or time domain, an averaging timescale must also be chosen. Frequency domain techniques require some choice of cutoff frequency, while time domain techniques require an averaging time. Note that the averaging time discussed here is not necessarily the same as the period T over which one flux measurement is averaged, although linear detrending algorithms often use the same period (i.e. each linear trend is calculated over one flux period). For running mean, the relevant parameter is the running mean window size. These time scales should be chosen to be long enough to cover multiples of the time scale associated with the slowest eddies, to account for turbulence statistics [16, 36, 42]. However, the period should still be short enough to exclude the low-frequency components from non-turbulent processes and instrument drift.

If a clear spectral gap exists between the low-frequency, deterministic signals and the high-frequency turbulent fluctuations of interest, then an averaging period corresponding to this gap should adequately remove the deterministic signals without excluding any flux-carrying eddies. For well-developed turbulence, the gap can be identified from the power spectrum of the velocity, as in Figure 1.6a. It can also be found by examining the cumulative cospectrum (ogive plot), which represents the integral of the cospectrum from high to low frequency, and theoretically asymptotes at some frequency to indicate that signals of a longer time period do not contribute significantly to flux [16]. An example of an ogive plot, along with the variance preserving spectrum of velocity, is shown in Figure 1.7.

The appropriate averaging time can also be identified without examining spectra. McGinnis et al. [40] conduct an analysis in which the flux is repeatedly calculated with increasing values of the running mean window size. As the window size increases, the flux incorporates lower frequency contributions; above a certain window size, the flux no longer increases (much like the ogive asymptote). The result of this analysis was found to match the flux determined by the ogive technique.

In practice, a clear spectral gap does not always exist, making it challenging to determine a low frequency cutoff for defining the averaging window (as in Figure 1.6b). Separation of turbulent components is still a major challenge in such situations [21, 40]. Averaging operations and time scales are discussed further in Appendix A, Section A.3.

The averaging time discussed here corresponds to the lower bound of the flux-contributing frequency range. In previous studies, this lower bound has ranged from 0.5 Hz (coastal ocean) to 0.003 Hz (lakes). The upper bound, which imposes demands on the instrumentation's high-frequency capabilities (see Section 1.3.3 on sensor requirements for EC), has ranged from 1 Hz (coastal ocean) to 0.2 Hz (lakes) [21]. In a more extreme case, contributions from frequencies

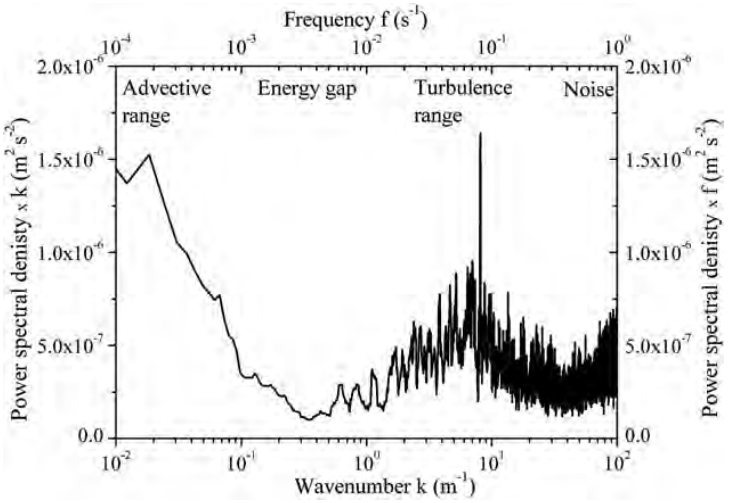

a) Power spectra of current (downstream) velocity showing a clear spectral gap between advective and turbulent components. Source: Lorrai et al. [21].

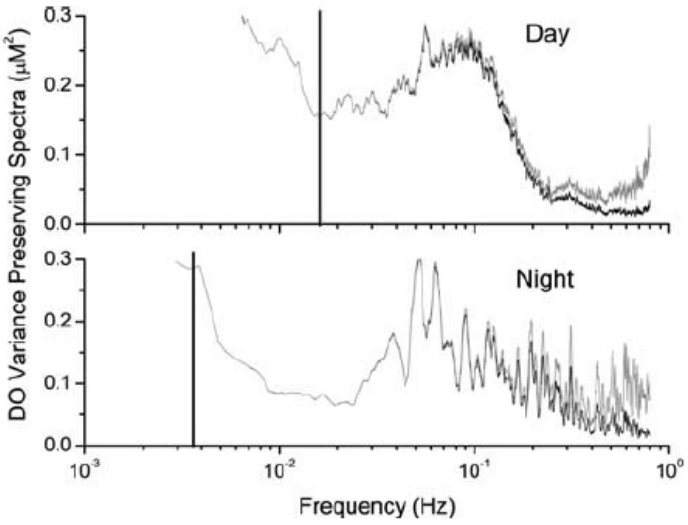

b) Power spectra of dissolved oxygen taken during an EC run; gray curve corresponds to DO data corrected for response time. Vertical lines represent estimates of the low-frequency cutoffs, consistent with the ogive plot, but no clear spectral gap is identifiable. Source: McGinnis et al. [40].

Figure 1.6: Variance-preserving spectra of different components of the EC measurement showing the spectral gap between advective and turbulent components.

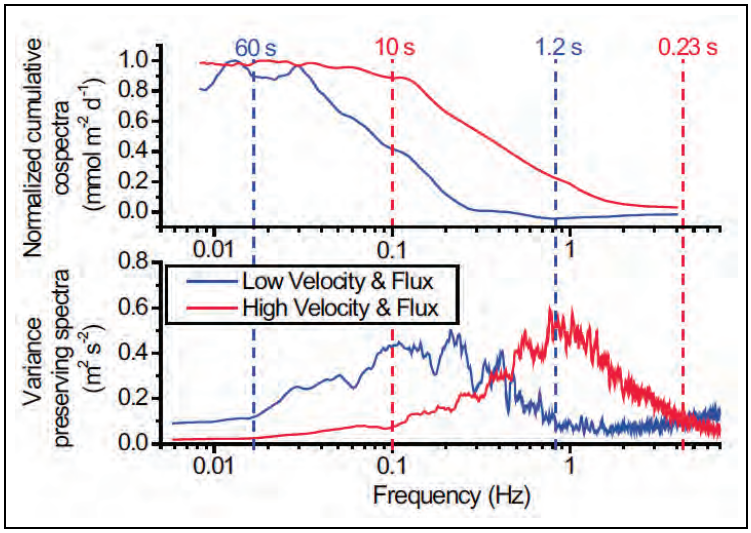

Figure 1.7: Ogive plot (top) and variance preserving spectra (bottom) for an EC deployment showing flux-contributing frequencies for low and high flux scenarios. The ogive plot, a cumulative cospectrum integrated from high to low frequency, plateaus past frequencies slower than the flux-contributing turbulent eddies. Source: McGinnis et al. [20].

as high as 4 Hz were found on a tidally driven continental shelf [10].

Flux calculations

Once the time series of w' and c' are determined in streamline coordinates, a flux for each averaging period T can be estimated by averaging the covariance ($w'c'$) over T. Alternatively, the flux for each period can also be derived by integrating the cospectrum of w' and c' for that period. The cospectra give the spectral contributions to flux; integrating over the cospectrum sums the contributions from all frequencies and is thus the vertical flux $\overline{w'c'}$.

The running integral of the cospectrum can be visually represented as the cumulative cospectrum (ogive plot, Figure 1.7), which gives the cumulative contribution of eddies from high to low frequency (short to long periods). The ogive plot should asymptote (converge) at low frequencies to the value of the flux, past the frequency where the corresponding time period is large enough to adequately sample the largest flux-carrying eddies [16, 21, 40, 42]. This is effectively saying that, at lower non-turbulent frequencies, the time series of velocity and concentration do not have statistically significant covariance (although their individual power spectra may carry components at those frequencies—those are the ones we want to take out with Reynolds' decomposition).

The period T of each flux estimate must also be chosen carefully. Note that this is not necessarily the same as the averaging time determined above for the Reynolds' decomposition, as discussed above; the running mean window size, for example, is often much shorter. T must be long enough for the covariance $w'c'$ to average over turbulence statistics. This is a longer time interval than is required for the averages of w and c individually, since the covariance has a higher relative scatter than the individual fluctuations w' and c' [21]. However, T must not be so long that it averages over lower-frequency trends in the flux[7]. Too short a T is equivalent to high pass filtering the measured flux signal, even if it is not used to define the coordinate rotation (as discussed by Finnigan et al. [45]); after all, the highest frequency that can be resolved at the flux level is $1/2T$, the Nyquist frequency given the measuring period.

[7]Note the distinction between lower-frequency fluctuations in w and c individually, which we went to great

An order-of-magnitude estimate of T based on existing EC data is provided by Lorrai et al. [21], who fit a histogram of instantaneous $w'c'$ values from an EC deployment to a Laplace distribution to extract the mean $\overline{w'c'}$ and variance σ^2. An 'adequate' number of samples N (which can be used to infer the necessary sampling duration as $N = f_s T$, where f_s is the sampling frequency) would reduce the error of the statistical average of $w'c'$ below some 'adequate' level of relative accuracy. For a target relative accuracy a, $N = \sigma^2 \big/ (a\overline{w'c'})^2$. In a sample deployment with DO sensors measuring at 1 Hz, an accuracy of $a = 20\%$ required a measurement duration of 1 h. An alternative measurement duration calculated as several times (5 to 10) the eddy scale for the environment was given as 15 min [21].

Some non-benthic aquatic EC studies, especially those in the open ocean where scales can be very large (e.g. eddies last several minutes [36]) and turbulence intermittent, have struggled with sampling a statistically significant number of eddies per flux period. These studies often utilized ensemble averaging over different runs and/or discarded large amounts of data [38, 39]; see Section 1.5.6 on aquatic EC studies for an expanded description. However, such techniques have not generally been employed in estimates of benthic flux.

1.4.4 Additional data processing corrections and checks

Time shift

A time shift is often applied to account for the chemical sensor response time (the DO sensors traditionally used have slower reaction time than than the velocimeters, so that a given concentration measurement is delayed relative to the corresponding velocity measurement) as well as the displacement between the two sensing volumes [40]. The expected temporal displacement of the two time series thus depends on the sensor response time as well as the travel time of the water parcel between the two sensing volumes, which in turn depends on the distance between the sensing volumes, flow velocity, and flow direction relative to instrument orientation [25].

Under unidirectional flow, the time shift can be calculated by shifting the concentration time series back in time relative to the velocity series[8] and calculating flux repeatedly for different time shifts, until the maximum correlation is observed between the two [40]. As current can vary over a deployment, the time shift correction may not be constant throughout the time series, and should be performed on segments with approximately steady conditions [21]. This procedure can substantially improve the precision of flux estimations, depending on the orientation of the chemical and velocity sensing volumes relative to the flow. However, in some situations—e.g. perpendicular orientations or larger spatial offsets, both of which have a higher probability that two sensors do not sample the same eddy structure—the time shift cannot fully compensate for the 'lost' flux. Donis et al. [25] found that if upstream, downstream and perpendicular orientations were equally considered, the time shift correction improved confidence and precision

lengths to remove in the Reynolds' averaging, and in the flux $\overline{w'c'}$, which we here want to preserve. Low-frequency variations in flux are certainly expected. If we maintain that turbulence is the dominant mode of transport in the water column [6, 7], then these lower-frequency fluctuations would manifest in an increased covariance of w' and c'. In contrast, the Reynolds' averaging discussed previously relates to extracting the w' and c' values in the first place.

of flux estimates in their laboratory setting by up to 30%.

For sites affected by wave motions, such as shallower sites with slower currents and surface gravity waves, a different time shift correction must be applied. The wave motions create an up and down motion of the natural concentration gradient (required for turbulent diffusion) that creates wave-frequency variations in concentration that are then correlated with velocity to produce a false flux. Using a model based on linear wave theory, Berg et al. [48] show that the time shift calculation described above can significantly overestimate flux or produce unreasonable fluxes (e.g. incorrect sign), and in fact produces the maximum time lag bias. They instead propose a time shift based on the instantaneous relative elevation of the water parcel $\tilde{z}$, found by integrating vertical velocity over time. For sediment consumption (positive concentration gradient where positive z is upward), if the sensing volumes are perfectly aligned then the measurement at a given point should give the lowest concentration when the wave displacement is highest (since the sensor is measuring the parcel that came from the lowest point that can reach it by wave motion). Thus, a time shift can be found, using a similar process as that for unidirectional flow, to produce this condition, i.e. the most negative cross-correlation between concentration and $\tilde{z}$. For sediment release, the correct time shift produces the most positive cross-correlation. This method requires a clear vertical gradient to be present, and a wave signal to be clearly identifiable.

Since horizontal wave velocity reverses direction with each wave cycle, the optimal time shift varies somewhat in time. Berg et al. [48] applied a single correction for each time interval, but note that this may be an oversimplification. An ideal time shift might include a constant component accounting for response time differences, and a smaller dynamic component of variable sign for the spatial separation which can then be determined from instantaneous velocities.

Frequency response correction

A frequency response correction can be applied to account for a slower sensor response time [21, 25]. The extent of the error depends on the speed of the sensor relative to the timescale of the turbulence, and is only of consequence at some sites (see Section 1.4.5 on site selection). In particular, sensor speed is problematic if the sampling rate is not at least twice the maximum frequency of the signal (order of magnitude values for frequencies are given in Table 1.1 on p. 39).

The attenuation of high-frequency contributions to the cospectrum can be given by the transfer function[9] [50]

$$T_{\mathrm{wc}} = \frac{(1+\omega^2\tau_{\mathrm{w}}\tau_{\mathrm{c}}) + \omega(\tau_{\mathrm{w}}-\tau_{\mathrm{c}})Q/Co}{(1+\omega^2\tau_{\mathrm{w}}^2)(1+\omega^2\tau_{\mathrm{c}}^2)} \tag{1.9}$$

[8] Perhaps up to a maximum of e.g. 4 s [25]. In general, the time shifts applied in EC studies have ranged from fractions of seconds to a few seconds.

[9] In atmospheric eddy correlation, the transfer function is used to estimate covariance attenuation by multiplying it with known empirical formulas for the cospectral distribution of turbulence covariance $Co_{\mathrm{wc}}(\omega)$ and integrating over frequency [21, 50]. This is possible because 'standard spectra' (empirical cospectra) exist for atmospheric fluxes, although their applicability in all scenarios is questionable [16]. Some EC studies in the water column have also compared to these 'standard spectra', but only as a basis for comparison [38].

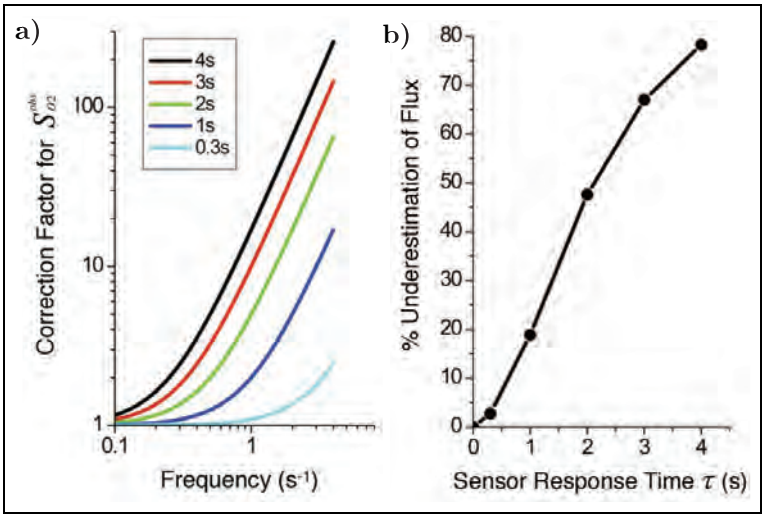

Figure 1.8
a) Frequency correction factor $1/1+(2\pi f\tau_c)^2$ for concentration sensors of different response times (τ_c) **b)** Underestimation of flux as a function of sensor response time, obtained by multiplying model-derived O_2 spectra with the appropriate correction factor. Based on experimental data from a racetrack flume with 7.4 m/s flow.
Source: Donis et al. [25].

where ω is the wavenumber ($\omega = 2\pi f$, where f is the frequency), τ_w and τ_c are the $1/e$ response times of the velocity and scalar measurement devices, Co is the covariance spectrum, and Q is the quadrature spectrum. For the case of a fast velocity sensor, $\tau_w \approx 0$ [21], and the quadrature spectrum of two collocated variables is commonly assumed to be negligible [50], so that the attenuation transfer function simplifies to

$$T_{wc}(\omega) = \frac{1}{1+\omega^2\tau_c^2}$$

The corrected cospectrum $C_{wc}^{corr}(\omega)$ can be found by using the inverse of the transfer function to enhance the measured cospectrum C_{wc}^{obs} as [25]

$$C_{wc}^{corr}(\omega) = (1+(\omega\tau_c)^2)C_{wc}^{obs} \tag{1.10}$$

The spectral corrections can be quite substantial when high frequency contributions are sampled with slower sensors, as shown in Figure 1.8. Donis et al. [25] found that a 3 s response time DO sensor underestimated flux by 67 % under 7.4 cm/s flow conditions. However, the frequency correction factor also amplifies high-frequency noise, and thus is sensitive to the high-frequency limit and can introduce artifacts if too amply applied.

1.4.5 Deployment site choice, planning and site-specific considerations

The quality of eddy correlation results is highly impacted by the characteristics of the deployment site and the suitability of the instrumentation for that site. Certain site characteristics require special care in interpreting results, and at some sites, eddy correlation is simply not possible.

The field site should have **turbulence characteristics** appropriate for the sensors. The turbulence determines the size and time scale of the eddies, and therefore the **size and speed requirements** of the instrumentation. At higher velocities, sensor response time can become

limiting, resulting in a loss of high frequency contributions. The extent of this error depends on the speed of the sensor relative to the speed of the turbulent processes; at manageable levels, it can be corrected with a frequency correction factor (described in the 'Additional corrections' subsection of Section 1.4.3). Based on laboratory tests and models, Donis et al. [25] recommend that, with the current recommended τ_{90} sensor response time of 0.2 s, flows higher than 20 cm/s should be avoided.

Sites with **low velocities, low particle counts, or low scalar measurements**, such as deep sea sites, stretch the **detection limits (sensitivity)** of the velocity or concentration sensors and can produce noisy or unreliable data [28, 29]. At the other limit, **biofouling** at more eutrophic sites can limit sensor functionality [12]. **Floating debris** can also interfere with measurements especially at sites with higher water velocities [7, 33]. Sites should be chosen with appropriate velocity and concentration characteristics for the sensors used.

Changing current directions pose an issue because they complicate the determination of an 'optimal' orientation of the sensors. Under unidirectional current, it is often possible to position the sensors to minimize physical interference with the flow (e.g. concentration sensor downstream of the sensing volume). In addition, the sensors can be positioned such that they are more likely to sample the same eddies; as discussed by Donis et al. [25], when the position of the velocity and concentration sensing volumes relative to each other is perpendicular to the current (as opposed to upstream or downstream), the correlation decreases and the resulting loss in measured flux cannot be fully corrected by a time shift. Fixing the orientation is not possible at sites with changing current direction, so these sites should be avoided if the two sensing volumes cannot be positioned close enough to obtain reliable fluxes (e.g. $<$1 cm separation).

Sites with more **complex flow conditions or complex topography** present several challenges. In the control volume derivation to arrive at Eq. (1.5), several rather restrictive assumptions about the flow field were made. The main assumptions relate to stationarity in time and homogeneity in space, including zero horizontal flux divergence ($\partial\overline{uc}/\partial x + \partial\overline{vc}/\partial y = 0$) and homogeneity of the source / sink within the EC footprint (see Appendix A for more details on the derivation). Conditions that deviate too far from these assumptions complicate data analysis and interpretation. For example, without **well-developed turbulence**, the separation between turbulent and advective components may not be clear, complicating the mean removal operation [40] and possibly allowing the calculated flux to be biased by deterministic components (as described in Appendix A, Section A.3 on the mean removal / averaging operation).

Highly dynamic systems, such as coastal systems, are particularly difficult. As discussed by Holtappels et al. [51], **transient processes (e.g. transient concentrations or velocities)** can add to the turbulent flux at h, creating an 'artificial' contribution to the measured flux that is not part of the target sediment uptake / release. In essence, the artificial flux arises from these processes occurring in the water column between the sediment and h. One such process relates to transient concentrations arising from the movement of water masses with different origins and therefore different solute concentration. These water masses do not move with uniform velocity, as the no-slip boundary results in smaller velocities closer to the sediment bed. Since these water masses carry a different concentration from the surrounding water, this differential advection results in a vertical concentration gradient, and thus a vertical flux. Separately, changing water

velocities can also cause an apparent flux through their effect on the turbulent diffusivity. The turbulent diffusivity depends on flow velocity and in turn defines the concentration profile of the solute. Thus, when current velocities change, so does the concentration profile; as the concentration profile transitions to its new steady state, a transient flux arises that is measured at h. Even moderate transients in concentration and velocity were estimated to cause the measured fluxes to deviate by up to 100 %

Deployments at sites with such transients should take special care. Careful analysis of the velocity and concentration time series to resolve their rate of change can help estimate the extent of such affects. Additional concentration, temperature and salinity sensors on the EC system can also provide an independent measurement to detect water masses of different origin [51]. In a study of the Oregon continental shelf, for example, significant correlation between the measured flux and the O_2 rate of change was used to infer the presence of differential advection and the mixing of different water masses [49]. Measuring the concentration gradient below the EC sampling volume can also help to monitor stationarity [42].

Longer deployments are also recommended for such dynamic systems [18]. Sampling periods should be multiples of the largest time scale [42], and longer sampling periods and/or deployments can allow low frequency components to average out to zero [35] or transient effects to average out to a more reliable mean flux [51]. In addition, long observations covering all possible directions of the mean flow field are required for the planar fit coordinate rotation, which has proven most successful so far for complex flow and complex topography [42]. However, the deployment time is also limited by other factors, such as biofouling [12] and battery life.

Sites with **waves** require some extra care in EC deployment, data processing, and interpretation. For example, a small instrument tilt can be a big problem when waves are present, because wave velocities are much more energetic than turbulence; any contamination by wave components can mask the actual turbulent flux (termed 'wave bias' and described in greater detail in Appendix A, Section A.4) [37]. Over a flat bed, these wave components can be removed by rotating coordinates based on the ADV's internal compass and tilt meter [44]. However, as discussed in Section 1.4.3 on EC data processing and in greater detail in Appendix A, Section A.2 on coordinate rotation for EC, rotating to a 'true vertical' as identified by the ADV is often insufficient. An alternative coordinate rotation method that minimizes wave bias has also been used, and has been shown to result in satisfactory leveling error [30, 35].

Waves also create complications in the calculation of the time shift (used to compensate for offsets in sensing volume and sensor response time). The traditional time shift calculation can result in significant error in the calculated flux, but an alternative time shift algorithm has been proposed that can be applied in certain circumstances [48] (described in the 'Time shift' subsection of Section 1.4.4). Another effect of waves, specific to O_2 concentration fluxes measured with DO microelectrodes, is the complication of the 'velocity effect' arising from the stirring sensitivity of the microelectrodes (described in further detail in Section 1.5.3 on studies of EC accuracy). Given the changing velocities and periodicity of waves, the stirring sensitivity can result in an artificial concentration signal out of phase with velocity. This effect can be reduced by measuring closer to the sediment (where wave-driven variations in w are reduced relative to u), and in settings with smaller ambient O_2 concentration (as the velocity effect scales with concentration) [30].

It should be noted that EC in the benthic boundary layer can be affected by both surface

gravity waves and internal waves. Surface waves have periods on the order of 5 s to 20 s (0.2 Hz to 0.05 Hz), while internal waves have periods on the order of a few minutes to tens of minutes (e.g. showing up in one study as a 'hump' in the spectra <0.002 Hz (>8.3 min)) [37]. The flux components they create at these frequencies (through mechanisms such as those described above) can thus overlap with flux-carrying frequencies, making them difficult to identify and disentangle. It is also difficult to separate artificial contributions and real flux, since flux may be facilitated by wave motion and thus occur at the wave frequency [30, 48]. Internal waves have the additional complication of having time scales on the order of EC flux measurements, potentially creating non-stationary transient advective events and/or flux divergence (see Appendix A, Section A.3 on mean removal operations for a greater discussion on how these violations of EC assumptions are considered). They are also geographically and temporally variable, nonlinear, and intermittent, further violating the assumption of stationarity of statistical variables within each burst [35, 37]. In general, deploying in deeper water can reduce the impact of wave action—for example, in a deployment 80 m to 85 m deep, surface waves shorter than ∼10 s could not be observed because of depth attenuation [35]. Sampling height can also affect the wave influence, as higher sampling heights experience stronger vertical wave components (e.g. $h = 30$ cm vs 15 cm) [30].

Measurements over a **heterogeneous sediment bed** run the risk of inadequate spatial averaging (to a value representative of the footprint), if turbulent horizontal mixing is incomplete at the measurement height h. This can be solved by placing the sampling volume at an adequate height over the sediment given the surface roughness of the sediment z_0 and the patch size of the heterogeneities X. Using a numerical model, Rheuban and Berg [19] presented empirical formulas for the necessary threshold heights to achieve horizontal variation in flux of less than 5 %, 10 %, and 20 % as

$$\begin{aligned} h_5 &= 2.01X^{0.534}z_0^{0.430} + 0.0840X - 0.903 \\ h_{10} &= 1.80X^{0.505}z_0^{0.458} + 0.0634X - 0.702 \\ h_{20} &= 1.54X^{0.478}z_0^{0.487} + 0.0440X - 0.516 \end{aligned} \quad (1.11)$$

However, although a higher measuring height allows greater horizontal mixing, it also increases the time delay between a change in flux at the sediment surface and the detection of the change at h. Based on the same model, an empirical relationship for the t_{90} response time (when 90 % of a change in flux is realized at h) was given as

$$\log t_{90} = 2.87 - 1.22(0.92^h) - \log u_* \quad (1.12)$$

where the friction velocity u_* combines the effect of z_0 and the average velocity at h, $\overline{u}$, as

$$u_* = \frac{\overline{u}\kappa}{\ln \frac{h}{z_0}} \quad (1.13)$$

where κ is the von Karmann constant [19].

This delay can complicate studies seeking to analyze the response of flux to fast-changing physical drivers in dynamic systems. It is particularly troublesome for interpreting dynamic fluxes if t_{90} is longer than the length of the burst (commonly 10 to 20 min), which is more likely in conditions of smooth sediments, low flows, and large measuring heights.

The choice of measuring height thus represents a tradeoff between spatial averaging and time response, depending on the characteristics of the site and study (e.g. size of heterogeneities, surface roughness, extent to which dynamic responses rather than long-scale time averages are desired, etc). However, other factors also limit the range of viable measuring heights. For example, for some given amount of flux, concentration gradients are stronger near the sediment (while eddies are smaller), allowing larger concentration fluctuations that are easier to detect [21]. In the limit, high above the sediment floor the gradient may be too weak for detectable fluxes, especially at sites with smaller fluxes. In addition, as discussed above, higher measuring heights can exacerbate the error caused by transient concentration or velocity fields [51], and increase the influence of waves [30].

On the other hand, measurements too close to the sediment floor can be infeasible due to limitations from the ADV measuring velocity, as reflections and reverberations from boundaries can create interference between the acoustic pulses used in the measurements. One or two 'weak spots' exist (relative to the sampling volume) where the presence of boundaries cause unreliability in the velocity measurements (see Section 1.8.4 on ADV weak spots), and measurement heights around these values should be avoided. Since this effect depends on the spacing between the pulses, the locations of the weak spots depend on the expected velocity range set for the instrument, which in turn depends on field conditions [52]. Measurements in the near-bed zone are also subject to ripple-flow interactions, which increase the level of turbulence [30].

The measuring height also affects the size of the footprint, which can be important depending on the goals of the study. Finally, the measuring height may not be clearly defined if the sediment height changes due to sediment resuspension, migration, or other events [49], and ripples or other bedforms on the sediment floor (or surface waves that act similarly) can create a flow-dependent hydraulic roughness [20]. Typical measuring heights in studies thus far have ranged from 8 to 80 cm [19].

For pilot studies, it can be easier to just avoid sites with spatial variations in the flow field or sediment uptake / release rate within the footprint, as suggested by Lorke, McGinnis, and Maeck [42]. In general, characteristics of 'easier' sites would include

- Unidirectional current flow with minimal change in speed or direction, little wave action, and well-developed turbulence
- Flat topography, no ripples, and homogeneous source/sink on the sediment bed
- Sufficient velocities, particles, concentration, and flux for sensors to measure, but not so much as to impede sensor functionality
- Eddy time scales within capability of sensor response times and achievable distance between the two sensors

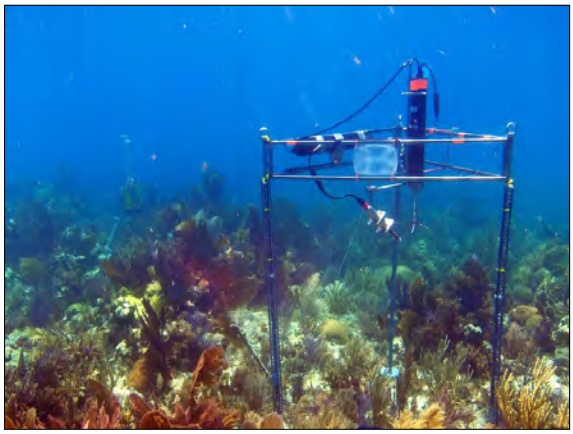

Figure 1.9: Eddy correlation deployment on a coral reef, using dissolved oxygen sensors. Credit: Jennie Rheuban and Matthew Long.

1.5 Current state of aquatic eddy correlation research

1.5.1 EC studies of benthic fluxes of dissolved oxygen

To date, the majority of EC studies at the sediment-water interface has focused on benthic fluxes of dissolved oxygen (DO), which are widely used as a proxy for mineralization [11, 33]. The concept of using EC with a DO microelectrode was first introduced by Berg et al. [4] in 2003. The technique has by now been used quite successfully to estimate benthic fluxes of DO in a wide variety of freshwater and marine settings, such as rivers [9, 20] (including an impounded river [53] and a smaller, second-order stream [7]), lakes [54], estuaries [9, 12], sea lochs [11, 33], Continental shelves [10, 35, 49], and deep ocean [27, 28]. It has also been used on a variety of sediments, such as muddy (cohesive) sediments [27, 31], permeable sediments [9, 10, 12, 31, 55], and even hard bottom substrates, where cores and chambers cannot be deployed at all [18]. It has proven useful for studying benthic ecosystems such as seagrass meadows [55], coral reefs [56], oyster beds [57], and live corraline algal beds [11], and has even been used in several novel deployments, including sideways deployment on a vertical cliff [18].

Eddy correlation can capture variabilities in benthic flux that are not captured by chamber or cores, allowing studies of the effect of local hydrodynamics on flux [9, 55]. For instance, EC measurements on permeable sediments, which are particularly troublesome for cores and chambers, have revealed a significant link between oxygen flux and current velocity [11, 33] and provided insight into the dynamics of sediment flushing and hyporheic exchange [7]. EC-measured fluxes have also been used with a diffusion-based box model model to provide insight into the dynamics of local, small-scale porewater advection in permeable sediments, and the mechanism by which turbulence dynamics drive flux variability [10]. In essence, as a result of its noninvasive property and spatial and temporal resolution, the eddy correlation technique has enabled studies of relationships between benthic oxygen fluxes and their controls that could not be revealed by other flux methods [5].

It is also worth noting that EC studies of dissolved oxygen are not constrained to the benthos. In fact, prior to its use in measuring benthic fluxes, EC had already been used in other aquatic settings, such as under Arctic sea ice [e.g. 36, 58] or in the main thermocline of the ocean [39]; see Section 1.5.6 for a greater description of aquatic EC beyond the sediment-water interface. More recently, researchers have begun to measure DO fluxes in some of these contexts as well,

enabled by the technology and methods developed for benthic flux measurement. For example, Long et al. [59] measured oxygen exchange and ice melt at the ice-water interface by deploying oxygen microelectrodes and temperature sensors alongside ADVs through holes in the sea ice. Oxygen flux measurements in the water column of lakes have also been made using systems mounted on tensioned mooring lines attached to subsurface floats; Kreling et al. [60] used such instrumentation to study oxygen fluxes at the pelagic and benthic oxyclines, while Weck and Lorke [29] measured oxygen alongside buoyancy (temperature) to study of mixing efficiencies in the thermocline.

An even newer development is the application of dissolved oxygen EC at the air-water interface to measure surface gas exchange (and, by extension, the gas transfer velocity). Air-water gas exchange is a key parameter in assessing ecosystems and biogeochemical cycles, but is highly complex and difficult to quantify. Both Berg and Pace [61] and Long and Nicholson [8] deployed underwater EC instrumentation from floating platforms to quantify the oxygen flux at the water surface, resulting in exchange measurements at a high frequency (hourly) that allowed the process to be examined with a level of detail that was previously not possible.

1.5.2 Validation of EC measurements in the field

Eddy correlation systems at the sediment-water interface are most commonly deployed alongside benthic chambers for comparison. Attard et al. [11] compiled a list of several dissolved oxygen EC studies that co-deployed and compared the two methods. In general, the two techniques have provided similar estimates for cohesive sediments that lack large macrofaunal species. However, for permeable sediments under dynamic flow conditions, the discrepancy between the two methods was larger and also more variable (EC-to-chamber ratios ranged from 0.5 to 4.1). This finding is often attributed to the inability of benthic chambers to recreate and/or capture turbulent dynamics and interactions in the benthic boundary layer, and any subsequent advective flux to or from the sediment. In support, EC-determined flux has been observed to increase with an increase in current velocity, which has been linked to a current-stimulated respiration and/or a more intense pumping / flushing / venting of oxygen deeper into the sediment [9, 10] that would be difficult for chambers to capture. However, some studies saw only variable contributions at wave frequencies (often linked to increased current velocities), indicating a possible inconsistency in effect or influence of other motions [49]. Some of the discrepancies between EC and benthic chamber flux estimates have also since been reduced as the eddy correlation technique is further refined and its limitations are better understood, e.g. with respect to the proper time shift for situations with wave motions [48] or asymmetric effects of water velocity on microelectrode measurements [30].

Attard et al. [11] also deployed a large number of benthic chambers (26 in total) alongside EC systems in a Scottish sea loch. They found a large variability between individual chambers–attributed to spatial heterogeneity–but generally good agreement between the mean chamber-measured flux and the EC-measured fluxes (average EC-to-chamber ratios of 0.8 ± 0.2 on a maerl bed and 1.2 ± 0.2 on sandy sediment). These findings provide confidence in the ability of EC to estimate benthic fluxes, as well as to integrate spatial heterogeneity, at least under the conditions of their deployment.

EC measurements have also been compared to sediment core incubations [4, 18] and diffusion

calculations from sediment microprofiles [9, 18, 27, 28, 35, 49]. However, as discussed in Section 1.2.2 on traditional methods of benthic flux measurement, these methods have their own sources of uncertainty. In addition, they cover different spatial and temporal resolutions, so that differences between the techniques can be expected. Microprofile estimates, for instance, are point measurements and can only capture diffusive flux; in fact, the difference between flux estimates from EC and from microprofiles has been used to estimate non-diffusive exchanges, such as fauna mediated uptake [18, 33]. Non-diffusive exchange can also arise from advective porewater transport in permeable sediments, and differences between EC-measured and microprofile-measured flux of up to 10 times are not uncommon [49]

Similarly, Koopmans and Berg [7] compared EC measurements to flux estimates from the open water technique, which covers a much larger footprint (in their study, 500 m versus eddy correlation's 10 m long ellipse). They found substantial differences in oxygen uptake, which they attributed to an influx of anoxic groundwater from stream banks. Again, the two techniques were used in a complementary manner to provide more information about the system.

Thus, not only do these 'traditional' methods of benthic flux measurements have their own limitations [4, 5], but oftentimes they are expected to be different, as they capture different scales and mechanisms than EC. Deployment alongside one of these methods can sense check the EC values, but it still does not necessarily confirm or refute EC measurements. As stated by Holtappels et al. [51], "so far, robust criteria to validate [EC] fluxes are missing." Consequently, many researchers have turned to a more bottom-up approach, by seeking to identify and quantify errors so that they can be addressed and/or processed out to get higher accuracy flux data.

1.5.3 Studies concerning the accuracy of benthic EC measurements

As eddy correlation becomes a more commonly used technique for determining benthic fluxes in aquatic systems, it has also become the subject of a growing body of literature on its accuracy and applicability in a variety of conditions. Errors that affect the quality of the measurements generally result from 1) sensor limitations, or 2) deviations from the assumptions about hydrodynamic settings that are embodied in the data analysis techniques [45]. Several recent papers have attempted to identify and quantify errors relating to both of these issues from a variety of angles and using a variety of techniques, including laboratory tests in flumes of various sizes [25, 30, 62] and three-dimensional numerical simulations [17, 19]. These studies often result in practical guidelines for EC deployment and data analysis, which are summarized in Section 1.4.5 on site selection and site-specific considerations.

Several studies relate to **sensor limitations**. In a study involving a large racetrack flume, Donis et al. [25] studied errors arising from sensor displacement and response times. Eddy correlation requires that velocity and concentration be measured instantaneously and at the same point, which in practice is impossible (at least with current instrumentation). However, the flux error caused by these non-idealities can be reduced by judicious sensor placement, depending on deployment site, as well as proper application of correction procedures (time shift and frequency correction).

The accuracy of velocity measurements can also be of concern. In a flume experiment, Reimers et al. [30] found that the Vector ADV (which is also used in this project) underevaluated the flow characteristics compared to nearby Vectrinos, a laboratory model from the same vendor.

This effect may also have been related to sensing volume interference and/or may be specific to the setting used (energetic wave motions).

Similarly, studies of sensor limitations are often specific to the chemical sensor used. For example, Holtappels et al. [62] and Reimers et al. [30] discuss the so-called 'velocity effect', which is relevant specifically to the Clark-type microelectrodes commonly used for EC measurements of dissolved oxygen. The diffusion/consumption-based mechanism of these microelectrodes sets up a spherical boundary layer surrounding the tip, so that the sensor's response depends on the current velocity (which changes the thickness of the diffusive boundary layer) in a manner that is nonlinear and asymmetric with respect to both flow speed and direction. The microelectrodes' 'stirring sensitivity' (a parameter which captures the change in signal strength resulting from changes in flow) is an inherent and fundamental sensor design tradeoff with response time. It is thus, to some extent, unavoidable when microelectrodes are used for eddy correlation. Models have been developed that estimate the artificial flux arising from this effect [30, 62], and have been applied to estimate artificial flux in some EC studies [11].

In a study of oxygen fluxes in a wave flume, Reimers et al. [30] found that two different microelectrodes produced highly variable velocity effects and a broad range of flux estimates that differed from each other, and in sign and order of magnitude from concurrent estimates made with sediment cores and microprofiles. Two models to predict the velocity effect-induced artificial flux were tested, but neither was found to produce adequate results, with various potential explanations for the discrepancy. To date, this study is the only we know of that has compared EC measurements to other concurrent measurements in a laboratory (flume) setting; the lack of agreement and obvious explanation may be specific, however, to the wave setting, under which velocity effects can combine with other effects (e.g. wave bias from tilt, time lag errors) to further complicate results.

Errors arising from failures to meet the **hydrodynamic criteria** for EC have also been the focus of several recent studies. As eddy correlation becomes more widely deployed, it is applied now to sites that are more challenging, with complex flow and terrain, in which data processing and interpretation are not straightforward [35].

One troublesome assumption is that the measuring height is sufficient to average out spatial heterogeneities in the flux footprint. As the contributions to flux are unevenly distributed within the footprint area, heterogeneities on the sediment floor can affect results even if they seem smaller than the 90 % footprint [19]. Especially in environments where flow direction and velocity change regularly, the variable footprint could cause significant variability in flux by picking up different patches of a heterogeneous sediment floor [18]. Using a three-dimensional numerical model, Rheuban and Berg [19] studied the measuring heights necessary to reduce the effect of such heterogeneities on flux results. They also studied the effect of the measuring height on the time lag before changes in flux at the sediment surface are realized at h, which can complicate interpretations of dynamic fluxes. Depending on the site, the measuring height should be chosen strategically. Several guidelines for selection of measuring height are given in Section 1.4.5.

In general, fluxes measured at h could fail to represent the target benthic fluxes at the sediment bed for a number of reasons. Not only can there be incomplete turbulent mixing, but the measurements could also be influenced by transport and other processes between the sediment floor and the measuring height, such as temporary horizontal inhomogeneous flow fields[10].

Holtappels et al. [51] studied the effects of transient unidealities, such as transient concentrations or water velocities. In dynamic environments where such phenomenon are expected (e.g. coastal environments), careful analysis of the rate of change of the velocity and concentration time series can indicate if such processes are occurring.

Finally, in situations with complex hydrodynamics, coordinate transformation to put velocity measurements into streamline coordinates is extremely important; however, incorrect rotation can introduce significant errors. Lorke, McGinnis, and Maeck [42] examined this issue in a study of an impounded river with a sloped bottom and highly variable man-made flow conditions. In those conditions, they found the flux results to be significantly dependent on coordinate rotation procedure and averaging time; see the 'Coordinate rotation' subsection of 1.4.3 for more information.

1.5.4 Expansion to other sensors

In EC studies, water velocity is typically measured by an Acoustic Doppler Velocimeter (ADV), whereas the concentration sensor used depends on the solute of interest. As described above, most eddy correlation studies of benthic fluxes to date have focused on DO fluxes, measuring concentration with a fast Clark-type microelectrode oxygen sensor (Figure 1.10a). Alternate oxygen sensors for DO fluxes are also now gaining popularity, often inspired by shortcomings of the traditional microelectrodes. For example, the fragility of the microelectrodes was a limiting factor in several studies [e.g. 18, 49]; McGinnis et al. [20] recommended deploying two sensors to improve robustness to debris and breakage, but some researchers have now turned to new O_2 sensors to replace the microelectrodes. Fiber-optic based oxygen optodes tipped with an oxygen-quenchable fluorophore have been used in some studies [12, 32], and an oxygen probe based on fluorescence lifetime measurements was also specifically developed as a more robust alternative to microelectrodes (Figure 1.10b) [5]. These alternate sensors often presented tradeoffs, e.g. robustness in exchange for a larger sensor tip and slower response time, which preclude their use in some hydrodynamic settings [5].

As discussed in Section 1.3.3 on the requirements of an EC sensor, EC can in principle be used to measure the flux of any substance, as long as a suitable chemical sensor exists for that substance. Temperature has now been measured in several aquatic EC studies, as thermistors exist that are small and fast enough for eddy correlation. Crusius et al. [6] used conductivity and temperature sensors to study submarine groundwater discharge, although the conductivity sensors were largely damaged during deployment. Long et al. [59] used conductivity, temperature, and DO sensors to examine fluxes across the ice-water interface, although again the conductivity sensor was damaged. In a stud of the thermocline of a lake, Weck and Lorke [29] deployed a temperature sensor alongside an oxygen sensor, extrapolating to buoyancy fluxes by using the temperature to calculate density. Berg et al. [5] also included a temperature sensor alongside their new oxygen probe, which was subsequently used in EC measurements at the air-water interface to quantify heat fluxes [61]. In fact, at the air-water interface, temperature variations (and the vertical turbulent heat flux) proved large enough to affect the readings of the oxygen

[10] Horizontally inhomogeneous flow can be coupled with vertical advection events, as described in Appendix A, Section A.3 on low-frequency components and mean removal operations. The vertical advection is ideally handled by the mean removal process, but the transients can also result in a turbulent flux at h that is not associated with sediment fluxes.

a) DO microelectrode mounted in EC system. Credit: Dirk Koopmans

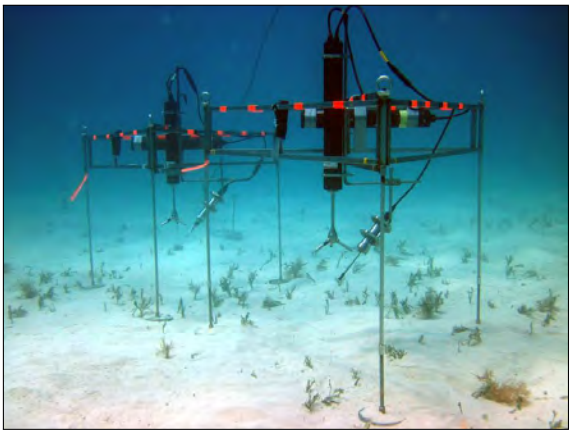

b) Robust oxygen sensor (foreground) and microelectrode (background) used in EC measurements. Credit: Markus Huettel

Figure 1.10: Concentration sensors currently used in eddy correlation systems.

sensor (temperature coefficient ∼3 %), and could bias the oxygen flux measurements by up to a factor of 3. It was therefore necessary to correct the oxygen readings using the temperature measurements.

Expansion to other compounds has been further enabled by innovations in sensor technology. McGinnis et al. [20] developed a low-noise, galvanically isolated picoamplifier with several features that made it especially suitable for use with microelectrodes in eddy correlation studies. They used it to not only with DO microelectrodes, but also with bisulfide microelectrodes to measure fluxes of H_2S in the anoxic waters of the Baltic Sea. Johnson et al. [31] used an In Situ Ultraviolet Spectrophotometer (ISUS) outfitted with a 1 cm optical probe (consisting of optical fibers in epoxy) to measure nitrate fluxes on an open continental shelf. To maintain a sampling rate of 1.8 Hz, UV spectra were stored and processed on shore; these measurements were synched with the velocity measurements by a periodic 5 V signal sent from the spectrophotometer to the ADV. Long et al. [12] used a fast H^+ Ion-Selective Field Effect Transistor (ISFET) to measure pH fluxes in a eutrophic estuary. The flat, light-sensitive sensor was contained in a flow-through pump-driven microcell made of 19 gauge stainless steel tubing, which was then coupled to an EC system that also had a dissolved oxygen sensor. By extrapolating through carbonate equilibria relationships, the pH and DO fluxes were used together to study carbon cycling and calcification. Finally, Swett [63] used an open-cell, single-channel Colored Dissolved Organic Material (CDOM) fluorescence probe to examine fluxes of dissolved organic material at several intertidal mudflats and a wetland.

Several of these eddy correlation sensors were deployed alongside other measurements of benthic flux, such as benthic chambers [12, 31] and porewater measurements, from which diffusion rates could be estimated [63]. These alternate techniques produced values that ranged from similar to EC fluxes to orders of magnitude different. Differences were indeed expected due to the failure of benthic chambers to capture flushing on permeable sediments, and the inability of the gradient method to include non-diffusive sources of flux, so the accuracy of these measurements could not be confirmed or refuted.

In a new development to the field, a slightly different approach has also been proposed for measuring eddy fluxes of compounds for which EC-suitable sensors do not exist. Lemaire, Noss, and Lorke [64] explored the idea of using the relaxed eddy accumulation (REA) technique, which, like EC, is borrowed from the field of micrometerology. REA is similar to EC except that fast concentration measurements are replaced by conditional sampling; velocity measurements are used to sort samples (via valves) into 'updraft' and 'downdraft' sample containers. After accumulation for periods of typically 0.5 h to 1 h, the samples can be analyzed using slower instrumentation or laboratory techniques, and their difference used to infer flux estimates. Using previous EC data of oxygen, temperature, and suspended particles (inferred from the backscattering strength of the ADV signal) to simulate REA measurements, the authors of this study concluded that REA is a promising technique for determining fluxes of difficult-to-measure solutes such as pollutants and nutrients, provided that several technical challenges can be overcome.

1.5.5 This sensor

The sensor developed for this project is an optical fiber spectrofluorometer with a built-in conductivity cell and fast, miniature thermistor. This project focused on benthic fluxes of fluorescent dissolved organic material (FDOM), which is present in many natural waters and typically provides a strong, broad signal. However, the instrument is readily extendable to directly measure other naturally fluorescing substances through adjustments or additions of excitation or detected emission wavelengths. In fact, it is possible that EC can provide useful measurements not only of dissolved fluxes, but also of algal or bacterial cells that are in the process of settling or being resuspended (algal cells fluoresce in the red region when excited by blue light, and bacterial density can potentially be estimated by thymidine fluorescence under deep UV excitation).

This functionality is a key difference from other optical devices that have been used in EC applications, such as the commercially available CDOM fluorometer used by Swett [63]. It not only enables fine-tuning for different compositions of FDOM in natural waters, as well as measurement of a wider range of analytes, but can also improve specificity with regard to individual categories of substances. For example, fluorescence data of FDOM at different excitation/emission pairs contains information regarding not only concentration but also age, nature, composition, and geochemical or anthropogenic origin of the organic material [65].

In addition to the fluorescence sensor, the trimodal sensor also includes a thermistor and conductivity cell that roughly meet the speed and resolution requirements for eddy correlation. As described above, temperature and conductivity have been measured in eddy correlation systems to quantify heat and salinity fluxes, which can then be used to infer submarine groundwater discharge [6]. The sensor developed here is unique in that the sensing volumes of the three sensors are nearly collocated. Thus, the sensor could potentially be used to measure three co-located fluxes, e.g. where submarine groundwater discharge is carrying a flux of dissolved organic material into a body of water of different salinity and temperature. Correlation between the three components, similar to the tracking Long et al. [12] found with pH and oxygen, can be used to sense check the instrument.

1.5.6 Aquatic eddy correlation beyond the sediment-water interface

This section provides a summary of EC studies in aquatic settings for measurements other than sediment-water fluxes. In many cases, they are not directly relevant to benthic flux studies. However, they can still offer some generally helpful insight and inspiration. In addition, they are becoming more relevant as techniques developed for benthic flux measurements (e.g. the measurement of dissolved oxygen) are increasingly applied to other aquatic settings.

Overview

As early as 1978, Partch and Smith [66] used eddy correlation to measure vertical turbulent fluxes of salinity, in order to study turbulent mixing through the density interface of a salt wedge estuary. More generally, EC has been used to study turbulent mixing processes in the open ocean (allowing, for example, better predictions of vertical fluxes of mass, heat, and nutrients [67]). One technique for open-ocean EC involves horizontal tows, which result in flux measurements (e.g. of density, for calculating mixing efficiency) at a single depth over a horizontal extent [38]. The average is over a spatial extent, rather than over time at a single point, as with benthic flux measurements. Horizontal tows are analogous to flights through the atmospheric boundary layer with a rack of probes mounted to an aircraft [67]. EC over a vertical spatial gradient (e.g. using a vertical profiler dropped over the side of a boat) have also been used, for example to study buoyancy fluxes in the main thermocline of the ocean, where turbulent patches are too sparse for a horizontal tow to sample [39].

Further down the water column, Shaw and Trowbridge [37] used EC in the bottom boundary layer to measure the vertical transport of heat and horizontal momentum[11], in order to study the dynamics of turbulent mixing driven by bottom drag. Similar to benthic flux measurements, benthic tripods were deployed on a seafloor; however, no concentration measurements were made, and the heat flux did not correspond to heat released from the benthos (e.g. due to submarine groundwater discharge). Instead, the temperature fluctuations were produced by surface waves in the presence of stable near-bottom stratification from a hurricane[12], and the focus was on the dynamics of the turbulence [37].

EC has also been used to study heat and momentum flux under sea ice in the Arctic, where it can be suspended through holes in the ice, sometimes with multiple clusters on a single line for a series of flux measurements at different depths. These studies often aim to better quantify and understand heat and mass transfer, as well as the mechanisms of turbulence, in the rotational boundary layer[13] [e.g. 26, 36, 58].

[11] Heat flux is obtained from the correlation of vertical velocity and temperature ($\overline{w'T'}$), while momentum flux is obtained from the correlation of horizontal and vertical velocity ($\overline{u'w'}$).

[12] "With sufficiently rapid entrainment relative to the turbulent intensity, the buoyancy flux due to entrainment creates density stratification in the boundary layer which cannot be eliminated by turbulent mixing" [68].

[13] The rotational boundary layer describes the region between the drifting pack ice and the underlying ocean, where the Coriolis force is important [69].

Instrumentation

Many of the studies described above used EC to measure heat flux. In such studies, temperature is usually quantified using CTDs (conductivity, temperature, depth sensors)[14]. Conductivity measurements were not generally used to estimate salinity fluxes, even when these fluxes were discussed [e.g. 26, 36], implying some challenges with salinity-based EC. Conductivity has been used alongside temperature and pressure to calculate density, which is then used as the scalar in EC calculations (to estimate density fluxes and mixing efficiencies) [38, 39]. However, 'spiking' in conductivity was not detectable, and the main fluctuations were observed in temperature [38].

Compared to benthic flux studies, the studies described in this section often used different instrumentation and methodologies, driven in large parts by fundamental differences in the settings. For example, scales of turbulence in the ocean range from "the order of 1 mm diffusive scales to eddy scales on the order of 1 m in the thermocline, to 10 m in the wind-mixed upper ocean, and to 100 m in the most energetic tidal mixing or convectively mixing flows" [67]. More concretely, one study under sea ice found eddy time scales on the order of minutes and the length scales on the order of ten meters; it was concluded that fluctuations faster than 20 s contributed <10 % of the heat flux [36]. In the tidal front, the vertical scale of flux-containing eddies appeared to be tens of meters (e.g. 40 m to 100 m) [38], and in the thermocline, the peak in the power spectrum of w' corresponded to a length scale (as converted from a time scale using the fall speed of the profiler) of ∼2 m [39]. In contrast, time scales in benthic flux studies range down to fractions of seconds, with length scales on the order of cm [21] (see Table 1.1, p. 39). This difference in scales allows and sometimes requires the use of different instrumentation. For example, open ocean studies may be concerned that the length scales in energetic flow fields are too large for the instrumentation [39], while benthic flux studies focus on achieving high enough spatial and temporal resolution.

Data analysis techniques

The data analysis techniques utilized by the aquatic EC studies described here also differ somewhat from those employed by the benthic flux community, as guided by their often different study goals.

One such technique is the analysis of the instantaneous $w'c'$ time series, as opposed to simply calculating the average $\overline{w'c'}$. In the derivation of the EC equations (presented in Appendix A, Section A.1), the averaging operation is required for several terms from the control volume analysis to disappear, including those corresponding to horizontal homogeneity (horizontal advection of the scalar, flow divergence, etc) and stationarity (accumulation or loss of the scalar in the control volume). However, studies described here are not measuring flux in a footprint on a surface some area below the measuring volume, and so the control volume is somewhat different. In effect, the instantaneous $w'c'$ series is used to represent simply the movement of the scalar, carried by eddies, at the exact measuring point. The horizontal divergence is thus

[14]Not all studies used CTDs. The bottom boundary layer study by Shaw and Trowbridge [37] in fact did not measure temperature directly, but calculated it based on sound speed (assuming a linear relationship between the two). Thus, temperature and velocity were measured using the same acoustic pulse-based current meters.

Box. 1.2: Example analysis of instantaneous flux time series

An example of $w'c'$ time series analysis is presented by McPhee [36] in a study of heat fluxes under sea ice. In the (filtered) instantaneous $w'T'$ series, eddy 'events' were observed as sharp positive or negative spikes an order of magnitude larger than the mean (the excursions could thus have a large impact on the mean, demonstrating "why it takes a while for turbulence statistics to 'settle down' "). The positive excursions tended to be larger than the negative, and the relatively large skewness[a] (i.e less symmetrical probability distribution function) indicated the efficiency with which heat was dispersed as the bigger eddies overturned. The values in the time series also tended to stay near zero between the events, and the resulting relatively large kurtosis[b] indicated that most of the heat transfer likely took place during intermittent events, and short-term estimates could be expected to be highly variable. The probability distribution functions themselves were also approximated for each time series, using 50-bin histograms of $w'T'$ normalized by standard deviation. The normalized pdfs for different time series and at different depths were all similar, indicating self-similarity of the turbulent exchange process. Thus, in this case the instantaneous time series were analyzed to better understand the basic characteristics of the process, as well as sense check the ability of the system to measure heat flux.

[a] Skewness is a measure of the asymmetry of the probability distribution function (pdf), with positive values representing a longer tail in the positive direction.

[b] Kurtosis is a measure of flatness of the pdf, with large positive values corresponding to abrupt peaks

also not necessarily zero[15]. An example of an analysis of the instantaneous flux series, and the kind of information it provides, is given in Box 1.2.

Many of the aquatic EC studies described in this section also faced challenges related to the sparseness of data, in part due to restrictions on the record length. For example, in a study of heat fluxes under sea ice, McPhee [36] used flux periods of 15 min, as longer flux periods could not be chosen because of low-frequency variability in sea ice drift. Gargett et al. [38] faced a similar restriction in analyzing fluxes from a horizontal tow through a tidal channel. In that case, the full towing record had to be segmented into smaller sections for flux calculations, because of the strong spatial inhomogeneities created by tidal fronts. For fluxes measured over a vertical gradient in the ocean thermocline, the record length was limited by the size of the turbulent patches [39].

The restriction on flux period time can be problematic because a representative flux value requires averaging over a certain number of independent flux estimates [38]. In essence, a statistically significant number of eddies is required in each flux period; the turbulence statistics need to 'settle down'. The 'degrees of freedom' (number of independent flux estimates, i.e. eddies, in the average) can be estimated based on the number of zero-crossings of w in the flux

[15] In fact, McPhee [36], observing changes in mean temperature, assumed a horizontal divergence arising from advective and horizontal turbulent fluxes; the integral of the vertical turbulent flux, combined with the observed temperature changes, was then used to estimate its value.

period, and combined with the standard deviation of flux[16] to estimate a 95 % error bound based on normal statistics. These estimated uncertainties often proved to be quite large due to the limited degrees of freedom, which resulted in a large random error (i.e. insufficient averaging over turbulence statistics). The statistical significance of the estimates was also assessed by comparing to a set of 'random' samples obtained by multiplying resampled w' and T' values. The result was often that many records were discarded. However, as discussed above, the studies were unable to increase statistical reliability by averaging longer because of non-stationarity over longer time frames [38, 39].

To reduce the random error to acceptable levels, flux estimates were often ensemble averaged over multiple runs. McPhee [36] smoothed or averaged the 15 min 'realizations' of flux ($\overline{w'T'}$) over periods of an hour or more, while Gargett et al. [38] averaged over all data from the cruise, classified based on statistical reliability. More generally, many studies presented spectra and cospectra as ensemble averages over many realizations [38, 39].

The sparseness of reliable samples in these studies often led to the exclusion of large amounts of data. For instance, in a study of buoyancy fluxes in the main thermocline, large amounts of data were excluded due to the intermittency of mixing events detectable by the instrumentation. The study focused only on the energetic parts of records, noting that the results thus cannot be generalized to a net flux [39]. In general, data screening is not uncommon with EC measurements in the water column or under sea ice; a set of objective criteria is often used to exclude segments where the assumptions for EC may be violated [26, 29]. Benthic flux studies, on the other hand, often seek to understand ecosystem processes or calculate cumulative, representative fluxes, and cannot be as generous with data exclusion.

[16] Gargett et al. [38] determined standard deviation based on mean flux calculations for different overlapping segments of the same time series, while Moum [39] used the standard deviation of $w'T'$ over the record.

1.6 Dissolved organic material and fluorescence spectroscopy of DOM

The material in this section derives from a paper completed for a class assignment.

Dissolved Organic Matter (DOM) is one of the largest pools of reduced carbon on the Earth's surface, and plays a significant role in the global cycles of carbon, nitrogen and phosphorous [70]. Present in all aquatic environments, it impacts the biology, chemistry and physics of aquatic ecosystems in numerous ways. For example, it 1) supplies energy to organisms, 2) binds metals and pesticides, affecting their mobility and toxicity, 3) affects the penetration of light and UV radiation into the water column, 4) serves as an important chromophore in aquatic photochemistry, and 5) influences particle aggregation [71].

DOM's role in natural environments is directly related to its concentration and composition. For instance, lower molecular weight DOM is more easily consumed by bacterioplankton than higher molecular weight DOM [72]. However, understanding DOM dynamics is complicated by difficulties in characterization and analysis [65]. DOM is a complex heterogeneous mixture of organic polymers that arises from sources such as degradation of terrestrial plant matter and production by phytoplankton. Thus, not only is it inherently difficult to characterize, but its composition also varies in time and space depending on proximity to sources and sinks and exposure to degradation processes [73]. Fluorescence spectroscopy is an especially attractive method for studying and monitoring DOM because it involves a relatively straightforward data collection process, provides information on both concentration and composition of DOM, and can be employed in situ and in real time [74].

1.6.1 Principles of fluorescence

Fluorescence is a phenomenon by which substances with certain chemical features emit light after absorbing light of a shorter wavelength (higher energy). The Jablonski diagram depicting the energy transitions is shown in Figure 1.11. The initial absorption results in excitation of an electron to a higher, unoccupied energy orbital; several possible excited energy states may be available, resulting in a range of possible transitions. Excitation is followed by nonradiative relaxation to the lowest sublevel of the excited state. Fluorescence is then one potential mechanism by which the electron can return to ground state [73].

The wavelengths of absorption and fluorescence are determined by the difference in energy states, which is defined by the chemical structure of the fluorescing compound. Thus, the absorption and emission spectra can provide insight into the chemistry of the material. For example, fluorescing molecules (fluorophores) most commonly have $\pi \rightarrow \pi*$ transitions, such as aromatic systems or conjugated double bonds [76]. Emission at longer wavelengths suggests greater conjugation, and excitation (absorption) at longer wavelengths suggests a compound more aromatic in nature or containing more functional groups [73]. In addition, since the fluorescence spectra are specific to the compound, they can be used not only to determine properties of the fluorescing molecule, but also in some cases to identify the fluorophore itself.

The intensity of fluorescence at a given emission wavelength λ_{em}, excited at a given wavelength λ_{exc}, depends on the intensity of the excitation light, the absorptivity at λ_{exc}, the concentration

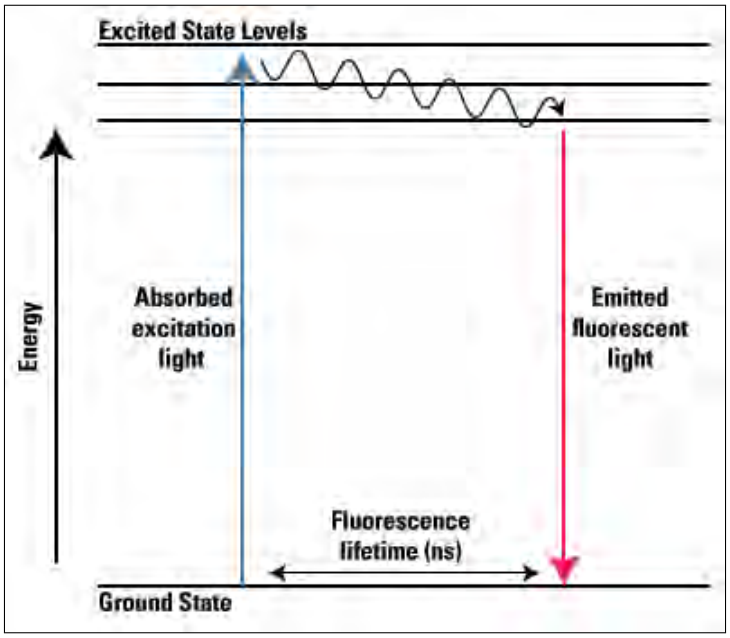

Figure 1.11: Jablonski diagram illustrating the mechanism of fluorescence. Source: ThermoFisher Scientific [75].

of the fluorophore, the path length, and $\phi(\lambda_{\text{em}})$, the quantum yield at λ_{em} [77, 78]. The quantum yield ϕ is a property of the fluorophore that represents the ratio of the fluorescing molecules to excited molecules; effectively, it is the probability that an excited molecule will fluoresce. It is through quantum yield that structural differences express themselves to make certain compounds 'strongly fluorescing' while others 'weakly fluorescing'. The quantum yield decreases with increasing temperature, and can also vary with pH, as structures are protonated or unprotonated [76]. However, in general, most factors determining fluorescence intensity are approximated as constant under reasonable and/or controlled measuring conditions, so that the intensity of emission can be used to infer concentration. In addition, the fluorescence signature of any given fluorophore of defined structure can be considered to be relatively constant, and can be used to identify the fluorophore or vice versa.

1.6.2 Fluorescence of dissolved organic material

Approximately 20 % to 70 % of DOM is estimated to be chromophoric DOM (CDOM) [70], i.e. absorbing radiation in the solar UV (290 nm to 400 nm) and visible (400 nm to 700 nm) ranges [72]. A subfraction of CDOM also fluoresces, and it is this fluorescent dissolved organic material (FDOM) that can be detected using fluorescence spectroscopy. Not only can FDOM concentrations inferred from fluorescence spectroscopy often be used to estimate DOM concentrations through site-specific ratios [79], but the actual fluorescent characteristics of the FDOM can provide information on its biochemical characteristics. In fact, constituent components with different characteristics can often be distinguished in the spectra, allowing fluorescence spectroscopy to be used to identify and trace different fractions of the DOM pool.

To date, two major types of DOM fluorescence have been identified: one associated with pro-

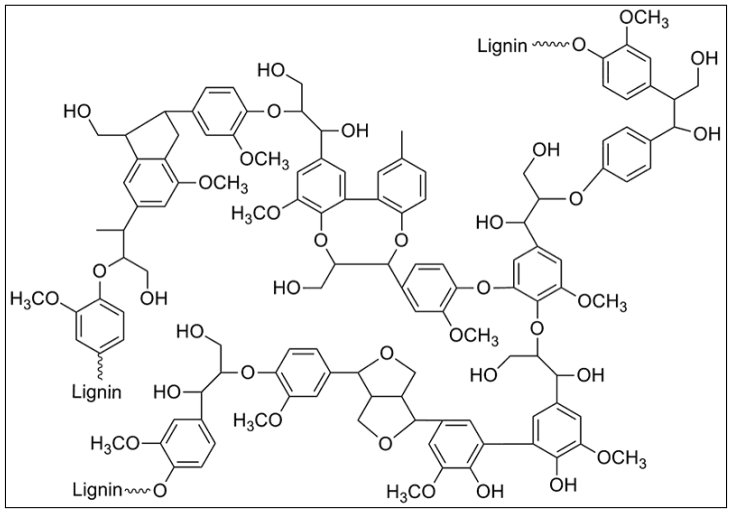

Figure 1.12: Chemical structure of a representative lignin fragment, showing a large number of aromatic rings. Source: Washburn [85].

teins, and the other with humic-like substances [65]. Protein-like fluorescence ($FDOM_P$) resembles the fluorescence from the aromatic amino acids tyrosine and/or tryptophan [80], and has been found to be correlated with their free form concentration [81]; however, it likely arises also from animo acids bound in protein [80], as well as other organic materials with similar fluorescence [65]. It has been associated with biological production by phytoplankton and bacteria [70], and is thus used as an indicator of biological activity and DOM bioavailability [65].

Compared to $FDOM_P$, fluorescence associated with humic-like substances ($FDOM_H$) typically has broader fluorescence peaks at longer wavelengths [70], indicating the presence of many conjugated fluorescence molecules [65]. This description is in line with the general understanding of humic substances as high molecular weight colored substances formed from the decay and transformation of plant and microbial remains [82, 83]. Although the definition of humic substances is not exact [84], the designation includes compounds such as lignin (Figure 1.12), tannins, polyphenols, and melanins [65], while examples of non-humic substances include amino acids, carbohydrates, fats, waxes, resins, and organic acids [82]. Humic substances are often classified into humic acids and fulvic acids, distinguished by the procedures used for fractionation and separation [82, 84].

$FDOM_H$ has been used extensively to trace terrestrial organic matter through aquatic ecosystems, as well as in carbon flux studies; it has also been associated with microbial oxidation and degradation of organic material [70]. Unlike $FDOM_P$, for which the relationship between molecular properties and fluorescence is poorly understood, the characteristics of different $FDOM_H$ spectra can be used to infer properties of the constituent compounds. For example, $FDOM_H$ spectra can been used to distinguish between autochthonous DOM (produced by biological activity within the water itself) and allochthonous DOM (e.g. from degraded terrestrial matter) [72]. In fact, various indices have been defined (e.g. the ratio of emission at one wavelength to another when excited at a given wavelength) that are used to provide information on properties such as aromaticity, age, extent of humification, and oxidation state, which can then be used to infer factors such as source and/or degree of degradation of the DOM [65]. These capabilities al-

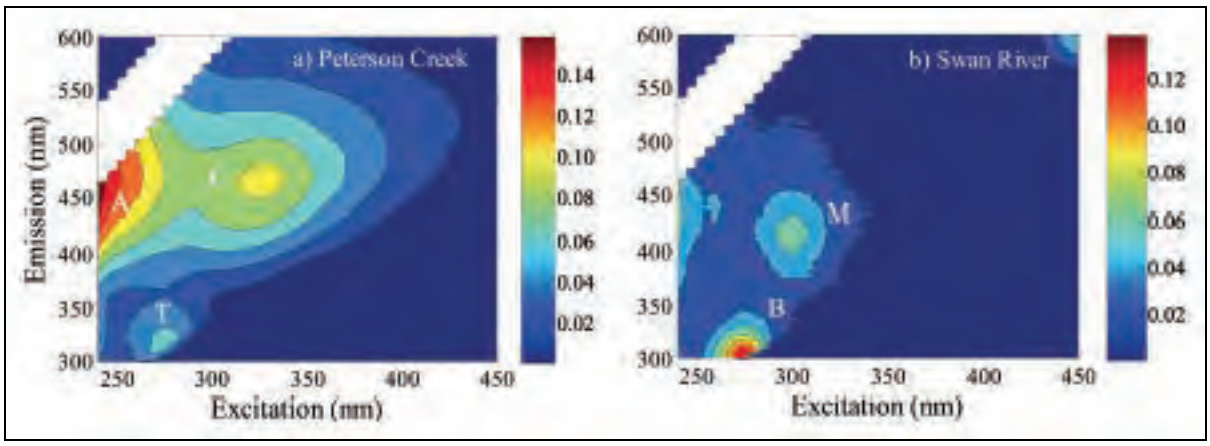

Figure 1.13: Examples of EEMs from two locations demonstrating the positions of the five primary fluorescence peaks. The white area in the upper left corner of each EEM is where excess scatter was removed. Source: Fellman, Hood, and Spencer [65].

low, among other things, the study of the transport and fate of DOM components as they travel through the ecosystem. For example, the variation of spectral properties of organic matter in sediments with depth and relative to overlying water can be used to infer the biogeochemical processes it undergoes in different sediment zones [86].

More information can be gleaned if emission spectra can be collected at a range of excitation wavelengths. The resulting information can be visualized with excitation-emission matrices (EEMs), three-dimensional matrices that provide a wealth of information on the abundance and nature of fluorophores present [65, 80]. Five commonly observed fluorescence peaks, first classified by Coble [80], are shown in Figure 1.13. Peaks A and C exhibit the broad, red-shifted emission maxima characteristic of FDOM_H, and are likely to comprise largely of degraded vascular plant material. Likewise, Peak M is also humic-like, but with shorter fluorescence wavelengths, indicating less aromaticity and lower molecular weight. It is generally associated with marine planktonic production, although it has been found in some studies in terrestrial and freshwater environments. Finally, peak B resembles the spectrum for tyrosine, and peak T for tryptophan [65].

Other peaks have also been identified, including some FDOM_H peaks that have been distinguished specifically as fulvic-like [73]. The distinction between fulvic acid and humic acid components can be of great importance in some applications, such as studies of sewage water treatment systems. In these systems, the procedures used to remove unwanted compounds often rely on the same chemical properties that distinguish fulvic and humic acids; consequently, the ratio of these materials can provide information on the system [87].

In fact, monitoring recycled water systems is one promising application of DOM fluorescence spectroscopy. Sewage material is notably different from natural waters in that it is much more rich in FDOM_P, particularly tryptophan-like fluorescence. This has been attributed to a larger fraction of organic matter originating from microbial activity, as opposed to plant material. As a result, the presence or absence of sewage water can be inferred from fluorescence measurements. In addition, fluorescence can be used to identify other contaminants, such as optical brighteners used in washing powder, which have a distinct horizontal spectral signature, as shown in

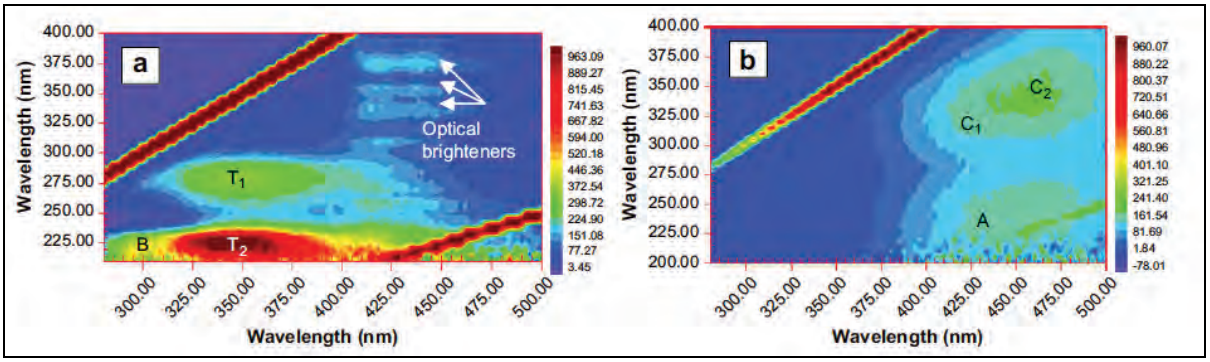

Figure 1.14: EEMs from a wastewater study for **a)** raw sewage, and **b)** clean river water. The peaks were identified as follows: B = tyrosine-like; T1 and T2 = tryptophan-like; A and C1 = fulvic-like; C2 = humic-like. Signals from optical brighteners are also noticeable in the sewage water. Source: Henderson et al. [87].

Figure 1.14. Thus, DOM fluorescence spectroscopy can potentially be applied to track sewage contamination and pollution in rivers; monitor water quality in natural aquatic environments; aid in process control in sewage treatment plants; identify specific pollutants in wastewater; and identify potential disinfection byproducts of drinking water treatment [87].

A more rigorous analysis of EEMs can be accomplished by applying multivariate data analysis techniques to leverage higher-order information contained in the matrices [87]. One popular method is parallel factor analysis (PARAFAC), which utilizes the trilinear structure of EEMs to decompose them into individual fluorescent components. The components (and their spectra) are determined in the model by minimizing the sum of squared error [73]. Among other things, the components identified through PARAFAC can be traced quantitively through a system, providing insight into the source, processing, fate, and uptake of different fractions of the DOM pool.

1.6.3 Challenges associated with DOM fluorescence studies

Practical difficulties in interpreting and comparing DOM fluorescence studies arise due to inconsistencies or errors in implementation. For example, measurements could be biased or inaccurate due to artifacts in the instrumentation, errors in sample acquisition or handling, or inconsistencies in data processing. An interlaboratory study comparing EEM results from 20 laboratories, conducted by Murphy et al. [74], revealed numerous procedural differences among the participating laboratories. Fluorescence results were found to be sensitive to, among other things, the instruments employed, correction algorithms adopted, and external standard used for normalizing the results (usually either the slope of a quinine sulfate dilution series or the area under a clean water Raman scatter peak). In addition, "almost half of the laboratories initially submitted one or more EEMs that were anomalous", with the anomalies appearing in large part to be related to human error or neglect in data processing [74]

Other challenges with DOM fluorescence spectroscopy are associated with 'matrix effects', which arise when components in the sample other than the analyte affect the measured values [87]. For instance, as discussed in Section 1.6.1, fluorescence intensity and spectra are potentially

influenced to various degrees by factors such as temperature, pH, and the presence of certain metal ions; isolating the effect of these elements to arrive at the 'true' spectrum is not always straightforward. Another example of a matrix effect is the inner filtering effect (IFE), which occurs when the sample matrix absorbs some of the excited or emitted radiation, thus reducing and/or distorting the emission spectra. Various approaches exist to correct for IFE, each with associated advantages and disadvantages [87]; results have been shown to be sensitive to the method used [74]. Studies assessing the potential of DOM fluorescence spectroscopy as a monitoring tool for recycled water systems have estimated the impact of inner filtering, temperature, pH and metal ions to be relatively unimportant [87]. However, they may factor more significantly in other applications, and should be considered when interpreting results.

1.6.4 In situ fluorescence spectroscopy

Much research is currently focused on such in situ fluorescence instrumentation. In situ spectrophotometers are generally designed to be portable and compact, and are often limited to measurements of one or two fixed emission wavelengths [87]. For example, the CDOM fluorometer piloted in eddy correlation studies of carbon fluxes was a single-channel device with 370 nm excitation and 460 nm emission detection [63], corresponding most closely to peak C. Other innovations include a submersible UV fluorometer designed to detect polycyclic aromatic hydrocarbons (excitation 254 nm, emission 360 nm, that was also found to respond to tryptophan-like material [88], and a portable light induced fluorescence (LIF) sensor utilizing an array of LEDs [89].

As fluorescence spectroscopy technology continues to develop, an increasing number of instrumentation configurations is becoming available. These designs all have their associated advantages and disadvantages, allowing choice based on the requirements of the particular application.

1.7 Optical fiber chemical sensors

To contextualize the sensor presented in this thesis, a brief review of optical fiber chemical sensors (OFCS) is presented here. The material in this section derives from a paper completed for a class assignment.

1.7.1 Basic definitions

Optical sensors are devices that detect changes in optical properties (e.g. reflection, dispersion, scattering, interference, absorption, refraction, or diffraction) to infer information about the measurand of interest. Optical sensors generally detect these changes by sending an input beam of light and measuring the subsequent modulation in wavelength, amplitude, phase, or polarization imparted by the measurand [90].

In extrinsic (as opposed to intrinsic[17]) optical fiber sensors, the optical fibers act only as waveguides to transmit the light. Thus, optical fiber(s) carry light from a source to the environment, where the measurand modulates the light extrinsically; the same or different optical fiber(s) then carry the light away to the processor.

Chemical sensors have been defined (the 'Cambridge definition') as "miniaturized device that can deliver real time and on-line information on the presence of specific compounds or ions in even complex samples" [92]. In the strictest sense, chemical sensors must respond to the target species (the analyte) reversibly, in order to allow continuous monitoring [93]. Note that the Clark-type microelectrodes commonly used in eddy correlation studies of dissolved oxygen consume small amounts of oxygen as part of their mechanism, and thus are not strictly chemical sensors, though the effect of this non-ideality is often negligible. However, the stirring sensitivity exhibited by these microsensors as a result of this mechanism can lead to potentially significant errors in EC-measured flux [62].

The advantages of using optical fibers in chemical sensors are numerous, and include immunity from hazardous chemical environments, low electrical noise, safety (due to lack of electrical power in the fiber), small sensor size, and low cost [90].

1.7.2 OFCS Instrumentation

The basic components of optical fiber chemic sensor instrumentation are a light source, optical fiber(s), transducer, detector, and signal processor (Figure 1.15).

Light source

The light source supplies the incident light to be modulated by the analyte. Since light from the source must be coupled into the optical fiber, ease of coupling is a major factor in determining

[17] In intrinsic sensors, the measurand directly interacts with light while it is in the optical fiber, i.e. the transducer is part of the optical fiber. Such sensors often utilize principles of evanescence, for example by relying on the interaction of the light with a modified region of the cladding [90, 91]. The sensor developed in this thesis is an extrinsic optical fiber sensor and intrinsic sensors will subsequently not be discussed.

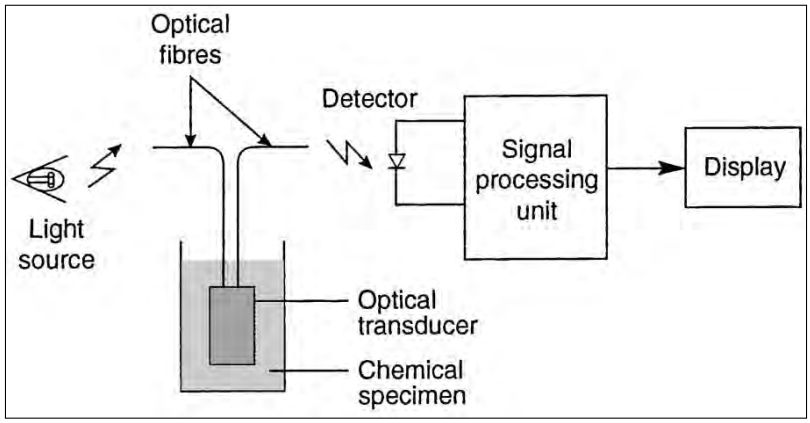

Figure 1.15: Schematic of typical OFCS instrumentation. Source: Taib and Narayanaswamy [90].

an appropriate light source for a given system. Other important considerations include output intensity, power requirement, wavelength, bandwidth, and stability. The most popular choice of light source for OFCS are light-emitting diodes (LEDs), which are cheap, reliable, and easily coupled to optical fibers via butt coupling [90].

Laser diodes (LDs) have also been used where higher output energy and/or monochromaticity is required, though they have much higher cost and power requirement. Today, monochromatic LEDs and LDs are commercially available that cover a quasi-continuous spectrum of output wavelengths from UV (240 nm) to near-IR 970 nm, and discrete wavelengths up to 1680 nm), at several output powers and encapsulations [94].

Optical fibers

Optical fibers are used to guide light between the source, sampling volume, and detector. Historically, the most common designs have been distal-type probes with an indicator (material that responds to the analyte by a change in optical properties [93]) affixed to or deposited at the tip [95]. More recent advances have enabled the varied and improved selection of configurations in use today. For example, distal probes utilizing the same fiber bundle to carry light to and from the sample can now be constructed with a central fiber to deliver light and outer fibers to collect the reflected light. Other distal probe designs separate the delivery and collection segments using a bifurcated optical fiber bundle or a U-bend [92].

The size of the optical fiber or fiber bundle used in OFCS must be chosen depending on application. Larger fiber bundles (e.g. diameter of several mm) allow easier interfacing with other optical elements, such as the source and detector, as well as higher throughput. However, the sensing tip may be too large for some applications. In contrast, single optical fibers offer small sensing tips (diameter on the order of microns), but have much lower throughput, sometimes necessitating laser sources and/or photon-counting or amplifying detectors [95].

Transducer

The transducer translates the analyte concentration into a modulation of light. Today, many OFCS transducer designs exist to sense analytes as diverse as pH, ions, gases, molecules, and biological compounds [92, 95].

Although transducer designs vary greatly depending on target analyte and modulation method, the most widely used techniques are based on absorption or luminescence (fluorescence). Sensors based on refractive index and reflectivity have also been developed [92]. Transducers can be categorized as either direct or reagent-mediated. Direct sensors measure an intrinsic property of the analyte, such as its intrinsic molecular absorption or fluorescence. In contrast, reagent-mediated sensors measure changes in the optical response of an intermediate indicator. The spectrophotometer designed in this thesis to measuring fluorescing compounds is a direct sensor, while the oxygen optodes used in other eddy correlation studies [5, 32] are reagent-mediated.

Detector

The detector is used to convert the modulated light output from the transducer into a photocurrent. Photodiodes are a common detector choice, with different types of photodiodes (e.g. silicon or avalanche photodiodes) suitable for different applications. Photomultiplier tubes (PMTs) are often used for low-intensity signals, when higher light sensitivity is required [94]. Monochromators or optical filters have also been used in conjunction with photodetectors to limit the non-signal intensity [96] and to select the wavelength(s) of interest [92].

Signal processor

The signal processor processes the photocurrent from the detector into a current or voltage suitable for interpretation as the analyte concentration. It may also perform functions such as noise reduction, amplification, demodulation, calibration, and conversion. Historically, the signal processor has comprised of electronic circuit components, but microprocessors and microcontrollers are now also capable of signal processing functions [94]. Many components are now commercially available that can be programmed and/or adapted for use in OFCS, allowing sensor development to be largely isolated from development of the signal processor.

1.7.3 Common Techniques Used With OFCS

Several techniques have been used to overcome challenges associated with OFCS or to improve their performance.

Source Modulation

All optical sensors must provide a means of discriminating the signal (produced by the source and modulated by the measurand) from ambient light. One approach is to simply perform

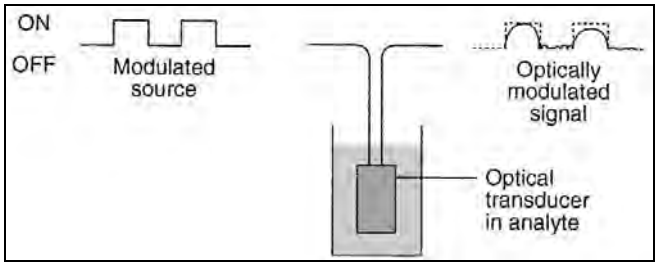

a) Principles of source modulation. Source: Taib and Narayanaswamy [90].

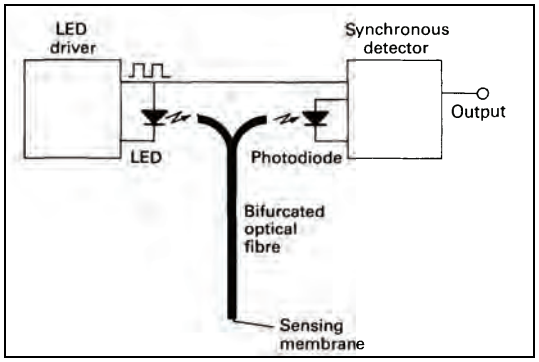

b) Example of OFCS setup with source modulation. Source: Hauser and Tan [96].

Figure 1.16: Block diagrams of modulation in optical fiber chemical sensors.

measurements in the dark, such as by covering the analyte with an opaque layer to block out ambient light [97]. Such an approach is not always practical, however. Thus, sensors often utilize source modulation, which provides both a method for discriminating ambient light, as well as a means of synchronization [90]. In this technique, the source is modulated, for example with a square wave. This modulated waveform is then further modulated by the analyte. Both the input square wave and modified square wave can then be processed by a demodulator, as shown in Figure 1.16. This technique has been used to successfully discriminate against ambient light that produced a photocurrent about 3-4 orders of magnitude higher than the signal of interest [96].

Referencing

A major limitation to intensity-based fiber-optic sensors is their susceptibility and sensitivity to variable losses in the system that are unrelated to the measurand. Potential sources of loss include connections and splices, microbending, macrobending, misalignment of light sources and detectors, and/or source intensity variation [91]. Referencing is a technique that can be used to calibrate out some of these variable errors.

The basic principle of referencing is that a reference beam of light bypasses the sensing region and is sent directly to the detector. The output is calculated as the ratio of signal to reference. In practice, many variations exist for implementation, involving any combination of single or multiple light sources, and single or multiple detectors [90].

Lifetime-based fluorescence sensing

Drawbacks to fluorescence sensing based on intensity modulation include the variable losses described above, as well as drift due to degradation or leaching of the dye [92]. Although referencing can be used to calibrate out some of these errors, steady-state intensity measurements are in general prone to error and often not reproducible, and data obtained with two different setups may not be consistent [93].

Lifetime-based sensing is a more robust fluorescence detection method based on measuring analyte-induced changes to the lifetime of the indicator. Some sensors directly measure lifetime (time domain measurements); others monitor it indirectly through phase measurement techniques (frequency domain measurements). Lifetime-based methods include rapid lifetime determination (RLD); dual-lifetime referencing (DLR), which combines lifetime sensing with referencing; and dual lifetime determination (DLD), which is especially useful for dual-analyte sensing [92, 93].

This instrument

The spectrophotometer developed in this thesis is an intensity (not lifetime) sensor that uses source modulation, but not referencing. Because of the short length of the optical fibers and the relatively simplicity of the source and coupling, as well as the relative insensitivity of eddy correlation measurements to instrument drift (due to the mean removal process), it was decided that such techniques were not as important for a first-pass prototype development.

1.8 Acoustic Doppler Velocimeters

The Acoustic Doppler Velocimeter (ADV) is the most commonly used velocity sensor for EC measurements of benthic fluxes. Some EC studies in flumes have used stereoscopic particle image velocimetry (PIV) [62], but this technique cannot be used in the field.

It is also worth noting that EC measurements in other aquatic environments (e.g. main thermocline of the ocean, or under Arctic sea ice) have used different sensors to measure water velocity[18]. These velocity sensors may be more suited to the larger length and time scales in these settings, the goals of the study (e.g. a vertical array of sensors can be deployed for a vertical series of flux measurements [e.g. 36, 37]), or the state of development of the sensors at the time of the study (e.g. for some time, ducted impeller clusters were the most suitable available instrumentation [69]; more modern studies in the same settings have also now used ADVs [26]). For benthic flux studies, ADVs are still the most commonly used velocity sensors, although concerns have also arisen regarding their ability to fully capture energetic flow characteristics [30]. Nevertheless, all sensors have their tradeoffs. Especially as ADV technology continues to develop, they are on the whole a reliable and commercially available instrument for the velocity portion of EC measurements.

1.8.1 Doppler-based instrumentation

Acoustic Doppler Velocimeters (ADVs) measure 3-dimensional velocity in small sensing volumes ('point measurement') at high frequency. Their measurement principle is based on the Doppler effect, which is the change in frequency of a wave when the source of the wave moves relative to the observer. For example, if the source is moving towards the observer, the time interval between the arrival of wave crests decreases steadily, which is perceived as a frequency shift (to higher frequencies). The frequency shift can be used to measure the relative speed.

Acoustic Doppler instruments can measure water velocity by transmitting a short pulse of sound ('ping') of known frequency from a transducer (device that converts energy from one form to another; in this case, electrical to acoustic). As it travels forward, some fraction of the sound pulse reflects off of small suspended particles in its path (e.g. zooplankton, sediment, or small air bubbles) and scatters in all directions. Some is echoed back to the source, which the instrument can then detect. A Doppler shift occurs if the particle is moving relative to the transmitter in the axis of the beam. The particles are assumed to move passively with the same speed as the water, and so the water velocity along the acoustic path can be calculated from the frequency shift between the ping sent and the echo received [52].

The velocimeter used in this study is a pulse coherent instrument, so it emits two pulses rather than one. Compared to the single-pulse system described above, pulse coherent profilers produce better accuracy and lower noise and can measure in smaller cell sizes [98]. These instruments calculate velocity from the phase difference between the backscatter from the two pulses in each

[18]Other water velocity sensors used have included: triplets of current meters consisting of ducted impellers with Hall effects sensors, at the density interface of a salt wedge estuary [66] or under arctic sea ice [36]; modified Acoustic Doppler Current Profilers (ADCPs) towed behind a boat through a tidal front [38]; airfoil probes and pitot tubes dropped through the main thermocline of the ocean [39]; Benthic Acoustic Stress Sensor (BASS) current meters measuring the differential travel time of acoustic pulses traveling in opposite directions, deployed in the bottom boundary layer of a continental shelf [37]; or ultrasonic current meters deployed under sea ice [58].

ping pair. This phase shift is directly proportional to velocity, and can be converted by scaling with the speed of sound as

$$V = \frac{\Delta\phi C}{4\pi f_{\text{src}} \Delta t} \tag{1.14}$$

where V is the current velocity, $\Delta\phi$ is the phase difference, C is the speed of sound (which varies with salinity and temperature and therefore may vary by deployment), f_{src} is the frequency of the source (the Nortek Vector used in this study uses 6 MHz, which was chosen by the manufacturer after considering accuracy, sampling volume, size, signal quality, etc [99]), and Δt is the time difference between the two pings, which is an adjustable setting (see Section 1.8.3 on phase wrapping) [52].

Pings have some noise, so each measurement at the chosen sampling (output) frequency averages over several ping pairs [52]. For the Vector, the actual ping rate is independent of the output frequency and instead depends on the 'Nominal Velocity Range' setting (250 Hz per pair for 0.1 and 0.3 m/s setting, and 125 Hz for 1, 2, 4, and 7 m/s setting; see Section 1.8.3 on phase wrapping for a greater description of this parameter). The instrument pings continuously, and each output represents the average of the ping measurements taken in that time period [Atle Lohrmann, Lee Gordon, Sven Nylund (Nortek AS), forum posts and personal communication 8 November 2015]. Thus, slower sampling rate averages over a greater number of pings and is less noisy.

1.8.2 Geometry and sensing volume

ADVs are bi-static instruments, i.e. the transmitter is separate from the receivers [52]. They generally have a central transducer that sends the ultrasonic pulse, while two to four receiving transducers, spaced around the emitter and angled inward, detect the reflected pulses. The intersection of their axes defines a sampling volume 5 cm to 18 cm away from the central transducer, depending on the ADV model [100]. Since the receiver and transmitter are separate and aligned to different axes, ultimately the Doppler shift perceived at each receiver is proportional to the velocity component along the bisector of the transmit and receive beams. That is, the actual axis along which velocity is measured is the bisector of the central transducer axis (z) and the tilted axis of the relevant receiver [52]. The geometry of the transmit and receive beams is shown in Figure 1.17.

The Vector used in this study has three receivers, allowing estimates of flow velocity in three directions. Raw velocity (in 'beam coordinates') is measured along the bisectors, which are angled relative to each other depending on the angle of the receivers; for the Vector, the receivers are angled 30° from center axis, so the bisectors are angled 15°. The bisectors define the axes of the beam coordinate system [52].

Velocity output from the Vector can be expressed in beam coordinates, a Cartesian instrument coordinate system ('XYZ' coordinates), or an Earth normal coordinate system ('ENU' coordinates, for East, North, Up). Velocities in beam coordinates can be transformed geometrically into the other two systems using a transformation matrix. The transformation matrix to XYZ instrument coordinates is preprogrammed into each instrument, with the orthogonal axes as defined in Figure 1.17; one of the receivers is marked to indicate the x direction, and the y and z axes are chosen to form a right hand orthogonal system with positive z pointing into

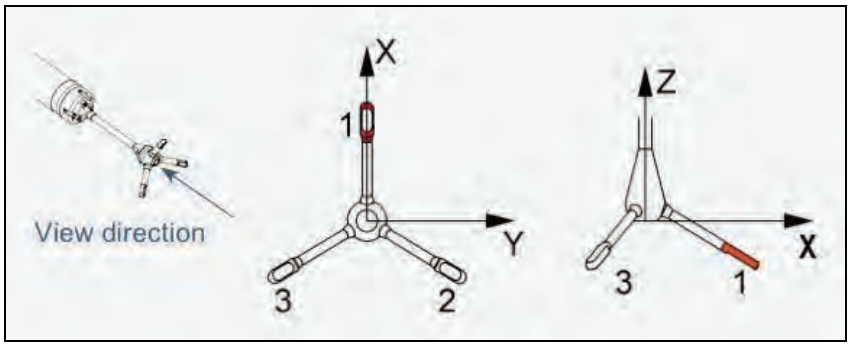

Figure 1.17: The Vector beam numbering convention and XYZ coordinate system as defined relative to the probe head. Positive x velocity is in the direction that Beam 1 (the labelled receiver) is pointing, and positive z velocity is flow into the central transducer. Source: Rusello [98].

the central transducer [98]. Due to this geometry, the instrument is more sensitive in the z direction than in x or y, and the z component of velocity yields the lowest uncertainty [52]. The transformation matrix to ENU coordinates is calculated and updated periodically based on the pitch, roll, and heading measured by external tilt and compass sensors in the instruments (and thus are only available for ADVs with these sensors, such as the Vector). The update rate for the ENU transformation matrix is not necessarily the same as the data measurement rate, which can create issues with moving instruments [98].

The sensing volume of the ADV is an irregular shape defined by the intersection of the transmission and receive beams [100], but which can be approximated as a cylinder some distance away from the transducer. Because of symmetry, the beams all intersect at the same point; that is, all three receivers are focused on the same volume, to obtain three simultaneous velocity components from that same volume.

For the Vector, the beams all intersect 157 mm from the transmitter. The pulse sent out by the transmit transducer covers ∼4 mm vertically, and the receivers listen to an echo that corresponds to ∼14 mm vertically. The sensing volume is approximated as a ∼14 mm diameter cylinder, ∼14 mm in height, as shown in Figure 1.18.

The sensing volume depends on the instrument; the Vectrino model, for example, has a sensing volume with a diameter of ∼6 mm [52]. In addition, the actual sensing volume may more complex. The Vectrino, for example, uses a complex spatial averaging scheme whereby localized velocity measurements are weighted by the return signal strength when acoustic backscatter is weak, but all tracer particles are weighted equally during strong backscatter. The weighting function within the sensing volume thus depends on particle type, particle loading, and ADV power level [100].

The sensing volume is defined not only by the intersection of the beams, but also by the range gating in time. Range gating refers to the subdivision of the received backscatter into different segments[19]. Both pulses in a ping pair are range-gated, and the phase difference is calculated for each range cell [52]. However, the focal point produces the strongest signal. The Vector does measure a full profile during a 'probe check', for example, but the signal strength is generally (and ideally) weak except for a Gaussian curve around the sampling volume. Thus, the signal normally reaches the noise floor (∼50 counts) in the area between the transmitter and the sampling volume, as well as beyond the sampling volume, unless there are reflections or interference in the system [Elin Bondevik (Nortek AS), personal communication, 2 May 2016

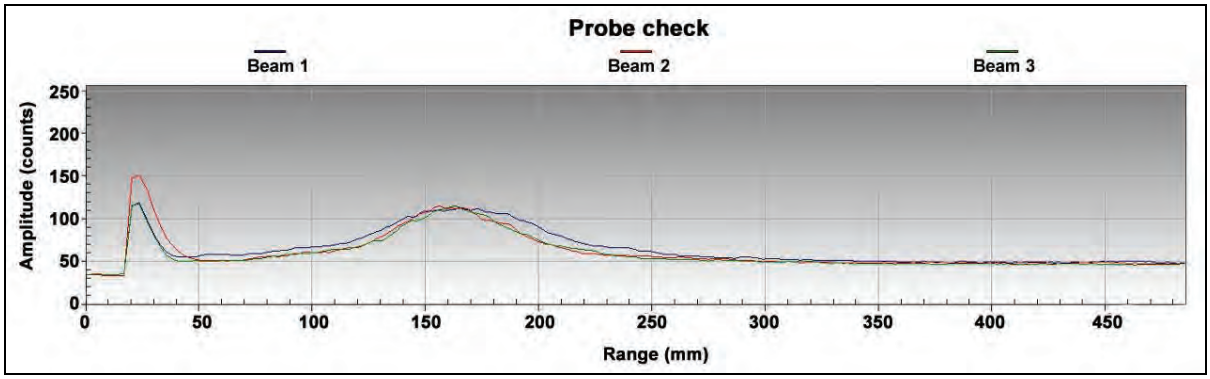

.

Figure 1.19: Sample Vector probe check showing a Gaussian curve around the sampling volume and low signal elsewhere. The signal at ∼20 mm is the transmit pulse from the Vector and electronic noise [Elin Bondevik (Nortek AS), personal communication, 2 May 2016]. A probe check is a profile measurement commonly taken at the beginning of a deployment (and/or periodically throughout) that shows how the signal varies with range. It provides information on the instruments' performance in the given environment, including sources of noise and the location of boundaries. Source: Elin Bondevik

/ 19 May 2016].

For the Vector (and Vectrino), the sampling volume ('cell size') is actually a user-configurable option, which sets the amount of time the instrument spends 'listening'. It should be optimized for the 'transmit length', another user-configurable option which sets the duration of each acoustic pulse. A shorter transmit length might be desirable for higher bandwidth, but it also results in less energy in the signal and thus lower SNR (see Section 1.8.5). These parameters usually do not require modification [PJ Rusello (Nortek AS), forum post, 25 July 2011].

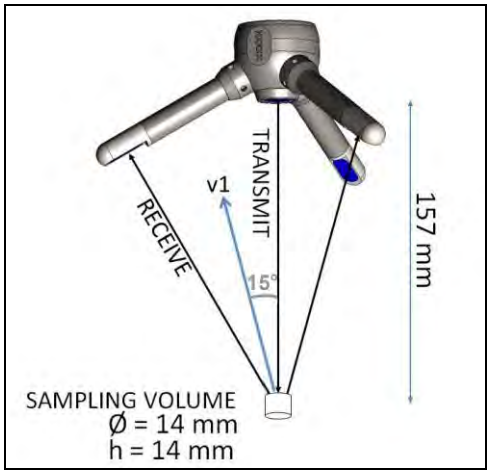

Figure 1.18: Approximate measuring volume of Vector ADV, defined by the intersection of transmit and receive beams. Source: adapted from Nortek AS [52].

1.8.3 Phase wrapping

As discussed in Section 1.8.1, the velocity is calculated from the phase shift between the two pulses of a ping pair. This phase shift itself is computed using the covariance method (a standard signal processing technique), which involves a four-quadrant arctangent computation that restricts the detectable phase shift angle to $[-\pi, \pi]$. If the actual phase shift lies outside this range, the calculation will wrap around the circle (introducing an additional 2π rad phase shift) and be represented as number

[19] Intuitively, the receivers pick up backscatter from particles all along the transmit pulse path, so only those signals received in a certain window of time correspond to the measuring volume on which the receivers are focused.

in the $[-\pi, \pi]$ range. This 'phase wrapping' manifests in the velocity trace as an abrupt, unrealistic change in the magnitude of the measured velocity. Phase wrapping is not always obvious in XYZ or ENU coordinates, since it can occur even when velocities appear to be far from their limit, due to the transformation that converts beam coordinates to the other coordinate systems [98].

Phase shift is directly proportional to velocity (as can be seen from Eq. (1.14)), so a larger velocity results in a larger phase shift. To avoid phase wrapping, the instrument should not be used to measure velocities above those that translate to $|\phi| = \pi$. The actual velocity at which the phase shift occurs depends on the lag time between the two pings (Δt), which is a configurable setting. A shorter lag 'gives' less time for the two pings to phase separate, and thus can handle larger velocities which move the particles farther (resulting in greater phase shift) in some given amount of time.

The Vector provides several options of time lags depending on the velocities to be measured (captured in the 'Nominal Velocity Range' parameter): larger velocities are measured with shorter lags to avoid phase wrapping, while smaller velocities are measured with larger lags for better resolution. Phase wrapped traces can also be 'unwrapped' in beam coordinates [98]. Alternatively, despiking algorithms applied to the resulting velocity data are also commonly used to remove the velocity spikes [34]. However, the best way to handle phase wrapping is to choose a proper velocity range to avoid the problem in the first place [98].

1.8.4 Weak spots

When measuring near boundaries, ADV measurements are susceptible to interference from reflected ping pulses. Specifically, 'weak spots' arise when the first pulse of a ping pair reflects off the boundary and reaches the sampling volume at the same time that the second pulse is passing through on its way out. This interference results in low SNR and correlation values, as well as noisy velocity data.

Weak spots depend on the the spacing between the pulses (which for the Vector is captured by the 'Nominal velocity range' parameter) relative to the distance to the boundary. Given that EC instruments are typically positioned 8 to 80 cm above the sediment floor [19], the relevant weak spots occur when the boundary is 46 cm (when measuring at velocity range of ± 0.1 m/s), 20 cm (when measuring at velocity range of ± 0.3 and ± 1.0 m/s), 9 cm (when measuring at velocity range of ± 2.0 m/s), and 8 cm (when measuring at velocity range of ± 1.0 m/s) away from the sampling volume. However, the location of the weak spots also depends on the speed of sound and the surface of the boundary, and so may occur a cm or more away from these values [52].

1.8.5 Amplitude, correlation, and SNR

The signal strength of the received echo is represented by the 'amplitude' metric, which is presented in the arbitrary unit of counts. The amplitude depends on the type and amount of particles in the water, scattering conditions, cell size, and the power level of the instrument [52]. It is not a measure of the actual velocity, but it often increases with velocity since higher velocities lead to more scatterers remaining in suspension [101]. Amplitude has actually been

used in some cases to estimate suspended solid concentrations [64], although its use in this capacity must be applied with caution.

The SNR (signal-to-noise ratio) is the ratio of the signal amplitude to the amplitude of noise. The noise level is determined at the beginning of each run when the transmitter is disabled, producing an amplitude value with no acoustic energy in the system. It is generally 50 counts or lower; a higher value could be the result of electronic noise (e.g. nearby motors or pumps), or signals picked up by the cable [101].

The SNR is presented in decibels (i.e. 20 times the ratio of $\log_{10}$ values, therefore representing the ratio of orders of magnitude) but is actually calculated as [102] [Atle Lohrmann (Nortek AS), forum post, 5 October 20015].

$$SNR = [\text{amplitude (counts)} - \text{noise level (counts)}] \times 0.43\,\text{dB/count} \tag{1.15}$$

since the metric of amplitude (counts) itself is a log-scale measure due to the use of a log amplifier[20] [Magnus Grøtterud (Nortek AS), forum post, 23 April 2015].

A low amplitude results in lower SNR and lower quality measurements, so ADV data quality checks often screen for low SNR. Data quality generally improves with SNR up to a value of around 15 or 20, beyond which SNR does not significantly affect data quality [101].

The 'correlation' metric is another measure of data quality. Correlation measures the similarity between the two pulse echoes, with 100 % corresponding to identical pulses. High correlation is desired because it indicates that the instrument measured the two pulses it sent out, echoing from the same particle, and is thus determining a valid Doppler phase shift. ADV data quality checks often consider correlations above 70 % to be sufficiently good quality data. However, high correlations are not always indicative of valid measurement of the flow, and it is best to examine the dataset carefully [98].

Low correlations can arise from low signal strength or high noise (i.e. low SNR); since noise, which is uncorrelated, has correlation values of around 10 %, the correlation values approach 10 % as the SNR drops. Other sources of low correlation include phase wrapping and pulse-to-pulse interference (e.g. from weak spots). Thus, solutions include increasing the amount of scatterers, setting an appropriate nominal velocity range, and avoiding weak spots [101].

Amplitude, SNR, and correlation are reported independently for each beam. However, with only 3 beams, a low quality signal in any one beam invalidates all three velocity measurements in XYZ or ENU coordinates. Some ADVs, such as the Vectrino, have 4 beams, in which case a poor measurement in one beam does not necessarily invalidate all transformed velocities.

[20] The number of counts is inversely proportional to the amount of gain that must be applied; a higher number of counts indicates less need for amplification, with 1 count $\approx$ 0.4 dB to 0.45 dB [52]. The 0.43 value in Eq. (1.15) is an estimate, as the exact scale factor differs with the hardware board. For the Vector used in this study, the scale factor is 0.54 dB/count [Elin Bondevik (Nortek AS), personal communication, 12 November 2015].

1.9 Conductivity measurements

1.9.1 Conductivity and salinity

Conductivity, the inverse of resistivity, is a measure of a medium's ability to pass an electrical current. In solutions, charge is carried by ions, so conductivity is directly dependent on the concentration of ions, as well as their mobility and valence, and the temperature [103, 104]. It is usually measured in microsiemens per centimeter (µS/cm) or some variation of these units. The siemen (also equivalent to a ℧) is a unit of conductance, which is the inverse of resistance ($1\,\mathrm{S} = 1\,℧ = 1\,\Omega^{-1}$). Conductivity is the specific unit of conductance (and a property of the solution), just like resistivity is the specific unit of resistance.

Salinity is the total concentration of dissolved salts in the water; operationally, it is the amount of material 'dissolved' enough to pass through a fine filter [105]. It is related to conductivity, since dissolved salts form ions (which conduct), but the two are technically different and do not scale directly. For example, two solutions with the same concentration of salts can have different conductivities if they have different composition (smaller ions have higher charge density and hence greater conductivity for the same concentration [104]) or temperature (see Section 1.9.4 for more information on temperature dependence). The increase in conductivity as salinity increases is also not linear. However, conductivity is often used to infer salinity; other methods, for example complete chemical analysis, are generally more involved.

Salinity derived from conductivity is known as practical salinity [106]. It is measured using the Practical Salinity Scale (PSS), where the salinity S of a sample is given by a complex, nonlinear function of the ratio of the conductivity of the solution to the conductivity of a reference KCl solution, with a correction for temperature [107]. S determined this way is often labeled with the 'unit' PSU, although it is actually unitless; the PSU designation just means it was measured with the PSS [108]. Because the PSS defines salinity using a conductivity ratio, solutions with different compositions but the same conductivity have the same salinity. This convention was chosen with the use of salinity to determine physical properties (e.g. density) in mind. The reference KCl solution (32.4356 g KCl in 1 kg solution) was chosen so that seawater with the same conductivity at 15 °C has a practical salinity of 35.000, which from previous methods had become known as the 'average' salinity of seawater [109].

A new standard adopted in 2010, TEOS-10, defines a more precise and accurate measure of salinity known as absolute salinity, which is given in units of g/kg solution [106]. TEOS-10 addresses a number of shortcomings of the PSS, such as slight differences in composition of seawater [107], to provide "the best available estimate of the mass fraction of dissolved matter" [105]. The standard defines a new thermodynamic equation of state for seawater; by approaching salinity through thermodynamics, it allows for consistency in thermodynamic relationships (e.g. density, sound, speed and heat capacity) [106]. The calculations are quite involved, and more information can be found in Millero [109].

Approximate conductivity and salinity ranges for typical environmental waters are given in Tables 1.2 and 1.3.

Total dissolved solids (TDS) is a metric describing the sum of all 'dissolved' particles (operationally, what passes through a fine filter, e.g. 2 µm) [106]. It is basically the same as salinity, although the term 'salinity' is used more often in oceanography, while 'TDS' is often used with

Table 1.2. Typical conductivity values for various bodies of water. Source: Fondriest Environmental Inc. [106].

	Conductivity range (µS/cm)
Deionized water	0.5 to 3
Melted snow	2 to 42
Tap water	50 to 800
Potable water in the US	30 to 1500
Freshwater streams	100 to 2000[a]
Industrial wastewater	∼10,000
Seawater	∼55,000

[a]The conductivity of freshwater is highly dependent on geology. The given range excludes estuaries. The conductivity of estuaries, which are influenced by both freshwater and saltwater flow, is highly variable and depends on many factors.

Table 1.3. Typical salinity values for various bodies of water, in parts per thousand. Source: Fondriest Environmental Inc. [106].

	Salinity range (ppt)
Freshwater	<0.5
Brackish / estuary	0.5 to 17
Black Sea	16
Ocean range	32 to 37
Average ocean	35

respect to freshwater and water quality standards [110]. TDS can be measured by gravimetry (evaporating and weighing) or from conductivity, using an empirical TDS constant that depends on the types of solids dissolved in the water. It is given in units of mg/L [106].

1.9.2 Conductivity electrodes

Conductivity measurements are conceptually simple. Conductance can be measured as

$$G = \frac{I}{V} \tag{1.16}$$

and thus can be accomplished by measuring the voltage across and current through two probes (electrodes) inserted in the solution of interest.

The conversion from conductance (total ability to pass current from one measurement point, e.g. electrode, to another) to conductivity (property of the material) depends on the geometry of the cell. For example, for parallel plate electrodes (and ignoring edge effects from the finite area of the plates),

$$G = g \times \frac{A}{l}$$

where g is conductivity, l is distance between the plates, and A is the surface area of the plate.

For more complicated geometries, the current flow field can be quite complex. In general, the geometry is captured in the cell constant K, where

$$g = G \times K \tag{1.17}$$

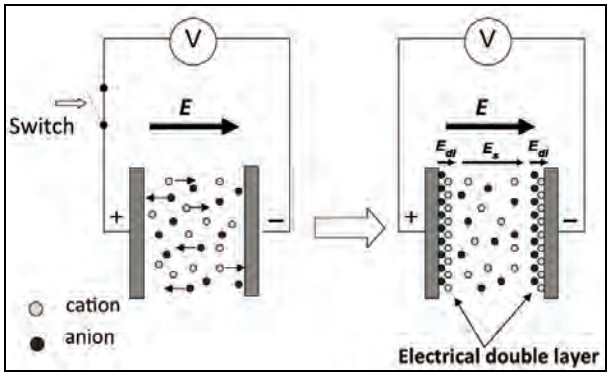

Figure 1.20: Schematic of electrode polarization. When an electric field E is applied, double layers of ions form at the electrode-solution interface, resulting in a large voltage drop E_{dl}. The actual field across the sample is small, as $E = E_{\mathrm{s}} + 2E_{\mathrm{dl}}$ and $E_{\mathrm{dl}} >> E_{\mathrm{s}}$. Source: adapted from Ishai et al. [112].

Thus, for the parallel plate electrodes, we would have

$$K = \frac{l}{A}$$

All conductivity meters have their own cell constant, which in simple cases can be calculated from the geometry of the probes, but is often found through a calibration. In fact, the cell constant is in essence the calibration factor to convert measured current and voltage into a conductivity value.

Cell constants are ideally fixed and constant (at some given temperature), but in reality can vary based on factors such as field effects (stray electric fields, which can, e.g. be broken by beaker walls), the conductivity of the solution, the measuring frequency (discussed more in section below), and cable resistance and capacitance [103, 111]. It can also change over time, so conductivity meters should be calibrated regularly. For two-pole cells (two-pole vs four-pole cells are discussed in the next section), one manufacturer recommends cell constants of $K = 0.1$/cm for pure water, $K = 0.4$ to $1\,1$/cm for environmental waters and industrial solutions, and up to $K = 10$/cm for high conductivity solutions [103]. This trend of cell constant makes intuitive sense; for higher conductivity samples, where resistance is lower, a longer length and smaller area can restrict the flow of current for a given voltage (or, alternately, produce a greater voltage for a given current).

1.9.3 Electrode polarization

Conductivity meters generally apply an alternating current between two active electrodes, and measure voltage, current, or both to calculate the impedance between the electrodes. In a two-pole cell, this impedance includes not only the resistance through the solution R_{s}, but also the electrode impedances from non-idealities like electrode polarization Z_{dl}. An inherent challenge in conductivity measurements is extracting the desired R_{s} while minimizing the error due to this additional impedance, which is described in greater detail below.

Under the influence of an applied electrical field (voltage), free ions in solution tend to move toward the electrode-solution interface. As shown in Figure 1.20, the migration of ions leads to the development of an ionic double layer, across which voltage drops rapidly. For a given applied voltage, the drop across the double layer detracts from the actual voltage applied across the

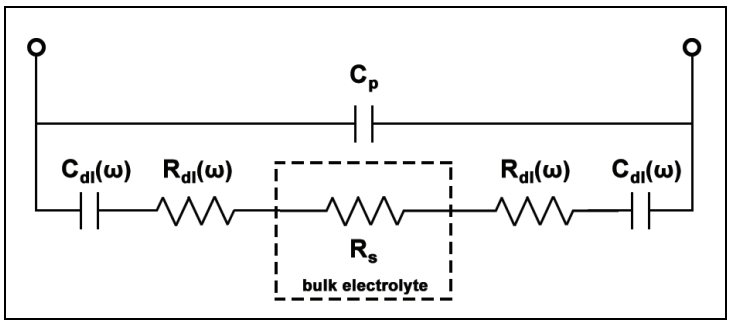

Figure 1.21: Equivalent circuit of two electrodes in solution, including impedance (R and C) from double layer formation at electrode surface.

bulk sample. The phenomenon is known as 'electrode polarization' (EP), since the distribution of charge reflects polarization of the electrode material [112].

If a DC current is applied between two electrodes, the double layer grows over time; in the limit, the current is zero and the system is essentially a giant capacitor (in practice, other non-idealities take over and the limit is not reached). AC excitation limits the growth of the polarization impedance Z_{dl}, but it can still be significantly non-negligible, especially at low frequencies (when capacitance can dominate) and with more conductive materials (when R_{s} is small and more easily swamped). Given that the boundary potential (ΔV_{dl} across the double layer) changes with current, the behavior of this electrode boundary can be characterized by a polarization impedance $Z_{\mathrm{dl}} = \Delta V_{\mathrm{dl}}/I$, which has resistive and capacitive components:

$$Z_{\mathrm{dl}} = R_{\mathrm{dl}} + \frac{1}{j\omega C_{\mathrm{dl}}}$$

that are generally modeled as two series components [113]. The effect of these EP components is especially pronounced for miniaturized electrodes, which have shorter path lengths and smaller cell constants [111].

An equivalent circuit is shown in Figure 1.21 that is generally valid as a model of a conductivity cell with AC excitation. A parasitic capacitance C_{p} has also been included in parallel with the electrolyte. This capacitance can arise from, for example, an effective 'capacitor' between the insulated bodies of the electrodes, or capacitance within the cable or wires.

Various theories and models exist for the actual physics at the electrode boundary [112], and the components of Z_{dl} can be further broken down into different resistance and capacitive elements deriving from different phenomena [111], but the end result is effective R_{dl} and C_{dl} that are both frequency dependent. Both decrease with increasing frequency[21] [113], as can be seen in Figure 1.22, which shows the measured impedance across a microelectorde array for three different solutions of different conductivity. The limiting values at high frequency correspond to the capacitance and conductance of the bulk electrolyte [114]. In contrast, the resistance from the double layer dominates the measurement at lower frequencies, so that the conductivity differences of the three solutions makes no difference.

[21] Note than a lower R_{dl} decreases the error in the measurement, while a lower C_{dl} increases it; a capacitance of 0 is effectively an open circuit ($Z = 1/(j\omega C) = \infty$, see Appendix B,Section C.1.1 for more discussion on capacitors). However, capacitance is generally less of an issue at higher frequencies due to the ω in the denominator of the complex impedance. Thus, given that C_{dl} decreases more slowly than frequency increases (slope in Figure 1.22a < -1), the net effect of the capacitance is still minimal at high frequencies.

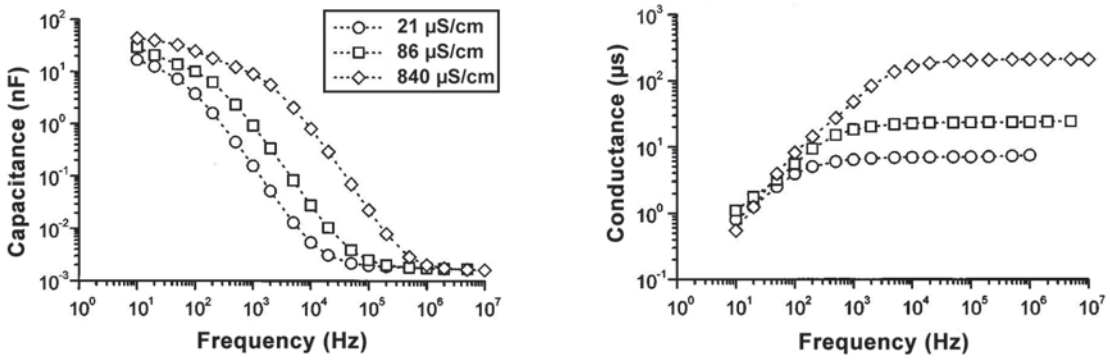

a) Capacitance. **b)** Conductance.

Figure 1.22: Capacitances and conductances measured (using an impedance analyzer) for a coplanar plate microelectrode array immersed in three different KCl solutions, as a function of frequency. Source: Green et al. [114].

In general, EP is a frequency-dependent phenomenon. As frequency of the AC excitation increases, the capacitive term becomes negligible and the R_{dl} term declines. Thus, high frequencies are favored for high conductivity measurements, when solution resistance is low and the series resistance and capacitance from EP play a larger role. However, at higher frequencies, parasitic stray capacitances also become more important; since C_{p} is in parallel with the electrode path, a smaller $1/(j\omega C_{\mathrm{p}})$ term would cause current to shunt through the capacitance. Thus, lower frequencies are favored for low conductivity measurements, when EP is less of an issue, but the higher solution resistance makes current shunted through the parallel C_{p} more problematic [103, 111]. Many conductivity meters adjust frequency automatically depending on the conductance of the sample; one manufacturer gives typical values of 94 Hz for a 4 to 40 µS range, and 47 kHz for a 400 to 2000 mS range [103].

Various algorithmic and hardware techniques have been used to reduce the effect of electrode polarization issues. Four-electrode designs have become commonplace, where in addition to the two active electrodes passing current, another two electrodes with high impedance are inserted to measure voltage (similar to a multimeter) [112]. These two electrodes draw negligible current and thus are not polarized, producing conductivity measurements directly proportional to the applied current [103]. These potential electrodes must also be small enough to not disturb the original potential distribution [111]. Then, EP impedances are theoretically eliminated; however, in practice, non-uniformity of polarization and parasitic influence from the potential-sensing electrodes can cause inaccuracies [112], including variations of the cell constant due to the finite size of the potential electrodes [111].

The material on the active surface of the electrodes also has a strong influence on the double layer and EP effects. In addition to proper choice of electrode material, coatings can be used to reduce the impedance at the electrode interface. Increasing the surface area, for example, can decrease impedance (as in a classic resistor, impedance increases as surface area shrinks); platinum black is a popular electrodeposited coating that provides a rough, porous surface with a large surface area. However, it is expensive and fragile, and the reproducibility of the deposition is poor. A larger surface area can also sometimes be achieved with mechanical rough-

Table 1.4. Typical temperature coefficient ranges for different electrolytes. Source: Radiometer Analytical SAS [103].

	Temperature coefficient (%/°C)
Acids	1.0 to 1.6
Bases	1.8 to 2.2
Salts	2.2 to 3.0
Drinking water	2.0
Ultrapure water	5.2

Table 1.5. Conductivity values at different temperatures for sample KCl and NaCl solutions. Source: Radiometer Analytical SAS [103].

	Conductivity (µS/cm)		
	KCl 7.5 % (1 M)	KCl 0.075 % (0.01 M)	NaCl 0.05 % (0.0085 M)
5 °C	74,140	896	628
15 °C	92,520	1147	814
25 °C	111,800	1413	1015
34 °C		1667	1206

ening. Other coatings to reduce the impedance interface include iridium oxide and conducting polymers, which each have their pros and cons [112].

Given that EP effects cannot be completely eliminated for two-pole electrodes, in practice one must be careful to calibrate near the measurement point. In thinking of the equivalent circuit as a voltage divider, one can see that, with some fixed R_{dl} (i.e. for a chosen excitation frequency) and fixed total voltage, the voltage across R_{s} is a nonlinear function of the resistance (and thus conductivity) of the solution. This translates to a nonlinear cell constant that changes with solution conductivity [103].

1.9.4 Temperature effects on conductivity measurements

Conductivity is highly temperature-dependent and mildly pressure-dependent [105]. In particular, conductivity rises with temperature, since an increase in temperature increases the mobility of ions; the number of ions may also increase as molecules dissociate. This dependence is captured by the temperature coefficient of variation, which gives the increase in conductivity, as a percentage, per 1 °C change in temperature [115]. The temperature coefficient varies with the measurement temperature, as well as with the ionic species (due to differences in the size of the ions and their charge density) [104]. It can be determined experimentally. A range of temperature coefficients for several solutions is given in Table 1.4, and the effect of temperature is also apparent in the conductivities of KCl and NaCl solutions at different temperatures (Table 1.5).

To facilitate comparison, conductivity values are often converted to values at a reference temperature (usually 20 °C or 25 °C). Conductivity sensors often include built-in temperature sensors, and many automatically convert the conductivity value before displaying (Automatic Temperature Compensation, ATC). Various temperature correction algorithms exist, with the simplest being a linear function using the temperature coefficient of variation as the slope. The method effectively linearizes around the reference temperature, i.e.

$$g_{\mathrm{Tref}} = g_{\theta} + \frac{\alpha_{\theta,\mathrm{Tref}}}{100} g_{\mathrm{Tref}} \times (\theta - T_{\mathrm{ref}}) \tag{1.18}$$

which is equivalent to

$$g_{\mathrm{Tref}} = \frac{g_\theta}{1 + (\alpha_{\theta,\mathrm{Tref}}/1\ 00)(\theta - T_{\mathrm{ref}})} \tag{1.19}$$

where θ is the measurement temperature, T_{ref} is the reference temperature (e.g. 25 °C), g_θ is conductivity measured at θ, g_{Tref} is the desired conductivity corrected to T_{ref}, and $\alpha_{\theta,\mathrm{Tref}}$ is the temperature coefficient of variation at T_{ref}.

Linear temperature compensation is accurate within a limited temperature range (where a nonlinear function can be approximated as linear), as well as to the degree that a suitable temperature coefficient is used. Many basic conductivity meters use simply a fixed temperature coefficient, e.g. 2 %/°C, which is a reasonable approximation for freshwater and many common dilute salts. However, since the temperature coefficient is not constant with temperature (i.e. the curve is not actually linear) and different ionic species have different coefficients, significant errors can arise in the reported conductivity. The error increases as the temperature of measurement ranges further from the reference temperature, which is why the temperature correction becomes less accurate as $|\theta - T_{\mathrm{ref}}|$ increases [103, 104, 115].

Non-linear temperature compensation may also be used. For example, the ISO/DIN7888 standard defines a non-linear correction for natural waters, in which a fourth degree polynomial is used to calculate the correction factor from the sample temperature to 25 °C [103]. As with the linear compensation, the non-linear compensation is only accurate to the extent that the compensation algorithm used is a good fit for the sample. Linear and non-linear compensation can provide different results, and it should not be assumed that the non-linear method is more accurate [115].

Different conductivity meters have varying degrees of sophistication in their ATC capabilities. Some allow, for instance, the user to input the temperature coefficient for use in a linear function, and some offer both linear and non-linear temperature compensation functions [104, 115].

Temperature effects present an additional challenge for miniaturized conductivity sensors, which may be susceptible to self-heating effects. These sensors often have a short path length through the solution, resulting in a large voltage drop across the double layer (electrode polarization). Not only does this increase the EP error in measurements, but it also results in greater power dissipation and, therefore, potential self-heating. Miniaturized sensors should be especially careful to limit currents; following this, highly sensitive and low-noise amplifiers are necessary to detect the smaller signals [111].

1.10 Temperature measurements

1.10.1 NTC Thermistors

Temperature is commonly measured using thermistors, thermocouples, or resistive temperature devices (RTDs). Thermistors (thermal resistors) are devices whose resistance depends on temperature in a predictable way. The resistance can either increase with temperature (Positive Temperature Coefficient, PTC) or decrease with temperature (Negative Temperature Coefficient, NTC). NTC thermistors are more common and are generally used in the range of $-55\,^{\circ}\mathrm{C}$ to $200\,^{\circ}\mathrm{C}$ [116, 117]. The temperature sensor used in this instrument is an NTC thermistor.

NTC thermistors have a nonlinear temperature response that is best approximated by the Steinhart-Hart equation, but in practice is often supplied by the manufacturer as a table. The nonlinearity poses a challenge for circuitry design, but NTCs are still widely used for their small size, fast response, and low cost. They are also sensitive to self-heating, which can occur with too much current; this property is in fact used in some applications.

NTCs are generally classified into three groups: bead (fast, fragile), disk and chip (larger, can handle larger currents), and glass encapsulated (bead type NTCs hermetically sealed in air-tight glass bubbles for stability and protection) [117]. Thermistor selection is very application-specific; important factors include the temperature range, resistance range, measuring accuracy, environment (surrounding medium), response time, and dimensional requirements [118]. For eddy correlation, the limiting factor is generally the speed; consequently, the thermistor also must be small, to allow for a smaller thermal mass (and faster response time). The NTC thermistor used in this study, the GP104L8F from U.S. Sensors, is a miniaturized glass encapsulated thermistor. The FP07 thermistor from GE used in other EC studies also consists of small-diameter glass-coated beads [6].

1.10.2 Thermistor circuitry

Thermistors are often used in conjunction with a Wheatstone bridge to convert the resistance to a measurable voltage (Figure 1.23). Compared to a simple voltage divider, the Wheatstone bridge is much more sensitive to change in resistance, as it measures a differential voltage between the thermistor and a different, similar voltage. This differential voltage can then be amplified by a suitable differential or instrumentation amplifier. Another option is to use a current source rather than a voltage source, and then convert the thermistor voltage (directly proportional to resistance) with another reference voltage [119].

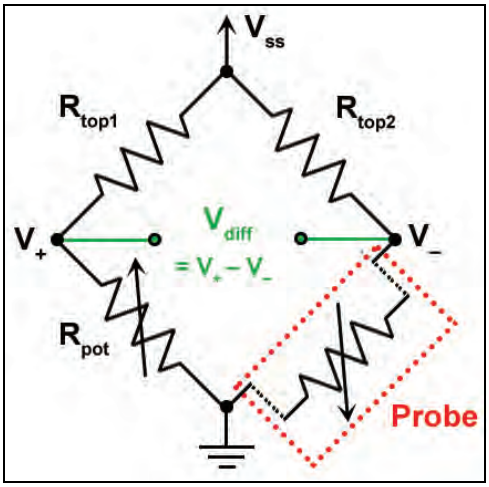

Figure 1.23: Wheatstone bridge.

One major challenge in designing for NTC thermistors is the nonlinear R-T curve. In principle, this nonlinearity can be handled in software; whatever voltage (and

hence resistance) is read in by the ADC, the microcomputer can map to the matching temperature. However, the R/T slope can change drastically across the desired temperature range. At the tail end of the curve, small changes in resistance must be detected for adequate accuracy; this requires an ADC with very high resolution (large number of bits), which is wholly unnecessary for other sections of the curve [120].

Thus, analog circuitry is often used to linearize the circuit response before digitization. For example, a resistor in parallel with the thermistor results in a flattened S-shape curve; however, this design decreases the sensitivity of the circuit [118]. Several other circuit designs exist to linearize the circuit as well [120]. Nevertheless, if the temperature range is known and not too wide, it is often easier to approximate the curve as locally linear. In the case of the Wheatstone bridge used in this project, the values of the resistors were chosen according to the target range, and the calibration curve was taken at a temperature similar to the sample temperature and approximated as locally linear.

1.11 Submarine Groundwater Discharge

One of the main applications of quantifying heat and salinity fluxes is the ability to measure submarine groundwater discharge (SGD) in certain locations.

Although the exact definition is subject to some debate, submarine groundwater discharge (SGD) in general is the discharge of groundwater out across the seafloor [121]. This includes not only fresh groundwater coming from terrestrial aquifers (e.g. groundwater is recharged by precipitation and then flows downhill to the ocean), but also oceanic processes such as convection (from seawater overlying freshwater), geothermal convection, tidal pumping, and waves. These processes can cycle seawater into the sediments, from which it is discharged as part of SGD [122].

Almost all coastal zones are subject to groundwater flow, either through submarine springs or disseminated seepage [121]. Freshwater environments can certainly also contain groundwater inputs or outputs, e.g. lateral inflow or outflow of a river. However, the processes are usually less complicated than in coastal ecosystems, so much of the research on groundwater discharge has focused on marine settings.

1.11.1 Importance of SGD

SGD is an important pathway by which solutes enter the ocean; in fact, due to the generally high concentration of dissolved solids in groundwaters (relative to surface waters), SGD can make a disproportionately large contribution to solute flux in coastal ecosystems [121]. It is also poorly understood and difficult to quantify, being essentially 'invisible', and thus is the "least studied element of water, salt, and nutrient budgets of the coastal oceans" [123].

Contaminants in the groundwater, such as nutrients, heavy metals, radionucleotides, and organic compounds, can have a large effect on the biogeochemistry, ecological balance, and water quality of receiving waters. For example, nitrogen outflow from groundwater contaminated by septic systems or agricultural runoff has created eutrophication issues at several sites. SGD can also impact the hydrological regime of the site, due to saltwater intrusion, as well as sediment stability of the shoreline [121]. Note that marine-origin SGD from seawater cycled through sediments can also be a source of significant geochemical flux, as it can undergo changes as it cycles through the pore spaces of the coastal aquifer [122]. Numerous examples and descriptions of the ecological impact of groundwater are given by Burnett et al. [121] and references therein.

The ability to quantify SGD is of great practical importance; if SGD is determined to be a significant factor in a particular area, it can inform and affect management decisions. For example, nutrient or other solute loading can be used as a basis for land-use planning, or water levels and fluxes can be managed through controls on withdrawal or alterations in recharge patterns. Managers can also influence the quality of the groundwater, e.g. through controls of land use or waste disposal. However, SGD must first be quantified to determine it's importance in the area of interest, which is quite challenging due to its complex nature and 'invisibility' [121].

1.11.2 Characteristics and drivers of SGD

As discussed above, SGD by definition includes both the movement of terrestrial groundwater flowing to the ocean, as well as seawater cycled through permeable sediments by marine processes. In addition, coastal aquifers can be quite complex, potentially comprising a combination of confined, semi-confined, and unconfined systems. Consequently, SGD is affected in complicated ways by a number of terrestrial and marine drivers, such as hydraulic gradient (water flowing downhill), tides, waves, and convection [121]. It can also consist of multiple components of different origin and character. The mixing zone of freshwater and seawater that is formed within the coastal plain and seafloor sediments has been termed the 'subterranean estuary', in recognition of its similarities to its surface counterparts [123].

The intrinsic components of SGD are fresh groundwater discharge (FGD), deep saltwater discharge (DSD), and intertidal saltwater discharge (ISD), delineated by saline recirculation zones above and below the freshwater discharge. These three components, which typically carry different solute loads to the sea, are influenced in different ways by different driving factors, and can evolve separately from each other (for example, the intertidal saltwater cell, which discharges ISD into the ocean during low tide, can appear and disappear with the lunar cycle) [23]. The relative amount of these components can vary; at some locations, recirculated seawater can account for 90 % or more of the discharge [121].

Since SGD is driven by a composite of factors that overlap in both space and time, it is difficult to define globally identifiable patterns, trends, or characteristics. Temporal trends have been observed on both shorter and longer time scales (e.g. semidiurnal or diurnal tidal relationships, versus seasonal shifts in the freshwater-seawater interface due to the annual recharge cycle) [121]. Discharge rates can also vary quite quickly; in a study of a fractured rock aquifer on the Brazilian coast, seepage rates were measured that changed as much as 110 cm/d over a 5 min interval [22].

SGD is also known to have high spatial heterogeneity. In the same fractured rock aquifer study, one benthic chamber measured an average of 8.2 cm/d (and up to 43.4 cm/d), while another device nearby measured an average of 190 cm/d (and up to 378 cm/d). Another pair of chambers 14 m closer to shore measured average rates of 5.5 cm/d and 4.3 cm/d. The spatial heterogeneity observed in this study was likely more pronounced than at many other sites, as the fractured rock aquifer shows an irregular bedrock surface where exposed, and preferential flow paths along rock fractures could be expected [22, 123].

Based on a series of five intercomparison experiments in different geological settings, Burnett et al. [121] conclude that SGD is fairly ubiquitous in the coastal zone, though spatial and temporal variation are common. Rates above 100 cm/d are considered high, while values below 5 cm/d are considered low. Spatially, it usually decreases with distance from shore, but is elevated near submerged springs.

1.11.3 Current methods of measuring SGD

Several well-developed methods exist to measure SGD; however, no one method has been established as the gold standard. Not only do the inherent spatial and temporal variability of

SGD make it challenging to capture comprehensively, but each method also has its own generalized assumptions and inherent errors. It is generally recommended to apply more than one approach, covering multiple geographic scales [121, 122].

The most common method of direct measurement is with **seepage meters**, which can be relatively simple, inexpensive, and accurate [122]. The basic seepage meter is analogous to a benthic chamber; a steel drum with a plastic bag is inserted into the ground, and the water that enters or leaves the bag is measured. Seepage meters cover small spatial scales, so that many must be deployed to adequately cover the spatial and temporal variability of groundwater flow. Several variations exist to automate the measurements and allow for continuous collection [121].

Another common technique is the use of **natural geochemical tracers**, such as ^{222}Ra or radium isotopes. Tracers are generally chosen that are enriched in the groundwater relative to the receiving water, as well as conservative and easy to measure. To quantify SGD by this approach, all sources and sinks of the tracer must be identified, as well as the residence time of the surface water body. Then, groundwater flow can be estimated from measured or estimated tracer concentrations (in both surface and groundwater) using a mass balance model [121]. Tracers provide an estimate of total SGD but cannot distinguish between different sources; they are also much more expensive and involved than seepage meters [122]. In addition, it is often difficult to quantify all sources and sinks. However, they provide an integrated signal and tend to smooth out small-scale variations in time and space [121].

Salinity differences have been used as tracers for freshwater SGD, but may not be useful for brackish or saline fluxes into a marine environment. Temperature differences between the ground and surface water have also been used as a tracer, using either temperature-depth profiles, or direct temperature differences in the two systems measured using infrared sensors or other methods [121].

Numerical simulations and models have also been used to estimate SGD. By simplifying features of the aquifer system, hydrological models enable better understanding of subsurface systems, as well as allow analysis of SGD movement under different hypothetical conditions [122]. However, they are limited by the inherent complexity of aquifer systems. For example, hydraulic conductivity can vary several orders of magnitude within short distances, so that obtaining a sufficiently representative value is challenging; models often also fail to capture some of the processes that drive SGD, which can be terrestrial or marine, vary in time, and drive all or part of the flow. Thus, model results often do not compare well with seepage meters and tracer measurements [121].

1.11.4 SGD measurement via eddy correlation

Crusius et al. [6] studied SGD using eddy correlation at a small estuary on Cape Cod, MA, by measuring heat and salinity fluxes using eddy correlation. The derivation from SGD flow using heat/salt balance equations are given in Appendix A, Section A.5. This technique requires knowledge of the temperature / conductivity of both the groundwater and surface water, which can be measured with probes above and below the sediment-water interface. The values measured in their study ranged from $T = 12.0\,^{\circ}\mathrm{C}$ and $S = 0$, likely representing fresh groundwater, to values close to the bottom-water values of $T \approx 19.3\,^{\circ}\mathrm{C}$ and $S \approx 29$. The authors

used the lowest estimates for their calculations, noting that if the cold, freshwater component of groundwater were mixing with more brackish porewater or groundwater, the calculated discharge would be higher.

Temperature was measured using a GE FP07 thermistor, which had a 90 % response time in the lab of 0.096 s for a transition from T =22 °C to 16 °C, and a mean amplitude of noise of 0.00084 °C in the field. The conductivity sensor was a four-electrode cell with four platinum wires and a sub-millimeter sensing volume. Its measured 90 % response time in the lab was 0.013 s for a transition from S =0 to 25, and the mean amplitude of noise was 0.0042 PSU. However, when used in the field, the signal contained abrupt spikes and changes of the mean, which were attributed to particles lodging in the electrodes at the sensor tip. As a result, conductivity measurements were only available for a short amount of the time. When available, SGD estimates from heat and salt, which can serve as two semi-independent tracers of each other, agreed reasonably with each other ((16.9 ± 2.9) cm/d for conductivity vs (20.7 ± 2.9) cm/d for heat) as well as with previous estimates made using seepage meters and tracer studies.

This study placed confidence in EC as another technique to estimate SGD. Note, however, that EC can only be used to estimate SGD where there is an appreciable temperature or conductivity (or, with our sensor, fluorescence) contrast between the groundwater and the surface water, creating a measurable heat or salinity (or fluorescence) flux. This technique also assumes that there is no momentum input, i.e. the groundwater advects into the surface water with such little momentum that the heat and salinity it carries subsequently move higher in the water column predominantly by turbulent diffusion only. The extent to which this assumption is valid at field sites of practical or scientific interest, and the extent to which EC can be applied or should be modified in cases where it is not (e.g. information can potentially be extracted from the 'mean' values removed in the Reynolds' decomposition), is a topic for future discussion.

1.12 Flux tracing

The trimodal sensor developed in this project enables testing of the hypothesis that the EC-measured flux of one chemical (or a parameter, such as conductivity or temperature) can be used to infer another. If true, then eddy correlation could potentially be used to measure fluxes of compounds for which EC-capable sensors do not exist, such as organic pollutants, toxic metals, and pesticides. The flux of these toxicants from sediments into surface waters create a significant environmental health risk, and the ability to measure them would be extremely helpful for the assessment and optimized cleanup of contaminated sediments.

This plausibility of 'flux tracing' is founded on the hypothesis that many mobile (i.e. dissolved or colloidal) chemicals in sediment porewaters are co-transported across the sediment-water interface. Whether by diffusion, advection, bioirrigation, or bioturbation, these transport processes should act on all chemicals similarly (with correction for, e.g., molecular diffusion coefficients in some cases). Thus, at any given site, the flux of chemicals from the sediment porewater into the overlying surface water might be expected to occur in proportion to their mobile concentrations in porewater.

Fluorescent dissolved organic matter (FDOM) is a promising choice as a naturally occurring tracer. As discussed in Section 1.6, it can be measured with fluorescence spectroscopy—in fact, its signal is often so strong as to interfere with weaker fluorescent signals, such as those from polycyclic aromatic hydrocarbons (PAHs). It is also likely to have a measurable benthic flux, due to is presence with elevated concentrations in many, if not most, sediments [e.g. 14, 86, 124]. Finally, not only is it plausible that it is co-transported with other compounds as discussed above, but natural organic matter has been known to bind some toxicants, such as PAHs and heavy metals (to varying degrees depending on a number of factors) [125, 126], and thus may be directly linked for co-transport.

The temperature and conductivity capabilities of the flux sensor can also be used for flux tracing, either as a sense check for FDOM, or as the principle tracer at sites that lack sufficient FDOM fluxes. As discussed in Section 1.11, submarine groundwater discharge is an important source of biogeochemicals to coastal ecosystems, and can potentially be inferred from heat or salinity fluxes. In addition, conductivity is itself a water quality parameter and can be expected to correlate with concentrations of contaminants. For example, in a study of two rivers in Brazil, Sousa et al. [127] found that electrical conductivity was strongly correlated with a variety of pharmaceuticals such as ibuprofen, likely because of their transport in wastewater and the conductivity contrast of wastewater with the receiving water.

Calculations for flux tracing would involve scaling the EC-measured flux of the tracer species (FDOM, conductivity, and/or temperature) by a site-specific ratio that relates the toxicant's concentrations to that of the tracer. The flux tracing concept is similar to the proposal by Holtappels and Lorke [128] to expand the suite of measurable solute fluxes, by combining measurements of solute gradients in the bottom boundary layer with DO flux measurements obtained using EC (flux ratio method). However, a technique with FDOM that calculates ratios from porewater samples avoids some of the challenges of measuring concentration gradients, such as the additional equipment required for simultaneous concentration measurements and the restriction to systems with low energy flow (in which concentration gradients can be detected).

Chapter 2

Optical fiber spectrofluorometer suitable for eddy correlation

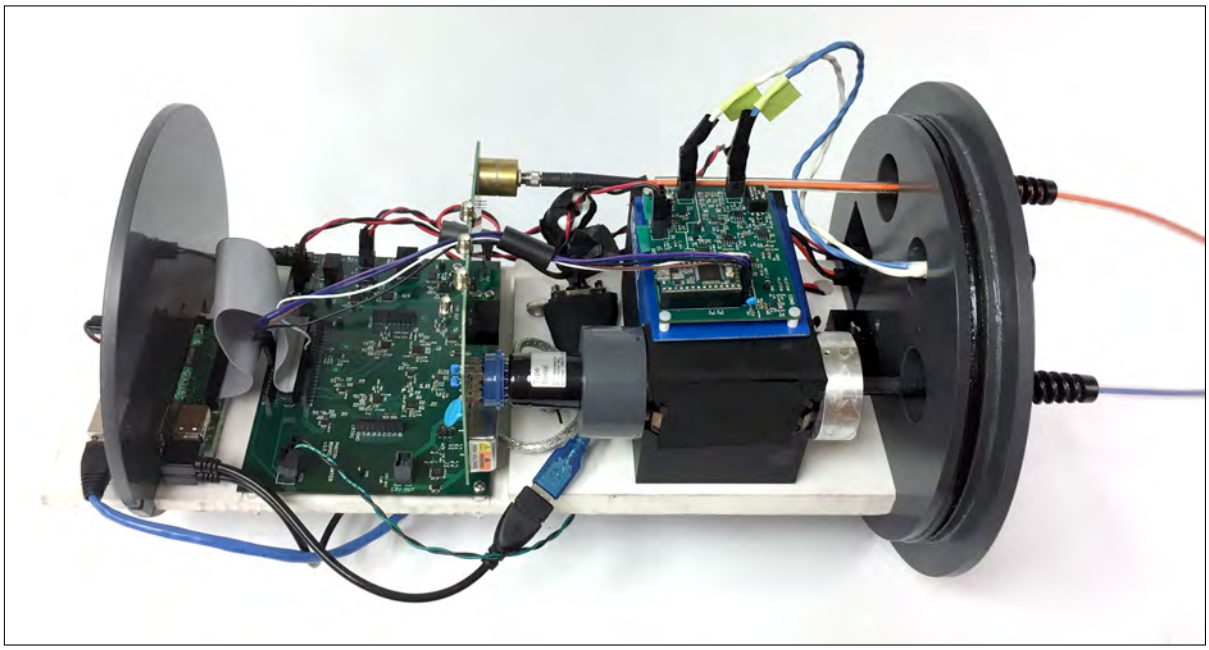

Figure 2.1: Interior electronics of instrument.

The instrument is shown in Figure 2.1.

2.1 Microcomputer

The instrument is centrally controlled by a Raspberry Pi 3 Model B microcomputer (1.2 GHz Broadcom BCM2837 64 bit CPU; Figure 2.2) running Raspbian, an operating system based on Debian (a Linux distribution) [129]. The Raspberry Pi is connected to the various components

it controls by USB and GPIO pins. Code is written in C++ and C and compiled by the g++ compiler; a summary of the code modules is available in Appendix F.

The user operates the instrument by communicating with the Raspberry Pi, which then controls and coordinates the different components of the instrument. Since wireless communication is unreliable underwater, communication with the Raspberry Pi is through wired Ethernet connection. All user communication with the Raspberry Pi is done by logging in remotely through Secure Shell (ssh and scp) using a terminal emulator on a separate computer. This then grants the user access to the Pi's command line. To enable the Pi to continue running the instrument even after the user disconnects, the terminal multiplexer tmux is used [130]. The user starts a tmux session upon logging in, starts the program and issues commands to measure, and detaches from the session before logging off. The user can then log in again at a later time and reattach to the session.

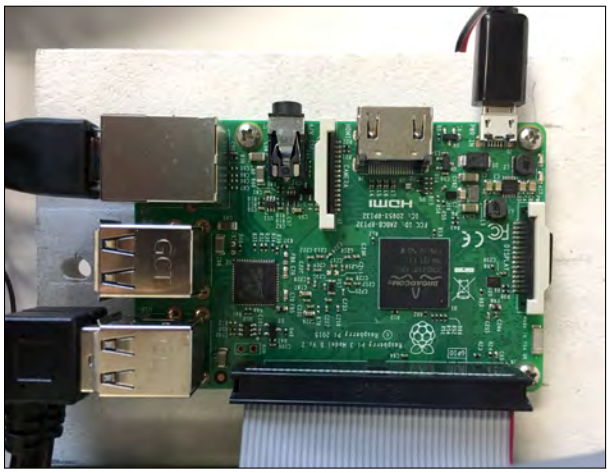

Figure 2.2: Raspberry Pi 3

2.2 Fluorescence sensor

The principle chemical sensor in the eddy correlation instrument is an optical fiber spectrofluorometer capable of high-speed, high-resolution *in situ* measurements of fluorescing compounds. A block diagram of the driving electronics is shown in Figure 2.3.

2.2.1 Excitation

The instrument utilizes a (375 ± 10) nm LED to excite fluorescence in the compound of interest (ThorLabs LED370E; Figure 2.4). This wavelength is suitable for detecting compounds such as humic substances (dissolved organic material), dyes such as fluorescein and rhodamine, and several fluorescing contaminants, including many polycyclic aromatic hydrocarbons (PAHs). The LED can also be easily exchanged for a different excitation source, such as a different wavelength LED to target other compounds, or a laser diode for greater signal. Optional modulation of the light source (with 50 % duty cycle) allows rejection of ambient light if necessary, and is described further in Section 2.2.7.

Figure 2.4: LED in lens tube

A typical driving voltage used for the LED is 3.83 V. From the measured I/V characteristics (Figure 2.5), this corresponds to a current higher than the manufacturer's maximum rating of 30 mA. In general, LEDs can be overdriven to produce higher intensity (especially when modulated), at the expense of operating life. During the course of development, LEDs were

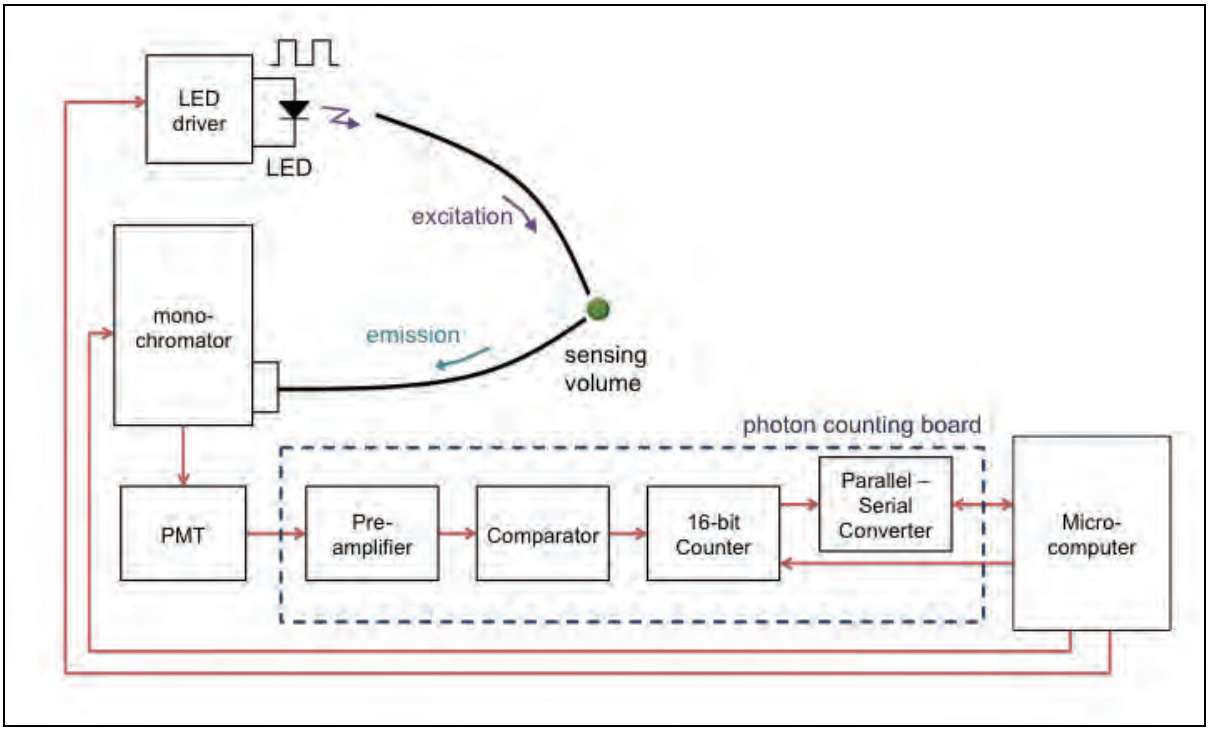

Figure 2.3: Block diagram of electronics for fluorescence sensor.

observed to experience a reduction in output light intensity as they aged, requiring higher and higher drive voltages until the LED was replaced.

The LED plugs into a circuit board containing its driving circuitry, which includes a thumbwheel potentiometer to adjust its drive voltage, and a bipolar junction transistor (BJT) that enables the microcomputer to turn it on and off. It is housed in a custom lens tube (two brass nuts soldered together and threaded with SM05 thread, then epoxied to the circuit board), which enables coupling with an optical fiber via an SMA905 connector. The LED and optical fiber are positioned as closely as possible; however, butt coupling in general is relatively inefficient, so that only a fraction of the LED output enters the optical fiber. Overdriving the LED as discussed above was thus found to be necessary to achieve the desired sensitivity.

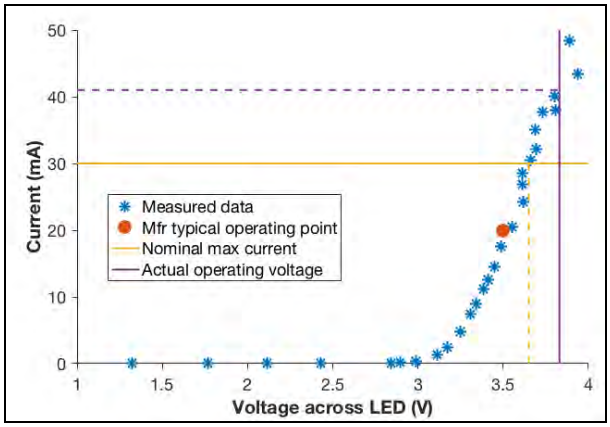

Figure 2.5: Measured I/V curve for a typical ThorLabs LED370E LED, along with 'typical operating point' given on manufacturer spec sheet. The specified maximum current (and corresponding voltage), as well as actual operating voltage (and corresponding current) chosen for this project, are also marked.

2.2.2 Optical fibers

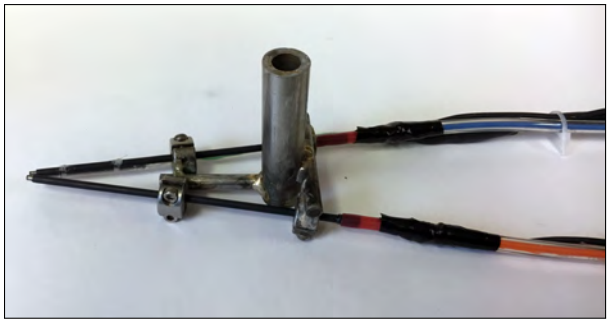

Figure 2.6: Optical fibers in holder

To carry light to and from the sensing volume, the system uses a pair of ⌀ 1000 µm core multimode silica optical fibers (ThorLabs FT1000UMT). These optical fibers have a numerical aperture of 0.39, and transmit light within the range of 300 to 1200 nm with less than 200 dB/km attenuation. They are cut to 2 m long, encased in ⌀ 3 mm (OD) PVC furcation tubing, and patched and polished for an SMA905 connector on one end and a bare fiber on the other end. The bare end of each optical fiber is epoxied into a 15 cm length of ⌀ 2 mm (OD) stainless steel tubing for stiffness and protection. Each optical fiber is then further encased with ⌀ 1/4 ” (OD) PVC Tygon tubing, which is plugged at each end with silicone RTV adhesive to prevent water entry.

The optical fibers are held at a 20 ° angle relative to each other, with the stainless steel-encased tips ∼1 mm apart at the closest point (Figure 2.6). One optical fiber carries light from the LED, while the other carries light back to the detector. The sensing volume is the intersection of the cones of excitation and acceptance. The choice of angle and spacing are discussed further in Sections 2.3.4 and 2.3.5 on optical optical fiber positioning and performance with humic acid, respectively.

The use of optical fibers allows the spectrofluorometer's sensing volume to be distal to the bulkier electronics package, to avoid disturbances to the flow field. It also provides flexibility in positioning so that the sensing volume can be aligned to the ADV's while minimizing interference with velocity measurements.

2.2.3 Monochromator

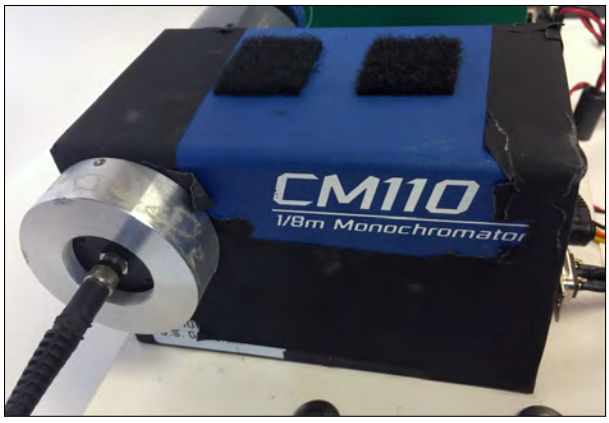

Figure 2.7: Monochromator

The first stage of the detector is the tunable monochromator (Spectral Products CM110, Figure 2.7), which filters the detected light to the target emission wavelength. The emission optical fiber couples light into the monochromator via a custom-made PVC connector threaded with SM1 thread and installed with an SMA905 connector. The output, consisting of emitted light at the target wavelength, is coupled to a photomultiplier tube (PMT) for detection via another custom PVC connector. Plastic was chosen for the connectors over metal to avoid electronic coupling from the monochromator's chassis. Both pieces secure onto the monochromator's flanges via three evenly-spaced #6 set screws.

The output wavelength of the monochromator is adjustable via software, which sends commands to turn the monochromator's grating. The commands are sent by the microcomputer via RS232 serial interface through a USB adaptor. The tunability of the monochromator enables the detected emission wavelength to be adjusted within the range of ∼185 to 650 nm. Thus, the instrument can potentially be used to target a variety of compounds that fluoresce at different wavelengths, as well as to characterize the fluorescent chemical composition of the environment by scanning the emission spectrum.

2.2.4 Photomultiplier tube (PMT)

To quantify the light, the system uses a fast photomultiplier tube (ET Enterprises 9111WB, Figure 2.8) in photon counting mode [131, 132]. The use of photon counting allows for maximum sensitivity in detecting small amounts of light, which is important in this system because the amount of light transmitted by the optical fibers is limited. The PMT is powered by an xp CA12N high voltage supply, a compact and economical supply capable of supplying up to −1250 V. Details regarding the circuitry are provided in the following section.

Figure 2.8: Photomultiplier tube

The PMT is secured in its PVC connector to the monochromator using a press-fit mechanism with two ultra-compressible -120 O-rings to hold the PMT steady, and a standard -120 O-ring as a stopper. During general use, the entire PMT and connector were encased in optical tape to reduce light leakage to the extremely light-sensitive device.

2.2.5 Photon counting circuitry

A labelled diagram of the photon counting circuitry is shown in Figure 2.9. For schematics and board layout, see Appendix E.

PMT voltage divider

The 10-dynode photomultiplier tube is driven by an anode-grounded voltage divider located directly on the photon counting circuit board. The resistor values for the voltage divider were chosen based on the PMT requirements, expected anode current, and desired gain for this application. The circuitry was also optimized for photon counting, with features such as RC filters, decoupling capacitors, and damping resistors, as well as proper choice of components and attention to high frequency layout [133–136]. For more information on the design of the PMT circuitry, see Appendix B, Section B.1. For more information on its performance, see Section 2.3.1.

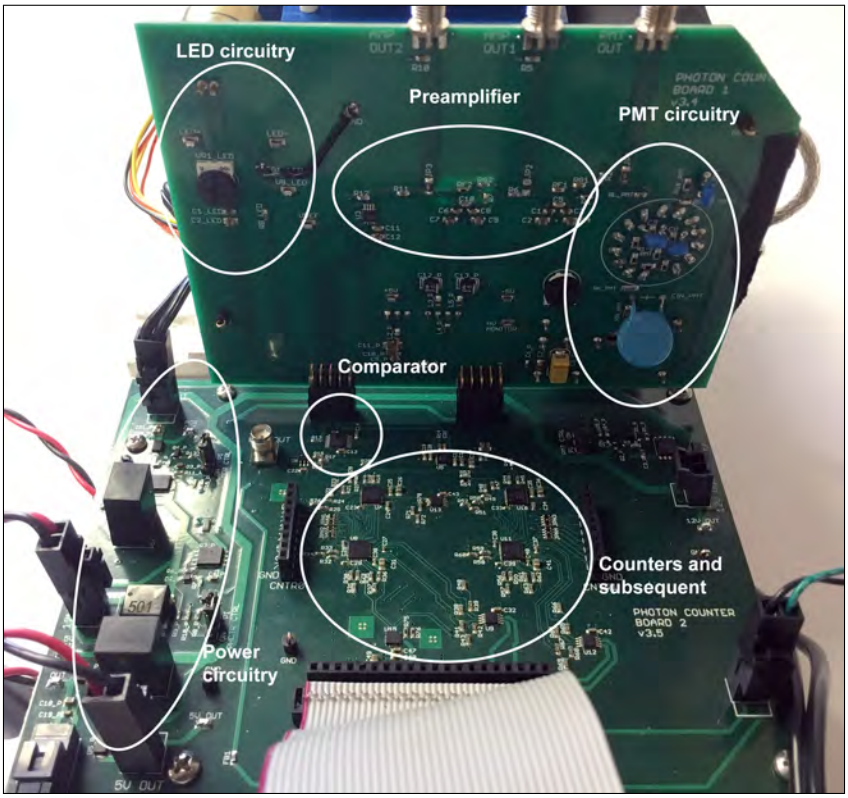

Figure 2.9: PMT and photon counting circuitry

Preamplifier

The electrical pulses from the photons, as output by the PMT, are short (on average a full width half maximum duration of 1 to 2 ns), small (down to 5 mV amplitude), and negative. Thus, the PMT output is amplified and inverted by a two-stage operational amplifier circuit in close proximity to the PMT voltage divider. High-bandwidth current-feedback operational amplifiers are used (Texas Instruments OPA695) to capture the small, fast photon pulses. The gain must also be carefully chosen; too low a gain will fail to amplify smaller pulses to a detectable level, while too high a gain can amplify noise into false signals, as well as widen the photon pulses (from the gain-bandwidth product) and potentially merge them. The gain values of -10 and $+8$ used here were chosen by observing output pulse characteristics (timing and amplitude) at different gains using a fast digital oscilloscope (Figure 2.10a).

Comparator

The amplitude of the photon pulses depends on the gain set by the PMT voltage divider, as well as the statistic emission of the PMT dynodes. In this application, they varied from -5 to several hundred mV as output by the PMT, with the amplified pulses directly reflecting their differing amplitudes. To standardize the photon pulses, a fast comparator (Analog Devices ADCMP553) is used, which produces an output pulse for only input pulses above a certain threshold (Figure 2.10b). The threshold of the comparator is connected to a digital

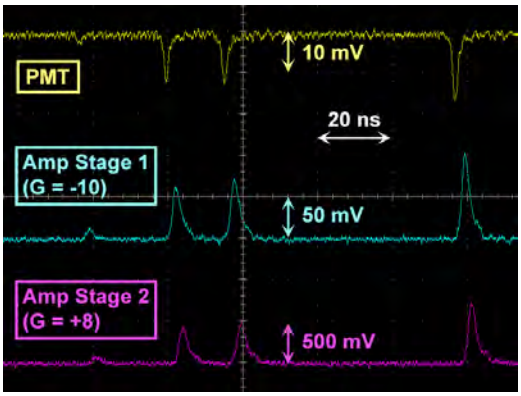

a) Successive stages of preamplifier output.

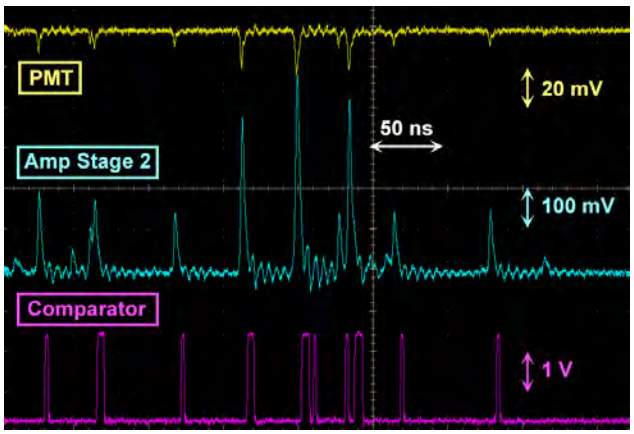

b) Preamplifier and comparator output (translated from LVPECL to TTL by a differential receiver).

Figure 2.10: Oscilloscope trace showing various stages of photon counting circuitry. The comparator translates photon pulses to a digital signal by standardizing all pulses above a given threshold.

Note: ringing in amplifier output in Figure 2.10b is due to impedance mismatch from using an on-board environment of 75 Ω, as recommended by the manufacturer, while terminating with 50 Ω within the scope. It would not be present in normal operation; instead, signals would more resemble those in Figure 2.10a, which was taken using a separate 50 Ω test board and thus does not exhibit ringing.

potentiometer and is thus controllable via software. A lower threshold allows greater sensitivity because even smaller pulses can be detected; however, too low a threshold may result in noise being falsely detected as photons. A default value of 200 mV was chosen based on the observed output of the second stage of the preamplifier.

The comparator effectively converts photon pulses to LVPECL differential signals. The use of differential signaling for the remainder of the circuitry is a natural choice for such high-speed digital data.

Counters and subsequent circuitry

The photon pulses, output as LVPECL signals by the comparator, are counted directly on the board by two chained 8-bit counters. The high-speed counters used, MC100EP016A (On Semi), have operational frequency > 1.3 GHz and produce 8 single-ended outputs each at LVPECL levels. The small voltage range of the LVPECL standard makes these outputs more susceptible to noise, but allow faster operation.

The 8-bit output of each counter is fed to a M100EP446 parallel to serial converter, which likewise accepts eight single-ended ECL inputs and is clocked by the microcomputer. The serial stream, presented as differential output, is translated to TTL signals by differential receivers before being read in by the Raspberry Pi.

In general, transmission of information to and from the Pi requires several translators, fanout buffers, and translating fanout buffers. The radiated noise from these fast-transitioning signals is often enough to trigger the sensitive, high-speed devices, and thus ferrite beads are used to

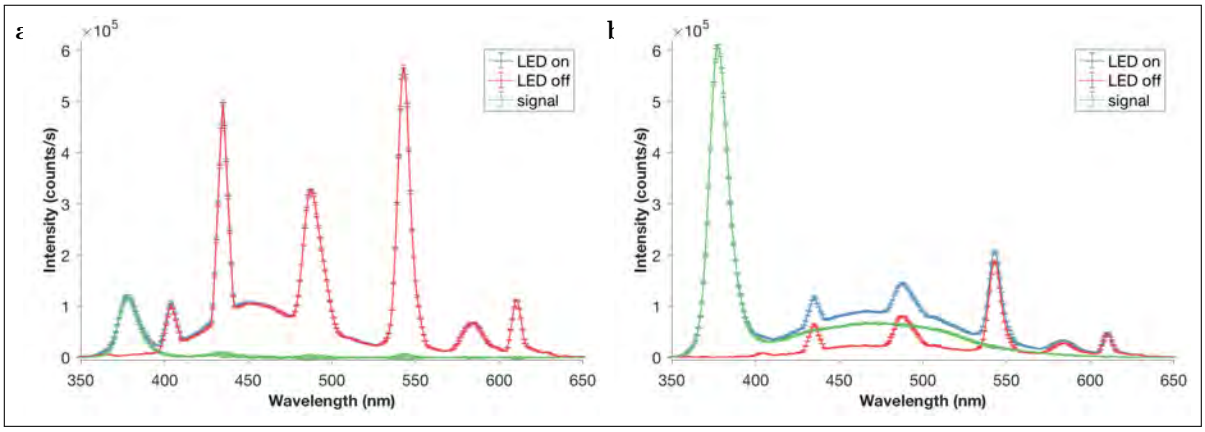

Figure 2.11: Demonstration of modulation through spectral scans of **a)** deionized water and **b)** 6 ppm humic acid solution taken in the presence of typical room lighting. Light levels are measured with both the LED on and LED off, and the difference represents only the fluorescence excited by the LED.

absorb some of the high-frequency switching noise [137, 138].

2.2.6 Raspberry Pi control

The Raspberry Pi microcomputer controls all operations, including starting and stopping counting, reading in the photon counts as a digital number, resetting the devices, and processing and storing the data. Some specific processing steps are required to handle counter rollover; see Box 2.1 for more information. The processing time incurred by the Pi is minimal, as described in Appendix B, Section B.2.

The Raspberry Pi also controls the monochromator and LED. Thus, through the programmed user interface, the instrument can be instructed to take a spectral scan (by stepping the monochromator in user-selectable increments), measure repeatedly in place and output aggregate results, or take a time series with some specified frequency. The integration time, as well as the frequency of the optional LED modulation, are also adjustable.

2.2.7 LED modulation

The optional modulation feature is demonstrated in Figure 2.11, which shows spectral scans of DI water and 6 ppm humic acid solution. The instrument alternates between measuring with the LED on and with the LED off, and subtracts the two to determine fluorescence excited by the LED. Ambient light, such as the large room light peaks shown in Figure 2.11, is detected when the LED is both on and off, and thus is subtracted out.

Source modulation is an incredibly useful technique for intensity-based optical sensors, as discussed in Section 1.7.3 (p. 77), and is essential in the presence of potentially changing ambient light levels. However, relative to measurements made completely in the dark and with the LED on, it does cut the effective integration time in half (for a 50 % duty cycle) for any given measurement speed since, for each data point, the instrument must spend time measuring with

Table 2.1. Pulse characteristics at various stages as observed by oscilloscope. Values are rough estimates, as testing conditions differed from actual operation conditions (measured on a standalone board, external connections to DPO, and voltage supply $-1035\,\mathrm{V}$ vs. $\sim -1100\,\mathrm{V}$ used in final instrument; the oscilloscope trigger of 100 mV on the stage 2 amplifier output also invariably influenced photon selection).

	Mean amplitude (mV)	Mean noise (mV)	FWHM[a] duration (ns)	Duration >100 mV[b](ns)
Test 1: Three channels connected to oscilloscope ($N = 145$)				
PMT output	-9.3 ± 2.7	0.43 ± 0.05	1.50 ± 0.25	
Amp stage 1	46 ± 15	1.80 ± 0.25	2.20 ± 0.28	
Amp stage 2	172 ± 61	4.5 ± 1.3	2.20 ± 0.18	1.80 ± 0.67
Test 2: First stage of amplifier disconnected ($N = 168$)				
PMT output	-9.1 ± 2.4	0.43 ± 0.06	1.50 ± 0.25	
Amp stage 2	176 ± 52	4.4 ± 1.2	2.10 ± 0.19	1.80 ± 0.58

both the LED on and off. The results in a loss of signal-to-noise ratio, as will be described in Section 2.3.2.

2.3 Performance of fluorescence sensor

2.3.1 Precision and accuracy

Photon characteristics

Table 2.1 summarizes pulses observed by a high-speed oscilloscope at the PMT output, first stage of the amplifier, and second stage of the amplifier. The amplifier is nominally set for gains of -10 and $+8$, but the actual gains may be lower due to the high bandwidth (gain-bandwidth product).

Signal quality

With this circuitry, the PMT produces single-photon electrical pulses that are only a few nanoseconds long with minimal ringing. Ringing is largely due to reflections from impedance mismatches in the current path [139]. It was observed in the first generation design of the instrument, which used a Hamamatsu H5783-03 PMT module with built-in high voltage supply and voltage divider (Figure 2.12a). The oscillations from ringing can continue for many cycles, potentially generating false positives while decreasing sensitivity by requiring a higher comparator voltage. For the second generation system, the custom PMT voltage divider (documented in Appendix B, Section B.1) included design components to reduce ringing, such as a dampening resistor, which substantially improved the quality of the photons (Figure 2.12b).

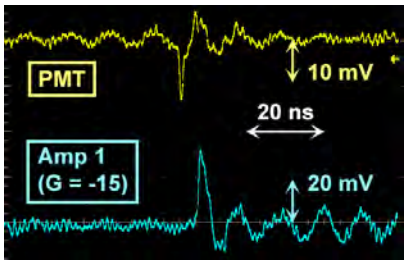

a) Photon pulses from Hamamatsu H5783-03 PMT module, exhibiting ringing characteristics.

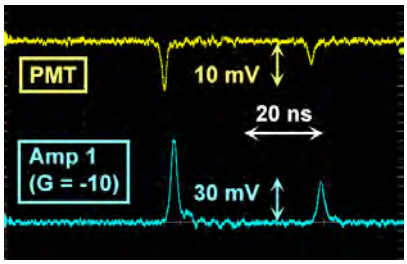

b) Photon pulses from current instrument with on-board PMT circuitry and amplifier, designed to reduce ringing and susceptibility to noise.

Figure 2.12: Oscilloscope traces showing photon pulses at PMT anode and after one stage of amplification.

More generally, the preamplifier circuit is extremely sensitive to noise (which has the same effect on photon counts as ringing), due to its high gain and bandwidth which are necessary for detecting the photon pulses. For example, the first generation of the instrument, which used a Hamamatsu PMT module that connected to the preamplifier circuit board via short BNC connectors, was observed to often pick up radiated RF (radio frequency) noise from the environment (Figures 2.13a and 2.13b). The FM radio band (89 to 110 MHz) was especially prominent in the Fourier transform of the amplifier output, while noise in the 50 to 88 MHz range was attributed to the monochromator (i.e. decreased substantially when it was off) (Figure 2.13c).

Sensitive analog circuits in general are incredibly susceptible to radiated electromagnetic interference (EMI). Radiated EMI makes its way into the circuit through antenna-like structures, cables, and sneak ground connections, where it can spike or otherwise impact the ground plane [140–142]. In this case, much of the noise was traced to the BNC connection, which might have acted as an antenna. It was addressed in the second-generation system by integrating the PMT, preamplifier, and subsequent circuitry onto one board, resulting in much cleaner, low-noise signals (Figure 2.14).

Noise arises not only from radiated EMI, but also from a variety of sources such as ground loops and cross-talk. Especially in a high-speed circuit like this one, it can degrade signal quality at any stage and/or lead to improper functioning. For example, the digital TTL signal from the microcomputer to initiate the counting was observed to spike the preamplifier signal and generate false counts. In this case, a series ferrite bead was sufficient to dampen the voltage spikes and prevent false positives. Much of the work on this sensor was dedicated to reducing noise to acceptable levels. Proper circuit layout was especially important, including attention to ground plane, board layering, mixed digital-analog layout, and other high-speed circuitry design considerations [139, 143–146]. The system also makes ample use of chokes, cores, and ferrite beads, which use magnetic inductance and lossy materials to dissipate noise of generally MHz-range frequencies (depending on the bead) [137, 138, 141].

Another factor affecting PMT performance in pulse-counting applications is the presence of afterpulses. Afterpulses are spurious pulses that appear in the output signal after true photon pulses, and can be problematic in obtaining an accurate photon count. One type of afterpulse appears with a short delay (several nanoseconds to tens of nanoseconds) and is caused by elastic

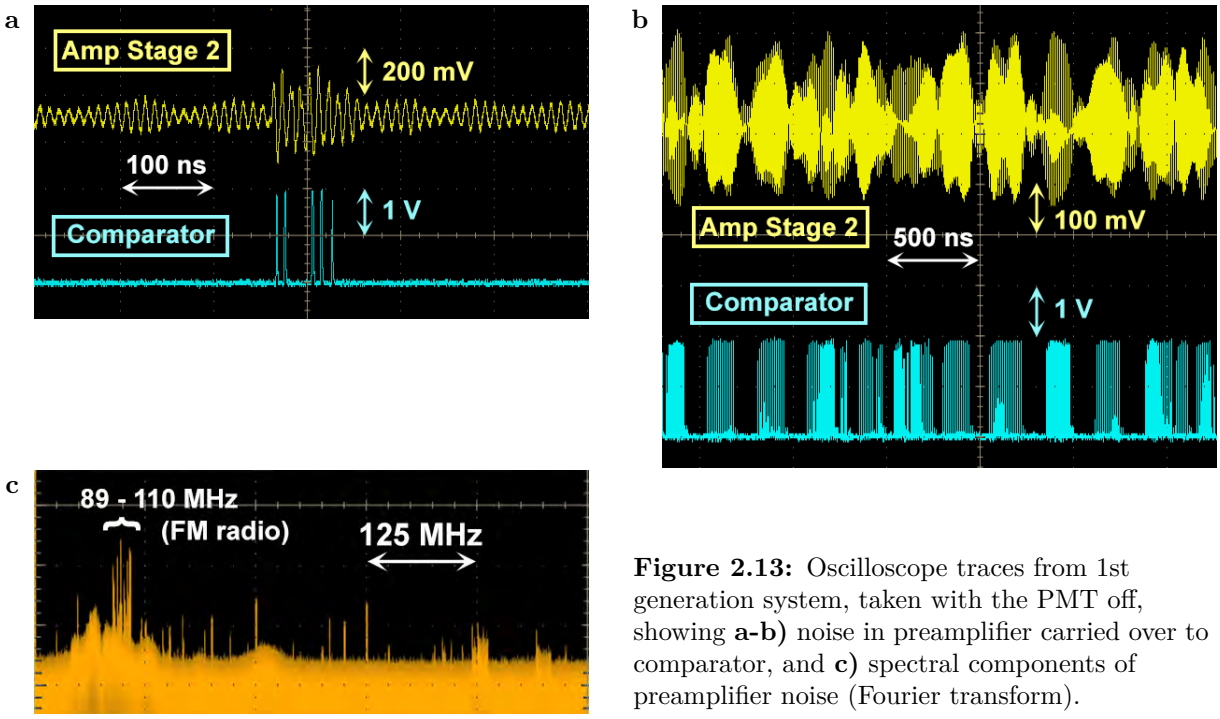

Figure 2.13: Oscilloscope traces from 1st generation system, taken with the PMT off, showing **a-b)** noise in preamplifier carried over to comparator, and **c)** spectral components of preamplifier noise (Fourier transform).

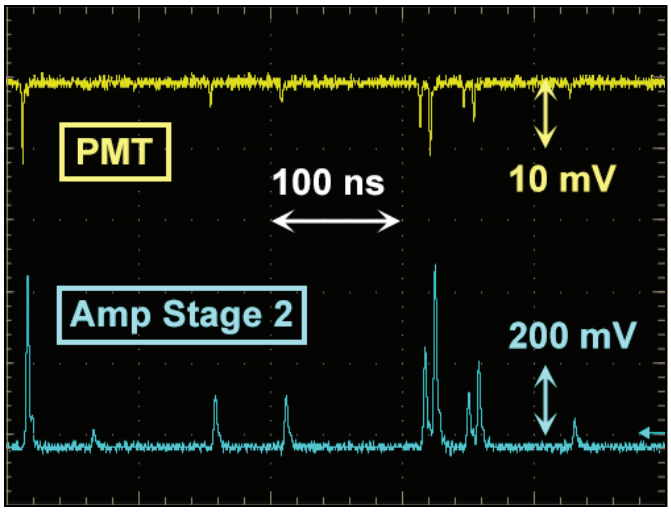

Figure 2.14: Oscilloscope trace showing photon pulses at PMT carried cleanly through the amplification stages, with minimal ringing and a quiet baseline.

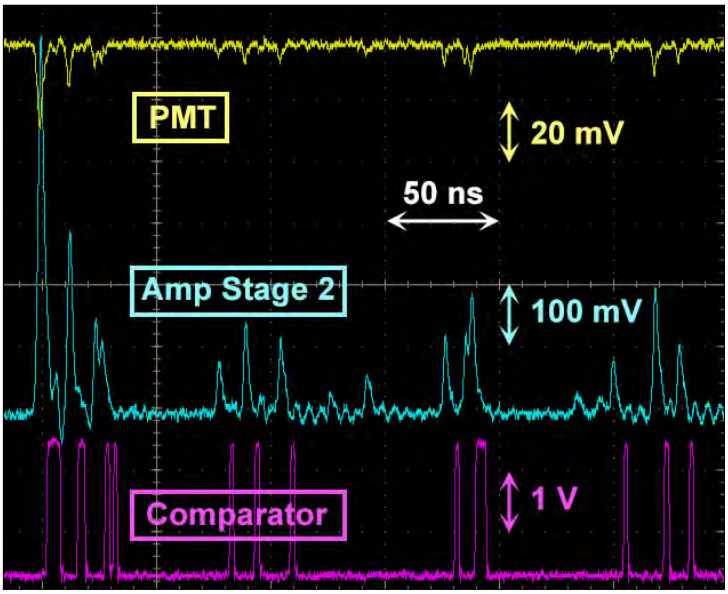

Figure 2.15: Oscilloscope trace showing potential PMT afterpulses transmitted through the circuitry to the comparator. The comparator's ability to 'detect' the small pulses depends on its reference voltage, here 112 mV; the final reference voltage used was 200 mV.

scattering of electrons on the first dynode [135]. These afterpulses are often ignored because they are faster than the subsequent circuitry, although for our instrument this may not be the case. The oscilloscope trace in Figure 2.15 shows several blocks of successive pulses that may or may not represent afterpulsing; some are averaged over, while others are conveyed faithfully to the comparator.

A second type of afterpulse appears with a longer delay (several hundred nanoseconds up to several microseconds) and arises from the ionization of residual gases within the PMT [135]. The amplitude of these afterpulses depends on the type of ions and the position where they are generated, and the delay time depends on the supply voltage [135]. Afterpulses are detectable in almost all conventional PMTs, and the propensity for afterpulsing is sometimes considered when evaluating the suitability of a particular model [147].

Our PMT does indeed at times exhibit afterpulse-like signals (e.g. Figure 2.15); a higher comparator reference voltage can screen some of these out, at the expense of missing real photons and subsequently reducing signal quality as per Eq. (2.1). In general, we rely on statistics to smooth out their effect; assuming that afterpulses have some given probability of occurring, they would be rolled into the calibration, albeit with some additional noise. Based on the good error performance of our instrument, as shown in Figure 2.16, it is judged that afterpulses do not pose a serious problem in this application.

2.3.2 Precision and accuracy performance

Because the arrivals of individual photons at the photocathode of the PMT can be treated as independent events, photon counting can be modeled with a Poisson distribution [148]. Thus, the theoretical standard deviation is given by the square root of the number of counts, so that the % standard deviation is

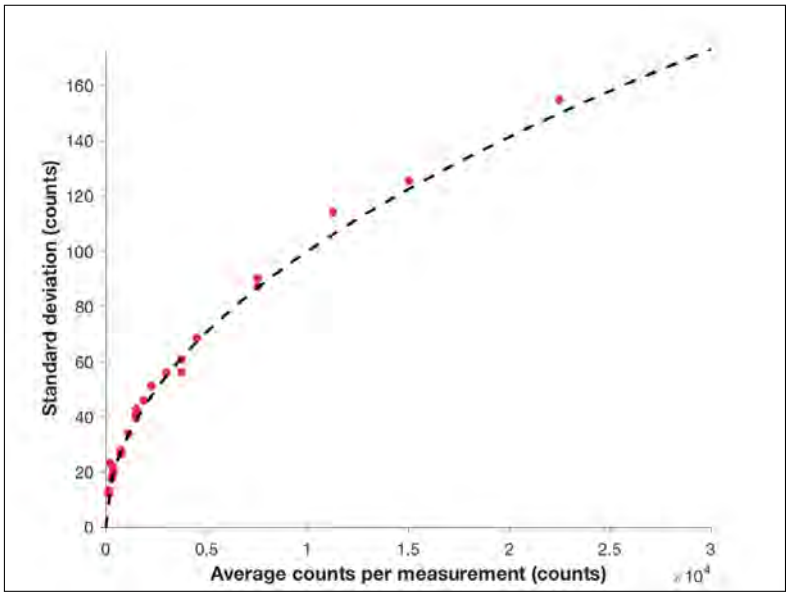

Figure 2.16: Observed error performance of spectrofluorometer. Standard deviation of counts is plotted against the average (N), over 300 measurements per data point. To achieve different average counts, measurements were taken at different integration times. The dashed line represents the theoretical $\sqrt{N}$ standard deviation.

$$Error\ \% = \frac{\sqrt{N}}{N} \tag{2.1}$$

where N is the number of observed counts. Note that the instrument output in units of counts/s is not necessarily the N that determines the error. The amount of time the instrument spends counting for any one data point ('integration time') depends on the measuring speed. For instance, to measure at 32 Hz, an integration time of 30 ms might be used (there is a small buffer for processing time; see Appendix B, Section B.2). The N counts measured in one integration are normalized to one second before outputting, but the error is still determined by the unscaled N.

The error performance of the instrument in repeated measurements is shown in Figure 2.16. Each point in the figure represents the average and standard deviation over repeated measurements at some given integration time and light level. The extremely good fit of observed standard deviation to the $\sqrt{N}$ line indicates that the instrument is operating close to the theoretical minimum level of variance, with little excess noise introduced by the circuitry, data processing, or PMT dark count.

However, at low photon counts (low N), which occur with lower light level and/or integration time, the error % can be non-negligible, as implied by Eq. (2.1). For example, in a humic acid solution with a measured total organic carbon content of 1.7 ppm, 2700 counts/s were observed. If 100 ms measurements were used, 270 counts would be observed in one integration, for a theoretical standard deviation of 6%. If 20 ms measurements were used, the error rises to 14%.

The acceptable level of noise for eddy correlation measurements will depend on environmental conditions. By Table 1.1, the expected fluctuations of DOC concentration ranged several orders of magnitude from 0.0001 ppm to 0.3 ppm, corresponding to 0.005 % to 15 % of a background of 2 ppm. If the noise level is comparable to the observed fluctuations in concentration, the EC results will rely on the even distribution of white noise to average out in the flux calculation (see

Section 1.3.3), and will thus produce noisier results. In practical use, the integration time of the measurements can be adjusted to trade off accuracy and speed, depending on the fluorescence strength, turbulence, and other characteristics of the site.

When modulation (described in Section 2.2.7) is used, the error is higher than for a non-modulated measurement of the same total speed, since the effective integration time with the LED on must be cut in half to accommodate measurements with the LED off. In addition, the calculation in Eq. (2.1) applies separately to measurements with the LED on and with the LED off. Consequently, the standard deviation of their difference N will not match $\sqrt{N}$, but will correspond roughly to the standard deviation with the LED on plus any uncertainty introduced by the LED off signal. This is generally not an issue when measuring in the dark, since the dark count is relatively low; however, under strong ambient light, detection of fluorescence becomes much more difficult as the error introduced by the LED-off signal becomes high.

The actual error performance of the instrument is more complicated; see Box 2.1.

Box. 2.1: More information regarding chaining of counters

Photons are counted on-board by two chained 8-bit counters, for a capacity of $2^{16} - 1 =$ 65,535 counts, after which they roll to 0. To avoid rollover when there are greater than 65,535 counts in an integration period, the system actually counts in subintervals of e.g. 0.5 or 1 ms that it then sums up to the full integration time. The subinterval can be as small as necessary so that, given the light level, the counters do not roll over in any one counting period; the downside of shrinking the subintervals is the extra processing time required to read and restart measurements.

The counters are configured such that, for proper cascading, the timing must be very precise of when the rollover photon pulse, fanned out by a fanout buffer, arrives at each counter[a]. With such high-speed signals, the system was observed to periodically miss a link (higher order counter fails to increment while lower counter resets), effectively dropping 255 counts. Occurring with some statistical regularity, this behavior simply shifts the average number of counts down for any given light level. However, sufficient averaging is required to smooth over this noise; put another way, the standard deviation is much higher, because some chain links are missed and some are not.

The data points given in Figure 2.16 correspond to only those where <255 counts were reliably measured in each subinterval, thus confining the counts to one counter and avoiding the linkage problem. The error performance relaxing this constraint is shown in Figure 2.17. If only one subinterval is 'summed up' for each integration period, then rollover issues occur at 255, 511, 767, 1023, etc. counts ($256n - 1$). The system can count up to 65,535 counts, but as the average number of counts nears or surpasses each of these thresholds, the error deviates a little more from the ideal. If five subintervals are 'summed up' for each period (e.g. 5 ms subintervals and total integration time of 25 ms), linkage issues occur when the average number of counts in each *integration time* exceeds $256 \times 5 - 1 = 1275$ (and 2555, 3835, 5115, etc.) counts. This is because an average of

1279 counts in the integration means that each subinterval (defining a counting period) has an average of 255 counts, which is when linkage to the higher order counter risks dropping 255 counts altogether[b](the other thresholds correspond to $[(256n - 1) \times 5]$). In Figure 2.17, vertical lines mark the average number of counts per integration where linkage issues would occur, given the number of subintervals per integration time (shown for three different values, represented by different colors). It can be seen that error performance of the instrument deviates from ideal as each threshold (for some given color) is crossed.

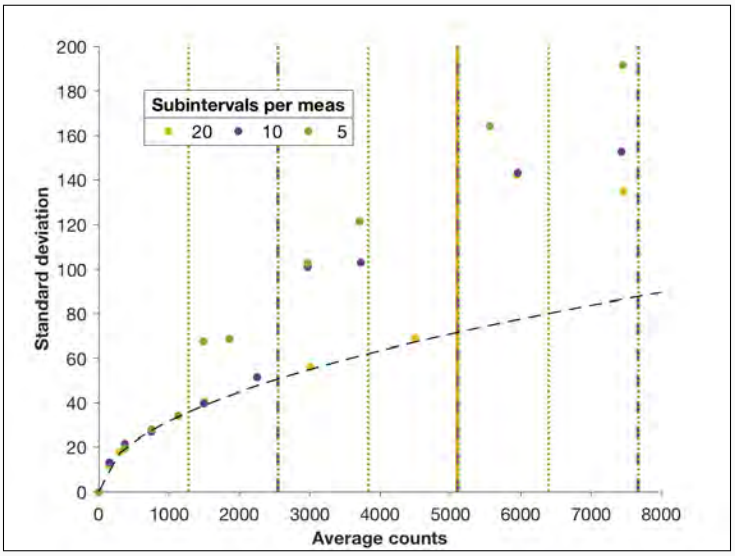

Figure 2.17: Observed error performance including errors from cascading counters; see text for details.

Ideally, the subinterval time is chosen such that the number of counts in any subinterval is <256, minimizing the error due to linking. For greater light levels, the subintervals should be smaller, at the expense of a minimal amount of processing time that is no longer available for counting; the choice of subinterval otherwise does not affect accuracy, as no difference in counts was observed between different subinterval times (for some given light level and integration time). The target integration time can then be achieved with close to ideal error. The use of chained counters allows the instrument to still function when light levels are unexpectedly high, as well as to avoid extremely short counting times (where processing time and/or small timing errors may add up). The utility of this feature (which, in prototyping at least, has proved very useful) is balanced against the extra complexity, board space, and power required by the second counter and its associated circuitry.

[a]The traditional architecture of feeding the output of one counter to the input of another is not possible because the high-speed counters accept a differential input but produce single-ended outputs.

[b]Linking issues actually occur for an average number of counts well less than 256n counts, since the counts distribution is a Gaussian curve around the average; thus, linkage issues can occur for data points on the positive side of the distribution.

2.3.3 Other performance metrics

Lower limit: Dark count

'Dark current', or 'dark count' when photon counting, is the current that flows through a PMT when it is operated in a completely dark state. It is caused by thermionic emission, leakage from the electrode support materials, and/or field emission [133, 135], and depends on the cathode type, cathode area, and temperature [147]. Dark count is important when the PMT is used to measure low amounts of light (e.g. <1000 counts/s [131]), because it contributes to uncertainty as per Eq. (2.1).

The manufacturer-specified dark count rate for our PMT model is typical 100 counts at 20 °C. For our system, at room temperature the lowest dark count observed (based on repeated measurements in the dark) was approximately 100 to 300 counts, though for most measurements it was higher. In fact, dark counts as high as several thousand counts per second were observed, generally after several weeks to months of disuse. This is not unexpected; one common recommendation to reduce dark count, especially after a long period of idleness, is to 'age' the PMT by running it continuously in the dark for several hours to several days [133].

Other potential causes of high dark count include exposure of the cathode to strong light, even if no voltage is applied; recovery can take from several hours to several days [133, 147][1]. Finally, as mentioned above, dark count is sensitive to temperature (as a major source is thermoionic emission). Depending on the cathode type, a 10 °C increase in temperature can increase the dark count by a factor of 3 to 10 [147]. For this reason, maximum sensitivity detector systems often utilize PMTs with thermoelectric or other cooling systems.

In our case, the system (specifically, the power-hungry counters on the photon counting board) does generate some heat within the housing, which could affect the PMT performance. This effect would be less of a problem when the instrument is submerged and heat can diffuse through the housing to the surrounding water. For laboratory tests, a small desktop fan was sometimes used to cool the system. However, in general the dark count was managed by properly aging the PMT (for, e.g. 24 h) prior to use. Such aging was observed to take dark counts from several thousand to a few hundred counts per second. It is possible that further aging, coupled with better cooling of the housing, would reduce the dark count to the manufacturer specification.

Even when properly aged, the dark count is initially much higher when the PMT is turned on, but drops within the first few minutes (Figure 2.18). This is normal for PMTs; one manufacturer [135] states that, after 30 minutes in a dark state, most PMTs approach the average dark current achieved after longer periods in the dark, although it does continue to decrease slowly. In general, a warm-up period is often recommended before each, whereby voltage is applied in the dark for perhaps 30 to 60 min. Along with aging, this warm-up period also improves the stability and reduces drift [135].

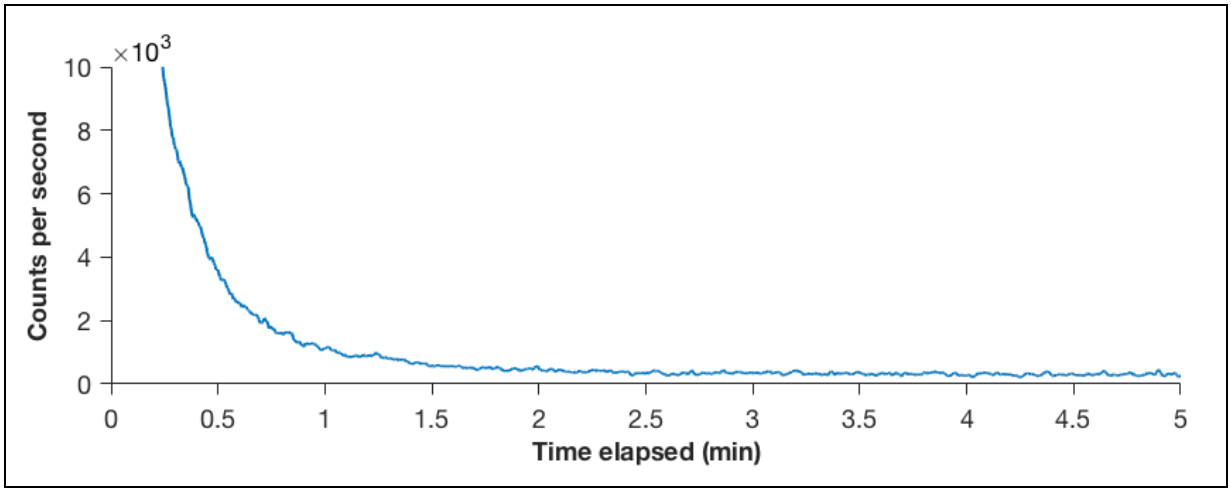

Figure 2.18: Observed dark count after turning on PMT (previously aged). Values dropped from an initial $\sim 4 \times 10^4$ counts/s at turn-on to a stable dark value within a few minutes, and did not decrease noticeably for the next 20 minutes (not shown). For a PMT in regular use, no significant difference was observed between data taken after resting (off) periods of 40 hours, 3 hours, or 10 minutes (also not shown).

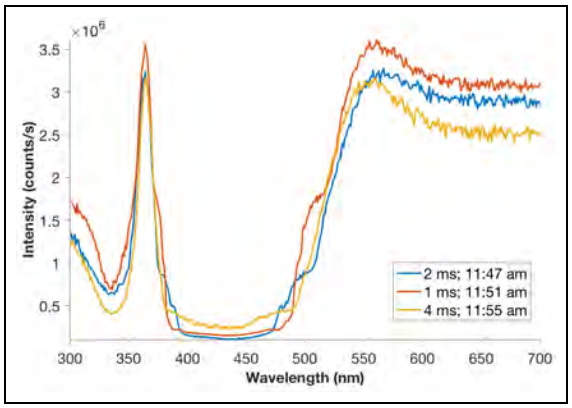

Figure 2.19: Spectral scans of daylight showing significant drop in signal due to overloading. Data are plotted for three different counting periods to demonstrate independence from counter rollover (see Box 2.1). 500 ms integration time.

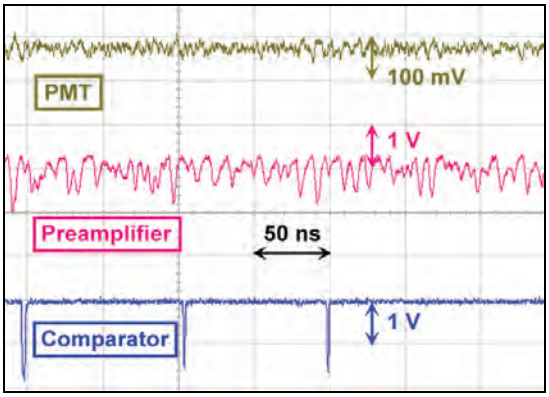

Figure 2.20: Oscilloscope trace for strong light signal demonstrating overload of the comparator. Due to the high rate of photons, the amplified pulses blend into one another and the comparator largely stays high.

Upper limit: Saturation

The maximum count that the instrument can measure is estimated to be $\sim 3.5 \times 10^6$ counts/s. This is estimated based on the data in Figure 2.19, which shows a spectral scan of strong daylight in which the signal drops over an order of magnitude (to $\sim 1 \times 10^5$ to 3×10^5 counts/s) at the wavelengths with the strongest light. This issue does not arise from counter capacity and is thus independent of counting period (see Box 2.1). Instead, it likely corresponds to photons being so close together that the comparator does not detect separate pulses (Figure 2.20).

The issue of 'pulse pile-up losses' is another known feature of photon counting [131]. The pulse-pair resolution, the minimum time interval at which pulses can be separated[2], can be influenced by any stage of the amplifier or comparator circuitry; its reciprocal determines the maximum count rate. However, due to the statistical nature of photon arrivals, pulse overlap begins to occur well below this rate. It is generally observed at about 1/10 of that calculated from the pulse-pair resolution [135].

From Table 2.1, the amplified photons have a width of ~ 2 ns, corresponding to a maximum rate of 5×10^8 counts/s, which is two orders of magnitude higher than the observed 3.5×10^6 counts/s (rather than the one order of magnitude observed in the literature, as stated above). Thus, it is likely that the observed pulse resolution is limited by the comparator, counters, or other circuitry, and not by the PMT or preamplifier circuit. However, the $\mathcal{O}(10^6)$ value corresponds well to other maximum count rate values in the literature of $10^6 \sim 10^7$ counts/s [131, 135].

Short of full overload (such as that observed in Figure 2.20, pulse overlapping does not necessarily invalidate all photon counting, but it causes the count rate to deviate from linearity. The measured count rate can be corrected to the true photon rate if the pulse pair resolution is known [131, 135]. For this instrument, such corrections are unnecessary, as with the current setup emission levels are unlikely to reach anywhere near these levels. Ambient light, of course, can reach such levels (Figure 2.19); in this case, the noise from such high counting rates would swamp out the fluorescence signal anyways, and so efforts have instead focused on reducing ambient light. A future iteration of the sensor might involve a parallel analog channel (measuring average PMT current) that can be used instead of photon counting at higher light levels. It will always be difficult to distinguish a small fluorescence signal from a large ambient light signal, but tactics such as a lock-in amplifier might in some situations provide enough precision for eddy correlation.

Spectral resolution and accuracy

The spectral resolution of the monochromator was estimated by connecting its output to a wavelength-dispersive spectrofluorometer module (Ocean Optics USB4000; measures all wavelengths simultaneously) under a wide broadband input (daylight), and observing the output at different wavelength settings. The results are shown in Figure 2.21 and Table 2.2.

[1] With strong enough light, e.g. an operating cathode exposed directly to daylight, the dark count can permanently increase by several orders of magnitude [147].

[2] The pulse-pair resolution is often also described in terms of the 'dead time' after each photon pulse during which the circuitry is unable to detect another pulse.

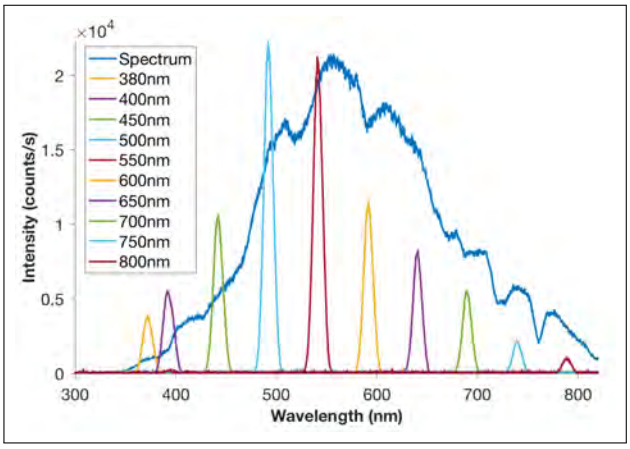

Figure 2.21: Light passed by the monochromator at different wavelength settings, as measured by a wavelength-dispersive spectrofluorometer.

Table 2.2: Monochromator resolution and spectral accuracy.

Nominal λ (nm)	**Peak** λ (nm)	**Discrep** (nm)	**FWHM** (nm)
380	372.1	7.9	11.3
400	391.6	8.4	12.5
450	442.6	7.4	11.2
500	492.2	7.8	10.9
550	540.8	9.2	11.1
600	592.0	8.0	11.1
650	641.1	8.9	10.1
700	689.3	10.88	10.5
750	739.4	10.6	9.1
800	788.6	11.4	8.6

The average of the spectral widths given is ∼11 nm, and represents the convolution of the spectral resolutions of the monochromator and the USB4000. The resolution of the USB4000 depends on grating and slit choices; for ours, it was estimated to be ∼8 nm. Approximating both responses as Gaussian curves and deconvoluting, the estimated FWHM value for the monochromator's bandwidth is $7 \sim 8$ nm. This value is reasonable, as the manufacturer specifies a bandpass of 1 nm using 0.150 mm slits and a 1200 grooves/mm grating [149], and the current setup uses the same grating but 2.4 mm slits.

For eddy correlation and/or measuring FDOM, which has a broad emission, high spectral resolution is not necessary; in fact, a wider spectral resolution may be desirable in some cases to allow more light.

From Table 2.2, it can be seen that the wavelength of the monochromator deviates from nominal all across its spectral range. The deviation is not constant across the spectrum, depends on the point used for calibration, and seemed to shift over time. Thus, it could not be fixed by calibration, at least for the monochromator unit used (age also affects the calibration performance). However, similar to the spectral resolution, spectral accuracy is not so important for our applications.

2.3.4 Optical fiber positioning

The spectrofluorometer's sensing volume is the intersection between the cones of acceptance and emission of the two optical fibers. Each cone is also weighted; the light farther from the fibers is more diffuse, since the intensity of light decreases with the square of path length. Thus, the location, size, and shape of the sensing volume, as well as the intensity of the detected fluorescence for any given solution, is highly dependent on the relative geometry of the optical fibers. This principle is shown graphically in Figure 2.22, which gives single-plane (2D) representations of the sensing volumes for different combinations of angles between the optical fibers (10 °, 20 °, and 30 °) and spacings between the fiber tips (touching, 1 mm, and 2 mm).

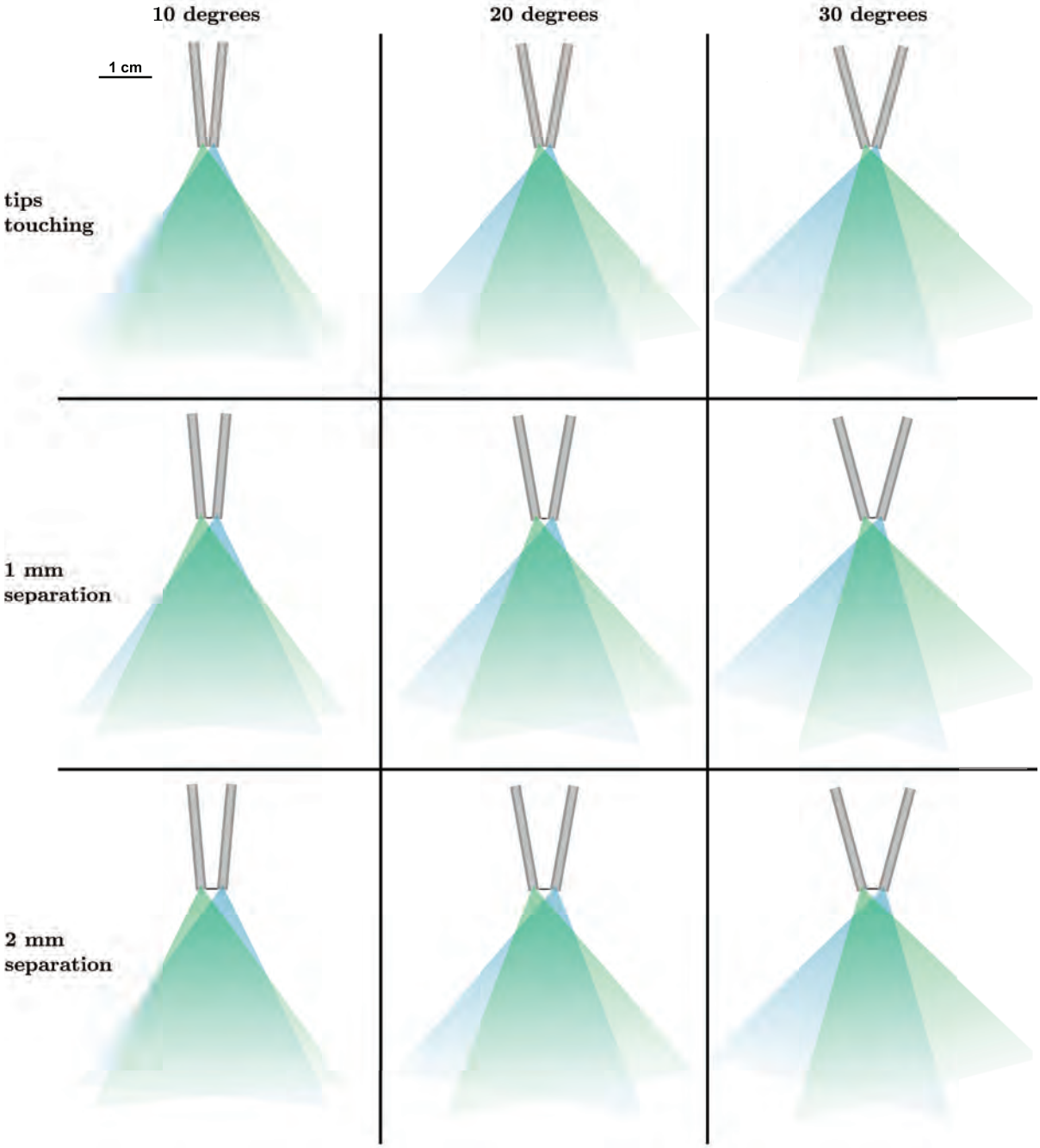

Figure 2.22: Single-plane (2D) representations of different combinations of angles (10 °, 20 °, and 30 °) and spacings (tips touching, 1 mm apart, and 2 mm apart) between the optical fibers. The optical fibers are modeled with ⌀ 1 mm core, 0.39 numerical aperture, and ⌀ 2 mm (OD) stainless steel tubing (the cladding and coating of the optical fibers, which for the FT1000UMT form a ⌀ 1.4 mm shell around the core, are not shown separately from the stainless steel tubing). The sensing volume is the intersection of the two cones. The colored weightings of the cones are not quantitative, but are used to demonstrate that the intensity of emission or acceptance falls off rapidly with distance to the optical fibers.

As described in Section 2.2.2, the positioning chosen for this instrument uses a 20 ° angle between the optical fibers, with the tips ∼1 mm apart at the closest point (Figure 2.6). The angle of 20 ° was chosen based on preliminary tests, in which the optical fibers were held at different, known angles by sandwiching between two foam-lined sheets of rigid plastic. These tests showed that the 20 ° angle produced a stronger fluorescence signal than with larger angles. Angles smaller than 20 ° were not tested because the difficulties they present in mounting and handling made them impractical.

Figure 2.22 shows why smaller angles might produce a larger signal—the volume of intersection increases as the two cones become more parallel. However, this advantage decreases as the tips are moved further apart, since the overlap of the high-intensity regions of the cones (near the fiber tips) decreases, more so than for the wider angles. The preliminary angle tests were conducted with the optical fiber tips touching, but the optical fibers in this instrument were ultimately spaced ∼1 mm apart. Based on Figure 2.22, 20 ° appears to be a reasonable choice of angle and possibly even has an advantage over 10 ° in terms of signal intensity at this separation distance.

Figure 2.22 also shows that the spacing between the optical fibers also has a strong effect on the location of the sensing volume and the intensity of the observed signal. Positioning the fiber tips farther apart leads to a sensing volume that is further from the tips of the optical fibers. The light in this more distal sensing volume is also more diffuse, leading to a weaker signal. When used to measure dissolved organic carbon, the longer path length also results in more inner filtering, as discussed in greater detail in Section 2.3.5 below.

In general, for eddy correlation, a tradeoff exists between reduced inner filtering and increased light output (for better signal quality) with closer tips, and a more distal sensing volume that can be positioned closer to the ADV's measuring volume with farther tips. The optical fibers provide flexibility to adjust the location of the sensing volume to explore and balance these tradeoffs, as well as to tailor positioning to site-specific characteristics (e.g. depending on the ambient concentration of DOM, or whether conductivity is also being measured). For this instrument, the majority of tests used a separation of ∼1 mm, which was chosen as a balance between the need for signal strength—which turned out to be the most immediate priority for the fluorescence sensor—and the requirements of the subsequently-introduced conductivity sensor, which necessarily requires some spacing between the fiber tips (see Chapter 3). The resulting sensing volume, as mapped experimentally, is discussed in Section 3.4.2 (p. 154).

2.3.5 Performance with humic acid; calibration curves

To test the ability of the instrument to be used for capturing DOM fluxes, the spectrofluorometer was tested in lab using solutions of a widely-used standard humic material, Sigma Aldrich humic acid (see Section 1.6 for more information on humic acid). The setup for these laboratory tests is shown in Figure 2.23. Figure 2.24 shows (inverse) calibration curves and spectral scans obtained with two different configurations of optical fibers: Configuration 1, in which optical fiber tips are touching, and Configuration 2, in which the tips are ∼1 mm apart.

As discussed in Section 2.3.4 above, positioning the fiber tips farther apart leads to more distal sensing volume with lower light intensities. This effect is quantified in Figure 2.24b, which shows that the ∼1 mm tip separation in Configuration 2 leads to a ∼50 % reduction in signal

Figure 2.23: Experimental setup used for optical fiber calibration and spectral scan measurements. Use of a wide-mouthed 500 mL amber jar minimizes light leakage and LED reflections from glass walls, which can create a fat spectral tail for the LED signal that bleeds into the emission wavelength range.

.

relative to Configuration 1 at lower concentrations of humic substances. The difference is even greater at higher concentrations, as the increased path length in Configuration 2 also increases the amount of inner filtering (see Section 1.6.3). Thus, while both calibration curves are quite linear at low concentrations, at higher concentrations the fluorescence intensity does not increase proportionally with concentration, with a more pronounced effect in Configuration 2. The effect of inner filtering is also confirmed by the spectral scans of the emission spectra of the humic acid (Figure 2.24c). For Configuration 2, the highest concentration of humic acid measured (35 ppm total organic carbon) exhibits both a reduced intensity and an overall shift towards longer wavelengths, as shorter wavelengths are self-absorbed.

A linear calibration curve is advantageous because it simplifies data processing and allows equal resolution across the entire range of measurable concentrations. However, global linearity of signal with concentration is not necessary for eddy correlation measurements, which are based on fluctuations around a mean. Even at high humic concentrations, a first order linear approximation of the curve will likely provide adequate accuracy to determine fluxes.

As described above, a separation of ∼1 mm was ultimately used in further tests to accommodate the conductivity sensor (see Chapter 3), which requires some spacing between the optical fibers. A piece-wise calibration curve for lower levels of humics (corresponding to relatively clear natural waters), measured with this configuration, is shown in Figure 2.25. The x error bars represent the observed standard deviation and correspond well to the theoretical minimum given by Eq. (2.1), given the 50 ms integration time[3]. The y error bars represent the corresponding error in DOC concentration calculated using the slopes of the fits, i.e. they are the observed uncertainty in measurements translated to DOC concentration. The uncertainty ('error') in y can be compared to the estimated DOC fluctuations, which from Table 1.1 range from 0.0001 ppm to 0.3 ppm (depending on DOC fluxes and the turbulence conditions). Thus, Figure 2.25 provides a visual representation of the discussion in Section 2.3.2 on precision and accuracy performance.

For this calibration curve, the uncertainty at higher background DOC levels (above ∼1 ppm)

[3]Measurements were taken in the dark to minimize deviation due to ambient light. In actual use, the presence of ambient light may further increase the observed uncertainty.

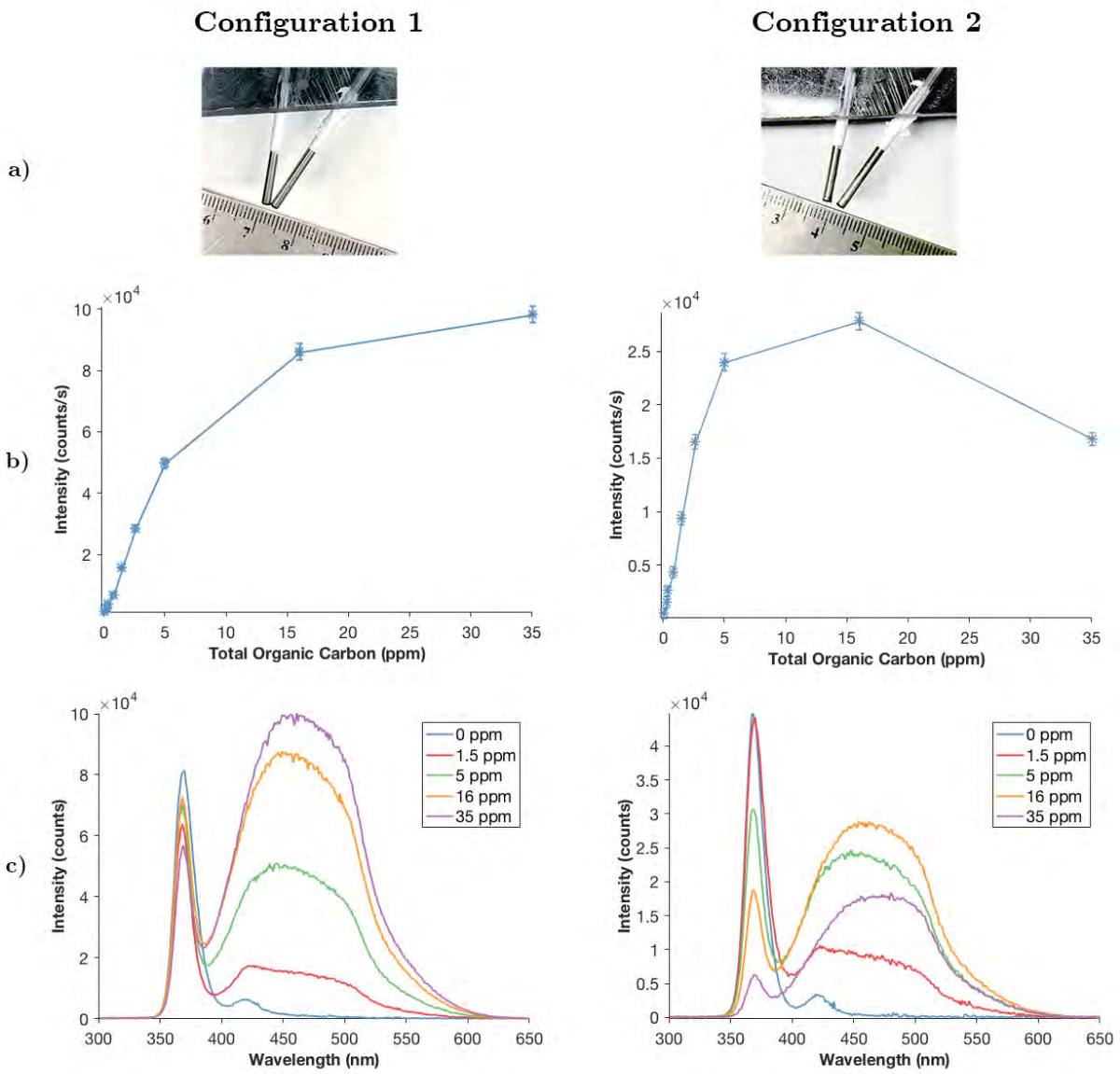

Figure 2.24: Humic acid measurements for two configurations of optical fibers. **a)** Images of optical fiber tips demonstrating the tip distance for each configuration. **b)** Calibration curves of humic acid (measured at 450 nm). **c)** Spectral scans of humic acid solution, showing the 380 nm LED excitation and resulting humic acid fluorescence. Configuration 2, in which the fiber tips are farther apart, demonstrates lower signal strength and a higher degree of inner filtering.

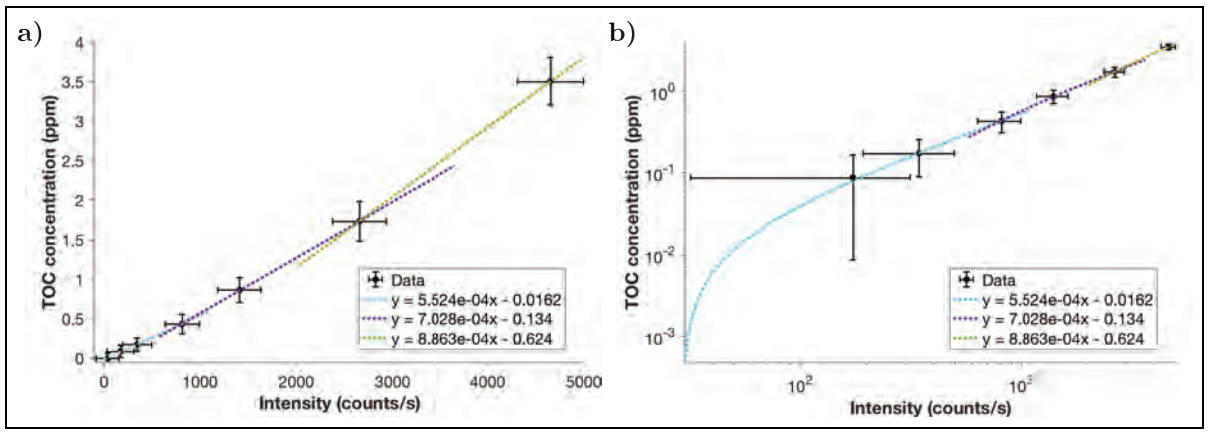

Figure 2.25: Piece-wise calibration of spectrofluorometer at low concentrations, shown with **a)** linear and **b)** log axes. All fits have $R^2 = 1.00$. Fits were used to scale standard deviations of photon counts to concentration error bars, which can be compared to expected fluctuations in concentration. Measured with 100 ms integrations (50 ms with LED on, 50 off); average and standard deviation over 600 are shown.

appears to exceed the largest fluctuations expected. The absolute uncertainty is less at lower background DOC concentrations, but is a higher percentage of the background concentration; measurements could still fail to fully resolve fluctuations, especially if lower background concentrations are correlated with lower fluxes. As discussed in Section 2.3.2, the flux calculations in such cases will rely on the even distribution of white noise to average out the uncertainty. Since the instrument is operating close to its theoretical detection limit, the uncertainty relative to the expected fluctuations can only be reduced by increasing the level of light (e.g. with a longer integration time, a more powerful excitation source, or better coupling into and out of the optical fibers), which would decrease the slope of the calibration curve and allow some given uncertainty in counts to translate to a smaller uncertainty in DOC concentration.

2.3.6 Spectral scans

Figure 2.24c shows the spectral scans of several solutions of humic acid, which were taken by stepping through detection wavelengths with the monochromator and measuring the light level. Spectral scans are generally useful for characterizing the environment and determining what fluorophores are present. In addition, the composition (and therefore emission spectrum) of dissolved organic material varies from site to site, as well as spatially and temporally within a given site (see Section 1.6, p. 69 on FDOM); spectral scans can therefore be used to identify site-specific optimal wavelengths for eddy correlation measurements, as well as to periodically characterize changes in chemical composition. The scattering of the LED signal can also be potentially used as an indicator of the scattering environment or turbidity (using a similar principle to nephelometry).

Another example of a spectral scan is shown in Section 2.3.6, which shows the emission spectra of humic acid and fluorescein solutions (taken separately). Fluorescein, a fluorescing dye commonly used in laboratory and field experiments, was used in many validation tests of this instrument and was observed to emit at 510 nm. Section 2.3.6 also shows LED peaks at ∼377 nm, whose intensities depend on the scattering and absorption environment, and the water Raman

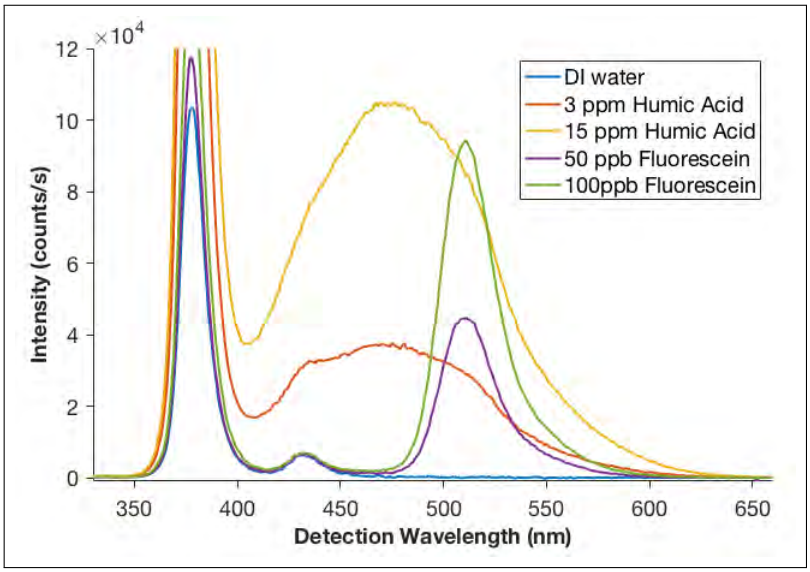

Figure 2.26: Spectral scan of solutions of humic acid and fluorescein dye. For these tests, the LED scattering peaked at ∼377 nm, and the water Raman peak appeared at ∼432 nm. The different emission spectra of humic acid (450 ∼ 500 nm) and fluorescein (peak ∼510 nm) are also apparent.

peak at ∼432 nm.

2.3.7 Sensor speed ('response time')

The term 'response time' is slightly misleading in this context because a fluorescence sensor responds almost immediately to a change in fluorophore concentration; the time scales involved are related to the emission of fluorescence and the movement of electrons through the circuitry. Instead, the sensor's speed performance is limited by the integration time necessary to produce a reliable signal, following the discussion in Section 2.3.2. The user must choose a measuring time to balance the requirements of speed and precision. This choice necessarily depends on environmental factors such as the type of fluorophore (specifically, its quantum efficiency), its concentration, and the ambient light level.

Thus, not only does the environment dictate the speed *requirements* of the sensor (following Section 1.3.3, p. 38), but in this case it actually influences the sensor's speed itself. It is consequently difficult to quantify the sensor's 'response time' so that it can be compared to the turbulence time scales. Nevertheless, to obtain a general sense of the instrument's ability to capture turbulent fluctuations, we conducted laboratory experiments that involved injecting a solution of humic acid into a beaker stirred by a stir bar. The optical fibers were pointed into the solution (similar to the setup of Figure 2.23 for calibration and spectral scan measurements), and the instrument was directed to measure a time series. At set times, humic acid was manually injected into the stirred flow using a micropipette.

The results (Figure 2.27) show that the instrument is able to observe the fluorescent material as it moves past the fiber tips. The humic acid swirls around the beaker after each injection before ultimately mixing into the bulk water. The measured end concentration does match the values expected based on the volumes of the injection and the beaker.

Measurements were made at 20 Hz, with each individual measurement comprising a 20 ms 'dark' measurement with no LED excitation, subtracted from a 20 ms measurement with excitation

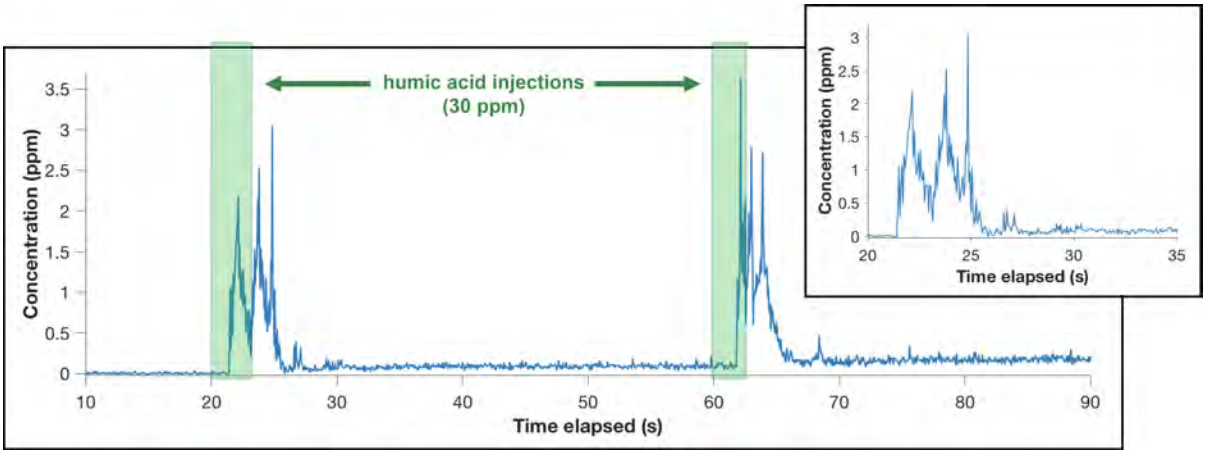

Figure 2.27: Time series of measurements from stirred beaker injected with small aliquots of 30 ppm humic acid solution. Injections were made at 20 and 60 s (shaded green in figure); inset shows a zoom-in of first injection. The instrument, measuring at 20 Hz, is able to pick up turbulent eddies before the fluorescent material diffuses into the solution.

(i.e. modulated). For EC, a few Hz is thought to be sufficient (see Section 1.3.3), so these results provide confidence that the instrument is able to measure with the speed and sensitivity required for eddy correlation measurements.

2.3.8 Comparison to other spectrometers; spectral response

The performance of the instrument was compared to two other commercially available spectrometers: the Ocean Optics USB4000 module and the Perkin Elmer LS50B desktop spectrofluorometer. The same optical fiber setup (Figure 2.23) and LED was used for the photon counter and the USB4000, while the desktop model used a 1 cm square cuvette. The optical fiber tips were ∼1 mm apart as in the final configuration.

Normalized calibration curves and emission spectra for the three instruments, taken using the same humic acid solutions, are shown in Figure 2.28. All three instruments produced linear calibration curves at lower concentrations and exhibited inner shielding at higher concentrations. The degree of inner shielding was greater for the desktop spectrofluorometer than for the optical fiber setups, even compared to the setup with 'larger' separation distance ('Configuration 2' in Figure 2.24), possibly because the 1 cm cuvette still has a longer equivalent path length.

Other differences in the data from the three instruments are related to the difference in spectral response, which is evident in Figure 2.28b. The photon counter, for example, has a better spectral response in the lower wavelength regions, mainly due to the quantum efficiency curve of the PMT (Figure 2.29). The USB4000, on the other hand, is more sensitive at higher wavelengths and thus its spectra appear to be 'red shifted' relative to the others.

In general, all spectrophotometers have their own spectral responses. Although this complicates direct comparison of spectra between instruments (see Section 1.6.3, p. 73 on challenges relating to fluorescence spectroscopy), it is not an issue for determining concentrations given correct calibration. Nevertheless, the spectral response is an important parameter. For example, this

a) Calibration curves from three instruments, normalized to value at 7 ppm. All are linear at low concentrations, but the desktop spectrofluorometer exhibits more inner shielding at higher concentrations. Measurements for the USB4000 and PE SF represent averages and standard deviations over a 2 nm-wide wavelength window, and for the photon counter, over repeated measurements in time.

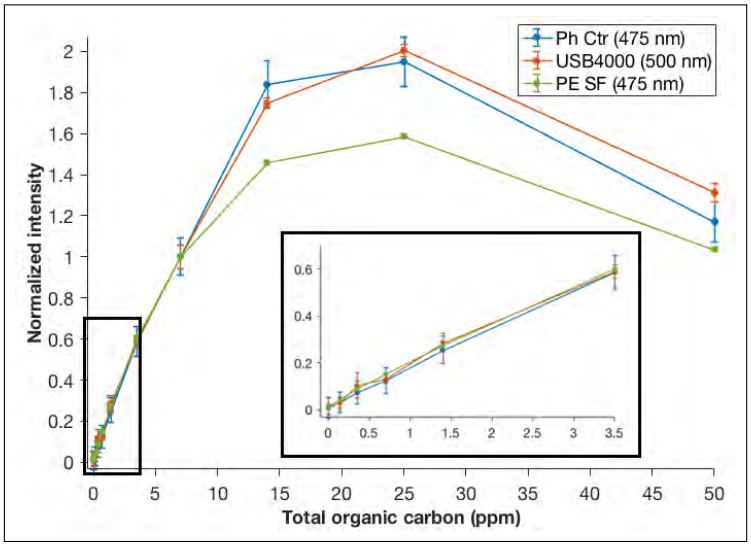

b) Spectral scans from three instruments using two different humic acid solutions, normalized to highest emission peak to visualize differences in spectral shape. Different spectral responses result in different curves, but the three instruments are consistent. The emission peak from the 40 ppm solution is red-shifted due to inner shielding.

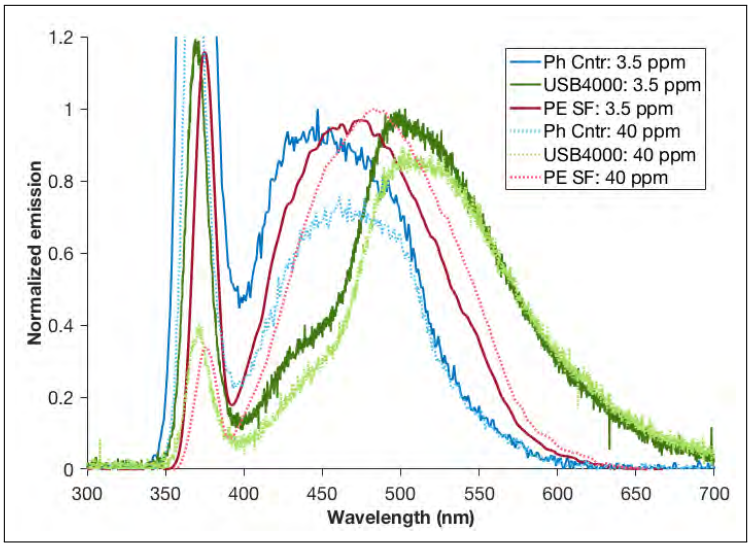

Figure 2.28: Comparison between three spectrofluorometers: 'photon counter' developed in this thesis, Ocean Optics USB4000 module, and Perkin Elmer desktop spectrofluorometer ('PE SF').

Test conditions: **Photon counter**: **a)** modulated 100 ms measurements (50 ms LED on, 50 ms off), average / stdev over 600 runs; **b)** modulated 20 ms measurements (10 ms LED on, 10 ms off), average / stdev over 25 runs at each wavelength. **USB4000**: 10 s integration, 0 boxcar, values in **a)** represent average and standard deviation over 2 nm-wide window. **PE SF**: 12 nm entrance and exit slits, scan speed 300 nm/min, excitation at 368 nm to match this particular LED; actual excitation peak is at 374.5 nm as shown in **b)**, possibly due to spectra responses or incorrect calibration. Values in **a)** represent average and standard deviation over 2 nm-wide window.

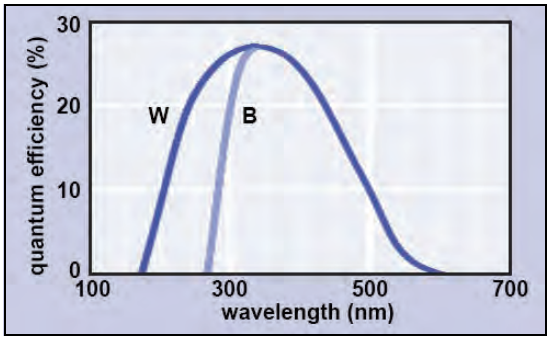

Figure 2.29: Quantum efficiency curve of ET Enterprises 9111WB showing a higher response in the UV range but minimal response past ∼600 nm wavelengths. The PMT used corresponds to the 'W' curve, indicating the use of a borosilicate glass window to allow wavelengths <250 nm to pass to the photocathode. Source: adapted from manufacturer spec sheet.

.

instrument could not be used to measure red wavelengths (∼700 nm) unless a different PMT is used[4]. It *can*, however, be used to measure green wavelengths; as shown in the spectral scan of Section 2.3.6, it was used to measure the emission of fluorescein dye at 510 nm. Although the instrument's response at this wavelength may not be as optimal as it would be at lower wavelengths, it is still able to detect the emission peak given a high enough fluorescein concentration.

[4]Finding a PMT that can measure at longer wavelengths is not trivial. Photons at longer wavelengths have less energy, and thus PMTs most commonly measure light in the UV / purple / blue range, while PMTs designed to measure light at longer wavelengths (green and higher) generally exhibit higher dark counts.

Chapter 3

Conductivity, temperature, and trimodal sensing

3.1 Conductivity and temperature sensors

After the fluorescence sensor was constructed and tested, the instrument was subsequently modified to enable conductivity and temperature sensing capabilities. This involved modifying the optical fibers to become conductivity electrodes, attaching a small thermistor to one fiber, and adding additional circuitry and code to process the signals from these sensors.

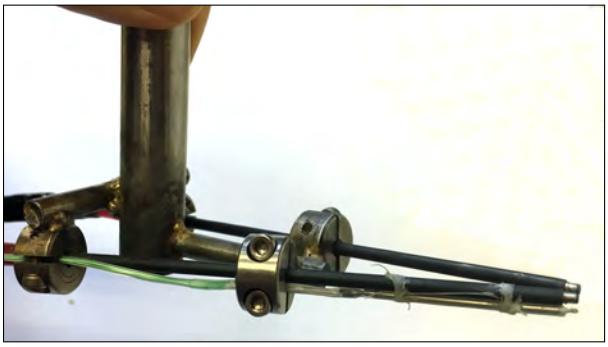

Figure 3.1: Conductivity cell and thermistor

The conductivity cell and thermistor are shown in Figure 3.1. Since the conductivity and temperature sensing volumes are roughly the same as the fluorescence sensing volume, use in eddy correlation studies would allow the simultaneous measurement of three different fluxes in the same place.

3.1.1 Physical construction

Conductivity probes

As described in Section 2.2.2, the sensing ends of the optical fibers consist of the $\varnothing$ 1 mm core optical fibers encased in $\varnothing$ 2 mm (OD) stainless steel tubing. The use of stainless steel presented a good opportunity to implement a built-in conductivity cell by insulating the bulk of the metal to expose only the tips, which can then be utilized as electrodes.

To modify the optical fibers for conductivity measurements, wires from a Subconn MCIL1M underwater cable (Micro Circular, one contact) were cemented onto the base of each stainless

steel tubing using silver epoxy. In future iterations, the wire may be soldered to the tubing using the appropriate stainless steel flux; however, as the optical fibers were already assembled in the present case, silver conductive paste was used to avoid heat damage.

The main body of the tubing, except for the tips, was encased in dual-wall moisture-seal heat shrink tubing. 1/8" flexible polyolefin tubing (Raychem TAT125) was used for the main body of the tubing; after shrinking around the stainless steel tubing, the diameter was measured to be ∼0.115" (∼3 mm). An additional ∼1" long piece of 0.183" semi-rigid polyolefin heat shrink (3M Heat Shrink TMW) was used to encapsulate the silver epoxy connection between the electrodes and the cable wire, with gaps filled in by thermoplastic adhesive tape (Raychem) to ensure water tightness.

A small amount of underwater epoxy was later added to the inside faces of the exposed stainless steel at the tips of the fibers. This change is described in Section 3.4.4 and does not apply to the results presented in this chapter.

Thermistor

The thermistor used is the GP104L8F (U.S. Sensor), which has a ⌀ 0.039" × 0.110" glass body. It is similar to the FP07 (GE) thermistor used in other eddy correlation studies [6], with some differences as described later in Section 3.3.2 (p. 149) on its timing performance.

Ultra-fast thermistors are tiny because the small thermal mass allows a faster response time, but the resulting fragility requires special care. To package the thermistor as a probe, the leads were first encased with 0.014" miniature heat shrink tubing, then epoxied with marine epoxy into the body of a stainless steel 1.5" gauge 18 needle (⌀ 0.050 " (OD)). Care was taken to ensure that the body of the thermistor was physically separated from the needle by epoxy, so that temperature measurements would not be affected by the thermal mass of the metal.

In later tests in a tank, which involved long periods of submersion, the thermistor appeared to exhibit signs of water leakage and/or electrical malfunction. Subsequent thermistor probes were made with special attention to the epoxy seals between the thermistor and the needle. In addition, a circuit board protective coating (Techspray Fine-L-Kote SR) was sprayed on the thermistor, leads, and heat shrink coating the leads.

The leads of the thermistor were then soldered to gauge 30 wire wrap wire, which was in turn soldered to the wire of a Subconn MCIL2M-G2 underwater cable (Micro Circular, two G2 contacts). The heat shrink and protective material is summarized in Figure 3.2.

To secure it to the optical fibers, the probe (⌀ ∼0.075" (2 mm) after encased by heat shrink) was tied to the stainless steel tubing of one of the fibers using two nail knots tied with 0.008" nylon fishing line, and a dab of marine epoxy (Figure 3.1).

3.1.2 Teensy microcontroller

The conductivity and temperature sensors are managed by a front-end microcontroller, the Teensy 3.2, which then communicates with the Raspberry Pi. A front-end microcontroller was chosen over direct control by the Pi to facilitate simultaneous measurement of fluorescence

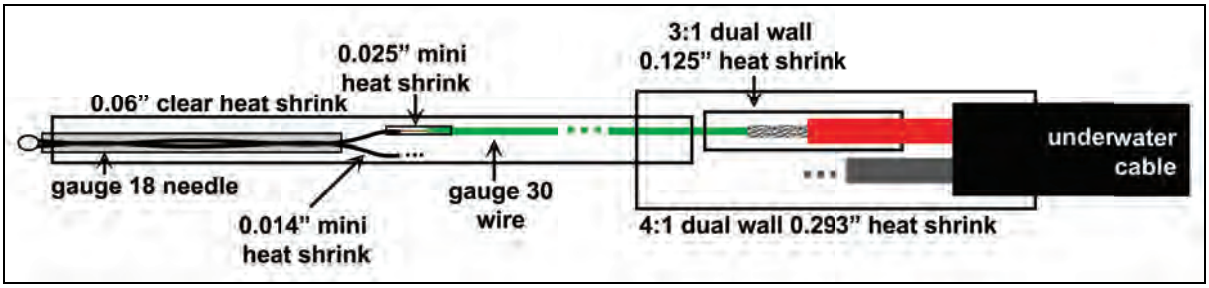

Figure 3.2: Protective material used to construct thermistor.

and conductivity/temperature: since the Pi is continuously engaged while counting photons, it would need to cut short the fluorescence measurement in order to read values for the other two sensors. The use of a front-end microcontroller was deemed an easier solution compared to an alternate approach like multithreading.

The Teensy 3.2 is a miniature (1.4" × 0.7") microcontroller with a 72 MHz microprocessor that can be programmed via the Arduino IDE [150]. Programs are directly loaded from a PC via USB (a summary of the code modules is available in Appendix F). In this application, the Teensy was disconnected from the PC once programmed and mounted directly on the conductivity/temperature circuit board, with a modification to allow it to run off board power rather than through USB.

The Teensy communicates with the Pi through SPI (a synchronous serial communication protocol), with the Teensy as slave and the Pi as master. Configuring the Teensy as slave is not supported with the traditional SPI library, and thus a user-provided library was used in which SPI slave mode is implemented with interrupts [151]. SPI was chosen over I^2C (another serial communication protocol, which has more library support) for speed considerations. Since the transfer time between the Teensy and the Pi cuts down on measuring time, the current SPI speed of 10 MHz has much less effect on integration times than the $\mathcal{O}$(kHz) I^2C speeds.

3.1.3 Circuitry

The conductivity and temperature circuit board is shown in Figure 3.3.

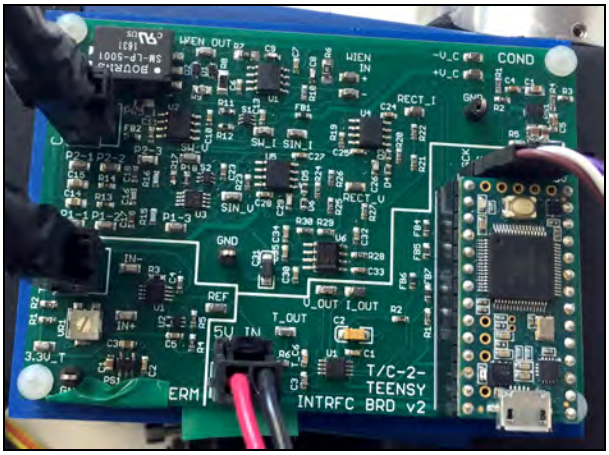

Figure 3.3: Circuit board for temperature and conductivity circuits; Teensy microcontroller is mounted on lower right.

Conductivity circuitry

The circuitry for the conductivity sensor was based on the system designed specifically for this application by Eck [152]. An oscilloscope trace showing the output of different stages of the circuit is shown in Figure 3.4. A sine wave excitation is provided by a Wien bridge, a self-oscillating circuit that takes advantage of the resonance frequency of RC circuits cou-

pled with positive feedback from an operational amplifier [153] (see Appendix B, Section B.4 for more information on Wien bridge circuit design). To power the 0 V-centered sine wave, the circuit uses a dual charge pump regulator with both positive and negative outputs (Texas Instruments LM27762) configured to produce ±3.3 V. An oscillation frequency of 72 kHz was chosen to avoid electrode polarization issues (see Section 1.9.3, p. 88, for background and Section 3.2.3 for results).

This signal excites the probes through a transformer, which galvanically isolates the probes from the rest of the instrument in order to prevent current from shunting to other unknown potentials in the seawater. The magnitude of the current and voltage through the transformer depends on the effective conductance between the probes. Rather than fixing one and measuring the other, this circuitry measures both (current and voltage) so that conductivity can be found from the quotient $g \sim I/V$. This makes the circuitry less susceptible to power supply drift. The current is measured with a transimpedance amplifier circuit (using a Texas Instruments OPA211, a general purpose op amp used in other conductivity circuit elements as well) on the primary side of the transformer. The voltage across the probes is measured across the transformer secondary, but galvanic isolation is maintained by capacitive coupling to the input of a suitable instrumentation amplifier (Analog Devices AD8220). To accommodate the large range of potential conductivities to be measured, the gain resistor for each amplifier is separately selectable by software-controlled switches. Each amplifier has a high-gain option that is three times its low-gain option (for current, gains of 10 and 3.3; for voltage, gains of 34 and 106). More information on the circuitry is given in Section 3.2.1.

Both current and voltage signals, as output by the amplifiers, are sine waves centered around 0 V. They are independently rectified with precision full-wave rectifier circuits [154] before being filtered by a Sallen-Key filter to analog outputs, which are then read in by two channels of the ADC.

The filter produces a value that is 0.637 of the amplitude of the sine wave, since the average over a rectified sine wave is $2/\pi$ times its amplitude. The maximum amplitude of the sine wave achievable with this circuitry (with e.g. very high or very low conductivity between the probes) is the supply voltage, assuming rail-to-rail capabilities for the amplifiers, which is the same as the ADC reference (3.3 V). Thus, the maximum output of the filter is only 0.637 times the ADC reference, and the circuit is unable to utilize the full range of the ADC. Future iterations of this circuit would include a post-filter amplifier, as in the design by Eck [152].

Temperature circuitry

The thermistor used, the GP104L8F, is an NTC thermistor (see Section 1.10.1, p. 93 for background on thermistors) with a nominal 25 °C resistance of 100,000 kΩ. Its resistance-temperature curve is given in Figure 3.5. Although the curve is nonlinear, it can be linearized locally to provide a linear calibration curve in a given range of temperature.

A Wheatstone bridge is used to convert the resistance to a measurable voltage. The resistor values were chosen based on the $R-T$ curve of the thermistor, the target temperature range, and the V_{out} vs V_{CM} curve of the amplifier; see Appendix B, Section B.3 for more information. The chosen values of ∼150 kΩ correspond to a center temperature of ∼17.5 °C.

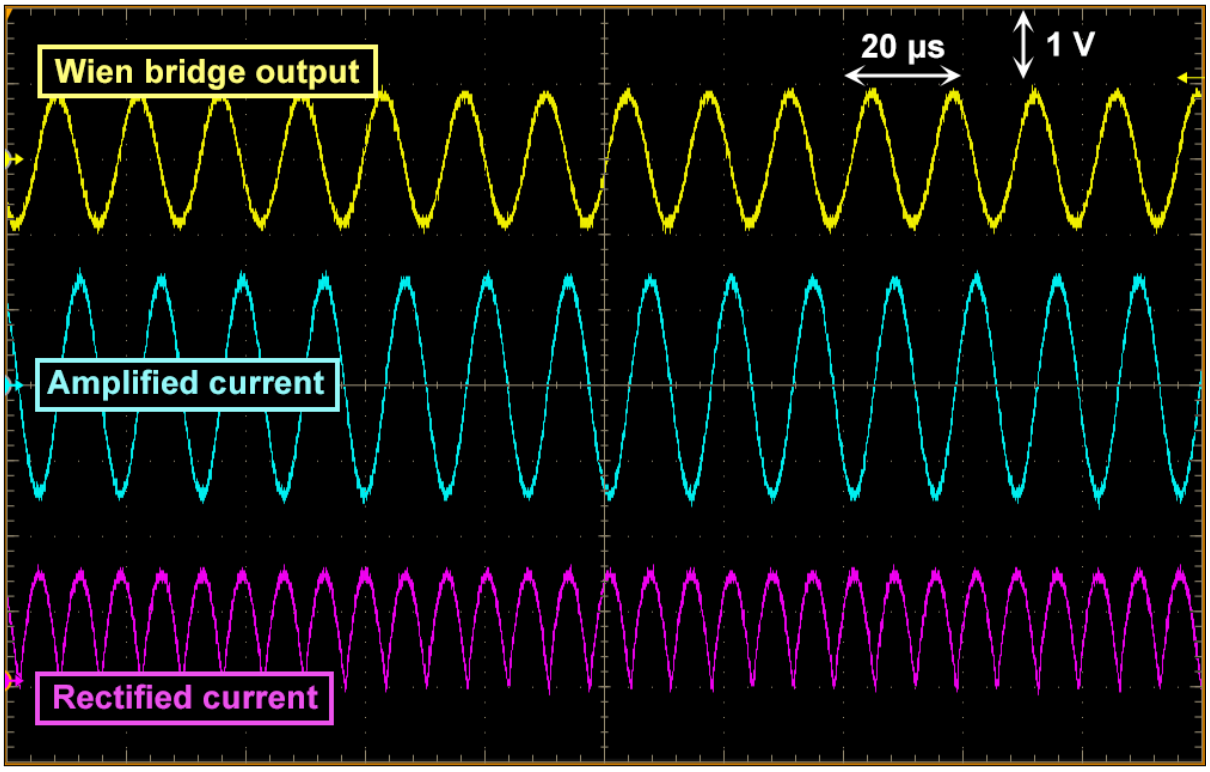

Figure 3.4: Oscilloscope trace showing different stages of the conductivity circuit.

The differential voltage from the Wheatstone bridge is fed to an instrumentation amplifier (Texas Instruments INA333), which amplifies and shifts it by a reference voltage. The reference voltage is set to $V_S/2$, to produce an output between 0 and V_S. A model of the output voltage with the gain and potentiometer values used ($G = 4$ and $R_{pot} = 138\,k\Omega$) is given in Figure 3.6. The theoretical effective range of the circuitry is roughly 7 °C to 25.5 °C. The potentiometer resistance can also be adjusted to fine tune the target temperature range, as shown in Figure 3.7.

Since the output of the temperature circuitry is an analog value that is sensitive to power supply noise and drift, a linear regulator (Texas Instruments TPS73133) is used rather than a noisier switching regulator, and the ADC is referenced to the power supply.

Analog to Digital Convertor

For simplicity, the conductivity and temperature circuits share an analog to digital convertor (ADC). The MAX11613 (Maxim Integrated) convertor used is a 12-bit I^2C ADC with four channels. The number of channels the ADC reads can be changed during operation by sending the appropriate commands. I^2C was chosen over the faster SPI because the Teensy is already an SPI slave (to the Raspberry Pi), and cannot be an SPI master at the same time. The MAX11613 is capable of 400 kHz operation, which is more than fast enough for these measurements.

Channels 1 and 2 are connected to the current and voltage measurements from the conductivity circuit, while channel 3 is the output of the temperature circuit. Channel 4 is connected to

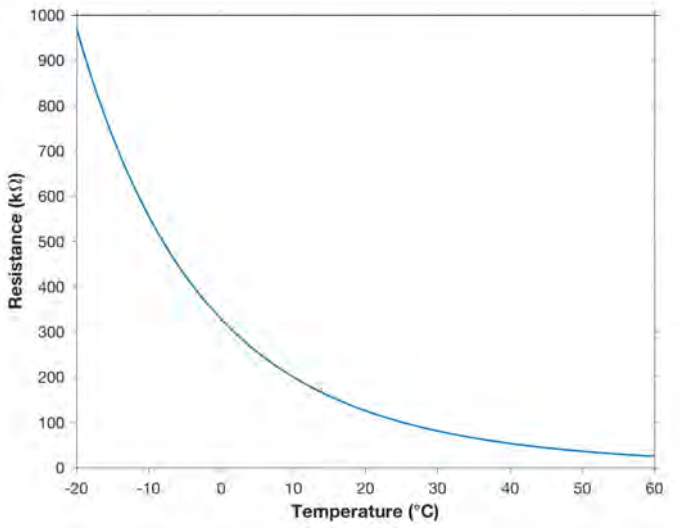

Figure 3.5: Resistance-temperature curve for GP104L8F thermistor. NTC thermistors exhibit nonlinear R-T curves, but are often approximated as linear within some range of interest.

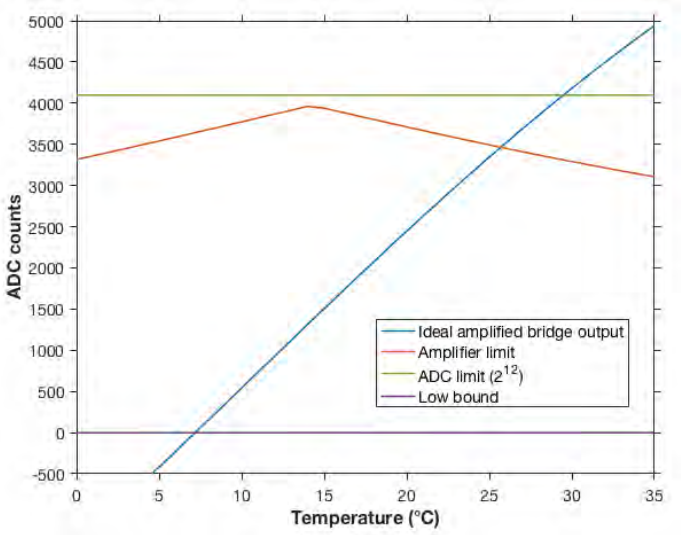

Figure 3.6: Modeled output of temperature measurements with $R_{\text{top}} = 150\,\text{k}\Omega$, $R_{\text{pot}} = 138\,\text{k}\Omega$, and amplifier gain = 4. The output of the Wheatstone bridge is roughly linear within the target temperature range, but nonidealities of the instrumentation amplifier limit output even below the ADC limit.

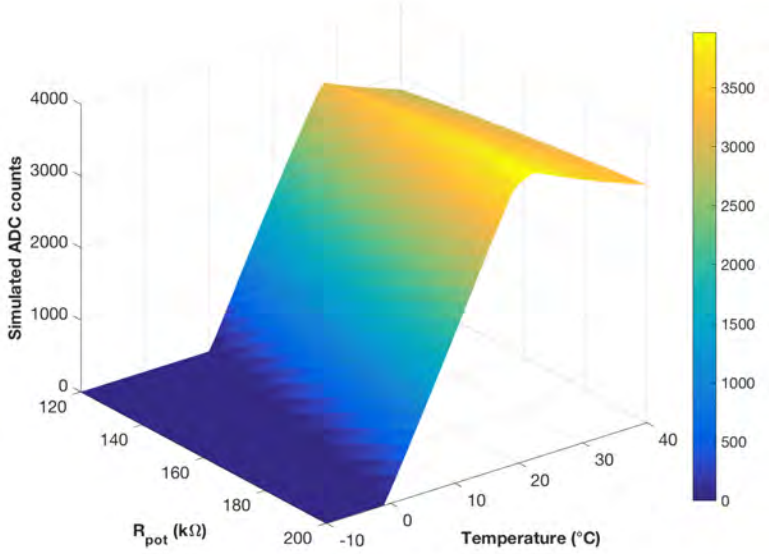

Figure 3.7: Modeled output of temperature measurements with $R_{\text{top}} = 150\,\text{k}\Omega$ and amplifier gain = 4. The potentiometer is controlled by a thumbwheel that can be tuned to target different temperature ranges. Graph shows the effective output value including consideration of amplifier limits.
Color bar is a representation of the z axis.

the supply voltage for the temperature circuit and is used as a reference when temperature is measured. So that the two sensors can operate independently, channel 4 is used as a reference only when temperature is measured. The reference for conductivity-only measurements, during which the temperature circuitry may or may not be on, is the ADC supply (provided by a regulator on the Teensy). Thus, the ADC reference for the conductivity circuitry depends on whether temperature is also measured, which in principle can lead to two calibration curves. However, all voltages are nominally 3.3 V, and in practice the effect of changing references was found to be minimal.

The ADC circuitry and architecture was later changed to utilize separate ADCs for conductivity and temperature. This change is described in Section 3.4.4 and does not apply to the results presented in this chapter.

3.1.4 Teensy control

As described in Section 3.1.2, the conductivity and temperature circuitry interface with a front-end Teensy microcontroller rather than with the Raspberry Pi directly. This enables the Teensy to continue to read conductivity and temperature measurements even as the Raspberry Pi is counting photons for fluorescence measurements, enabling simultaneous measurement. With the ADC speed of several hundred kHz, the Teensy is generally able to read multiple ADC values per fluorescence measurement. Thus, the Teensy averages many ADC values for each measurement, which reduces the impact of circuitry and ADC noise.

Whether the Teensy measures conductivity, temperature or both depends on a 'state' that is set independent of the measurement. The Teensy stores its state as an internal variable, which then determines how many and which ADC channels it reads. It can also turn temperature and/or conductivity on and off separately, check their voltages, and adjust the conductivity gain. Finally, it instrument can also auto-select gain values by comparing the numbers read in with given threshold values. The thresholds are calculated based on the relative gains of the resistors.

The user interacts only with the Raspberry Pi, which then communicates with the Teensy. SPI, the communication protocol used between the Teensy and the Pi, is implemented with interrupts. The code is structured such that the Teensy is ready and waiting with its values when the Pi sends an interrupt. This is implemented using relatively precise knowledge of the speed at which the Teensy reads its ADC; see Appendix B, Section B.2 for more information on the calculation. For more information on the breakdown of operations between the Teensy and the Pi, refer to the source code (available upon request).

3.2 Performance of conductivity sensor

3.2.1 Circuit analysis

The conductivity circuit is by nature quite complicated. It contains several sources of non-idealities, and their propagation through the circuitry is not immediately obvious. To better understand the behavior of the circuit and how and under what circumstances it deviates from

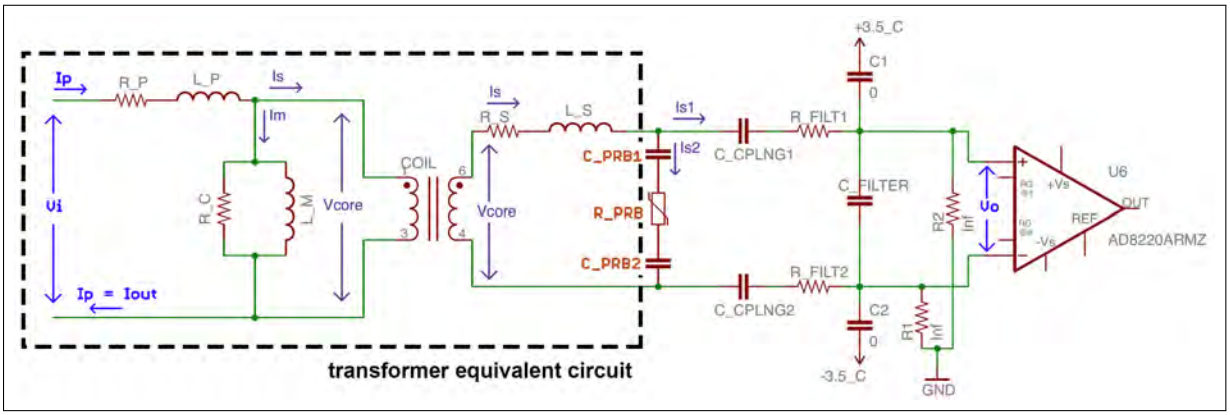

Figure 3.8: Model of transformer including transformer unidealities.

ideal behavior, as well as to aid in design choices and provide a basis for troubleshooting, a model was implemented in MATLAB based on basic circuit analysis.

The model was based on the pre-amplifier circuitry[1] shown in Figure 3.8. An AC voltage V_{in} is applied on the primary of the transformer, and the resulting current 'passes through' the probe resistance via coupling across the transformer coils. Given a fixed amplitude V_{in}, and neglecting transformer non-idealities (discussed in greater detail below), the current on the primary I_{p} should be proportional to the conductance across the probes. Thus, by measuring the primary current I_{p}, conductance across the probes can be approximated without direct electrical contact (i.e. galvanic isolation).

In practice, the driving input V_{in} is not always stable, and the measurements need to correct for its potential drift or change. One option is to reference the ADC to the amplitude of V_{in}, as done by Eck [152] in the first generation of the conductivity circuitry design. The second generation design, however, uses a self-oscillating circuit (Wien bridge) to produce the input sine wave[2], which has an amplitude independent of any supply. To account for changes in the input amplitude, the circuitry instead measures the voltage across the cell directly, in addition to the primary current I_{p}.

Voltage is measured on the transformer secondary, where it is capacitively coupled (to maintain galvanic isolation) to the AD8220 instrumentation amplifier through capacitors C_{cpling1} and C_{cpling2}. A filter is also in place at the amplifier input, as recommended by the manufacturer, comprising $R_{\text{filt1/2}}$, C_{filter} and $C_{1/2}$. The remaining external circuit elements in Figure 3.8, R_1 and R_2, are for input bias current of the amplifier, which is negligible. Thus, the measured output voltage V_{o} ultimately corresponds to the voltage across the secondary after passing through the coupling capacitors and the filter circuitry.

From the results of the model implemented in MATLAB (Figure 3.9), most of the external elements between the transformer and the voltage amplifier did not appear to significantly influence the sensor's response. However, the filter circuitry creates some nonlinearities at very low conductivity (high voltage, low current), even causing a 'hook' in the calibration

[1] Everything beyond the amplifiers is roughly linear.

[2] This change was driven by the availability of components compatible with the 3.3 V system, as opposed to the 5 V system used by Eck [152].

curve whereby the measured I/V actually rises as conductivity decreases (Figure 3.9c). The effect appears to arise from the filter branch (of the filter–probe parallel circuit) becoming non-negligible as the voltage across the probe branch increases. Lower capacitance and higher resistance bring the filter closer to an open circuit and minimize the effect; the values $C_{\text{filter}} = 1\,\text{nF}$ and $R_{\text{filt1}} = R_{\text{filt2}} = 20\,\text{k}\Omega$ were chosen based on this consideration as well as manufacturer recommendation.

In practice, this 'hook' in the calibration curve was indeed observed, although it did not seem to arise from a drop in voltage as predicted by the model (Figure 3.9b) but instead by a rise in current (results are presented in Figure C.5 of Appendix C, Section C.1.3 since they correspond to the 1 kHz system). After the frequency was increased to 72 kHz, it was no longer observed, possibly due to the effect of other circuit elements that become more prominent at higher frequencies.

Transformer non-idealities, shown in the labelled equivalent circuit in Figure 3.8, may play a bigger role in circuit nonlinearity. In particular, the finite magnetizing inductance L_{M} and core losses R_{C} shunt current around the probe, adding to the measured current on the primary side and thereby introducing an offset in current (and subsequently conductivity) [152]. This magnetizing current I_{M} is nonlinear with the conductance across the probes in the parallel branch, as can be seen in the model output in Figure 3.10

This behavior causes the current (Figure 3.9a) to be nonzero at infinitesimal probe conductance, and to increase nonlinearly as G increases.

On the other hand, the nonzero DC resistances on the primary and secondary sides, R_{p} and R_{s}, affect the behavior of the circuit at higher conductivities. As the resistance between the probes becomes comparable to the values of these series resistances, they form a voltage divider. If other circuit elements are disregarded (including potential reactive elements in the probes themselves, represented in Figure 3.8 as C_{probe}; see Appendix C, Section C.1 for a further discussion of probe capacitance), then

$$\begin{aligned} I_0 &= V_{\text{in}} \frac{1}{R_{\text{p}} + R_{\text{s}} + R_{\text{probes}}} \\ V_0 &= V_{\text{in}} \frac{R_{\text{probes}}}{R_{\text{p}} + R_{\text{s}} + R_{\text{probes}}} \end{aligned} \tag{3.1}$$

At very high conductivities, the probes approach a short circuit; $R_{\text{p}}+R_{\text{s}} >> R_{\text{probes}}$, and R_{probes} in the denominator of Eq. (3.1) becomes negligible. Shown graphically in Figure 3.9, the current asymptotes at $V_{\text{in}}/(R_{\text{p}} + R_{\text{s}})$ (for the $R_{\text{p}} = R_{\text{s}}$ values used here, this would be $3\,\text{mA} \times V_{\text{in}}[V]$), while the voltage decreases linearly toward zero. The 72 kHz situation exhibits greater deviation from this behavior, indicating the influence of other circuit elements; differences between the different frequencies reflect the influence of the reactive elements in the circuit.

The voltage divider (Eq. (3.1)) does introduce some nonlinearities where R_{probes} is comparable to $R_{\text{p}} + R_{\text{s}}$, which for the transformer used corresponds to $G \approx 3000\,\mu\text{S}$. These appear in Figure 3.9 as inflection points in I, V, and/or I/V around this value.

The last transformer non-idealities included in the model are the nonzero leakage inductance on each side, L_{p} and L_{s}, arising from imperfect magnetic coupling. The other labelled variables in Figure 3.8, $I_{\text{s}} = I_{\text{s1}} + I_{\text{s2}}$ and V_{core}, represent intermediate variables used to aid the modeling (current on the secondary side and voltage coupled across the transformer, respectively).

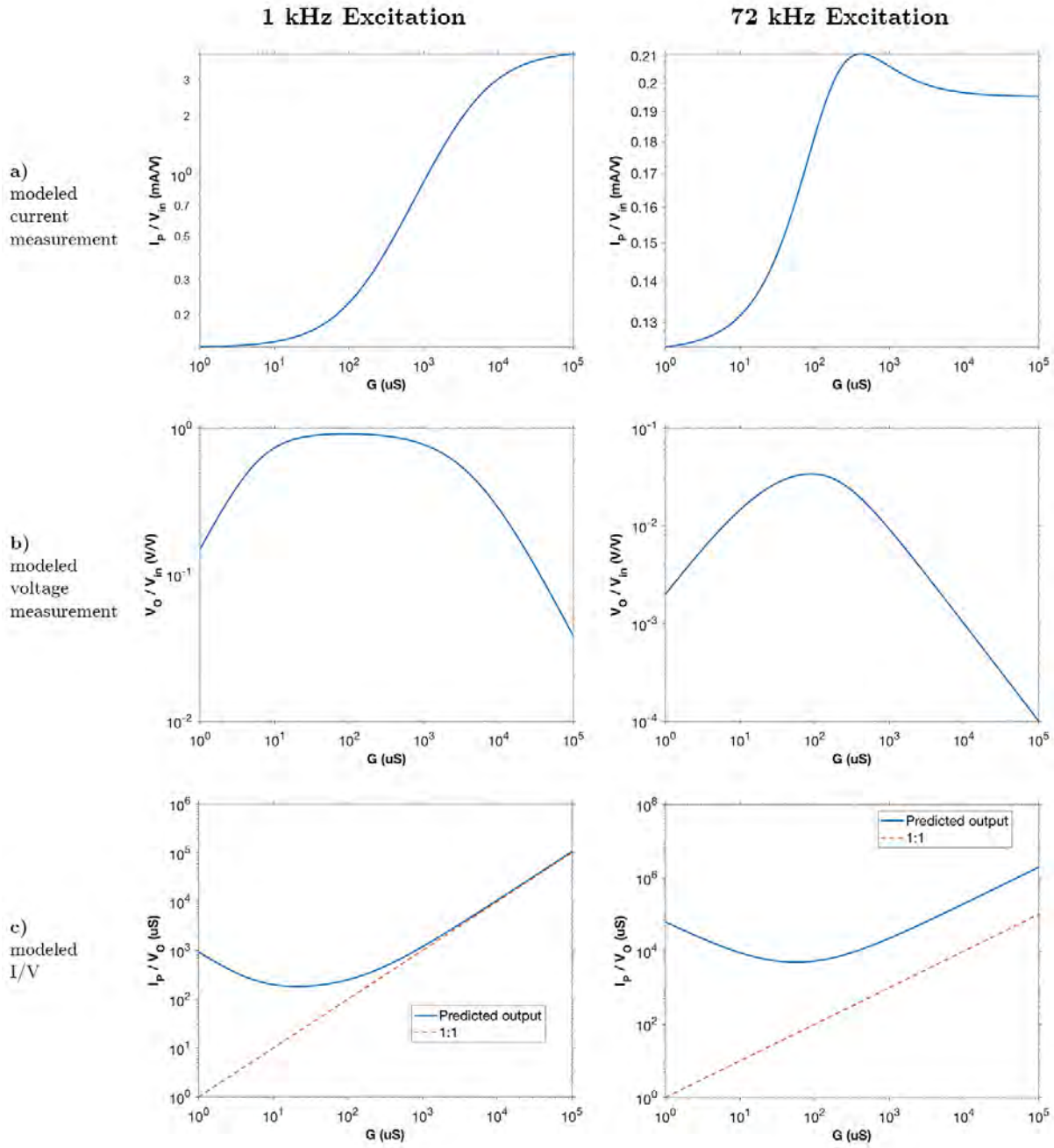

Figure 3.9: Output of MATLAB model based on circuitry in Figure 3.8. Amplitude of **a)** current I_p and **b)** voltage V_o are shown relative to the amplitude of the input voltage V_in. Their **c)** resulting quotient I/V is used to calibrate to conductivity. Ideal output is a zero-intercept, positive-slope line for current, a flat (fixed) voltage, and a I/V value that matches actual G on the $1:1$ line. However, the circuits differ from ideal due to transformer non-idealities and other circuit elements. To show frequency dependence of the phenomenon, results are shown for two excitation frequencies: 1 kHz, the original frequency used, and 72 kHz, the actual frequency used due to electrode polarization issues (see Section 3.2.3). Both current and voltage values are much smaller for the higher frequency, requiring more gain (leading to more noise and less precision). The deviation of the I/V vs G curve with 72 kHz is in principle not an issue because it simply adjusts the calibration, but it indicates the effect of non-idealities on the absolute values measured.

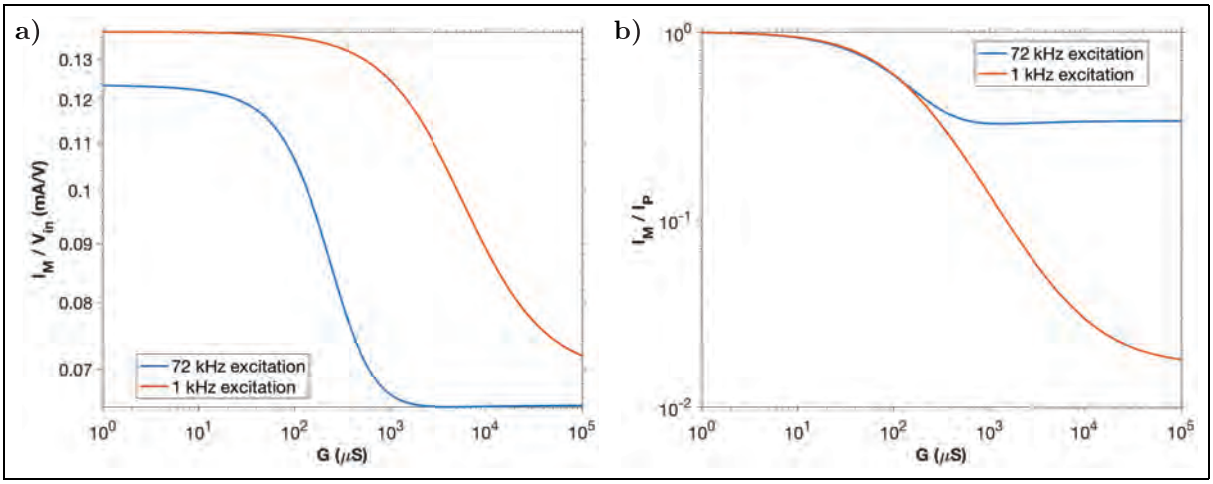

Figure 3.10: Output of MATLAB model of **a)** magnetizing current I_{M} shunted around the probe, and **b)** its proportion to the total current measured by the system ($I_{\mathrm{p}} = I_{\mathrm{M}} + I_{\mathrm{s}}$).
As $G_{\mathrm{probes}} \to 0$ ($R_{\mathrm{probes}} \to \infty$), the equivalent resistance of the two parallel branches increases towards $R_{\mathrm{C}} + j\omega L_{\mathrm{M}}$, the current passes exclusively through the shunt, and the magnetizing current—*and* the primary current I_{p}—trends toward $V_{\mathrm{in}}/R_{\mathrm{C}} + j\omega L_{\mathrm{M}}$ (leftside asymptotes). As $G_{\mathrm{probes}} \to \infty$ ($R_{\mathrm{probes}} \to 0$), the shunt branch becomes negligible compared to the probes and almost no current passes through it (rightside asymptotes). The transition region in the middle show the range where $R_{\mathrm{C}} + j\omega L_{\mathrm{M}}$ and R_{probes} are comparable.
The total current I_{p} changes as the equivalent impedance across the two branches changes, but the proportion shunted around the probes changes as well with the changing relative impedances. This results in slightly different transition points for the magnetizing current (**a**) and its ratio to total current (**b**).
Comparison between the two excitation frequencies indicates that the absolute magnetizing current is slightly less for the higher frequency, but it never decreases (as conductivity increases) to as small a proportion of the primary current as with the lower frequency, because at higher frequencies the series inductances are more significant and limit the overall current as the probes approach a short circuit.

In a transformer, more wire is required for higher magnetizing inductance, so DC resistance (DCR) increases with L_M. This presents a fundamental tradeoff between the non-idealities of finite L_M and nonzero DCR [152]. However, DCR is less of a problem for this circuit; a lower value would shift the inflection points to higher conductivities, but either way the calibration curve is still nonlinear[3]. A transformer was therefore chosen with a very high magnetizing inductance of 3.8 H. Its DCR is 115 Ω on each side (i.e. this transformer is symmetrical; there is no real primary or secondary), which is actually quite low given its high L_M. These parameters, along with a shunt resistance R_c of 7500 Ω and leakage inductance $L_p = L_s$ of 6 mH, were used in the MATLAB model to produce the results given in Figures 3.9 and 3.10.

The probes in the circuit diagram Figure 3.8 are shown as a series C–R–C circuit, which includes the capacitance from the double layer formation at the electrode surface, as in Figure 1.21 (p. 89). For Figures 3.9 and 3.10, this component was modeled as a simple resistor (with $R = 1/G$), which effectively assumes an infinite C_{probe}. In a modification of the model that showed results for a range of C_{probe} values, the probe capacitances were found to have negligible impact; see Appendix C, Section C.1.2 for more information. The probe capacitance did, however, have an effect on the time response of the sensor, as discussed in Section 3.2.3.

Figure 3.9 represents the expected behavior of the circuit, including expected deviations from ideal $I/V = G$ behavior. Not all non-idealities were included so further deviations in the actual performance are not necessarily anomalous, although they should not be too significant.

3.2.2 Actual behavior: calibration curve and cell constant

A calibration curve of the conductivity sensor is shown in Figure 3.11. As discussed in Section 3.1.3, two gain options are available each for the conductivity and voltage measurements, to achieve better resolution even for low I or V values. Thus, Figure 3.11 shows separate calibration curves for the different combinations of gain settings. The 'both low' gain setting is broken into two calibration curves; due to the non-idealities discussed in Section 3.2.1, the calibration curve is not linear across the full dynamic range. With this piece-wise calibration, the low gain setting is in fact usable across the entire range of conductivities. However, use of high current gain at low conductivities, and high voltage gain at high conductivities, increases the resolution of the measurements.

Conductivity probes in general do not have global linearity, which is usually not an issue, as most natural settings would not exhibit a range of conductivities that could not be captured by a single linear curve. Instead, it is recommended to always calibrate around the measurement point [103]. For eddy correlation, any errors from nonlinear calibration are further minimized because the absolute number is less important than deviations around a mean.

The performance of the sensor can be seen in greater detail by looking at the measured current, voltage, and I/V as a function of conductivity, in analogy to the model results in Figure 3.9[4]. Results are presented in Figure 3.12 for a set of fixed resistors, as well as the probes immersed ∼2 cm into solutions of various conductivities. The solutions used included distilled water, tap

[3]DCR is a not a problem here for high conductivities because both current and voltage are measured. If only current were measured and then compared to the fixed V_{in}, as in the first generation design, then the DCR would restrict the dynamic range at high conductivities [152].

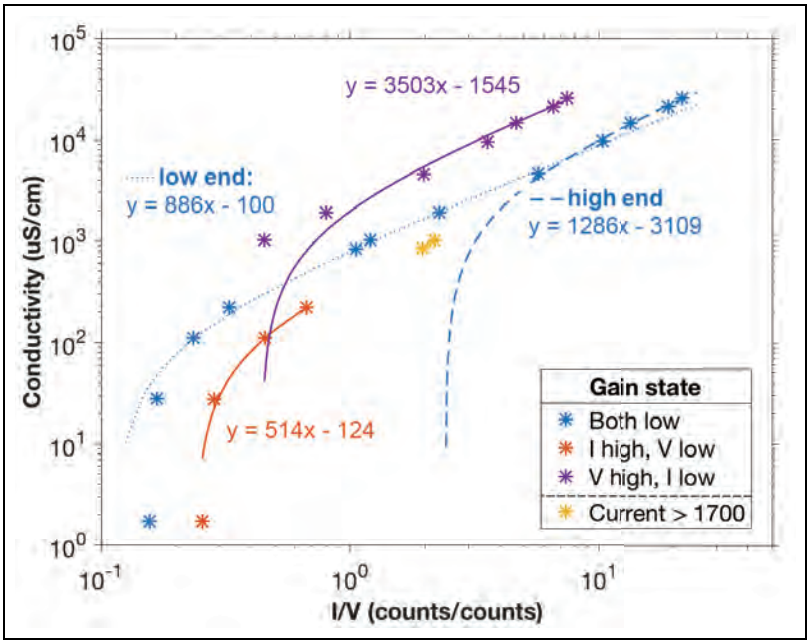

Figure 3.11: Calibration curves of conductivity sensor, showing separate curves for high current / low voltage gain, high voltage / low current gain, and low current / low voltage gain settings. Data points where the current measurement came out to >1700 counts are marked separately, as the high current draw appears to affect the voltage measurements.

water, NaCl solutions of various concentrations (0.001 to 0.1 %), brackish water collected from Boston Harbor (filtered with a 0.2 µm filter), and mixes of the brackish water and freshwater. Their conductivities were measured separately with a commercial handheld conductivity meter (Amber Science Model 604).

The results exhibit some but not all of the features predicted by the model. Namely, the current asymptotes at both low and high conductance, and the voltage decreases linearly with conductance past ∼300 µS. The 'hook' at low conductivity and the 'bump' in current predicted by the model were not seen, possibly due to other features of the circuit that were not captured (e.g. series resistance from electrode polarization). The three gain settings correspond well to each other and are relatively linear in their respective ranges, which allows the linear calibration curves shown in Figure 3.11.

The results for resistors (vs conductance G) and probes (vs conductivity g) can be combined to estimate the cell constant of the probes. As shown in Figure 3.13, this was accomplished by first using data measured with the resistors to map the sensor's I/V output to conductance values. Relatively high-order fits (third-order) were used in an attempt to capture circuit non-linearities that would affect both conductance and conductivity measurements. These fits were then used to map the I/V values measured by the probes to the corresponding conductance values, as shown in Figure 3.13b. Finally, the cell constant K was calculated by dividing conductance by conductivity. The ideal conductivity-conductance characteristic is a zero-intercept line with slope equal to the cell constant, and the ideal cell constant is a fixed constant.

The cell constant found here is relatively constant ($K \approx 1.5\,\mathrm{cm}^{-1}$) in the range of $g =$ 200 to 5000 µS/cm. This value falls well in the range recommended by one manufacturer of 0.4 to 1 cm^{-1} for environmental waters, and up to $K = 10\,\mathrm{cm}^{-1}$ for high conductivity solutions

[4]The y axis values here cannot be compared directly to the model, even with an estimate of V_{in}, because they represent amplified, rectified, and filtered outputs. The amplifier may deviate from its ideal gain due to gain-bandwidth limitations. However, the shapes of the curves should be comparable.

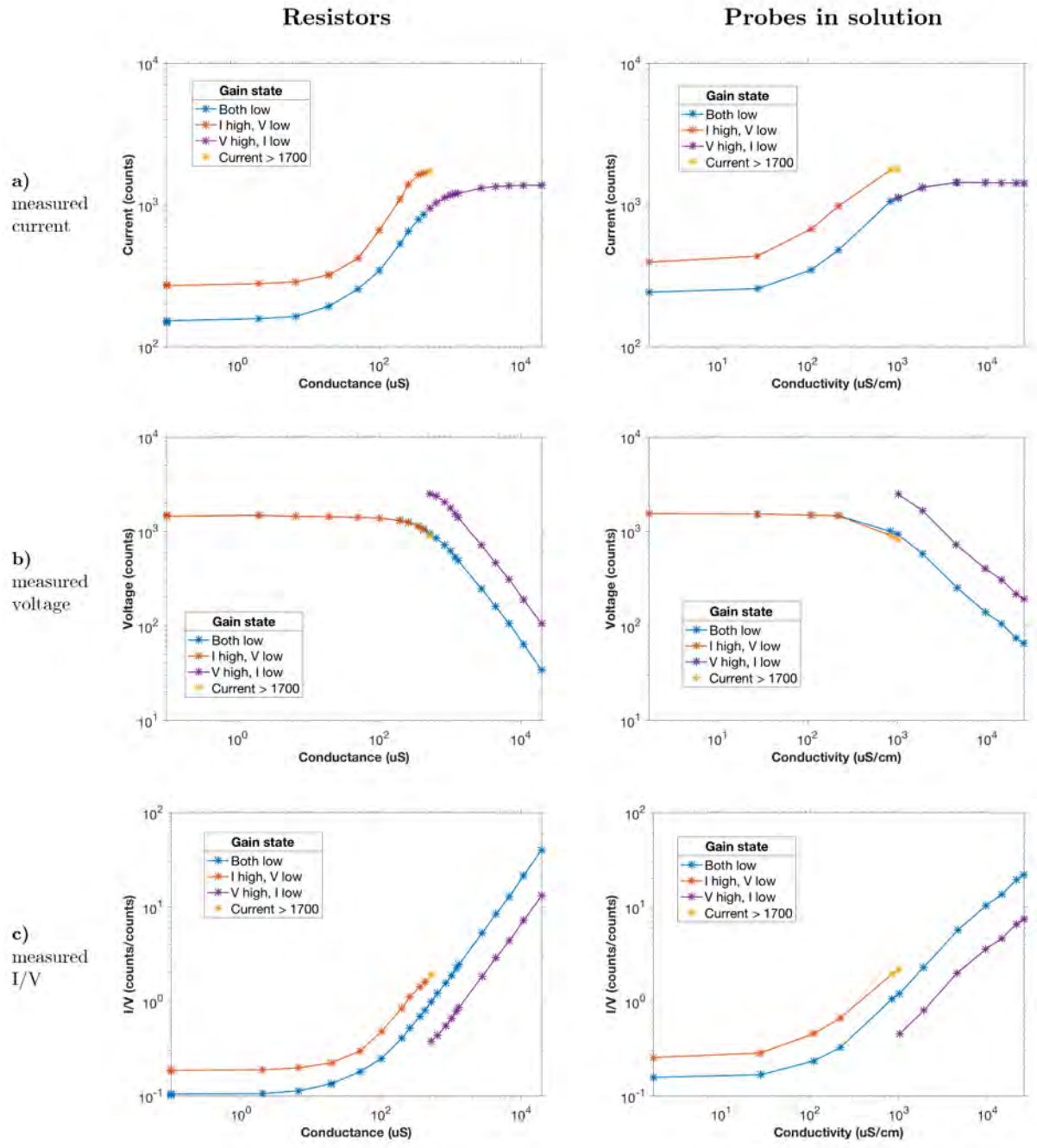

Figure 3.12: Measured output of conductivity circuitry for **a)** current and **b)** voltage, as seen by the ADC after all circuit processing (including amplification, rectification, and filtering, which occur past the circuitry shown in Figure 3.8). Their **c)** resulting quotient I/V is used to calibrate to conductivity. Results are shown for measurements taken with fixed resistors (vs conductance G) and with probes immersed in solutions of various conductivities (vs conductivity g as measured by a commercial conductivity meter). The Wien excitation frequency was 72 kHz and measurements were taken with a fan blowing on the circuitry to avoid thermal drift (see Section 3.2.4).

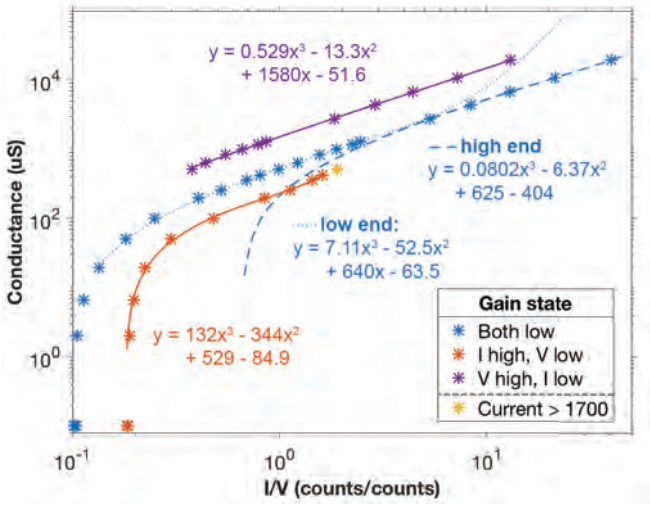

a) 'Calibration curve' mapping measured I/V to conductance, as measured from fixed resistors. Third-order fits were used to capture some of the nonlinear features.

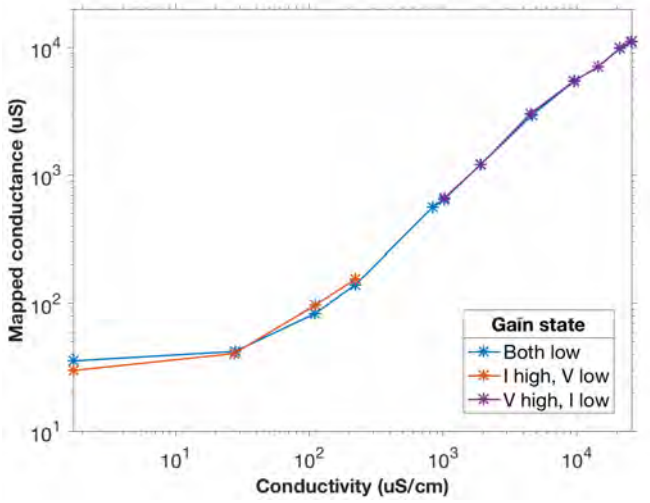

b) Measurements of probes in fixed conductivity solutions, mapped to equivalent conductance through the I/V values and the curve fits derived from resistors (**a**).

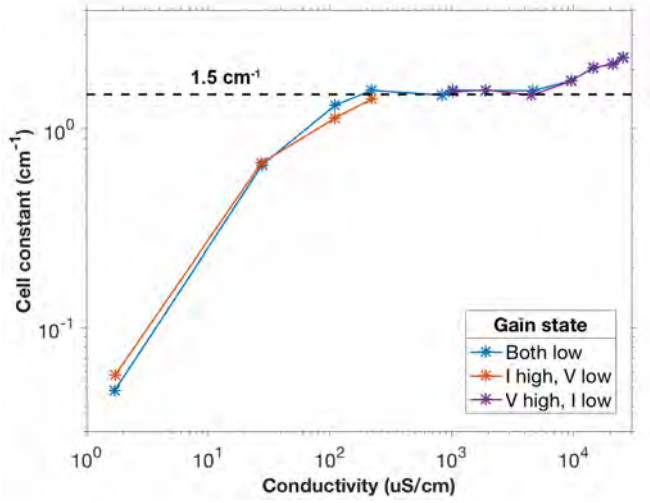

c) Estimated cell constant of probes as a function of conductivity, found by dividing the mapped conductance (**b**) by the conductivity (x axis).

Figure 3.13: Derivation of cell constant for the optical fiber probes used by combining measurements of resistors (various conductances) with probe measurements taken in solutions of various conductivities.

[103]. The cell constant also appears to be smaller at lower frequencies, and larger at higher frequencies.

Especially for low frequencies, this deviation may be partially due to the inability of the resistor curve fit to capture low-conductance values, and may not represent the true cell constant. In general, however, deviation at lower and higher conductivities is not surprising given the bigger role played by small errors when either current or voltage measurements are low. As discussed in Section 1.9.2 (p. 87) on background information for conductivity electrodes, various factors influence the cell constant—not only conductivity but also, for example, field effects (so placement of the probes in the beakers becomes important).

The nonlinearity of the cell constant impacts sensor performance by translating to nonlinearities in the calibration curve. Thus, it is likewise not a problem, since the range of conductivities in any one sample will not be large enough to be affected by the nonlinearity. However, knowledge of the cell constant is useful for characterizing and understanding the behavior of the conductivity cell.

3.2.3 Time response

The time response of the conductivity sensor is difficult to measure by transferring quickly between beakers of different solution, because it is sensitive to field effects from the degree of immersion (resulting in a drop in perceived conductivity every time it is lifted out of the water). Thus, to qualitatively assess the time response of the conductivity sensor, its performance was compared to that of the other two sensors. Under flow in a small racetrack flume, a warm, salty, fluorescent dye—which should be picked up by all three sensors—was injected near the sensing volume. The three sensors are not expected to track perfectly, and the influence of the difference in sensing volume vs response time is not clearly distinguishable (see Section 3.4.3). However, a qualitative assessment is possible by comparing the shape of the responses.

Two scenarios are shown in Figure 3.14. The conductivity sensor was initially designed using a 1 kHz excitation wave, but in the flume tests, the conductivity time series were found to exhibit less well-resolved peaks than both the fluorescence and the temperature (Figure 3.14a). The capacitive-looking features (e.g. gradual decays rather than sharp peaks) were hypothesized to arise from electrode polarization (Section 1.9.3, p. 88), and the AC excitation frequency was subsequently changed to 72 kHz by adjusting the resistors and capacitors of the Wien bridge[5]. The resulting conductivity time series, shown in Figure 3.14b, has sharper features and a faster response time.

Although these experiments cannot be used to quantify or even quantitatively compare response time, the results in Figure 3.14 indicate that some capacitive elements were present at 1 kHz that are no longer present at 72 kHz. These results, which are completely reasonable and in line our electrode polarization hypothesis, put confidence in the ability of this sort of comparison to identify a slower time response. In addition, they indicate that the higher frequency conductivity cell is able to achieve a reasonable response time, likely faster than the temperature sensor.

[5]There is nothing particularly special about the frequency 72 kHz; it was chosen based on the immediately available components. Excitation at 7.2 kHz was also tested, but was found to not completely eliminate the capacitive features seen in Figure 3.14a.

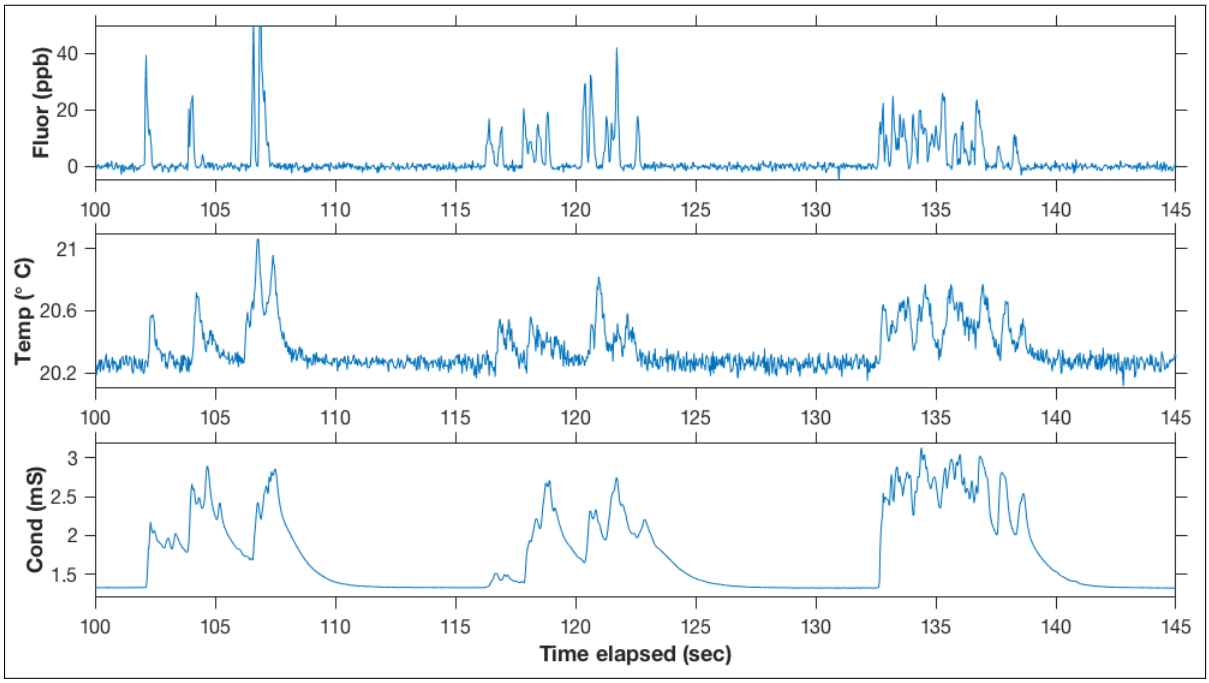

a) With 1 kHz excitation for conductivity.

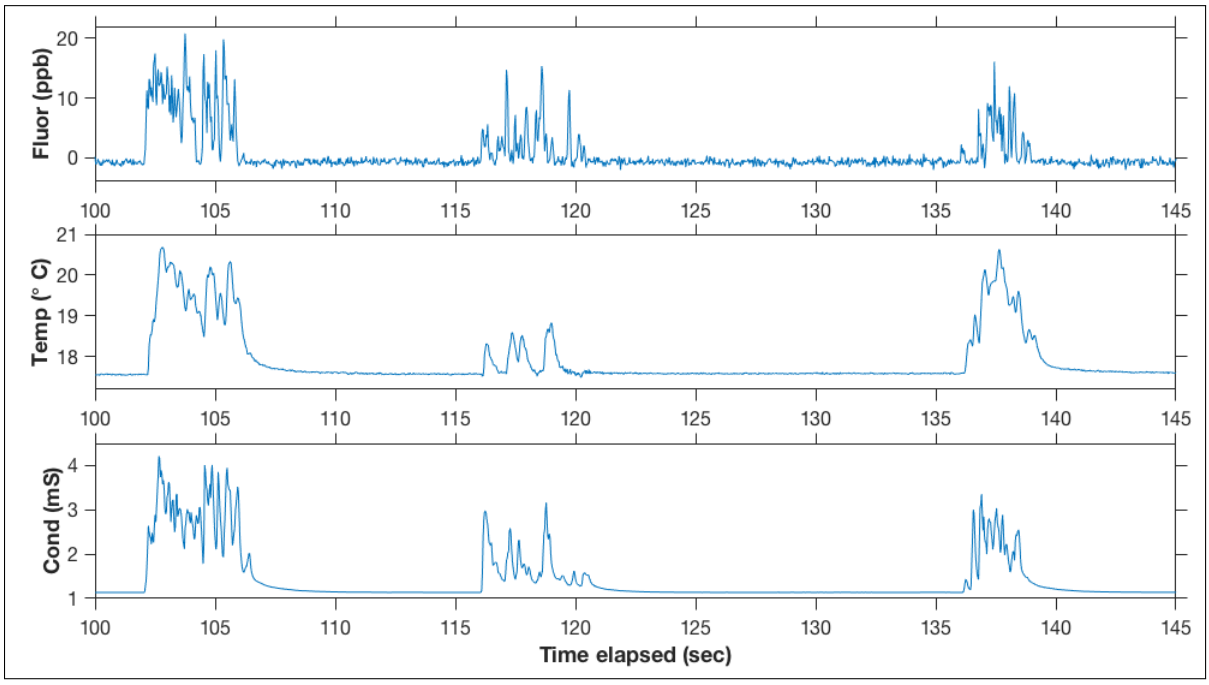

b) With 72 kHz excitation.

Figure 3.14: Simultaneous measurements of injected warm, salty, fluorescent dye, under flow. Shape of conductivity response relative to other sensors was used to qualitatively assess the conductivity's time performance.

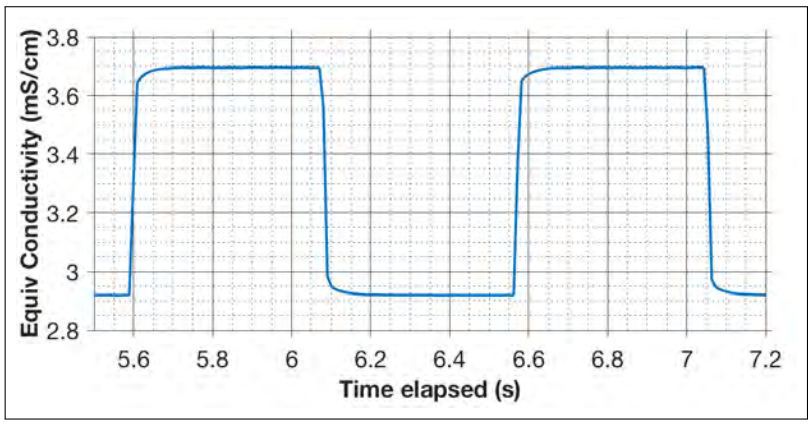

Figure 3.15: Electronic response time of conductivity sensor. Resistors were used in place of the probes, with a pulse generator used to switch between two different resistors at 1 Hz. The electronic response time is only fractions of a second, indicating that it was not responsible for the slower response observed in Figure 3.14a.
The sensor measured at 100 Hz and used an AC excitation frequency of 1 kHz.

The increase in excitation frequency does introduce other issues. For instance, the transformer is not designed for such high frequencies, and both the current and voltage signals are smaller. This effect is in fact captured by the model of Figure 3.8. To accommodate the smaller signals, the gains on the amplifiers were increased (from the 1 kHz values of 3.3 / 1.1 for current and 6 / 13.5 for voltage, to new values of 10 / 3.3 for current and 34 / 106 for voltage for 72 kHz excitation).

The electronic response time of the circuit itself was also tested separately. The probes were replaced by two parallel resistors, with a relay in one branch that was connected to a pulse generator. The pulse generator alternately opened and closed the relay so that the resistance across the probe was either R_1 or $R_1 /\!/ R_2$. Results for one set of resistors are shown in Figure 3.15. Based on these results, it was judged that the electronic response time was not responsible for the capacitive features seen in Figure 3.14a.

Subsequent tests in the flume revealed a potential time response issue relating to hydrodynamic artifact; see Section 3.4.4 for more information.

3.2.4 Drift over time

Conductivity cell constants are known to change over time [103], but this sensor was observed to exhibit variation in measurements even over the course of a single experiment. To better understand the source of this variation and whether it is of concern for eddy correlation, continuous measurements were taken of both a fixed resistor value of 680 Ω, as well as probes immersed in a solution of 1865 µS/cm. Both the resistor value and the solution were chosen because they were found to produce for this circuit values for both current and voltage that were reasonably high but not too high.

Results are shown in Figure 3.16. Both the current and voltage were observed to drop initially and then rise and fall with a period on the order of 40 min ∼ 50 min. By probing with a Keithley 2100 digital multimeter, it was found that the Wien bridge characteristics (voltage and frequency) varied in tandem with the measured current and voltage values (Figure 3.17). Theoretically, a varying V_{in} amplitude would affect both current and voltage equally—as both are directly proportional to V_{in}—and therefore not affect their quotient. However, the resulting

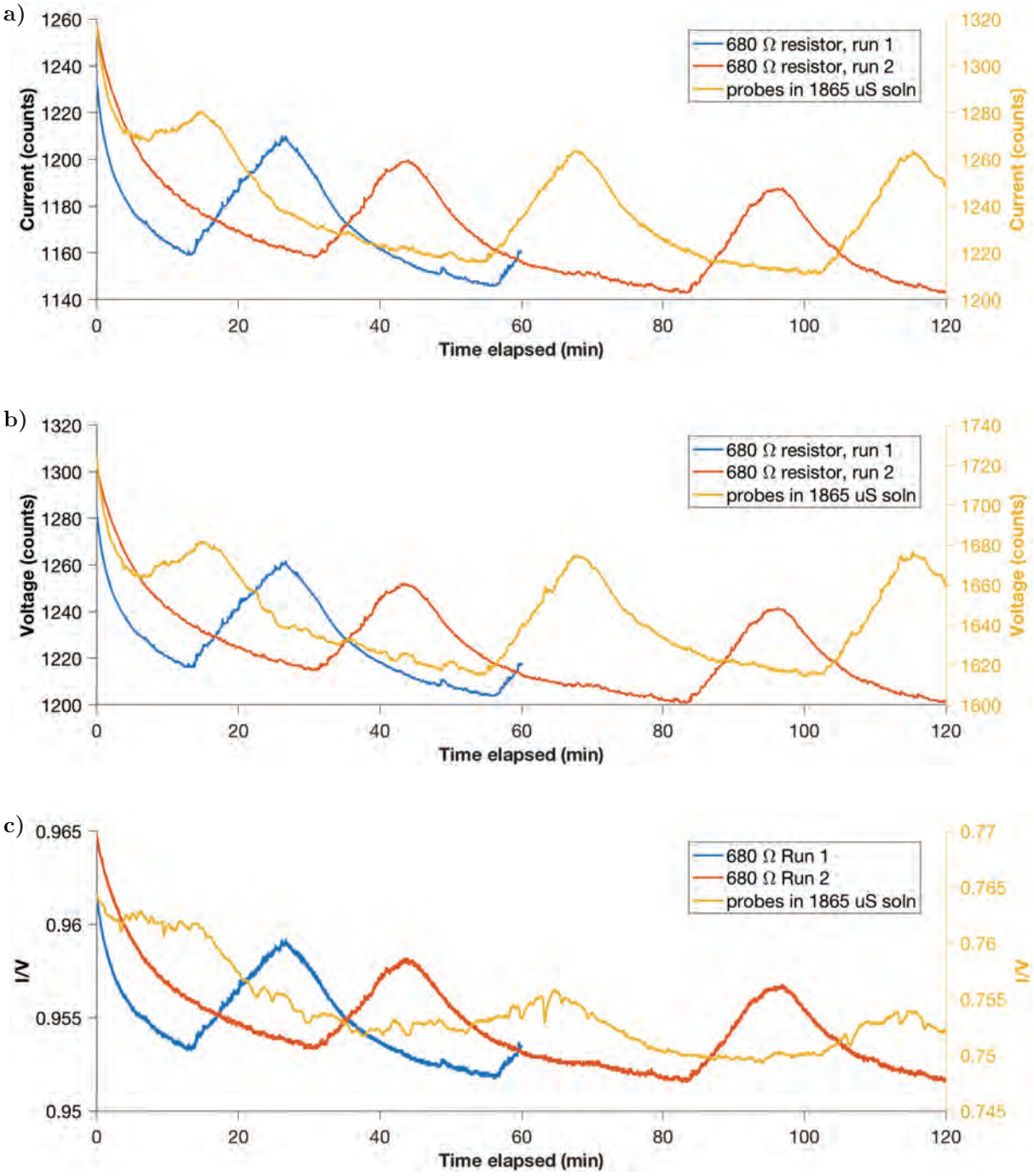

Figure 3.16: a) Current, **b)** voltage, and **c)** quotient I/V time series with fixed resistors and probes in solution, showing drift over time.

a)
Frequency.

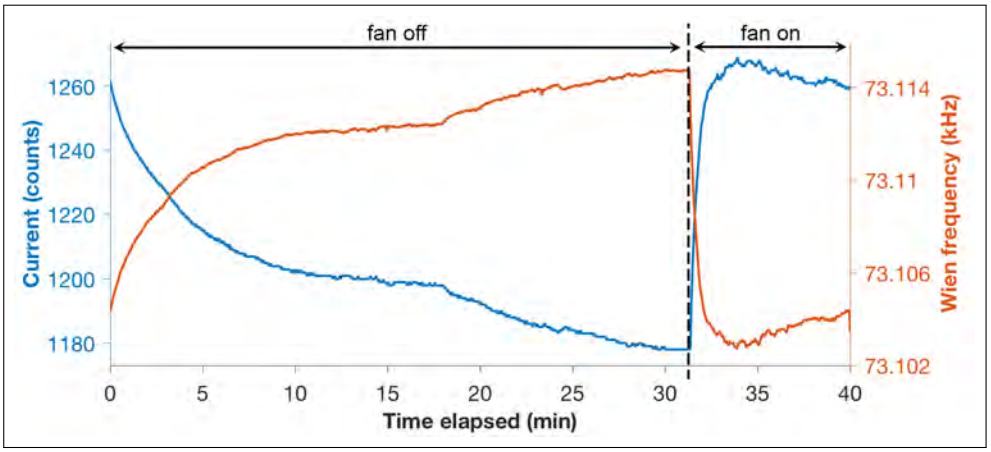

b)
Amplitude.

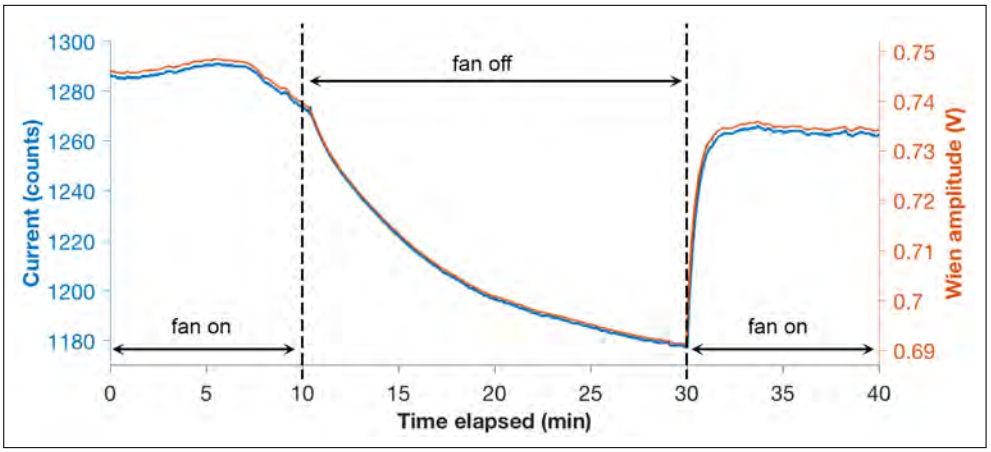

Figure 3.17: Time series of current as measured by conductivity sensor, alongside **a)** frequency and **b)** amplitude of the excitation signal provided by the Wien bridge. The observed drift in the current and voltage measurements appear to arise from drift in the Wien bridge, and was mitigated by blowing a fan on the circuitry.

I/V was observed to vary as well, possibly due to the magnetizing current which creates a fixed offset in current (Figure 3.10).

In addition, the variation was substantially reduced when a small AC fan was blown on the circuitry, indicating the influence of circuit board heating. It is likely that the warming and cooling of the resistors and capacitors of the Wien bridge affected its characteristics (see Appendix B, Section B.4 for a description of the Wien bridge oscillator). The amount of change required to produce the observed effect is small. For example, Figure 3.17a shows a change in frequency of 73.102 kHz to 73.114 kHz. Given a fixed C of 1 nF, this Δf would occur if both resistors of the Wien bridge changed from 2177.2 Ω to 2176.8 Ω. Alternatively, given a fixed R of 2200 Ω, the frequency shift could be explained by a change in both capacitors from 0.9896 nF to 0.9894 nF. These values correspond to a 0.018 % change for resistance, or a 0.02 % change for capacitance. The temperature coefficient of the ±0.1 % resistors used was likely ±15 ppm/°C, which corresponds to 0.0015 %/°C. The capacitors used were C0G (NPO) ceramic capacitors, which are known for their temperature stability; a typical temperature coefficient is ±30 ppm/°C [155]. If all four components changed in the same direction, a 5 °C change in local temperature might produce the observed effect.

In the future, more attention can be paid to heat tolerance, although the components chosen are already considered temperature-stable. However, for eddy correlation, small drift over this sort of time scale is not an issue, since it can be removed with the mean during the isolation of the fluctuating components. [which is indeed done - reference ch 4]

Thermal drift from self-heating of the cell itself was not investigated. In general, conductivity is sensitive to temperature (as described in Section 1.9.1, p. 86), and changes in temperature—whether from self-heating or from actual temperature fluctuations associated turbulent heat flux—could be expected to affect conductivity. In another dual-sensor EC study involving temperature-sensitive oxygen probes, Berg and Pace [61] found that temperature fluctuations from heat flux were large enough at the air-water interface to substantially bias oxygen eddy flux calculations; the temperature measurements were used to correct the O_2 sensor readings. Similarly, in our case, temperature measurements from the nearly collocated thermistor can be used to correct the conductivity if necessary.

3.3 Performance of temperature sensor

3.3.1 Calibration curve

A calibration curve of the thermistor is shown in Figure 3.18. As described in Section 3.1.3 (p. 132), the circuitry is designed to allow a linear calibration within an approximate range of 7 °C to 25.5 °C. The experimental data show valid measurements up to ∼28 °C, indicating that the instrumentation amplifier is able to amplify past its nominal limit.

3.3.2 Time response

The time response of the temperature sensor was estimated by moving it quickly between two beakers of water at different temperatures. An example of the resulting signal is shown

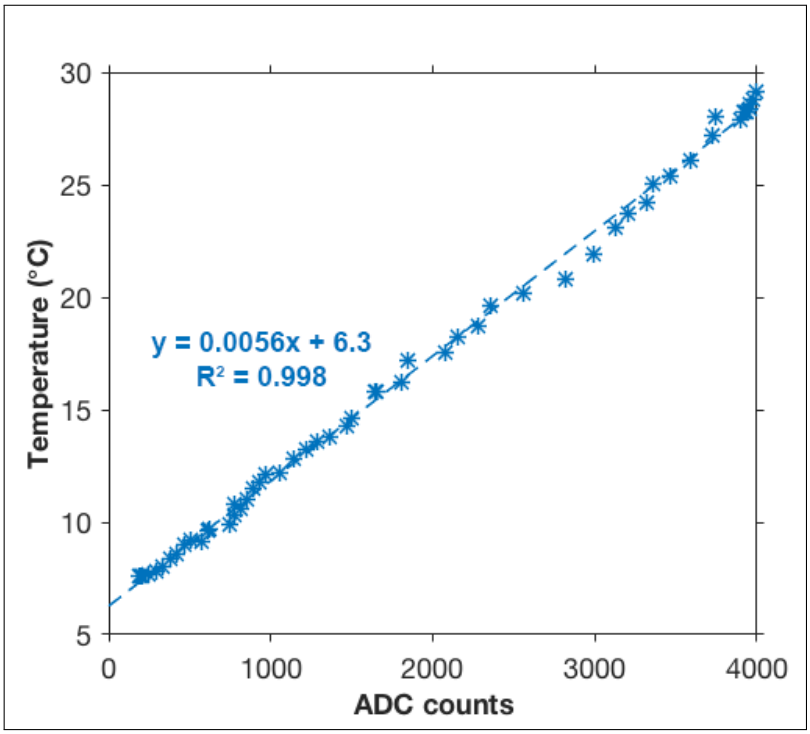

Figure 3.18: Calibration curve of temperature sensor.

in Figure 3.19. The 90 % response time, t_{90}, was calculated as the time from the start of a transition to the point where 90 % of the difference between the two values is reached. The start of a transition is defined here operationally as the point where 6 % of that difference has been reached, to account for noise in the starting value.

Based on these results, the t_{90} is estimated to be between 0.5 and 1 s. This value was not dependent on the magnitude of the change, but did vary from transition to transition. Based on the expected speeds of fluctuation given in Table 1.1 (p. 39), this response time may or may not be fast enough for eddy correlation, depending on the turbulence levels.

To determine the limiting factors of the time response, the electronic response time of the circuitry was measured separately. The thermistor was replaced by two parallel resistors, with a relay in one branch that was connected to a pulse generator. The pulse generator alternately

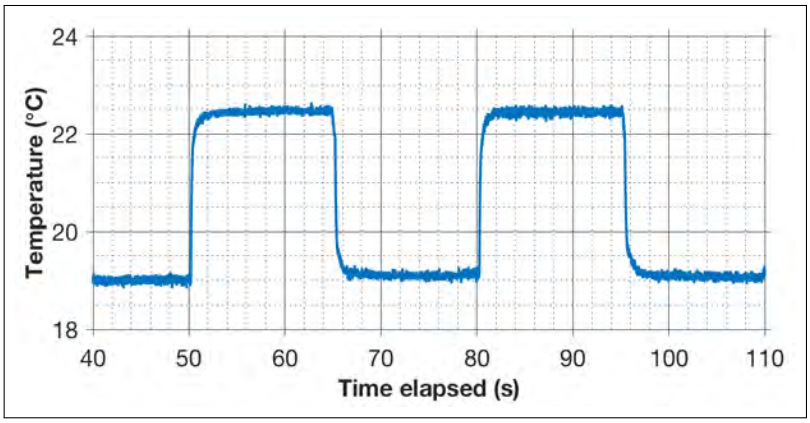

Figure 3.19: Response time test for temperature sensor conducted by transferring thermistor rapidly from one beaker of water to another.

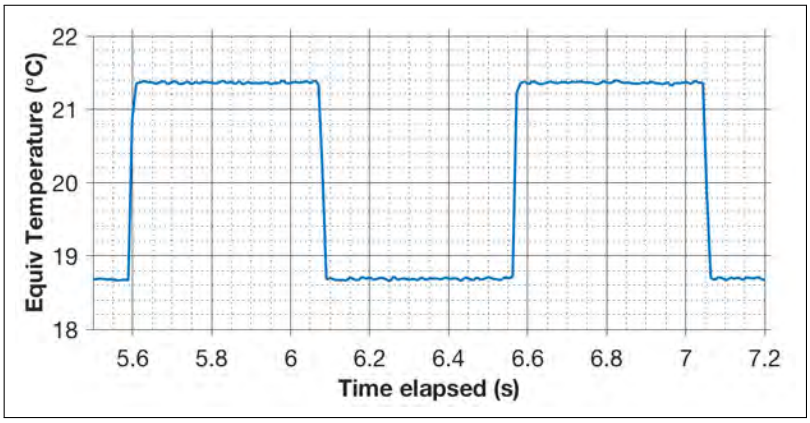

Figure 3.20: Electronic response time of temperature sensor. Resistors were used in place of the thermistor, with a pulse generator used to switch between two different resistors at 1 Hz. The sensor measured at 100 Hz

opened and closed the relay so that the resistance across the probe was either R_1 or $R_1 /\!/ R_2$. Results for one set of resistors are shown in Figure 3.20. Based on these results, the electronic response time is much faster than the observed transitions in Figure 3.19. Thus, the temperature sensor's response time is most likely due to the thermal mass of the thermistor

The time response of the temperature sensor could be improved by switching to a different thermistor. The thermistor used, the GP104L8F, has a nominal thermal time constant of 0.20 s in stirred oil. In contrast, the FP07 thermistor used by many in the EC community has a nominal time constant of 0.10 s in still air, and 7 ms when plunged into water. The GP104L8F was chosen for this project due to its much lower cost, but as the system continues to improve we are likely to switch in the FP07 for a faster time response.

3.3.3 Drift over time

Temperature was measured alongside current and voltage as part of the drift tests described in Section 3.2.4 for the conductivity sensor. The sensor's temperature measurements were found to be stable and did not exhibit the same oscillations as the conductivity circuit.

Over longer periods of time, the sensor's response may drift slightly. For instance, in the calibration curve shown above, the best fit calibration line had an equation of $y = 0.0056x + 6.3$ where x is the sensor's response (ADC counts) and y is the actual temperature. A calibration curve measured 5 months later produced a best fit calibration line $y = 0.0055x + 6.6$. This amount of drift is relatively insignificant; a temperature fluctuation of $\Delta T = 0.3\,°\text{C}$, the highest expected value for eddy correlation (see Table 1.1), would produce a Δx of $0.3 \div 0.0056 = 53.6$ LSB (ADC 'least significant bit' increments) if the first curve were correct. If the second curve were used to interpret the results, this would produce a $\Delta T = 0.0055\Delta x = 0.29\,°\text{C}$ (instead of 0.3 °C). Thus, especially for eddy correlation (where the mean is discarded), the temperature sensor can be used for some amount of time without recalibration.

However, it should be noted that the calibration may differ slightly for different regions of the calibration curve, even within the 'usable region' for our circuitry. A calibration curve taken a few months later for the $25 \sim 26\,°\text{C}$ range produced a best fit calibration line of $y = 0.0069x + 2.5$. The slope is now 0.0069 °C per LSB rather than 0.0056 °C per LSB. Following the above results, if the new curve were used to interpret results that should have been calibrated with the old

curve, the detected temperature fluctuation would be $\Delta T = 0.0069 \times 53.6\,\text{LSBs} = 0.37\,^{\circ}\text{C}$. In the grand scheme of calculated flux, however, the $\sim$20 % discrepancy here is relatively small.

3.4 Trimodal sensing

The ability of the instrument to measure all three properties (fluorescence, conductivity, temperature) was evaluated using tests conducted in a tabletop racetrack flume. A warm, salty, fluorescent dye, which should be detectable by all three sensors, was injected into the flow such that it was carried into and past the instrument's sensing volume. In the turbulent flow, the injection fluid is transported by eddies, and so the heat, salinity, and fluorescein were expected to travel together (i.e. their turbulent diffusivities are not substantially different). Three sensors measuring simultaneously and in the same location should pick up the same exact signal. Thus, we used comparisons between their measurements to gain insight into the differences between the sensors, the extent to which they are collocated in space and time, the overall ability of the instrument to make trimodal measurements, and any limitations which might affect its ability to make trimodal eddy correlation measurements of benthic flux.

3.4.1 Experimental setup

The experimental setup is shown in Figure 3.21. The flume had a channel width of $\sim$16 cm, a height of $\sim$20 cm, and a length of $\sim$6 m on each side. It was filled to $\sim$17 cm depth with tap water. The optical fibers were mounted at $\sim$8.6 cm depth and oriented to face into the flow. A heated solution of fluorescein dye in seawater was injected at a distance of $\sim$2 cm $\sim$ 10 cm in front of the optical fibers. The solution was made by mixing 100 ppm fluorescein solution with seawater before heating in an oven, and generally had a fluorescein concentration of $\sim$5 ppm, a conductivity of $\sim$20 mS, and a temperature of 40 °C to 60 °C. The flume generally started with no fluorescein, a conductivity of 950 µS $\sim$ 1050 µS, and a temperature of $\sim$17 °C, all of which changed as solution was injected and the flume water warmed in the ambient air[6]. It was assumed that the turbulent diffusivities of heat, salinity, and fluorescein were not substantially different, so that the three would travel together as they were carried toward the sensing volume by the turbulent flow. Injections were made with either a 5 mL micropipette for a quick turbulent burst, or a syringe pump connected a ⌀ 1/8 " (OD), ⌀ 0.055 " (ID) ($\sim$1.4 mm) stainless steel tubing outlet for a steady, narrow stream with minimal input of momentum. The latter is shown in Figure 3.21.

Videos of the injections were recorded by a downward-facing camera mounted above the flume, and a side-facing camera mounted on a tripod next to the flume. A black light (405 nm) was positioned nearby to excite sufficient fluorescence for the cameras to image the dye. Since this fluorescence is considered 'background' by the sensor (which modulates its LED to reject these signals), it contributes to the noise of the fluorescent measurements as described in Section 2.3.2 (p. 112). Thus, the position and orientation of the black light were adjusted to reduce the amount of light reaching the sensing volume while still allowing the cameras to adequately image the dye. The videos and the time series measured by the instrument were synched by

[6] Experiments were done in winter; tap water entered the flume at 10 °C

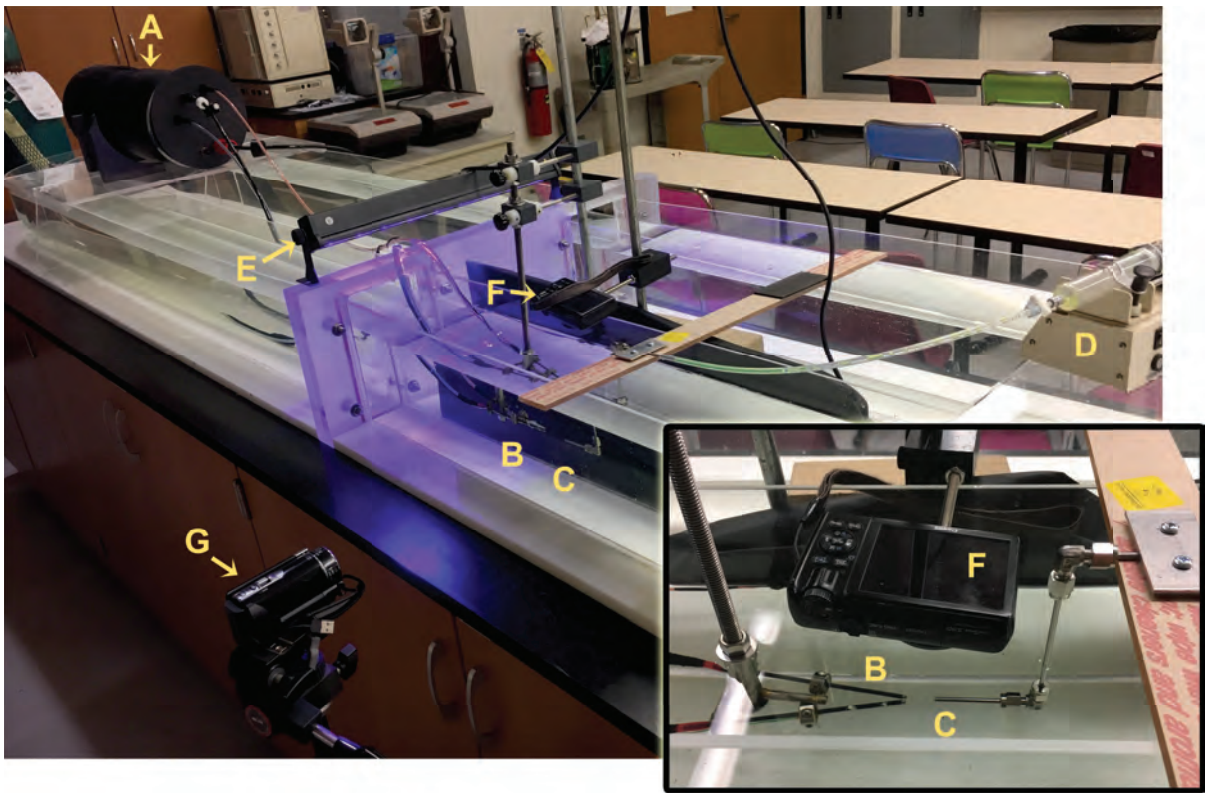

Figure 3.21: Setup in tabletop racetrack flume to test ability of instrument to simultaneously measure fluorescence, conductivity, and temperature; inset shows angled top view of sensing volumes. Labeled as follows: **A)** body of sensor in pressure housing; **B)** optical fibers at sensing volume end; **C)** stainless steel tubing and **D)** syringe pump, for injection of fluorescent, salty, warm solution; **E)** black light to allow imaging of injection dye by cameras; **F)** downward-facing camera; **G)** sideways-facing camera.

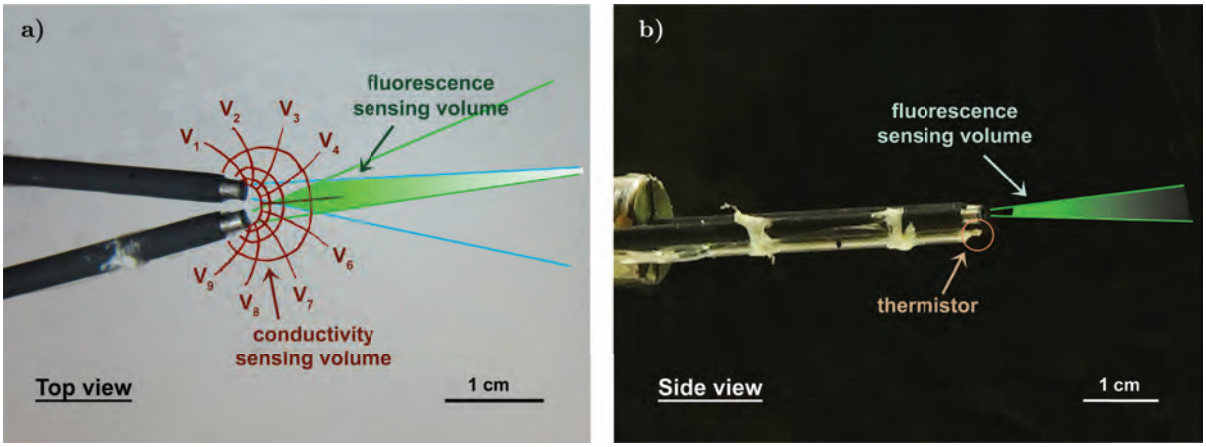

Figure 3.22: Estimated sensing volumes of three sensors viewed from **a)** top and **b)** side. See text for derivation. Temperature sensing volume is not visible in top view; conductivity sensing volume is not shown in side view due to difficulty of representation in the 2D plane.

flashing a pulse of light at the beginning of each time series, which was identifiable in both the videos and the measurements.

3.4.2 Sensing volumes

Estimates of the sensing volumes were paired with the video recordings to determine if, when, and to what extent any discrepancies between the measurements could be explained by differences in the location, size, and shape of the sensing volumes. The estimates used are shown in Figure 3.22, and their derivations are described in greater detail below.

Fluorescence

The sensing volume of the fluorescence sensor is discussed in theoretical terms in Section 2.3.4 (p. 119). Here, the sensing volume was identified empirically by assembling a composite of video frames in which the beam of the LED was visible by the more intense emission of fluorescein within its cone. Since the visibility of the beam was consequently dependent on the distribution of fluorescein, multiple semi-transparent frames representing different snapshots of the turbulence were stacked to produce identifiable boundaries for the cone of emission. The cone of emission was marked in this way for both the top and side views. For the top view, the cone of acceptance was assumed to be identical but tilted by 20 °. Their overlap was marked as the sensing volume, with coloring to indicate heavier weighting for the more proximal area (i.e. the overall detected fluorescence contains a greater contribution from the fluorescing compounds in the more proximal areas). The area for the side view was also colored accordingly, with the ∼3 mm directly in front of the tips omitted to indicate area of non-overlap. All image processing was done using Adobe Photoshop CS6.

Conductivity

A two-dimensional approximation of the conductivity sensing volume was estimated using a flow net, where the bodies of the electrodes are modeled as equipotential surfaces with different electrical potential (i.e. the voltage difference across the probes). Intermediate equipotentials V_{n} are marked in Figure 3.22a, along with three perpendicular streamtubes that run from one electrode to the other. The flow net is drawn for a uniform conductivity solution; patches of lower or higher resistivity would necessarily change the distribution of equipotentials and streamtubes (as $V = IR$), but a good first-order approximation can still be achieved without this complication.

As by flow net theory, an equal amount of current travels through each streamtube. Thus, the current density is higher for smaller streamtubes, and the sensing volume is weighted towards the proximal end (i.e. the volume of solution in the streamtube closest to the fibers contributes more to the effective total resistance between the electrodes, than the solution in the farther streamtubes). See Box 3.1 for a more detailed explanation of flow net relationships in terms of electrical properties.

The equipotentials and streamtubes between the fibers on their 'inside edge' (side facing each other) are not shown. This region contains the same number of equipotentials as the electrical field between the 'outside edges' (which is shown in Figure 3.22a), and consequently a large number of streamtubes as well. In other words, this area between the fiber tips contains a strong electrical field and high current density.

One might expect that the total measured conductivity is weighted heavily towards the conductivity of the solution in this volume. This is likely true, but the situation is complicated by the physical body of the fibers. This region could potentially be 'blocked' from the flow by the fibers themselves, resulting in stagnant region that would contribute only a fixed resistance (or conductivity) to that measured by the probes, and could therefore be removed with the mean (assuming proper adjustment to calibration). However, it was later found to be somewhat problematic; see Section 3.4.4.

Figure 3.22a is a two-dimensional approximation of the conductivity sensor's sensing volume; the three-dimensional form is difficult to represent, but the single-plane form shown here is roughly valid because of the symmetries of the conductivity cell. In the side view of the sensor, the dimensionality becomes more important. The sensing volume is not shown in Figure 3.22b, the side view of the sensor, because the streamlines would be largely radiating into or out of the plane of view. However, they would also radiate to some extent above and below the plane of the optical fibers, with a larger weighting closer to the fiber tips.

Temperature

The thermistor measures the temperature of the liquid touching its surface, and can be considered a point measurement (see Box 3.2 for a more detailed discussion of this approximation). Since the point measured is collocated with the physical body of the thermistor, some degree of offset with the other sensors is necessary to avoid interference with the other measurements. This is the same principle as for dissolved oxygen sensors, and the reason that all DO sensors in EC are positioned outside of the ADV's sensing volume.

Box. 3.1: An electrical view of flow nets

By flow net theory, all streamtubes have equal 'flow' (here, current), and here they traverse the same potential. As an electrical circuit, then, the streamtubes must have the same resistances (since $V = IR$); in electrical parlance, the three streamtubes are parallel channels with equal resistance and equal current in each channel. In this uniform-conductivity scenario, they also have equal resistivity (per-volume resistance). Of course, the unequal weighting of one streamtube over another is inconsequential in a uniform-conductivity situation, but it still exists. So, with equal resistance and equal resistivity, how does the 'weighting' of one streamtube over another arise?

In fact, this understanding is completely congruent with flow net theory. For a given cell,

$$R = \rho \frac{L}{A} \tag{3.2}$$

where R is resistance, ρ is resistivity, L is length of the current path (from one equipotential to the other) and A is cross-sectional area. In terms of A, the two-dimensional representation shown here assumes a uniform thickness, and so it is only the width of the streamtube that matters.

Flow nets are specifically drawn so that each cell has equal length and width. In this case, one can see by Eq. (3.2) how all cells have the same resistance R, since L and A (or rather, width) scale together. L and A, however, are different between the streamtubes, with the closer streamtubes having smaller dimensions. The volume of solution in these streamtubes has a 'greater contribution' to the total resistance on a per-volume basis only. This is captured by its higher *current density* (amount of current per cross-sectional area); in the narrower streamtubes, there is less area (or width) across which to disperse the same amount of current[a]. Of course, the relative contribution of streamtubes is merely an abstract concept in the case of uniform conductivity. However, it becomes important as perturbations in conductivity are introduced, because patches with 'greater contribution' to total resistance will have a greater weighting in the total effective conductivity.

Thus, even when the per-volume resistance (the resistivity), total voltage, and total current are the same, the per-volume current is not. This concept of geometry is excluded by design in the circuit diagram view of parallel resistors. It is also not incorporated in the $V = IR$ representation of the circuit, although it is hidden in the specifics of R and V and their relationship to the volume- and length-normalized properties of resistivity and potential gradient ($V = IR$ is equivalent to $\mathrm{d}V/\mathrm{d}L = J\rho$ where the current density $J = I/A$).

[a]This is geometrically necessary because the equipotentials are much closer; since shorter length is less resistance, the same total resistance (and total current) is achieved with a smaller cross-sectional area. In non-discrete terms, the shorter length results in a a steeper potential gradient, which results in higher current density.

In this case, the thermistor is mounted beneath one of the fibers. Its sensing volume is located beneath and slightly farther back than the other sensing volumes, as shown in Figure 3.22b. The sensing volume is smaller compared to the others and will necessarily have a larger offset from the velocity sensing volume.

3.4.3 Results

In general, the time series measured by each of the sensors were consistent with the video observations and with each other. Dye injected with the micropipette generally travelled past the sensing volume as turbulent eddies, which were observed by the sensors as burst events. The extent to which these events were captured by the sensors depended largely on the location, angle, and speed of the injection. On the other hand, dye injected with the syringe pump and outlet generally travelled past the sensing volume as distinct, narrow jets.

Figure 3.23 gives an example of a time series covering four micropipette injections. The turbulent features of the dye were picked up by all three sensors, although with some differences. A major source of discrepancy was the response time; a faster response time leads to sharper peaks and steeper tail-offs. As expected, the temperature was the slowest, while the fluorescence was nearly instantaneous.

In fact, the three time series could be made to more closely resemble each other by applying a low pass filter to the fluorescence (and to a lesser extent, conductivity) series. An example is shown in Figures 3.24 to 3.27. A series of bursts are shown in Figure 3.24, and again in Figure 3.25 but with a 0.2 s-window running mean filter applied to fluorescence and 0.1 s-window running mean to conductivity. The filter parameters were chosen based empirically, based on a subjective judgment of qualitative similarity. However, they can still provide an order-of-magnitude idea for the difference in response time between the sensors. The improvement in match can also be seen in the plots of one time series vs another ('cloud plots'), shown in Figures 3.26 and 3.27; more information on interpreting the cloud plots is given in Box 3.3.

A low pass Butterworth filter was also analyzed in the same way as the running mean filter above, and independently produced a similar estimate for sensor response times. Results are given in Appendix C, Section C.2.

In addition to the different response times, the slightly different sensing volumes, as described in Section 3.4.2, is another major source of discrepancy. The different *locations* of the sensing volumes would introduce a time shift between the three measurements, depending on the direction of the eddy (which in turn was dependent on the specifics of the injection) relative to the spatial offset. Consistent with this, the time series were often better aligned after one was shifted relative to the other. Similar to the above analyses with the filters, rough estimates of 'appropriate' time shifts were determined empirically by shifting the series and qualitatively comparing the results (more detailed results are given in Appendix C, Section C.2). The time shifts varied slightly based on the eddy but were in general <0.15 s, which provides an order of magnitude estimate for typical time discrepancies between the three sensors. However, the extent to which this time shift can be applied to future measurements depends heavily on the current speed, which unfortunately was not measured in these experiments.

The difference in sensing volume locations not only cause the sensors to detect the same features

Box. 3.2: A more nuanced view of the thermistor's sensing volume

Practically speaking, there must be a finite volume of water surrounding the thermistor's body that contributes to its measurement. An estimate of the size of this sensing volume could possibly be obtained by estimating the volume of water whose 'heat' can reach the thermistor in the time it takes for it to react to a change in temperature. This timespan can be approximated by the response time of the thermistor, which was estimated (Section 3.3.2) as between 0.5 and 1 s.

Heat 'reaches' the thermistor by diffusing through the water. Assuming that the thermistor is fast enough to capture the eddies involved with turbulent diffusion (as EC sensors must be), the effective sensing volume is then dictated by thermal diffusion. There is some finite, though perhaps very thin, layer around the thermistor where heat can diffuse quickly enough that it is registered by the thermistor within its response time. Note that time and space are conflated here, since heat from another location has in fact reached the thermistor; the thermistor is not remotely measuring the temperature of some slightly displaced patch of water. However, in order to arrive at an effective sensing volume, we 'mark off' the spatial extent of surrounding water where this can happen within the thermistor's response time, making the sensing volume largely a consideration of how its response time compares to the rate of thermal diffusion.

The thermal diffusivity of water is analogous to molecular diffusivity and gives a measure of the rate of transfer of heat in a material:

$$\frac{\partial T}{\partial t} = \alpha \nabla^2 T \tag{3.3}$$

where T is temperature, t is time, and α is the thermal diffusivity ($0.143\,\mathrm{mm}^2/\mathrm{s}$ for water at 25 °C). From the Laplacian (double divergence) in Eq. (3.3), we see that the extent to which the temperature changes at a point depends on the temperature difference as well as its distance. A sharp temperature difference farther away might still reach the sensing volume to some degree, whereas if the temperature of the water is uniform, the concept is meaningless. The concept of a sensing volume is therefore a bit complicated.

Rather than try to map out variable and poorly defined parameters, then, we here draw analogy to the concept of molecular diffusion. Under turbulence, molecular diffusion is generally only significant in a thin layer near the boundary. Here, we consider the layer around the thermistor that is within diffusion range for some reasonable amount of heat to be thin enough that the temperature can be considered a point measurement.

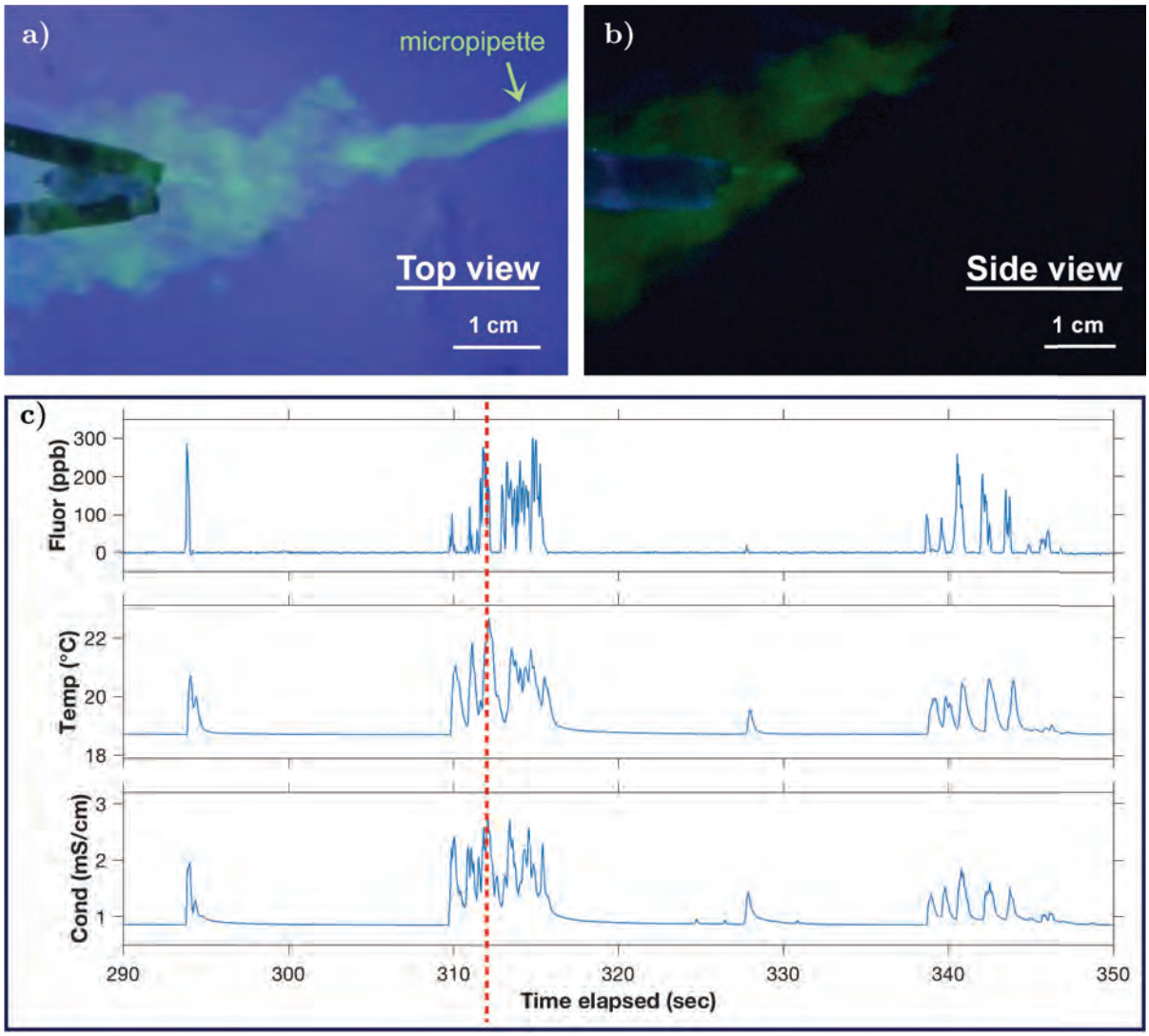

Figure 3.23: Example of event registered by all three sensors. A warm, salty, fluorescent dye was injected into the flow in front of the sensing volume using a 5 mL micropipette. **a)** Top and **b)** side images taken by cameras show turbulent features of the dye, which are reflected in the **c)** time series measured by the three sensors. The time series show four different micropipette injection events, and the dashed red line indicates the moment shown in the screenshots. All three sensors captured similar features but were not exactly the same, likely due to differences in their response times and sensing volumes.

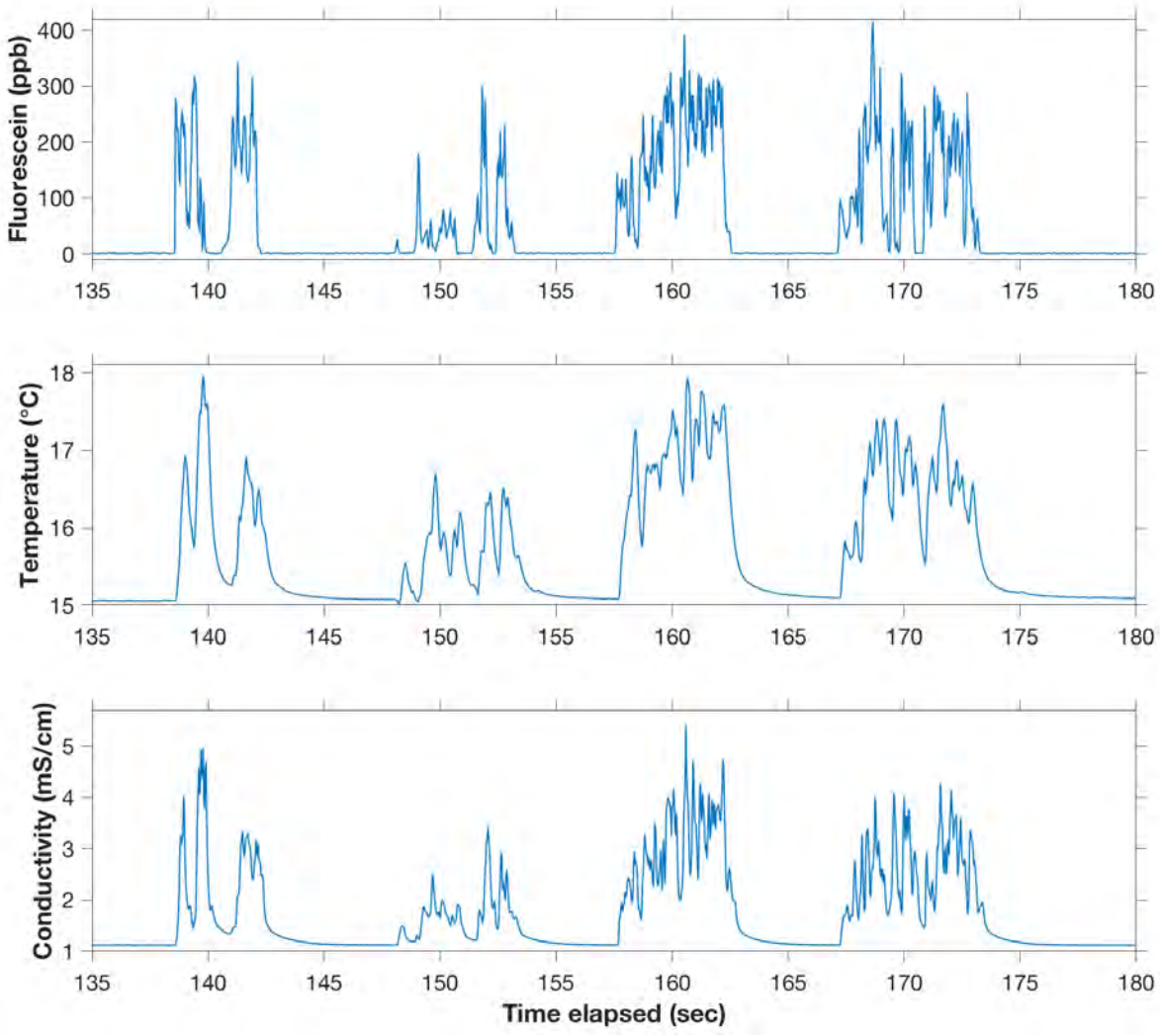

Figure 3.24: Series of bursts from micropipette injection of a warm, salty, fluorescent dye into the flow in front of the sensing volume. Differences in response time between the sensors are reflected in the 'sharpness' of their detected features.

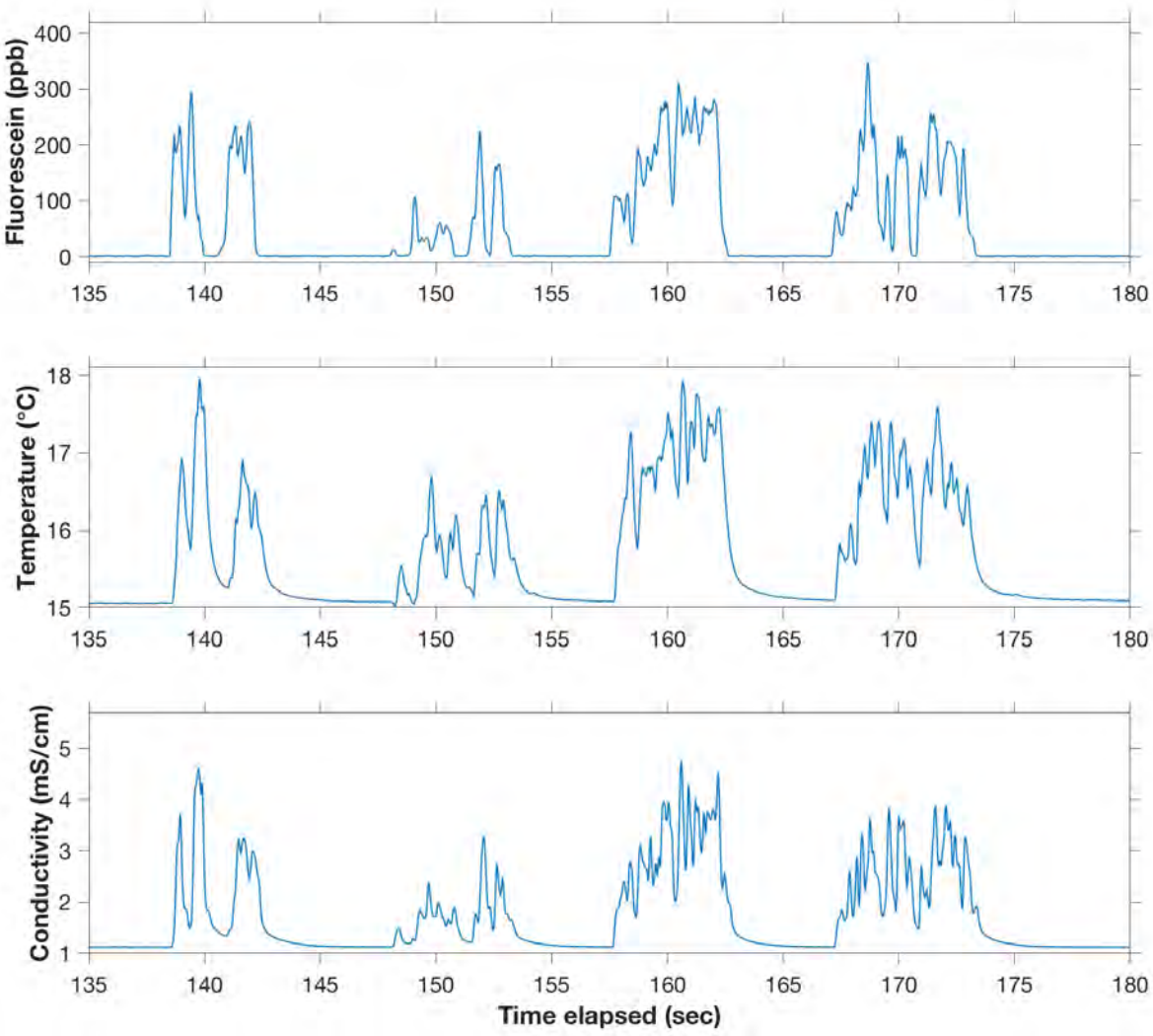

Figure 3.25: Same time series as Figure 3.24, but with a 0.2 s-window running mean filter applied to fluorescence and 0.1 s-window running mean to conductivity, which improves qualitative similarity between series. The window length for the running mean provides an order-of-magnitude estimate for differences in time response in this setting.

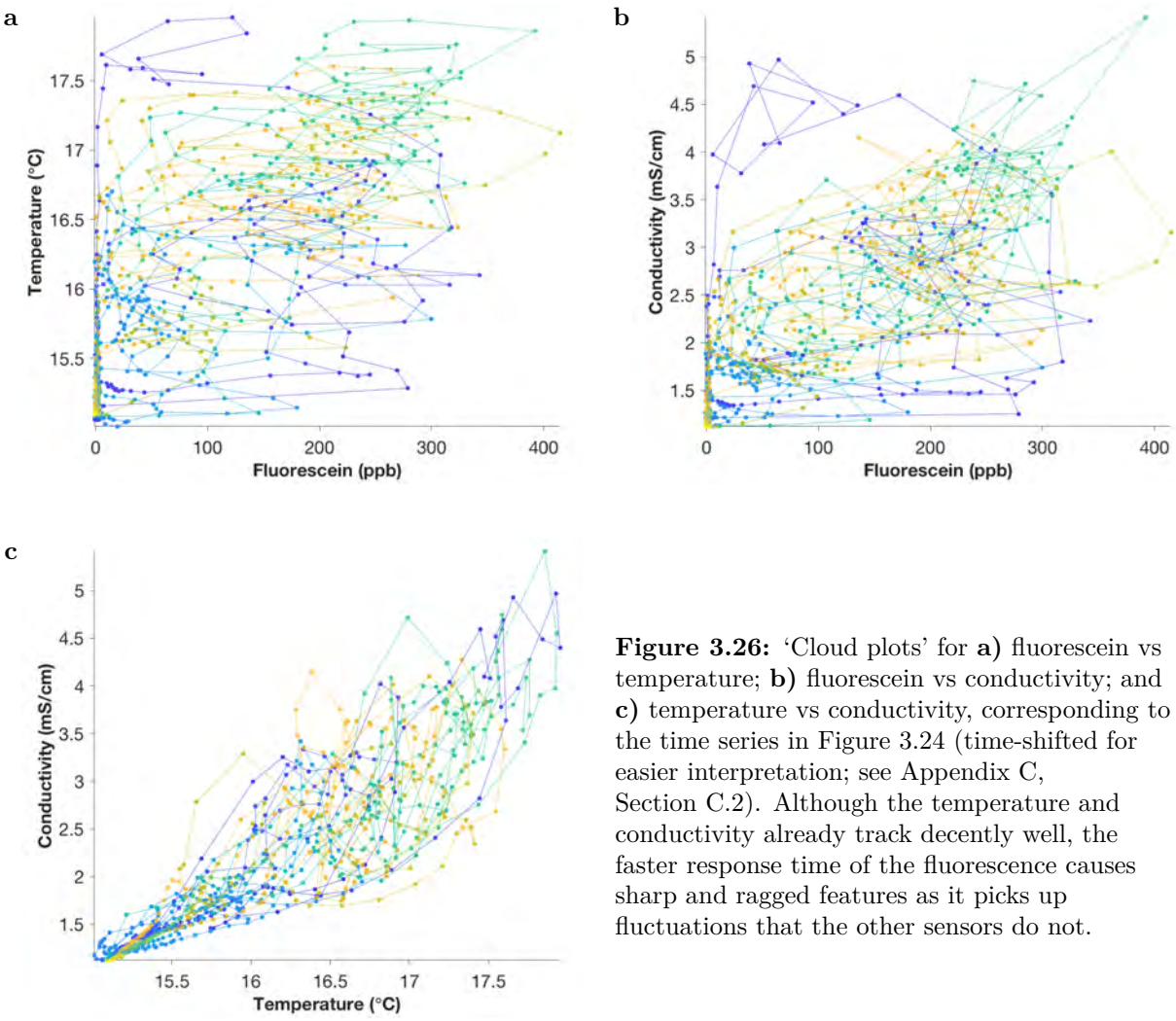

Figure 3.26: 'Cloud plots' for **a)** fluorescein vs temperature; **b)** fluorescein vs conductivity; and **c)** temperature vs conductivity, corresponding to the time series in Figure 3.24 (time-shifted for easier interpretation; see Appendix C, Section C.2). Although the temperature and conductivity already track decently well, the faster response time of the fluorescence causes sharp and ragged features as it picks up fluctuations that the other sensors do not.

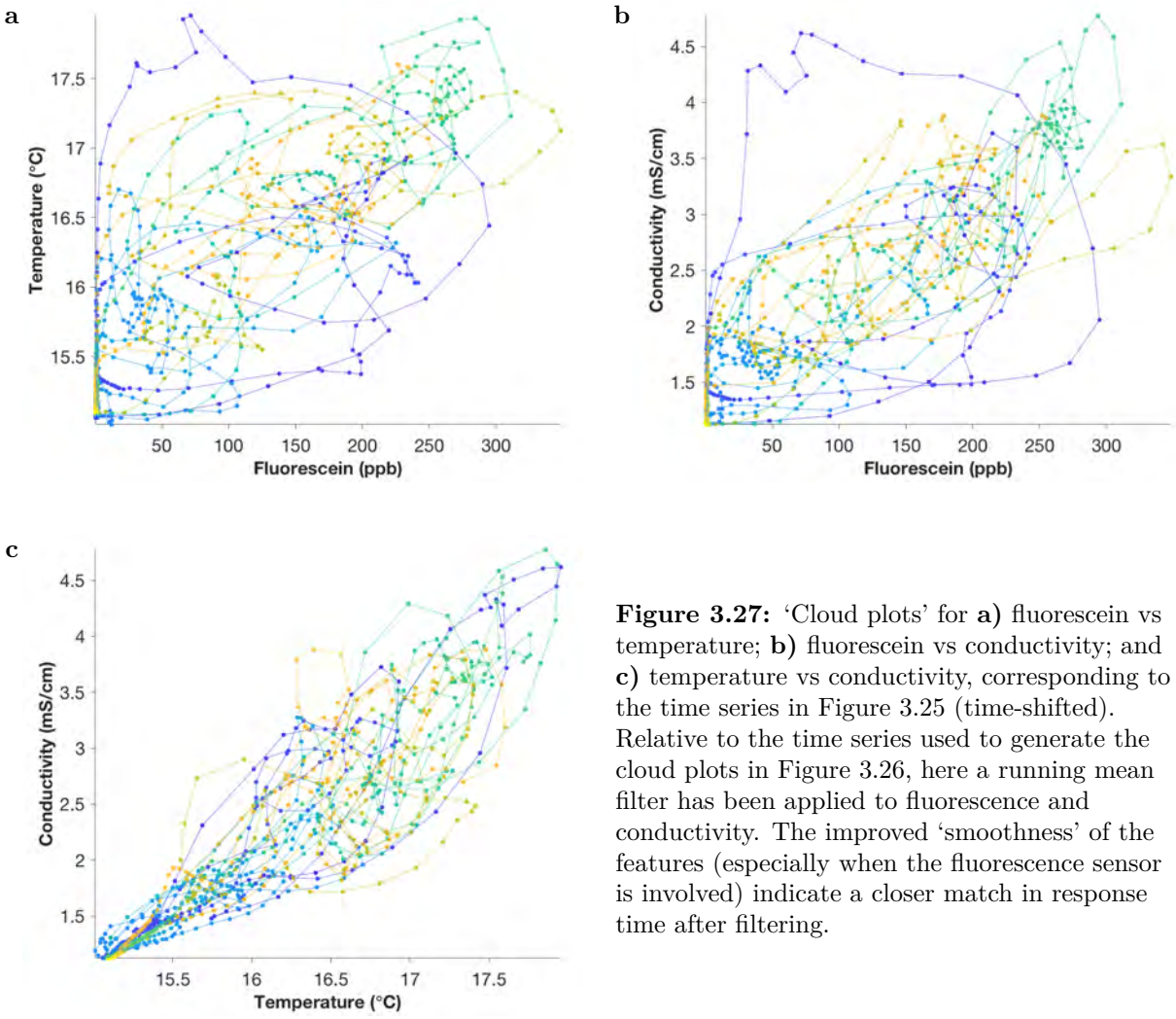

Figure 3.27: 'Cloud plots' for **a)** fluorescein vs temperature; **b)** fluorescein vs conductivity; and **c)** temperature vs conductivity, corresponding to the time series in Figure 3.25 (time-shifted). Relative to the time series used to generate the cloud plots in Figure 3.26, here a running mean filter has been applied to fluorescence and conductivity. The improved 'smoothness' of the features (especially when the fluorescence sensor is involved) indicate a closer match in response time after filtering.

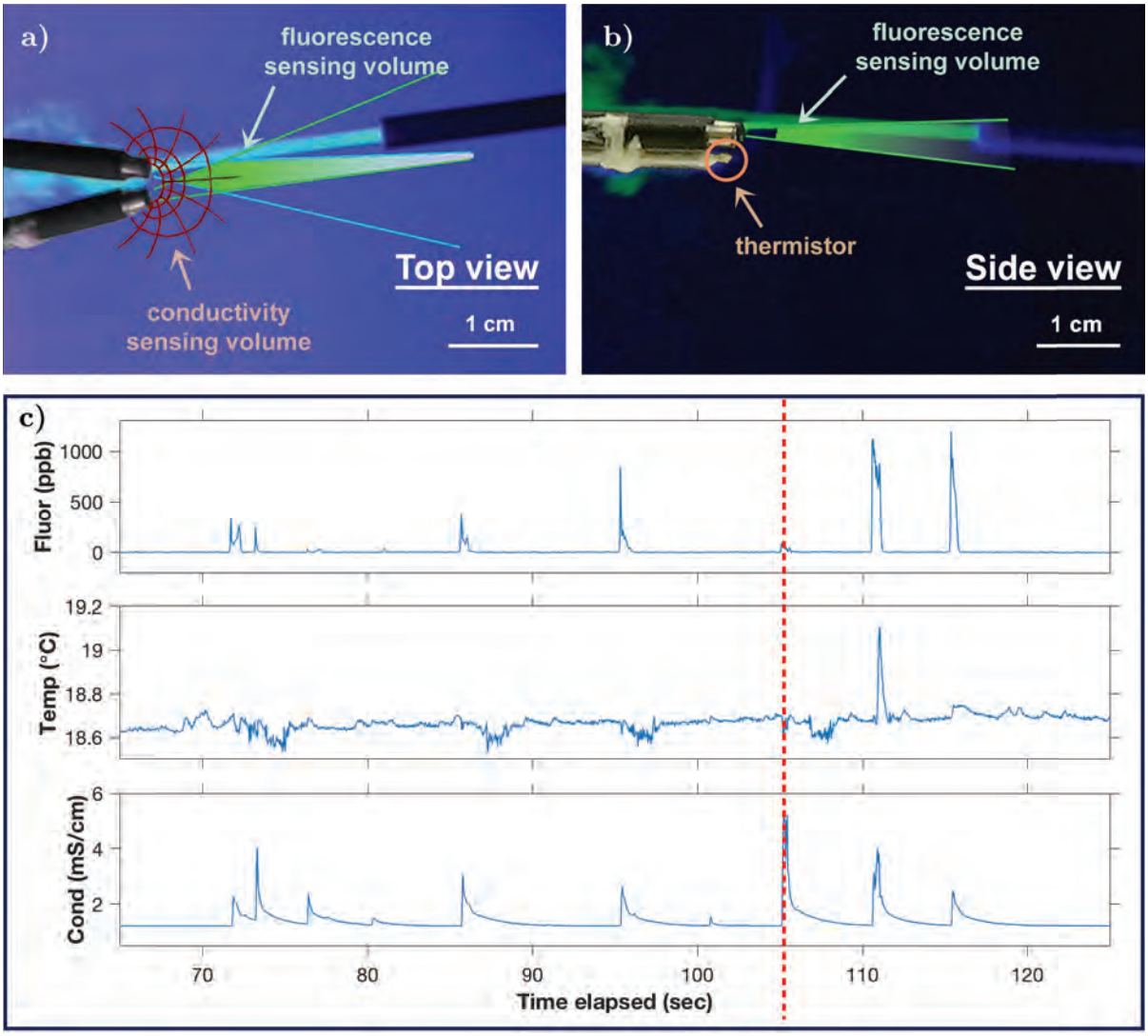

Figure 3.28: Example of event detected differently by the three sensors. A $\varnothing \sim 1.4\,\text{mm}$ jet of warm, salty, fluorescent dye is injected into the flow out of an outlet connected to a syringe pump. **a)** Top and **b)** side images with sensing volumes superimposed show that the jet grazes the fluorescence's sensing volume, enters the conductivity's, and misses the temperature's, which is reflected in the **c)** time series measured by the three sensors. The time series shows several jet events, and the dashed red line indicates the moment shown in the screenshots. The negative dips in temperature and fat tails for conductivity are discussed separately.

Box. 3.3: Interpreting cloud plots

The 'cloud plots' shown in Figures 3.26 and 3.27 represent plots of one sensor's measurements vs another's, for the time frame shown in Figures 3.24 and 3.25. They show, to some degree, how well the time series track

1. If the two time series tracked perfectly, the plot would be a diagonal line. The closer to a diagonal line that the plot is, the more closely the two series are tracking.
2. Large 'circles' indicate a time shift, i.e. one sensor both starts and stops seeing an eddy before the other. Differences in response time could still exist, depending on the separation between points along one edge of the 'circle' vs another, but are difficult to distinguish. A small time shift can make a big difference in 'untangling' the cloud plots so that other features can be seen (see Appendix C, Section C.2). For this reason, the plots shown in Figures 3.26 and 3.27 correspond to time-shifted series.
3. Skewed 'circles' (a diagonal line on one edge only) indicate a response time difference, and are often only different from the large circles by a small time shift. For example, in Figure 3.27a, the rising edge of the fluorescence generally coincides with the rising edge of temperature (as fine-tuned by the time shift), although temperature rises more slowly (small-slope diagonals in lower part of graph). The same eddies circle around as fluorescence returns to 0, but the temperature measurements are still high due to the slower response time. If the response times were more evenly matched, the shape would be closer to a single diagonal. The tendency of the temperature and conductivity sensors to 'trail' at the end of each burst is also apparent in the cluster of points along their axes (fluorescein = 0 ppb).
4. Smoother circles (or other shapes) indicate a more similar response time than jagged features, which imply that one sensor is seeing fluctuations that another isn't.

at different times (solved by a time shift), but could also cause them to sample different parts of the same eddies, resulting in different turbulent features being detected. This effect is tied to the difference in *size* and *shape* of the sensing volumes, which also causes the sensors to sample different parts of the same eddy and to different extents.

As an example, Figure 3.28 shows a jet of dye injected into the flow through the narrow outlet. The event shown is picked up by the conductivity sensor, but barely by the fluorescence and not by the thermistor at all. This is consistent with the estimated sensing volumes of the three sensors, as shown in the figure.

Thus, it can be seen that the three sensing volumes are not actually collocated, which is theoretically necessary to estimate three simultaneous fluxes using EC. In practice, the slight differences in sensing volume location and size may not be a problem for trimodal flux sensing. The jet shown in Figure 3.28 is only ∼1.4 mm in diameter; given the typical dimensions of eddies (e.g. values given in Table 1.1, p. 39), any significant flux-carrying eddies encountered in the natural environment will likely be larger and will enter all three sensing volumes to some degree. However, it is still helpful to map out and recognize the differences in sensing volumes, which may be important in some situations.

Finally, note that it is not possible to separate the effects of differing time responses and sensing

volumes; time and space are effectively intertwined. A larger sensing volume will sense areas that may be detected at separate times by a smaller sensing volume, thus averaging over over both time and space.

3.4.4 Improvements identified through flume experiments

Results from the flume experiments revealed some shortcomings of the sensor that were subsequently corrected for future experiments.

Anomalous negative dips in temperature signal

The negative dip observed in the temperature signal in Figure 3.28 was attributed to persistence in the ADC. In the design used for these experiments, the temperature shared an ADC with the current and voltage measurements for conductivity, and a 'scan' command was used to measure all three as described in Section 3.1.3). The 'scan' is a built-in function of the ADC by which the three channels are read in succession and the results transmitted to the Teensy with one command; thus, three measurements could be taken with the timing cost of only one I^2C transmission sequence.

The dips in temperature (Channel 3) were traced to persistence from the conductivity's voltage signal in Channel 2. The high conductivity spikes in Figure 3.28 correspond to a low spike for voltage, which would cause the subsequent temperature measurement to be lower than it otherwise would have been (in this case, baseline value, since the jet missed the thermistor). In other words, the value in Channel 2 was affecting the value read for Channel 3. The manufacturer of the ADC agreed that this could be a flaw in the ADC, arising from crosstalk on the analog input multiplexer as well as a potential timing issue, and noted that it could not be fixed except by switching ADCs [Samantha Morehead (Maxim Integrated), personal communication, 7 Aug 2018].

A software solution was implemented that involved reading each channel separately. Although this fixed the issue of channel interference, it required separate I^2C commands for each read and thus substantially decreased the number of reads possible in a given time period. In subsequent EC tests, the noise on the temperature measurements proved problematic for resolving temperature fluctuations. Ultimately a hardware solution was implemented whereby the current measurements were routed to Channel 1 of the ADC, and voltage measurements to Channels 2 and 3. The three channels could be read in succession using a 'scan' command (one I^2C command), and Channel 2 discarded to avoid interference of the voltage measurement by the current. The temperature measurements were then routed to a separate ADC (ADC121C027 from Texas Instruments) on a flyout board, as shown in Figure 3.29.

The ADC121C027, a compact, single-channel I^2C device, allows several measurements to be read with one I^2C command. To take advantage of the associated time savings, the code was restructured to read the temperature and conductivity measurements in blocks. That is, the temperature and conductivity measurements were no longer completely interleaved, although the blocks were small enough that they could still effectively be considered simultaneous. Further information on the block architecture and its implications for timing are given in Appendix B,

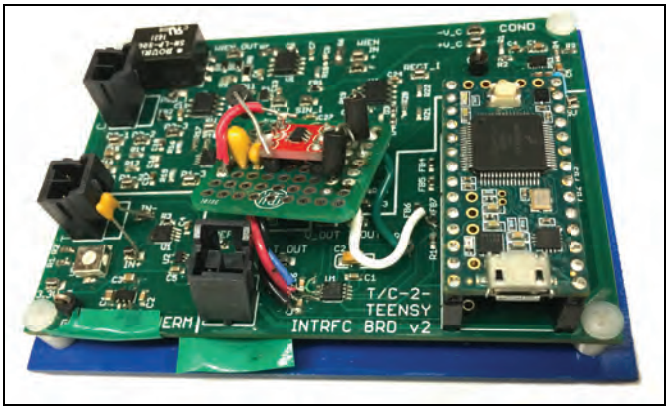

Figure 3.29: Circuit board for temperature and conductivity circuits, showing flyout board for new ADC implemented to avoid cross-contamination of signals. Also visible is a 1 µF capacitor on the thermistor input, added to reduce noise in the temperature measurements.

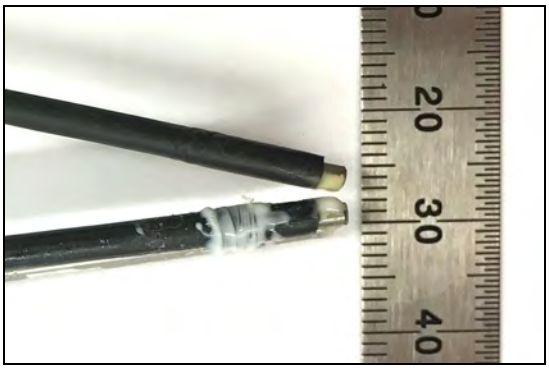

Figure 3.30: Modification of conductivity cell (optical fibers) to reduce susceptibility to hydrodynamic trapping of dye, which was observed to interfere with the sensor's ability to detect fine features. The inside-facing regions of the probes were coated in marine epoxy for electrical insulation.

Section B.2.2. The gain auto-adjustment feature for the conductivity sensor (described in Section 3.1.4 on Teensy functionality) was also unfortunately removed, as it was deemed not worth the amount of time it cost.

Conductivity fat tail

The fat tail in the conductivity signal in Figure 3.28 was of particular concern because of the fast response times required for EC. It was ultimately attributed to a hydrodynamic artifact; dye was sometimes observed to persist in the area between the optical fibers, especially when injected using the jet from the ⌀ 1.4 mm outlet. Thus, it was hypothesized that the fat tail was due to the trapping of the dye by the physical sensor body / geometry of the optical fibers. Supporting this hypothesis, the fat tail was observed to be much more pronounced under slow flow. The relative insensitivity of the fluorescence and temperature sensors could be explained by differences in sensing volume; the conductivity has a sensing volume that is much closer to the solid surface than the fluorescence, and much more dispersed than the temperature. In addition, the conductivity sensor is particularly sensitive to the area between the electrodes, as described in Section 3.4.2.

To better visualize this phenomenon, the flume experiment was repeated without the fluorescence. Instead, dyes of different salinity and temperature, colored with food coloring, were injected. Figure 3.31 shows the injection of a red dye with mildly elevated conductivity and temperature. The dye indeed persisted in the area behind the fiber tips, which coincided with the fat conductivity tail in the time series. It should be noted that, while the 'trapping' of the dye by the sensor body is indeed an issue (as in Image 3 of Figure 3.31), the persistence of the dye in the flow (e.g. the trail of dye in Image 2) also creates a similar effect. Persistence of dye in the flow is a property of the flow field and the injection, and an accurate sensor would indeed detect it as a lingering signal.

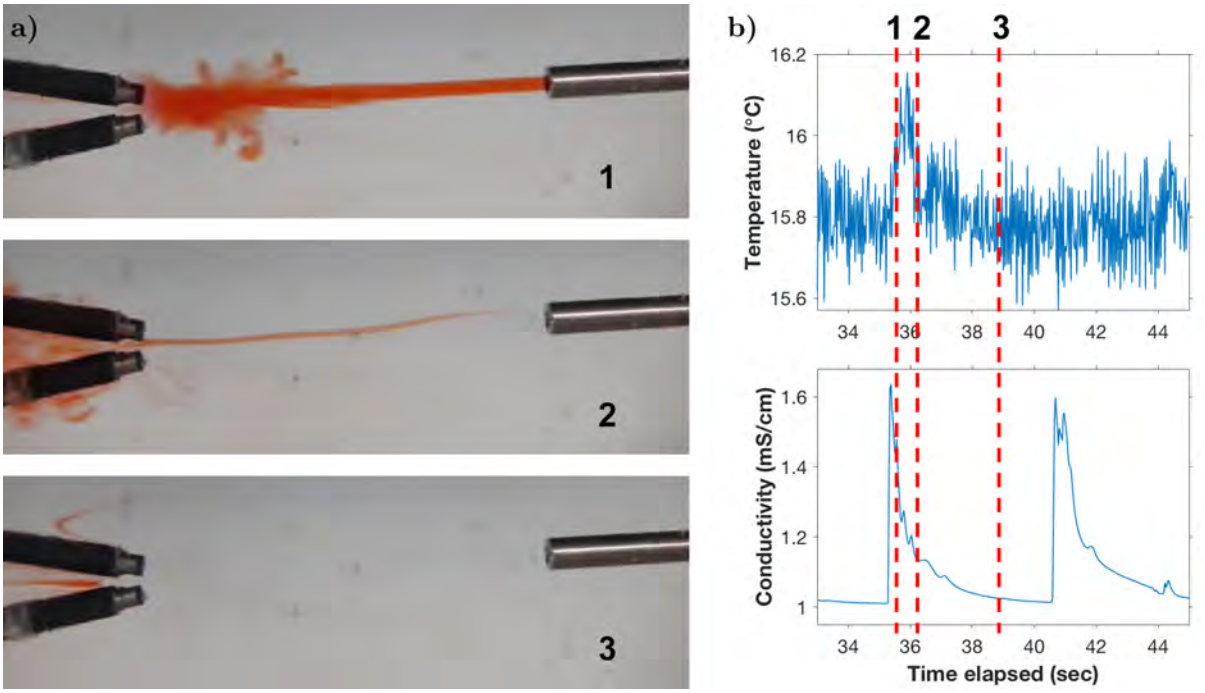

Figure 3.31: Injection of a red dye ($C \approx 4.7\,\mathrm{mS/cm}$, $T \approx 40\,^{\circ}\mathrm{C}$ when prepared) into ambient flume water ($C \approx 1\,\mathrm{mS/cm}$, $T \approx 15.3\,^{\circ}\mathrm{C}$) under flow. **a)** Top view images of three stages of the same burst, corresponding as labelled to the red lines in the **b)** time series measured by the sensor. The persistence of dye trapped by the optical fiber geometry is seen to coincide with the fat tail of conductivity, implying a hydrodynamic origin of the tail.

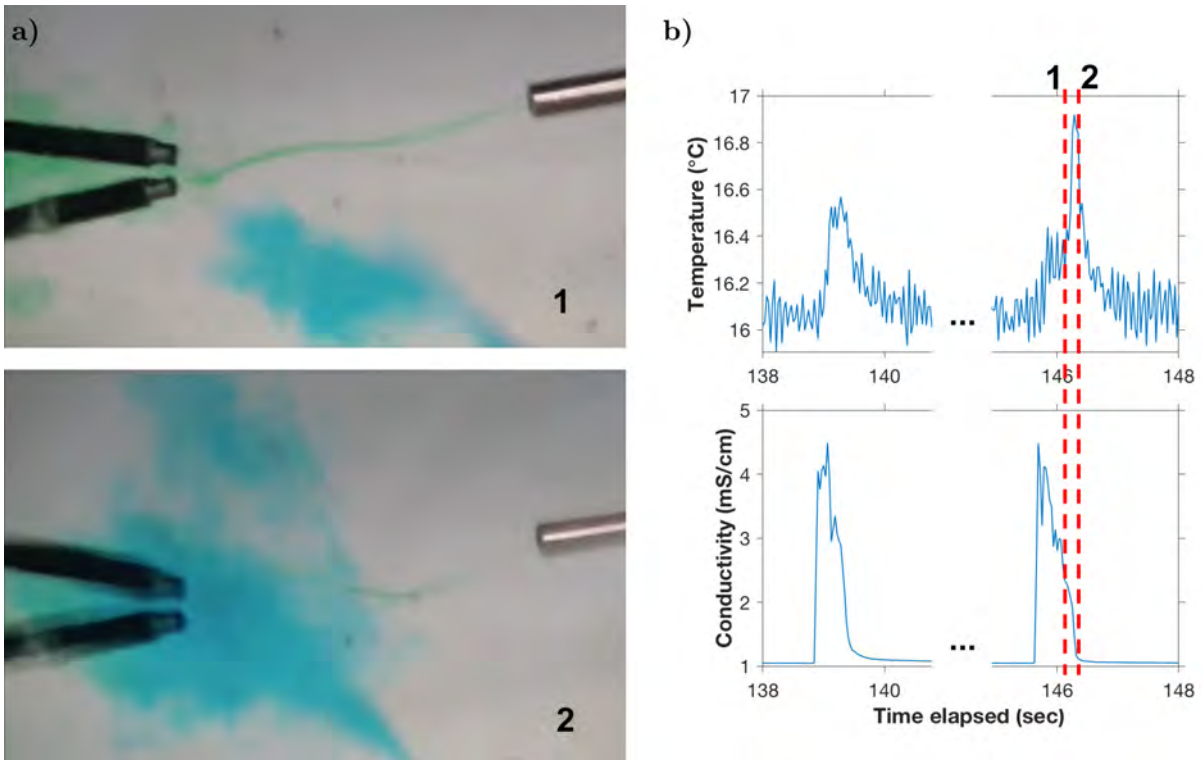

Figure 3.32: Injection of a green dye ($C \approx 23\,\mathrm{mS/cm}$, $T \approx 60\,^{\circ}\mathrm{C}$ when prepared) into ambient flume water ($C \approx 1\,\mathrm{mS/cm}$, $T \approx 16.1\,^{\circ}\mathrm{C}$) under flow, followed immediately by a burst of blue dye ($C \approx 1\,\mathrm{mS/cm}$, $T \approx 19.4\,^{\circ}\mathrm{C}$) to flush the region. **a)** Top view images of two stages of the same burst pair, corresponding as labelled to the red lines in the **b)** time series measured by the sensor. The blast of blue dye with properties similar to the ambient water was observed to eliminate the fat tail.

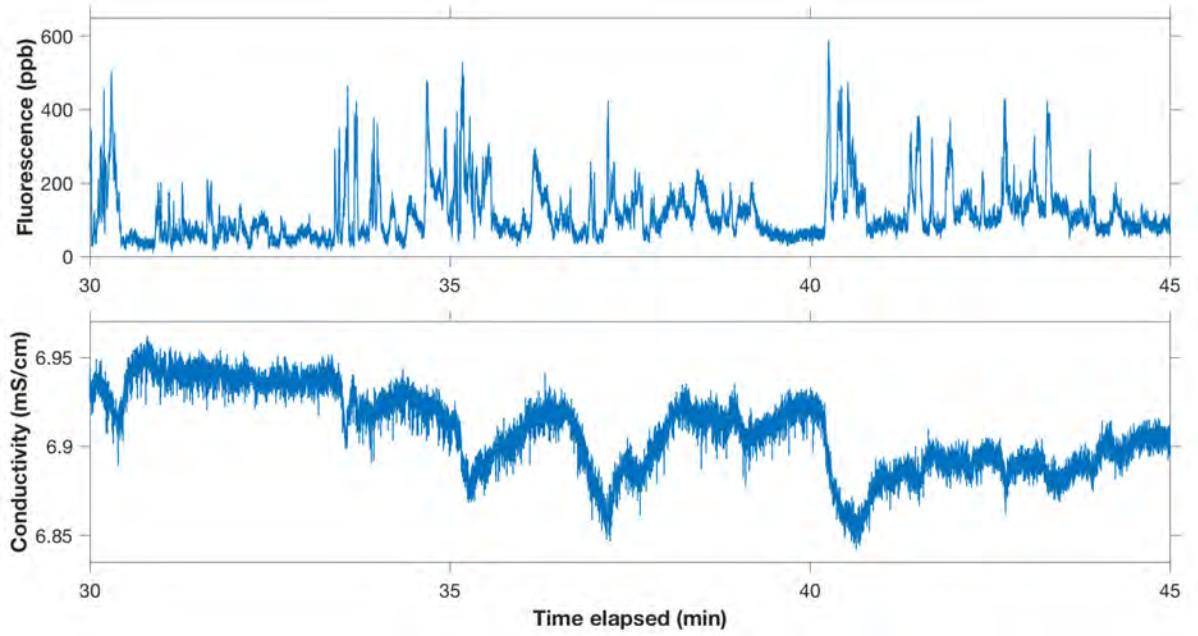

Figure 3.33: Time series of fluorescence and conductivity taken from an EC run (described later in Section 4.5.1). The inability of the conductivity sensor to pick up the fine features observed by the fluorescence sensor was hypothesized to arise from the same hydrodynamic interference that created the fat tail in flume measurements.

Figure 3.32 shows a similar test in which a jet of green dye with highly elevated conductivity and temperature is directed at the sensing volume, followed closely by a burst of blue dye (delivered with a micropipette) of roughly the same conductivity and temperature as the ambient water. In this case, the fat tail was no longer present, presumably flushed out by the second burst of dye.

It was unclear whether this hydrodynamic disturbance would present a problem for eddy correlation measurements. It was possible that the effect was only significant with a large concentrated blob, while the conductivity fluctuations carried by the eddies in natural waters would represent much smaller variations. Furthermore, for properly turbulent bursts, as in Figure 3.23, the conductivity was not observed to be particularly slow.

In later EC tests, the conductivity failed to pick up the same fine features as the fluorescence sensor (Figure 3.33), raising concerns that it was averaging over eddies. It was hypothesized that this was again due to the trapping of solution by the optical fiber bodies, possibly in or near the high-E-field region between the fiber tips. Attempts to 'plug' this region (e.g. with clay, balls of Teflon tape, etc.) did not improve the characteristics of the conductivity time series. Ultimately, the electrodes were insulated on the inside faces with marine epoxy (Marine Tex RM321K Flex Set underwater epoxy), as shown in Figure 3.30. Approximately half the circumference of exposed stainless steel at each fiber tip was coated, and the fibers were mounted in the holder such that the coated regions were facing each other[7].

[7]The additional electrical insulation changes the calibration curve and cell constant from those presented in Section 3.2.2. Measurements with resistors and the I/V-to-conductance mapping of Figure 3.13a would be unchanged, but the probes would produce different I/V values for a solution of given conductivity.

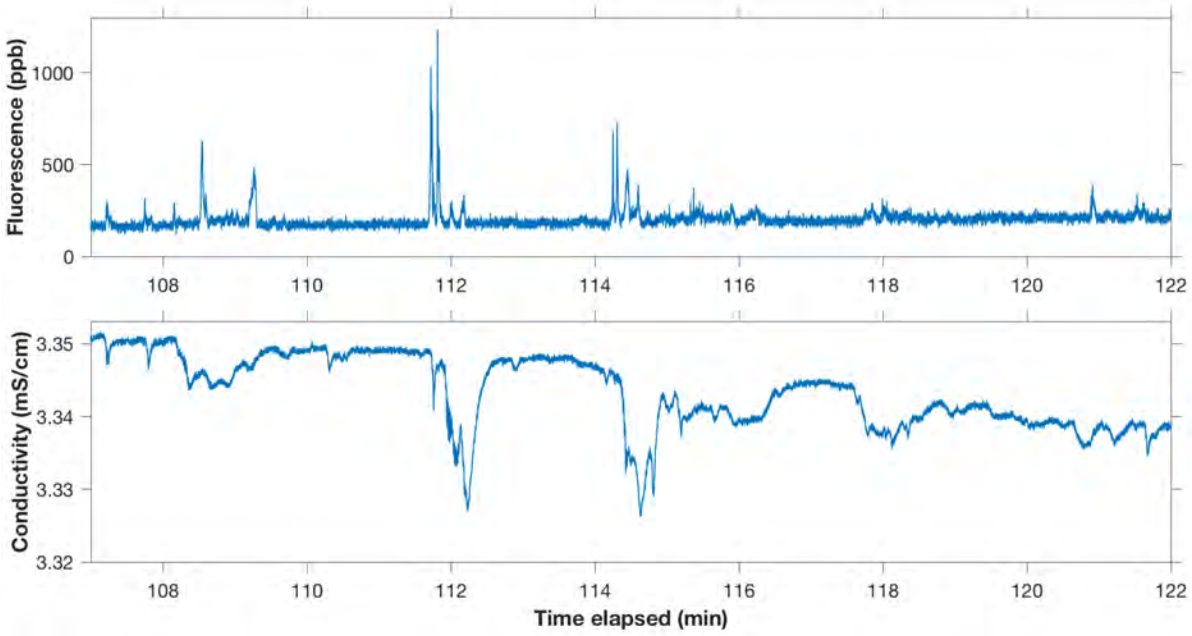

Figure 3.34: Time series taken from an EC run after the modification shown in Figure 3.30 to improve the time response of the conductivity sensor. Following this modification, the conductivity sensor was able to pick up some fine features, though many features remained largely averaged. Note that the EC run shown here inherently had much less turbulence than that shown in Figure 3.33 due to different parameters of the run.

In subsequent tests, the conductivity sensor was found to pick up some sharp peaks (Figure 3.34), showing that under some circumstances it is capable of detecting fine features, and that some of the averaging observed previously could indeed be ascribed to dye in the sensitive region between the electrode tips. However, the conductivity sensor appeared to still somewhat merge the eddy-like features picked up by the fluorescence sensor, possibly due to its larger, more dispersed sensing volume. The impact of this will be explored further in ch 5. In future iterations of the instrument, a solution might be to redesign the geometry of the conductivity cell, e.g. by fully insulating the stainless steel tubing and instead attaching fly-out electrodes.

Chapter 4

Integration with ADV and eddy correlation

In this chapter, the trimodal sensor is referred to as 'EDDI' (Eddy Diffusion Detection Instrument)[1]. EDDI includes the Raspberry Pi, fluorescence sensor (including monochromator, PMT, and photon counting circuitry), the conductivity / temperature / Teensy circuitry, and the power controls, as well as the housing and physical sensor heads (e.g. optical fibers). It does not include the ADV, although the ADV is controlled by EDDI for EC measurements.

4.1 Power and Battery

4.1.1 Battery

A 14.8 V, 10,400 mAh lithium ion battery (Tenergy) is used to power the electronics for EDDI. The battery uses a four-series, four-parallel configuration of 18650 lithium ion cells with PCB protection for shorts, overcharging, and overdischarging. It produces an output voltage that, in practice, ranges from ∼16.5 to 13.5 V. All components used in the system (e.g. DC/DC regulators) were chosen to be compatible with this input voltage range, although many of the devices are nominal 12 V input. The high voltage regulator for the PMT, in particular, is specified for a maximum input voltage of 15.5 V. Thus, the battery should not be fully charged while the PMT is in use. However, the 4-series battery was still chosen over a 3-series lithium ion combination (nominal 11.1 V) due to the physical configuration of batteries available that would fit in the pressure housing, as well as the monochromator's requirement of a nominal 15 V input voltage. A future iteration of the board may include a diode to reduce the voltage seen by the PMT's regulator.

To facilitate easy usage, the charge and discharge characteristics of the battery were also estimated by measuring its voltage while charging or in use. The charge curve obtained using a Tenergy TLP-4000 Universal 1 A charger is given in Figure 4.1. The discharge curve obtained under normal use of the photon counter, without temperature and conductivity circuitry, is

[1]Name credit: Tom O'Reilly

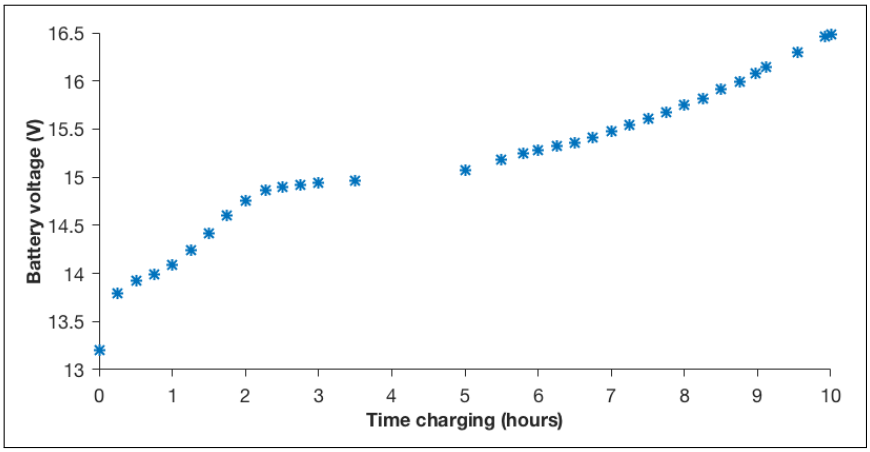

Figure 4.1: Charge curve of 14.8 V, 10,400 mAh lithium ion battery using a 1 A charger.

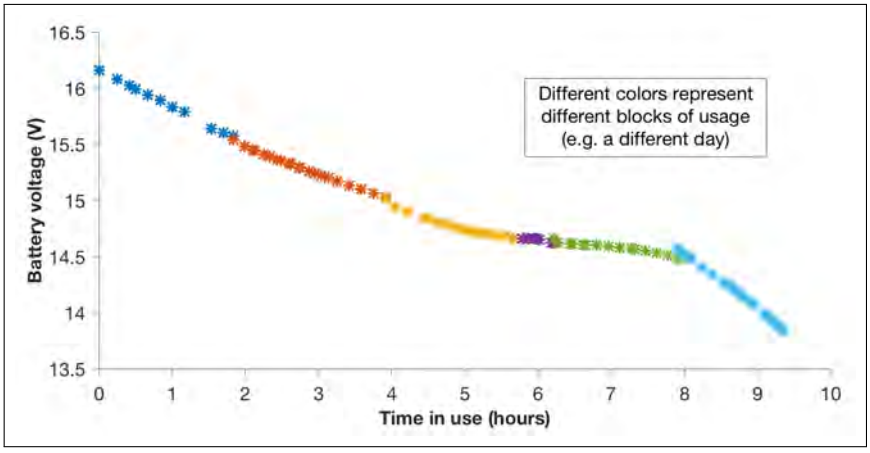

Figure 4.2: Discharge curve of battery under normal usage of photon counter.

given in Figure 4.2. The circuit has a protective diode at the battery's input with a voltage drop of $V \approx 0.3\,\mathrm{V}$; the voltages given in Figures 4.1 and 4.2 were measured for the battery itself, so the voltage seen by the circuitry is ∼300 mV less than that shown in the figures.

4.1.2 Reed switch and power control

The battery is connected to the circuitry through a reed switch (Standex-Meder PR126253001), which is installed on the lid of the pressure housing (Figure 4.3). The reed switch closes in the presence of a magnetic field, even one applied to the outside of the housing. Thus, it provides an on/off mechanism for the instrument that requires no through-holes in the housing, reducing the potential for leakage. The housing is described in Section 4.2 and the reed switch is shown installed on the lid in Figure 4.5.

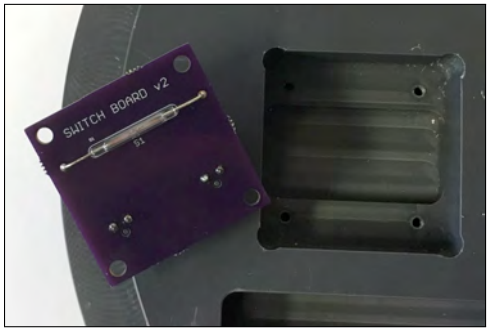

Figure 4.3: Reed switch.

Activating the reed switch connects the battery to a 5 V regulator (Recom R-78B5.0-1.5), powering on the Raspberry Pi and Teensy; all other parts of the circuitry are turned on by the Raspberry Pi through GPIO pins. The reed switch could not be connected to the entire circuitry because the current load would damage the switch, which has a 1.5 A maximum switching current (relatively high for a reed switch). More information is given in Appendix B; Section B.5 discusses the power control circuitry, and Section B.5.3 discusses the reed switch and its circuitry.

4.1.3 Power consumption

EDDI's power consumption was measured using a Keithley 2700 scanning digital multimeter. The multimeter was set to simultaneously measure voltage across and current through the battery, with their product as power. Differences in power draw as various parts of the instrument were turned on, off, or set to measure were used to estimate power consumption by the individual components of the instrument. An example is shown in Figure 4.4, and resulting power estimates are given in Table 4.1.

The regions of high noise in Figure 4.4 occurred when the the photon counting boards and/or PMT were off. When the MOSFET switches for these components are off (see Appendix B, Section B.5), the large capacitors at the input of their regulators have no contact with the main power. There are no capacitors directly bypassing the main power, because a capacitive load would cause a large inrush current for the reed switch and likely melt its contacts together (see Appendix B, Section B.5.3). The 5 V regulator driving the Raspberry Pi and Teensy does not require an input capacitor, and the monochromator's bypass capacitors are on the other side of a protective diode.

The noisiness of the power measurements when the capacitors are disconnected does not necessarily represent a noisy power rail. The noise could also arise from the circuitry used to measure the power itself, which contained a large number of free wires and alligator clips. However, ei-

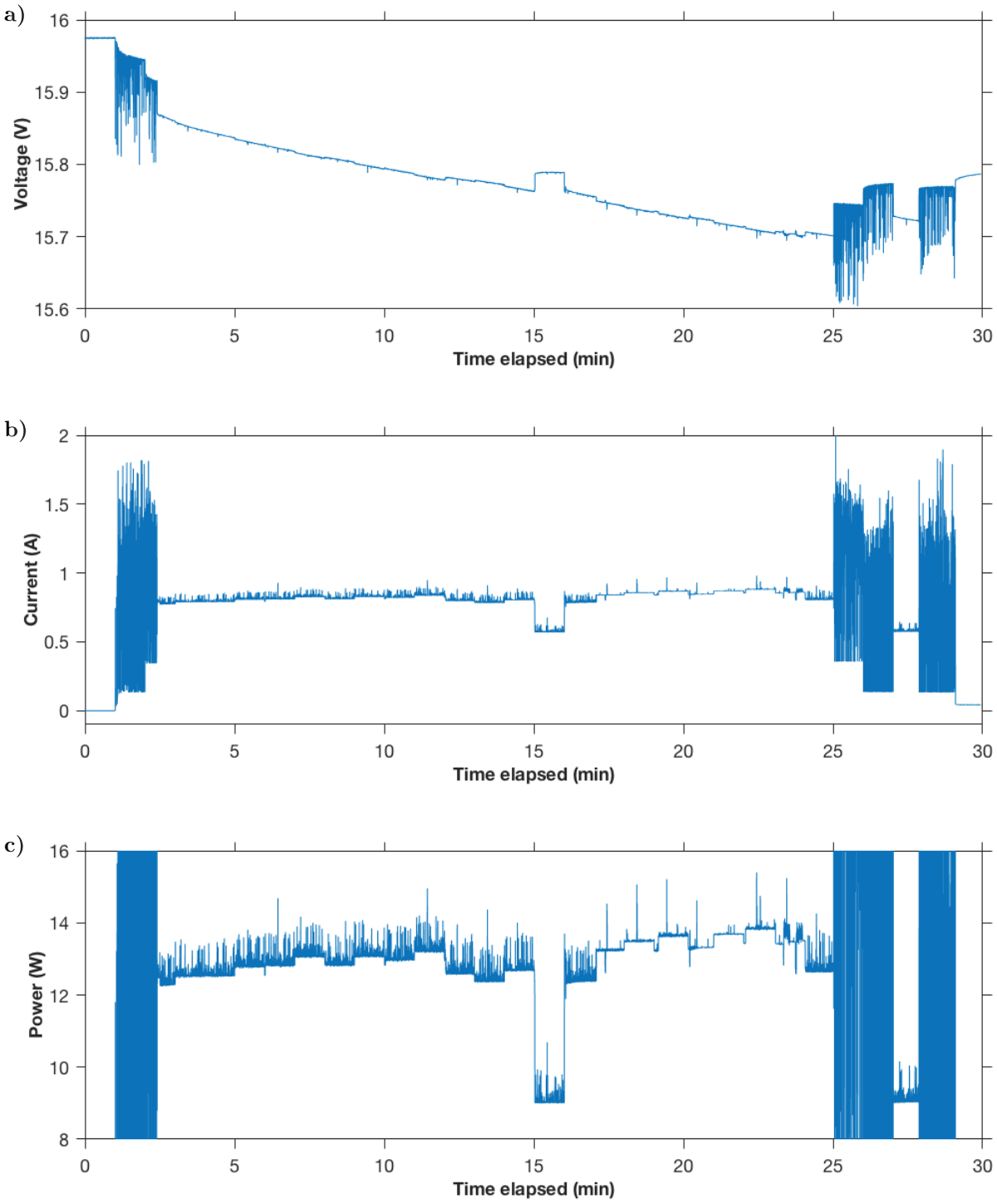

Figure 4.4: Example of test to determine power consumption of individual parts of the EDDI instrument. Various parts of the instrument were turned on, off, or set to measure, in increments of 1 min, and the difference between average power consumed during different segments was used to estimate power consumption by different parts of the instrument. A digital multimeter was used to measure **a)** battery voltage and **b)** total current output by the battery. Their product is the power (**c**).

Table 4.1. Estimated power consumption of instrument.

Static power usage while on (W)	
Baseline[a]	0.6 – 0.7
Raspberry Pi	2 – 2.2
Photon counting circuitry	6.5 – 7
PMT (dark)	0.7 – 0.8
+ strong light	+ 0.1 – 0.2
Monochromator	3.3 – 3.4
LED	0.3
Teensy	0.2 – 0.25
Temperature circuitry	<0.01
Conductivity circuitry (low g)	0.25 – 0.3
+ high g	+ 0.1

Extra power consumption while active (W)	
Counting photons (dark)	0.25 – 0.27
+ strong light	+ 0.2
Measuring T and/or C (low g)	0.2 – 0.25
Simultaneous photon and T/C measurement (dark, low g)	0.3

Power consumption under normal use	13 W − 14.5 W
with MCR off	9.5 W − 11 W

[a]'Baseline' power consumption includes e.g. power dissipated by the reed switch. This amount depends on the switch's contact resistance and the current draw; for example, the reed switch used has a contact resistance of 100 mΩ, so a typical 0.9 A current for the draw would result in 81 mW power dissipation. The 'baseline' consumption also includes losses due to the efficiency of the 5 V DC/DC convertor that is permanently on. Efficiency losses depend on the input voltage and current draw. As the battery voltage drops, the system generally becomes more efficient and dissipates (and therefore consumes) less power.

ther the photon counting boards or the PMT had to be on to obtain a clean estimate of power consumption.

4.2 Packaging, housing and construction

The housing for EDDI's electronics is constructed from a 13" length of ⌀ 8"-nominal PVC pipe, with the appropriate (8" nominal) cap and coupling cemented at the two ends. Diagrams of the interior layout are given in Appendix G. For robustness, all components are fastened to a PVC platform that is secured to the lid using a cotter pin. The PMT is connected to the monochromator by the connector described in Section 2.2.3, and plugs directly into a socket on one of the circuit boards. To reduce light leakage, the PMT is wrapped with optical tape (loosely, as the high voltage between leads can start a fire if 'shorted' by the tape), as are all LED-containing connectors (e.g. RS232-to-USB convertors).

EDDI's electronics are contained in three custom circuit boards that were designed in Eagle CAD software (Autodesk) and fabricated by an external fab shop. All three circuit boards were reflow soldered due to the presence of leadless IC packages. A bill of materials is included in Appendix E.

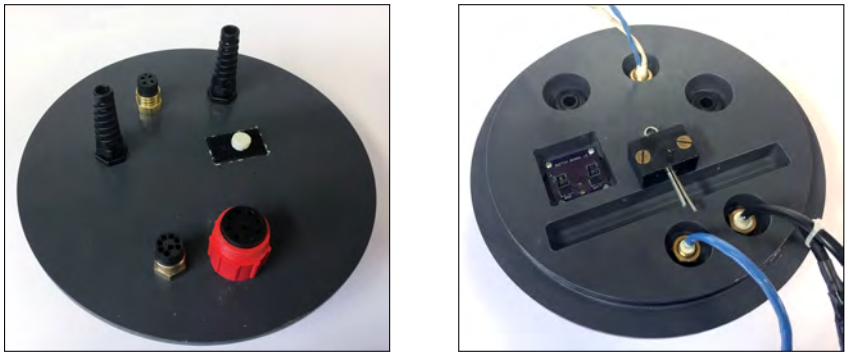

Figure 4.5: Lid of pressure housing showing underwater connectors, submersible cord grips, and magnet for reed switch.

a) Front. **b)** Back.

The lid of the housing is shown in Figure 4.5; diagrams of the layout are given in Appendix G. The lid was designed in Mastercam X6 and milled on a CNC router from a piece of 1"-thick, 12" × 12" PVC. It is installed with a -276 Buna-N O-ring (∼1/8" fractional width, ∼11" ID) around its circumference. It contains underwater connectors for the ethernet (Subconn Ethernet Circular 8-pin), temperature/conductivity (Subconn Micro-circular G2 4-pin[2]), and ADV (Impulse 8-pin). It also contains two plastic submersible cord grips for the optical fibers. The cord grips are installed with O-rings for water tightness, and can be loosened or tightened to release vacuum when opening or closing the lid from the housing. The reed switch (Section 4.1.2) is also mounted to the inside of the lid, with a corresponding strip of Velcro on the outside to hold the magnet when the instrument is powered on. The magnet, made of Neodymium Iron Boron, is coated in marine-grade epoxy (Flex-Set) to prevent corrosion, with Velcro epoxied to one side to allow attachment to the lid of the housing.

[2]The 4-pin connector for temperature/conductivity connects to the temperature (2-pin) and conductivity (2 × 1-pin) cables via a custom ordered Y-split cable.

Figure 4.6: Holder for optical fibers, designed to reduce solid bulk while holding fibers at a 20 ° angle.

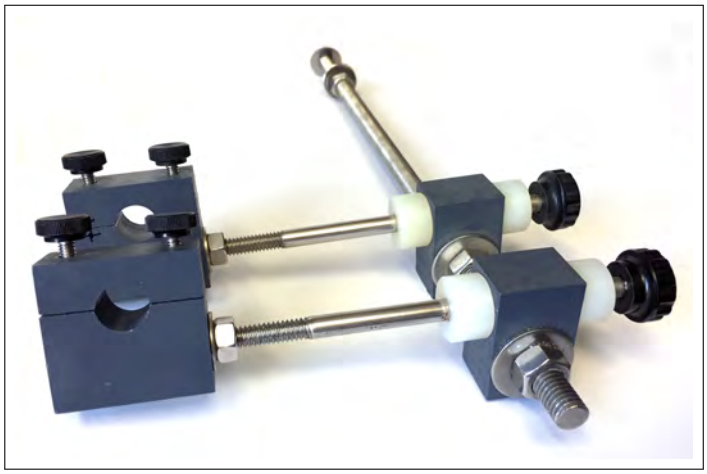

Figure 4.7: Connector to mount optical fiber holder to ADV stem. ADV stem fits in PVC pieces, while holder is secured at the end of the threaded rod using washers and screws.

All components and electronics for EDDI, except the sensor heads, are housed in this pressure housing. The ADV is held separately and also uses its own internal battery. It is connected to EDDI by its Impulse cable (see also Appendix B, Section B.7 for more information on the ADV's cable and connector).

4.3 Optical fiber holder

The custom holder for the optical fibers is shown in Figure 4.6. It was designed to hold the optical fibers securely and rigidly at the desired angle of 20 °, with special attention to reducing the solid bulk (thought to interfere with the ADV measurements; see Section 4.4.3 and Appendix C, Section C.3 on interference tests). It is constructed out of stainless steel rods, two-piece shaft collars (sized for the optical fibers after they are encased with heat shrink to form the conductivity cell, $\varnothing\,3\,\mathrm{mm}$), and a spacer. The parts were machined as necessary and then brazed together using silver solder. Designs for the holder, drafted in AutoCAD software (Autodesk Inc.), are given in Appendix G.

For the EC system, the holder is mounted to the ADV stem rather than to the external framework as in some other deployments, to minimize the risk of relative movement between the velocity and concentration sensors. The device constructed for this purpose is shown in Figure 4.7. It allows adjustment of vertical height, horizontal distance, and rotation around the z axis, so that the optical fibers can be positioned in the desired location close to the ADV's sensing volume.

4.4 Acoustic Doppler Velocimeter

Acoustic Doppler Velocimeters and some of the considerations involved in their use are described in Section 1.8 (p. 80). The ADV used for this eddy correlation system is a Vector (Nortek AS).

The Vector is a field instrument with its own battery and recorder for storing data. Its sensing volume is approximately a ∼1.4 cm diameter cylinder of ∼1.4 cm height located 15.7 cm away from the central transducer [52].

4.4.1 Synching with the ADV

Many of the existing eddy correlation systems use the ADV's recorder to store concentration data, by connecting the chemical sensor to the ADV's optional analog input. However, for the photon counter, the concentration data is not analog but digital. With many factors considered, it was decided that the master controller would be EDDI (specifically, the Raspberry Pi (RPi)), rather than the ADV.

The Vector used in this system is wired to accept a TTL 'synch in' signal, and is configured (via Nortek software) to initiate a velocity measurement on each synch pulse. The RPi is then able to initiate a velocity measurement by sending the appropriate GPIO signal, enabling easy synchronization with concentration measurements. The RPi also interacts with the ADV through the serial port using an RS-232 connection to check the user configuration information, receive data, interact with the ADV's recorder, and communicate for other functions.

The Vector stores all velocity information on its recorder, which is then read into the RPi at the end of an eddy correlation run. The Vector's data can also be live-streamed during the EC run; however, this method was not used due to timing considerations. For more information, see Appendix B, Section B.6.

4.4.2 ADV interference with EDDI

Fluorescence

The Vector was found to radiate electromagnetic signals associated with its acoustic ping pairs. As discussed in Section 2.3.1 (p. 109) on the fluorescence sensor performance, the photon counter is extremely sensitive to radiated noise. The ping pairs were clearly visible in the output of the amplifier, with a timing dependent on the ADV's settings (Figure 4.8). Each ping caused a burst of noise in the amplifier; these signals were indistinguishable from photon counts and were propagated through the comparator, as shown in Figure 4.9. A Fourier transform of the burst signal showed strong frequency components at 18, 30, 54, 60, 66, and 78 MHz, as well as other harmonics of the Vector's 6 MHz acoustic signal.

As discussed in Section 2.3.1, much of this problem was resolved in the second generation design by integrating the PMT with the circuit boards. In addition, Nortek AS (the manufacturer of the ADV) worked with us to design and build a custom harness for the Vector with a filter that reduces its radiated EMI. See Appendix B (Section B.7) for more information on the harness and filter.

a) Nom. velocity range = 0.3 m/s.

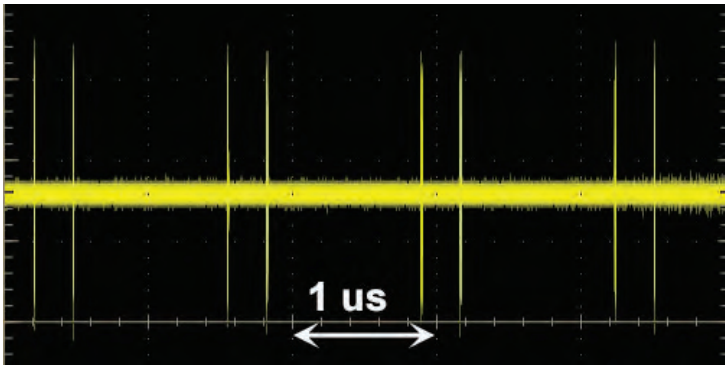

b) Nom. velocity range = 4 m/s.

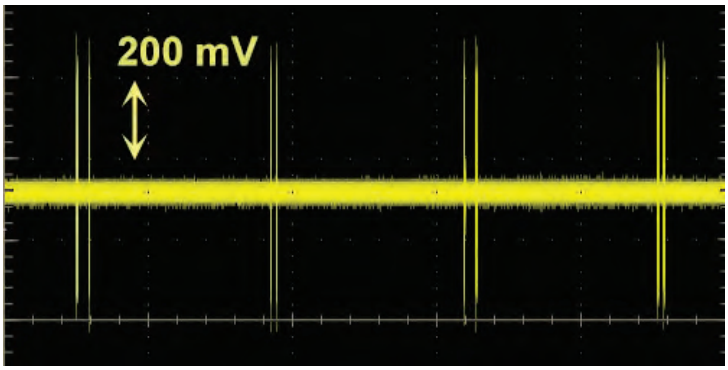

Figure 4.8: Oscilloscope trace of the photon counter's preamplifier output, showing interference from ADV ping pairs. The timing between the pings of each pair depends on the ADV's nominal velocity range setting, while the timing between the pairs is determined by the Vector's internal ping rate. Thus, the user-configured measuring rate determines the number of ping pairs averaged per output velocity data point.

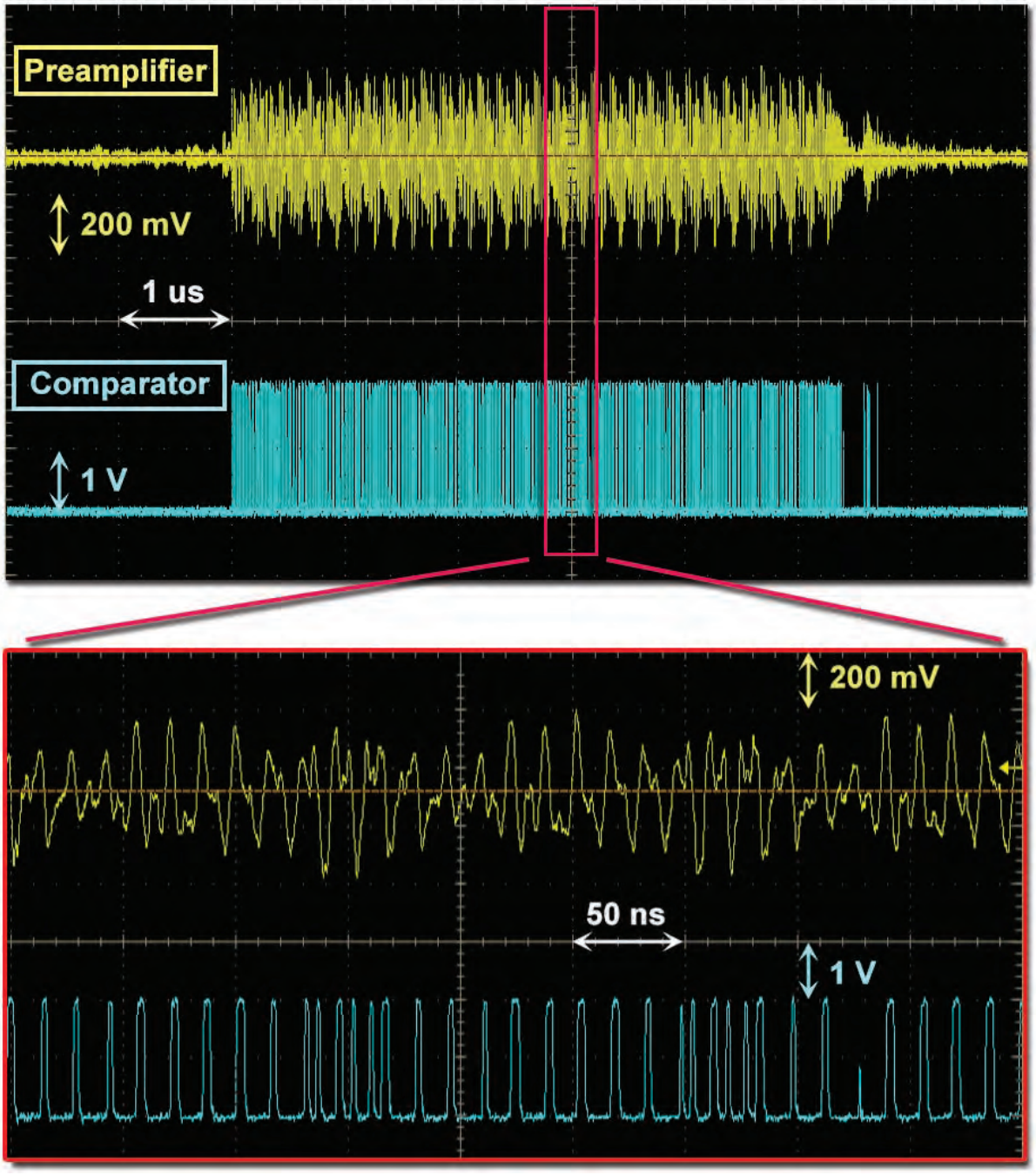

Figure 4.9: Oscilloscope trace of the photon counter's response to a single ADV ping, showing substantial and periodic noise in the preamplifier output that was registered by the comparator as photon counts.

Conductivity

In conducting EC tests in the tank (see Section 4.5), the ADV was also found to electrically interfere with the conductivity sensor by its serial streaming, resulting in steady 1 Hz downward spikes in the conductivity reading. The interference was only present when the ADV was streaming data through its cable during measurement. It was hypothesized to arise from some coupling of the ADV's electronics with the water in the tank, which had a conductivity elevated above freshwater (∼3.5 mS/cm.

The serial streaming of data should actually have been disabled because the ADV was configured to record onto its recorder rather than stream data live (see Section 4.4.1 and Appendix B, Section B.6 on Vector integration notes). However, a bug was found in the Nortek software/firmware whereby streaming during recorder measurement, a configurable feature, was automatically re-enabled after measuring velocity live by streaming to the PC (conducted prior to all EC runs to check the signal quality). It could only be disabled by initiating a recorder run from the Nortek software, where it was actually off by default. Thus, the workaround until Nortek fixes the bug is to start and stop a 'shadow' recorder run via the PC prior to switching cables to the Pi, so that the setting for no streaming is stored.

4.4.3 EDDI interference with ADV

Eddy correlation theoretically requires concentration and velocity to be measured in the exact same location. However, this is currently not possible with any instrumentation that we or other researchers know of [25, 48]. Oxygen probes, for example, measure O_2 concentration at their probe tip, which cannot be placed inside the ADV's sensing volume because it would interfere with the velocity measurements. The probe tip is therefore positioned right outside the ADV's sensing volume, e.g. a few mm away [11, 33] for the traditional microelectrodes, 5 mm for a conductivity/temperature sensor [6], or up to 2.5 cm for a more robust oxygen optode [5, 48] (see Section 1.4.2, p. 43). The offset in sensing volumes can be somewhat adjusted for with a relative time shift, but it is ideal to have the two sensing volumes as close as possible. See Section 1.4.4 (p. 51) on corrections to EC measurements for more information about time shifts.

Our fluorescence sensor has a sensing volume that is slightly displaced from the optical fiber tips (see Section 3.4.2, p. 154) presenting a unique opportunity to reduce the spatial discrepancy between the sensing volumes. To test the minimum distance between the optical fiber tips and the ADV's sensing volume, we conducted a test similar to that of Berg et al. [5]. In stagnant, unseeded water, the optical fibers were mounted at difference distances from the ADV's sensing volume, and the ADV's signal was recorded for at least 5 min at each distance.

Interference was assessed using the ADV's amplitude output, which represents the strength of the backscatter signal (see Section 1.8.5, p. 84). The amplitude would normally be quite low in particle-free stagnant water, but it would be higher if the ping pairs scatter off of an object fixed too close to the sensing volume. The concurrently measured parameter of correlation can also be used as an indicator. Similar to amplitude, low correlations are expected in particle-free water, but the presence of an object will result in extremely high correlations.

The optical fibers were aligned to the edge of the sensing volume (representing 0 mm offset),

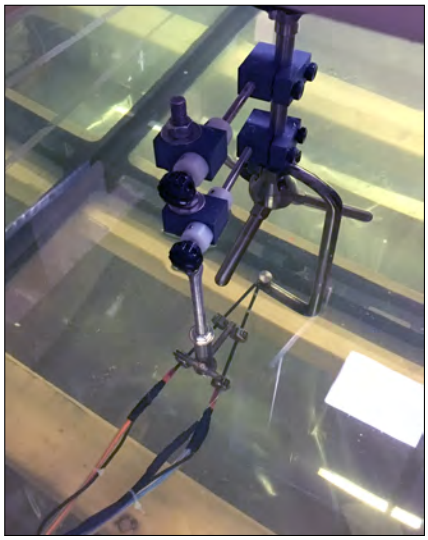

a) Top view.

b) Side view.

Figure 4.10: Setup for tests of sensor interference with velocity measurements. Alignment piece attached to ADV was removed after aligning sensors.

between Beams 1 and 2, with the aid of a specially constructed stainless steel alignment piece as shown in Figure 4.10. After each measurement, the sensor was offset further from the sensing volume by turning the partially threaded rods that control horizontal alignment. Since the threading is 1/4"-20, there are 20 threads per inch (and the rod is $\varnothing$ 1/4"), so each revolution corresponds to $1/20 = 0.05" = 1.27\,\text{mm}$ additional offset.

The level of interference was also sensitive to rotation, both of the fiber holder around its three rotational axes, and of the entire assembly around the axis of the ADV. For the rotation of the holder itself, best attempts were made during the interference tests to keep the holder level, although in general tilting the holder to reduce interference is acceptable as long as the fibers remain pointed at the ADV's sensing volume. For rotation around the axes of the ADV, the optical fibers were placed between two beams (Beams 1 and 2 for the interference tests), but sensitivity to rotation is discussed further in Appendix C (Section C.3).

Results are given in Figure 4.11. Note that the offset given in the x axis represents the distance between the edge of the velocity sensing volume and the optical fiber tips, and hence the main bulk of the conductivity and temperature sensing volumes. However, the fluorescence sensing volume is slightly offset from the optical fiber tips, and would overlap more with the velocity sensing volume when the optical fibers are a few mm away.

The amplitude plot, Figure 4.11a, shows interference past 1 cm offset. Correlation results (Figure 4.11b) are noisier, but show interference that tapers past ~0.5 cm. From Figure 4.11, it appears that backscatter from the body of the other optical fibers and holder continues to interfere with velocity measurements, even when the objects are not physically in the ADV's sensing volume or in the path of its beams. This effect was even more noticeable in preliminary tests, where a different fiber holder was observed to interfere with velocity measurements even when it was 2 cm away (see Appendix C, Section C.3). The similar test conducted by Berg et al. [5] for their dual oxygen-temperature probe appeared to show such an effect as well.

We hypothesize that this 'remote' interference arises from the nature of the sound pulses used in the Doppler measurements, which can reflect off of solid surfaces and bounce around. We first

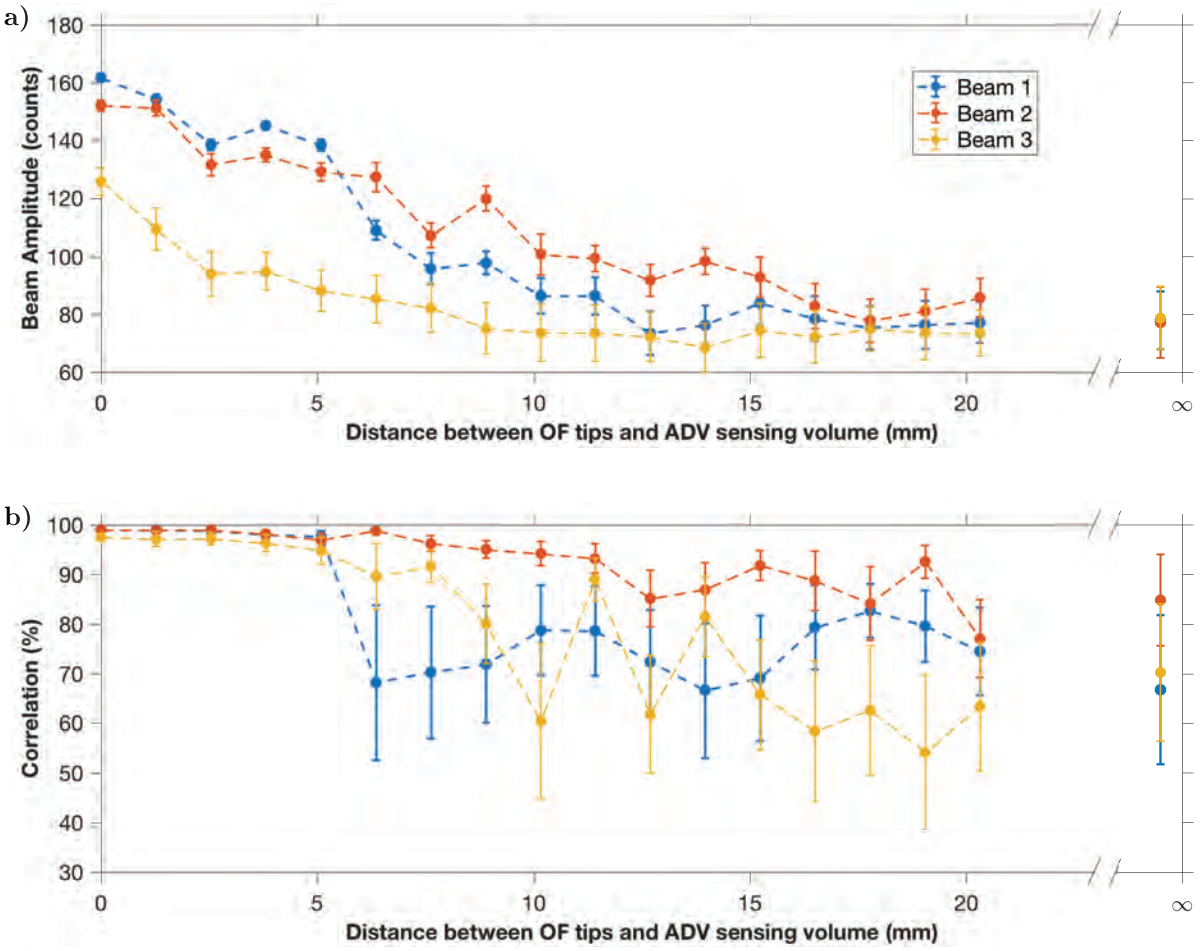

Figure 4.11: a) Amplitude and **b)** correlation of ADV measurements, averaged over 5 min, as a function of the distance between the optical fiber tips and the edge of the ADV's cylindrical sensing volume. As measurements were conducted in unseeded, stagnant water, high amplitude and high correlation signify interference of the ADV's measurements by the presence of the concentration sensor.

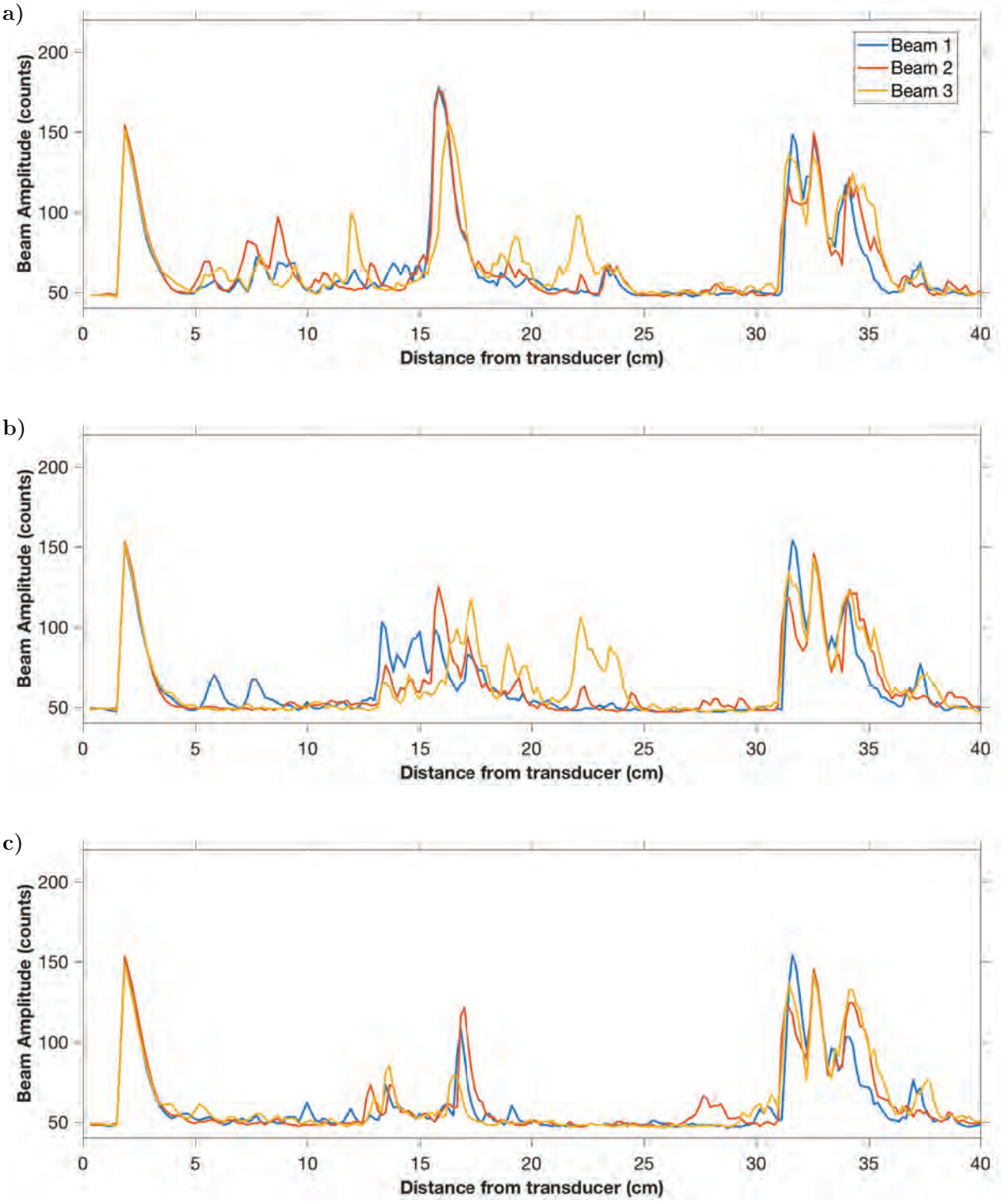

Figure 4.12: Probe checks taken with the optical fiber tips positioned **a)** at the edge of the ADV sensing volume (0 mm offset), **b)** at a typical distance for EC measurements (7.6 mm), and **c)** without optical fibers or their holder. The probe checks show 'spiky' signals from reflections off of the optical fibers, as well as the walls of the tank.

noticed the issue of reflections during baseline measurements in the 120 gallon glass aquarium, where 'spiky' signals in the probe checks[3] and intermittently low correlation values were eventually traced to reflections from the glass surfaces of the aquarium. For these tests, some degree of noise was also anticipated due to the low amplitudes (characteristic of the low-particle, low-turbulence environment). Indeed, as might be expected given low signal-to-noise ratio (SNR), the probe checks appeared to be somewhat stochastic, here due to the broadband noise[4]. Thus, the instant snapshot given by each profile is not fully representative of the average amplitude profile, although it can still provide a general visualization of interference.

In the probe checks for these tests (Figure 4.12), 'spiky' features associated with reflections are quite prominent at the distance corresponding to the sensing volume ($\sim$15 cm). Some of the spikes are due to reflections off the enclosed aquarium (Figure 4.12c), but the interference is much more noticeable when the optical fibers are present (Figures 4.12a and 4.12b). Interference can also be seen at distances in the 5 cm to 10 cm range. However, these measurements correspond to a different beam geometry than for the actual sensing volume (i.e. flatter tetrahedron), so interference in the receive paths do not necessarily indicate trouble for actual velocity measurements in the sensing volume [Elin Bondevik (Nortek AS), personal communication, 19 May 2016].

Berg et al. [5] base their assessment of 'adequate' offset (to avoid interference) on the backscatter from natural particles. As long as the natural backscatter is 15 dB[5] (with a translation of 0.54 dB/count for our instrument, this corresponds to 28 counts) greater than the interference, the velocity measurements should still be reliable. However, such quantitative analysis is difficult with our measurements, since the background level was variable and exhibited higher values than those given by Berg et al. [5], despite using the same model ADV. Due to the nature of the environment, our aquarium was not completely particle-free, so it is likely that some of the amplitude is due to natural scattering off particles or the aquarium walls.

The EC test presented in this thesis typically used a separation of 5 mm $\sim$ 8 mm. This value is based on the results in Figure 4.11, as well as baseline values measured before each run to ensure the holder is not interfering too significantly. Distances that produced amplitudes of 90 $\sim$ 110 counts in unseeded stagnant water seemed to be a reasonable tradeoff between interference and collocation, where increasing the distance further does not decrease the amplitude significantly.

[4]Probe check measurements represent full profiles of backscatter and ideally show a Gaussian curve around the sampling volume (see Figure 1.19, p. 83).

[4]The stochastic nature of turbulence has been previously discussed in reference to EC theory. Turbulence is indeed stochastic, but the randomness of amplitude discussed here is independent of the randomness of turbulence, as signal strength for ADVs does not reflect the velocity itself; see Section 1.8 (p. 80).

[5]Recall that the amplitude unit of 'counts' is a log-scale measure due to the use of a log amplifier, as described in Section 1.8.5, p. 84.

4.5 EC experiments in a laboratory tank: Methodology

4.5.1 Experimental setup

Further information and specifications of the experimental setup are given in Appendix B, Section B.8. Steps to prepare for the experiment are given in Section B.9. Many different EC runs and other tests were conducted in the tank, to troubleshoot the instrument and the environment. Results will be shown only for the trial conducted on 12 September 2018; where relevant, all provided settings will correspond to this run.

Tank setup and dye input mechanism

EC experiments were conducted in a 120 gallon glass aquarium with approximate dimensions $2 \times 4 \times 2$ ft ($0.6 \times 1.2 \times 0.6$ m). A wooden frame was constructed to hold a turbulence-generating mechanism over the tank, as shown in Figure 4.13. The mechanism controlled four linearly oscillating plungers at the corners of the tank, suspended 32.5 cm to 39 cm above the tank floor depending on the phase of the oscillation. The plungers were offset by 45 ° from each other, and oscillated at a frequency depending on the driving voltage to the motor (controlled via a benchtop power supply). For the EC run described here, the oscillation frequency was ∼0.9 Hz, but would vary depending on the shifting and rubbing of parts.

The tank was filled to ∼46 cm with tap water, salted as to be described. During operation of the fluorescence sensor, the tank was draped in blackout cloths to prevent ambient light from reaching the sensor (which would increase the noise of the fluorescence measurements).

The ADV was held over the tank by a specially constructed holder clamped to cross-beams directly mounted to the tank. The ADV was not mounted to the wooden frame to avoid coupling of vibrations. The optical fibers were mounted to the ADV stem as described in Section 4.3. For the test described here, the separation distance between the optical fiber tips and the ADV sensing volume was ∼6 mm, as shown in Figure 4.16.

The sensing volume was suspended in the tank over a specially constructed plate for dye release, as shown in Figure 4.14. For the EC run described here, the measuring height was estimated to be 11.2 cm above the plate, based on ADV probe check measurements. The measured height of the plate is 2.4 cm, so the distance of the sensing volume to the floor of the tank was ∼13.6 cm.

The 12” (∼30 cm) diameter plate was designed for a uniform release across its surface area. It was paired with a detachable lid, which could be secured to the plate by press fit to form an O-ring seal. The lid comprised mainly of a piece of mesh stretched over the shallow surface reservoir of the plate. The mesh constrained the dye within the reservoir, while allowing a steady diffusion into the tank. Dye was pumped into the plate via two channels of a peristaltic pump (Rainin Dyanamx RP-1), using ⌀ 1/8 ” (ID) Tygon tubing (OD ⌀ 3/16”). The remaining two channels of the pump were used to pull dye out of the opposite side of the plate.

The plate could be operated in two different ‘modes’. In ‘flushing’ mode, dye was pumped in one side and out the other; the purpose was to pull dye through the plate to fill the reservoir, in preparation for an even release across its area. The plate was designed so that a relatively

Figure 4.13: Experimental tank for conducting EC experiments. The wooden frame on which the tank rests holds a motor-driven mechanism with four oscillating plungers to generate turbulence.

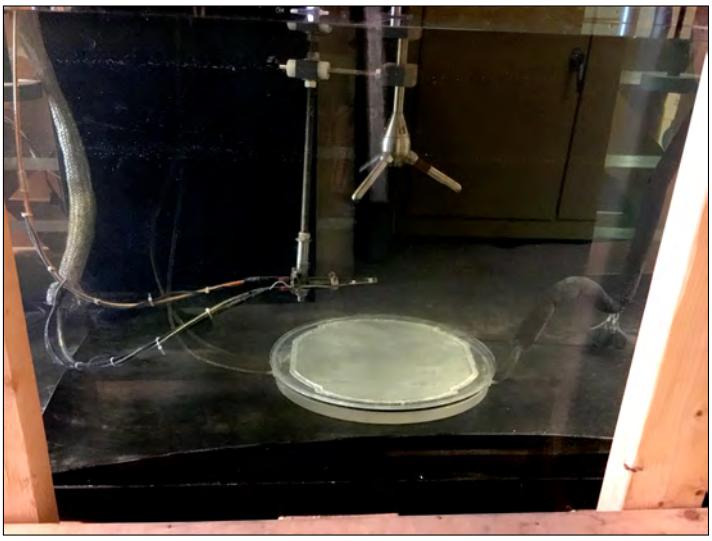

Figure 4.14: Side view of tank showing optical fibers mounted to ADV stem, with sensing volumes ∼14 cm above a plate designed to release dye for detection.

Figure 4.15: Benchtop setup of dye input system, including peristaltic pump with two channels for inflow and two channels for outflow. Inflow is connected to a carboy holding input dye, shown sitting in an ice bath. Outflow is directed to a separate bottle. The glass beaker with spigot used for inputting ambient tank water is also shown in the center.

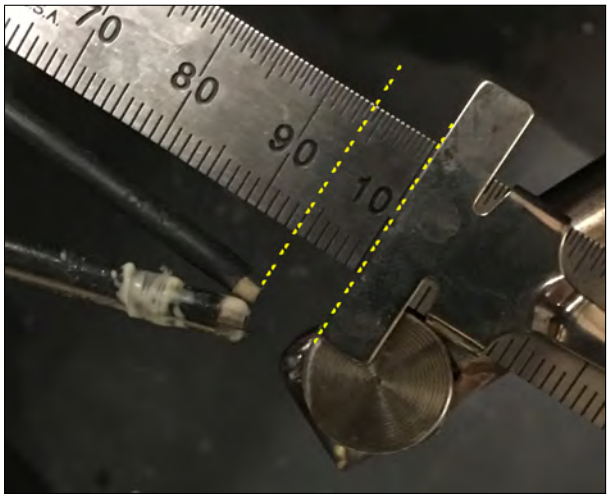

Figure 4.16: Actual alignment of optical fibers to ADV sensing volume for tank test described in this section. The alignment piece used to represent the ADV's sensing volume is shown in Figure 4.10.

uniform distribution could be achieved this way. In 'pumping' mode, only the input tubings were connected to the pump. Thus, dye was actively input into the tank at a rate controlled by the peristaltic pump, and entered the water through the mesh. The ideal entry would be momentum-less, with transport dominated by turbulent diffusion. The plate release would thus be analogous to an advective discharge (e.g. submarine groundwater discharge) into the benthos that would then be quickly swept up by the turbulence.

The dye input system is shown in Figure 4.15. Input liquid (dye or ambient tank water) was pumped to the plate from a suitable container with a barbed hose connection. For the dye, the container used was a 5 L polypropylene carboy with a valved spigot. For ambient liquid (from the tank), the container used was a glass beaker with a hose connection. When flushing ambient tank water, the system could be set to recirculate flow by directing the outlet tubings back to the beaker.

Of the user-configurable rates provided by the peristaltic pump, only the 'prime' rate (intended to be used to prime the tubes) and the nominal '30 mL/min' rate were used. All 'flushing' was done under prime speed, while pumping was done with either the prime speed or the 30 mL/min speed. The actual pump rates were measured separately. With our tubing, and using two channels, the measured pump rate for 'prime' speed was 57 mL/min, and for the nominal 30 mL/min speed was 35 mL/min. These rates were found to be relatively insensitive to the head difference overcome by the pump.

Dye solution

The experiment involved the release of a 'dye solution' at a controlled rate from the floor of the tank. The solution is referred to as 'dye' because it contains fluorescein dye, but it was actually created to be detectable by all three EDDI sensors, similar to the solution used in the tabletop flume tests described in Section 3.4.

The solution contained 2 ppm fluorescein dye, diluted using distilled water from a 100 ppm stock created using fluorescein salt and 0.1 M sodium bicarbonate solution. Unlike the injection solution described in Section 3.4, however, the dye was of lower temperature and conductivity than

the ambient tank water. Since the dilution was done with distilled water, the conductivity of the dye was generally $\sim$250 µS/cm, with most of the conductivity attributable to the fluorescein salt. To create a conductivity contrast, the tank was salted with aquarium salt (Instant Ocean) to a conductivity of $\sim$3500 µS/cm. To ensure dissolution and mixing of the salt in the tank, the salt was first stirred into the tank, and then left overnight under recirculating flow created by a bilge pump.

For temperature contrast, the dye (in the carboy) was chilled in a cold room overnight before experiments. During experiments, the carboy was kept in an ice bath, as shown in Figure 4.15. Although the cold room was nominally 4 °C, the measured temperature of the dye prior to experiments was often closer to 8 °C. To increase the temperature contrast, the tank was also warmed using two aquarium heaters set to a temperature of slightly over 26 °C. The heaters were removed prior to the experiments, as their input heat flux could overwhelm any detectable fluxes.

The temperature difference proved particularly difficult to maintain, even with foam tube insulation around the pump tubing. A long probe thermistor[6] inserted into the tank $1 \sim 2$ mm above the plate during trial runs generally read $20 \sim 24$ °C. Although temperatures measured above the plate may not correspond directly to the temperature of the thin layer of dye within the plate's reservoir, the large difference in measured temperatures from the dye's supposed 8 °C indicated that heat was likely lost between the carboy and the tank.

The conductivity and temperature differences were chosen so that the solution would be as close to neutrally buoyant as possible. To achieve this, the buoyancy effects from the conductivity and temperature differences had to offset each other. Initial tests using a warm, salted dye sank to the bottom of the tank upon release. The temperature of the dye was limited by the temperature ratings of the carboy, tubings, and pump. Thus, a cold freshwater input was chosen instead of a warm, salty input. Such an input is more analogous to a groundwater discharge; in a natural system, however, buoyancy considerations would not be as much of an issue, as natural gradients would exist (e.g. the water at the bottom would already be cooler). Here we just aimed to achieve a low enough buoyancy contrast that most of the transport would be carried by turbulent diffusion.

Because the temperature difference was so hard to maintain, and it was desired to measure a heat flux, the temperature contrast between dye and tank was chosen to be as large as possible. The tank temperature of $\sim$26 °C is at the upper bound of EDDI's range, while the cold room was the best means we had of cooling the dye. These temperatures were then fixed in trial runs, and the salinity was adjusted to achieve the desired buoyancy.

The salinity of the tank was chosen based on repeated trials observing dye release under a black light. If the salinity of the tank was too high, the dye could be observed to form buoyant plumes and rise preferentially from the side of the plate closest to the release. If the salinity was too low, the dye could be observed to flow over the sides of the plate and sink. In practice, neutral buoyancy is impossible to achieve, and the final conditions were chosen based on the observed

[6]The long probe thermistor was created using the same GP104L8F thermistor as used in EDDI, similarly packaged into a needle. A series of telescoping stainless steel tubings formed the body, with thinner tubings near the bottom to avoid disturbing the bottom layer, and a $\varnothing$ 1/4 in (OD) tubing as the main body of the probe. It was connected to a scanning digital multimeter, which provided resistance readings that could be calibrated into temperature.

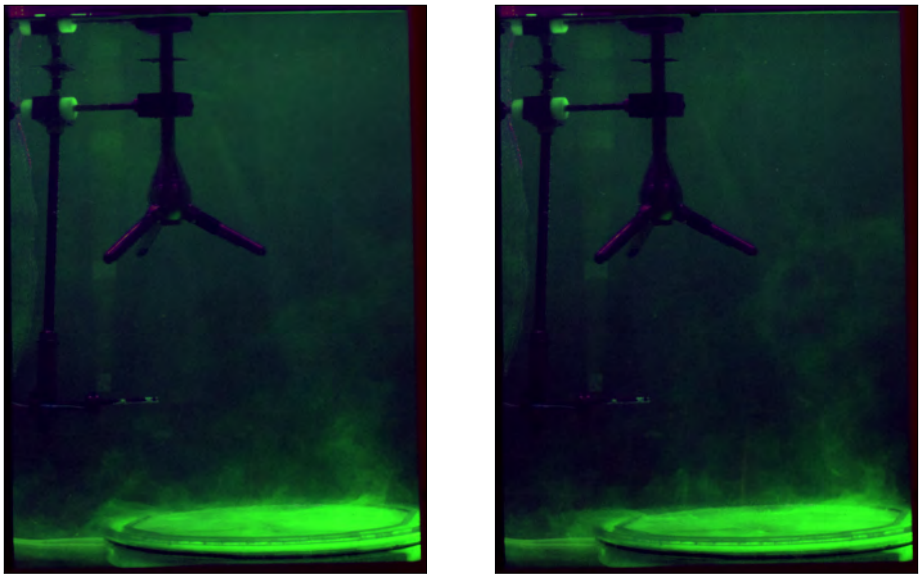

Figure 4.17: Release of dye from plate at two different release rates. Images are processed; see Appendix B, Section B.11 for more information. The plate is purposefully off center because flow patterns tended to push the dye leftward.

a) 35 mL/min release. **b)** 57 mL/min release.

release patterns of the dye from the plate. It is likely that the dye was slightly positively buoyant, although portions of the dye were also observed to spill over the edge of the plate and sink to the bottom. The position of the plate within the tank was also important, as the flow patterns generated by the plungers created some asymmetries (e.g. dye observed to drift toward the center of the tank as it rose, but preferentially on one side). The final position of the plate and ADV, as well as the orientation of the optical fibers, was chosen based on repeated tests with various permutations of the setup.

The final conductivity chosen for the tank, $\sim$3.5 mS/cm (corresponding to a salinity of $\sim$1.7 ppt), was only slightly elevated above the dye ($S = 0$ ppt). Based on the temperature difference, the dye should have been heavier than the ambient tank water; however, as discussed, the temperature difference was difficult to maintain and the dye was often observed to rise.

Dye releases during the experiment, imaged using a Nikon D5300 camera under a 405 nm, are shown in Figure 4.17. Note that the dye release was not completely even, due to the circulation patterns within the tank and the imperfect buoyancy. The higher release rate (Figure 4.17b) appeared to be more uneven than the lower rate. The plume at the right side of the plate, closest to the inlet tubings, in particular appeared to be skewed towards the back of the tank (into the page).

Accommodations for EDDI

The temperature measurements were initially affected by a significant amount of noise that exceeded the expected fluctuations. A capacitor across the thermistor input successfully reduced much of the noise, and a separate ADC (not shared with conductivity) was installed for temperature to increase the averaging time (see Section 3.4.4, p. 166). The capacitor did not appear to affect the response time of the temperature measurements. In addition, some of the noise and irregularity could be traced to broken thermistors and/or leakage through the

thermistor packaging, which was fixed with new thermistors.

However, much of the noise was also traced to the cable, so that it was significantly reduced when the cable was curled up rather than being extended (such as when hanging in the tank). A Fourier transform of fast (160 Hz) temperature measurements showed an extremely strong 60 Hz signal, indicating interference by building power. Such interference would not be expected in field measurements, but obviously was a problem for our laboratory measurements. It may have been specific to the particular room or location, or it may have been present but unnoticed in previous tests (e.g. flume tests in Section 3.4) where temperature fluctuations were larger.

To counter this radiated noise, a braided copper interference-shielding sleeving was installed around the conductivity/temperature cable and consequently the optical fiber to which it was attached. The sleeving, which can be seen in Figure 4.14, encased most of the length of the cable and optical fiber and was thus grounded to the tank water. It was also grounded to the temperature/conductivity board using an alligator patch cable. It was used for these particular tank tests but should not be necessary in the field.

Accommodations for the ADV

As mentioned in Section 4.4.3 (p. 184) in reference to interference with the ADV's signal, baseline measurements in the glass aquarium initially produced 'spiky' signals in the probe checks and intermittently low correlation values. These issues were eventually traced to reflections from the glass walls and floor of the aquarium. Subsequently, the floor and most of the walls were lined with neoprene rubber sheets (1/8" and 1/16" thick), some of which are visible in Figures 4.13 and 4.14 (some rubber sheets were removed from the walls for viewing). The rubber sheets were essential to achieving usable data with the ADV, and were likely necessary due to the enclosed nature of the system and the high reflectivity of glass.

The ADV signal was also observed to decline in quality over the course of the EC runs, reaching unacceptable levels of noise within the first 30 min. Specifically, the amplitude (and relatedly, the SNR) was observed to drop, but could be revived with vigorous stirring. It was hypothesized that the seed particles (scatterers added to improve amplitude) used were settling, possibly because the environment was not turbulent enough (velocity data is presented in Section 4.6.1). An alternative brand of seed particle was found to stick to the glass walls. Ultimately, we sourced seed particles from Ubertone, a French company, that were found to stay afloat for several hours at a time. These polyamide seed particles have a density of 1.01 g/mL, which is very similar to water, resulting in a slow settling velocity of 0.03 mm/s.

Configurable parameters for the Vector were chosen as follows:

- **Measurement speed**: 64 Hz. Because the ADV is controlled by the Pi, its true measurement speed is dictated by the user-selected measurement speed for the EC run. The Vector's own configurable measurement speed is only relevant because it dictates when the Vector samples its pressure sensor, which is ideally in the middle of the measurement [Sven Nylund (Nortek AS), personal communication, 11 August 2015]. The final measurement speed used for these experiments was 48 Hz, so either the 32 Hz or 64 Hz options for the Vector would have been most appropriate.

Table 4.2. Program for EC run described in this section.

	Time range	**Input to tank**	**Notes**
1	0 - 10 min	Flush ambient (recirculating flow)	Baseline turbulence characteristic
2	10 - 20 min	Pump ambient 57 mL/min	Observe for momentum input
	18 min	Pushed plate toward center of tank (more centered under sensors)	
3	20 - 30 min	Flush ambient	
4	30 - 40 min	Flush dye	A small amount of flux is sometimes observed in this stage due to positive buoyancy; bright green color of outflow liquid indicated that most dye was pulled through
5	40 - 80 min	Pump dye 35 mL/min	
6	80 - 120 min	Pump dye 57 mL/min	
7	120 - 161 min	Pump dye 35 mL/min	
8	163 - 170 min	Flush ambient (non-recirculating)	Shorter flush stage combined with subsequent pumping was observed to clear the plate of remaining dye
9	170 - 195 min	Pump ambient 57 mL/min	Large puffs of dye were often observed near the beginning of this stage as dye cleared from the plate
10	195 - 240 min	Flush ambient (recirculating flow)	

- **Nominal velocity range**: 0.3 m/s. This parameter is specific to the turbulence regime created. Although the velocities in our system appeared to be quite low, we still ran into low correlations when using a lower velocity range, possibly due to phase wrapping in beam coordinates (see Section 1.8.3, p. 83 for a description of phase wrapping).

- **Coordinate system**: XYZ.

- **Power level**: Low. Due to the quiescent z velocity in our system, we observed some acoustic streaming, and so chose the low power level to minimize its effect.

- **Start on Synch, Sample on Synch**: Enabled. This is required for the Vector to be controlled by the RPi.

- **Recorder settings**: Serial streaming disabled, to avoid interference with the conductivity (see Section 4.4.2. In addition, the recorder run must have a name, to avoid errors. Both of these parameters were set by running a 'shadow' recorder run after pre-run ADV checks, before disconnecting from the PC.

All other parameters used the manufacturer default values.

4.5.2 Experimental procedure

The procedures for setting up and preparing the experiment are given in Appendix B, Section B.9. The experiment was 4 hours long and followed the program given in 4.2. Note that all changes in expected flux occur in increments of 40 min, which would thus represent the longest flux period that could be used for calculations.

For the EC run described here, measurements were made at 48 Hz, with a 20 ms integration time (see Appendix B, Section B.2 for a discussion of integration time vs measuring frequency for this instrument). 48 Hz was chosen because it is a relatively high frequency that can be averaged down to standard measuring frequencies of, e.g. 16 Hz or 8 Hz. In addition, an active measuring period (integration time) could be chosen (20 ms) that would make nearly maximal use of the entire time between samples (20.8 ms). With the photon counter modulated at 1 kHz, the integration time is ideally a multiple of 2 ms, since each LED on/LED off pair is 2 ms long[7]. Thus, 48 Hz was chosen over 62 Hz, for which a natural choice for integration time might have been 15 ms.

4.5.3 Calibrations and unit conversions

The EDDI sensors were calibrated based on measurements taken before and after the EC run, as well as measurements taken before and after other EC runs conducted within a few weeks. Calibration curves are given in Figure 4.18. More calibration points were achieved for conductivity and temperature calibration by draining the tank after the EC run, adding tap water back to the original depth, and taking a measurement.

It should be noted that conductivity calibrations were done using a commercial meter with temperature compensation disabled, since EDDI's conductivity sensor measures actual conductivity at ambient temperature. Temperature compensation for EDDI can be done separately on the calibrated results; see Box 4.1.

The fluorescence sensor was calibrated based on the estimated concentrations of fluorescein in the tank before and after the run[8]. The pre-run concentration is 0 ppm, although the sensor may not register 0 counts, because strong excitation scattering—especially prominent with seed particles in the water—could bleed into the emission wavelength. The end concentration was estimated based on the volume of water in the tank at the end (given the tank dimensions and measured water depth), and the amount of dye pumped into the tank (based on Table 4.2; 'flush' periods were not counted as dye input).

[7] Odd integration times would result in the photon counter sitting idle for 1 ms, which is an unnecessary loss of counting time. Faster modulation is also possible, but would result in an increased amount of data processing time.

[8] To check the fluorescence calibration, separate measurements were also made with a benchtop setup using optical fibers suspended in a 500 mL amber jar (similar to the calibration setup shown in Figure 2.23, p. 122). However, direct comparison was complicated by differences in the water (unseeded), as well as strong reflections from the amber jar that depended on the positioning and angle of the fibers. The slope of the benchtop calibrations was found to compare decently well to that of the tank calibrations (0.0036 vs 0.0029 ppb/count; for flux measurements, it is only the slope of the calibration curve that matters, since the mean is removed). Given the scale of flux uncertainties, even a factor of two in the slope would not be the greatest source of uncertainty.

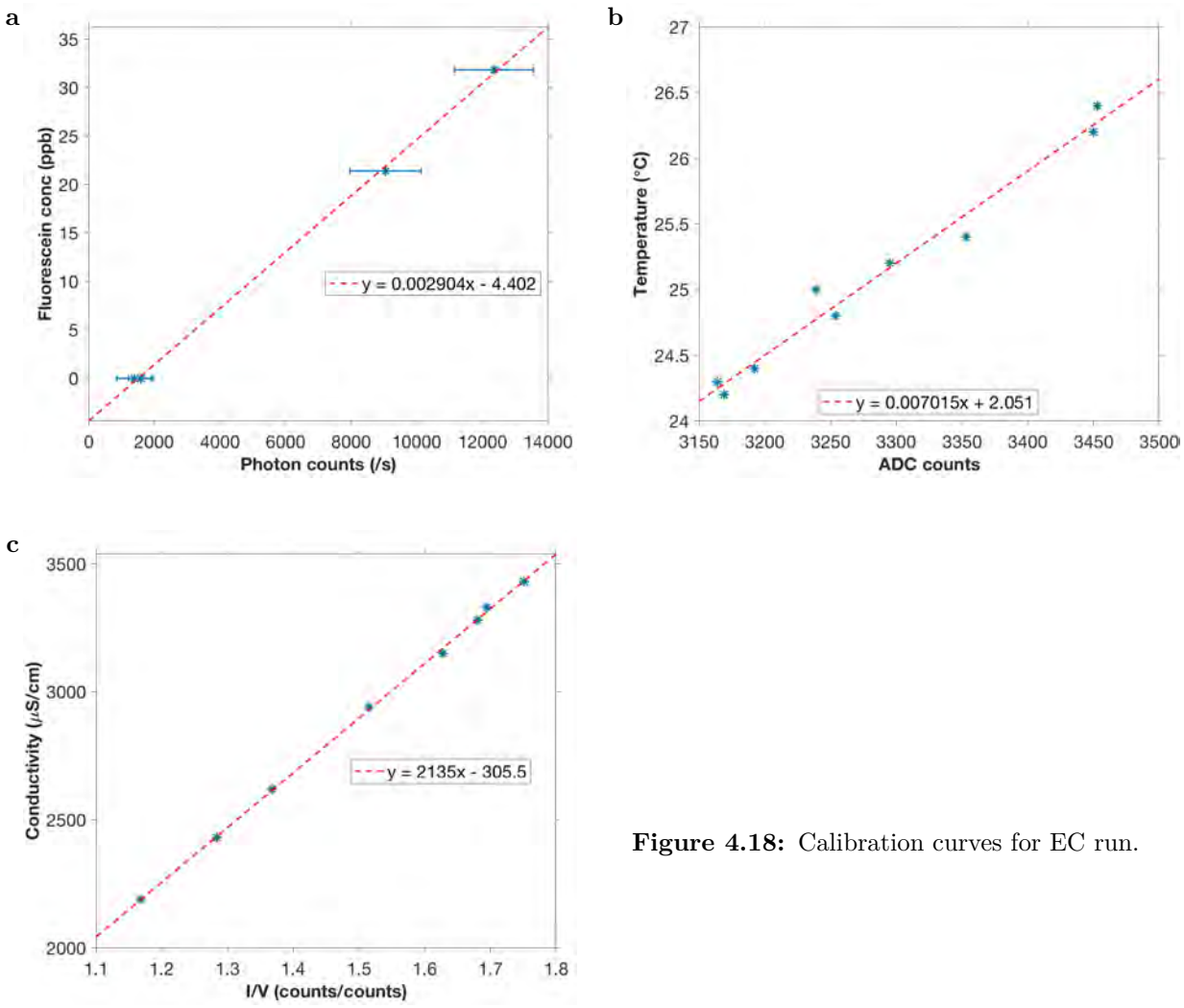

Figure 4.18: Calibration curves for EC run.

Conversion to flux units

The calibrated output of the sensor was given in ppb for fluorescein, °C for temperature, and µS/cm for conductivity. For flux, the concentration units multiply velocity (m/s), ideally to arrive at a rate of mass (or heat) per area per unit time. For fluorescein, ppb = µg/L = mg/m^3 is multiplied by m/s for velocity, to arrive at mg/(m$^2 \cdot$ s). For temperature, the flux is of heat content (kJ). Thus, the temperature in °C is multiplied by the specific heat and density of water (factor of $4.186\,\mathrm{J/(g \cdot °C)} \times 1\,\mathrm{g/mL} \times 10^6\,\mathrm{mL/m^3} \times 0.001\,\mathrm{J/kJ}$) to arrive at a 'concentration' unit of kJ/m^3. This unit is then multiplied by the velocity's m/s for flux units of kJ/(m$^2 \cdot$ s).

For conductivity, measurements had to first be converted to salinity (see Section 1.9.1, p. 86 for a description of conductivity vs. salinity). This conversion was done using a linear fit around the conductivity range of interest ($2 \sim 5$ mS/cm), based on salinity-conductivity values for 25 °C (close to the tank temperature) from a lookup table [24]. The resulting fit, made using S =1, 2, and 3 ppt, was given by the equation $y = 0.54x - 0.2$ where y is salinity in ppt = g(salt)/kg(water) and x is conductivity in mS/cm (note factor of 1000 from measurement units). The resulting salinity is multiplied by the density of water (a factor of $1\,\mathrm{kg/L} \times 1000\,\mathrm{L/m^3}$), to arrive at a concentration unit of g(salt)/m^3(water). This unit is then multiplied by the velocity's m/s for flux units of g/(m$^2 \cdot$ s).

The flux units were then scaled to units of concentration/m^2/d, a factor of 3600×24 (seconds to days), due to the small numbers that would be observed for flux per second.

Conversions to/from inflow rates

One of the main advantages of this laboratory system is the ability to compare measured fluxes to some independent measure, in this case the pumping rate. The pumping rate, expressed in volume per time (mL/min converted to m^3/d) can be converted to units of flux (based on the pumping rate, concentration of the dye, and release area), to arrive at an expected flux rate for each measurand. Alternatively, the measured flux rates can be converted to inflow units.

In both cases, an estimate of the flux area is required—EC measures the flux rate per unit area, so the volume pumped in, spread over some release area, should be divided by area to arrive at an expected inflow rate in m/d. However, the flux area was not immediately clear. Dye rose from the plate's area, but because the plate did not cover the entire floor of the tank, some also diffused sideways rather than upwards. In addition, as mentioned in Section 4.5.1 in reference to the dye solution, some of the dye was observed to spill over the edge of the plate and spread across the floor, rather than diffuse upwards. Thus, two areas were used as the bounds of expected flux or inflow: the plate's release area, calculated to be $\sim$0.07 m^2, and the area of the entire interior tank floor, calculated to be 0.675 m^2. In practice, the expected fluxes calculated using the plate's release area were much larger than those observed, and so were omitted from the graphs. The expected fluxes plotted in Section 4.6 correspond to the tank's floor area, and represent a lower bound on expected value.

The conversions between mass (or heat) flux and inflow is similar to the calculations for submarine groundwater discharge (derived in Appendix A, Section A.5). For our calculations, we simplified by using the same density and specific heat for both the inflow and ambient solutions, as the factor to account for these differences would be negligible. Then, analogous to the

groundwater inflow calculation, the implied inflow for each measurand is given by

$$q = \frac{\text{calculated fluorescein flux}}{F_{\text{inflow}} - F_{\text{tank}}} \tag{4.1}$$

for fuorescein, where F_{inflow} and F_{tank} are the fluorescein concentrations of the dye solution and ambient tank water, respectively;

$$q = \frac{\text{calculated heat flux}}{s\rho(T_{\text{inflow}} - T_{\text{tank}})} \tag{4.2}$$

for temperature, where s is the specific heat of water, ρ is the density of water, and T_{inflow} and T_{tank} are the temperatures of the dye solution and ambient tank water, respectively; and

$$q = \frac{\text{calculated salt flux}}{\rho(S_{\text{inflow}} - S_{\text{tank}})} \tag{4.3}$$

for conductivity, where S_{inflow} and S_{tank} are the salinities (converted from conductivities; note that this is really just a scaling by the slope of the conversion equation) of the dye solution and ambient tank water, respectively.

The denominator of each calculation is thus, essentially, the input-ambient contrast in property of interest, but converted as for flux above to the proper per-volume-water unit (e.g. heat per volume of water, or grams salt per volume of water). In doing this calculation, we used for the 'bulk tank value' the mean measured value in the tank for the corresponding flux period. The value for the inflow solution was the known or measured value of the dye, except in the case of temperature, where a higher value of 15 °C was used (as a rough approximate) to account for temperature changes as the dye travels to the tank.

The conversion of known inflow rate to an expected flux for each measurand is the reverse of these calculations (know q, solve for flux). The expected flux rate can then be calculated for each time point, using as the 'bulk tank value' the mean concentration observed in the data (as calculated by the Reynolds' decomposition).

The expected inflows and flux rates were then scaled to account for mixing in the tank. The tank appeared to be well-mixed at the end, based on the time series and cospectra. Thus, of the total mass of dye entering the tank, the net amount predicted to cross the measuring height was scaled by a factor of $(d - h)/d$, where d is the water depth (46 cm) and h is the measuring height (14 cm), for a scale factor of 0.7. The scaling is intuitive if one imagines a uniform release of dye from the floor, some of which stays in the volume below h with a net increase in mean concentration, while the rest crosses the $z = h$ boundary as flux. In practice, the circulation patterns in the tank are more complicated, but the scaling factor provides a first-order estimate.

4.5.4 Processing steps for eddy correlation

The data processing steps are as follows, roughly matching those presented in Section 1.4.3 (p. 44) for EC measurements in general. All data processing was done in MATLAB.

1. **Data conditioning.** Velocity data from the ADV was screened for quality by discarding measurements with SNR ≤ 5 and correlation $\leq 70\,\%$. Fluorescence data was also removed where the UV light had been turned on for imaging, resulting in higher levels of noise in the fluorescence measurement. All removed data was replaced using linear interpolation.

   Data was averaged from 48 Hz to 16 Hz using bin averaging. The velocity data was despiked using the acceleration method of Goring and Nikora [34], using a $0.3\,\mathrm{m/s^2}$ acceleration threshold and 100 iterations. Concentration data from EDDI was calibrated to fluroescein concentration, conductivity, and temperature.

2. **Coordinate rotation.** Velocity data was rotated using fixed angle rotation based on the Vector's internal sensors. Fixed angle rotation was chosen because the experimental setting was relatively flat and contained; in addition, the flow patterns in the tank and possibility of acoustic streaming meant that a non-zero z velocity (w) may actually have existed, and forcing it to 0 could be incorrect. For the run described in this section, the fixed angle rotation used a pitch angle (α) of -0.114 ° and roll angle (β) of 2.32 °. The double rotation calculation identified a yaw (θ) angle of 176 ° and pitch (ϕ) of -66 °, while planar fit identified pitch of 10 ° and roll of -18 °, which are all unrealistic.

3. **Optional filtering.** The conductivity sensor exhibited features at a much slower time scale than the other sensors, possibly due to spatial averaging. The temperature sensor was also slower than the fluorescence, likely due to its slower time response. Thus, some analyses were conducted in which the concentration time series were low-pass-filtered with a running mean, to observe if the three signals and subsequently calculated fluxes could be made match more closely.

4. **Optional removal of excursions.** The data collected in this system almost universally exhibited large excursions in concentration, with those in conductivity especially prominent. These excursions often lasted several minutes, which is too long for turbulent eddies. Thus, for some analyses, we removed these excursions from the dataset in order to examine flux carried by smaller scale motions. The process for removing excursions was a best-attempt approach described in Appendix B, Section B.10.1. The same time points were removed for velocity and all three concentrations.

5. **Mean removal (Reynolds' decomposition).** Several mean removal techniques were tested and evaluated for their effect on the concentration measurements. The effect on the vertical velocity was not evaluated as carefully, as the complicated flow patterns in the tank made it difficult to interpret the velocity measurements. However, as the mean w was already quite small, the velocity measurements were simply handled using the same technique as for concentration.

   The concentration data had an underlying linear trend, due to the effects of the closed system (i.e. concentration would continue to increase in the tank as dye was added). Because the tank was heated, the temperature also exhibited a consistent downward trend as heat was lost to the surrounding air. Finally, the conductivity sensor exhibited thermal drift, as shown in Section 3.2.4 (p. 146), on the order of 10 min. Thus, the first mean removal technique used was a **10 min linear detrend** (i.e. a 10 min linear trend was calculated and them subtracted). This detrend was interpreted as removing the effects of the closed system, the natural temperature loss, and the conductivity sensor drift. The

calculated trend was quite smooth, indicating that it reflected only the effects of linear processes such as these.

The second mean removal technique used was the subtraction of a **30 s running mean**. The running mean isolates slower components, so *subtracting* them from the original series allows us to look only at contributions from components *faster* than 30 s. This technique was applied to data with excursions removed, since the presence of the excursions created some artifacts in the apparent fluctuations (see Appendix B, Section B.10.1).

It should also be noted that, for many of the time series graphs shown in this section, a 40 min linear detrend was applied for visualization purposes only (i.e. to allow better visualization of the fluctuations without a stretched y axis). As the goal was visualization, not accurate isolation of fluctuating components for flux calculations, the window length did not correspond to that used for flux calculations. Instead, a longer window was used to minimize the amount of processing in the dataset, as well as avoid discontinuities in plots. 40 min was considered the largest acceptable detrend window because, as can be seen from Table 4.2, expected changes in flux occurred in increments of 40 min. Thus, in terms of the effects of a closed system, the slopes might be expected to change every 40 minutes. In terms of the other effects the detrend was meant to remove, the change in slope due to radiant heat loss should be small and gradual. The third effect, the conductivity sensor drift, would not removed by the longer window (and can be seen in the data provided in Appendix C, Section C.4), but it was considered acceptable for data visualization.

6. **Flux calculation.** Fluxes were calculated by multiplying the fluctuating components of velocity and concentration, with the appropriate unit conversions as described in Section 4.5.3. Expected inflow and flux values were also calculated based on the pump rate.

7. **Spectral calculations.** Power spectra (PSDs) of the velocity and concentrations were used to visualize the frequency components in each time series. For velocity, spectra were calculated after removal of a fixed mean value (which was effectively already 0 for x and y velocities), as the 0-frequency component was found to cause sidelobes in the Discrete Fourier Transform calculation. For the concentrations, spectra were calculated on the fluctuating components around a 40 min-window linear trend. The detrend was done as a practical consideration to help in visualization, as the long linear trends discussed above caused low-frequency components to dominate (and even caused some sidelobes) in the PSDs for temperature and conductivity. The use of a 40 min window removes the effects of the closed system (as all changes in flux are in 40 min blocks) but does not remove the effects of the conductivity drift, which for the PSD would manifest as increased components at the drift frequency.

   For one set of spectra, calculations were done separately for different periods of time: 10 to 30 min (before any dye was input into the system), 40 to 160 min (during dye input), and 180 to 240 min (after dye input). Linear detrending was done on the original dataset, which was then segmented for the spectral calculation. Segmentation allowed examination of the turbulence by itself, as well as isolation of the frequency components related to the dye release. This set of spectra also included PSDs calculated from a 60 min measurement in stagnant but seeded water in the tank, for comparison to a baseline noise floor.

Table 4.3. Velocity statistics for EC run.

	Average velocity (cm/s)			**Standard deviation** (cm/s)		
	x	**y**	**z**	**x**	**y**	**z**
EC run pre-dye	−0.21	0.04	−0.08	0.49	0.43	0.21
EC run during dye input	-0.10	0.004	-0.16	0.48	0.42	0.20
EC run post-dye	-0.01	-0.06	-0.18	0.44	0.46	0.20
stagnant water	-0.003	-0.02	-0.14	0.35	0.28	0.10

A second set of spectra was calculated on the full EC run. Spectra were calculated for z velocity and the three concentrations and normalized by the total variance of the original time series (after a 40 min linear detrend), so that they could all be displayed on the same graph. Appendix B, Section B.10.1 and Appendix C, Section C.4 also show other spectra that were calculated with slightly different data processing, described therein.

Spectra were calculated using the pwelch function in MATLAB, which uses Welch's modified periodogram technique for estimating spectral components. A window size of 8192 datapoints was used, with 50 % overlap; longer datasets would result in the averaging of more windows. The spectra were evaluated at a number of frequency points equal to the window size, and in this case the frequencies of evaluation were specified as an even distribution in log scale in the range of 0.001 Hz (corresponding to ∼16.7 min) to 8 Hz (the Nyquist frequency for the 16 Hz data). The spectra could be multiplied by frequency to arrive at the variance preserving spectra, as discussed in Section 1.4.3 (p. 44).

Cospectra between vertical velocity and concentration were also calculated on the fluctuations identified by the Reynolds' decomposition. This calculation used the cpsd function in MATLAB. The cospectra were summed in reverse, using the cumtrapz function, to arrive at cumulative cospectra (ogive plots). Cospectra were calculated separately for each 40 min segment of the data. They could be calculated on shorter segments as well, to identify spectral contributions to flux in more granular time windows. In our data, these generally produced messier cospectra that did not always converge, possibly due to the presence of phenomena of a time scale larger than the flux window, or lack of stationarity due to too few events (discussed in Section 4.6).

4.6 EC experiments in a laboratory tank: Results and discussion

4.6.1 Velocity measurements and the turbulence regime

Mean velocities and standard deviations (representing turbulence), measured by the ADV, are given in Table 4.3. Power spectra are given in Figure 4.20. x is the longitudinal axis of the tank.

As can be seen, the turbulence in the tank was overall quite low, at least at the measuring

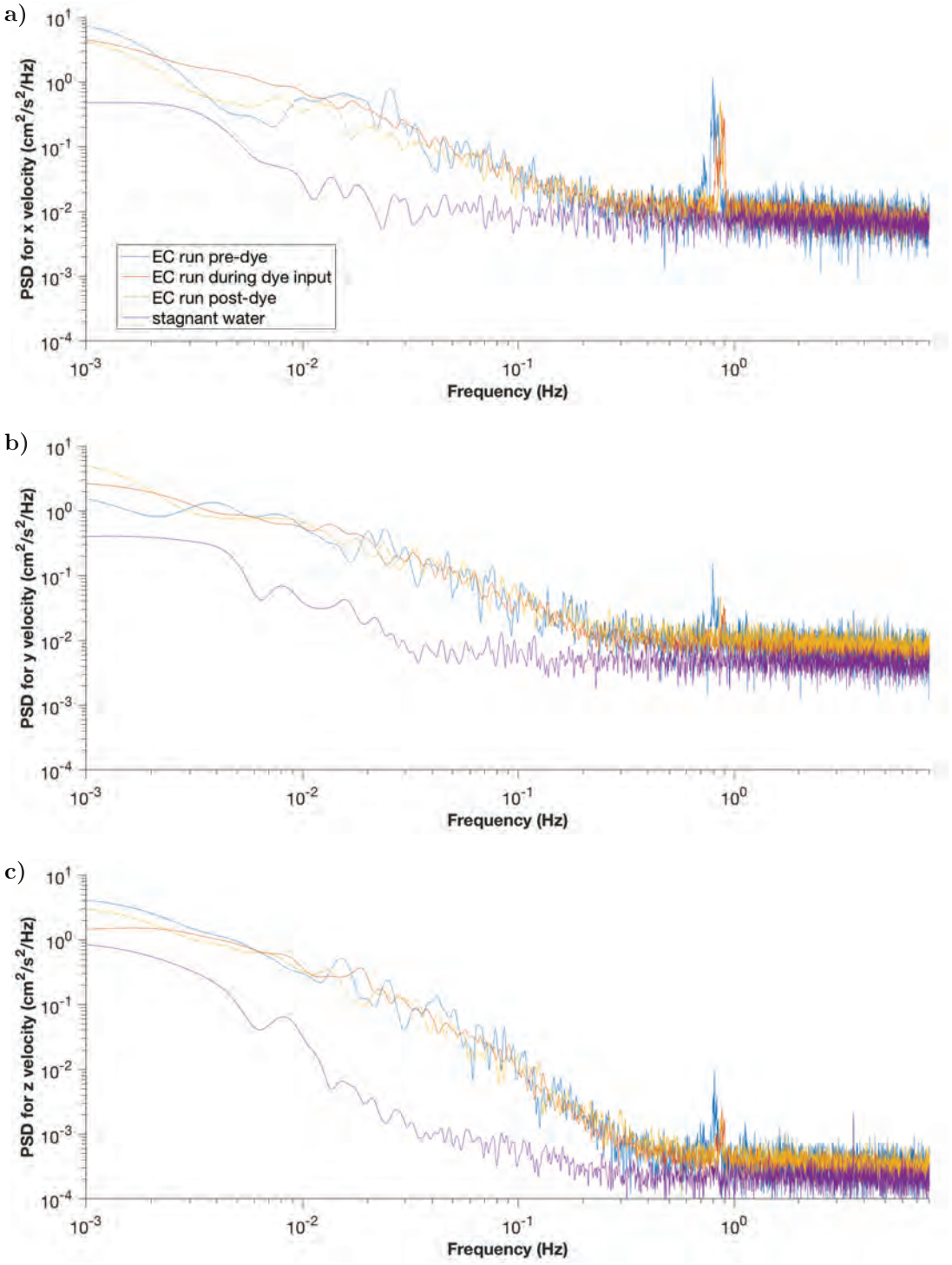

Figure 4.20: Power spectra of **a)** x velocity (u), **b)** y velocity (v), and **c)** z velocity (w)

point. In fact, the net negative z velocity, although small, was similar for both the turbulent and stagnant cases; it could be due to acoustic streaming, which is only prominent in quiescent situations. Compared to the reference values given in Table 1.1 (p. 39) for estimates of sensor requirements, the turbulence observed here is similar to the 'low turbulence' situation. Thus, this system would be less demanding on the sensors (speed and sensitivity) than for the same flux in a 'high turbulence' situation.

The frequency of the plungers, which was slightly less than 1 Hz (but changing, as described in Appendix B, Section B.8.1), can be seen as a strong signal in the PSDs. However, interestingly, most of the 'turbulence' observed was at lower frequencies, while values above ∼1 Hz were not significantly different than the noise floor[9]. It appears that, although the plungers oscillated at ∼1 Hz, they were not in fact directly creating turbulence, but instead set up secondary circulations or motions that were then causing the turbulence. The plunger frequency signal seen in the PSDs could, in fact, be due partly to vibrations of the ADV stem, and thus not represent movement of water at that frequency.

4.6.2 Trimodal 'concentration' measurements with EDDI

Time series measured by EDDI are shown in Figure 4.21, alongside z velocity for completeness. Lines mark the different segments of the program, as detailed in Table 4.2. Segmented time series, zoomed to show features, are given in Appendix C, Section C.4.

Overall, the three time series picked up similar features, with positive spikes in fluorescence corresponding to negative excursions in temperature and conductivity (the dye was positively fluorescent but depressed in temperature and conductivity relative to the tank). The performance of the sensors was consistent with previous observations from the trimodal flume experiments, described in Section 3.4.3 (p. 157). The extremely fast fluorescence detected features that were much sharper than those detected by the other two sensors[10]. In contrast, the conductivity signal was characterized by large, prominent events, which could possibly be explained by its larger and more dispersed measuring volume (discussed in Section 3.4.4, p. 166 with reference as well to hydrodynamic trapping).

The conductivity tracked quite well with the temperature signals, which were also on the slower side. In the case of the temperature, the 'bluntness' of features was likely due not to spatial averaging, but to temporal; the thermistor's response time is known to be the slowest, as was observed in the flume experiments. However, it is actually not outrageously slow ($t_{90} < 1$ s), and some of the 'bluntness' in its time series can likely also be attributed to another problem: lack of resolution.

Figure 4.22 shows the temperature time series plotted in its original 48 Hz. A substantial amount of discretization can be seen in the measurements, with the features corresponding to variations of only a few LSB. As given by the slope of its calibration curve, one LSB corresponds

[9] Reimers et al. [30] also identified the frequency range of $f \geq 1$ Hz as noise; studying EC in a wave flume, they identified turbulence as $0.35\,\text{Hz} \leq f \leq 1\,\text{Hz}$, while lower frequencies were attributed to waves or seiching within the flume.

[10] In many of the graphs presented in this section, the fluroescein time series seem to have sharp 'spikes' that are difficult to see because of the x axis resolution. These spikes do in fact correspond to true features and not single-datapoint spikes. These features can be seen when further zoomed in x, as in Figure C.23 in Appendix C.

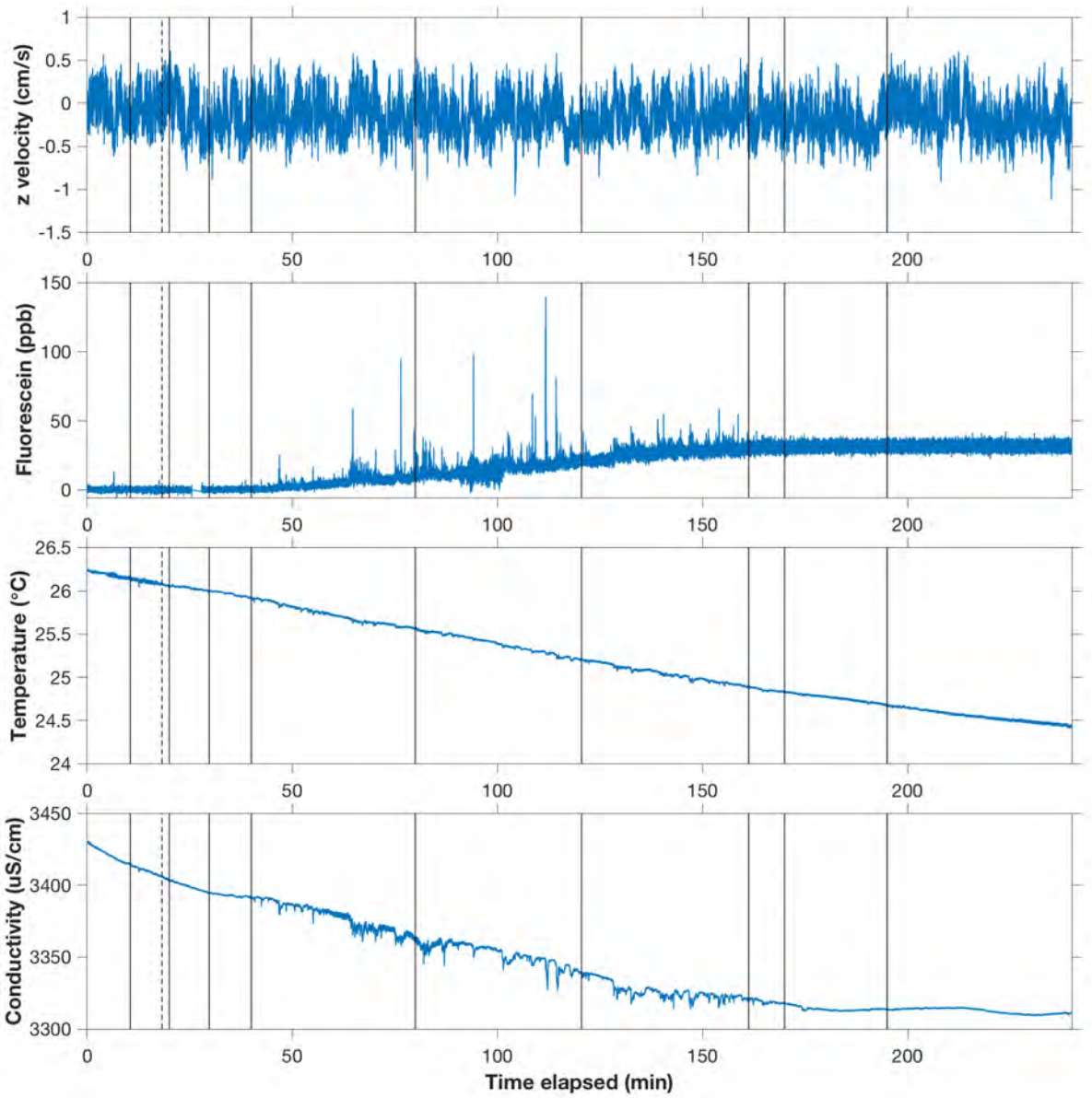

Figure 4.21: Full time series for EDDI and w measurements taken during EC run in test tank.

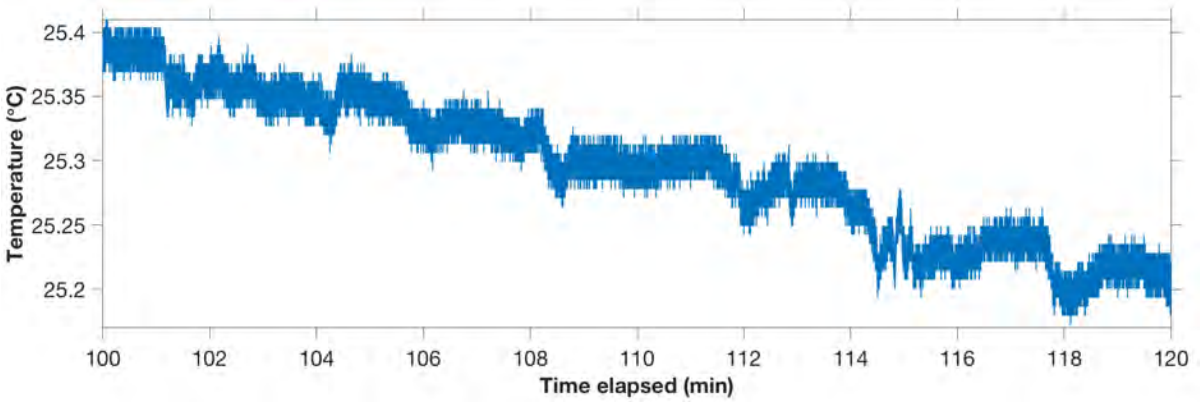

Figure 4.22: Original 48 Hz time series of temperature measurements, showing a substantial degree of discretization.

to 0.007 °C. Lack of resolution is a site-dependent problem, since the 'required' resolution of the sensor depends on the size of the features, which in turn depend on the turbulence and flux. The sensitivity demands on the sensor when used in a natural setting may not be the same as those here. However, based on the sensor requirements given in Table 1.1 (p. 39), a greater degree of resolution than 0.007 °C/LSB may be required, especially since 1 LSB is hardly enough to pick up a fluctuation.

The resolution of the temperature sensor can actually be improved relatively easily by adjusting its valid range. The centerpoint of the range of valid temperatures can be adjusted with the potentiometer (see Section 3.1.3, p. 131 on the temperature's circuitry) and the gain of the amplifier can be increased, which would reduce the valid range but increase the resolution within that range. In the future, we are likely to switch to the faster FP07 thermistor which has a different $R - T$ curve and would require some recalculation of resistor and gain values. This switch would be an opportune time to increase the resolution of the thermistor.

Next, to explore the extent to which differences in the three time series can be explained by spatial and temporal averaging (as opposed to other phenomenon like sensor malfunction), we applied a low pass filter to the fluorescence and temperature time series and compared the results. The filter used for this purpose was a 10 s running mean for fluorescence and a 1 s running mean for temperature; for the latter, it also served to smooth over the discretization, which was less pronounced but still apparent at 16 Hz.

Results for a single section, corresponding to the higher rate of dye release (57 mL/min), are shown in Figures 4.23 and 4.24, respectively. With the filter applied, the time series were found to match quite well, indicating that the sensors were likely detecting the same features but with differing amounts of spatiotemporal averaging. Note that averaging the time series here corresponds to both spatial and temporal averaging, due to movement of and within the eddies. A small sensing volume averaging over many different points of an eddy as it drifts by is similar to a single, fast measurement by a large sensing volume that is simultaneously sampling the whole eddy at once.

The filters required to achieve good qualitative agreement for these data are much slower than those used in in the flume experiments. The filters used in the flume experiments, e.g. a

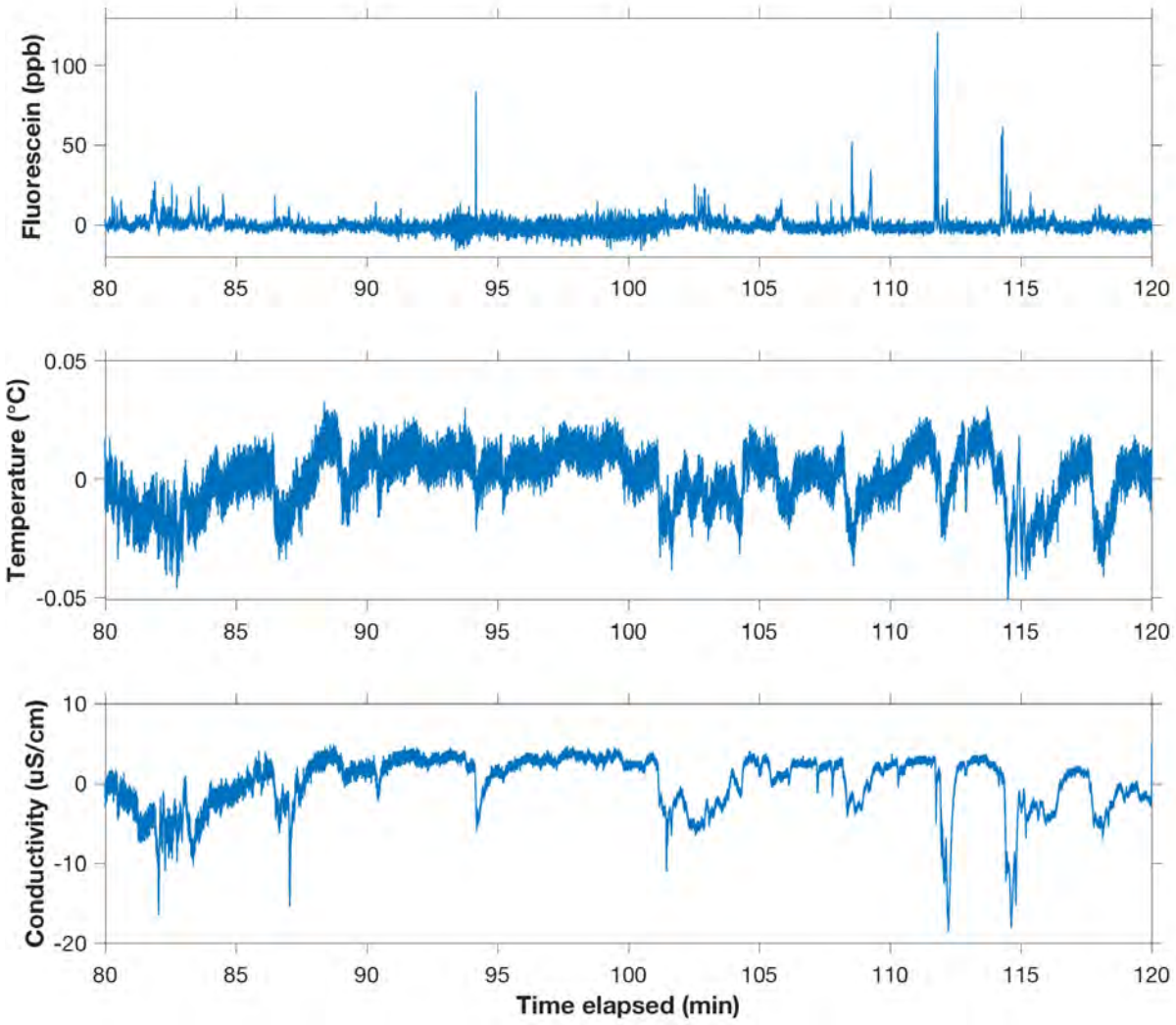

Figure 4.23: Zoom in on section of time series corresponding to 57 mL/min dye release, with linear trend removed. The features measured by the three sensors roughly match, although fluorescence features are much sharper. The burst of noise around $t = [93, 101]$min is likely due to somebody turning on lights in the room.

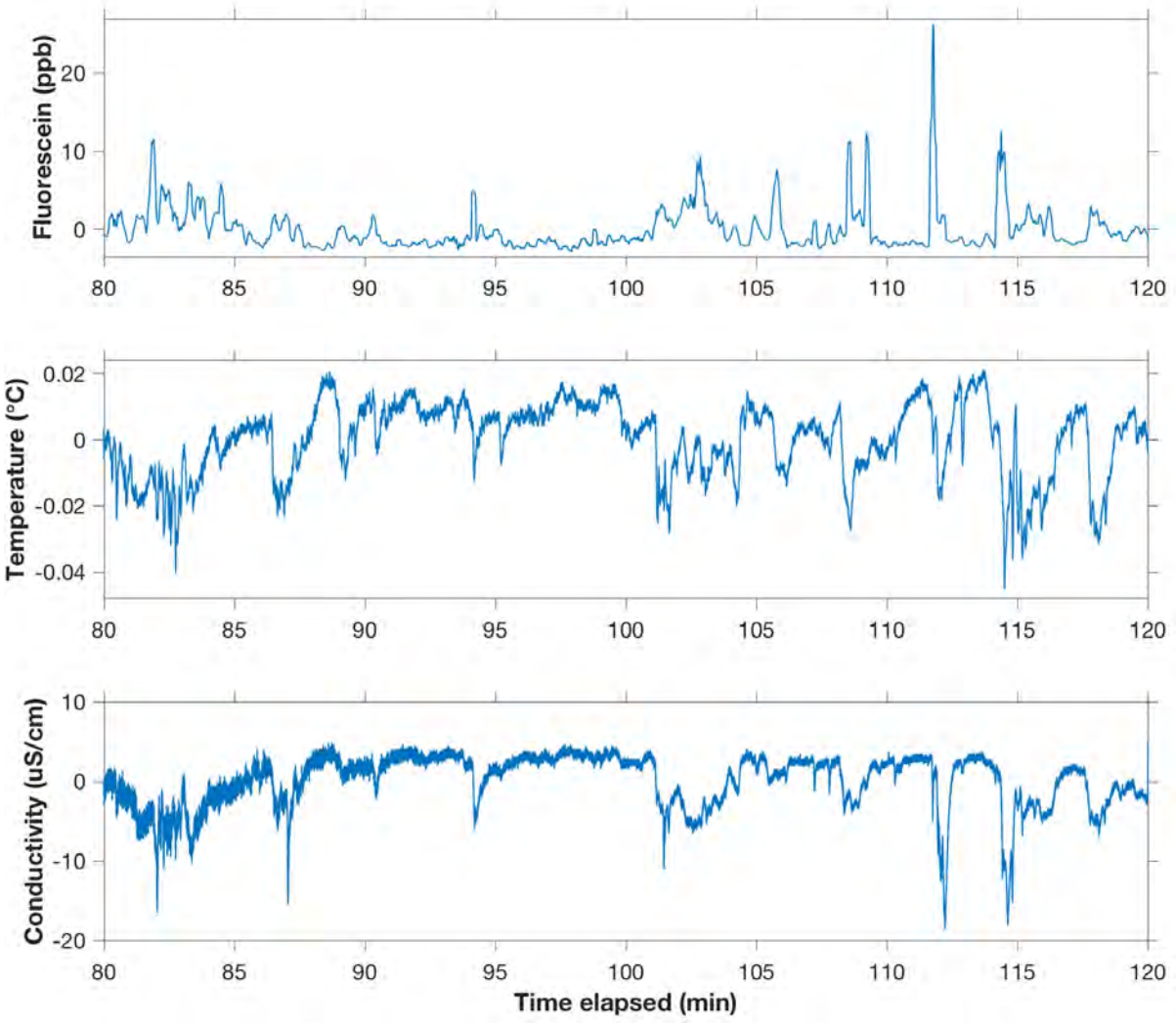

Figure 4.24: Same time series as Figure 4.23, but with a 10 s running mean filter applied to fluorescence, and a 1 s running mean applied to temperature. The good agreement between the three time series implies that the sensors are detecting the same features but with differing amounts of spatiotemporal averaging.

0.2 s running mean for fluorescence, produced nearly no difference in the time series in the present case. It appears that, under the low turbulence of the tank, the spatial averaging of the conductivity played a more prominent role, causing it to be the slowest. However, the results from the previous flume experiments showed that the conductivity is *not*, in general, 10× slower than the fluorescence sensor. It is likely instead that this particular setting (see Section 4.6.5) interacted with the conductivity's more dispersed sensing volume to produce the large features.

4.6.3 Calculated fluxes

Fluxes calculated in 5 min windows are shown separately for each EDDI sensor in Figure 4.25. The implied inflows for the sensors are given in Figure 4.26. The absolute values of the fluxes are reasonable, and of similar order of magnitude to the lower bound of expected values based on the pumping rates. Notably, however, all three sensors can be seen to underpredict flux in the $t = [40, 60]$min and $t = [80, 100]$min time periods. These time periods both correspond to the first 20 min after an increase in the pumping rate (from 0 to 35 mL/min at $t = 40$ min, and from 35 mL/min to 57 mL/min at $t = 80$ min). This discrepancy, along with a more general comparison to the pumping rate, will be returned to in the conclusion (Section 4.7).

A 5 min window is actually too short to provide a representative value of flux (see Section 4.6.4 and Figure 4.34), but it was used here to highlight the tendency of the fluxes to track each other. Indeed, it can be seen the fluxes calculated by all three sensors are similar in both pattern and magnitude, even when they differ from the values expected based on the pumping rate (e.g. the underpredictions immediately after increasing the pumping rate at $t = 80$ min). Nevertheless, some differences between the three sensors are still present. Some of these discrepancies likely arise from differences in spatiotemporal averaging; in support of this idea, fluxes are generally lower for the conductivity, which was observed in the time series to have the most averaging.

To further test whether differences in averaging could be responsible for discrepancies in calculated fluxes, we repeated the flux calculation process using filtered time series. Unlike the filter applied to Figure 4.24 to show qualitative matching of the time series, we here applied the same running mean filter to all three sensors. To the extent that the differences between the calculated fluxes were indeed due to higher frequency components, then such a filter should still bring the fluxes to closer convergence, since it should not affect the slower sensors that were unable to detect them.

The results are shown in Figure 4.27. It is apparent that the filters almost universally bring the flux down, as they should (if filtered enough, flux should be 0!), but effects are not very noticeable for windows smaller than 20 s. So the filters applied for Figure 4.24, despite achieving 'qualitative' similarity between the time series, were actually not enough to substantially affect flux. However, all three sensors were affected by filters >20 s. The fluorescence, which originally had the largest fluxes and is also the fastest sensor, was affected the most. This implies that some of the flux difference was from its higher spatiotemporal resolution. From comparing the fluorescence and conductivity results in Figure 4.27c, we can see that filtering the fluorescence time series does appear to bring the calculated inflows closer to the 1 : 1 line.

However, a 1 min running mean is quite a large filter, and the loss in flux could also be due to

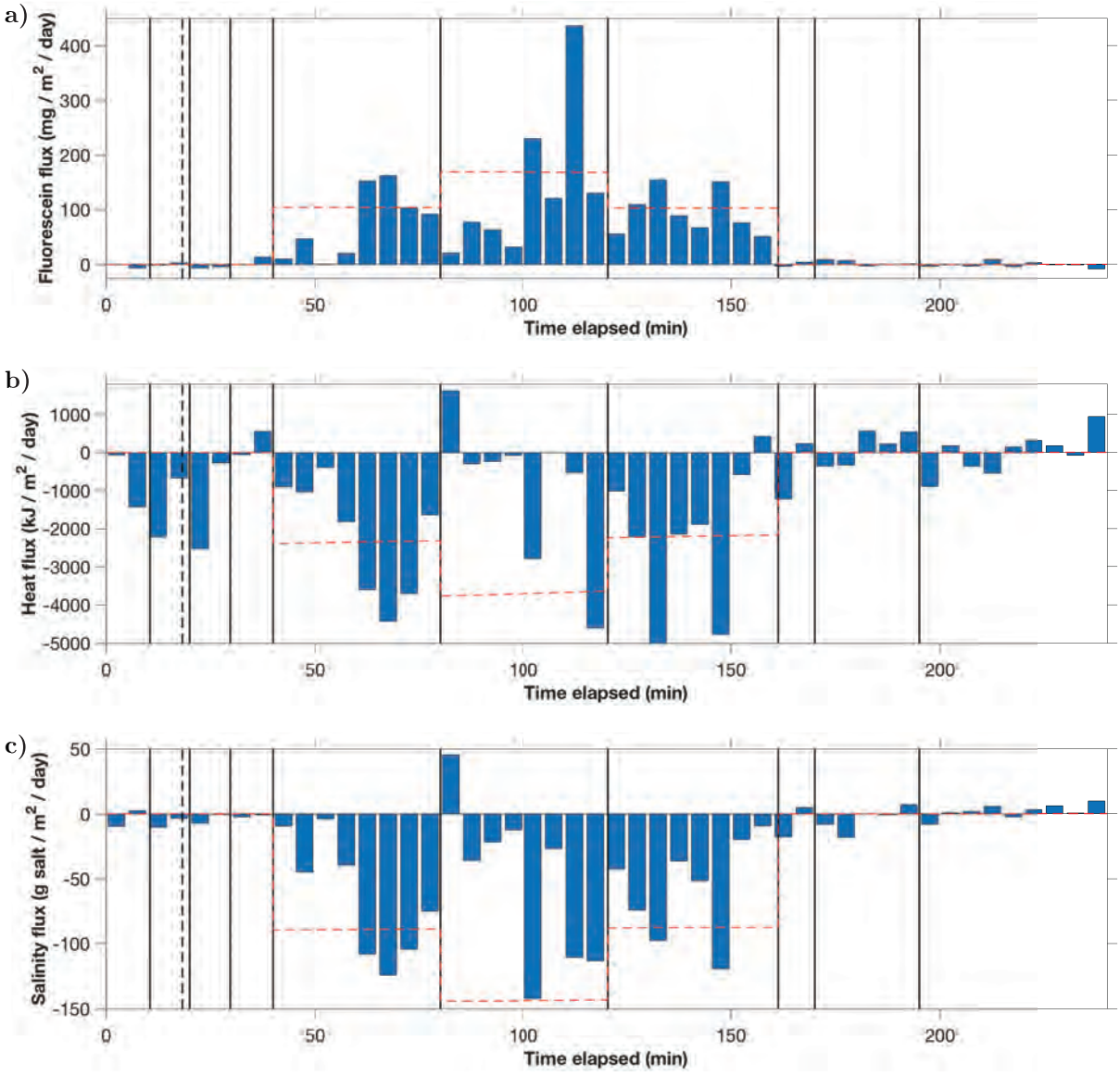

Figure 4.25: Calculated fluxes for **a)** fluorescein, **b)** heat, and **c)** salt. Dashed red line shows lower bound of expected value based on pumping rate.

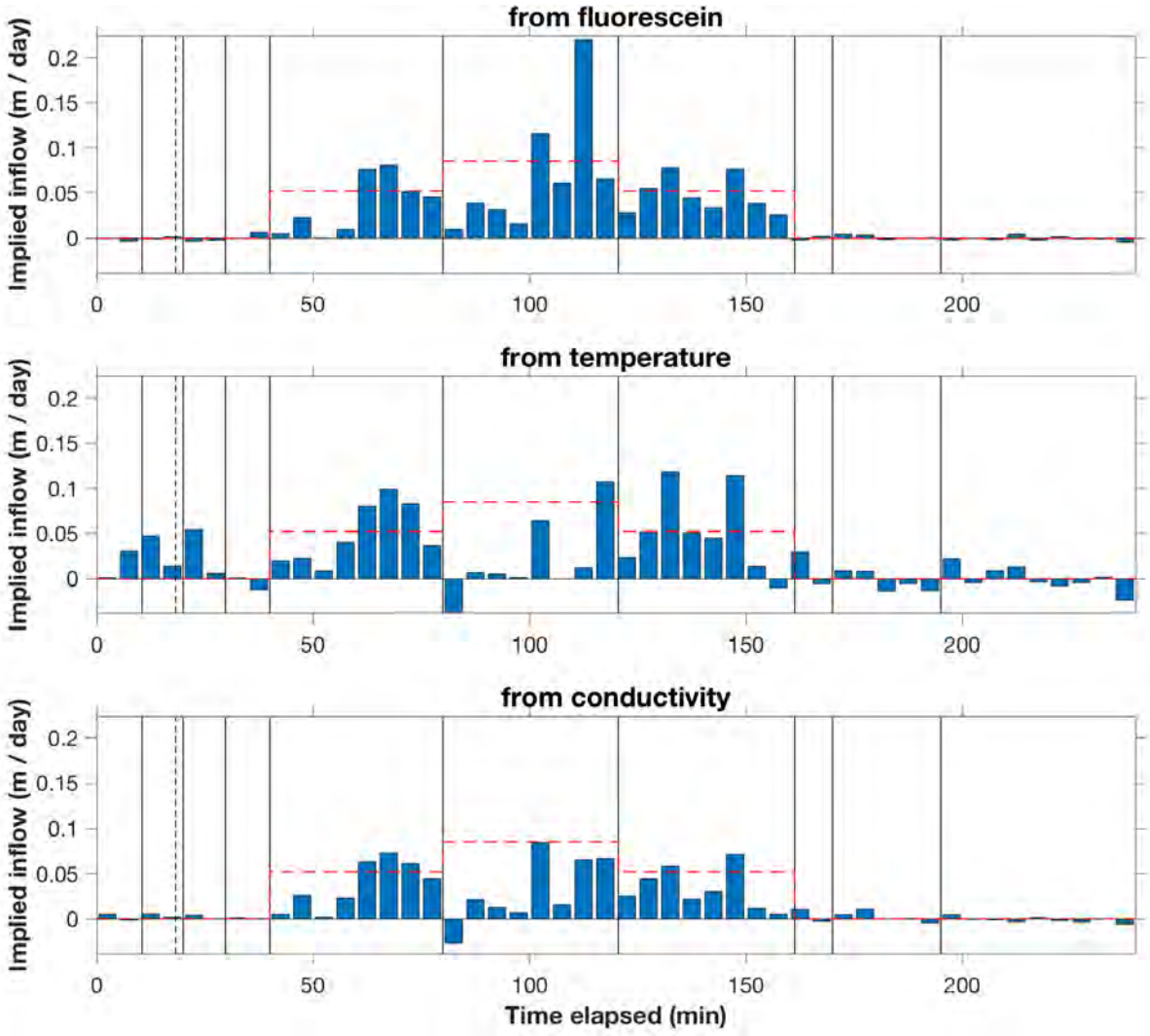

Figure 4.26: Implied inflows calculated from EC measurements with each of EDDI's sensors. Dashed red line shows lower bound of expected value based on pumping rate.

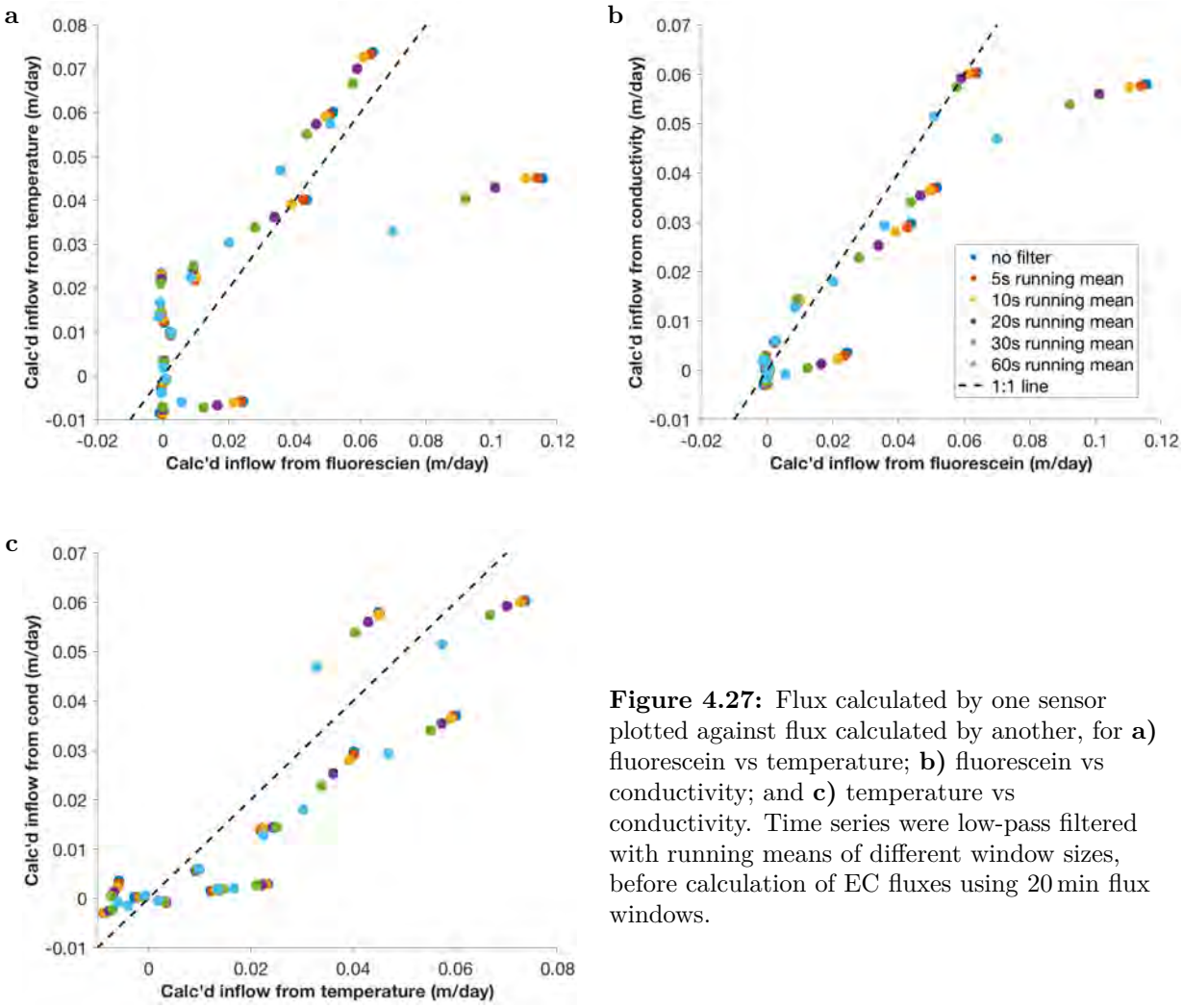

Figure 4.27: Flux calculated by one sensor plotted against flux calculated by another, for **a)** fluorescein vs temperature; **b)** fluorescein vs conductivity; and **c)** temperature vs conductivity. Time series were low-pass filtered with running means of different window sizes, before calculation of EC fluxes using 20 min flux windows.

distortion of the time series. With such a large window, it is not guaranteed that the patterns observed in Figure 4.27 were due only to removal of high-frequency components. Thus, we sought to better understand the differences in flux by examining the w' and c' series on the same graph.

An example is shown in Figure 4.28, and more are given in Appendix C, Section C.4. For these examples, the fluorescence times series was filtered with a 1 min running mean for visualization purposes (otherwise the spikes are very sharp and high and make it impossible to see other features); as discussed above, this has little effect on the flux calculations. For better visualization, the axes for the temperature and conductivity fluctuations are also flipped, so that an upward fluctuation coinciding with a positive velocity fluctuation indicates upward dye movement. Note also that these series were detrended using a 10 min linear trend, and so discontinuities in the time series at 10 min intervals could be due to this process.

Figure 4.28 shows the time period from $t = [80, 120]$min, which corresponds to some of the largest discrepancies between the three calculated fluxes, as well as to the expected release rate. From Figures 4.28b and 4.28c, it can be seen that the negative flux observed for temperature and conductivity in the $t = [80, 85]$min range was due to a negative excursion of w' that coincided with a positive burst of dye. The event was actually also detected by the fluorescence sensor, but apparently to a lesser extent and/or more finely, with values returning to 0 in between fast fluctuations. It thus appears that there was indeed a real 'downward flux' event, but it was detected slightly differently by the three sensors, with resulting differences in calculated flux. In this case, then, the discrepancies in flux can be largely attributed to differences in response time as well as sensing volume size and location. However, this case also highlights how one event can bias the entire result, especially for short flux windows. In effect, the record is not stationary over this period; more events are needed for a statistical representation.

In another example, the extremely high positive flux in fluorescence in the $t = [105, 110]$min range can be seen to arise from two large events picked up by the fluorescence sensor that perfectly coincide with increases in w'. The conductivity and temperature appeared to pick up these events as well, but in slightly different form; for example, for the event at $t = 112$ min, both sampled a small spike corresponding to the rise in w', but did not sample a large excursion until ~30 s later. Thus, it is likely that the different sensing volume *locations* of the sensors caused them to sample different parts of the same 'eddy' and/or the same 'eddy' at different times. In this case, it was sensing volume offset, and not spatiotemporal averaging, that caused the sensors to underpredict. The averaging in the filter analysis of Figure 4.27 brought the fluorescence-predicted flux closer to the other two not because it compensated for spatiotemporal averaging, but because it is blanket reduced flux by melting away features that the other two failed to even detect.

When it comes to sensing volume location, the fluorescence sensor's sensing volume is closer to the ADV's than the temperature or conductivity, since it is slightly displaced from the optical fiber tips (as described in Section 3.4.2, p. 154, where the sensing volumes are overlaid; recall also that the fiber tips are 6 mm away from the ADV's sensing volume). The fluorescence sensor is therefore most likely to be 'accurate' when discrepancies arise from sensing volume location. However, the offsets between the three sensing volumes are actually not so large, $\mathcal{O}$(mm). In a system with unidirectional flow, given proper sensor orientation the eddies would tend to be carried past all three sensing volumes, so that the effect of the offset on flux would be small or at

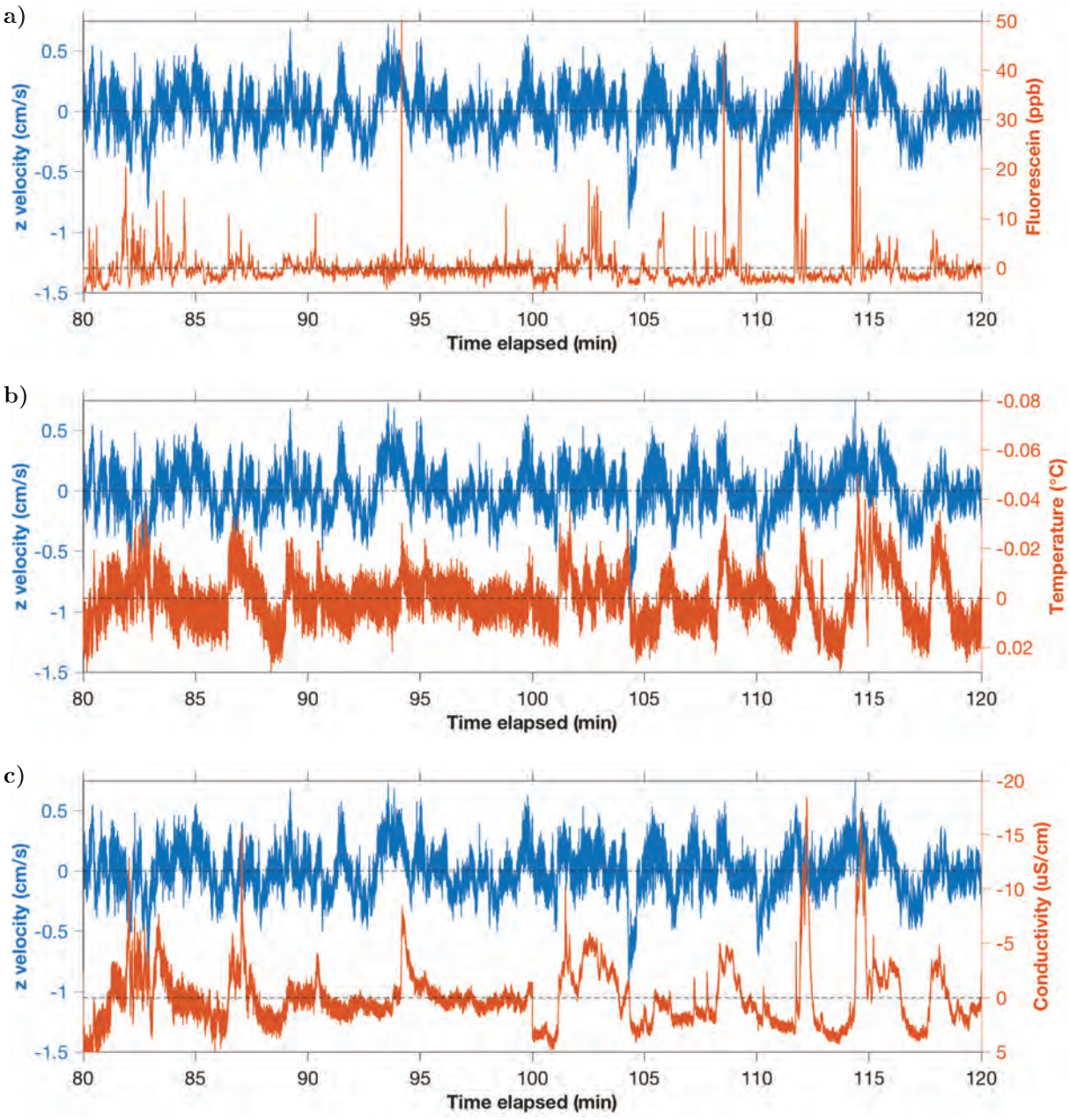

Figure 4.28: Time series of fluctuations in **a)** fluorescein, **b)** temperature, and **c)** conductivity, overlaid with concurrently measured w fluctuations, for one segment of the EC run. Axes are flipped for temperature and conductivity. Close analysis of the time series reveals sources of discrepancy for individual flux points.

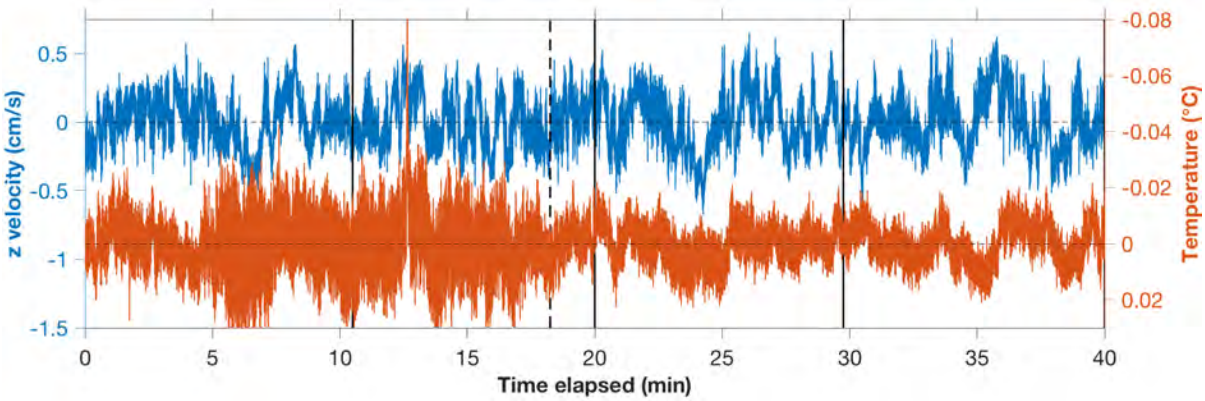

Figure 4.29: Time series of temperature fluctuations (axis reversed) overlaid with concurrently measured w fluctuations for the beginning of the run, where negative heat flux was observed despite the lack of dye input.

least could be compensated with a time shift[11]. The effect of the offset is therefore exacerbated in this setting by the nature of the flow regime.

The temperature fluxes also merit some discussion. The temperature sensor observed a negative flux of heat (which would correspond to a positive dye flux) in the $t = [5, 30]$min range, when there was no dye input at all. It is possible that this was due in some degree to radiant, convective, or conductive loss of heat to the surrounding environment, as the tank was heated above room temperature. Indeed, the temperature time series (shown in Figure 4.21) was observed to continue to trend downward even in periods of no dye input, whereas the other two sensors did not, indicating an alternative source of heat loss. The beginning of the run was when the tank was at its warmest, and thus would experience the highest losses. However, a similar effect but to a lesser extent would still be expected at the end of the run, and no significant net fluxes were observed.

Time series analysis, similar to those shown in Figure 4.28 above, reveal that there was indeed some covariance in temperature and vertical velocity (Figure 4.29). Despite the burst of noise at $t = [5, 20]$min and the temperature sensor's resolution issues, the negative heat flux does appear to be real. Possibly there was some thermal stratification that developed in the tank but was stirred up by the plungers, which were turned on $10 \sim 15$ min before the EC run. The ambient tank solution in the beaker also could have cooled to room temperature before entering the tank.

In general, simulating a temperature flux is quite difficult, and so the temperature fluxes were expected to have some degree of noise. As discussed in the 'Dye solution' subsection of Section 4.5.1, it is likely that the dye had already picked up some heat on its way into the tank. Then, once inside, it was surrounded by water of a different temperature; under such slow turbulence, the process of thermal diffusion could be comparable to turbulent diffusion. If any

[11] The time shift required here to align the large feature seen by T and C with the velocity event is 30 s. Such a time shift was indeed found to produce a large flux in conductivity and temperature for this time period, but 30 s is much larger a time shift than those typically implemented in EC runs (e.g. 'up to 4 s' [25]). However, the typical time shifts are calculated based on current flow, whereas this system has no directional flow and only slowly drifting eddies. In general it does not make sense to apply time shifts to this data, where the 'most appropriate' time shift is inconsistent in both direction and magnitude.

of the heat flux was due to thermal diffusion, it would not have been picked up by EC. Such concerns would not be relevant in a natural setting, where the bottom temperature is likely depressed and the turbulence is faster.

4.6.4 Spectral analyses

Variance-preserving spectra for all three concentrations and z velocity are given in Figures 4.30 and 4.31, reflecting the distribution of power by frequency; power spectra in log form are given in Figure C.29 in Appendix C (Section C.4). Note that the $\sim$0.0012 Hz ($\sim$14 min) humps for pre-dye and post-dye signals in Figure 4.30c for conductivity likely reflect thermal and/or analog drift, which was removed for flux calculation but not for spectral calculations. The temperature PSD also has a strong peak at 4 Hz, likely due to electromagnetic interference from the building's 60 Hz power lines (the greatest common denominator of 60 and 16, the measurement frequency, is 4; i.e. signals with period 16.67 ms and 62.5 ms are only periodic together in blocks of 250 ms). This interference was previously observed in temperature measurements and confirmed to be 60 Hz when measured with higher frequencies, and was already greatly reduced by using braided copper shielding as described in Section 4.5.1 (p. 192).

As discussed in Section 4.6.1, the turbulence regime was quite low frequency ($<$0.3 Hz, corresponding to $>$3 s), which can be seen in Figure 4.31. The z velocity frequency distribution was also relatively insensitive to dye input. On the other hand, the spectra for the concentrations reveal lower-frequency contributions that were only present during dye input. The fluorescence sensor experienced contributions as fast as $\sim$1.5 Hz (0.7 s), but the contributions were slower for the other two sensors.

Figure 4.32 shows spectra for the full EC run (i.e. combining pre-dye, dye input, and post-dye sections) before and after removal of excursions. As described in Section 4.5.4, the 'excursions' refer to large deviations from baseline observed in the concentration time series[12]. Spectra for the three concentrations and z velocity are shown together, normalized by the total variance for each under the original time series.

It can be seen that fluorescence features in the $0.001 \sim 1.5$ Hz range, which from Figure 4.30a appear to arise only during dye input, are largely associated with the excursions. On the other hand, for temperature and conductivity, the spectral components associated with the excursions are at lower frequency. These results are in line with the observations made in Section 4.6.2 that the large features are sharper for fluorescence than for conductivity or temperature, possibly due to differences in spatiotemporal averaging.

However, even with excursions removed, spectral components still remain for velocity and all concentrations across a large frequency range. Some of these components are due to drift (e.g. the $\sim$0.0012 Hz hump in temperature and conductivity), while others likely reflect actual features observed by the sensors in the time periods between the excursions. Higher frequency components in particular would be expected to be largely unaffected by removal of the excursions, which were relatively slow and large. This can indeed be observed in Figure 4.32, although it should be noted that the spectral components observed at higher frequencies ($>$1 Hz or so) likely include some element of noise as well as true contributions from faster eddies.

[12]The excursions are shown in time domain in Appendix B, Section B.10.1, along with additional spectra. Flux results after their removal are given in Section 4.6.6.

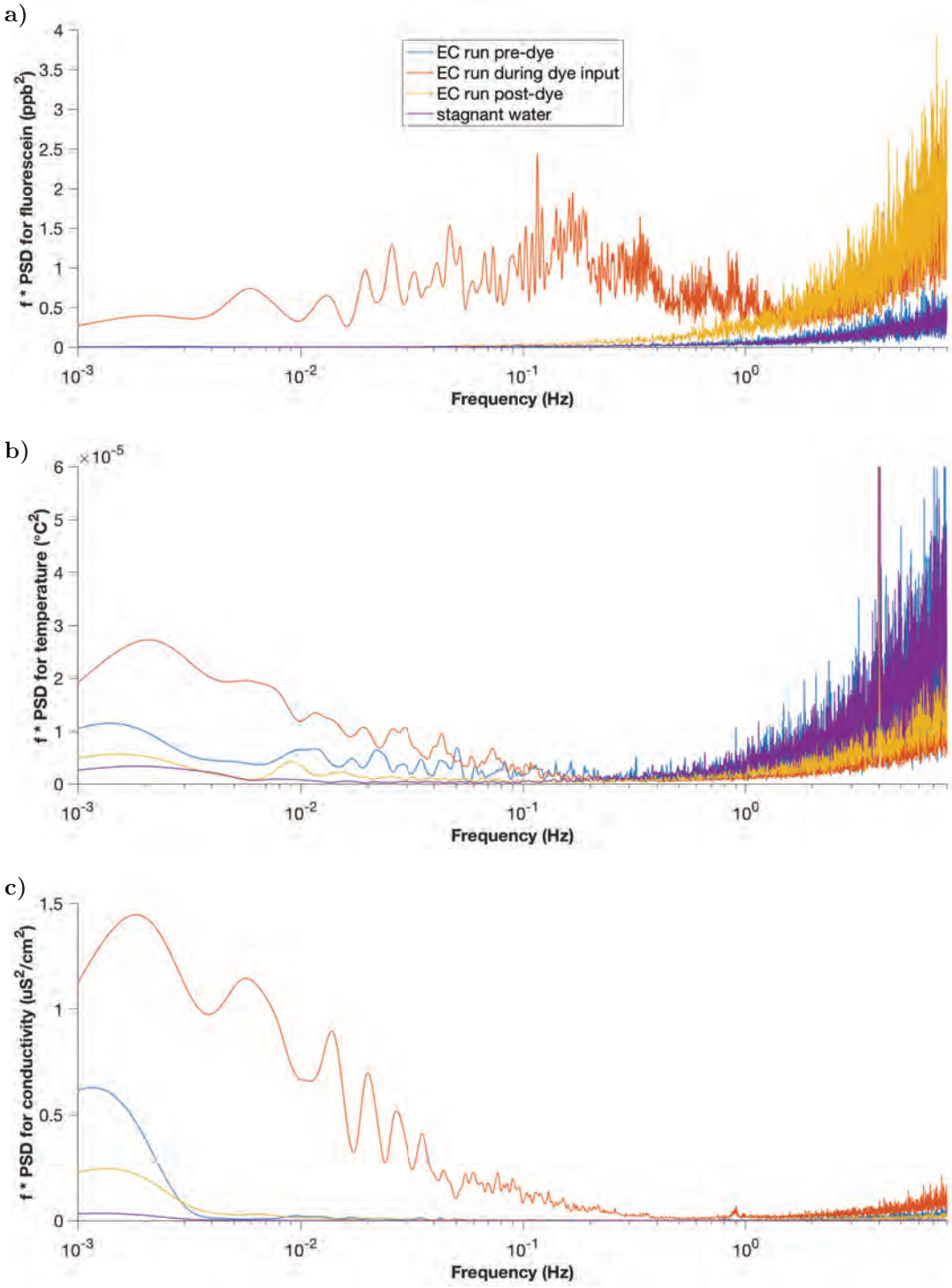

Figure 4.30: Variance-preserving spectra of **a)** fluorescein, **b)** temperature, and **c)** conductivity

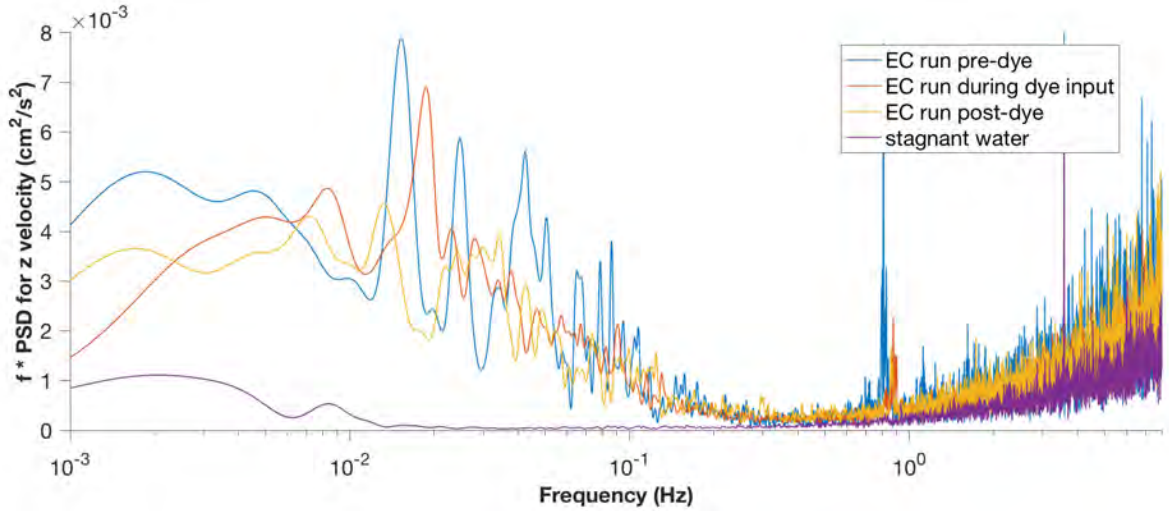

Figure 4.31: Variance-preserving spectra of z velocity (w).

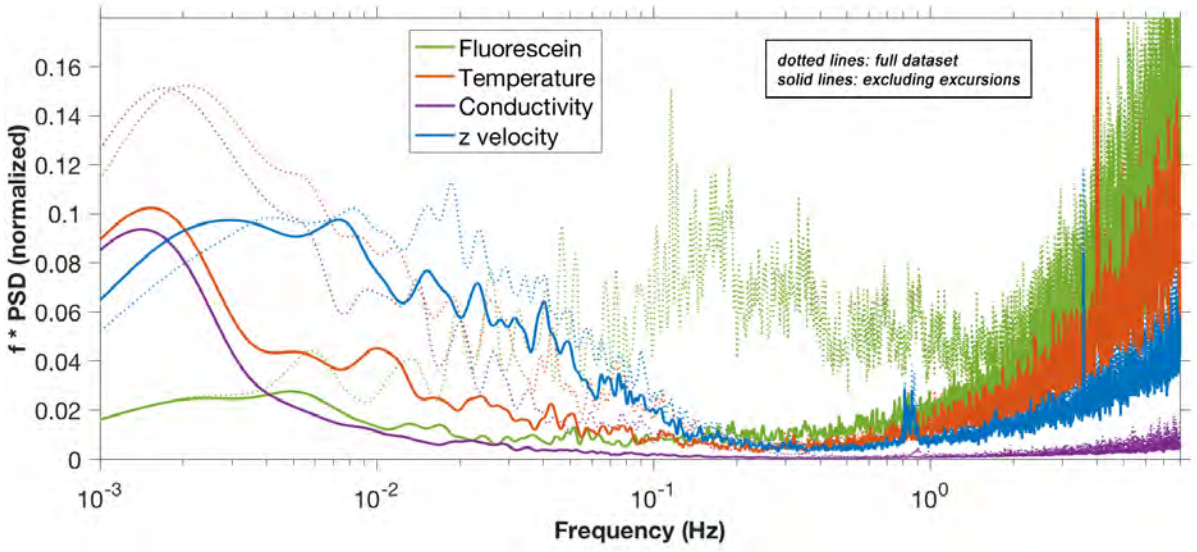

Figure 4.32: Normalized variance-preserving spectra for full EC run, before (dotted lines) and after (solid lines) removal of excursions. Spectra were normalized by the total variance of the original time series after a 40 min linear detrend (i.e. for each measurand, solid and dotted lines were both normalized by the total variance corresponding to the dotted line).

The fluorescence and conductivity sensors also appear to have some contribution at the plunger frequency (slightly less than 1 Hz), which is only noticeably present for dye input and thus unlikely to be caused by vibrations (it would not have been outrageous had the conductivity sensor been sensitive to field effects). Finally, based on comparisons of the spectra before, during, and after dye input, it appears that the system was well-mixed at the end of the run, rather than continuing to mix due to gradients set up during dye input.

Cumulative cospectra (of fluctuations in velocity and concentration) are shown in Figure 4.33. As can be seen, contributions faster than 0.1 Hz (10 s) are negligible. The spectra also do not converge (toward low frequencies) until around 0.001 Hz (16.7 min). This is consistent with our understanding of a low-turbulence system with low-frequency motions and flux carried by larger, slower events.

Based on the cospectra, flux periods of >15 min or so should produce more reliable fluxes. Figure 4.34 shows inflows calculated using flux periods of 20 min, which still (possibly accurately) underpredict the amount of flux, but are all generally positive and in agreement with each other.

4.6.5 'Real' turbulence vs. other circulations

The time series of EDDI measurements qualitatively make sense, exhibiting large excursions that can be explained as dye entering the sensing volume as it is released from the plate. However, the excursions observed last for several minutes, which is too slow for turbulence. The time scale of the largest eddies depends on the measuring height and vertical velocity scale (see Table 1.1); for our measuring height of $h = 14$ cm and z turbulence of $w' \sim 0.2$ cm/s, the largest timescale expected would be $\tau_{\mathrm{LE}} = h/w' = 70$ s. Although the fluorescence indeed picked up features in this range or faster, those observed by the temperature and conductivity sensors were much slower. In addition, they appeared to correlate with z velocity, and thus to carry flux.

We hypothesize that the excursions represent large-scale processes that are not technically turbulent eddies, but can still carry flux in a similar way: higher concentrations released at the bottom are brought upward by positive w, and lower concentrations are brought downward with negative w. Thus, the eddy correlation methodology can still be applied. Our instrument is capable of measuring the flux carried by these eddies, as evidenced by the flux numbers in Figures 4.25, 4.26 and 4.34 and their reasonable agreement with the input rates. There is some noise in flux numbers with the shorter 5 min flux periods, as the eddies are large compared to the flux window and thus a single window may not provide a representative average. However, averaged long enough (i.e. over several excursions) the system becomes stationary, as implied by the convergence of the cospectra when using 40 min flux windows. In line with this picture, the contributions in the power spectra and cospectra are at quite low frequencies.

What exactly are these motions, and can they reasonably be expected to arise in this setting? We hypothesize that they represent small plumes that were pushed out of the plate, possibly with some buoyancy effects. However, they were not so buoyant that they traveled upward immediately. Instead, they drifted slowly in the low-turbulence region in the bottom center of the tank. This view is consistent with what was observed when imaging the dye during the runs, as well as with the characteristics of the turbulence described in Section 4.6.1.

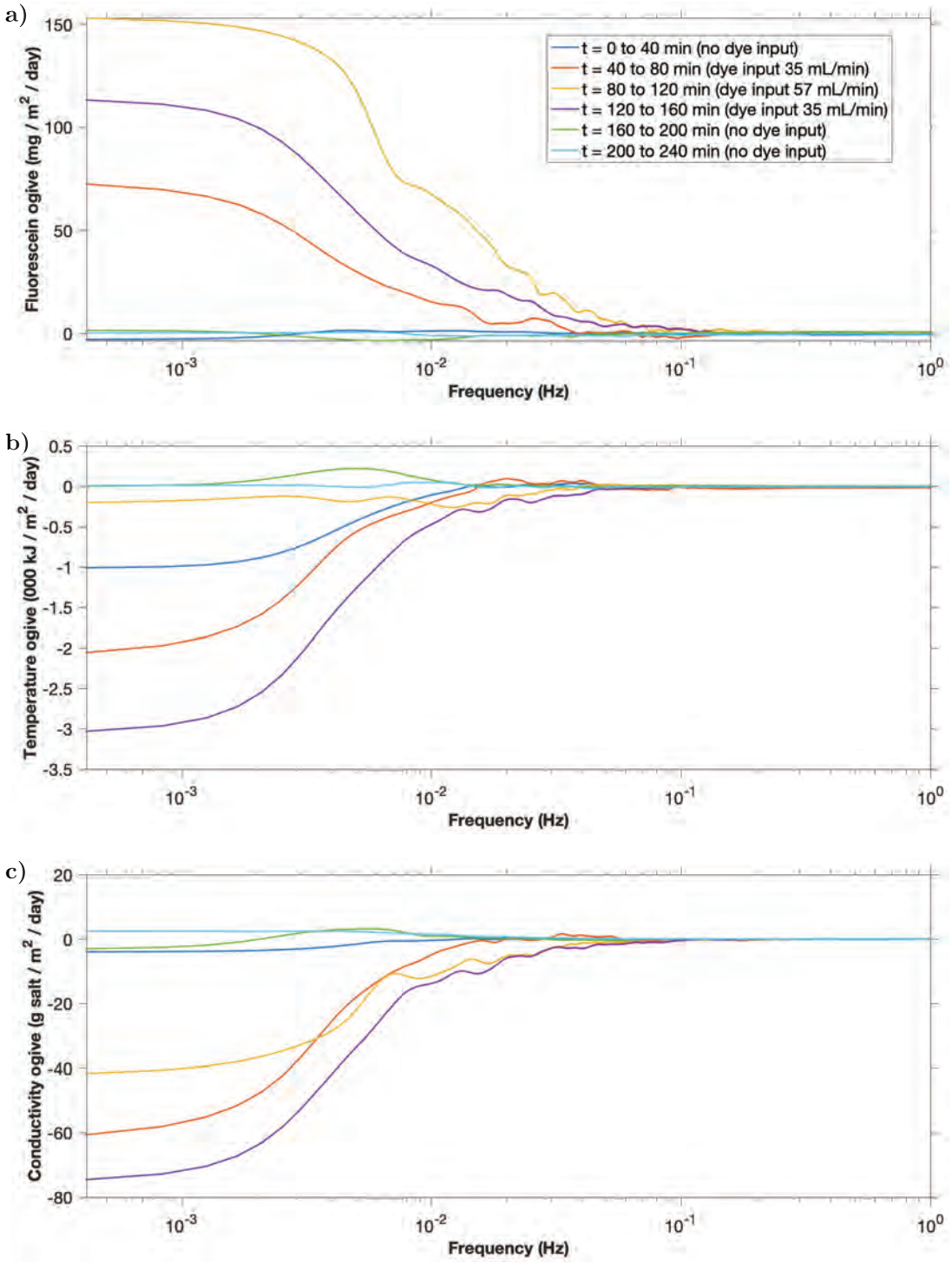

Figure 4.33: Cumulative cospectra (ogive plots) for **a)** fluorescein, **b)** temperature, and **c)** conductivity.

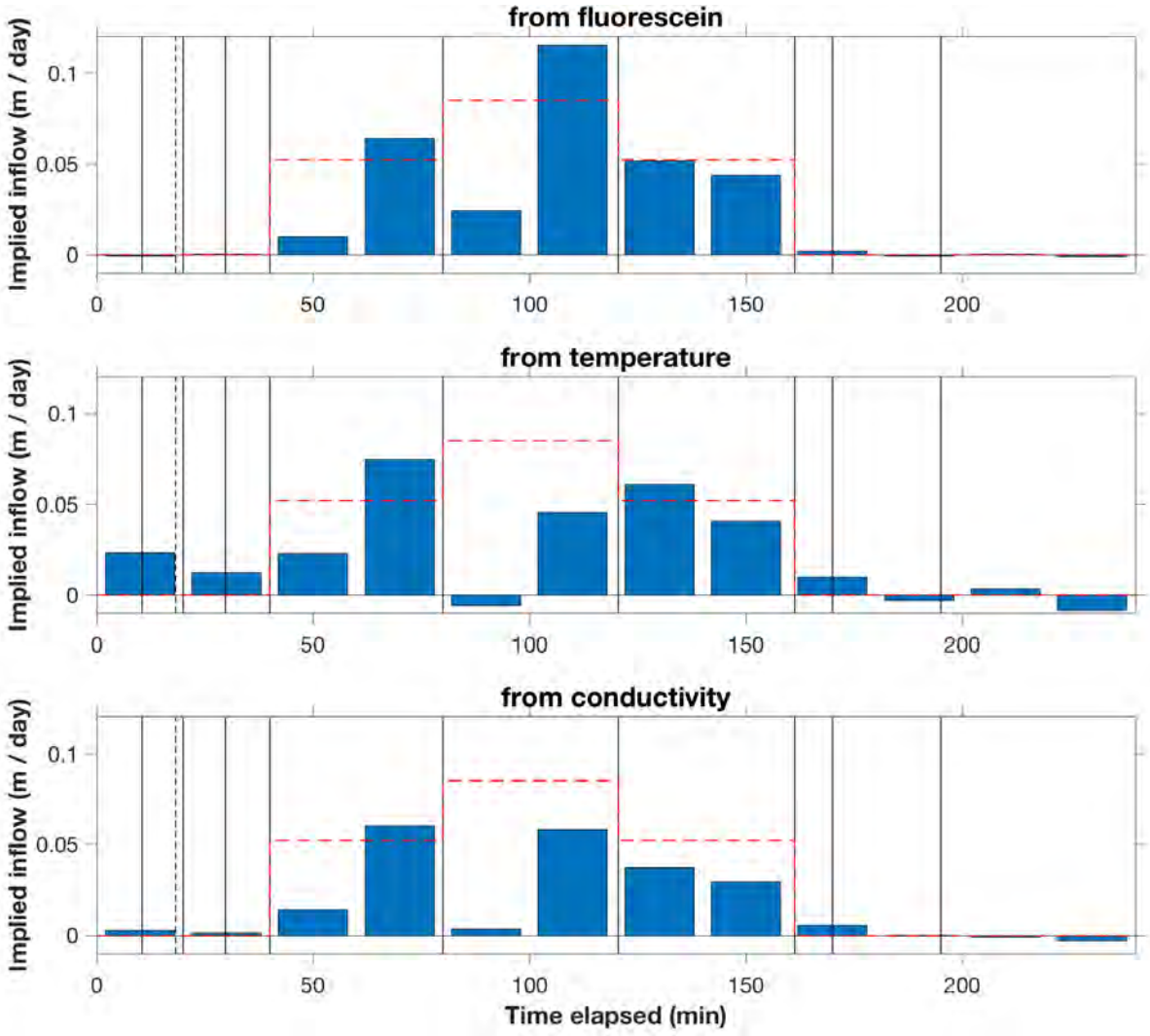

Figure 4.34: Implied inflows calculated from EC measurements with each of EDDI's sensors, using a 20 min flux window for hopefully converging fluxes.

It is somewhat surprising that the turbulence in the tank is low enough to give rise to this phenomenon; however, it is also possible that the turbulence created by the plungers, at a height of $30 \sim 40$ cm above the floor, was simply not reaching the base of the tank. This notion is consistent with turbulence profiles measured in the center of the tank (shown in Figure C.33 in Appendix C, Section C.4).

In other test experiments, the plungers were observed to push dye in the plate if it was located directly underneath them. This indicates that the motions created by the plungers can in fact reach the tank floor, but likely only in a localized area underneath them; such dynamics would tend to set up secondary circulations within the tank.

Thus, plumes are thought to have risen from the plate possibly due to buoyancy, where they drifted slowly in the area of low turbulence. Eventually, they floated high enough to hit the turbulent areas, were carried away by secondary circulations, or were otherwise dissipated. But while they persisted in the region above the plate, they were detected by the EDDI sensors as large excursions, and carried the flux through their slow drift. The fluorescence sensor may still have picked up faster features because its fast response time and targeted sensing volume allowed it to see features within the drifting plumes, as implied by the events seen in the time series in Figure 4.23. In more turbulence and especially with some amount of flow, the other two sensors should also be able to see features on these scales.

4.6.6 Flux mediated by 'true' eddies

Although most of the flux seems to be carried by large events, we do still expect some amount of flux due to true turbulence. Thus, to estimate the flux mediated by turbulent eddies, we excluded the excursions from the dataset (see Appendix B, Section B.10.1) and re-calculated flux. Implied inflow results for a 30 s running mean are shown in Figure 4.35, and for a 10 min linear detrend are shown in Figure 4.36.

Figure 4.35 shows that the flux mediated by fast (<30 s) eddies is quite low, especially compared with overall flux in the system. However, the fluxes are still generally positive when they should be (with the exception of the $t = [40, 60]$min time window) and the relative trends over time agree between the three sensors. With turbulent flux, we expect the spatiotemporal averaging of the sensors to play a larger effect, since the components should be of higher frequency. Consistent with this, the faster fluorescence sensor did indeed measure higher flux than the other two sensors.

To further sense check our results, we conducted a similar analysis as in Figure 4.27 by calculating flux after applying different lengths of running mean filter. The results are shown in Figure 4.37. The results appear to be generally consistent with our understanding; 1 s running mean filters, which had little effect on fluxes before exclusions were removed, now do tend to pull the fluxes closer to 0.

From Figure 4.36, it can be seen that using the long linear detrend yields higher flux numbers than the short running mean, even with the excursions removed. This indicates that there are some lower frequency components in the system (which would be removed by the running mean) that contribute to flux, even beyond the excursions. Even so, the flux calculated using the conductivity sensor is quite low, indicating that for salinity especially, much of the detected

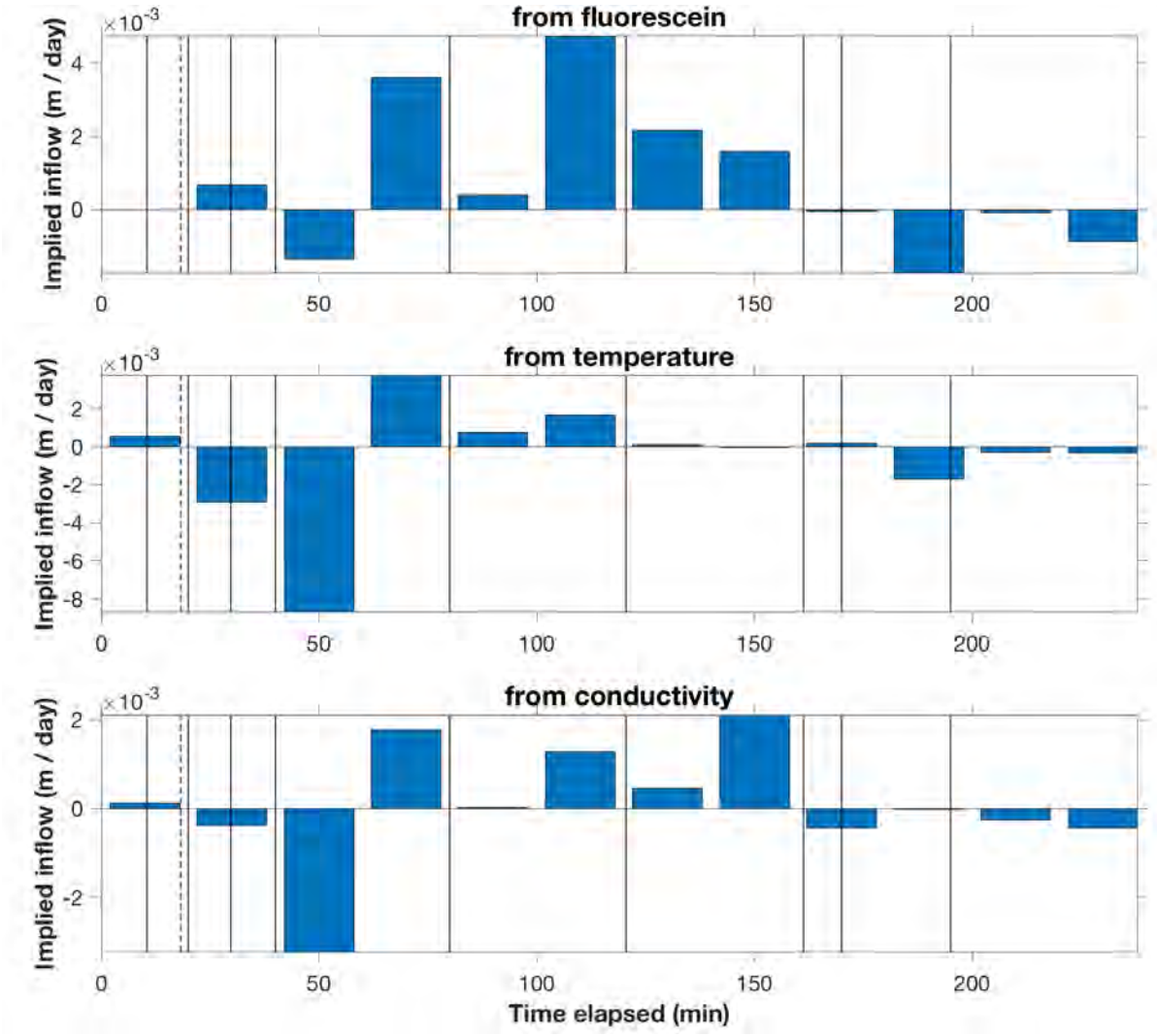

Figure 4.35: Implied inflows calculated for dataset with excursions removed, using a 30 s running as the mean removal algorithm. Note that the y axes for the three sensors are different.

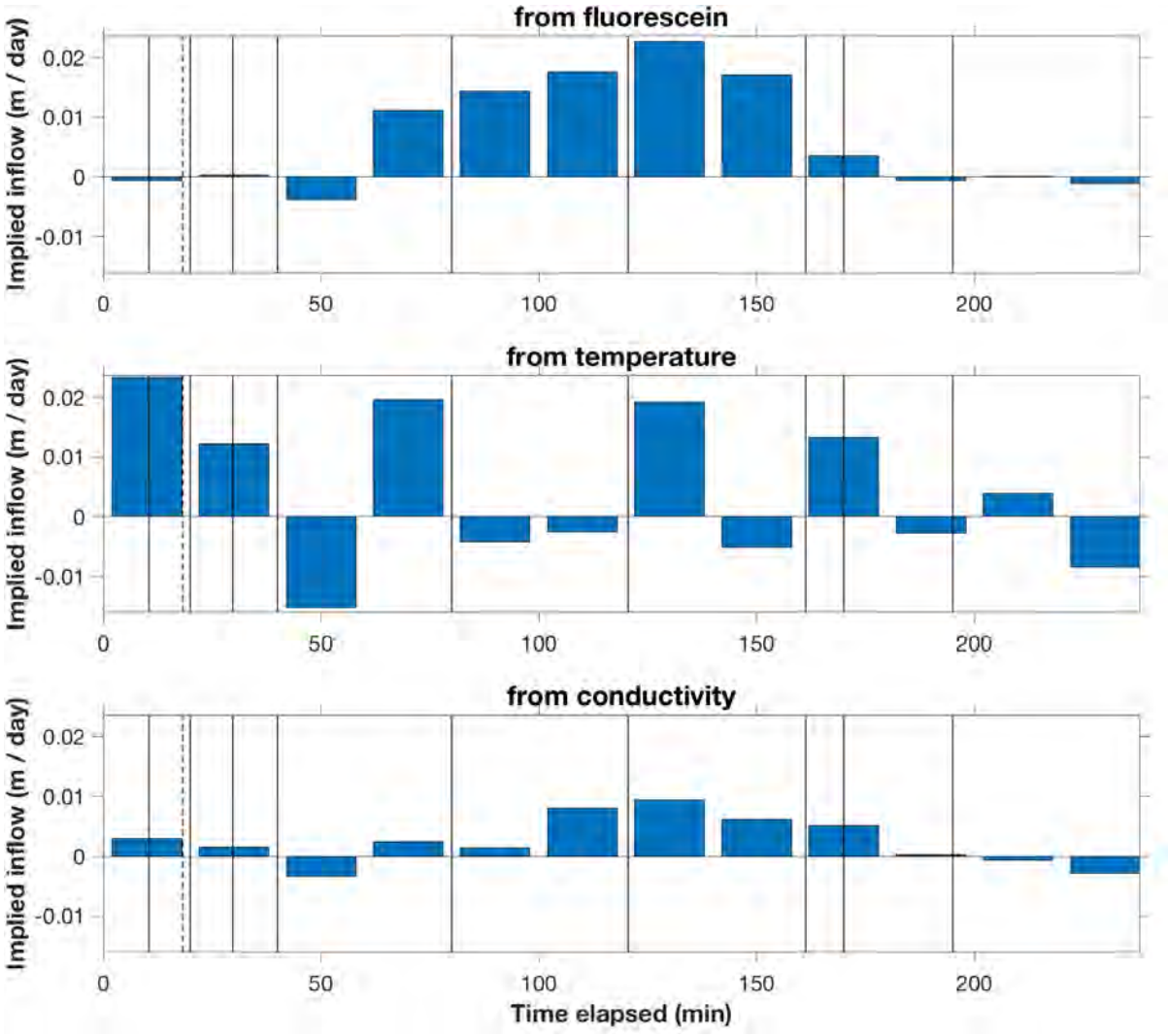

Figure 4.36: Implied inflows calculated for dataset with excursions removed, using a 10 min linear detrend as the mean removal algorithm.

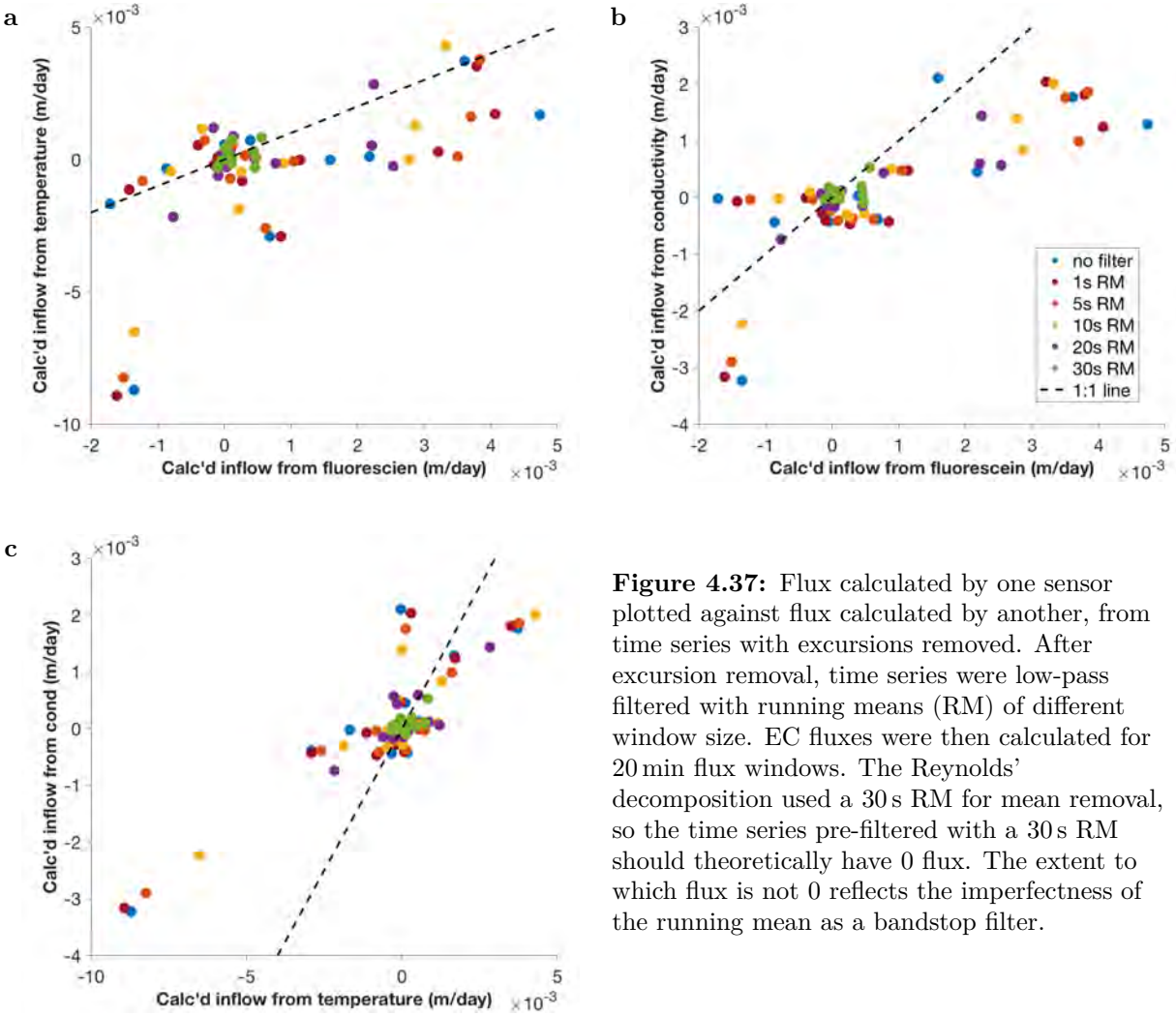

Figure 4.37: Flux calculated by one sensor plotted against flux calculated by another, from time series with excursions removed. After excursion removal, time series were low-pass filtered with running means (RM) of different window size. EC fluxes were then calculated for 20 min flux windows. The Reynolds' decomposition used a 30 s RM for mean removal, so the time series pre-filtered with a 30 s RM should theoretically have 0 flux. The extent to which flux is not 0 reflects the imperfectness of the running mean as a bandstop filter.

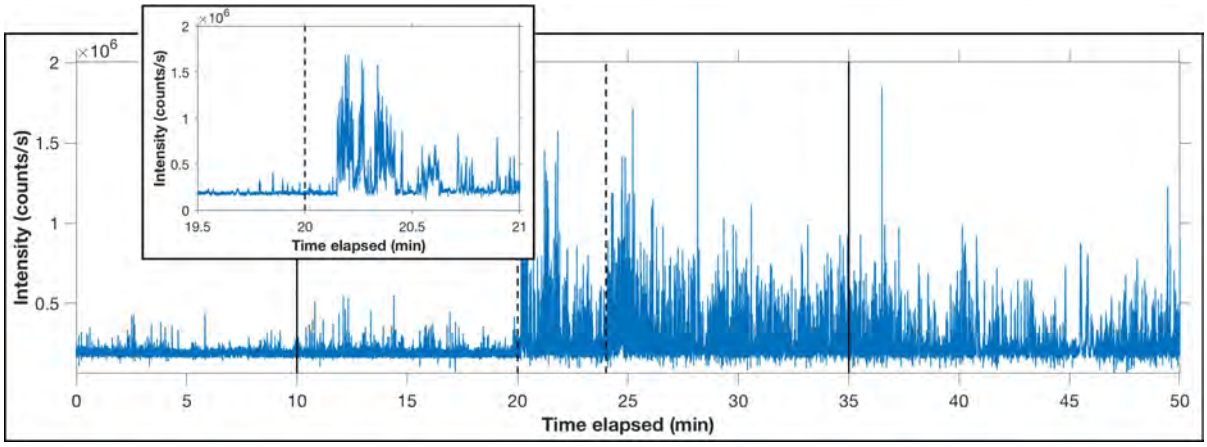

Figure 4.38: Time series of measurements at LED scattering wavelength. Dashed lines correspond to the addition of seed particles, while solid lines correspond to turning on turbulence (at 10 min) or turning it off (at 35 min). Inset shows a zoom-in of the first addition of seed. Features observed resemble eddies, suggesting future expansion to nephelometry.

flux was mediated by the large events. Possibly the spatial averaging of the conductivity sensor caused it to roll faster flux components into the bigger events.

Finally, regardless of mean removal technique, fluxes calculated from the dataset with excursions removed had some degree of noise. Removing the excursions removed large portions of the dataset especially in the time periods of dye input, reducing the number of eddies (though smaller and more frequent than the large events) in each averaging window. Cumulative cospectra corresponding to the 'turbulent' fluctuations (corresponding to the fluxes in Figure 4.35) are given in Figure C.31 in Appendix C, Section C.4, and do show few contributions slower than ∼1 min (i.e. the spectra converge). However, the cospectra were calculated for 40 min windows, while smaller windows resulting in noisier spectra that did not converge. The issue of stationarity, i.e. that a statistically representative number of events be present, is related to but distinctly different from the size of the features contributing to the flux.

4.6.7 LED scattering

A side observation from tank tests was that the presence of seed particles in the water would cause large spikes in the LED scattering peak for the fluorescence sensor. Actual fluorescence at emission wavelengths appeared to unaffected, but the spikes were noticeable in spectral scans taken before and after the measurements.

Figure 4.38 shows a time series taken at the LED peak wavelength (376 nm under the monochromator's current calibration), where eddy-like features are observed after the addition of seed particles. The features were observed both with and without turbulence; possibly the particles, which are also used for laser doppler velocimetry, were particularly reflective. These results suggest that the LED scattering may, in a future version of the instrument, be used to detect scattering by particles (i.e. nephelometry), which could be correlated with velocity for particle flux measurements.

In spectral scans of fluorescence, strong signals at one wavelength have been observed to 'bleed'

into surrounding wavelengths (i.e. taller peaks are also fatter). This 'spectral bleeding' of strong light is likely due to the way light passes through the monochromator. Strong LED scattering signals were observed to sometimes bleed as far as the emission wavelength, and would be subsequently removed in the calibration (as a fixed intercept for 0 concentration). This case was potentially concerning because the LED scattering did not appear to be constant. However, baseline measurements taken at the emission wavelength did not exhibit features similar to those observed in Figure 4.38, indicating that the variable scattering in this situation did not affect fluorescence measurements at 510 nm.

4.7 Conclusions

This thesis focused largely on instrument development, with the challenge of developing sensors that were fast, small, and accurate enough for EC, and integrating them with a velocimeter. The three EDDI sensors designed to this end were shown in tests throughout their development to be capable of measuring c' at a resolution that is likely sufficient (to varying degrees) for capturing turbulent flux. For the w' measurements, a commercially developed ADV was used that was previously shown to be capable of the necessary resolution. Then, given that the instruments were integrated in such a way as to avoid interference in either direction, it should be able to measure both c' and w' to the resolution necessary for eddy correlation.

As a final test that the instrument can work as a full package for flux measurement, experiments were conducted in the tank whereby the $\overline{w'c'}$ measured by the instrument could be compared to an independent estimate of flux. A match between the flux estimates would require that a) the instrument is capable; b) eddy correlation is 'correctly' applied in the data processing; and c) eddy correlation is valid in the environment generated by the tank.

We can only assume, based on all our data, that the w and c measured by the instrument are correct and of sufficiently good 'quality'. This is not to say that the instrument was assumed to be correct and capable a priori, in which case the tank experiments would be slightly pointless—there is no real practicality in constructing an artificial environment and testing if EC can be used in it. Instead, the tank tests were used to identify and address new issues, until there appeared to be no more issues related to the sensors[13]. Then, we try to explain any remaining discrepancies by other factors.

For b), mean removal and other choices do present a difficulty, but we compared various techniques and made informed decisions based on what we understood of the tank environment. To the best of our ability, the data processing chosen is the 'best choice' for the given system. Of course, if c) is not true, then there may be no data processing technique that allows us to arrive at the flux that we want; for example, the concept of 'fluctuating components' could be ill-defined in the system. It could also be that flux at the measuring point, even if correctly represented by the measured $\overline{w'c'}$, fails to represent the desired sediment flux. In such cases, EC as a whole is not valid in this system.

[13] We did have some known concerns for the sensors individually—slower response times, larger sensing volumes, etc—whose effect on flux could be tested, to some degree, by comparisons with the other sensors (e.g. if the thermistor's response time were insufficient, it would detect substantially less flux than fluorescence). The data seemed to indicate that all of the sensors were generally capable in this setting.

In our experiment, we found that flux measured by all the sensors were of the same order of magnitude as the lower bound of expected rates. In addition, all three sensors were generally in good agreement. The differences in response time and sensing volumes were not completely without effect, but mostly did not impede the ability of the sensors to measure tracking fluxes, which bodes well for future extensions to flux tracing. The biggest discrepancies in measured flux were likely due to differences in the sensing volume locations, which would have less effect on flux estimates in settings with actual flow.

However, the experiment also highlighted the complex flow circulation patterns in the tank. Although the instrument was designed to measure turbulent flux, it appears that relatively little turbulence was actually present at the measuring volume. Instead, different processes were occurring on a larger scale, which were detected by the instrument as large events. When these events were included (by choice of Reynolds' decomposition parameters) into the calculated fluctuations c' and w', the resulting fluxes provided a relatively good match to the predicted fluxes. Thus, it appears that these larger events were carrying most of the flux that emanated from the 'sediment bed' (tank floor). It also appears that the eddy correlation technique—i.e. the correlation of fluctuating components of concentration and velocity—can still provide a reasonable estimation of sediment flux when applied to these events, even if they do not represent true turbulence.

Although the measured fluxes were reasonably in line with the predicted fluxes (i.e. same order of magnitude), they also across the board underpredicted the flux, even from the supposed 'lower bound' estimate. Fluxes were especially low, or even negative, for around 20 min each time the pump rate was increased (at $t = 40$ min and $t = 80$ min). These measured fluxes did appear to be 'real' (i.e. not due to sensor malfunction), as the pattern was observed by all three sensors, which otherwise produced fluxes in the expected ranges for the rest of the EC run. In addition, a deeper dive into the most prominent discrepancy—the negative flux measured by the temperature and conductivity sensors in the $t = [80, 85]$min time period—revealed features that looked like a true covariance between velocity and concentration (Figure 4.28).

We thus tentatively attribute the underpredictions in these time periods to the intricacies of the dye release system. It is possible that, when the pumping rate is first increased, temporary changes in the pattern of release occur as the system transitions to a new steady state. For instance, the abrupt increase in inflow might create local pressure micro-gradients within the mesh of the plate, which would then create localized releases. The system's measurements during these time periods would then correctly reflect instances where the rising plume missed the sensing volume, or created secondary circulations that resulted in a downward flux at the sensing volume.

In general, some amount of mismatch between the measured and expected inflow rates is expected. The lower bound estimate of expected rate was calculated assuming a uniform release of the dye across the floor of the tank, that rises evenly to the level of the sensing volume. In fact, the dye was released from a 0.7 m area. The smaller release area would result in a higher per-area flux rate, but the flux could also completely miss the sensing volume if it did not rise or diffuse evenly, such as in the micro-gradient scenario described above. This was in fact observed during our experiment described[14]. The situation echos that of other EC studies grappling with heterogeneous sediment beds and incomplete mixing [e.g. 19]. However, here we cannot, for example, measure higher in the water column to smooth out heterogeneity, since

the problem is tied to the complex flow field in the artificial tank environment.

The tank environment was characterized by spatially heterogeneous turbulence, secondary circulations, and possibly buoyancy effects, and transport appeared to be dominated by these larger tank-scale processes. With such large, flux-carrying processes at play, it would be impossible to pick up all of the transport with a single point measurement. For example, buoyant plumes or secondary circulations that carry mass upward in other regions of the tank would not be detected; on the flipside, a large plume that rises exactly into the sensing volume would produce a large apparent flux. If the processes were random (stochastic), then the flux could be averaged over a long enough period (for which it is stationary). However, given that the plungers create distinct patterns of fluid motion in the tank, it is unlikely that they were all stochastic.

In essence, it is quite possible that our instrument was correctly measuring the vertical flux at the sensing volume, but that the vertical flux at that sensing volume was an imperfect representation of the average vertical flux across the tank bed. In other words, EC—as a technique to measure flux from the sediment bed (and not at a single point somewhere above it!)—is not completely applicable in this particular system. Discrepancies between the measured and expected fluxes are likely a result of this factor, and reflect the limitations of the tank design as a system to create and detect benthic fluxes. Understanding these limitations, the measured fluxes appear to be quite reasonable, raising confidence in the ability of the instrument to measure fluxes in a different environment.

[14]The position of the plate was chosen based on observed patterns so that, in the x (longitudinal) direction of the tank, the dye tended to drift toward the sensing volume. However, during the particular EC run described here, the biggest plumes were observed to rise at an offset in the y direction (closer to the back of the tank if viewed as in Figure 4.14). Unlike systems with unidirectional flow, the tank is in fact a three-dimensional system, leading to all manner of complex flow patterns.

Box. 4.1: Temperature compensation of conductivity

In principle, the near collocation of EDDI's thermistor and conductivity sensor provide a good opportunity to temperature compensate the conductivity. This idea was explored using a linear compensation with a standard coefficient of $\alpha = 0.2$ (see Section 1.9.4, p. 91 on conductivity dependence on temperature). However, this compensation produced unrealistic results. For example, compensated conductivity appeared to rise at the end of the EC run, although uncompensated conductivity was flat; the conductivity is not expected to change when there is no dye input, although the temperature can continue to drop due to losses to the surrounding environment. The temperature compensation was also observed to remove the downward trend of conductivity, which should be present due to lower-salinity dye being added to a closed system.

These results, shown in Figure 4.19, indicate that the compensation methodology or coefficient was not suitable, perhaps overcorrecting the conductivity values. Temperature compensation was not subsequently attempted, as it would likely have little results on the fluxes anyways. Compensation for a trending mean would be removed by the Reynolds' decomposition. Compensation for temperature fluctuations, on the other hand, although important in principle, would likely have minimal impact on the fluxes due to the small size of the fluctuations; this was also observed in other EC studies of benthic flux [5].

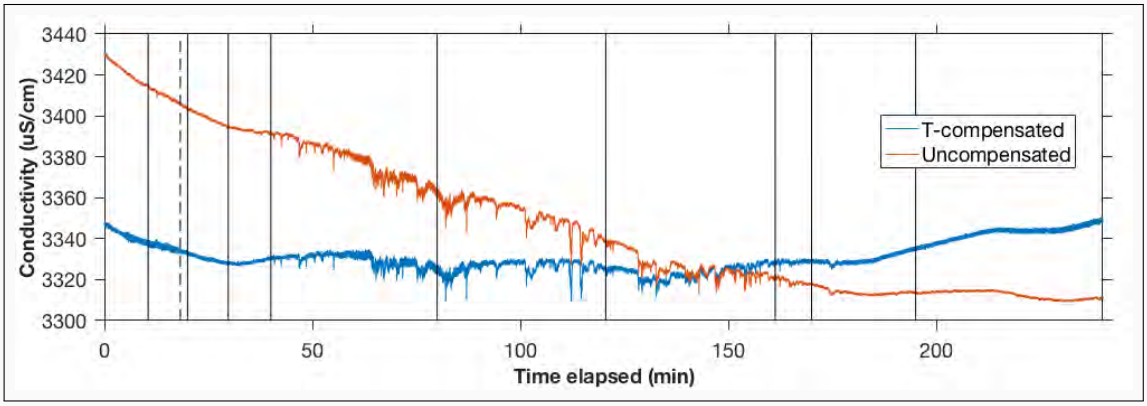

Figure 4.19: Temperature compensation of conductivity measurement for EC run.

Chapter 5

Preliminary field notes

Figure 5.1: Deployment at Upper Mystic Lake on 15 September 2017. Additional photos are included in the photo gallery in Appendix D.

The EC system was packaged for the field and deployed in preliminary trials at Upper Mystic Lake in Medford, MA. Upper Mystic Lake does not meet many of the guidelines described for ideal EC field sites in Section 1.4.5 (p. 53), such as having unidirectional flow. However, it was chosen as a convenient location for preliminary tests aimed at developing a field protocol and identifying new field-related issues.

5.1 Benthic lander

The benthic lander designed for the instrument is shown in Figure 5.2, and diagrams are given in Appendix G. The lander was designed using AutoCAD (Autodesk) and fabricated by the MIT Central Machine Shop. It is constructed of Type 304 square stainless steel tubing (1" × 0.065" wall for the frame; 1.25" × 0.065" wall and 1.5" × 0.083" wall for the legs), welded together.

Figure 5.2: Benthic lander with all equipment assembled.

Holes were drilled in the stainless steel tubings so that the lander would fill when underwater and drain above water, to avoid difficulties with buoyancy.

The design of the lander was based on those used by other EC researchers (Figure 1.5, p. 45), as well as the needs of our own instrument. A tripod was chosen because of the stability and stiffness afforded by three legs; stiffness is especially important for eddy correlation because vibrations can affect the measurements, which specifically look at fluctuations. However, the tilted legs of a tripod are more disruptive to the flow than directly vertical legs, which can be arranged with ample space between them. Thus, as a compromise, the lander was designed to be a truncated pyramid.

The lander has telescoping legs, so that the height can be adjusted from 50 cm to 120 cm, with a corresponding equilateral triangle base of side 70 cm to 100 cm. The lander is stored and transported in its shortest form, but for deployment, the height can be adjusted based on the water depth, desired sampling volume height, and flow field.

The pyramid has two tiers, as can be seen in Figure 5.2. The two bars on the 'front' face of the lander are directly vertical of each other (unlike the other two sides), so that the ADV can be mounted in true vertical. The ADV holders use a similar principle to that used in the lab (shown in Figure B.11 in Appendix B), in which PVC blocks with foam-lined cutouts are screwed tightly around the ADV using socket screws. Behind the ADV, two PVC bars across the lower tier form a platform for the EDDI housing, which is attached using two giant hose clamps. The lander thus has a 'front' face and a preferential flow direction, but in situations with changing flow, it can be adjusted to minimize disruptions by widening the base.

The feet were designed as octagons cut from 6" plates. The relatively large feet are suitable for soft sediments, but a 3/8" hole is also provided so that a stake can be attached, if necessary, for other sediment types.

Figure 5.3: Benthic lander shown with clamp-on wheels for easier transport.

5.2 Deployment

Initial field deployments were done by wading. A field equipment checklist is given in Appendix D, along with a checklist of the field procedure. The lander was deployed at a shallow site close to shore, and controlled by a computer on shore via the 10 m underwater ethernet cable. Three deployments were attempted.

In the first deployment, the lander was found to be quite heavy and difficult to move, especially with EDDI and the ADV loaded on it. Thus, for the second deployment, the equipment was instead assembled at the deployment location, so that each component (lander, ADV, EDDI) was carried into the water separately. The sensing volumes also had to be aligned underwater, which could be quite a lengthy process since it can require some iteration with ADV measurements to ensure no interference. In general, the deployment process required several trips back and forth between the shore and the site.

For the second deployment, buoys were tied to each leg of the lander to aid in transporting it to the chosen measurement point. The buoys 'lightened' the load of the lander once it was deep enough for them to take effect. In principle they would be removed once the lander was in place, although this was generally not necessary for the preliminary trials in shallow water. They can be seen in the deployment photos in Appendix D.

EDDI is also positively buoyant from the large amount of empty space in the housing, making it relatively easy to carry once in the water. The main difficulty lay in carrying the optical fibers, which were attached to the EDDI housing (as it could only be opened on shore). The sensing ends of the fibers were pre-mounted into their holder and could not be protected, and so extra care was required to not damage the delicate fiber tips as the housing was transported to the measurement location.

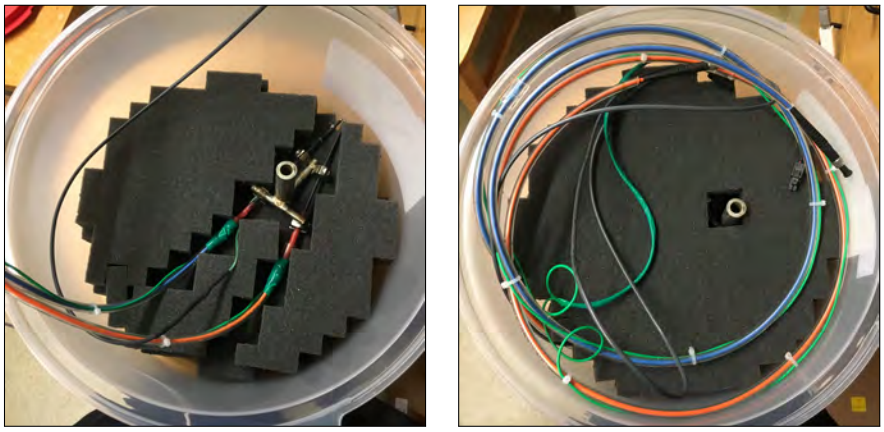

Figure 5.4: Carrier for optical fibers. Optical fibers are shown before installation of underwater cables for temperature and conductivity.

After the first field season, the lander was subsequently modified to enable easier transport while on land. Two 8" cushion-loaded casters[1] (wheels) can now be clamped to the two back feet using low-profile C-clamps, as shown in Figure 5.3. 5 ft stainless steel square tubings with rectangular grips can also be clamped on, so that the lander can be wheeled around like a wheelbarrow. With the lander now easier to transport on shore, it may be possible to pre-assemble the entire package while on shore, before wheeling into the water, removing the wheels, and attaching the buoys. These new developments will be tested in the next field season.

Another logistical issue in field deployments was the protection of the optical fibers during transport to and from the field site. When not mounted, the connector ends of the optical fibers can be protected with standard SMA caps, and the free ends can be protected using rubber push-on caps of the appropriate size (i.e. larger for the fiber with the thermistor). However, we ultimately decided it would be more advantageous to preload the optical fibers in their holder, so that the same calibrations from lab measurements would be maintained. It was also advantageous to avoid loading the fibers in the field, as the process is a bit delicate.

To protect the exposed optical fibers during transit, a container was prepared using a standard cake carrier, with foam cubes arranged as a mold around the optical fibers in their holder, as shown in Figure 5.4. The optical fibers could then be coiled on top for easy transit.

5.3 Light contamination

The main takeaway of the initial field deployments related to the role of light contamination in the quality of the measurements. The field deployments all occurred in late morning to early afternoon, and coincidentally on days of rather strong sunlight. In initial spectral scans, the daylight spectrum was found to overload the photon counter measurements, as in Figure 5.5a (see also Figure 2.19, p. 117 demonstrating spectral overload). The wavelength chosen for humic acid emission, 475 nm, unfortunately coincided with some of the strongest daylight signal. The ambient light completely swamped out the fluorescence of any humic acid in the water; even though LED modulation theoretically removes ambient light, the statistical noise of the high

[1] These particular casters were chosen for their large plate.

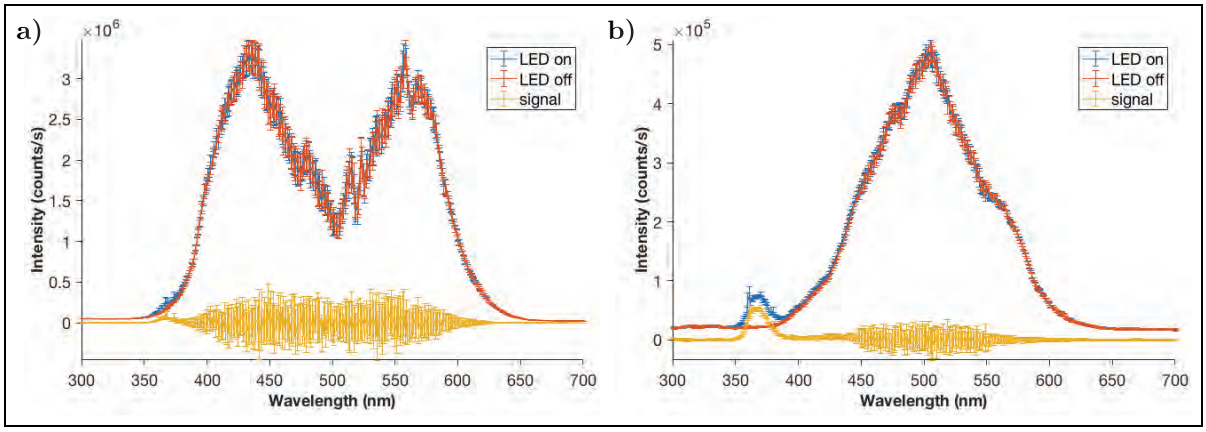

Figure 5.5: Modulated spectral scans taken from field deployments taken **a)** before and **b)** after installation of a floating dark sheet above the measuring area. Strong daylight signals are apparent in both spectra, creating an unacceptable amount of noise in the modulated difference, although the dark sheet reduced this effect by about an order of magnitude. Spectra were taken as the average / standard deviation over 20 measurements of 20 ms each (10 ms each with LED on and off).

photon counts (discussed in Section 2.3.2, p. 112) was larger than the expected fluorescence. Upper Mystic Lake also has a rather low humic content, with total organic carbon of around 1 $\sim$ 2 ppm (as measured by a Shimadzu TOC from grab samples of the lake water).

For the second deployment, a light shield was constructed to cover the entire surrounding area above the sensing volume. The shield was made from a 10 ft × 25 ft, 0.004"-thick black polyethylene (LDPE) film, with anchors tied to ropes at the corners. When in place, the film covered the lander and floated on the surface of the surrounding water. It can be seen in the pictures in Appendix D. Obviously the shield may affect some of the natural processes in the area of interest, but for now it was used to enable proof-of-concept tests by separating the problem of light contamination. Another option would have been to conduct tests at night.

The shield was found to reduce the light level by about an order of magnitude, as seen in Figure 5.5b. However, the amount of light was still considered too high to detect fluctuations in humic acid.

Subsequent ex situ tests revealed that there was some light leakage through the housing, mainly through the joint between the pipe and the coupling which happened to coincide with the location of the PMT inside the housing. Covering the joint with a few layers of optical tape reduced this light leakage significantly, although the presence of the floating dark shield also reduced its impact.

The main source of light contamination proved to be light coming directly in through the receiving optical fiber. Diffuse light above or to the side of the fibers did not produce such strong signals. Instead, the strongest signals arose from light in the cone of acceptance of the receiving fiber, e.g. from reflections of sunlight off of objects facing the fibers. A dark cardboard cutout at some distance in front of the fibers could almost completely block out the light contamination, though the necessary area for the sheet increased with its distance from the fiber tips, as per the geometry of a cone. A 12" × 12" sheet was found to cut the ambient signal approximately in half when placed ~4 ft away, and to reduce it by a factor of ~10 when

placed 1 ft away.

In a first attempt at a solution, we constructed a rigid, black plastic sheet that could be attached to a leg of the lander using elastic cable ties. The optical fibers could be turned sideways (relative to the flow) to directly face the plastic sheet, which was hopefully large enough given the distance of the ADV mount to the edge of the leg. However, the third deployment failed when the pressure housing flooded, so this solution has not yet been tested in the field. The sideways orientation of the optical fibers also positions the concentration sensing volumes perpendicular to the flow (relative to each other and to the ADV sensing volume), which is less ideal for sampling the same eddies; the impact of this factor will also be tested in the next field season.

Bibliography

[1] National Research Council Committee on Contaminated Marine Sediments. *Contaminated Marine Sediments: Assessment and Remediation*. The National Academies Press, 1989. ISBN: 9780309086714. URL: http://www.nap.edu/openbook.php?record%7B%5C_%7Did=1412.

[2] Steven C Nadeau and Merton M Jr. Skaggs. "Analysis of Recontamination of Completed Sediment Remedial Projects". In: *4th International Conference on Remediation of Contaminated Sediments*. Savannah, GA, 2007. URL: http://www.smwg.org/presentations/Battelle/Nadeau%20and%20Skaggs%202007%20-%20Analysis%20of%20Recontamination%20of%20Completed%20Sediment%20Remedial%20Projects.pdf.

[3] Nancy P Kohn and Nathan R Evans. "Year 6 Post-Remediation Biomonitoring and Phase II Source Investigation at the United Heckathorn Superfund Site, Richmond, California". English. In: (Apr. 2004). DOI: 10.2172/15010621. URL: http://www.osti.gov/bridge/product.biblio.jsp?osti%7B%5C_%7Did=15010621.

[4] Peter Berg et al. "Oxygen uptake by aquatic sediments measured with a novel non-invasive eddy-correlation technique". In: *Marine Ecology Progress Series* 261 (2003), pp. 75–83. ISSN: 0171-8630. DOI: 10.3354/meps261075. URL: http://www.int-res.com/abstracts/meps/v261/p75-83/.

[5] Peter Berg et al. "A new robust oxygen-temperature sensor for aquatic eddy covariance measurements". In: *Limnology and Oceanography: Methods* 14.3 (Mar. 2016), pp. 151–167. ISSN: 15415856. DOI: 10.1002/lom3.10071. URL: http://doi.wiley.com/10.1002/lom3.10071.

[6] John Crusius et al. "Eddy correlation measurements of submarine groundwater discharge". In: *Marine Chemistry* 109.1-2 (Feb. 2008), pp. 77–85. ISSN: 03044203. DOI: 10.1016/j.marchem.2007.12.004. URL: http://linkinghub.elsevier.com/retrieve/pii/S0304420307002940.

[7] Dirk J. Koopmans and Peter Berg. "Stream oxygen flux and metabolism determined with the open water and aquatic eddy covariance techniques". In: *Limnology and Oceanography* 60.4 (July 2015), pp. 1344–1355. ISSN: 00243590. DOI: 10.1002/lno.10103. URL: http://doi.wiley.com/10.1002/lno.10103.

[8] Matthew H Long and David P Nicholson. "Surface gas exchange determined from an aquatic eddy covariance floating platform". In: *Limnology and Oceanography: Methods* 16.3 (Mar. 2018), pp. 145–159. ISSN: 15415856. DOI: 10.1002/lom3.10233. URL: http://doi.wiley.com/10.1002/lom3.10233.

[9] Peter Berg et al. “Eddy correlation measurements of oxygen fluxes in permeable sediments exposed to varying current flow and light”. In: *Limnology and Oceanography* 58.4 (2013), pp. 1329–1343. ISSN: 0024-3590. DOI: 10.4319/lo.2013.58.4.1329. URL: http://aslo.org/lo/toc/vol%7B%5C_%7D58/issue%7B%5C_%7D4/.

[10] Daniel F McGinnis et al. “Quantifying tidally driven benthic oxygen exchange across permeable sediments: An aquatic eddy correlation study”. In: *Journal of Geophysical Research: Oceans* 119.10 (Oct. 2014), pp. 6918–6932. ISSN: 21699275. DOI: 10.1002/2014JC010303. URL: http://doi.wiley.com/10.1002/2014JC010303.

[11] KM Attard et al. “Benthic oxygen exchange in a live coralline algal bed and an adjacent sandy habitat: an eddy covariance study”. en. In: *Marine Ecology Progress Series* 535 (Sept. 2015), pp. 99–115. ISSN: 0171-8630. DOI: 10.3354/meps11413. URL: http://eprints.gla.ac.uk/111085/1/111085.pdf%20http://www.int-res.com/abstracts/meps/v535/p99-115/.

[12] Matthew H Long et al. “Oxygen metabolism and pH in coastal ecosystems: Eddy Covariance Hydrogen ion and Oxygen Exchange System (ECHOES)”. In: *Limnology and Oceanography: Methods* 13.8 (Aug. 2015), pp. 438–450. DOI: 10.1002/lom3.10038. URL: http://doi.wiley.com/10.1002/lom3.10038.

[13] David J Burdige et al. “The Role of Benthic Fluxes of Dissolved Organic Carbon in Oceanic and Sedimentary Carbon Cycling”. In: *Geophysical Research Letters* 19.18 (Sept. 1992), pp. 1851–1854. ISSN: 00948276. DOI: 10.1029/92GL02159. URL: http://doi.wiley.com/10.1029/92GL02159.

[14] Brooke L Holcombe, Richard G Keil, and Allan H Devol. “Determination of pore-water dissolved organic carbon fluxes from Mexican margin sediments”. In: *Limnology and Oceanography* 46.2 (2001), pp. 298–308. ISSN: 0024-3590.

[15] Cinzia De Vittor et al. “Oxygen, carbon, and nutrient exchanges at the sediment,Äìwater interface in the Mar Piccolo of Taranto (Ionian Sea, southern Italy)”. In: *Environmental Science and Pollution Research* 23.13 (July 2016), pp. 12566–12581. ISSN: 0944-1344. DOI: 10.1007/s11356-015-4999-0. URL: http://link.springer.com/10.1007/s11356-015-4999-0.

[16] John Moncrieff et al. “Averaging, Detrending, and Filtering of Eddy Covariance Time Series”. In: *Handbook of Micrometeorology*. Ed. by Xuhui Lee, William Massman, and Beverly Law. Vol. 29. Atmospheric and Oceanographic Sciences Library. Dordrecht: Kluwer Academic Publishers, 2005. Chap. 2, pp. 7–31. ISBN: 978-1-4020-2265-4. DOI: 10.1007/1-4020-2265-4_2. URL: http://link.springer.com/10.1007/1-4020-2265-4%7B%5C_%7D2.

[17] Peter Berg, Hans Røy, and Patricia L Wiberg. “Eddy correlation flux measurements: The sediment surface area that contributes to the flux”. In: *Limnology and Oceanography* 52.4 (July 2007), pp. 1672–1684. ISSN: 0024-3590. DOI: 10.4319/lo.2007.52.4.1672.

[18] Ronnie N Glud et al. “Benthic O2 exchange across hard-bottom substrates quantified by eddy correlation in a sub-Arctic fjord”. In: *Marine Ecology Progress Series* 417 (Nov. 2010), pp. 1–12. ISSN: 0171-8630. DOI: 10.3354/meps08795. URL: http://www.int-res.com/abstracts/meps/v417/p1-12/.

[19] Jennie E Rheuban and Peter Berg. "The effects of spatial and temporal variability at the sediment surface on aquatic eddy correlation flux measurements". In: *Limnology and Oceanography: Methods* 11 (2013), pp. 351–359. ISSN: 15415856. DOI: 10.4319/lom.2013.11.351. URL: http://apps.webofknowledge.com/full%7B%5C_%7Drecord.do?product=WOS%7B%5C&%7Dsearch%7B%5C_%7Dmode=CitingArticles%7B%5C&%7Dqid=3%7B%5C&%7DSID=2AQtD3Q7L1dahMKS71r%7B%5C&%7Dpage=1%7B%5C&%7Ddoc=1%20http://www.aslo.org/lomethods/free/2013/0351.html.

[20] Daniel F McGinnis et al. "Simple, robust eddy correlation amplifier for aquatic dissolved oxygen and hydrogen sulfide flux measurements". In: *Limnology and Oceanography: Methods* 9 (Aug. 2011), pp. 340–347. ISSN: 15415856. DOI: 10.4319/lom.2011.9.340. URL: http://www.aslo.org/lomethods/free/2011/0340.html.

[21] Claudia Lorrai et al. "Application of Oxygen Eddy Correlation in Aquatic Systems". In: *Journal of Atmospheric and Oceanic Technology* 27.9 (Sept. 2010), pp. 1533–1546. ISSN: 0739-0572. DOI: 10.1175/2010JTECHO723.1. URL: http://journals.ametsoc.org/doi/abs/10.1175/2010JTECHO723.1.

[22] Henry Bokuniewicz et al. "Direct measurements of submarine groundwater discharge (SGD) over a fractured rock aquifer in Flamengo Bay Brazil". In: *Estuarine, Coastal and Shelf Science* 76.3 (Feb. 2008), pp. 466–472. ISSN: 02727714. DOI: 10.1016/j.ecss.2007.07.047. URL: https://www.sciencedirect.com/science/article/pii/S0272771407003708.

[23] Elena Abarca et al. "Transient groundwater dynamics in a coastal aquifer: The effects of tides, the lunar cycle, and the beach profile". In: *Water Resources Research* 49.5 (May 2013), pp. 2473–2488. ISSN: 00431397. DOI: 10.1002/wrcr.20075. URL: http://doi.wiley.com/10.1002/wrcr.20075.

[24] Envco. *Conversion Table for Changing Conductivity into Salinity*. 2009. URL: http://envcoglobal.com/files/u5/Envco%20Conductivity%20to%20salinity%20conversion%20table.pdf (visited on 02/11/2018).

[25] Daphne Donis et al. "An Assessment of the Precision and Confidence of Aquatic Eddy Correlation Measurements". EN. In: *Journal of Atmospheric and Oceanic Technology* 32.3 (Mar. 2015), pp. 642–655. ISSN: 0739-0572. DOI: 10.1175/JTECH-D-14-00089.1. URL: http://journals.ametsoc.org/doi/abs/10.1175/JTECH-D-14-00089.1.

[26] Algot K. Peterson et al. "Turbulent heat and momentum fluxes in the upper ocean under Arctic sea ice". In: *Journal of Geophysical Research: Oceans* 122.2 (Feb. 2017), pp. 1439–1456. ISSN: 21699275. DOI: 10.1002/2016JC012283. URL: http://doi.wiley.com/10.1002/2016JC012283.

[27] Peter Berg et al. "Eddy correlation measurements of oxygen uptake in deep ocean sediments". In: *Limnology and Oceanography-Methods* 7 (2009), pp. 576–584. ISSN: 1541-5856.

[28] Daphne Donis et al. "Assessing benthic oxygen fluxes in oligotrophic deep sea sediments (HAUSGARTEN observatory)". In: *Deep Sea Research Part I: Oceanographic Research Papers* 111 (May 2016), pp. 1–10. ISSN: 09670637. DOI: 10.1016/j.dsr.2015.11.007. URL: http://www.sciencedirect.com/science/article/pii/S0967063716300292.

[29] Julika Weck and Andreas Lorke. “Mixing efficiency in the thermocline of lakes observed from eddy correlation flux measurements”. In: *Journal of Geophysical Research: Oceans* 122.1 (Jan. 2017), pp. 291–305. ISSN: 21699275. DOI: 10.1002/2016JC012188. URL: http://doi.wiley.com/10.1002/2016JC012188.

[30] Clare E. Reimers et al. “Microelectrode Velocity Effects and Aquatic Eddy Covariance Measurements under Waves”. In: *Journal of Atmospheric and Oceanic Technology* 33.2 (Feb. 2016), pp. 263–282. DOI: 10.1175/JTECH-D-15-0041.1. URL: http://journals.ametsoc.org/doi/10.1175/JTECH-D-15-0041.1.

[31] Kenneth S Johnson et al. “Nitrate and oxygen flux across the sediment-water interface observed by eddy correlation measurements on the open continental shelf”. In: *Limnology and Oceanography: Methods* 9 (Nov. 2011), pp. 543–553. ISSN: 15415856. DOI: 10.4319/lom.2011.9.543. URL: http://www.aslo.org/lomethods/free/2011/0543.html.

[32] Lindsay Chipman et al. “Oxygen optodes as fast sensors for eddy correlation measurements in aquatic systems”. In: *Limnology and Oceanography: Methods* 10 (2012), pp. 304–316. ISSN: 15415856. DOI: 10.4319/lom.2012.10.304. URL: http://www.aslo.org/lomethods/free/2012/0304.html.

[33] Ronnie N. Glud et al. “Benthic Carbon Mineralization and Nutrient Turnover in a Scottish Sea Loch: An Integrative In Situ Study”. In: *Aquatic Geochemistry* 22.5-6 (Dec. 2016), pp. 443–467. ISSN: 1380-6165. DOI: 10.1007/s10498-016-9300-8. URL: http://link.springer.com/10.1007/s10498-016-9300-8.

[34] Derek G Goring and Vladimir I Nikora. “Despiking Acoustic Doppler Velocimeter Data”. en. In: *Journal of Hydraulic Engineering* 128.1 (Jan. 2002), pp. 117–126. ISSN: 0733-9429. DOI: 10.1061/(ASCE)0733-9429(2002)128:1(117). URL: http://ascelibrary.org/doi/abs/10.1061/(ASCE)0733-9429(2002)128:1(117)%20http://ascelibrary.org/doi/10.1061/(ASCE)0733-9429(2002)128:1(117).

[35] Clare E Reimers et al. “Benthic oxygen consumption rates during hypoxic conditions on the Oregon continental shelf: Evaluation of the eddy correlation method”. In: *Journal of Geophysical Research* 117.C2 (Feb. 2012), p. C02021. ISSN: 0148-0227. DOI: 10.1029/2011JC007564. URL: http://doi.wiley.com/10.1029/2011JC007564.

[36] Miles G. McPhee. “Turbulent heat flux in the upper ocean under sea ice”. In: *Journal of Geophysical Research* 97.C4 (Apr. 1992), p. 5365. ISSN: 0148-0227. DOI: 10.1029/92JC00239. URL: http://doi.wiley.com/10.1029/92JC00239.

[37] W. J Shaw and J. H Trowbridge. “The Direct Estimation of Near-Bottom Turbulent Fluxes in the Presence of Energetic Wave Motions”. In: *Journal of Atmospheric and Oceanic Technology* 18.9 (Sept. 2001), pp. 1540–1557. ISSN: 0739-0572. DOI: 10.1175/1520-0426(2001)018<1540:TDEONB>2.0.CO;2. URL: http://journals.ametsoc.org/doi/abs/10.1175/1520-0426%7B%5C%%7D282001%7B%5C%%7D29018%7B%5C%%7D3C1540%7B%5C%%7D3ATDEONB%7B%5C%%7D3E2.0.CO%7B%5C%%7D3B2.

[38] Ann E. Gargett et al. “Mixing Efficiencies in Turbulent Tidal Fronts: Results from Direct and Indirect Measurements of Density Flux”. In: *Journal of Physical Oceanography* 25.11 (Nov. 1995), pp. 2583–2608. ISSN: 0022-3670. DOI: 10.1175/1520-0485(1995)025<2583:MEITTF>2.0.CO;2. URL: http://journals.ametsoc.org/doi/abs/10.1175/1520-0485%7B%5C%%7D281995%7B%5C%%7D29025%7B%5C%%7D3C2583%7B%5C%%7D3AMEITTF%7B%5C%%7D3E2.0.CO%7B%5C%%7D3B2.

[39] James N Moum. “Energy-containing scales of turbulence in the ocean thermocline”. In: *Journal of Geophysical Research: Oceans* 101.C6 (June 1996), pp. 14095–14109. ISSN: 01480227. DOI: 10.1029/96JC00507. URL: http://doi.wiley.com/10.1029/96JC00507.

[40] Daniel F McGinnis et al. “Measurements of eddy correlation oxygen fluxes in shallow freshwaters: Towards routine applications and analysis”. In: *Geophysical Research Letters* 35.4 (Feb. 2008), p. L04403. ISSN: 0094-8276. DOI: 10.1029/2007GL032747. URL: http://doi.wiley.com/10.1029/2007GL032747.

[41] William J. Emery and Richard E. Thomson. *Data analysis methods in physical oceanography*. Second. Amsterdam: Elsevier, 2004, pp. 422–423. ISBN: 0-444-50756-6.

[42] Andreas Lorke, Daniel F McGinnis, and A. Maeck. “Eddy-correlation measurements of benthic fluxes under complex flow conditions: Effects of coordinate transformations and averaging time scales”. In: *Limnology and Oceanography: Methods* 11 (2013), pp. 425–437. ISSN: 15415856. DOI: 10.4319/lom.2013.11.425. URL: http://www.aslo.org/lomethods/free/2013/0425.html.

[43] Xuhui Lee, John Finnigan, and Kyaw Tha Paw U. “Coordinate Systems and Flux Bias Error”. In: *Handbook of Micrometeorology*. Ed. by Xuhui Lee, William Massman, and Beverly Law. Vol. 29. Atmospheric and Oceanographic Sciences Library. Dordrecht: Kluwer Academic Publishers, 2005. Chap. 3, pp. 33–66. ISBN: 978-1-4020-2265-4. DOI: 10.1007/1-4020-2265-4_3. URL: http://link.springer.com/10.1007/1-4020-2265-4%7B%5C_%7D3.

[44] Jeremy D. Bricker et al. “Spectral Wave,ÄìTurbulence Decomposition”. In: *Journal of Atmospheric and Oceanic Technology* 24.8 (Aug. 2007), pp. 1479–1487. ISSN: 0739-0572. DOI: 10.1175/JTECH2066.1. URL: http://journals.ametsoc.org/doi/abs/10.1175/JTECH2066.1.

[45] John Finnigan et al. “A Re-Evaluation of Long-Term Flux Measurement Techniques Part I: Averaging and Coordinate Rotation.” In: *Boundary-Layer Meteorology* 107.1 (2003). ISSN: 0006-8314.

[46] James M. Wilczak, Steven P. Oncley, and Steven A. Stage. “Sonic Anemometer Tilt Correction Algorithms”. en. In: *Boundary-Layer Meteorology* 99.1 (2001), pp. 127–150. ISSN: 00068314. DOI: 10.1023/A:1018966204465. URL: http://link.springer.com/article/10.1023/A:1018966204465%20http://link.springer.com/10.1023/A:1018966204465.

[47] John Finnigan. “A Re-Evaluation of Long-Term Flux Measurement Techniques Part II: Coordinate Systems”. In: *Boundary-Layer Meteorology* 113.1 (Oct. 2004), pp. 1–41. ISSN: 0006-8314. DOI: 10.1023/B:BOUN.0000037348.64252.45. URL: http://link.springer.com/10.1023/B:BOUN.0000037348.64252.45.

[48] P. Berg et al. “Technical note: Time lag correction of aquatic eddy covariance data measured in the presence of waves”. In: *Biogeosciences* 12.22 (Nov. 2015), pp. 6721–6735. DOI: 10.5194/bg-12-6721-2015. URL: http://www.biogeosciences.net/12/6721/2015/.

[49] Kristina McCann-Grosvenor, Clare E. Reimers, and Rhea D. Sanders. "Dynamics of the benthic boundary layer and seafloor contributions to oxygen depletion on the Oregon inner shelf". In: *Continental Shelf Research* 84 (Aug. 2014), pp. 93–106. ISSN: 02784343. DOI: 10.1016/j.csr.2014.05.010. URL: http://www.sciencedirect.com/science/article/pii/S0278434314001915.

[50] T. W. Horst. "On Frequency Response Corrections for Eddy Covariance Flux Measurements". In: *Boundary-Layer Meteorology* 94.3 (Mar. 2000), pp. 517–520. DOI: 10.1023/A:1002427517744. URL: http://link.springer.com/10.1023/A:1002427517744.

[51] Moritz Holtappels et al. "Effects of transient bottom water currents and oxygen concentrations on benthic exchange rates as assessed by eddy correlation measurements". In: *Journal of Geophysical Research: Oceans* 118.3 (Mar. 2013), pp. 1157–1169. ISSN: 21699275. DOI: 10.1002/jgrc.20112. URL: http://doi.wiley.com/10.1002/jgrc.20112.

[52] Nortek AS. *Comprehensive Manual*. Tech. rep. 2013.

[53] Andreas Lorke et al. "Effect of ship locking on sediment oxygen uptake in impounded rivers". In: *Water Resources Research* 48.12 (Dec. 2012), n/a–n/a. ISSN: 00431397. DOI: 10.1029/2012WR012483. URL: http://doi.wiley.com/10.1029/2012WR012483.

[54] Andreas Brand et al. "Intermittent oxygen flux from the interior into the bottom boundary of lakes as observed by eddy correlation". In: *Limnology and Oceanography* 53.5 (Sept. 2008), pp. 1997–2006. ISSN: 00243590. DOI: 10.4319/lo.2008.53.5.1997. URL: http://www.aslo.org/lo/toc/vol%7B%5C_%7D53/issue%7B%5C_%7D5/1997.html%20http://doi.wiley.com/10.4319/lo.2008.53.5.1997.

[55] Andrew C Hume, Peter Berg, and Karen J McGlathery. "Dissolved oxygen fluxes and ecosystem metabolism in an eelgrass (Zostera marina) meadow measured with the eddy correlation technique". In: *Limnology and Oceanography* 56.1 (2011), pp. 86–96. ISSN: 00243590. DOI: 10.4319/lo.2011.56.1.0086. URL: http://www.aslo.org/lo/toc/vol%7B%5C_%7D56/issue%7B%5C_%7D1/0086.html.

[56] Matthew H Long et al. "In situ coral reef oxygen metabolism: an eddy correlation study." In: *PloS one* 8.3 (Jan. 2013), e58581. ISSN: 1932-6203. DOI: 10.1371/journal.pone.0058581. URL: http://www.pubmedcentral.nih.gov/articlerender.fcgi?artid=3594154%7B%5C&%7Dtool=pmcentrez%7B%5C&%7Drendertype=abstract.

[57] Matthew A. Reidenbach et al. "Hydrodynamics of intertidal oyster reefs: The influence of boundary layer flow processes on sediment and oxygen exchange". In: *Limnology and Oceanography: Fluids and Environments* 3.1 (Feb. 2013), pp. 225–239. ISSN: 21573689. DOI: 10.1215/21573689-2395266. URL: http://doi.wiley.com/10.1215/21573689-2395266.

[58] Kunio Shirasawa, R. Grant Ingram, and Eric J.-J. Hudier. "Oceanic heat fluxes under thin sea ice in Saroma-ko Lagoon, Hokkaido, Japan". In: *Journal of Marine Systems* 11.1-2 (Feb. 1997), pp. 9–19. ISSN: 09247963. DOI: 10.1016/S0924-7963(96)00023-1. URL: https://www.sciencedirect.com/science/article/pii/S0924796396000231%20http://linkinghub.elsevier.com/retrieve/pii/S0924796396000231.

[59] Matthew H Long et al. “Oxygen exchange and ice melt measured at the ice-water interface by eddy correlation”. In: *Biogeosciences* 9.6 (June 2012), pp. 1957–1967. ISSN: 1726-4189. DOI: 10.5194/bg-9-1957-2012. URL: http://www.biogeosciences.net/9/1957/2012/.

[60] Julika Kreling et al. “Physical controls of oxygen fluxes at pelagic and benthic oxyclines in a lake”. In: *Limnology and Oceanography* 59.5 (Sept. 2014), pp. 1637–1650. ISSN: 00243590. DOI: 10.4319/lo.2014.59.5.1637. URL: http://doi.wiley.com/10.4319/lo.2014.59.5.1637.

[61] Peter Berg and Michael L. Pace. “Continuous measurement of air,Äìwater gas exchange by underwater eddy covariance”. In: *Biogeosciences* 14.23 (Dec. 2017), pp. 5595–5606. ISSN: 1726-4189. DOI: 10.5194/bg-14-5595-2017. URL: https://www.biogeosciences.net/14/5595/2017/.

[62] Moritz Holtappels et al. “Aquatic Eddy Correlation: Quantifying the Artificial Flux Caused by Stirring-Sensitive O2 Sensors”. In: *PLOS ONE* 10.1 (Jan. 2015), e0116564. ISSN: 1932-6203. DOI: 10.1371/journal.pone.0116564. URL: http://journals.plos.org/plosone/article?id=10.1371/journal.pone.0116564%20http://dx.plos.org/10.1371/journal.pone.0116564.

[63] Michael P Swett. “Assessment of Benthic Flux of Dissolved Organic Carbon in Estuaries Using the Eddy Correlation Technique”. PhD thesis. 2010.

[64] Bruno J. Lemaire, Christian Noss, and Andreas Lorke. “Toward relaxed eddy accumulation measurements of sediment-water exchange in aquatic ecosystems”. In: *Geophysical Research Letters* 44.17 (Sept. 2017), pp. 8901–8909. ISSN: 00948276. DOI: 10.1002/2017GL074625. URL: http://doi.wiley.com/10.1002/2017GL074625.

[65] Jason B Fellman, Eran Hood, and Robert G M Spencer. “Fluorescence spectroscopy opens new windows into dissolved organic matter dynamics in freshwater ecosystems: A review”. In: *Limnology and Oceanography* 55.6 (Nov. 2010), pp. 2452–2462. ISSN: 0024-3590. DOI: 10.4319/lo.2010.55.6.2452.

[66] Eric N. Partch and J. Dungan Smith. “Time dependent mixing in a salt wedge estuary”. In: *Estuarine and Coastal Marine Science* 6.1 (Jan. 1978), pp. 3–19. ISSN: 03023524. DOI: 10.1016/0302-3524(78)90038-5. URL: https://www.sciencedirect.com/science/article/pii/0302352478900385?via%7B%5C%%7D3Dihub%20http://linkinghub.elsevier.com/retrieve/pii/0302352478900385.

[67] James N Moum. “Quantifying Vertical Fluxes from Turbulence in the Ocean”. In: *Oceanography* 10.3 (1997), pp. 111–115. ISSN: 10428275. DOI: 10.5670/oceanog.1997.02. URL: https://tos.org/oceanography/article/quantifying-vertical-fluxes-from-turbulence-in-the-ocean.

[68] L Mahrt and Jean-Claude André. “On the stratification of turbulent mixed layers”. In: *Journal of Geophysical Research* 88.C4 (1983), p. 2662. ISSN: 0148-0227. DOI: 10.1029/JC088iC04p02662. URL: http://doi.wiley.com/10.1029/JC088iC04p02662.

[69] Miles G McPhee. “A rigid, cable-lowered instrument frame for measuring turbulence and internal waves in the Arctic”. In: *IEEE Journal of Oceanic Engineering* 14.2 (Apr. 1989), pp. 203–207. DOI: 10.1109/48.16834. URL: http://ieeexplore.ieee.org/document/16834/.

[70] Linda Jorgensen et al. "Global trends in the fluorescence characteristics and distribution of marine dissolved organic matter". In: *Marine Chemistry* 126.1-4 (Sept. 2011), pp. 139–148. ISSN: 0304-4203. DOI: 10.1016/j.marchem.2011.05.002.

[71] Bryan D Downing et al. "Quantifying fluxes and characterizing compositional changes of dissolved organic matter in aquatic systems in situ using combined acoustic and optical measurements". In: *Limnology and Oceanography-Methods* 7 (Jan. 2009), pp. 119–131. ISSN: 1541-5856.

[72] Luca Bracchini et al. "Spatial and seasonal changes in optical properties of autochthonous and allochthonous chromophoric dissolved organic matter in a stratified mountain lake." In: *Photochemical & photobiological sciences : Official journal of the European Photochemistry Association and the European Society for Photobiology* 9.3 (Mar. 2010), pp. 304–14. ISSN: 1474-9092. DOI: 10.1039/b9pp00129h. URL: http://www.ncbi.nlm.nih.gov/pubmed/20221456.

[73] Colin A Stedmon, Stiig Markager, and Rasmus Bro. "Tracing dissolved organic matter in aquatic environments using a new approach to fluorescence spectroscopy". In: *Marine Chemistry* 82.3-4 (Aug. 2003), pp. 239–254. ISSN: 0304-4203. DOI: 10.1016/S0304-4203(03)00072-0.

[74] Kathleen R Murphy et al. "Measurement of Dissolved Organic Matter Fluorescence in Aquatic Environments: An Interlaboratory Comparison". In: *Environmental science & technology* 44.24 (Dec. 2010), pp. 9405–9412. ISSN: 0013-936X. DOI: 10.1021/es102362t.

[75] ThermoFisher Scientific. *Fluorescent Probes*. URL: https://www.thermofisher.com/us/en/home/life-science/protein-biology/protein-biology-learning-center/protein-biology-resource-library/pierce-protein-methods/fluorescent-probes.html (visited on 01/03/2018).

[76] Diana Wong. *Fluorescence and Phosphorescence*. 2017. URL: https://chem.libretexts.org/Core/Physical%7B%5C_%7Dand%7B%5C_%7DTheoretical%7B%5C_%7DChemistry/Spectroscopy/Electronic%7B%5C_%7DSpectroscopy/Fluorescence%7B%5C_%7Dand%7B%5C_%7DPhosphorescence (visited on 01/02/2018).

[77] Tomas Persson and Margareta Wedborg. "Multivariate evaluation of the fluorescence of aquatic organic matter". In: *Analytica Chimica Acta* 434.2 (May 2001), pp. 179–192. ISSN: 00032670. DOI: 10.1016/S0003-2670(01)00812-1. URL: http://www.sciencedirect.com/science/article/pii/S0003267001008121%20http://linkinghub.elsevier.com/retrieve/pii/S0003267001008121.

[78] Qun Gu and Jonathan E Kenny. "Improvement of inner filter effect correction based on determination of effective geometric parameters using a conventional fluorimeter." In: *Analytical chemistry* 81.1 (Jan. 2009), pp. 420–6. ISSN: 1520-6882. DOI: 10.1021/ac801676j. URL: http://www.ncbi.nlm.nih.gov/pubmed/19063673.

[79] Giovanni M Ferrari. "The relationship between chromophoric dissolved organic matter and dissolved organic carbon in the European Atlantic coastal area and in the West Mediterranean Sea (Gulf of Lions)". In: *Marine Chemistry* 70.4 (June 2000), pp. 339–357. ISSN: 03044203. DOI: 10.1016/S0304-4203(00)00036-0. URL: http://linkinghub.elsevier.com/retrieve/pii/S0304420300000360.

[80] Paula G Coble. "Characterization of marine and terrestrial DOM in seawater using excitation-emission matrix spectroscopy". In: *Marine Chemistry* 51.4 (Jan. 1996), pp. 325–346. ISSN: 03044203. DOI: 10.1016/0304-4203(95)00062-3. URL: http://linkinghub.elsevier.com/retrieve/pii/0304420395000623.

[81] Y Yamashita and E Tanoue. "Chemical characterization of protein-like fluorophores in DOM in relation to aromatic amino acids". In: *Marine Chemistry* 82.3-4 (Aug. 2003), pp. 255–271. ISSN: 0304-4203. DOI: 10.1016/S0304-4203(03)00073-2.

[82] F J Stevenson. *Humus Chemistry: Genesis, Composition, Reactions*. New York: John Wiley & Sons, 1982, p. 443.

[83] International Humic Substances Society. *What are Humic Substances?* 2017. URL: http://humic-substances.org/ (visited on 03/19/2018).

[84] Roberto Baigorri et al. "Complementary multianalytical approach to study the distinctive structural features of the main humic fractions in solution: gray humic acid, brown humic acid, and fulvic acid." In: *Journal of agricultural and food chemistry* 57.8 (Apr. 2009), pp. 3266–72. ISSN: 1520-5118. DOI: 10.1021/jf8035353. URL: http://www.ncbi.nlm.nih.gov/pubmed/19281175.

[85] Newell R. Washburn. *Lignin*. 2015. URL: http://www.chem.cmu.edu/groups/washburn/res-lignin.html (visited on 01/03/2018).

[86] M.M.D Sierra et al. "Fluorescence and DOC contents of pore waters from coastal and deep-sea sediments in the Gulf of Biscay". In: *Organic Geochemistry* 32.11 (Nov. 2001), pp. 1319–1328. ISSN: 01466380. DOI: 10.1016/S0146-6380(01)00100-0. URL: http://apps.webofknowledge.com/full%7B%5C_%7Drecord.do?product=UA%7B%5C&%7Dsearch%7B%5C_%7Dmode=GeneralSearch%7B%5C&%7Dqid=17%7B%5C&%7DSID=2DnQok36THZcOHEhtTx%7B%5C&%7Dpage=1%7B%5C&%7Ddoc=2.

[87] R K Henderson et al. "Fluorescence as a potential monitoring tool for recycled water systems: A review". In: *Water research* 43.4 (Mar. 2009), pp. 863–881. ISSN: 0043-1354. DOI: 10.1016/j.watres.2008.11.027.

[88] Marc Tedetti, Catherine Guigue, and Madeleine Goutx. "Utilization of a submersible UV fluorometer for monitoring anthropogenic inputs in the Mediterranean coastal waters". In: *Marine pollution bulletin* 60.3 (Mar. 2010), pp. 350–362. ISSN: 0025-326X. DOI: 10.1016/j.marpolbul.2009.10.018.

[89] Jason E Dickens et al. "An LED array-based light induced fluorescence sensor for real-time process and field monitoring". In: *Sensors and Actuators B-Chemical* 158.1 (Nov. 2011), pp. 35–42. ISSN: 0925-4005. DOI: 10.1016/j.snb.2011.04.077.

[90] Mohd N Taib and Ramaier Narayanaswamy. "Solid-state instruments for optical fibre chemical sensors. A review". In: *The Analyst* 120.6 (1995), p. 1617. ISSN: 0003-2654. DOI: 10.1039/an9952001617. URL: http://xlink.rsc.org/?DOI=an9952001617.

[91] Eric Udd. "An Overview of Fiberoptic Sensors". In: *Review of Scientific Instruments* 66.8 (Aug. 1995), pp. 4015–4030. ISSN: 0034-6748. DOI: 10.1063/1.1145411.

[92] Colette McDonagh, Conor S Burke, and Brian D MacCraith. "Optical chemical sensors". In: *Chemical reviews* 108.2 (Feb. 2008), pp. 400–22. ISSN: 0009-2665. DOI: 10.1021/cr068102g. URL: http://www.ncbi.nlm.nih.gov/pubmed/18229950.

[93] Matthias I J Stich, Lorenz H Fischer, and Otto S Wolfbeis. "Multiple fluorescent chemical sensing and imaging." In: *Chemical Society reviews* 39.8 (Aug. 2010), pp. 3102–14. ISSN: 1460-4744. DOI: 10.1039/b909635n. URL: http://www.ncbi.nlm.nih.gov/pubmed/20571676.

[94] Luis Fermín Capitán-Vallvey and Alberto J Palma. "Recent developments in handheld and portable optosensing-a review." In: *Analytica chimica acta* 696.1-2 (June 2011), pp. 27–46. ISSN: 1873-4324. DOI: 10.1016/j.aca.2011.04.005. URL: http://www.ncbi.nlm.nih.gov/pubmed/21621030.

[95] Mark A Arnold. "Fiber optic chemical sensors". In: *Analytical Chemistry* 64.21 (Nov. 1992), 1015A–1025A. ISSN: 0003-2700. DOI: 10.1021/ac00045a001. URL: http://pubs.acs.org/doi/abs/10.1021/ac00045a001.

[96] Peter C Hauser and Susie S S Tan. "All-solid-state instrument for fluorescence-based fibre-optic chemical sensors". In: *The Analyst* 118.8 (1993), p. 991. ISSN: 0003-2654. DOI: 10.1039/an9931800991. URL: http://xlink.rsc.org/?DOI=an9931800991.

[97] N Benaim, K T V Grattan, and A W Palmer. "Simple Fiber Optic Ph Sensor for use in Liquid Titrations". In: *Analyst* 111.9 (Sept. 1986), pp. 1095–1097. ISSN: 0003-2654. DOI: 10.1039/an9861101095.

[98] Peter J Rusello. *TN-027: A Practical Primer for Pulse Coherent Instruments A Practical Primer for Pulse Coherent Instruments*. Tech. rep. NortekUSA, 2009. URL: https://www.nortekgroup.com/assets/documents/A-Practical-Primer-for-Pulse-Coherent-Instruments.pdf.

[99] Nortek AS. *Principles of Operation: Acoustic Doppler Velocimeters*. 2009. URL: http://www.nortekusa.com/usa/knowledge-center/table-of-contents/velocimeters (visited on 09/09/2015).

[100] C. M. Poindexter, P. J. Rusello, and E. A. Variano. "Acoustic Doppler velocimeter-induced acoustic streaming and its implications for measurement". In: *Experiments in Fluids* 50.5 (May 2011), pp. 1429–1442. ISSN: 0723-4864. DOI: 10.1007/s00348-010-1001-2. URL: http://link.springer.com/10.1007/s00348-010-1001-2.

[101] Nortek AS. *FAQ*. 2018. URL: https://www.nortekgroup.com/faq/ (visited on 02/28/2018).

[102] NortekAS. *Nortek Forum*. URL: http://www.nortek.no/en/knowledge-center/forum (visited on 11/16/2015).

[103] Radiometer Analytical SAS. *Conductivity Theory and Practice*. Tech. rep. Lyon, 2010. URL: http://www.analytical-chemistry.uoc.gr/files/items/6/618/agwgimometria%7B%5C_%7D2.pdf.

[104] Jenway. *AN A02-001A: The effect of temperature on conductivity measurement*. Tech. rep. Bibby Scientific, 2009. URL: http://www.jenway.com/adminimages/A02%7B%5C_%7D001A%7B%5C_%7DEffect%7B%5C_%7Dof%7B%5C_%7Dtemperature%7B%5C_%7Don%7B%5C_%7Dconductivity.pdf.

[105] Rich Pawlowicz. "Key Physical Variables in the Ocean: Temperature, Salinity, and Density | Learn Science at Scitable". In: *Nature Education Knowledge* 4.4 (2013), p. 13. URL: https://www.nature.com/scitable/knowledge/library/key-physical-variables-in-the-ocean-temperature-102805293.

[106] Fondriest Environmental Inc. *Conductivity, Salinity and Total Dissolved Solids*. 2014. URL: http://www.fondriest.com/environmental-measurements/parameters/water-quality/conductivity-salinity-tds/ (visited on 07/06/2017).

[107] Francisco Souza Dias. *Salinity sensors*. 2013. URL: http://www.marbef.org/wiki/Salinity%7B%5C_%7Dsensors (visited on 01/20/2018).

[108] Frank J Millero. "What is PSU?" In: *Oceanography* 6.3 (1993), p. 67.

[109] Frank J Millero. "History of the Equation of State of Seawater". In: *Oceanography* 23.3 (2010), pp. 18–33. URL: http://www.teos-10.org/pubs/Millero%7B%5C_%7DHistory%7B%5C_%7DEOS.pdf.

[110] Clean Water Team (CWT). "Electrical conductivity/salinity Fact Sheet". In: *The Clean Water Team Guidance Compendium for Watershed Monitoring and Assessment*. 2nd ed. Sacramento, CA: Division of Water Quality, California State Water Resources Control Board (SWRCB), 2004. URL: https://www.waterboards.ca.gov/water%7B%5C_%7Dissues/programs/swamp/docs/cwt/guidance/3130en.pdf.

[111] Zbigniew Moroń. "Considerations on the Accuracy of Measurements of Electrical Conductivity of Liquids". In: *XVIII Imeko World Congress* 2 (2006), pp. 17–22. URL: http://citeseerx.ist.psu.edu/viewdoc/download?doi=10.1.1.521.5188%7B%5C&%7Drep=rep1%7B%5C&%7Dtype=pdf.

[112] Paul Ben Ishai et al. "Electrode polarization in dielectric measurements: a review". In: *Measurement Science and Technology* 24.10 (Oct. 2013), p. 102001. ISSN: 0957-0233. DOI: 10.1088/0957-0233/24/10/102001. URL: http://stacks.iop.org/0957-0233/24/i=10/a=102001?key=crossref.9efe09e2e85ae2736ef0a0951a223501.

[113] H. P. Schwan. "Electrode Polarization Impedance and Measurements in Biological Materials". In: *Annals of the New York Academy of Sciences* 148.1 Bioelectrodes (Feb. 1968), pp. 191–209. ISSN: 0077-8923. DOI: 10.1111/j.1749-6632.1968.tb20349.x. URL: http://doi.wiley.com/10.1111/j.1749-6632.1968.tb20349.x.

[114] N. G. Green et al. "Fluid flow induced by nonuniform ac electric fields in electrolytes on microelectrodes. I.,ÄÉExperimental measurements". In: *Physical Review E* 61.4 (Apr. 2000), pp. 4011–4018. ISSN: 1063-651X. DOI: 10.1103/PhysRevE.61.4011. URL: https://link.aps.org/doi/10.1103/PhysRevE.61.4011.

[115] John J Barron and Colin Ashton. *The Effect of Temperature on Conductivity Measurement*. Tech. rep. 3. Reagecon Diagnostics Ltd, 2007. URL: https://www.reagecon.com/pdf/technicalpapers/Effect%7B%5C_%7Dof%7B%5C_%7DTemperature%7B%5C_%7DTSP-07%7B%5C_%7DIssue3.pdf.

[116] Nick Davis. *Introduction to Temperature Sensors: Thermistors, Thermocouples, RTDs, and Thermometer ICs*. 2017. URL: https://www.allaboutcircuits.com/technical-articles/introduction-temperature-sensors-thermistors-thermocouples-thermometer-ic/ (visited on 01/23/2018).

[117] ResistorGuide. *NTC thermistor*. 2012. URL: http://www.resistorguide.com/ntc-thermistor/ (visited on 04/22/2016).

[118] EPCOS AG. *NTC Thermistors Application notes*. Tech. rep. March. TDK, 2013. URL: https://en.tdk.eu/download/531110/a3be527165c9dd17abca4970f507014f/pdf-applicationnotes.pdf.

[119] John Bishop. *SLOA052: Thermistor Temperature Transducer to ADC Application*. Tech. rep. September. Texas Instruments, 2000, pp. 1–9. URL: http://www.ti.com.cn/cn/lit/an/sloa052/sloa052.pdf.

[120] Bonnie Baker. *AN685: Thermistors in Single Supply Temperature Sensing Circuits*. Tech. rep. Microchip Technology, 1999. URL: http://ww1.microchip.com/downloads/en/AppNotes/00685b.pdf.

[121] W.C. Burnett et al. "Quantifying submarine groundwater discharge in the coastal zone via multiple methods". In: *Science of The Total Environment* 367.2-3 (Aug. 2006), pp. 498–543. ISSN: 0048-9697. DOI: 10.1016/J.SCITOTENV.2006.05.009. URL: https://www.sciencedirect.com/science/article/pii/S0048969706003445.

[122] C.A. McCoy and D.R. Corbett. "Review of submarine groundwater discharge (SGD) in coastal zones of the Southeast and Gulf Coast regions of the United States with management implications". In: *Journal of Environmental Management* 90.1 (Jan. 2009), pp. 644–651. ISSN: 0301-4797. DOI: 10.1016/J.JENVMAN.2008.03.002. URL: https://www.sciencedirect.com/science/article/pii/S0301479708000881.

[123] Thomas Stieglitz, Makoto Taniguchi, and Skyler Neylon. "Spatial variability of submarine groundwater discharge, Ubatuba, Brazil". In: *Estuarine, Coastal and Shelf Science* 76.3 (Feb. 2008), pp. 493–500. ISSN: 02727714. DOI: 10.1016/j.ecss.2007.07.038. URL: https://www.sciencedirect.com/science/article/pii/S0272771407003125.

[124] S. Otto and W. Balzer. "Release of dissolved organic carbon (DOC) from sediments of the N.W. European Continental Margin (Goban Spur) and its significance for benthic carbon cycling". In: *Progress in Oceanography* 42.1-4 (Dec. 1998), pp. 127–144. ISSN: 00796611. DOI: 10.1016/S0079-6611(98)00031-7. URL: https://www.sciencedirect.com/science/article/pii/S0079661198000317.

[125] Yu Ping Chin and Philip M Gschwend. "Partitioning of polycyclic aromatic hydrocarbons to marine porewater organic colloids". In: *Environmental Science & Technology* 26.8 (Aug. 1992), pp. 1621–1626. ISSN: 0013-936X. DOI: 10.1021/es00032a020. URL: http://apps.webofknowledge.com/full%7B%5C_%7Drecord.do?product=UA%7B%5C&%7Dsearch%7B%5C_%7Dmode=GeneralSearch%7B%5C&%7Dqid=32%7B%5C&%7DSID=2DnQok36THZcOHEhtTx%7B%5C&%7Dpage=1%7B%5C&%7Ddoc=4.

[126] Liping Weng et al. "Complexation with dissolved organic matter and solubility control of heavy metals in a sandy soil". In: *Environmental Science and Technology* 36.22 (2002), pp. 4804–4810. ISSN: 0013936X. DOI: 10.1021/es0200084. URL: http://pubs.acs.org/doi/abs/10.1021/es0200084.

[127] Diana Nara Ribeiro de Sousa et al. "Electrical conductivity and emerging contaminant as markers of surface freshwater contamination by wastewater." In: *The Science of the total environment* 484 (July 2014), pp. 19–26. ISSN: 1879-1026. DOI: 10.1016/j.scitotenv.2014.02.135. URL: http://apps.webofknowledge.com/full%7B%5C_%7Drecord.do?product=UA%7B%5C&%7Dsearch%7B%5C_%7Dmode=GeneralSearch%7B%5C&%7Dqid=26%7B%5C&%7DSID=2DnQok36THZcOHEhtTx%7B%5C&%7Dpage=1%7B%5C&%7Ddoc=1%20http://www.ncbi.nlm.nih.gov/pubmed/24686141.

[128] Moritz Holtappels and Andreas Lorke. "Estimating turbulent diffusion in a benthic boundary layer". In: *Limnology and Oceanography-Methods* 9 (2011), pp. 29–41. ISSN: 1541-5856. DOI: 10.4319/lom.2010.9.29. URL: http://apps.webofknowledge.com/full%7B%5C_%7Drecord.do?product=UA%7B%5C&%7Dsearch%7B%5C_%7Dmode=GeneralSearch%7B%5C&%7Dqid=3%7B%5C&%7DSID=4ELaaYCTeIgIt6aiQZv%7B%5C&%7Dpage=1%7B%5C&%7Ddoc=2.

[129] Raspberry Pi Foundation. *Raspberry Pi*. 2017. URL: https://www.raspberrypi.org/ (visited on 07/28/2015).

[130] Nicholas Marriott. *tmux*. 2017. URL: https://github.com/tmux/tmux.

[131] ORTEC. *AN51: Pulse-Processing Electronics for Single-Photon Counting*. Tech. rep. ORTEC, 2000. URL: http://www.ortec-online.com/library/index.aspx.

[132] C C Garrard. *RP096: Practical photon counting*. Tech. rep. ET Enterprises, 2011.

[133] Burle Industries. *Photomultiplier Handbook*. 1980. URL: http://psec.uchicago.edu/links/Photomultiplier%7B%5C_%7DHandbook.pdf.

[134] Photonis imaging sensors. *Photomultiplier tubes basics*. Tech. rep. 2005. URL: http://particle.korea.ac.kr/lab/cata%7B%5C_%7Dbasic.pdf.

[135] Hamamatsu Photonics. *Photomultiplier Tubes: Basics and Applications*. 3a. 2007. URL: https://www.hamamatsu.com/resources/pdf/etd/PMT%7B%5C_%7Dhandbook%7B%5C_%7Dv3aE.pdf.

[136] ET Enterprises. *RP069: Voltage Divider Design*. Tech. rep. 2011. URL: http://www.et-enterprises.com/files/file/technical-information/rp069%7B%5C_%7Dvoltage%20divider%20design.pdf.

[137] Jefferson Eco and Aldrick Limjoco. *AN1368: Ferrite Bead Demystified*. Tech. rep. Analog Devices, 2015. URL: http://www.analog.com/media/en/technical-documentation/application-notes/AN-1368.pdf.

[138] Chris Burket. "All Ferrite Beads Are Not Created Equal". In: *In Compliance* (Aug. 2010), p. 7. URL: https://incompliancemag.com/article/all-ferrite-beads-are-not-created-equal-understanding-the-importance-of-ferrite-bead-material-behavior/.

[139] Alexander Weiler and Alexander Pakosta. *SCAA082: High-Speed Layout Design*. Tech. rep. Texas Instruments, 2006. URL: http://www.ti.com/lit/an/scaa082a/scaa082a.pdf.

[140] H. Ward Silver. "The Myth of the RF Ground". In: *QST* (2015), pp. 63–64.

[141] Jim Brown. *Understanding How Ferrites Can Prevent and Eliminate RF Interference to Audio Systems*. Tech. rep. Audio Systems Group, Inc., 2005. URL: http://audiosystemsgroup.com/SAC0305Ferrites.pdf.

[142] Maxim Integrated. *Tutorial 2045: Understanding Common-Mode Signals*. Tech. rep. 2003. URL: https://www.maximintegrated.com/en/app-notes/index.mvp/id/2045.

[143] Hank Zumbahlen. "Staying Well Grounded". In: *Analog Dialog* 46.06 (2012). URL: http://www.analog.com/en/analog-dialogue/articles/staying-well-grounded.html.

[144] Tim Williams. "The ground plane: Lord of the Board". In: *EMC Journal* 72 (2007). URL: http://www.elmac.co.uk/Lord%7B%5C_%7Dof%7B%5C_%7Dthe%7B%5C_%7Dboard.pdf.

[145] Henry Ott. *Tech Tips*. 2002. URL: http://www.hottconsultants.com/tips.html (visited on 08/07/2016).

[146] David B Fancher. *ILB, ILBB Ferrite Beads: Electro-Magnetic Interference and Electro-Magnetic Compatibility*. Tech. rep. Vishay Dale, 1999. URL: https://www.vishay.com/docs/34097/ferritenote.pdf.

[147] Wolfgang Becker and Axel Bergmann. *Detectors for High-Speed Photon Counting*. Tech. rep. Berlin: Becker & Hickl GmbH, 2018. URL: https://www.becker-hickl.com/pdf/spcdetect1.pdf.

[148] Samuel W. Hasinoff. "Photon, Poisson Noise". In: *Computer Vision*. Boston, MA: Springer US, 2014, pp. 608–610. DOI: 10.1007/978-0-387-31439-6_482. URL: http://link.springer.com/10.1007/978-0-387-31439-6%7B%5C_%7D482.

[149] Spectral Products. *Digikröm CM110/CM112 Monochromator / Spectrograph*. Tech. rep. 2006.

[150] Paul J Stoffregen. *Teensy Technical Specifications*. 2017. URL: https://www.pjrc.com/teensy/techspecs.html (visited on 04/21/2017).

[151] Btmcmahan. *Teensy 3.0 SPI Master & Slave*. 2013.

[152] Michael Ben Eck. "Fast Conductivity Sensor for Eddy Correlation Measurement of Benthic Fluxes". Undergraduate. Massachusetts Institute of Technology, 2015, p. 28.

[153] Wayne Storr. *Wien Bridge Oscillator Tutorial and Theory*. 2014. URL: http://www.electronics-tutorials.ws/oscillator/wien%7B%5C_%7Dbridge.html (visited on 05/04/2017).

[154] Ting Ye. *TIDU030: Precision Full-Wave Rectifier, Dual-Supply*. Tech. rep. Texas Instruments, 2013, p. 24. URL: http://www.ti.com/lit/ug/tidu030/tidu030.pdf.

[155] James Lewis. *Understanding Ceramic's Capacitance Over Temperature Performance*. 2016. URL: https://ec.kemet.com/understand-ceramics-capacitance-over-temperature (visited on 03/27/2018).

[156] Yadvinder Malhi, Keith McNaughton, and Celso Von Randow. "Low Frequency Atmospheric Transport and Surface Flux Measurements". In: *Handbook of Micrometeorology*. Ed. by Xuhui Lee, William Massman, and Beverly Law. Vol. 29. Atmospheric and Oceanographic Sciences Library. Dordrecht: Kluwer Academic Publishers, 2005. Chap. 5, pp. 101–118. ISBN: 978-1-4020-2265-4. DOI: 10.1007/1-4020-2265-4_5. URL: http://link.springer.com/10.1007/1-4020-2265-4%7B%5C_%7D5.

[157] J. Sievers et al. "Estimating surface fluxes using eddy covariance and numerical ogive optimization". In: *Atmospheric Chemistry and Physics* 15.4 (Feb. 2015), pp. 2081–2103. ISSN: 1680-7324. DOI: 10.5194/acp-15-2081-2015. URL: http://www.atmos-chem-phys.net/15/2081/2015/.

[158] J. H Trowbridge. "On a Technique for Measurement of Turbulent Shear Stress in the Presence of Surface Waves". In: *Journal of Atmospheric and Oceanic Technology* 15.1 (Feb. 1998), pp. 290–298. ISSN: 0739-0572. DOI: 10.1175/1520-0426(1998)015<0290:OATFMO>2.0.CO;2. URL: http://journals.ametsoc.org/doi/abs/10.1175/1520-0426%7B%5C%%7D281998%7B%5C%%7D29015%7B%5C%%7D3C0290%7B%5C%%7D3AOATFMO%7B%5C%%7D3E2.0.CO%7B%5C%%7D3B2.

[159] Claudio Talarico. *Slides taken from: Feedback: Part C ,Äì Oscillators*. 2007. URL: http://web.ewu.edu/groups/technology/Claudio/ee331/Lectures/L8.pdf (visited on 05/04/2017).

[160] ON Semiconductor. *AND9093: Using MOSFETs in Load Switch Applications*. Tech. rep. 2014.

[161] Tim Skovmand. *AN53: Micropower High Side MOSFET Drivers*. Tech. rep. Linear Technology, 1993. URL: http://cds.linear.com/docs/en/application-note/an53.pdf.

[162] Vishay Silconix. *AN804: P-Channel MOSFETs, the Best Choice for High-Side Switching*. Tech. rep. 1997. URL: https://www.vishay.com/docs/70611/70611.pdf.

[163] NXP Semiconductors. *AN11158: Understanding power MOSFET data sheet parameters*. Tech. rep. 2014. URL: https://assets.nexperia.com/documents/application-note/AN11158.pdf.

[164] National Instruments. *Reed Relay Protection*. 2015. URL: http://www.ni.com/white-paper/3953/en/ (visited on 07/26/2016).

[165] Littelfuse. *Sensors: Product Catalog & Design Guide*. Tech. rep. 2015.

[166] MEDER electronic. *Reed Switch Characteristics: Basic Electrical Parameters of Reed Switch Products*. Tech. rep. 2014, pp. 22–29.

[167] Hamlin Inc. *AN108A: Inductive Load Arc Suppression*. Tech. rep. 2013. URL: http://www.hamlin.com/specSheets/AN108A-Inductive-Load-Arc-Suppression.pdf.

[168] EAO AG. *Preventing HMI and Switch Damage from DC Inductive Loads*. Tech. rep. 2014. URL: http://eao.com/fileadmin/documents/PDFs/en/08%7B%5C_%7Dwhitepapers/EAO%7B%5C_%7DTA%7B%5C_%7DHMI-Inductive-loads-and-flyback-voltages%7B%5C_%7DEN.pdf.

[169] Hamlin Inc. *AN107: Capacitive Loads*. Tech. rep. 2007.

[170] EPCOS AG. *NTC Thermistors for Inrush Current Limiting*. Tech. rep. October. TDK, 2013.

[171] Hamlin Inc. *AN104: Reed Switch and Reed Sensor Activation*. 2008. URL: http://www.hamlin.com/specSheets/AN104.pdf (visited on 05/19/2016).

[172] Ken Parker. *Coupling Capacitors*. Tech. rep. IEEE, 2001. URL: http://grouper.ieee.org/groups/1149/6/doc/Coupling%7B%5C_%7DCaps%7B%5C_%7D200104261.pdf.

Appendices

Appendix A

Eddy correlation theory

A.1 Derivation of EC governing equation from conservation of mass

Much of the derivation in this section is based on that presented by Finnigan et al. [45].

A.1.1 Mass conservation at a point

The statement of conservation of mass or energy at a point is given as [42, 45]

$$\frac{\partial c}{\partial t} + \boldsymbol{\nabla} \cdot (\vec{u}c) = \boldsymbol{\nabla} \cdot (D_{\mathrm{M}} \nabla c) + S(\vec{x}, t) \tag{A.1}$$

where $c = c(\vec{x}, t)$ represents the scalar (e.g. concentration, temperature, or conductivity), which is a function of both space and time; $\vec{u} = (u, v, w)$ is a velocity vector corresponding to position vector $\vec{x} = (x, y, z)$; D_{M} is the molecular diffusion coefficient; and $S(\vec{x}, t)$ represents the sum of sources and sinks at that point. Note that the divergence of a vector field represents the volume density of flux emanating from an infinitesimal volume around a point; here, it represents both the 'advective' and 'turbulent' movements of c.

Molecular diffusion can be ignored, as it is negligible except in the diffusive boundary layer very close to the surface. Water column sources and sinks are also often considered negligible [21, 51], so that the S term only has a nonzero value at the sediment-water interface.

A.1.2 Mass conservation in a control volume

Given the presence of fine-scale spatial heterogeneity, we are looking for a (spatial) average flux over a representative patch of surface. Thus, we must integrate over this patch and normalize by the area to arrive at a flux density independent of surface area. In addition, since the water column between the sediment-water interface and the instrument height h is also affected by mass transport processes, we must integrate the mass transport equation to h if we are to arrive at an expression representing what is measured at h.

Following the derivation by Finnigan et al. [45], we use a control volume defined by the axes of a Cartesian coordinate frame[1]. The 'floor' is a square of side length $2L$ with its center at $(0, 0, 0)$, and vertically the volume extends from $z = 0$ (the sediment-water interface) to $z = h$ (measurement height). We are interested in the flux over the representative patch of area $4L^2$ that is the bottom face of the control volume.

The variables in Eq. (A.1) are functions of time as well as space. Given the statistical nature of turbulent transport, any conclusion must represent a (temporal) average over some period of time long enough for the mean to converge; our goal is therefore a time-averaged flux. Averaging in time is an addition operation, and is associative with differentiation and integration, so it can be applied to the argument of any derivative or integral.

Averaging in time, integrating in space, and normalizing by area, yields

$$\int_0^h \left[\frac{1}{4L^2} \int_{-\mathrm{L}}^{L} \int_{-\mathrm{L}}^{L} \overline{\frac{\partial c}{\partial t}} \,\mathrm{d}x \,\mathrm{d}y \right] \mathrm{d}z + \int_0^h \left[\frac{1}{4L^2} \int_{-\mathrm{L}}^{L} \int_{-\mathrm{L}}^{L} \left\{ \frac{\partial \overline{uc}}{\partial x} + \frac{\partial \overline{vc}}{\partial y} \right\} \mathrm{d}x \,\mathrm{d}y \right] \mathrm{d}z + \frac{1}{4L^2} \int_{-\mathrm{L}}^{L} \int_{-\mathrm{L}}^{L} \int_0^h \frac{\partial \overline{wc}}{\partial z} \,\mathrm{d}z \,\mathrm{d}x \,\mathrm{d}y = \frac{1}{4L^2} \int_{-\mathrm{L}}^{L} \int_{-\mathrm{L}}^{L} \overline{S}(x, y, 0) \,\mathrm{d}x \,\mathrm{d}y \quad \text{(A.2)}$$

where the overbar represents average in time. Note that the source term is an area integral evaluated at $z = 0$, since as mentioned above, water column sources and sinks are considered negligible.

The second and third terms on the left hand side of Eq. (A.2) represent the flux divergence terms $\overline{\boldsymbol{\nabla} \cdot (\vec{u}c)} = \partial\overline{uc}/\partial x + \partial\overline{vc}/\partial y + \partial\overline{wc}/\partial z$ broken into horizontal and vertical components. The z term $\partial\overline{wc}/\partial z$ has been rearranged so that the integral over z is computed first, and can be given as

$$\int_0^h \frac{\partial \overline{wc}}{\partial z} \,\mathrm{d}z = \overline{wc}(h) - \overline{wc}(0)$$

If we consider all covariance (and resulting flux) at the sediment-water interface $z = 0$ to be a part of the source term S[2], then $\overline{wc}(z = 0)$ is 0, representing no influx from this term. The third term of Eq. (A.2) then becomes

$$\frac{1}{4L^2} \int_{-\mathrm{L}}^{L} \int_{-\mathrm{L}}^{L} \overline{wc}(x, y, h) \,\mathrm{d}x \,\mathrm{d}y$$

The covariance term $\overline{wc}$ is now an area integral evaluated only at the top boundary of the control volume, and Eq. (A.2) becomes

[1] See Section A.2 for further discussion about coordinate systems.

[2] Solute can enter the water column from sediment porewaters through a variety of mechanisms, including groundwater advection, molecular diffusion, bioturbation, and bioirrigation. Upon entering the benthic boundary layer, turbulent diffusion takes over. In this derivation, we follow Finnigan et al. [45] in considering all of these 'sources' of solute to be part of the term S, which is then the target flux we are trying to measure. This is as opposed to other derivations, e.g. that of Lorrai et al. [21], which neglects S but keeps an eddy diffusion term $\overline{w'c'}(0)$, that is then the target flux to measure. This is a difference in definition only.

$$\int_0^h \left[\frac{1}{A} \iint_{\mathrm{A}} \overline{\frac{\partial c}{\partial t}} \, \mathrm{d}x \, \mathrm{d}y \right] \mathrm{d}z + \int_0^h \left[\frac{1}{A} \iint_{\mathrm{A}} \left\{ \frac{\partial \overline{uc}}{\partial x} + \frac{\partial \overline{vc}}{\partial y} \right\} \mathrm{d}x \, \mathrm{d}y \right] \mathrm{d}z + \frac{1}{A} \iint_{\mathrm{A}} \overline{wc}(x, y, z = h) \, \mathrm{d}x \, \mathrm{d}y = \frac{1}{A} \iint_{\mathrm{A}} \overline{S}(x, y, z = 0) \, \mathrm{d}x \, \mathrm{d}y \quad \text{(A.3)}$$

where the term on the right hand side (integral of S) represents the time-averaged, space-averaged sediment-water exchange from a representative patch of sediment of area $A = 4L^2$.

A.1.3 Simplifying assumptions

In practice, it is not possible to measure all of the terms in Eq. (A.3). Thus, a number of simplifying assumptions must be made so that the sediment-water exchange S can be estimated.

One assumption is that a 'blending height' h_b exists above which horizontal variations of the mean vertical flux are negligible, and that the instrumentation is located at $h > h_\mathrm{b}$; i.e. the mixing power of the turbulent flow is assumed to be an adequate spatial averaging operator [47]. Then, $\overline{wc}(x, y, h) = \overline{wc}(h)$ is a single value, and there is no need to average in space. In addition, we can assume that the flux measured at h represent an average over a representative patch of sediment, which allows $\overline{S}(x, y, 0)$ to also reduce to its area average at $z = 0$ [45]. In practice, the patch of sediment whose flux is measured is an upstream footprint whose size, shape, and location depends on environmental conditions and measuring height [17].

We also assume horizontal homogeneity of the flow field (no horizontal advection of the scalar and no flow divergence), so that the horizontal gradients of $\overline{uc}$ and $\overline{vc}$ disappear. This assumption is valid if the sediment bed is flat and homogeneous [42], but becomes complicated in less ideal conditions. A coordinate system is often chosen to minimize the error from assuming zero horizontal divergence; see Section A.2 for more detailed discussion about coordinate systems. Finally, the term $\overline{\partial c / \partial t}$ also disappears if we assume the flow field is stationary (non-transient), in which case there is no accumulation or loss of c in the control volume.

With these assumptions, Eqn A.3 becomes

$$\begin{aligned} \overline{wc}(h) &= \overline{S} \\ &= \overline{Flux} \end{aligned} \quad \text{(1.1 revisited)}$$

Note that other derivations are sometimes presented that use an infinitesimal-area control volume, as by Finnigan [47] and Lorke, McGinnis, and Maeck [42]. Instead of explaining away the spatial integrals, these derivations account for the fact that we only have measurements at a single point by allowing the area $A = 4L^2$ in Eq. (A.2) to shrink to an infinitesimal $\mathrm{d}x \, \mathrm{d}y$; or, equivalently, by integrating in z only [47]. Equation (A.3) would then be given by

$$\int_0^h \overline{\frac{\partial c}{\partial t}} \, \mathrm{d}z + \int_0^h \left\{ \frac{\partial \overline{uc}}{\partial x} + \frac{\partial \overline{vc}}{\partial y} \right\} \mathrm{d}z + \overline{wc}(0, 0, h) = \overline{S}(0, 0, 0) \quad \text{(A.4)}$$

The same terms cancel out by assuming horizontal homogeneity and stationarity, leaving only $\overline{wc}(0,0,h)$ and $\overline{S}(0,0,0)$. The same assumption of measuring above the blending height h_b is required for the former at h to be representative of the latter in the footprint area. With this assumption, Eq. (A.4) likewise simplifies to Eq. (1.1).

A.1.4 Separation of turbulent components (Reynolds' decomposition)

This expression of the sediment-water flux in Eq. (1.1), $\overline{wc}(h)$, represents the total covariance between vertical velocity and concentration, measured at the instrument height h. It includes the turbulent flux at h, as well as other low-frequency components and trends.

Turbulence is a chaotic but stationary process (mean and variance do not change over time), which enables its analysis by statistical methods (e.g. averaging over time to obtain a mean representation). However, trends and other low-frequency components add non-stationarity to the measurements, and it is generally desirable to separate the 'true' turbulent processes from the deterministic signals [45].

Thus, a Reynolds' decomposition is used to break down the instantaneous values $c(t)$ and $w(t)$ into mean values ($\overline{c}(t)$ and $\overline{w}(t)$) and fluctuations around the mean ($c'(t)$ and $w'(t)$), i.e.

$$\begin{aligned} c(t) &= \overline{c}(t) + c'(t) \\ w(t) &= \overline{w}(t) + w'(t) \end{aligned} \qquad \text{(1.2 revisited)}$$

The mean flux can then be expressed as

$$\begin{aligned} \overline{Flux} &= \overline{wc} \\ &= \overline{\overline{w}\overline{c}} + \overline{\overline{w}c'} + \overline{w'\overline{c}} + \overline{w'c'} \end{aligned} \qquad \text{(1.3 revisited)}$$

Note that two different averaging operations are represented by the overbars in Eq. (1.3): 1) the flux is averaged over a measuring period T, so that one period T produces one flux data point; and 2) an averaging operation is performed on the individual w and c time series to separate high and low frequency components. Operationally, (2) can also be a block mean over T; however, it can be accomplished with a different 'averaging' operator as well.

An 'averaging operator' is here defined to also include detrending (e.g. linear) and filtering (e.g. with a running mean), as by Moncrieff et al. [16]. These averaging operators allow removal of low frequency components that are not included as part of turbulent flux (to be discussed). Strictly speaking, this is not the mean implied by the overbars in Eq. (1.3). Rather, Eq. (1.3) can also be expressed as by Reimers et al. [35] as

$$\begin{aligned} c(t) &= \overline{c} + c_\mathrm{lf}(t) + c'(t) \\ w(t) &= \overline{w} + w_\mathrm{lf}(t) + w'(t) \end{aligned}$$

where $\overline{c}$ and $\overline{w}$ represent the block means over the entire deployment, $c_\mathrm{lf}(t)$ and $w_\mathrm{lf}(t)$ represent low frequency components of concentration and velocity that are separated using detrending or filtering (and are therefore dependent on the burst length and separation), and $c'(t)$ and $w'(t)$ represent the high-frequency components that can be found by subtracting the mean and low-frequency components from the total signal.

In this document, we use the term 'mean' to refer to the low-frequency portion separated by the detrending or filtering operation, which includes the scalar block mean over the full deployment (i.e. 'mean concentration' $= \overline{c} + c_{\mathrm{lf}}$). Our 'mean' can thus itself be a function of time (i.e. $\overline{w}(t)$ rather than simply $\overline{w(t)} = \overline{w}$).

If the averaging operator obeys the Reynolds averaging properties, then the $\overline{\overline{w}c'}$ and $\overline{w'\overline{c}}$ terms disappear [16], and Eq. (1.3) becomes

$$\overline{Flux} = \overline{\overline{w}\overline{c}} + \overline{w'c'} \tag{1.4 revisited}$$

This simplification is intuitive when the averaging operator is a simple block average; then the mean is constant over the averaging period, and the w' and c' terms by definition average to zero. However, detrending and filtering operations do not, in general, follow the Reynolds averaging properties. For example, with linear detrending, the $\overline{\overline{w}c'}$ and $\overline{w'\overline{c}}$ terms do not disappear, although they are in practice small. Filtering operations (i.e. that operate as a window function in the frequency domain, and thus a convolution in time) in general also do not follow the Reynolds' averaging properties, although the running mean does [16].

It is also assumed that the mean vertical velocity, $\overline{w}$, is 0 over the averaging time. This is generally true if the measurements are expressed in streamline coordinates (see Section A.2 on coordinate systems). Then, the $\overline{\overline{w}\overline{c}}$ term disappears, and we arrive at

$$\overline{Flux} = \overline{w'c'} \tag{1.5 revisited}$$

The mean flux over the averaging time is equal to the covariance of the fluctuating components of velocity and concentration. This form of the mass balance is convenient because the term $\overline{w'c'}$ is often the term that we can measure with the most confidence [47].

As a final remark regarding the derivation, the Reynolds' decomposition could also be done before the assumptions of horizontal homogeneity whisk away the horizontal divergences, as by Finnigan [47] and Lee, Finnigan, and Paw U [43]. Then, for e.g. the x direction we would get

$$\begin{aligned}\frac{\partial uc}{\partial x} &= \frac{\partial\left\{(\overline{u}+u')(\overline{c}+c')\right\}}{\partial x} \\ &= \frac{\partial(\overline{u}\overline{c}+\overline{u}c'+u'\overline{c}+u'c')}{\partial x}\end{aligned}$$

Taking the time average over the entire thing to account for turbulent statistics, the $\overline{u}c'$ and $u'\overline{c}$ terms disappear as above. The same can be done in the y direction. The divergence terms in Eq. (A.4) can then be substituted to get

$$\int_0^h \left\{\frac{\partial \overline{uc}}{\partial x} + \frac{\partial \overline{vc}}{\partial y}\right\} \mathrm{d}z = \int_0^h \left\{\frac{\partial \overline{u}\overline{c}}{\partial x} + \frac{\partial \overline{v}\overline{c}}{\partial y}\right\} + \int_0^h \left\{\frac{\partial \overline{u'c'}}{\partial x} + \frac{\partial \overline{v'c'}}{\partial y}\right\} \tag{A.5}$$

We see that the horizontal divergence has an advective term (involving the mean values) and a turbulent term (involving fluctuations). Horizontal advective fluxes disappear if the sediment surface is flat, and the turbulent divergence disappears if the surface is homogeneous [42]. These assumptions, which must both be made for EC, are quite restrictive; however, they can be more closely approximated in a properly chosen coordinate system.

A.2 Coordinate systems and coordinate transformation

A.2.1 Streamline and Cartesian coordinates

The above derivation uses a Cartesian coordinate system, which is well suited for 1-dimensional flow in homogenous terrain. Such systems have strong symmetries in the velocity and scalar fields, so that their mean values changes in only one direction (normal to the surface). If the z axis of a Cartesian coordinate system is aligned with this direction, which is the main direction of flux, then the horizontal divergence terms $\frac{\partial \overline{uc}}{\partial x}$ and $\frac{\partial \overline{vc}}{\partial y}$ disappear, and $\overline{w}$ is also 0 without a problem [47]. The assumptions made above are valid, and the flux can be estimated from a single point measurement using Eq. (1.5).

Moving away from 'ideal sites' to more complex terrain with two- and three-dimensional flow, the choice of coordinate frame becomes more involved. In general, it is not possible to obtain values for all of the mass balance terms from a point measurement. However, by taking advantage of symmetries in the velocity and scalar fields, we can improve our ability to estimate flux from the values that we do have. This is because the choice of coordinate system affects the mathematical form of the divergence term in Eq. (A.1), and can make it easier to estimate the divergence terms we do not know. We thus would like a coordinate frame which a) allows us to express our measurements (e.g. by rotating from instrument coordinates), and b) optimizes our ability to estimate the terms of the divergence $\boldsymbol{\nabla} \cdot (\vec{u}c)$, given the terms that can be measured [43].

For example, as stated above, Cartesian coordinates were used to move from Eq. (A.1) to Eq. (A.2) by allowing the divergence to take the form

$$\boldsymbol{\nabla} \cdot (\vec{u}c) = \frac{\partial uc}{\partial x} + \frac{\partial vc}{\partial y} + \frac{\partial wc}{\partial z}$$

so that the time averaged form of Eq. (A.1), neglecting molecular diffusion and including the Reynolds' decomposition, is given by

$$\overline{\frac{\partial c}{\partial t}} + \frac{\partial \bar{u}\bar{c}}{\partial x} + \frac{\partial \bar{v}\bar{c}}{\partial y} + \frac{\partial \bar{w}\bar{c}}{\partial z} + \frac{\partial \overline{u'c'}}{\partial x} + \frac{\partial \overline{v'c'}}{\partial y} + \frac{\partial \overline{w'c'}}{\partial z} = S(\vec{x}, t)$$

In complex terrain, a more useful coordinate system is the mean streamline coordinate system, which is defined by the (velocity) flow field. In this coordinate system, the x axis is tangent to the local mean streamline (of velocity); the z axis is orthogonal to x, and perpendicular to the plane of the local terrain[3]; and the y axis is oriented to form a right-handed coordinate system [46]. Since the vector basis is defined by the time average of the instantaneous flow field, the coordinate frame is also dependent on the way the flow is averaged [47] (averaging operations and time scales are discussed further in Section A.3).

In the absence of flow separation, the mean streamlines closely parallel the surface, so the mean streamline coordinate system follows the terrain and the z axis is everywhere normal to the

[3]The z axis is aligned with the *principle normal* to the streamline, which is in a tangent plane to the streamline and in the direction of greatest curvature; a more rigorous definition is given by Finnigan [47].

surface [46]. The gradients of the mean velocity and scalar fields will be largest in the surface-normal direction, and thus this coordinate system takes advantage of the strongest symmetries in the mean fields [47]. In essence, the point of coordinate rotation is to seek symmetries, which allow simplification of the mass balance terms that cannot be measured.

The streamline coordinate system is, like Cartesian coordinates, an orthogonal right-handed system. However, the orientation of the vector basis depends on position, and the form of the divergence is different. A greater discussion on calculations in such 'curvilinear' systems, as well as the form of the mass conservation equation and its extension to an integral mass balance, is provided by Finnigan [47].

Streamline coordinates simplify the advection term in the mass balance equations (i.e. the $\partial\bar{u}\bar{c}/\partial x + \partial\bar{v}\bar{c}/\partial y + \partial\bar{w}\bar{c}/\partial z$ terms simplify to just the streamline component $\overline{u}\,\partial\overline{c}/\partial x$), but cause the divergence term to take a form that requires knowledge of the local radii of curvature of the streamline and the y axis. These values are not impossible to obtain; for atmospheric boundary layer measurements, they can be estimated from a contour or digital elevation map of the terrain [47]. However, this information is not generally available underwater. It is common to instead approximate the stream surfaces as planes, and the streamline coordinates as rectangular [42]. We can use what is basically a Cartesian coordinate system, and the forms of the mass balance given in Section A.1, although deviations of the actual system from this approximation can result in errors in the calculated flux. For example, a coordinate system aligned to the mean velocity at the measuring point $\vec{x} = (0, 0, h)$ may not necessarily align with streamline at the upstream footprint or even at the local sediment surface [42, 47].

A.2.2 Coordinate transformations

The instrument measuring velocity outputs the vector result in its own coordinate system (instrument coordinates). The position of this coordinate system relative to the rest of space and the mean flow depends on the placement of the instrument. However, in order to calculate a vertical flux, we must know the orientation of the measured velocity vector relative to the local topography.

As discussed above, expressing values in streamline coordinates can simplify the mass balance equations to enable calculation of flux from a single point measurement. It is thus important to rotate the velocities as expressed in instrument coordinates to their values in streamline coordinates (or a close approximation), so that the assumptions used to derive the EC equations are valid. Importantly, the z axis must be normal to the local streamline. Otherwise, if the velocity measurements are represented in a tilted coordinate system (e.g. if the instrument is physically tilted relative to the surface), errors can arise from the cross-contamination of velocities [46]. That is, high horizontal flux magnitudes can exist, and the projection of these into the vertical plane will dominate the measured flux and mask the true sediment-water flux [42].

Identification of the 'proper' coordinate system can be quite complicated in situations of complex flow conditions or sloped topography [42, 45]. The coordinate rotation schemes are based on fitting the measured velocity vectors in instrument coordinates to assumed characteristics about the flow field. For example, in streamline coordinates, $\overline{w}$ is theoretically 0 over some averaging time period. However, a nonzero $\overline{w}$ can arise from artifacts of the deployment, such

as instrument leveling errors, or flow deflection by the frame or sensor supports [35]. It can also be real, as when vertical advection is balanced simultaneously by transient horizontal advection events caused by complex flow events; in this case, the $\overline{w}$ will be nonzero but should be ignored. Different schemes attempt to resolve these factors by making different assumptions regarding the flow dynamics [45].

The following coordinate rotation procedures and equations are as described by Wilczak, Oncley, and Stage [46].

Fixed-angle rotation

It is sometimes possible to use instrument coordinates directly, without depending on the measured velocity vectors. On flat terrain and in simple flow conditions, if the tilt of the velocimeter relative to the surface is known and small, these angles can sometimes be used directly to correct small tilt errors. For instance, velocimeters typically use a built-in compass to give their pitch (α, rotation around the y axis) and roll (β, rotation around the x axis). The yaw angle around the z axis is not as important for eddy correlation, where the orientation of the z axis is what matters.

The measured velocities $(u_\mathrm{m}, v_\mathrm{m}, w_\mathrm{m})$ are rotated relative to the 'true' coordinate system (u, v, w) as

$$\begin{bmatrix} u_\mathrm{m} \\ v_\mathrm{m} \\ w_\mathrm{m} \end{bmatrix} = \mathbf{A} \begin{bmatrix} u \\ v \\ w \end{bmatrix} \tag{A.6}$$

where

$$\mathbf{C} = \begin{bmatrix} 1 & 0 & 0 \\ 0 & \cos(\beta) & -\sin(\beta) \\ 0 & \sin(\beta) & \cos(\beta) \end{bmatrix}, \qquad \mathbf{D} = \begin{bmatrix} \cos\alpha & 0 & \sin\alpha \\ 0 & 1 & 0 \\ -\sin(\alpha) & 0 & \cos(\alpha) \end{bmatrix}, \qquad \mathbf{A} = \mathbf{CD} \tag{A.7}$$

Note that $\mathbf{C}$ and $\mathbf{D}$ are not commutative; however, for most situations of small tilt, the order of the pitch and roll rotations is not important [46].

The correction can then be done as

$$\begin{bmatrix} u \\ v \\ w \end{bmatrix} = \mathbf{A^T} \begin{bmatrix} u_\mathrm{m} \\ v_\mathrm{m} \\ w_\mathrm{m} \end{bmatrix} \tag{A.8}$$

since the matrix $\mathbf{A}$ is orthogonal and its inverse is equal to its transpose, $\mathbf{A^{-1}} = \mathbf{A^T}$.

In situations with more complex flow or topography, this transformation is not sufficient to place the velocity vectors in a coordinate system acceptable for eddy correlation. For example, over sloped topography, the 'true vertical' measured by the instrument will not be the desired local normal.

Double and triple rotation

For a **double rotation**, the x and y axes are first rotated around z to set the average v to 0; then the new x and z are swung around y to set the mean w to 0. This effectively aligns the

x axis with the local mean streamline, since the mean velocity vector has no components in v and w.

The first rotation produces the rotated velocity (u_1, v_1, w_1) as

$$\begin{aligned} u_1 &= u_\mathrm{m}\cos(\theta) + v_\mathrm{m}\sin(\theta) \\ v_1 &= -u_\mathrm{m}\sin(\theta) + v_\mathrm{m}\cos(\theta) \\ w_1 &= w_\mathrm{m} \end{aligned}$$

where

$$\theta = \mathrm{atan}\left(\frac{\bar{v_\mathrm{m}}}{\bar{u_\mathrm{m}}}\right)$$

The second rotation produces the final velocity (u, v, w) as

$$\begin{aligned} u_2 &= u_1\cos(\phi) + w_1\sin(\phi) \\ v_2 &= v_2 \\ w_2 &= -u_1\sin(\phi) + w_1\cos(\phi) \end{aligned}$$

where

$$\phi = \mathrm{atan}\left(\frac{\bar{w_1}}{\bar{u_1}}\right)$$

With only two rotations, the location of the y and z axes in the y-z plane is not specified, i.e. they can rotate freely about x, and any combination will satisfy $\overline{v} = \overline{w} = 0$. The orientation in the coordinate system used depends on the initial orientation. For this reason, a third rotation is often applied to set the cross-stream stress $\overline{vw}$ to 0. However, this **triple rotation** scheme relies on an ideal form of the stress tensor that is rarely observed, creating a closure problem and often results in noisy or physically unrealistic values for the third rotation angle. Finnigan [47] concludes that "the best one can do using this procedure is to avoid applying the third rotation".

The angles θ and ϕ can be calculated on a period-by-period basis, i.e. coordinates are rotated every flux period based on the mean wind vector for that period. Alternatively, the rotation can be calculated based on an ensemble of flux data points; that is, the coordinates are aligned to the mean wind vector for an entire deployment (consisting of multiple flux periods, NT). This choice is discussed further below in Section A.2.3 in reference to the implicit assumptions behind these choices.

A number of shortcomings to the double rotation scheme, especially at less ideal sites (e.g. that do not have homogenous 1-D flow), are given by Lee, Finnigan, and Paw U [43]. These include over-rotation due to, e.g. electronic offset in the instrument, deflection by the sensor frame or supports (dependent on the direction of current, which can change), and horizontal flow, especially a problem in low flow conditions which can result in unrealistically large rotation angles.

Planar fit

The planar fit assumes the existence of a local streamline plane over which the mean velocity vectors from successive averaging periods are generally aligned [42]. By calculating the mean

velocity over several averaging periods, the 'best fit' orientation of this plane can be solved with a multiple linear regression analysis, i.e. by minimizing the residuals (the difference between the mean velocity vectors and the plane). The z axis is perpendicular to this plane, and the x and y axes can be rotated within the streamline plane to align with the streamwise direction (zeroing out v) either on a period-by-period basis or for the entire deployment [47]. Alignment within the xy plane is important, for example, when measuring cross-stream momentum flux $\overline{v'w'}$, as is often done in atmospheric applications. For eddy correlation of scalar fluxes, such as all sediment-water interface studies so far, this is not as relevant.

The mathematical solution for the planar fit is given by Wilczak, Oncley, and Stage [46], along with a sample implementation; an alternate implementation is given by Lee, Finnigan, and Paw U [43]. The basic principle is that the components of velocity in the target streamline coordinates (corresponding to the streamline plane) u_p, v_p, and w_p can be expressed as a linear combination of the components in the tilted coordinate system in which they are measured (u_m, v_m, and w_m):

$$\overrightarrow{u_\mathrm{p}} = \mathbf{P}(\overrightarrow{u_\mathrm{m}} - \vec{c}) \tag{A.9}$$

where $\mathbf{P}$ is the planar fit rotation matrix, similar to $\mathbf{A^T}$ in Eq. (A.8), and $\vec{c} = (c_\mathrm{x}, c_\mathrm{y}, c_\mathrm{z})$ is an offset error due to instrument error. Since the tilt coefficients are most sensitive to the vertical offset, and the offsets in the horizontal components cannot be obtained by planar fit but do not cause significant error, the c_x and c_y components can be ignored (considered 0) [46].

The coefficients of the linear combination, the elements of $\mathbf{P}$, define the transformation from one coordinate system to another. Since the mean w_p is 0 (or we are trying to get it as close to 0 as possible), any component of w_m in our tilted coordinate system is some linear combination of u_m and v_m, i.e.

$$\begin{aligned}\overline{w_\mathrm{p}} &= p_{31}\overline{u_\mathrm{m}} + p_{32}\overline{v_\mathrm{m}} + p_{33}(\overline{w_\mathrm{m}} - c_\mathrm{z}) \\ &= 0\end{aligned}$$

and thus

$$\begin{aligned}\overline{w_\mathrm{m}} &= c_\mathrm{z} - \frac{p_{31}}{p_{33}}\overline{u_\mathrm{m}} - \frac{p_{32}}{p_{33}}\overline{v_\mathrm{m}} \\ &= b_0 + b_1\overline{u_\mathrm{m}} + b_2\overline{v_\mathrm{m}}\end{aligned} \tag{A.10}$$

so that b_1 and b_2 are defined by the (yet unknown) rotation matrix $\mathbf{P}$, and the b_0 accounts for a fixed instrument offset error in the z direction.

With many such data points, a linear regression can be used to obtain vales for b_0, b_1 and b_2 by minimizing the sum of square residuals

$$S = \sum_{\mathrm{i}=1}^{N} (\overline{w_\mathrm{i}} - b_0 - b_1\overline{u_\mathrm{i}} - b_2\overline{v_\mathrm{i}})^2 \tag{A.11}$$

where $i = 1...N$ represents the individual data runs over which each mean is calculated. S can be minimized by setting up three equations in which $\partial S/\partial b_0$, $\partial S/\partial b_1$, and $\partial S/\partial b_2$ are set to 0, which then provides a linear systems of equations that can be solved for b_0, b_1 and b_2.

From the b_1 and b_2 coefficients, the p_{31}, p_{32} and p_{33} components can be calculated using the orthogonality condition $p_{31}^2 + p_{32}^2 + p_{33}^2 = 1$, and then used to determine values of the pitch and

roll angles (α and β) by equating $\mathbf{P}$ to $\mathbf{A^T} = \mathbf{D^T C^T}$ in Eq. (A.7). With α and β, the rest of the transformation matrix $\mathbf{P} = \mathbf{D^T C^T}$ can be calculated.

The time scale over which to average velocities for the planar fit can be the same or different as the flux period T, but should be smaller than the time scale of the low-frequency flow variations. This allows the velocity vectors to represent averages over turbulence and instrument noise, but still encompass different directions of mean flow. In a study of an impounded river, Lorke, McGinnis, and Maeck [42] used time periods of 512 s to calculate mean velocities based on an observed spectral gap, but found that the coordinate rotation parameters were not significantly different for longer averaging intervals.

Alternate coordinate rotation methods

More complicated situations may require different techniques. In a study of the Oregon continental shelf, Reimers et al. [35] rotated coordinates to minimize wave bias, as they saw surface wave signals whether rotating coordinates every period or fixing the rotation frame. This rotation aligned the vertical velocity at wave frequencies with the vertical velocity derived via linear water wave theory from the ADV's pressure signal, thus minimizing the wave signal in the vertical velocity component. The remaining contributions at wave frequencies were considered to be real flux contributions from, e.g. wave- or pressure-driven exchange processes. A subsequent study of oxygen fluxes in a wave flume found little leveling error when this rotation method was used, based on examinations of the velocity and shear stress time series [30].

A.2.3 Comparison of rotation techniques and sensitivity of flux results

Assumptions behind coordinate rotation techniques

One way to compare the different coordinate rotation methods, in order to make an informed choice of the most appropriate, is to examine the underlying assumptions behind each method.

As mentioned on Section A.2.2, double or triple rotations can be calculated on a period-by-period basis (i.e. a separate rotation for each flux period), or based on an ensemble of periods (e.g. using the global mean over the entire deployment). If calculated by period, the implicit assumption is that horizontal homogeneity holds for every observational period, and the mean velocity vector is 'always' parallel to the surface [43]. Note that this assumption is inherently dependent on the chosen flux period T, as it is the mean velocity vector over this period that must always be aligned to the surface [45]. In contrast, rotating based on the mean wind vector for an ensemble of periods assumes that the mean velocity over a long period of time is parallel to the surface.

The planar fit method assumes the existence of a local streamline plane over which mean velocity vectors in the long term are generally aligned; the vertical velocity averaged over the entire data set is close to 0. The residual mean vertical velocity in the long-term coordinate is optimized to be small, but is sometimes nonzero. Various hypotheses exist to account for this residual, including random noise, vertical advection, low-frequency contributions, and measurement artifacts [43].

Both the ensemble rotation and planar fit allow for nonzero mean vertical velocity for any given period. The implicit assumption is that, in the actual physical system, the mean over a single period of the velocity can intercept the surface and it would therefore be incorrect to force it to 0 [43]. Nonzero means could arise from, for example, sampling limitations or mesoscale motions [46], such as transient vertical advection events that are simultaneously balanced by transient horizontal divergence (whereas over a longer period of time, the transients would average out). Then, rotating to force $\overline{w}$ to 0 would over-rotate the coordinates for that period.

As discussed mathematically by Finnigan et al. [45], rotating by period rather than based on the ensemble mean velocity effectively high pass filters the signal (trends longer than the flux period T are not captured), and folds horizontal components into the calculated vertical flux $\overline{w'c'}$ due to over-rotation. The recommendation is to rotate by ensemble.

More concrete guidance

In a study of an impounded river with a sloped bottom and highly variable flow conditions, Lorke, McGinnis, and Maeck [42] tested several coordinate rotation schemes and their effect on the measured flux. The operation of ship locks at this sites created surges which reflected back and forth horizontally to produce several distinct spectral peaks; the observance of the surge peaks in the vertical velocity signal was attributed to sensor misalignment. However, the double and triple rotation actually increased these low-frequency ($>3 \times 10^{-3}$ Hz, $\sim$5 min) spectral peaks in the vertical. In addition, the cumulative cospectrum did not converge to a flux value at lower frequencies, indicating that the resultant flux is dependent on the choice of averaging time scale (see Section A.3 on the mean removal / averaging operation). The planar fit, on the other hand, was able to remove the low-frequency and wave-related components from the vertical velocity, and produced a flux estimate.

In general, both double rotation by deployment and planar fit are likely to produce reasonable results in 'gentle' topography, but the planar fit generally produces more stable results in steep or complex topography [47]. In addition, the planar fit is more robust to interference from the instrument frame, since it uses information from all water velocity directions, and is impervious to instrument offset as long as that offset is constant [43]. However, it is restricted to longer term measurements that cover time periods of directional changes in mean flow, such as periodic current variation, internal waves, tidal variations, or seiching of lakes [42]; if the 'realizations' of $\overrightarrow{u}$ are nearly parallel, the coordinate system is not stable [47].

Thus, the time scale over which to average velocities for the planar fit should be smaller than the time scale of the low-frequency flow variations. Consequently, it also may be unsuitable for settings with high-frequency flow variations [42], necessitating different techniques such as the wave bias minimization described above (p. 263). In the study described therein, surface waves were observed with periods of 11 s to 16 s (surface waves with periods <10 s would not have been observable at the depths involved), which is well within the range of turbulence. Flux may indeed be influenced by processes related to surface wave motions (by affecting the rate of oxygen consumption in the sediment), but projections of the horizontal velocities onto the vertical can also create strong (and spurious) flux contributions. A rotation to minimize wave biases was found to greatly reduced flux contributions at surface wave frequencies, and what remained was inferred to be real flux contributions from, e.g. wave- or pressure-driven exchange

processes [35].

Finally, as mentioned by Berg et al. [48] and is also intuitively reasonable, neither double rotation nor planar fit can be calculated if the current velocities are too small, e.g. $<2\,\mathrm{cm/s}$. In such cases, other rotation techniques must be used. This is not necessarily a game changer; the fixed-angle rotation is not a bad choice over flat terrain and under simpler flow conditions. In a study of wind waves over a flat bed, Bricker et al. [44] found that tilt errors due to wave bias (described further in Section A.4) could be adequately removed using the fixed-angle rotation based on the ADV's tilt sensors.

A.3 Mean removal, detrending, and filtering

Another central data processing decision to be made in EC measurements is the choice of averaging operator and averaging time for the Reynolds' decomposition ('mean removal'). This choice is tied to the choice of coordinate rotation, as the double, triple, or planar fit rotations all require the calculation of a mean velocity over some chosen time scale.

A.3.1 Source of low-frequency trends and purpose of mean removal

The purpose of the Reynolds' decomposition is to separate low-frequency signals and trends from the turbulent components, so that they can be excluded from the flux calculations. Theoretically, if the assumptions for EC are valid, then performing this operation on a collected dataset should be unnecessary for velocity[4] and simple for concentration. However, in general, more complicated operations are necessary. To understand why, and to better make an informed choice of technique, we must understand what low-frequency signals exist in the data that should not be considered part of the turbulent diffusion process.

Low-frequency signals and trends can arise from sources such as instrumental drift, projections of horizontal velocities into the vertical, and actual deterministic (i.e. advective) environmental processes [16, 42]. Note that the mean removal is typical done after coordinate rotation, so ideally any contamination from horizontal velocities should be minimal.

Instrumental drift often appears as linear trends, making linear detrending particularly intuitive. Its effect can be reduced or at least identified with procedures like periodic re-calibration, duplicate deployment, or concurrent deployment of a more stable but slower instrument. The ability and/or necessity of mean removal is actually advantageous from an instrumentation point of view; flux results are relatively robust to instrumentation drift, since low frequency signals and trends are removed in the data processing.

On the other hand, removing the effects of actual environmental processes that might introduce non-stationarity can be quite complicated, especially in complex terrain with complicated flow patterns. In atmospheric boundary layer research, where the technique was largely developed,

[4] If the flux period T is long enough for a statistical representation of turbulence (which it must be to be meaningful) then the mean vertical velocity $\overline{w}$ should already be 0, since by definition there is no flow normal to the streamline. However, as discussed above in Section A.2.3 on the different coordinate rotation techniques, this is not always the case when the math is said and done. These nonzero and potentially period-varying $\overline{w}$ are a first example of why the mean removal step merits some discussion.

low-frequency atmospheric motions occur that are described as "features of the wider landscape that are not related to the local surface" [156], and are considered "highly site-specific and characterized by significant uncertainty" [157]. As discussed above in Section A.2.3 comparing different coordinate rotation techniques, low-frequency components in vertical velocity can arise from vertical advection events that do not contribute to flux from the interface, but instead balance out unmeasured transient horizontal advection or changes in the storage term [45]. In other words, low-frequency components may arise from the temporary violation of some of the assumptions of EC, such as zero horizontal flux divergence or stationarity in time. Several atmospheric EC studies discuss atmospheric motions that can induce such transients [e.g. 45, 156], but the general conclusion is not specific to atmospheric applications: "even in horizontally homogeneous terrain, the flow field is only horizontally homogeneous when averaged over a period much longer than that of any significant temporal perturbation to the flow" [45]. In terms of coordinate rotation, this factor justifies rotating over the long term rather than individual periods; in terms of mean removal, it also explains the presence of low-frequency w components that do not contribute to the target flux at the interface[5].

The goal of mean removal, and the reason it should be done even if instrument drift and horizontal projections are accounted for, is to obtain some sort of "rational separation" between the "strong and active" part of transport (turbulence) that is handled with statistical techniques (e.g. averaging flux over T to arrive at a representation for that period), and any slower, deterministic processes that might bias the statistical results [16]. The different mean removal techniques, such as linear detrending or running mean, attempt to match the form of these slower processes, so that they can be 'discarded' (as perhaps nonzero and non-constant for this period, but averaging out to zero in the long run). For an example of some such processes in an aquatic environment, see Section A.3.4.

A.3.2 Choice of mean removal technique

Two commonly used methods for mean removal are linear detrending and running mean. As mentioned in Section A.1.3 on assumptions made in the derivation of EC, linear detrending does not obey the Reynolds' averaging properties, but in practice the extra terms are small. Running mean is a filtering operation that does, in fact, obey the Reynolds' averaging properties.

Moncrieff et al. [16] analyzed the frequency domain representation and associated errors of several averaging operators, and examined some empirical cases from atmospheric EC. They concluded that "the best method will be very dependent on conditions at a given site, including the data processing system being used. A comparison of alternative approaches is often wise." For aquatic EC, Lorrai et al. [21] found that, at study sites with steady, unidirectional flow,

[5]Sievers et al. [157] suggest that the necessity of this process depends on the application of the study. Since the low-frequency motions are considered non-local and not driven by the local turbulence, "long-term net ecosystem-exchange studies in which the flux estimates are understood to be site-specific" may not require isolation of the turbulent components. On the other hand, "process-oriented studies", in which fluxes are linked to local biogeochemical processes to provide more universal insights, require that only the "locally meaningful" turbulent fluxes are measured [157].

Aquatic eddy correlation studies generally fall in the latter category. The sediment-water flux is often used as a proxy for some biogeochemical process in the sediment; for example, dissolved oxygen fluxes are used to infer the rate of benthic carbon mineralization [11, 33]. The relevant parameter is the extent to which the sediment is a source or sink of the compound of interest.

linear detrending and running averaging generally produced similar results. Nevertheless, for systems affected by internal waves, seiching, or other dynamic processes, especially those with flow reversals, they recommended the running mean, as the filtering operation is better able to remove large-scale signals over a broad frequency range.

Other frequency-domain techniques, though less common, have also been used. In a study of density fluxes in the water column, a high-pass Butterworth filter was used to isolate the fluctuating components of density ('concentration'). This study did not filter w, to aid in data screening specific to their setting [38]. A low-pass filter has also been suggested for identifying low-frequency components that can subsequently be subtracted from the signal [35, 49]. For example, a low-pass filter can be used to precisely remove long-period fluctuations due to tides ($<\sim$0.0001 Hz), for EC runs long enough to capture such trends [35]. In general, though, such filters have more commonly been proposed in the context of waves. Even beyond EC applications, spectral techniques have been suggested to remove or reduce wave frequencies in the vertical velocity spectra, in order to counter wave bias (defined in Section A.4) [44]. Other artifacts at wave frequencies could also potentially be removed spectrally, such as time lag bias (described in Section 1.4.4 on time shift and other corrections) and the 'velocity effect' observed in oxygen microelectrodes (described in Section 1.5.3 on studies of EC accuracy). However, this technique must be used with care, as the flux may be facilitated by wave motion and thus occur at the wave frequency.

Frequency filters have the advantage of enabling precise understanding and selection of frequency content. However, time-domain operations are in general easier to implement and understand, and are more commonly used in EC studies of benthic flux.

A.3.3 Choice of time scale

In addition to choice of averaging operation, an averaging time (or, for frequency-domain techniques, a cutoff frequency) must be chosen. Note that the averaging time discussed here is not necessarily the same as the period T over which one flux measurement is averaged, although linear detrending algorithms often use the same period (i.e. each linear trend is calculated over one flux period). For running mean, the relevant parameter is the running mean window size, which defines the separation of the components [40]. The period T is still relevant, however, for defining the coordinate rotation time scale, properly averaging over turbulence statistics, resolving variations in flux, etc.

The averaging time scale should be chosen that is long (low frequency) enough to adequately sample all flux-contributing eddies, i.e. it must be long enough to cover multiples of the time scale associated with the slowest flux-contributing eddies, to account for turbulence statistics [16, 36, 42]. However, the period should still be short enough to exclude the low-frequency components from non-turbulent processes and instrument drift.

f a clear spectral gap exists between the low-frequency, deterministic signals and the high-frequency turbulent fluctuations of interest, then an averaging period corresponding to this gap should adequately remove the deterministic signals without excluding any flux-carrying eddies. For well-developed turbulence, the gap can be identified from the power spectrum of the velocity, as in Figure A.1a. It can also be found by examining the cumulative cospectrum (ogive plot), which represents the integral of the cospectrum from high to low frequency, and

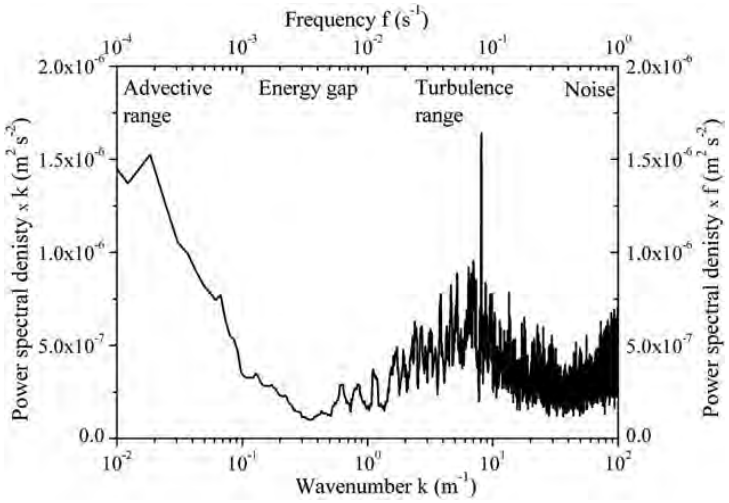

a) Power spectra of current (downstream) velocity showing a clear spectral gap between advective and turbulent components. Source: Lorrai et al. [21].

b) Power spectra of dissolved oxygen taken during an EC run; gray curve corresponds to DO data corrected for response time. Vertical lines represent estimates of the low-frequency cutoffs, consistent with the ogive plot, but no clear spectral gap is identifiable. Source: McGinnis et al. [40].

Figure A.1: Variance-preserving spectra of different components of the EC measurement showing the spectral gap between advective and turbulent components. Reprint of Figure 1.6.

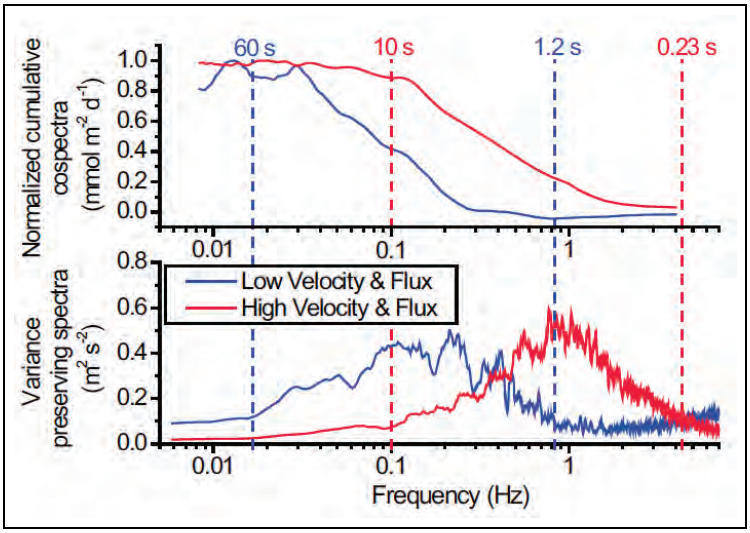

Figure A.2: Ogive plot (top) and variance preserving spectra (bottom) for an EC deployment showing flux-contributing frequencies for low and high flux scenarios. The ogive plot, a cumulative cospectrum integrated from high to low frequency, plateaus past frequencies slower than the flux-contributing turbulent eddies. Reprint of Figure 1.7. Source: McGinnis et al. [20].

theoretically asymptotes at some frequency to indicate that signals of a longer time period do not contribute significantly to flux[6] [16]. The ogive contains the same information as the cospectrum, which can also be visually examined to identify the spectral gap. An example of an ogive plot, along with the variance preserving spectrum of velocity, is shown in Figure A.2.

The appropriate averaging time can also be identified without examining spectra. McGinnis et al. [40] conduct an analysis in which the flux is repeatedly calculated with increasing values of the running mean window size. As the window size increases, the flux incorporates lower frequency contributions; above a certain window size, the flux no longer increases (much like the ogive asymptote). The result of this analysis was found to match the flux determined by the ogive technique.

However, in practice, a clear spectral gap does not always exist. A range of frequencies could contain both turbulent and advective contributions; Sievers et al. [157] note that the observed fluctuations are "likely to reflect some degree of convolution between signals of local turbulent contributions and site/time-specific low-frequency contributions". An example of such a case is shown in Figure A.1b. Separation of turbulent components is still a major challenge in such situations [21, 40]. Sievers et al. [157] propose a method that involves calculating cospectra for a large number of permutations of flux periods and running mean window sizes, and then fitting the resulting density pattern to an ogive model. To our knowledge this technique has not been applied in the aquatic field, possibly because the extent of uncertainty in the spectral gap has not justified the computational complexity.

A.3.4 Examples

An example of an aquatic eddy correlation study that required careful evaluation of mean removal techniques is given by Reimers et al. [35]. In this study of the Oregon continental

[6]Failure of the ogive to converge indicates that the result is sensitive to the averaging time scale for the Reynolds' decomposition [42], since the flux estimation continues to change as lower frequency components are included.

shelf, low-frequency contributions on the scale of hours to days were observed, and attributed to natural phenomenon like tidal forcing or upwelling fronts; they were expected to average to zero over multiple cycles. Oscillations on the order of minutes to tens of minutes were also observed, consistent with nonlinear internal waves. These low-frequency components had both positive and negative contributions to flux which, again, should average out over longer time series. The turbulent flux $\overline{w'c'}$, on the other hand, is net nonzero, representing net consumption or production in the sediment.

The ideal choice of averaging operator would separate the low-frequency components from the fluctuations in velocity and concentration associated with turbulent eddies. This would retain only turbulent diffusion in the $\overline{w'c'}$ term, and all transient advective flux would be rolled into the lower frequency terms involving $\overline{w}$ and $\overline{c}$ [7].

The authors compared linear detrending, running mean, and low-pass frequency filtering techniques, but found that calculated fluxes were found to be very sensitive to the averaging operation. The results were also sensitive to the averaging time (e.g. size of the running mean window), as some velocity oscillations appeared to have periods greater than the burst durations. In fact, the deployment pattern of <15 minute bursts (with 5 min gap in between) proved quite restrictive, in that it also limited the extent to which the low-pass filter could be applied. The authors ultimately concluded that linear detrending (in conjunction with a rotation to minimize wave bias, as described on p. 263) was the most appropriate for their situation, but noted that it was somewhat of a judgment call [35].

In another study, results were also found to be extremely sensitive to averaging time in cases where the vertical velocity was contaminated with advective components from the horizontal direction [42]. However, these studies represent cases with complex flow patterns, and in less complicated situations, the choice of averaging operator and time are not as challenging.

A.4 Wave bias

Wave bias is a particular form of instrument leveling error that is applicable to aquatic but not atmospheric systems. It refers to the contamination of EC measurements by surface and/or internal waves; since wave velocities can be several orders of magnitude larger than turbulent eddies, the flux signal they generate can swamp out the true turbulent flux. Wave bias has been studied more extensively in the context of shear stress, which can be measured as the covariance between horizontal and vertical velocities ($\overline{u'w'}$), but it can apply to all eddy flux measurements.

Wave bias in the context of eddy correlation can be illustrated by incorporating waves into the mathematical expressions describing EC measurements and examining the terms that arise. Along the lines of Shaw and Trowbridge [37], Bricker et al. [44], and others, we model a simplified velocity vector with two components, horizontal (u) and vertical (v). For the Reynolds' decomposition, we include (alongside the mean and fluctuations) a variable representing wave

[7] [35] note that water column turbulence may not be the only driver of net nonzero sediment-water flux; other processes related to surface wave motions or pressure gradients around small-scale sediment topography may also contribute, and would be included in $\overline{w'c'}$.

fluctuations. Thus, $w = \overline{w} + \tilde{w} + w'$, representing components for mean current, waves, and turbulence, respectively. The concentration scalar is similarly decomposed as $c = \overline{c}+\tilde{c}+c'$.

For eddy correlation, we take these measured time series w_m and c_m, remove the mean, calculate the covariance, and recognize that the result represents the desired vertical turbulent flux $w'c'$ to the extent that the EC assumptions are valid. If the mean removal algorithm does not remove the wave fluctuations (i.e. $\tilde{w}$ is separate from $\overline{w}$), then in fact the covariance calculated would be between $(\tilde{w} + w')$ and $(\tilde{c} + c')$ instead of only w' and c'. In addition, in the presence of a small uncorrected instrument tilt θ the covariance becomes, to first order in θ [37]

$$\mathrm{cov}(c_\mathrm{m}, w_\mathrm{m}) = \overline{c'w'} + \overline{\tilde{c}\tilde{w}} + \theta(\overline{c'u'} + \overline{\tilde{c}\tilde{u}}) \tag{A.12}$$

Cross-terms between turbulence and wave terms, $\overline{\tilde{c}w'}$ and $\overline{c'\tilde{w}}$, have been removed under the definition of turbulence as motions that do not correlate with waves [44].

The target vertical turbulent flux can be seen as the first term on the right hand side of Eq. (A.12), but now there are additionally three more terms. The second term is a wave bias representing vertical transport by waves. The third and fourth terms are 'apparent' turbulence- and wave-induced biases arising from the instrument tilt [37]. In the context of the coordinate rotation discussion of Section A.2, θ here is the pitch angle α, and from matrix $\mathbf{D}$ in Eq. (A.7) we see that $w_\mathrm{m} = -u\sin(\theta) + w\cos(\theta)$. The Taylor expansions around $\theta = 0$ for sine and cosine give first order terms $\sin(\theta) = \theta$ and $\cos(\theta) = 1$, so that for small θ the measured vertical velocity used to calculate the covariance would be $w_\mathrm{m} = -u\theta + w$. From here it is easy to see how the tilt terms in Eq. (A.12) arise.

For 'gentle' conditions and small θ[8], the turbulence bias is generally small. However, the wave bias can be much larger (e.g. an order of magnitude, for momentum fluxes). Thus, while in principle this wave bias could be rendered negligible by rotating coordinates to align with the wave-induced velocity field, the level of accuracy to which the coordinate orientation must be known is impossible to achieve [37, 158]. Note again, however, that wave bias has mainly been studied in the context of shear stress measurements, which involve *two* velocity components that directly reflect instrument tilt and high wave velocities.

Rather than coordinate rotation, techniques to remove wave bias instead involve removing the wave signals from the velocity time series ('wave-turbulence decomposition'), which makes them more analogous to mean removal. Several of these methods require additional instrumentation to measure e.g. displacement of the free surface (whose motions are considered to be due to waves), or velocity at an appropriately nearby location (where wave motions are considered to correlate between the two sensors, and turbulence is not). Spectral techniques in the frequency domain can also be used, although care must be taken because the wave peak often occurs at frequencies at which turbulence is also energetic [44].

Bricker et al. [44] compared different methods of removing wave bias in stress measurements, for wind waves over a flat bed. They found that the wave bias was minimal when the velocity measurements could be corrected using the instrument's internal compass and tilt meter (not all velocimeters have these sensors). Of course, this simple fixed-angle rotation cannot be applied

[8]Coordinate rotation fits in here in that its goal is to achieve a system where any remaining tilt θ is small enough that the bias term is negligible.

for more complicated topography, leading to the need for more involved coordinate rotation procedures (as described in Section A.2), which are now further complicated in the presence of waves.

For eddy correlation of scalar variables, the velocity measurements are still subject to wave bias. As described on p. 263, Reimers et al. [35] developed a coordinate rotation technique specifically to minimize wave bias, that was found to produce little leveling error in a subsequent study in a wave flume [30]. In another study at a shallow water site (dense seagrass meadow) with low current velocities and short-period waves, the wave bias was estimated to have a marginal effect of 2 % based on fluxes calculated with and without rotation. Frequency filters can also be used to remove wave bias (from tilt) and other wave-frequency artifacts (e.g. time lag, velocity effect of microelectrodes). These filters can be used on the time series as part of mean removal (as described in Section A.3.2), or even on the eddy fluxes themselves; however, they must be used with care, as real fluxes can occur at wave frequencies, e.g. when wave motions give rise to eddies or water parcel ejections [30, 48]. A description of the kinds of waves that affect EC measurements of benthic flux is given in Section 1.4.5 on site selection and site-specific considerations (p. 55).

A.5 Quantifying groundwater discharge from heat and salinity fluxes

As discussed in Section 1.3.1, groundwater discharge can be extrapolated from heat and salinity fluxes if the groundwater has a different temperature or conductivity, respectively, than the overlying water. Quantifying the rate of groundwater from heat and salinity fluxes requires some additional steps beyond Eq. (A.3).

As given in Crusius et al. [6], heat balance in a control volume above the sediment-water interface can be given as

$$H_{\mathrm{g}} - H_{\mathrm{w}} - H_{\mathrm{ec}} = 0 \tag{A.13}$$

where H_{g} is the heat that enters the control volume with the discharging groundwater, H_{w} is the heat that exits the control volume with the displaced water column water, and H_{ec} is the turbulent flux of heat across the top of the control volume located at the instrument height, h. In other words, Eq. (A.13) recognizes that heat content enters and leaves the control volume from the convection associated with the groundwater inflow, in addition to the heat that exits due to turbulent diffusion; however, it is only the last of these that is measured by eddy correlation. Note that heat flow due to horizontal temperature differences are neglected, in line with the zero horizontal divergence simplification made for eddy correlation.

Each of the three terms in Eq. (A.13) can be expressed in terms of the temperature, specific heat, and density of the groundwater and surface water:

$$H_{\mathrm{g}} = T_{\mathrm{g}} s_{\mathrm{g}} \rho_{\mathrm{g}} q_{\mathrm{g}} \tag{A.14}$$

$$H_{\mathrm{w}} = T_{\mathrm{w}} s_{\mathrm{w}} \rho_{\mathrm{w}} q_{\mathrm{g}} \tag{A.15}$$

$$H_{\mathrm{ec}} = \overline{u'_{\mathrm{z}} T'_{\mathrm{w}}} s_{\mathrm{w}} \rho_{\mathrm{w}} \tag{A.16}$$

where T is mean temperature (°C), s is the specific heat (J/(g · °C)), ρ is the density (g/cm^3), and the subscripts g and w denote properties of the groundwater or water column water. q is the discharge rate of groundwater into the control volume (cm/s), which is also the same as the outflow of the displaced water column water. $\overline{u'_z T'_w}$ (cm · °C/s) is the turbulent temperature flux which can be estimated through eddy correlation.

Thus, along with the eddy flux of temperature, calculation of the groundwater discharge rate requires measurements or knowledge of the specific heat, density, and temperatures of both water column and groundwater. Then, the discharge rate can be solved for as

$$q_g = \frac{\overline{u'_z T'_w} s_w \rho_w}{\rho_g (T_g s_g - T_w s_w)} \qquad \text{(1.6 revisited)}$$

Crusius et al. [6] also gives the result for a similar calculation based on salt balance, i.e. in cases where the turbulent flux of conductivity is measured with eddy correlation. The calculation of q_g is essentially the same as that for heat, except that $T \cdot s$, the specific heat content (J/g), is replaced by salinity S.

$$q_g = \frac{\overline{u'_z S'_w} \rho_w}{\rho_g (S_g - S_w)} \qquad \text{(1.7 revisited)}$$

Appendix B

Implementation details

B.1 Photomultiplier tube circuitry

The gain of a PMT depends on the voltage applied between cathode and anode. This voltage is then split among the dynodes by the voltage divider, to power each amplification stage. For the 9111WB PMT used in this instrument, the maximum gain is specified as 7.1×10^6. For photon counting, it is advantageous to have the gain as high as possible (i.e. higher voltage) so that photons can be more easily distinguished.

Another requirement of the voltage divider, aside from overall voltage, is that its current I_D must be much greater ($\sim$100 X is thought to be sufficient) than the signal current I_a that is measured out of the anode. This is because all electrons sent from dynode to dynode and eventually to the anode are supplied by the divider current; diverting too significant a fraction of the divider current would affect the voltages between the dynodes, which reduces linearity of the output signal amplitude. Linearity is less important for photon counting since the sizes of the photons only need to be sufficient; however, it is still a desired property.

The anode current was estimated using a gain of 5×10^6, which multiplies 1.6×10^{-19}coulombs per photoelectron to achieve a charge of $q_\mathrm{a} = 8 \times 10^{-13}$ coulombs per photoelectron generated at the cathode (q_a = charge out of anode per photoelectron at cathode = $textgain\times$ charge per photoelectron). The electrical output at the anode from a single photon is approximated by a 3 ns square wave (based on pulses observed on an oscilloscope), which would produce a "peak" current of 0.27 mA for the duration of the 3 ns pulse ($q_\mathrm{a} \div$ pulse duration). However, the anode current generally used for calculations is the average current, which takes into account the time between photons, during which no current flows through the anode. At a rate of 2×10^6 photons/s (close to the highest observed; see the 'Upper limit' section of Section 2.3.3, p. 118), the average current I_a would be $q_\mathrm{a} \times 2 \times 10^6 = 1.6\,\mu\mathrm{A}$. Thus, a voltage divider current $I_\mathrm{D} \geq 100 \times I_\mathrm{a} = 0.16\,\mathrm{mA}$ would be sufficient.

The voltage from cathode to the first dynode, $V_\mathrm{k-d1}$, is often recommended by the manufacturer; for the 9111WB, the spec sheet gives a maximum value of 300 V. As other reference points, the standard Zener diode-based voltage dividers offered by the manufacturer fix $V_\mathrm{k-d1}$ at 150 V. On the other hand, the manufacturer's non diode-based voltage dividers use $V_\mathrm{k-d1} = 3R$ and $V_\mathrm{d-d} = R$, i.e. voltage from cathode to the first dynode is three times the voltage between each

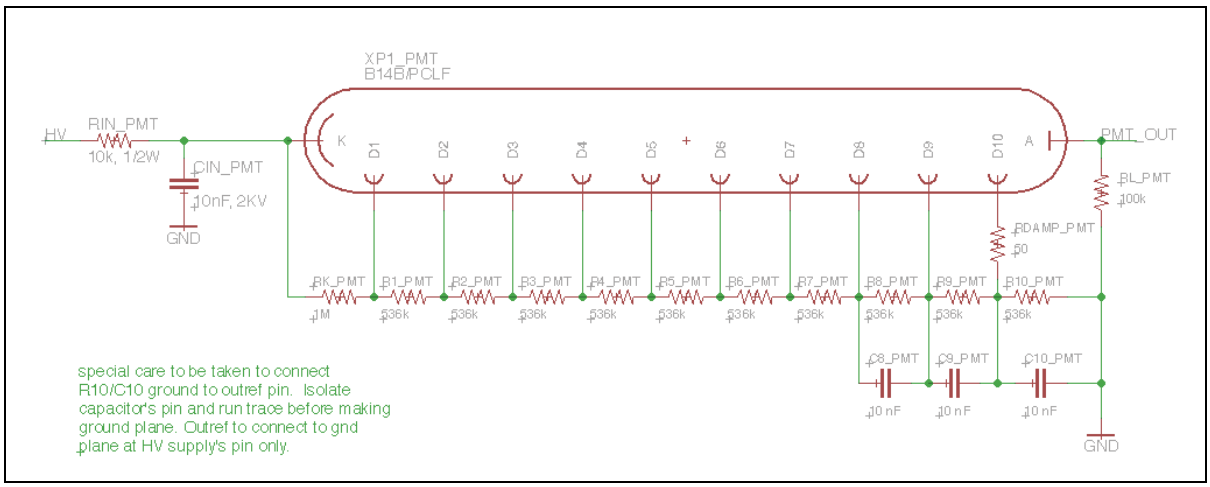

Figure B.1: Schematic of PMT circuitry in present instrumentation.

dynode pair. Thus, the voltage between the cathode and first dynode is $V_{\mathrm{k-d1}} = \frac{3}{13} V_{\mathrm{S}}$. For a supply voltage of 1100 V (close to the maximum 1250 V of the power supply), the voltage from cathode to first dynode would be $V_{\mathrm{k-d}} = 254\,\mathrm{V}$, which is higher than the 150 V reference point mentioned above. These voltage dividers were likely designed for lower voltage (lower gain); many applications look at the analog output of photons averaged together, which is sensitive to amplitude and can saturate if the gain is too high.

For the higher voltage desired in this application, a $V_{\mathrm{k-d1}}$ of $2R$ was chosen to keep the cathode-first dynode voltage closer to 150 V ($V_{\mathrm{k-d1}} = 2/12\ V_{\mathrm{S}} = 183\,\mathrm{V}$ for $V_{\mathrm{S}} = 1100\,\mathrm{V}$). The divider current is then $I_{\mathrm{D}} = V_{\mathrm{S}}/12R$ and a target divider current I_{D} of 0.16 mA would require $R = 573\,\mathrm{k\Omega}$. The chosen values of $R_{\mathrm{d-d}} = 536\,\mathrm{k\Omega}$ and $R_{\mathrm{k-d1}} = 1\,\mathrm{M\Omega}$ (Figure B.1) are based on these calculations.

The PMT circuitry also includes other features to improve its performance in this particular application. Referring to Figure B.1, the input filter from R_{in} and C_{in} reduces noise on the input power, which would cause fluctuations in gain. The capacitors C_9 to C_{13} help to reduce the effect of the anode current draw from the divider current in the final stages of the voltage divider (i.e. smoothing the "peak" current mentioned above), thus improving linearity. The damping resistor R_{damp} reduces the undesirable ringing effect often observed in the process (see Section 2.3.1, p. 109). The load resistor R_{l} is necessary for protecting the circuitry.

B.2 Calculating processing time for microcomputers

B.2.1 Raspberry Pi for photon counting

When counting photons, the integration time t_{intgr} and measuring frequency f_{meas} are specified separately. In the absence of any processing time, choosing $t_{\text{intgr}} = 1/f_{\text{meas}}$ maximizes the integration time for a given measuring speed (and vice versa). However, because of processing time, the instrument must leave some buffer t_{buf} such that $t_{\text{buf}} + t_{\text{intgr}} \leq 1/f_{\text{meas}}$. We wish to choose the largest acceptable value of t_{intgr}, which requires some knowledge of the processing time.

Right now the instrument does not automatically maximize the integration time given a measurement frequency; both are specified by the user. However, the instrument does check that a sufficient buffer is provided so that the measurements appear with the correct specified frequency. For this check, the instrument must estimate the processing time, which was determined below and then hard-coded into the code. Future versions of the instrument may involve automatic calculation of t_{intgr} when measuring time series.

Due to the capacity of the counters, the instrument actually counts in subintervals of e.g. 0.5 or 1 ms that it then sums up to the full integration time t_{intgr} (see Box 2.1). A major component of the processing time that must be accounted for is associated with each subinterval (e.g. signaling the circuitry, reading the numbers, adding numbers, resetting the circuitry, etc.) and thus depends on the number of subintervals summed up for one full measurement of t_{intgr} duration (which therefore depends on the chosen subinterval time relative to the integration time). The system also incurs some fixed processing time for each measurement, regardless of how many subintervals are summed up (e.g. timing calculations, storing numbers, looping counts, etc).

To estimate the processing time, time series were measured where the chosen t_{intgr} matched $1/f_{\text{meas}}$ exactly, i.e. no buffer for processing was allowed. The output timestamps would then deviate from the ideal measuring interval of $1/f_{\text{meas}}$ because the instrument is programmed to complete all measurements for t_{intgr} time regardless. The processing time was estimated from the observed deviations. Figure B.2 shows the measured timing deviation incurred by processing time plotted against the number of subintervals summed per measurement. No statistical difference was observed between modulated and unmodulated measurements. From the fit of the curve, the estimated fixed cost is 3 µs, and the estimated variable cost per subinterval is 4 µs. However, because of the scatter, a much larger buffer should be allowed so that no measurements deviate. Thus, a value of 10 µs fixed cost per measurement, plus an additional 10 µs per subinterval summed, were chosen for calculating the buffer.

The processing time incurred turns out to be minimal (fractions of ms) for most measurements. However, these values were calculated for the Raspberry Pi 3 running at 1.2 GHz. The instrument initially used the slower Raspberry Pi 1 Model B+ running at 700 MHz, whereby similar calculations produced values of 10 µs for the fixed cost and ∼9 µs variable cost. After inflating to account for variation, these delays did affect the measurements (which can be as fast as, e.g. 15 ms) in a nontrivial way. The Pi 3 is much faster and made this analysis sort of useless; but as a side note, the Pi 3 is so fast that it created other problems with the circuitry.

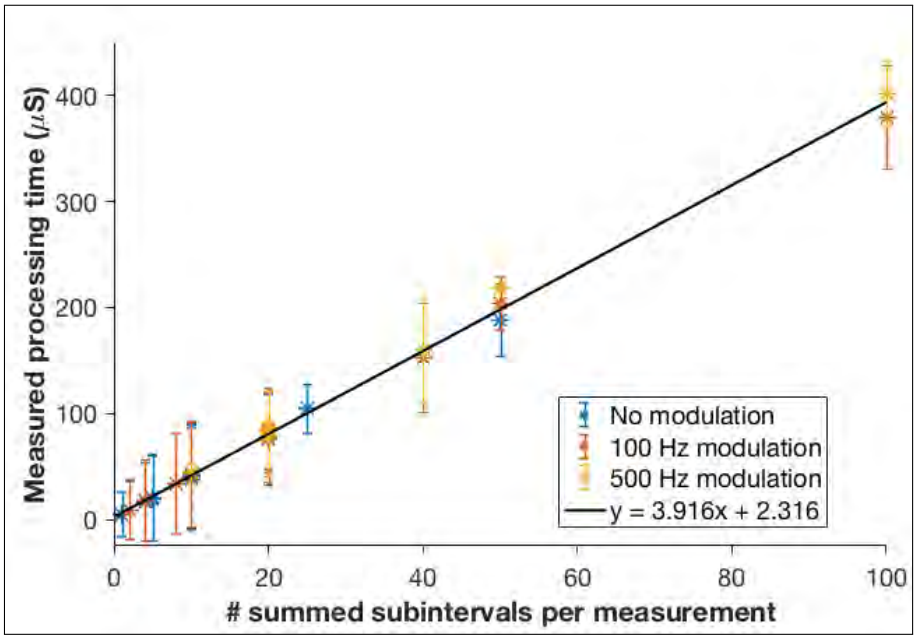

Figure B.2: Pi 3 timing tests.

B.2.2 Teensy for conductivity/temperature measurements

A similar analysis was conducted for the Teensy, which controls conductivity and temperature measurements and communicates with the Pi via a 10 MHz SPI channel. The system uses a 400 kHz (corresponding to 2.5 µs) ADC, so multiple ADC reads can be averaged (to reduce noise) in one 'measurement' (integration time, $\mathcal{O}$(ms))—ideally, as many as possible. In the chosen code structure, the Teensy and Pi agree before each measurement on the number of reads the Teensy will make, based on the target total integration time. Calculating this number requires some knowledge of the timing.

Again, for each total integration there is a fixed cost (e.g. SPI transfer, averaging operation) and a variable cost associated with each ADC read that the Teensy is making on its own, before the Pi checks back for the aggregate number. For the initial one-ADC design (see Section 3.4.4, p. 166), the variable cost for each ADC read itself had a fixed component (one I^2C handshake transferring 16 bytes per channel), and a component that varied with the number of channels. Temperature, current, and voltage each had their own channel, so that temperature-only measurements read one channel, conductivity-only measurements read two channels, and measuring both temperature and conductivity read three channels.

ADC read times were measured by having the Teensy take timestamps before and after each command. Plotted vs the number of measurements in the average (Figure B.3a), the linear fits give estimates of the fixed cost (intercept) and variable cost (slope). Based on the fits, the Pi was programmed to allow 96, 155, and 214 µs per read, depending on the number of active channels. The fixed cost from these tests was not used, as it was associated largely with operations that would not occur in normal use of the instrument (e.g. calculating time elapsed and printing output). Instead, to estimate the fixed cost, the SPI transfer was timed in the same way (using Teensy timestamps) and generally came to $\leq$21 µs. Ultimately, however, a fixed cost of 600 µs was determined experimentally to be necessary.

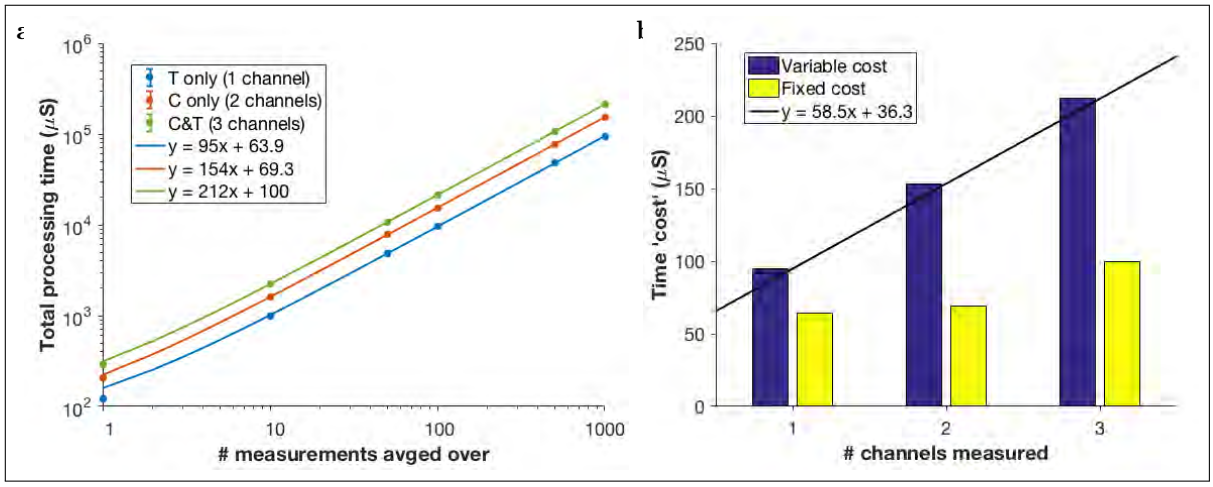

Figure B.3: Teensy timing graphs for single-ADC system.

The variable cost itself was also broken down into a fixed component and variable component, as described above. Figure B.3b shows the variable cost plotted against the number of channels (for completeness, the fixed cost associated with Teensy printouts, etc. is plotted as well). The breakdown appeared to be ∼60 µs per channel (reading 16 bits each) and ∼40 µs for setting up the I^2C call.

It was later found that the ADC exhibits some persistence from channel to channel, so that conductivity measurements, for example, would interfere with temperature readings (see Section 3.4.4). The code was subsequently changed to avoid this issue. The new code required three separate I^2C calls per measurement (each sampling one channel only). New timing estimates were based on the ∼100 µs estimated above for one I^2C call reading one channel. Three calls was estimated to take 300 µs, so that for each measurement, 300 µs per channel read plus 600 µs fixed cost were budgeted in calculating the number of ADC reads per integration period. This obviously substantially reduced the number of reads averaged per measurement.

The noise for the temperature sensor was subsequently found to be unacceptably high for EC measurements, requiring a hardware fix that would bypass the inefficiency of sending separate I^2C calls for each channel. As described in Section 3.4.4 (p. 166), the conductivity now occupies three channels of the ADC (which could be read with one I^2C transfer), while the temperature is routed to its own ADC. The ADC for the temperature allows several measurements to be read with one I^2C command, so to take advantage of the associated time savings, the code was slightly restructured to read the temperature and conductivity measurements in blocks. A block size of 255 reads was chosen based on an I^2C buffer size of 512 bytes. The Teensy would then read 255 temperature values, followed by 255 conductivity values (each a scan of three channels requiring one I^2C call), repeated until it had reached the number of ADC reads dictated by the Pi.

New timing tests were performed, again using Teensy time outputs to track measurement times. The resulting read times were very consistent and followed clear trends with little variation. For the temperature, each ADC read within one block was observed to take 51.6 µs (slope of read time on y vs number of reads on x) and each block incurred a cost, related to the I^2C command and other associated processing, of 93 - 94 µs (intercept of the graph divided by the number

of I^2C calls, repeated for different block counts). For conductivity, each read was observed to take 212 µs with little to no extra cost from processing blocks. For state 3 measurements (both C and T), the cost per read was observed to be 264 µs (neatly the sum of the temperature and conductivity) and the cost per additional block was similar to that of temperature-only measurements. Based on these numbers, the Pi now allows 53, 215, and 265 µs per read, with 95, 10, and 100 µs per block (number of blocks calculated by microcomputers based on block size and total number of reads), and a fixed cost per total measurement of 600 µs.

B.3 Thermistor circuitry Wheatstone bridge

As described in Section 3.1.3, a Wheatstone bridge (Figure B.4) is used to convert the resistance of the NTC thermistor to a measurable voltage. Compared to a simple voltage divider, the Wheatstone bridge is much more sensitive to change in resistance, as it measures the difference between a voltage divider containing the thermistor and a voltage divider at some close, fixed voltage (as set by the potentiometer).

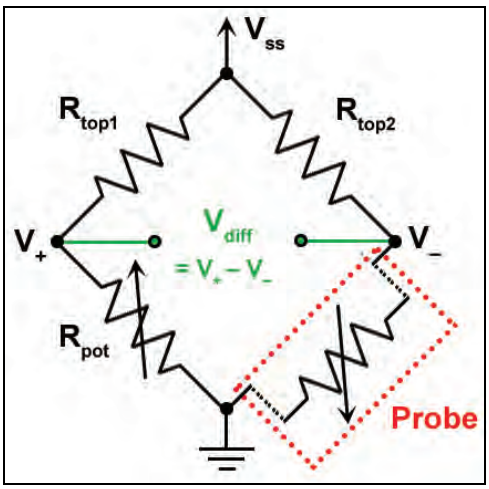

Figure B.4: Wheatstone bridge (reprint of Figure 1.23).

The differential voltage from the Wheatstone bridge is fed to an instrumentation amplifier (Texas Instruments INA333). The in amp amplifies the differential voltage, which can be either positive or negative, and shifts it by a reference voltage, here set to $V_S/2$, to produce an output between 0 and V_S. The INA333 is capable of nearly rail-to-rail output; however, due to the internal architecture of the instrumentation amplifier, the achievable output voltage also depends on the input common mode voltage V_{CM} (average of the two inputs V_+ and V_-, relative to ground). The INA333 was chosen in part for its relatively less restrictive output vs V_{CM} curve, in addition to its low input bias current and low offset voltage.

The resistor values for the Wheatstone bridge were chosen based on the *R-T* curve of the thermistor, the target temperature range, and the V_{out} vs V_{CM} curve of the amplifier. In general, all resistor values should be roughly similar to the resistance of the thermistor at a target "center temperature". If the potentiometer resistance R_{pot} is significantly different from the probe resistance, the differential voltage would not be centered around 0, which reduces the range of the shifted output. If the top resistors R_{top} are significantly greater than the probe voltage, the voltage divider output $V_- = R_{probe}/(R_{probe} + R_{top})$ curve is too nonlinear. If the probe voltage is significantly greater than R_{top}, the voltage divider output is too flat, and the common mode voltage is too high for an optimum amplifier output. The chosen values of $\sim$150 kΩ correspond to a center temperature of $\sim$17.5 °C.

To inform the choice of resistor and gain values, a simple MATLAB model was used to simulate the output of the amplifier. Results using a gain value of 4 and the potentiometer value of 138 kΩ used in the final system (chosen empirically by turning the pot wheel and measuring the results) is given in Figure 3.6 (p. 134). The effective range of the circuitry is roughly 7 °C to 25.5 °C. Figure 3.7 (p. 134) shows how the potentiometer resistance can be adjusted to fine tune the target temperature range.

B.4 Wien bridge

The AC excitation of the conductivity circuit is provided by a Wien bridge oscillator, a circuit that self-oscillates sinusoidally with a frequency depending on the components used. Specifically, the oscillation is provided by the combination of a series RC network and parallel RC network as shown in Figure B.5a, which select for a resonance frequency as

$$f = \frac{1}{2\pi R_{\mathrm{o}} C_{\mathrm{o}}} \tag{B.1}$$

In addition,

$$V_{\mathrm{out}} = \frac{1}{3} V_{\mathrm{in}} \tag{B.2}$$

where both equations can be derived from circuit analysis of the circuit shown in Figure B.5a [153].

The original circuit with a target of 1 kHz oscillation used $R_{\mathrm{o}} = 15.8\,\mathrm{k\Omega}$ and $C_{\mathrm{o}} = 10\,\mathrm{nF}$ as in an example circuit provided by Talarico [159]. To increase the oscillation frequency to avoid electrode polarization issues (Section 3.2.3, p. 144), the components were subsequently changed to $R_{\mathrm{o}} = 2.2\,\mathrm{k\Omega}$ and $C_{\mathrm{o}} = 1\,\mathrm{nF}$, for a frequency of 72.3 kHz. This choice of components was driven largely by the selection of immediately available components that fit the circuit board and had temperature tolerance $\leq 0.1\,\%$, although this tolerance appears to be insufficient for handling the self-heating of the board (Section 3.2.4, p. 146).

A Wien bridge oscillator is formed by connecting this RC circuit to an operational amplifier, as shown in Figure B.5b. V_2, the 'output' voltage of Figure B.5a, is fed to the non-inverting input of the amplifier, and the amplifier's output is fed back to the RC circuit, creating a positive feedback loop [153]. The gain of the amplifier is set by the negative feedback loop on its inverting input (R_{F1} and R_{F2} voltage divider in Figure B.5b), with corresponding gain of $1 + R_{\mathrm{F1}}/R_{\mathrm{F2}}$ as for a classic non-inverting amplifier configuration. Following Eq. (B.2), if the gain is set to 3 or higher, then the circuit will oscillate.

The traditional behavior for positive feedback with gain > 1 (in this case, it is the product of the gain and the attenuation from the RC circuit as given in Eq. (B.2) that matters) is an exploding amplitude (instability). This is because any increase in either the input or output, e.g. due to noise or transients, will cause the other to increase, which will cause the first to increase again. In fact, this is how the oscillation in the circuit begins in the first place. The negative feedback ensures that the output is $1 + R_1/R_2$ times the input, but it does not prevent the instability. There is nothing in the $R_{\mathrm{O1/O2}} C_{\mathrm{O1/O2}}$ circuitry that fixes the amplitude.

Instead, Wien bridges usually include some form of amplitude stabilization. Ours uses diode stabilization, as shown in Figure B.6. When V_{out} is low, the diodes are off (no current can flow at such low voltages), so the effective $R_{\mathrm{F1}} = R_{\mathrm{F3}}$ of the figure. Using the values given in the figure [159], this gives a gain of $1 + 21/10 = 3.3$, which is slightly larger than the required $G = 3$; the amplitude begins to increase. However, as V_{out} increases, the diodes turn on and allow current to flow through the R_{F4} branch. The two diodes allow multidirectional current, since the signal is AC. In the limit of $V_{\mathrm{out}} >>$ the voltage drop across the diode V_{D}, then the effective $R_{\mathrm{F1}} = R_{\mathrm{F3}} /\!\!/ R_{\mathrm{F4}}$. For the example given, this yields an effective $R_{\mathrm{F1}} = 19\,\mathrm{k\Omega}$ for a gain of 2.9. The gain is reduced below 3 and the amplitude decreases again.

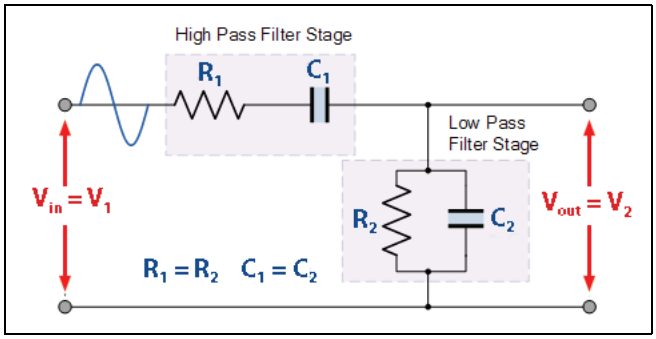

a) Combination of series and parallel RC circuits that provide the oscillation for the Wien bridge. The combination of the high-pass and low-pass filters selects for a resonance frequency.

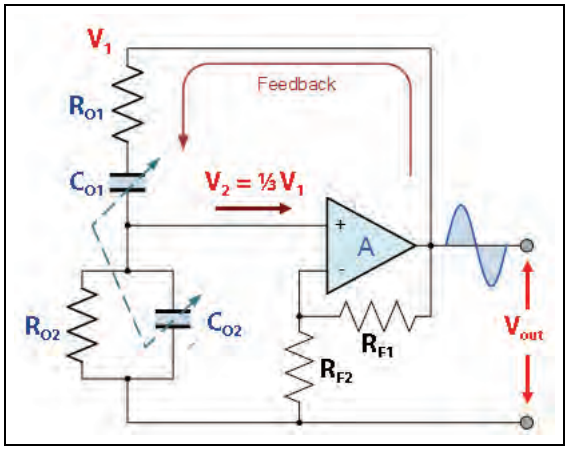

b) Full Wien bridge oscillator using an inverting amplifier with positive feedback to maintain oscillations, and negative feedback to set the gain.

Figure B.5: Wien bridge circuit diagrams. Source: adapted from Storr [153].

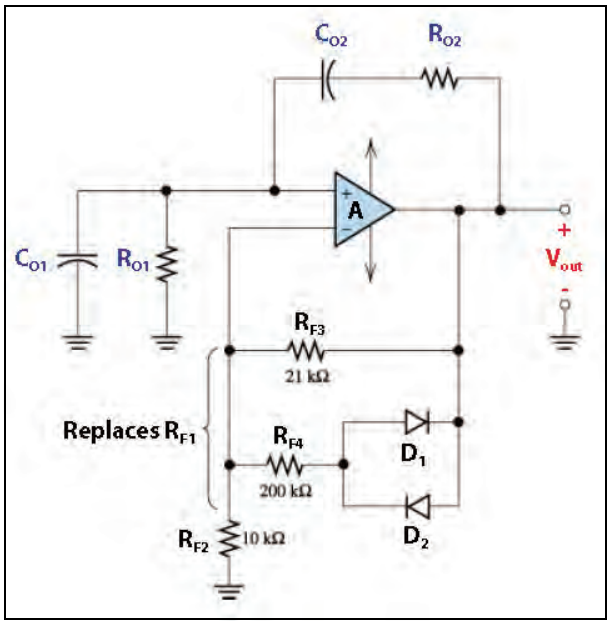

Figure B.6: Circuit diagram of Wien bridge with amplitude stabilization via a pair of diodes. Source: adapted from Talarico [159].

The voltage across the diodes, V_{D}, pushes more of the current through the R_{F3} branch than R_{F4} (relative to the situation where $V_{\mathrm{D}} = 0$), so it sets the effective R_{F1} somewhere in between R_{F3} and $R_{\mathrm{F3}} /\!\!/ R_{\mathrm{F4}}$. Eventually, an equilibrium is reached where the gain is exactly right that the circuit oscillates with stable amplitude; any spikes in one direction or the other are pulled back by the self-adjusting gain. The final amplitude of V_{out} is set by the relative values of feedback resistors R_{F2}, R_{F3}, and R_{F4} and the $I - V$ characteristic of the diode. For example, for a fixed set of resistor values, the circuit is stable when the gain is precisely set by a V_{D} of a certain amount; V_{D} depends on the current through the diode, which in turn directly corresponds to a given V_{out} amplitude.

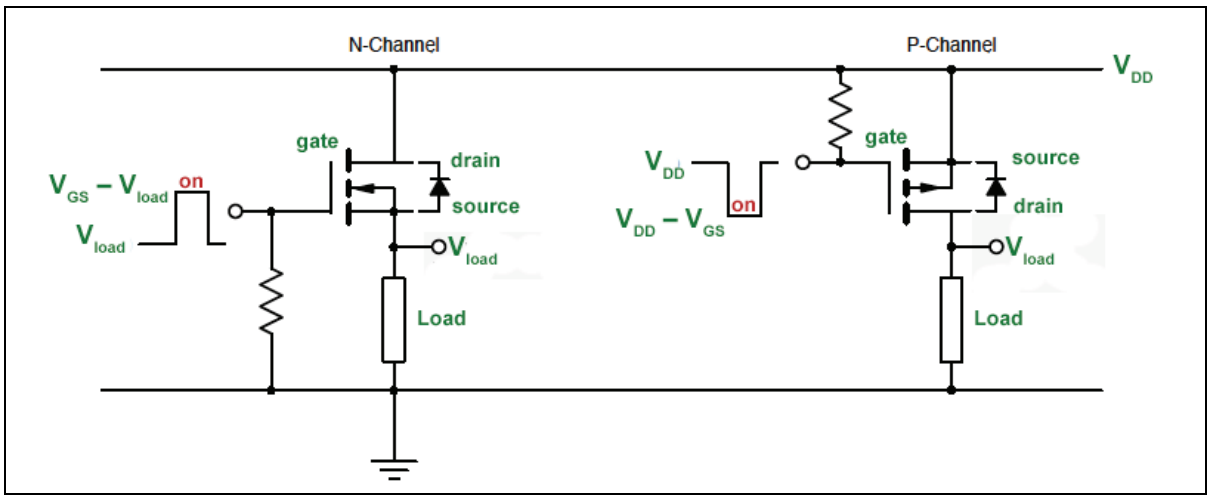

Figure B.7: N-channel and p-channel high-side switching. Source: adapted from Vishay Silconix [162].

B.5 Power controls

As described in Section 4.1.2, the instrument is powered 'on' by applying a magnet to a reed switch, which then closes the circuit to power the Raspberry Pi and Teensy. Closing the reed switch does not power on the rest of the circuitry, as the current load would damage the switch.

B.5.1 Fluorescence sensor power control

For the fluorescence sensor, power to the monochromator, PMT, and circuitry is independently controlled by the Raspberry Pi via MOSFET switches [160]. MOSFET switches were chosen over relays because, given the current demanded by the circuitry, the higher relay resistances would result in excessive 'on'-state power loss.

A high-side switching circuit (load between FET and ground) was chosen over low-side switching (load between source and FET) to avoid ground mismatches. P-channel transistors are generally more suitable than n-channel for high-side switching, because of the high gate voltage that would be required of an n-channel (Figure B.7) [161, 162]. For this application, a p-channel transistor with low drain-source resistance was chosen (Vishay Silconix SI7157) to minimize power losses [163]. The Raspberry Pi GPIO voltage level of 3.3 V is not sufficient to fully turn on a MOSFET, which would result in a higher drain-source resistance. Thus, the gate is controlled by a bipolar junction transistor circuit that is in turn controlled by the Pi GPIO.

The MOSFET switches activate power to the DC/DC convertors driving the relevant parts of the circuitry. Due to on-board capacitances, the photon counting circuitry has a ramp-up time of ~20 ms, as observed in oscilloscope traces, before the full 3.3 V is reached. To avoid damaging the devices, the Raspberry Pi is specifically programmed to wait for the appropriate duration before sending signals to the components.

Box. B.1: Considerations informing transistor circuit design

Transistors require a certain gate-to-source voltage V_{GS} (e.g. 5 V to 10 V), known as the 'threshold voltage', to turn 'on'. If V_{GS} is too low, then the drain-source resistance R_{DS} will be too high to pass significant current, as given by their R_{DS}-V_{GS} curves. In high-side switching, the supply voltage to the load V_{load} is the 'bottom' of the transistor (source for n-channel, drain for p-channel); i.e. the voltage powering the load is equal to the overall circuit supply voltage V_{DD}, less power dissipated in the transistor due to R_{DS}. Low R_{DS} is preferred so that less power is wasted. With low R_{DS}, then, V_{load} is close to V_{DD}, which in this case is the battery voltage ($\sim$15 V). With an n-channel resistor, the gate voltage would need to be several volts greater than the source, meaning several volts greater than 15 V relative to ground. With a p-channel transistor, the gate voltage is pulled down from the source voltage (V_{DD}), and so is somewhere between 0 V and V_{DD}. This is easier to achieve because it does not require 'boosting' a voltage above the board power supply.

B.5.2 Conductivity / temperature power control

The Teensy is automatically turned on alongside the Raspberry Pi when the reed switch is closed by an external magnet. This architecture was chosen as a practicality given the structure of the existing circuitry (for the fluorescence sensor) when the conductivity and temperature sensors were introduced. The impact on power consumption is small (see Table 4.1, p. 177); additionally, the code is written to accommodate the Teensy staying on without reset even if the program is restarted.

The Teensy controls power to the conductivity and temperature voltage regulators separately. Both the regulator for the conductivity (Texas Instruments LM27762) and temperature (Texas Instruments TPS373133) have enable pins, allowing easy on/off functionality via GPIO. The LM27762 for conductivity additionally has an output pin to indicate whether the power output is at the desired value. The value of the TPS373133 for temperature can also be checked by reading in the fourth channel of the ADC, to which it is connected. Thus, both the conductivity and temperature circuitry provide features to check the performance of their voltage regulators.

B.5.3 Reed switch

A reed switch consists of two ferromagnetic blades (reeds) inside a sealed glass tube, which is filled with an inert gas to prevent oxidation of the contacts. For a normally open (NO) switch, the contacts close in the presence of a magnetic field; in its absence, the spring force of the reeds pulls the contacts apart. The sensitivity of the reed switch (i.e. amount of magnetic field required to actuate the switch) is determined by the relative stiffness of the blades, the size of the gap, and the overlap between the two contacts [164, 165]. Also described as 'pull-in', it is specified in units of ampere-turns (AT), which is a measure of magnetic field strength [166]. Lower AT means a more sensitive switch; typical sensitivities range from 10 AT to 30 AT [165].

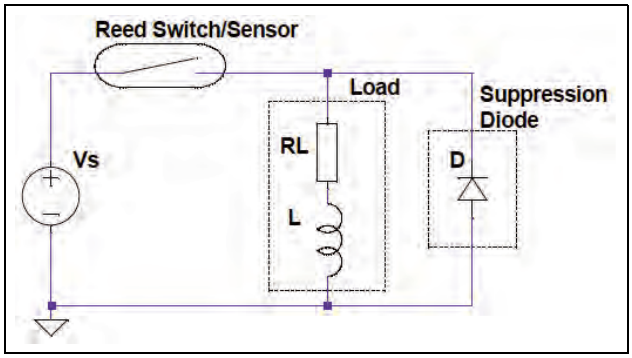

Figure B.8: DC reed switch circuit with protective diode. Source: Hamlin Inc. [167].

Reed switches are subject to damage from arcing, which occurs when the switch is driving a circuit with inductance. When the switch opens, the current changes abruptly, and the inductance causes current to flow backwards through the circuit. The inductor acts like a power source with a potential governed by the inductor equation $V = L\,\mathrm{d}I/\mathrm{d}t$ (i.e. proportional to the rate of change of current). This voltage can be extremely large, up to several thousand volts. This large voltage causes arcing across the small gap between the switch contacts, which can melt part of the contact surface. As the reeds initially 'bounce' on opening and closing, the contacts can solidify in a closed position. If the spring force of the reeds is not sufficient to break the micro-weld, then the reed is stuck closed. Either way, arcing can severely shorten the lifespan of the switch by damaging its contacts [164, 167, 168].

In DC circuits, the high voltage from arcing is typically prevented with a diode (often called a suppression diode, flyback diode, freewheeling diode, or catch diode), as shown in Figure B.8 [167]. The diode is not active under normal operation of the circuit, but for the reverse inductor current, it creates an alternative path that goes back through the inductor without passing through the switch. The inductor draws current from itself (hence the name 'flyback') in a continuous loop until the energy is dissipated through wire and diode losses. From the circuit, it can be seen that the diode should be chosen with a reverse voltage greater than the normal operating voltage, and a forward current greater than the maximum current induced by the inductor. The diode should also be placed as close to the inductive load as possible, to avoid radiation of electrical noise by cables [168].

For this system, the flyback diode is located on the same board as the switch, which is separated from the load (the photon counting board, which has an inductive choke at its input) by a ∼12" twisted wire pair. A future iteration might include the flyback diode directly on the photon counting board, but in this case, the boards were already fabricated, assembled, and in use by the time the switch was installed. The switch board also includes a protective diode to prevent damage from accidentally reversing polarity of the power source.

Capacitive loads, which even in the absence of capacitors can arise from other components such as long cables and MOSFET gates [169], are also troublesome for reed switches. When the switch closes, the capacitor acts as a transient short circuit (see Section C.1.1 for a tutorial in capacitor intuition), which can generate a high inrush current. The current usually decreases quickly to the steady state value as the capacitor is charged, but the initial current can be very high. It is limited by the elements in series with the capacitor and the switch—without an additional resistor or inductor, this comprises only the resistance of the contacts and the wire. The power dissipated (as heat) through the contact resistance ($P = I^2R$) can be sufficient

to melt the contacts and cause them to stick. Contact bounce can also subject the relay to multiple inrushes per activation, resulting in greater damage [164].

Inrush current can be limited by a series resistor, whose value can be chosen based on the driving voltage and the switching current limit of the switch [164]. An inductor can also be used, or an NTC thermistor [169]. NTC thermistors (inrush current limiters) are useful because they have high initial resistance, which decreases as the circuit is energized and the thermistor self-heats [170].

For this project, it was decided that, given the relatively high (for a portable instrument) steady state current of the instrument, a series resistor of the necessary value would needlessly dissipate too much power. The NTC thermistor as well had too high a resistance, even at its maximum current and temperature. (A 1 Ω resistance may not seem high; but with a 1 A current, it would dissipate 1 W, which is quite a lot of power for a portable instrument. This resistance would be less of a problem with, for example, a higher driving voltage, which for a given power requirement of the load would result in a smaller current). A series inductor would also require a rather high inductance. It was decided instead to limit the capacitance of the direct load. This involved removing the input capacitor of the 5 V regulator that is connected directly to the switch. The capacitor is not necessary for the regulator's functioning, and there are no other capacitors directly connected to the switch's load (see Section 4.1.3, p. 175 on power consumption, in reference to noise in power measurements).

In addition, some reed switches can handle capacitance better than others; in general, lower sensitivity switches can handle more capacitance. The reed switch used in this project, the Standex-Meder PR1262530, was chosen for its high current capacity. Reed switches have two current ratings: the maximum *switching current* that the switch can handle as it opens or closes, and the maximum *carry current* for when the contacts are already closed [166]. The carry current rating is generally higher, although too high a carry current can also melt the contacts together [164]. The PR126 model has a max switching current of 1.5 A and a carry current of 2.5 A. It should be noted that turning on some of the elements of the circuit exposes the power supply to some very large capacitors, which would cause a momentary large current draw that could exceed the carry current rating of 2.5 A. In practice, the switch was observed to stick semi-regularly, an issue that might be addressed in a future iteration of the instrument.

The reed switch chosen has a pull-in range of 25 - 30 AT, which is a relatively low sensitivity (as a tradeoff for greater current capacity). Sensitivity was a potential concern for this instrument because the switch must be activated through the wall of the housing's PVC lid, creating a minimum distance between the magnet and the switch.

In general, the interaction of the magnetic field and the switch, which defines the necessary activation distance, is quite complicated. It depends on the magnet's orientation and location relative to the switch, as well as its strength and shape [171]. With a wall thickness of 3/16", a relatively strong Neodymium Iron Boron magnet (0.5" diameter, 0.2" height; Radial Magnet Inc. 8177) was found to be sufficient to activate the switch.

B.6 Vector integration notes

Two methods exist for acquiring data from the ADV; both are implemented in the software. The ADV can be instructed to store data on its internal recorder (memory), which can then be read by the Pi after the measurement run. Data can also be streamed 'live' from the ADV to the Pi over serial port at the end of every measurement. Using the ADV's internal recorder results in some amount of data being discarded, since of the recorder stores in multiples of 256 bytes. However, reading data during collection reduces the amount of time spent measuring, as the Pi must receive and process the RS-232 signals. In addition, when used in tests in the laboratory tank (a relatively small system), the ADV's serial streaming was found to spike the water potential and interfere with conductivity measurements (see Section 4.4.2, p. 180). Ultimately, the final code for eddy correlation uses the recorder method, especially as the amount of data loss is small compared to the amount collected in an EC run.

Special care was also taken in programming the Pi to read the data bytes transmitted by the ADV. The Pi's speed is such that it often received and processed the data faster than the data could be made available; thus, the code specifically checks for and accommodates such situations.

B.7 EMI-reducing filter for Vector

As discussed in Section 4.4.2 (p. 180), the Vector was found to emit electromagnetic radiation associated with its ping pairs that interfered with the photon counting measurements. Nortek AS, the manufacturer of the ADV, worked with us to design and build a custom harness for the Vector with a filter that reduces its radiated EMI.

When we bought our Vector, the original harness we specified had 14 wires (that would be carried by two underwater Impulse cables, 8-pin and 6-pin) to allow a variety of signals in or out of the Vector. However, the prototype filter designed by Nortek could accommodate only 5 signals. Based on our application, the new harness was designed with a filter for the following signals:

- Ground
- RS232 TX
- RS232 RX
- Synch In
- Power out

The harness, including the filter, is shown in Figure B.9. The filter was designed to reduce emission of the 6 MHz acoustic signal as well as its harmonics. Data shared by the Nortek engineer showed a substantial reduction in a majority of the harmonics, including the strong 18 MHz harmonic (observed in our tests to be one of the strongest harmonics). As an example, the filter almost completely removed the 6 MHz signal, reduced the 18 MHz harmonic by 17 dB, and reduced the 100 MHz signal by 12 dB [Terje Peterson (Nortek AS), personal communication, 6 Jun 2016].

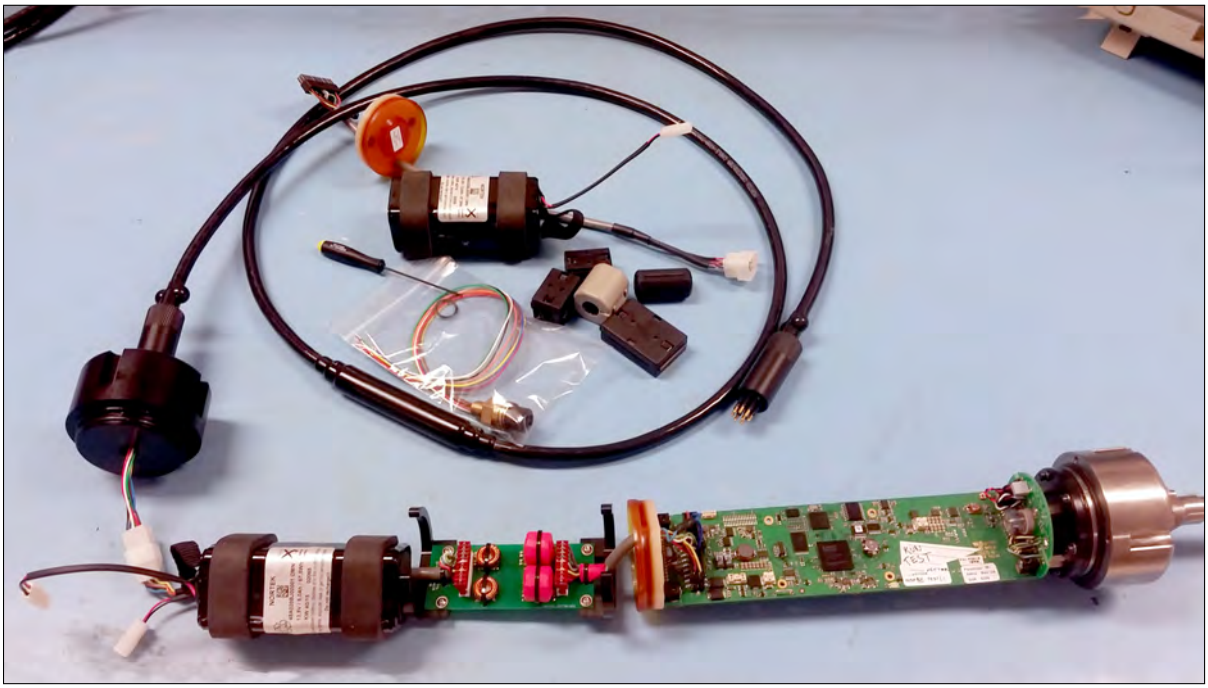

Figure B.9: Custom harness with filter designed by Nortek AS to reduce electromagnetic radiation from the Vector ADV. The filter sits between the ADV's circuit board (connected to the transducer) and the battery (connected to the endbell), occupying the space of a second battery. Credit: Terje Peterson.

Tested in our system, the new harness did indeed substantially reduce the radiated interference, to levels that could be screened out by setting the comparator reference voltage appropriately. Coupled with the integration of the PMT and the circuit boards in the second generation of the instrument, the issue was largely eliminated.

As described above, the harness was originally wired for 14 signals, but the filter could only accommodate five signals. This did not impact the functionality of the instrument, as the signals that were eliminated were not used (e.g. analog input, Sync Out, etc.) The harness was also wired with a 'Power In' to accommodate an external power source, i.e. from an AC adaptor. The Power In and its associated ground were not filtered; the Nortek engineer checked that they would not be a significant source of radiated noise.

The final 8-pin connector on the harness carries the signals for Power In, its associated ground, RS232 TX, RS232 RX, Synch In, Power Out, and ground, as well as one unconnected pin. The pinout was chosen to be compatible with the standard cable supplied for the original 8-pin connector. This cable broke out the Power In wire and its associated Ground to a separate barrel plug, while the rest of the signals were wired to a DB9 connector for RS232 communications with a PC. For our application, we used this cable to control the Vector directly through the Nortek software (e.g. check conditions, adjust Vector settings, test ADV functionality), often before deployments or to troubleshoot the ADV. For eddy correlation, a separate cable with underwater connectors on both ends was used to connect the Vector to the instrument. A mating connector was installed on the lid of the instrument's housing; inside, the RS232 lines were connected to a DB9 connector for communication with the Raspberry Pi, and the Synch In was wired to a separate plug on the board as a TTL signal. The Ground wire was split into

two and sent to both connections.

Thus, Synch In is not connected to anything when a PC is used to control the Vector, and the Power In and its ground are not connected to anything when the Vector is plugged in to the instrument (the Vector must operate from its own battery when it is controlled by the Pi; the Power In option is present to save power when using it with a PC). The Power Out, which is used to supply power from the Vector's internal battery to external instruments, has not been used so far and is not connected to anything in either setup.

B.8 Description of apparatus for EC tests in a tank

Dimensions and/or designs for many of the components described here are given in Appendix G.

B.8.1 Tank and turbulence mechanism

EC experiments were conducted in a 120 gallon glass aquarium with approximate dimensions $2 \times 4 \times 2$ ft ($0.6 \times 1.2 \times 0.6$ m). A wooden frame was constructed to hold a turbulence-generating mechanism over the tank, as shown in Figure B.10. The mechanism consists of a motor connected by a V-belt to a gear reducer (scavenged from a lawn mower). The shaft of the gear reducer is held by a mounted bearing with shaft collars to prevent sliding. It is attached to two timing pulleys, which in turn drive (via timing belt) two other pulleys at the other two corners of the tank. These two pulleys are connected to each other using a steel shaft secured to a raised wooden platform by mounted bearings.

The pulleys are modified to hold a crankshaft-like mechanism, enabled by shoulder screws, which drives vertical linear motion in four PVC plungers constructed of 0.5" PVC rod cemented to $\varnothing$ 3" PVC disks. The plungers are guided by pipe flanges mounted underneath the wooden platforms, and are set 45 ° degree out of phase with each other. The voltage-controlled motor is powered by a benchtop DC power supply.

The end result is that turbulence in the tank is generated by four linearly oscillating plungers at the corners of the tank, suspended $33 \sim 39$ cm above the tank floor, at a frequency that can be controlled by setting the voltage of the power supply. For the EC run described in Chapter 4, the power draw on the power supply was $\sim$2.25 A at $5.6 \sim 5.7$ V, which corresponded to a frequency of $\sim$0.9 Hz. However, the frequency was found to vary, as small misalignments in the mechanism would cause parts to rub, with a corresponding slow-down due to the friction. With enough rubbing, some parts would shift or be pushed, resulting in less friction and a faster speed. Over the course of an EC run, the amount of friction between different rubbing parts would vary, with corresponding variation in frequency.

The ADV was held over the tank by a specially constructed holder (Figure B.11), which was clamped to a wooden cross-beam. The cross-beams were mounted to the tank using rails held by friction fit to the rim of the tank. The ADV was not mounted directly to the wooden frame to avoid coupling of vibrations, which could cause false signals in velocity by vibrating the ADV stem, as well as interfere with the detection of smaller eddies.

Figure B.11: ADV mount.

Other features that can be seen in Figure 4.13 include a second wooden frame beneath the tank, which served as a containment structure in case of leaks; it was lined with plastic and equipped with a sump pump. The tank was also taped for protection in case of glass shattering, but much of the tape was removed for viewing.

a) Angled side view of tank. Reprint of Figure 4.13.

b) View of short end of tank (left-right is y axis), with instrument in housing at side.

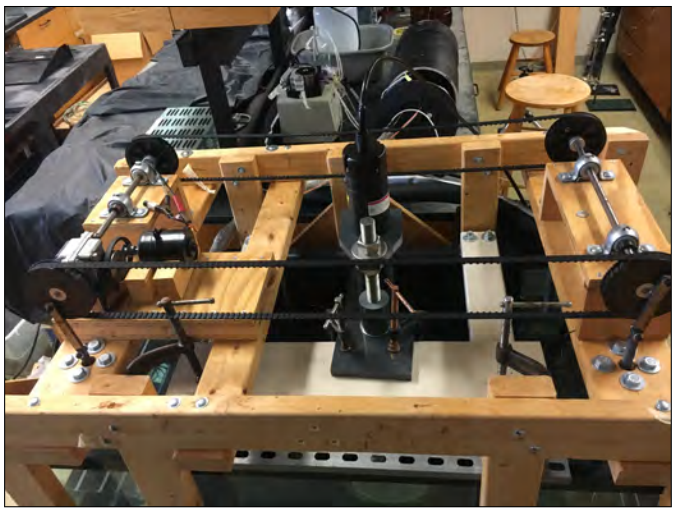

c) Top view of tank showing mechanism for generating turbulence.

Figure B.10: Experimental tank for conducting EC experiments. The wooden frame on which the tank rests holds a motor-driven mechanism with four oscillating plungers to generate turbulence.

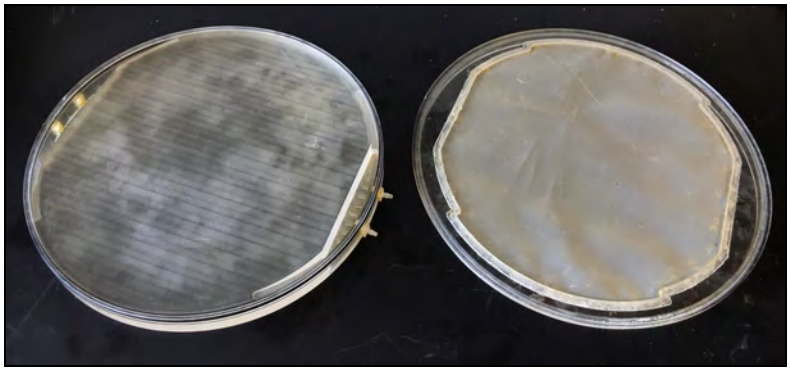

Figure B.12: Dye release plate (left) and lid with mesh (right).

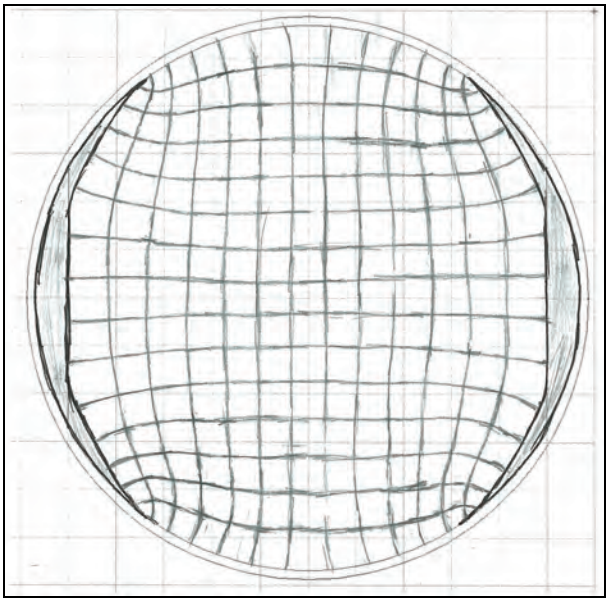

Figure B.13: Flow net used to design reservoir shapes for chemical release plate.

B.8.2 Dye release plate

The dye release plate was the product of several trials and iterations, in order to arrive at a design that could achieve a relatively even release across its surface. The final version was made mainly using a CNC mill with Mastercam CAD software, and is shown in Figure B.12.

The base of the plate was a circular 1" thick, 12" diameter piece of acrylic. The surface of this plate was milled down, except at the rim, to form a 1/16"-depth reservoir. The reservoir was designed to hold a shallow layer of dye that would then uniformly diffuse upward out of the lid. The shallow depth was chosen to avoid long set-up times (during the 'flushing' stage), as the pump rate would be quite slow. To allow dye to enter and exit the plate, two deeper reservoirs were milled at opposite ends of the plate. The shape of the side reservoirs (which have wings) was chosen based on a flow net, drawn to model 2-D flow through the plate given uniform head within each reservoir; the wings allow a more uniform distribution of dye across the entire plate as it moves from one reservoir to another. The flow net is shown in Figure B.13, and previous drafts used to arrive at this design are given in Appendix G.

Each of the side reservoirs was installed with 2 barbed tube fittings (for 1/8" ID tubing), epoxied into through-holes drilled through the side of the plate, for external attachment of the

tubing. An O-ring groove was also milled around the circumference of the plate and installed with a 1/8" width -276 O-ring (11" nominal ID). The lip of the lid, which fit over the O-ring to prevent leakage of dye, was constructed by cutting a 1/4" piece from a 12" diameter, 1/8"-wall cast acrylic tubing. The lip was bonded to the lid, which was constructed from an acrylic sheet milled into a circle slightly larger than the lip (to form a rim). The center of the acrylic sheet was milled out in the center in a shape matching the shallow reservoir of the underlying plate. A piece of 121 × 121 polypropylene mesh, cut to fit, was stretched over the shape and epoxied. The role of the mesh was to hold the dye within the reservoir so that it could be released at a controlled rate, as set by the peristaltic pump.

The performance of the mesh appeared relatively insensitive to the mesh / opening size, based on preliminary experiments. However, the material of the mesh was relatively important; an earlier iteration of the plate used nylon, which ballooned underwater and caused the reservoir to form a dome under the mesh. The resulting system, although capable of releasing dye (and, in fact, requiring a shorter flushing phase to achieve an even distribution, possibly due to mixing of the dye with ambient liquid underneath the dome), represented a slightly different release system than the one desired.

B.8.3 Dye release system

The benchtop setup of the dye release system is shown in Figure 4.15 (p. 189).

Fluid was pumped into or out of the plate using a 4-channel peristaltic pump (Rainin Dynamax RP-1). The pump required 3/16" OD tubing, with the ID of the tubing determining the flow rate for a given speed setting. For our application, we used 1/8" ID Tygon tubing, the largest that can be accepted (and thus the largest flow). The max flow rate per channel for this size tubing is specified by the manufacturer as 28.2 mL/min.

The original tubing supplied by the manufacturer was bonded with fixed collars to hold the tubing in the pump head at the proper tension. Tubing tension and diameter (which can be altered by constant tension) affect the reproducibility of the flow rate. However, the original tubing supplied by the manufacturer was no longer functional, so we used our own laboratory Tygon tubing. To prevent slipping in the pump head, small pieces of larger Tygon tubing (OD 5/16 in, ID 3/16 in) were cemented to the outside of the pump tubing using PVC cement, acting as collars.

The input tubing to the plate was insulated in foam insulation tubes to help maintain the temperature difference between the dye and the ambient water. The foam insulation used underwater was a 1/2"-wall, ⌀ 1/4 " (ID) Buna-N/PVC tube with the ends sealed with foam adhesive; both pump tubings were inserted inside for a snug fit. The portion of the pump tubings above water (i.e. between pump and the sealed insulation tube described above) was insulated in a split foam tube, which was filled with ice during runs.

Input liquid (dye or ambient tank water) was pumped to the plate from a suitable container with a barbed hose connection. For the dye, the container used was a 5 L polypropylene carboy with a valved spigot. When flushing dye through the plate, the outlet tubings (pulling liquid from the plate) were directed to a separate bottle that could then be emptied.

The container used when flushing or pumping ambient liquid (from the tank) was a glass beaker

with a hose connection. When flushing ambient liquid, the system could be set to recirculate flow by directing the outlet tubings back to the beaker. When pumping ambient liquid, the beaker, which had a 600 mL capacity, was periodically refilled by scooping water from the tank.

Both the carboy and the glass beaker had 3/8" barbed hose connections, so the same tubing could be used for both. The larger 3/8" ID tubing was connected to the two smaller pump tubings (1/8" ID) by a series of tube fittings including a Y-splitter, expander, and valve. The input solution was switched between the beaker and the carboy by momentarily turning off the pump, closing the valves, and switching the tubing from one container to the other.

B.9 Experimental steps for tank tests

Advance preparation steps to set up the experimental include:

- Align optical fibers with ADV sensing volume using a ruler and camera (easier if done before filling tank) to a separation distance of 5 mm $\sim$ 8 mm.
- Make dye solution, put in cold room overnight.
- Check EDDI's battery voltage; charge or discharge if necessary.
- Check PMT dark count; age overnight if necessary (a benchtop power supply can be used to power the instrument to conserve batteries).
- Prepare tank:
  - Put in most of the rubber sheets on the floor and walls (some rubber cannot be added until after the heaters are removed).
  - Fill tank with tap water from sink to a depth of $\sim$46 cm.
  - Add salt to a conductivity of $\sim$3500 µS/cm.
  - Put in heaters, set to a temperature of slightly over 26 °C.
  - Recirculate flow in the tank overnight using a bilge pump, to allow salt to dissolve, temperature to equilibriate, and oxygen bubbles to dissolve out of solution.
  - Following overnight recirculation, check conductivity and adjust if necessary by adding salt, or pumping out water and adding tap water.

Preparation steps done immediately before the experiment include:

1. Turn off recirculating pump and connect turbulators to power supply; check turbulence setting.
2. Remove heaters; finish lining walls of tank with black rubber.
3. Connect ADV to PC using standard cable for pre-run checks:

- Configure ADV to settings described in Section 4.5.1 (p. 193), except Start and Sample on Synch, and start measuring by streaming data to PC.
- Before adding seed, check for large amplitudes indicating interference by the optical fibers, and adjust fibers if necessary, until sufficiently low amplitudes ($<$110 counts in all beams) are achieved.
- Turn on turbulence and add seed to achieve reasonable amplitudes ($\geq$110 counts in all beams). Check correlations and troubleshoot if necessary.
- Finish the ADV check by changing settings to enable Start and Sample on Synch, and running a shadow recorder run, ensuring that the recorder file has a name and that streaming is disabled (default). Disconnect the ADV from the PC and connect it to EDDI. Turbulence can be turned off again.

4. Set up dye input system:
   - Prepare ice bath and set carboy in it.
   - Set up recirculating flow system for the plate by connecting the glass beaker to the input and filling with tank water, and directing the output back to the same beaker.
   - When tubes are properly primed (no air bubbles), put lid on plate underwater and position plate under sensing volume but slightly offset (due to circulation patterns in tank).
5. If imaging with a camera, check camera settings (time lapse images were generally used at a rate of one image per 5 s), focus, and battery. Install black light on frame with a small clamp.
6. Using commercial instruments, measure conductivity, temperature, and depth of tank, and conductivity and temperature of dye solution (for calibration purposes).
7. Cover tank with blackout cloths, especially areas directly facing the optical fibers.
8. Set up EDDI:
   - Power on EDDI, connect via ssh, start tmux, and start the program.
   - Set up and turn on the desktop fan. Slightly open the housing to expose the C/T board and possibly the PMT, but cover any exposed areas tightly with a blackout cloth. Turn off lights.
   - Tune monochromator to a dark wavelength (e.g. 700 nm) and turn on PMT to allow the initially high dark count to drop.
   - Turn on conductivity and temperature sensors to allow thermal drift to settle.
   - Wait $\sim$10 min, and do not proceed until dark count has dropped to acceptable levels ($\sim$700 counts/s were generally acceptable, as the dark count would continue to drop during the remainder of the pre-run checks).
9. Turn on turbulence.
10. Take baseline measurements with EDDI:

- Take baseline modulated fluorescence scan (e.g. 300 to 700 nm) to check for proper LED signal and extent of spectral bleeding into fluorescence range.
- Set the monochromator to the correct wavelength for emission. 506 nm was used for the experiment described in Chapter 4; the emission wavelength of fluorescein is higher, but 506 nm was found to produce the highest emission for our unit at the time of experiments, likely due to calibration drift.
- Turn the monochromator off to conserve power.
- Measure fluorescence, temperature, and conductivity, for calibration purposes as well as to check that all sensors are working properly (e.g. temperature range is not exceeded, conductivity cables have not come loose).

11. Wake up ADV and start EC measurements.

The 'baseline measurements' (spectral scan and fluorescence / temperature / conductivity measurements) were also repeated at the end of the run.

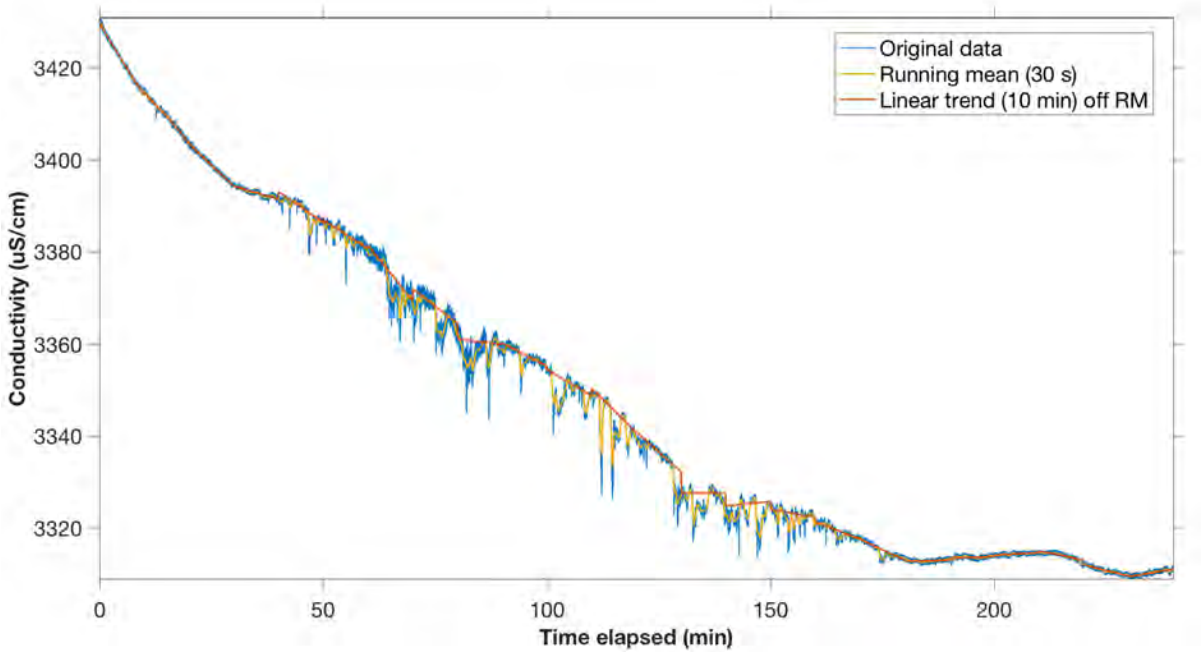

Figure B.14: Original data conductivity, 30 s running mean, and 10 min linear detrend of running mean, calculated as the first steps in identifying excursions.

B.10 Data processing for EC tests

B.10.1 Removal of excursions

As described in Section 4.5.4 (p. 199), for some of the analyses, the large, minutes-long excursions were removed from the dataset in order to examine flux carried by smaller scale motions. Given that there is inherently some subjectivity in deciding what comprises an 'excursion', the algorithm for removing the excursions is a best-attempt approach that produces reasonable results.

Algorithm for identifying excursions

The algorithm to identify excursions was applied to the conductivity data only, which had the largest and most prominent excursions. Then, time segments identified in this way were cut out of the original dataset for all of the sensors and the vertical velocity. They were left as gaps in the data, bypassed by the subsequent mean removal and flux calculations.

The basis for identifying the excursions is the calculation of a 30 s running mean, and the identification of segments where it is changing. The running mean smooths over smaller and faster fluctuations, so a changing mean indicates a larger feature.

However, due to the underlying linear trend in the data, the running mean was always changing. Thus, rather than simply looking for segments where the mean is flat, the algorithm looks for 'outliers' of the mean from a 10 min linear detrend (of the running mean). 10 min was chosen

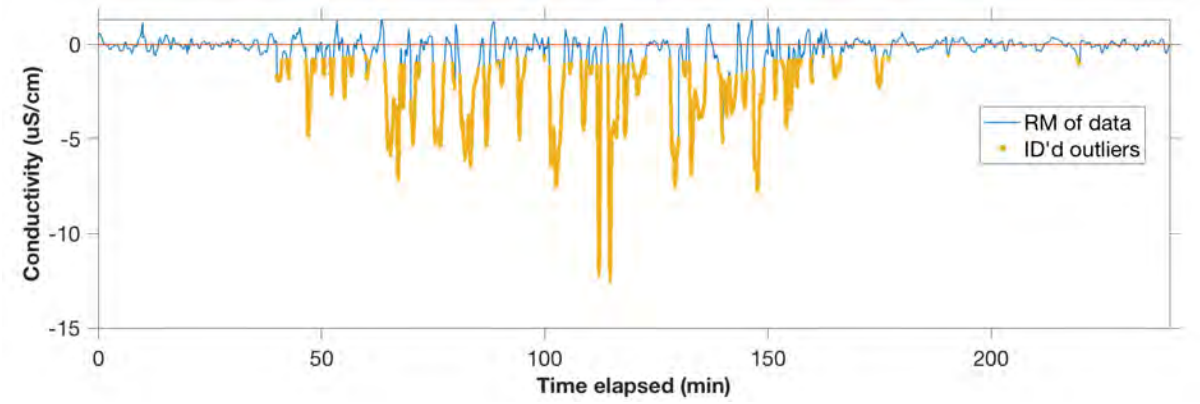

Figure B.15: 30 s running mean of conductivity data, with 10 min linear detrend subtracted, showing points identified as outliers.

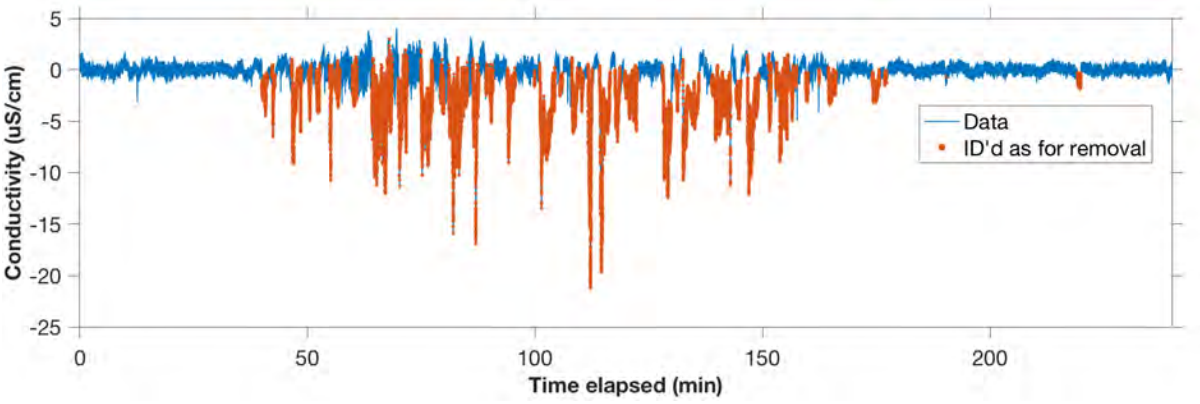

Figure B.16: Original dataset, with 10 min linear detrend subtracted, showing points identified by the algorithm as excursions.

due to the thermal drift of the conductivity sensor. The original data, running mean, and linear fit to the running mean are shown in Figure B.14.

For each 10 min block, outliers were identified as more than 2× the noise level away from the calculated linear trend, where the noise was calculated as the fluctuations around the linear trend in the first period (where there were no excursions). The process was iterated, i.e. the linear fit was recalculated with the outliers removed, since the original outliers could bias the fit; and outliers were re-identified. The detrended data, along with the identified outliers, is shown in Figure B.15. For this plot, the linear fit was subtracted from the data to aid in visualization, at the expense of slightly distorting the data.

Finally, the time points corresponding to outliers identified in the running mean were labelled as 'excursions'. The results for the conductivity dataset, again shown with mean removed to aid in visualization, are given in Figure B.16. It can be seen that, although the outliers identified in Figure B.15 for the running mean appear to be somewhat of a flat cutoff some distance away from the baseline (Figure B.15), in the original dataset they do correspond to what can reasonably be identified as excursions.

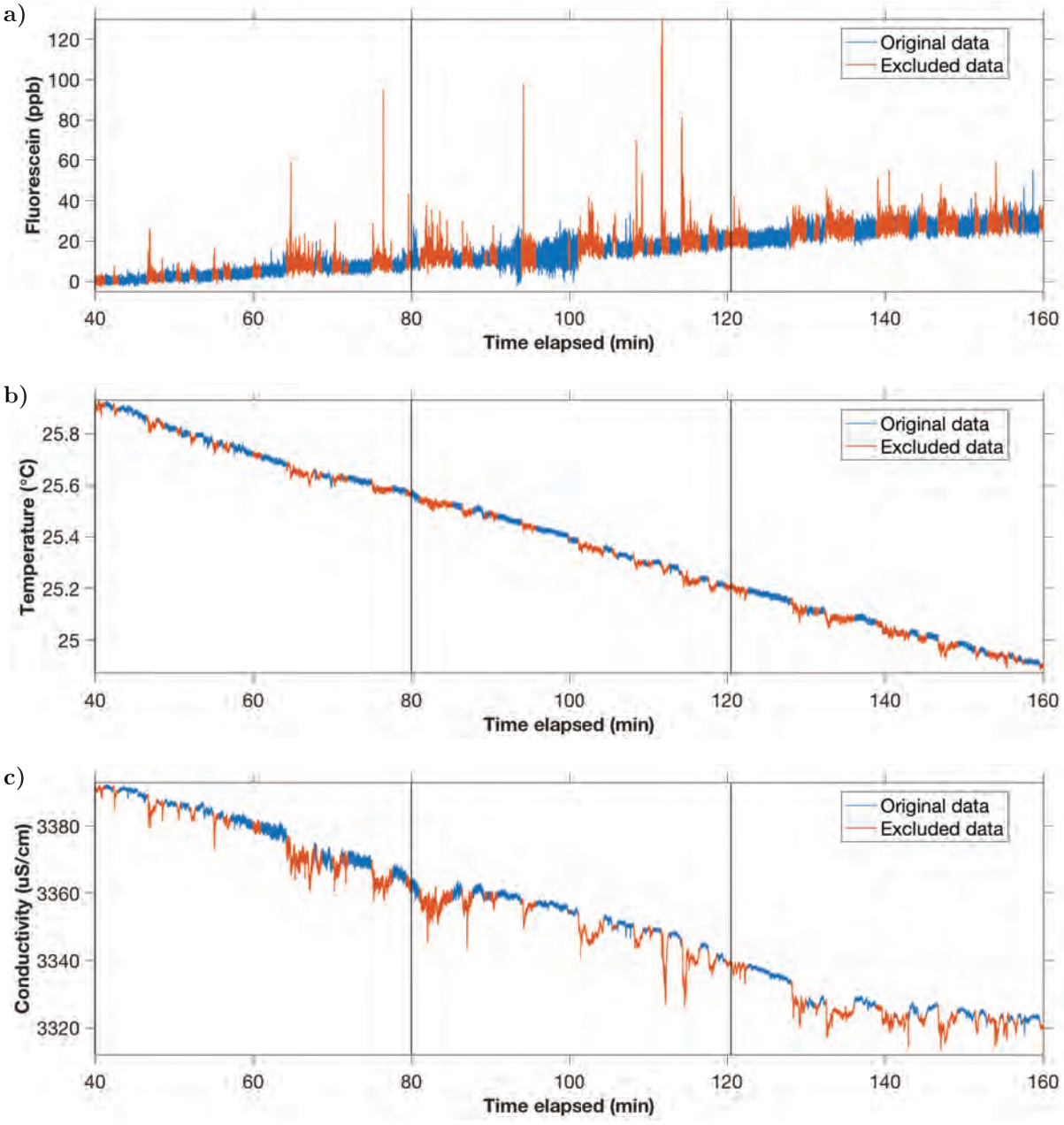

Figure B.17: Zoomed time series of un-detrended **a)** fluorescein, **b)** temperature, and **c)** conductivity, showing segments identified as excursions based on the conductivity running mean.

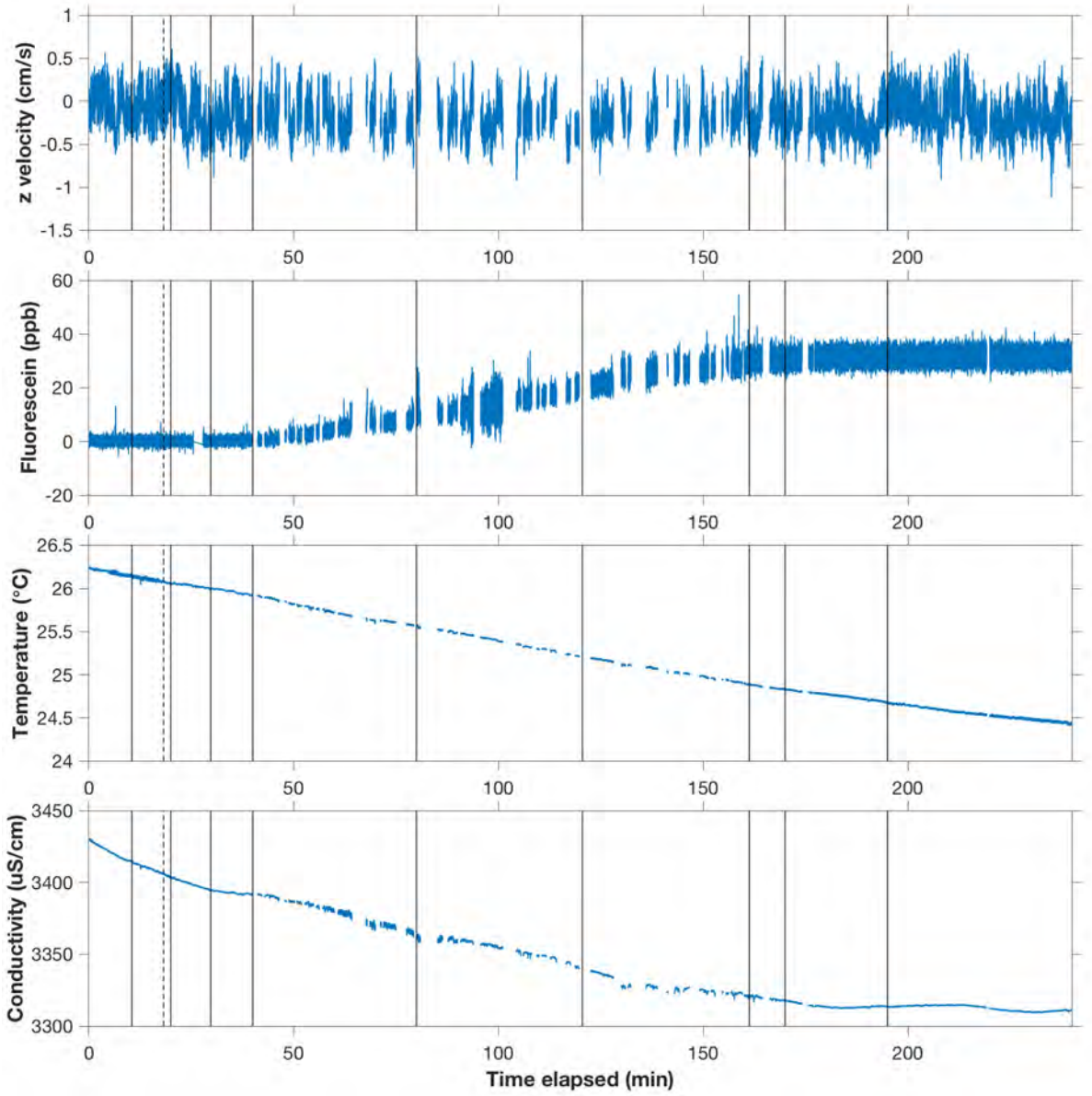

Figure B.18: Full time series for EDDI and w measurements taken during EC run in test tank, with excursions removed as described.

As described above, the time segments identified this way were removed from all three EDDI measurements (concentration and velocity values were replaced by 'NaN' in the MATLAB data for the identified time points). The results are shown for one time segment, as an example, in Figure B.17. The final full time series with excursions removed is shown in Figure B.18, which can be compared to the original time series in Figure 4.21 (p. 204).

Spectral calculations on data with excursions removed

Calculation of spectra and cospectra after removing excursions is not straightforward, because of the gaps created in the data. For flux calculations, the gaps can simply be ignored while the remaining data is used to calculate the running mean or linear trend, subtracted from to identify fluctuations, and multiplied to obtain covariance. However, Fourier transforms cannot be calculated on data with gaps, requiring some additional or alternate treatment.

One option is to calculate spectra on continuous segments individually, and then ensemble average them as done by other EC practitioners when 'events' are sparse (see Section 1.5.6, p. 65 on aquatic EC in non-benthic settings). However, the implementation for this approach is quite complex. As we did not require great precision in the results (the spectra were used for rough comparisons and high-level analyses), we opted for a more approximate approach that involved approximating the excursion-removed data as one continuous dataset, i.e. by 'removing' or 'filling in' the gaps.

'Removing' the gaps would, in the simplest interpretation, involve excluding the gaps and splicing together the remaining segments. We decided against this approach because, given the relatively large number of splices and short length of the segments, artificial contributions from treating distinct segments as continuous could become significant. Instead, we chose to interpolate across each excursion with a two-point interpolation based on the data points to either side of the gap, i.e. each excursion was replaced by a line. Then, similar to the procedure for the original datasets, either a 40 min linear trend or a 30 s running mean was calculated and subtracted from the data (to remove large components at low frequency from the trending baseline, or to look at fluctuations, respectively) before transforming to frequency domain.

The spectra are thus somewhat approximate, since the interpolated line across each gap could still create spectral contributions, and would also affect the calculations of the linear trend or running mean. However, the approximation was considered acceptable since, with excursions removed, all the data was relatively close to a trending baseline (or 0 for the velocity). Consequently, the interpolations would likely lie relatively close to the linear trend or running mean, and would therefore have small contributions to the fluctuations used to calculate spectra.

Effect and necessity of removing excursions

It could be argued that the excursion removal process is unnecessary; a low-frequency filter like the 30 s running mean should identify all low frequency components, which could then be subtracted from the data in the Reynolds' decomposition. Since the excursions were large events, they should be removed with the mean.

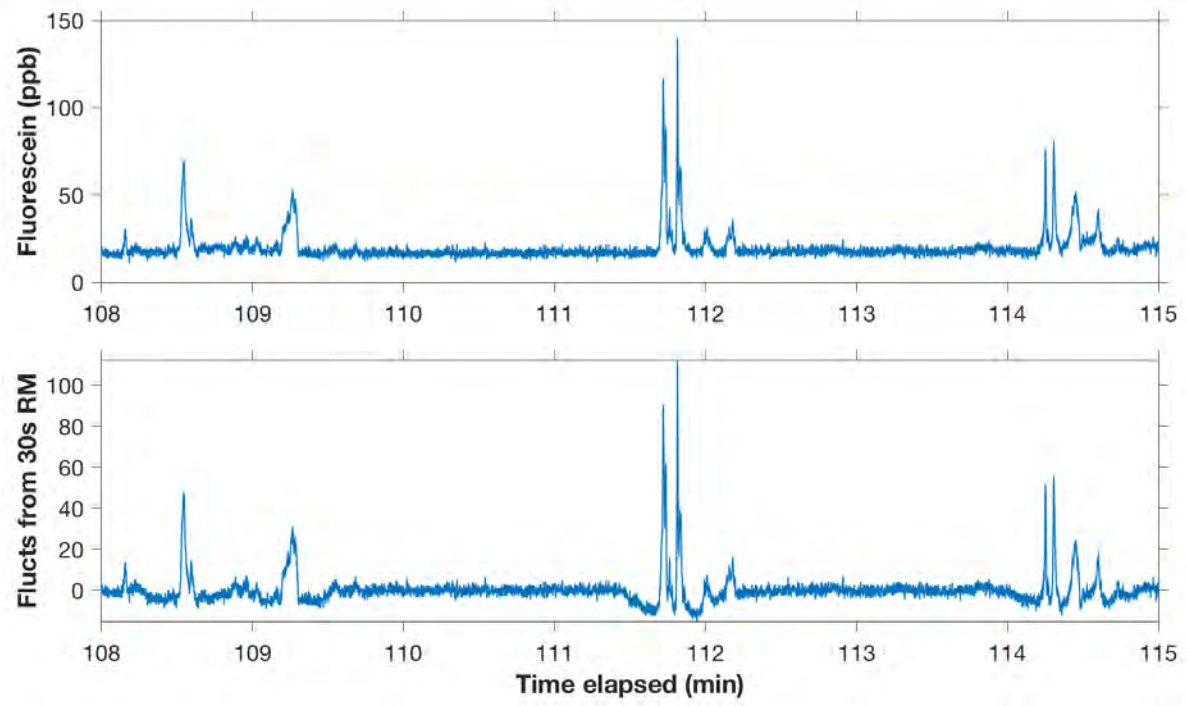

Figure B.19: Time series of fluorescein, along with fluctuations after subtracting a 30 s running mean. The fluctuations have apparent depressions around the large features, due to their effect on the mean.

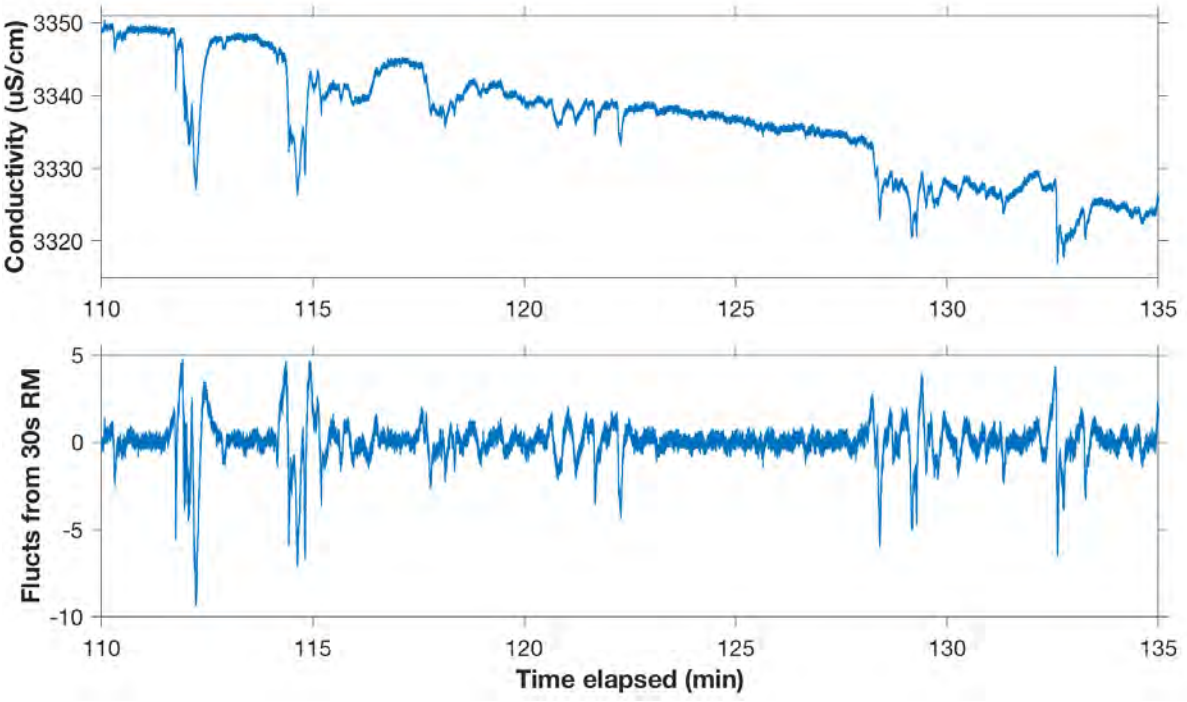

Figure B.20: Time series of conductivity, along with fluctuations after subtracting a 30 s running mean. The fluctuations have sharp upward spikes around the large features, due to their effect on the mean.

However, we found that the excursions were so large that they would noticeably affect the running mean, creating artifacts in the apparent fluctuations. Examples for fluorescein and conductivity are shown in Figures B.19 and B.20. It can be seen that, although the trending baseline in the original dataset appears to be relatively linear, the subtraction of a 30 s running mean created apparent fluctuations in the opposite direction.

In Figures B.21 and B.22, variance-preserving spectra from the original time series are shown alongside spectra calculated after subtracting a 30 s running mean (i.e. corresponding to the time series shown in Figures B.19 and B.20). Each graph also shows an analogous pair of spectra calculated from the data with excursions removed.

If the running mean were an ideal filter with a 30 s cutoff, its subtraction would remove all spectral components below 0.03 Hz while maintaining exactly the components at higher frequencies. A running mean is, of course, not an ideal filter, so the spectral cutoffs in Figures B.21 and B.22 are not sharply at 0.03 Hz; however, it can be seen that components below $\sim$0.01 Hz are still generally removed. For reference, the filter characteristics of a 30 s running mean are shown in Figure B.23, and the frequency domain representation of the mean removal process is shown in Figures B.24 and B.25 using normalized variance preserving spectra.

Interestingly, after subtracting the running mean the signals appeared to have some components in the $0.03 \sim 0.1$ Hz range that were actually *greater* than the original series. These components possibly correspond to the artificial fluctuations shown in Figures B.19 and B.20. Technically, this should not be possible, since the running mean filter can only attenuate the original spectrum, and a subtraction in frequency is a subtraction in time. The 'production' of spectral components is thus somewhat mysterious from the perspective of a frequency domain analysis. However, it is congruous with the idea that fluctuations are 'created' around excursions when subtracting a running mean.

This pattern also occurred after removal of excursions, which is at odds with the argument for removing excursions to avoid artificial contributions. However, as discussed above, the spectra for these data are somewhat more approximate due to the way they were calculated; the 'production' of spectral components after removing the running mean could arise from the interpolation. In addition, even though the excursion-removed dataset shows greater power at some frequencies after mean removal than before, the post-removal spectra (suspected of containing artificial contributions) are still generally across the board lower than the original data without excursion removal.

In the absence of artifacts, fluxes calculated using fluctuations around a 30 s running mean would ideally be the same whether or not excursions are removed, since the excursions are relatively low frequency. We found that fluxes calculated using the original dataset (i.e. the data in Figures B.19 and B.20) were larger than those calculated using the data with excursions removed. The larger fluxes may be due to the artifacts, or they may be due to actual fluctuations (eddies) 'within' the excursions. We cannot rule out that excluding excursions causes some real fluxes to be missed, in addition to being a slightly artificial process. However, we decided to err on the side of caution and present data interpreted as 'fluxes during non-excursion segments'. In future similar situations, a different low pass filter may be able to remove lower frequencies without artifacts, and thus obviate the need to remove excursions.

The excursions actually affect all mean calculations, unless very long windows are used, which

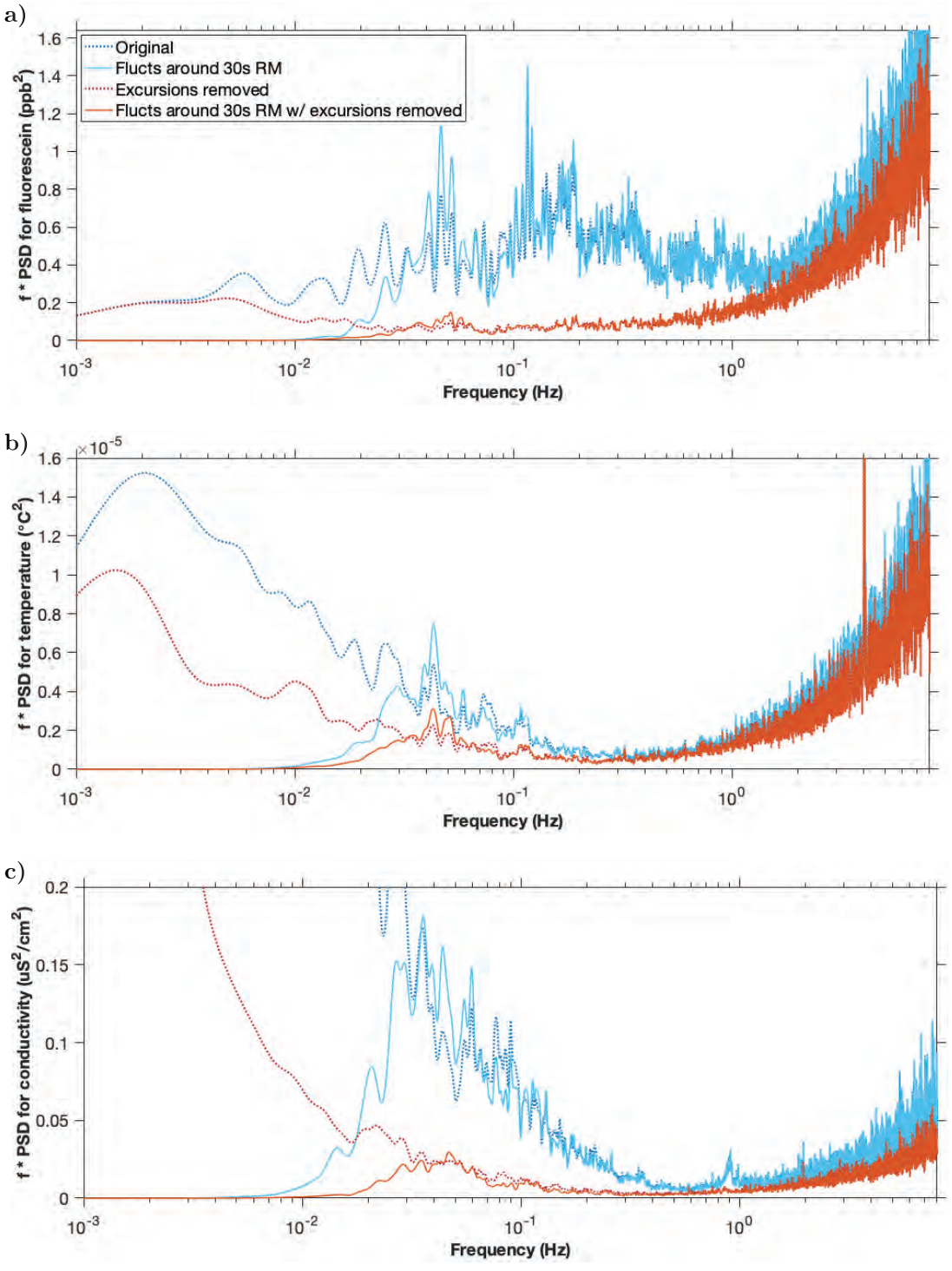

Figure B.21: Variance-preserving spectra of **a)** fluorescein, **b)** temperature, and **c)** conductivity for the full EC run. Spectra are shown for the original time series (with a 40 min linear trend removed), fluctuations around a 30 s running mean (i.e. original time series with a 30 s running mean subtracted), the time series with excursions removed, and fluctuations around a 30 s running mean calculated from the time series with excursions removed.

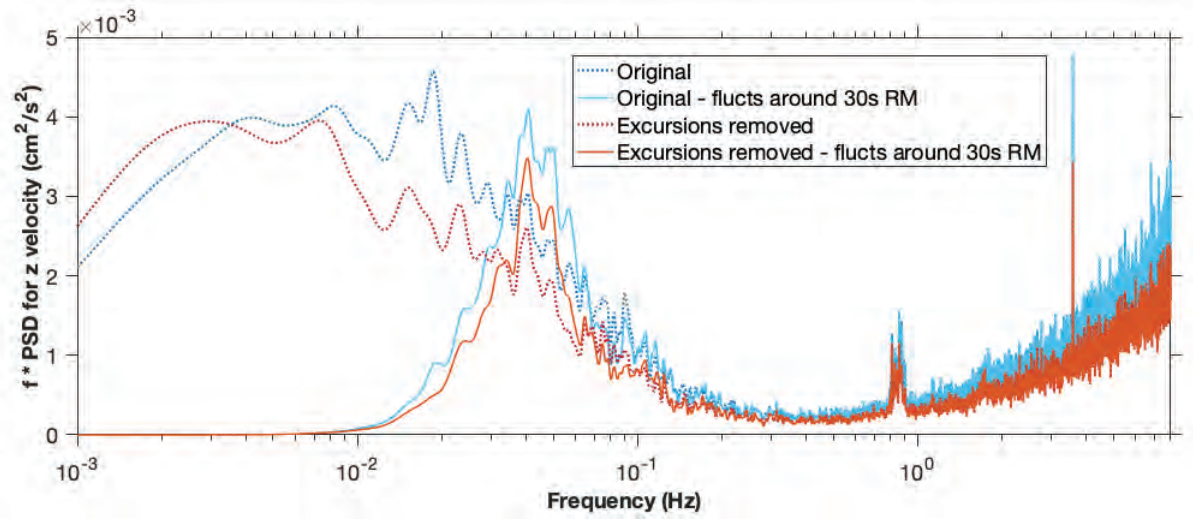

Figure B.22: Variance-preserving spectra of z velocity (w), similar to the time series shown for the concentrations in Figure B.21.

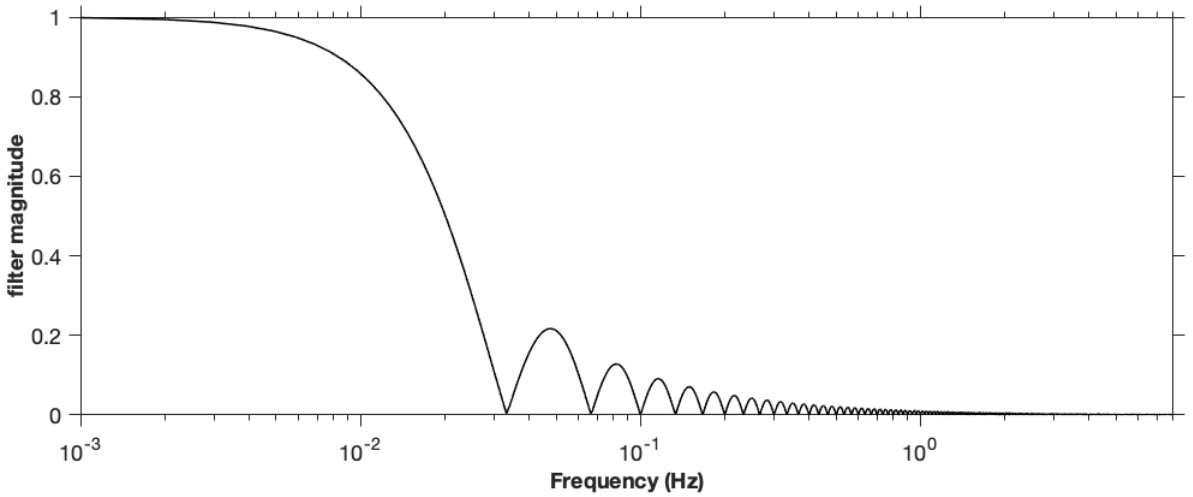

Figure B.23: Spectral representation of a 30 s running mean filter.

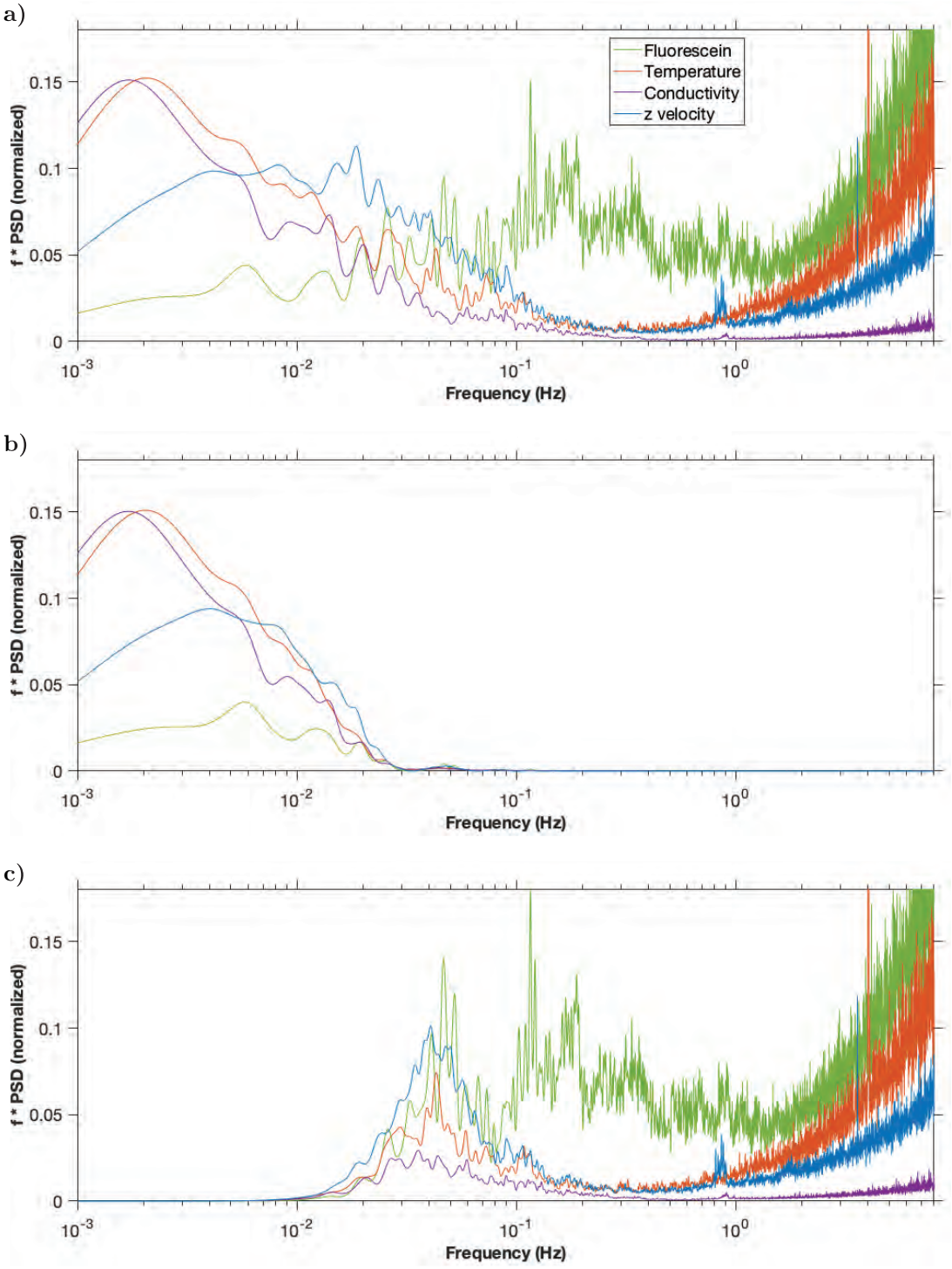

Figure B.24: Normalized variance-preserving spectra of **a)** original time series (with a 40 min linear detrend), **b)** 30 s running mean of original time series (also detrended), and **c)** fluctuations around a 30 s running mean (i.e. **a)** minus **b)**). All three concentrations and z velocity are shown together in each graph, normalized by the total variance of the original time series after a 40 min linear detrend (i.e. total area under **a)**). Note that **a)** is identical to what is shown in Figure 4.32 (p. 217), and **a)** and **c)** are represented in non-normalized form in Figures B.21 and B.22.

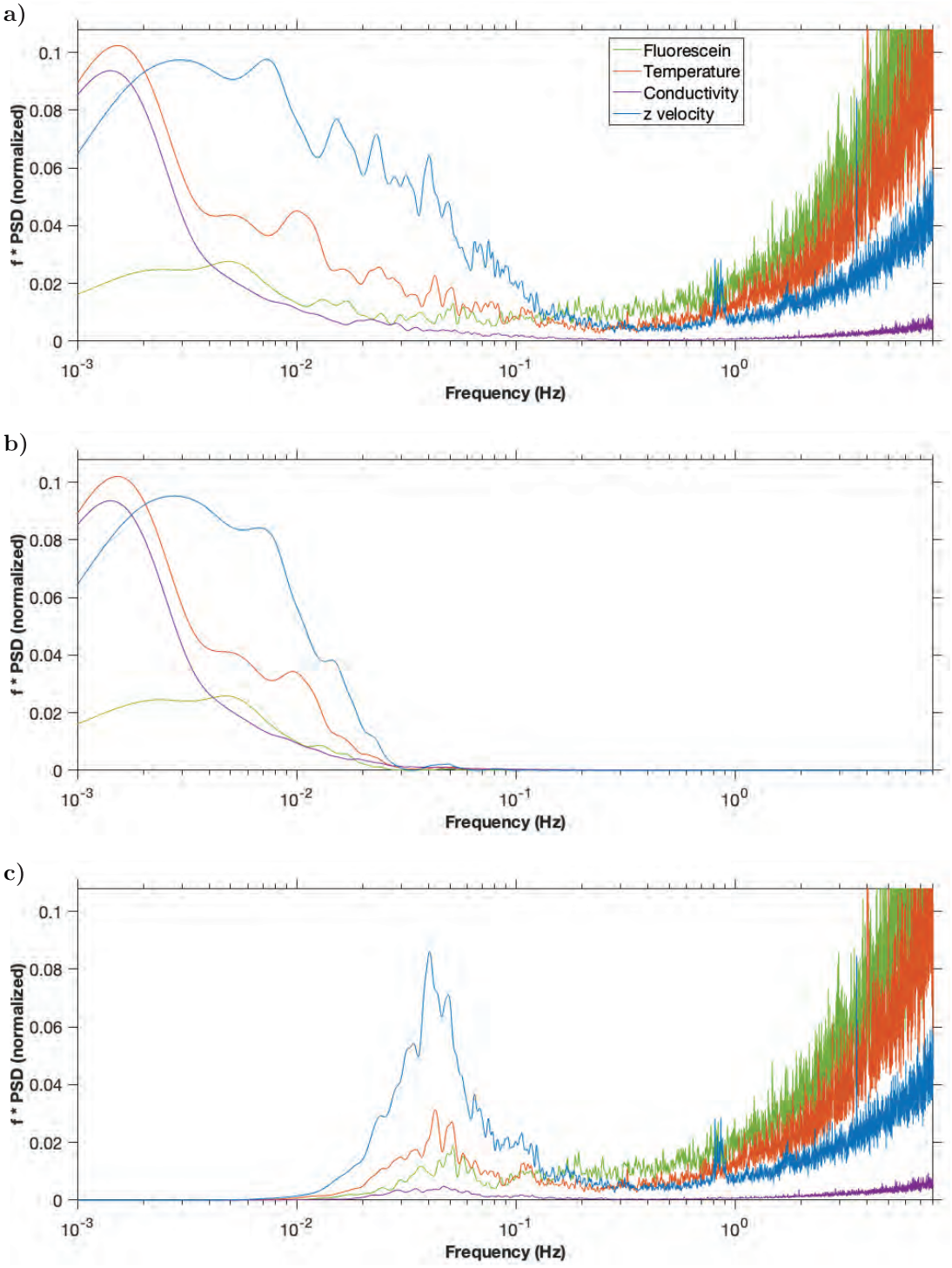

Figure B.25: Normalized variance-preserving spectra of **a)** excursion-removed time series (with a 40 min linear detrend), **b)** 30 s running mean of excursion-removed time series (also detrended), and **c)** fluctuations around a 30 s running mean (i.e. **a)** minus **b)**). All three concentrations and z velocity are shown together in each graph, normalized by the total variance of the *original* time series (including excursions) after a 40 min linear detrend (i.e. total area under Figure B.24a). Note that **a)** is identical to what is shown in Figure 4.32 (p. 217), and **a)** and **c)** are represented in non-normalized form in Figures B.21 and B.22.

is problematic if the data is interpreted as a trending baseline with events. A linear trend would still be biased by the excursions—which could be large and several minutes long, at least for conductivity and temperature—and deviate from the apparent baseline. This was indeed observed for the 10 min linear detrend used in many of the flux calculations, where portions of the 'baseline' for the conductivity and temperature measurements would appear instead as positive fluctuations. We did explore a linear detrending method that excluded outliers, which resulted in a trending mean that more closely followed the baseline. However, the effect on the fluxes was small. In addition, it is also possible that some portions of the baseline do in fact represent 'positive fluctuations' (e.g. in the view of a solute-carrying eddy, the downward movement of bulk liquid could be considered part of the diffusion as the mean values are changing). Given the complicated interpretation, and the fact that the effect on fluxes was small, we erred on the side of less data processing and ultimately did not use this technique.

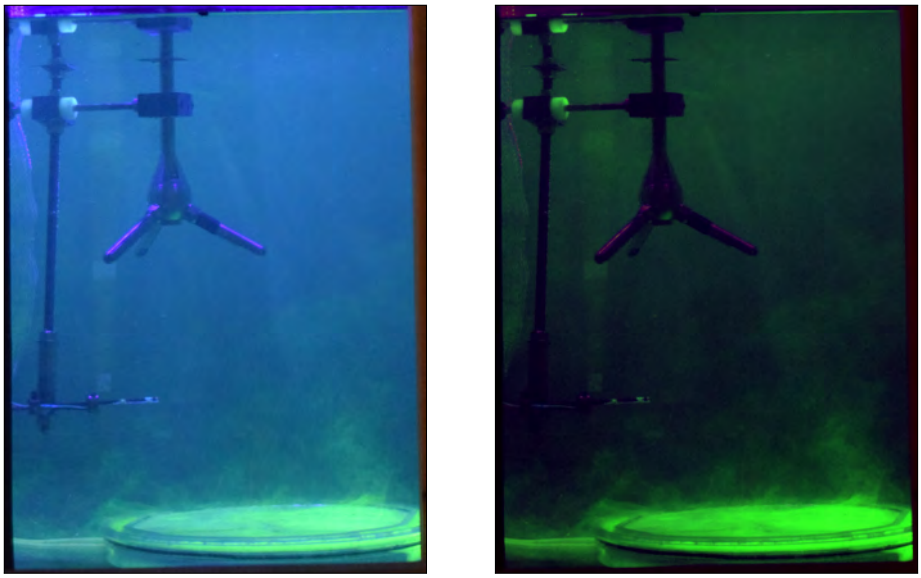

Figure B.26: Image processing of Figure 4.17a to reduce blue and red components, as well as darken 'background' green components.

a) Original image.

b) Reprint of Figure 4.17a.

B.11 Image processing

Many images of the instrument in this thesis were processed slightly in Adobe Photoshop to provide a clearer view of the instrumentation. Processing included enhancing brightness and contrast and removing backgrounds.

The images of rising dye in the tank tests, shown in Figure 4.17 (p. 192), were processed more heavily, to make it easier to see the eddy-like features in the plumes. Processing involved using the 'Levels' feature in Photoshop separately to reduce the blue (and red) components. Blue in particular was a problem because the light from the UV lamp used to excite the fluorescence could mask some of the features in the green fluorescence. In the future, a SCHOTT glass longpass filter for ~495 nm (assuming fluorescein emission is 510 nm) would likely provide better results, since it has a sharp cutoff for frequencies shorter than the target frequency (longer frequencies were not considered a problem, since the photos were found to have little red content). Afterprocessing images taken without the filter relies on the camera's blue and green detectors to separate the frequencies, and it is likely that undesired blue-tinged components would make their way into the green pixels.

The green channel was also edited using 'Levels' to enhance the appearance of the features of interest. Figure 4.17a is shown again in Figure B.26 alongside its original photo. For this image, the only enhancement of the green channel was to raise the minimum input to 75 (from 0), which means that all pixels with camera-recorded values darker than 75 are output as 0 (black). This served to darken the background so that the brighter features would be more noticeable. The maximum output of the blue channel was also changed to 60, and of the red channel to 125, meaning that all values recorded as higher (more brightly blue or red) by the camera are displayed at that level. All the numbers are somewhat arbitrary and were chosen based on subjective evaluations of image quality.

Another example of image processing is shown in Figure B.27, which shows a dye release from

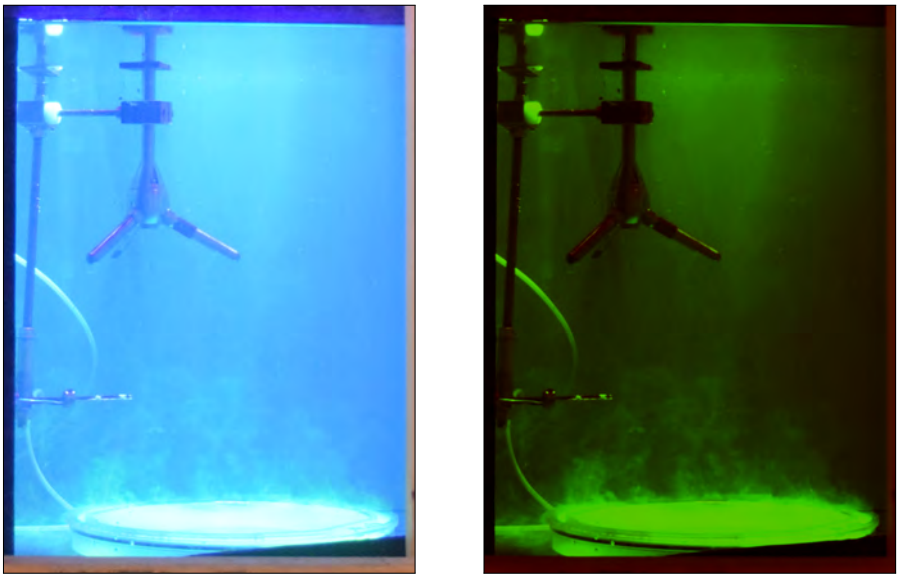

Figure B.27: Image processing of a dye release photo with a stronger excitation source, requiring adjustments to contrast.

a) Original image.

b) Processed image.

a different eddy correlation run (6 September 2018). Although this image was not included in the main thesis, it can be used to demonstrate some features of image processing. The UV lamp was much closer to the water in this run, so the blue components are more prominent. In addition, because the light was stronger, the fluorescence from the plate was very bright and dominates the green channels; the more dilute features in the sensing volume are difficult to see.

Processing for this image involved raising the minimum input of the green channel to 75, as well as changing the γ value to 0.32. The γ represents the curvature of the input-output curve and is normally 1 (straight line). $\gamma < 1$ increases the contrast (steeper slope) for darker elements (lower numbers), so that changes in the input pixel number are magnified in the display output. It also reduces the contrast for lighter elements. In this case, it serves to increase the contrast for the fainter dye features in the sensing volume. The blue output was also capped at 0 (no blue) and the red at 100. The green shades in the overlying water that appear to correspond to the beam of light from the UV lamp could be components of the strong 405 nm excitation that the camera registered as having some green (and thus stored values in the green pixel). They could also correspond to dye that was already mixed into the system at the point that the picture was taken, and was then excited into fluorescence by the strong UV light.

Appendix C

Supplementary results

C.1 Electrode polarization in the conductivity cell

C.1.1 Background: capacitor tutorial

The governing equation for a capacitor is

$$C = \frac{Q}{V} \tag{C.1}$$

or permutations thereof, where C is the capacitance, Q is the charge, and V is the voltage. Thus, the capacitance of a capacitor defines the amount of charge it can hold for a give amount of voltage drop across it.

In terms of current, the equation is often presented as

$$I = \frac{\mathrm{d}Q}{\mathrm{d}t} = C\frac{\mathrm{d}V}{\mathrm{d}t} \tag{C.2}$$

where I is the current.

By Eq. (C.1), $C = \infty$ means that any amount of charge can exist without any voltage drop; by extension and Eq. (C.2), any amount of current can flow even if voltage is not changing. Thus, infinite capacitance means that the capacitor behaves as a short circuit. On the flip side, $C = 0$ represents an open circuit.

The intuition for capacitors is often that large capacitors can store lots of charge and result in a slower time response, which may seem at odds with the near-short circuit. In fact, all finite capacitances are open circuits ('storing charge') for DC voltages. In a DC context, the slow time response can be seen in the behavior of a series RC circuit in reaction to a step input, e.g. after a DC voltage source has been added or removed. Charge must accumulate or leave the capacitor so that it reaches its open circuit voltage, but with a series resistor limiting the current, this can only happen so quickly. Thus, the change in voltage across any given element (and therefore the current, which is directly proportional to voltage across the resistor) is limited. For a given R, the change is slower for capacitors with higher C, since it will take more current to achieve the necessary voltage. For a given C, the change is slower for large R,

because the current is more limited. The time response is often characterized by the RC time constant.

In terms of open and closed circuits, a capacitor by itself or in parallel with a resistor is a short circuit immediately after the step input, in which case current rushes in (or out) to quickly charge (or discharge) the capacitor to match the input voltage. A larger C would draw a higher inrush, a longer duration inrush, or both, to accumulate more charge.

For AC signals, the voltage and current are constantly changing; there is no step response. The impedance of the capacitor is purely reactive, as

$$Z_{\mathrm{C}} = \frac{1}{j\omega C} \tag{C.3}$$

since $Z = V/I$ and Eq. (C.2) in complex form (applied to sinusoidals) is given as

$$I_0 e^{j\omega t} = C\frac{\mathrm{d}}{\mathrm{d}t}\left(V_0 e^{j\omega t}\right) = j\omega C V_0 e^{j\omega t} \tag{C.4}$$

where I_0 and V_0 are the amplitudes of the current and voltage.

A capacitor in series with the voltage source and other circuit elements, such as C_{probe} in Figure C.1 (which models C_{dl} in Figure C.2), is a *coupling capacitor*. This means it allows AC (or otherwise changing) signals while blocking DC. More specifically, it blocks signals below a certain frequency, depending on its capacitance. Since voltage is changing (sinusoidally), an infinite capacitance is now more accurately a short circuit. For example, as potential on one side of a parallel plate capacitor changes with the voltage source, current will flow to or from the capacitor and will draw equal current from the other side to balance out the charge. There is a phase shift from one side of the capacitor to the other, but if C is large, lots of current can flow with little change in voltage across the capacitor, so the relationship of current to voltage is dictated by other circuit elements and is essentially independent of the capacitor. However, if C is small, then voltage across the capacitor can change noticeably as current flows. If this voltage builds quickly but the voltage source is not changing fast enough—the AC frequency is too low—then the relative voltage difference between the source and the capacitor decreases, and the current slows. This can also be thought of in terms of signal decay [172], whereby for a given AC input, too small a capacitor will cause the signal to decay too quickly. In that case, the capacitor equalizes with the driving voltage and current ceases to flow.

Thus, small capacitors only allow high frequencies, whereas larger capacitors also allow lower frequencies—and behave like short circuits for a wider range of signals. In parallel to the above scenario, the series resistance will limit (or dictate, depending on how you look at it) the current. It does this by 'setting' the current in lockstep with the input voltage, which is changing sinusoidally; in other words, by dictating the amplitude of the current. As for the capacitor, assuming it is large enough, it behaves as a short circuit.

The capacitor does not behave completely like a short circuit, however. It is invisible in the sense that, in a steady state with a large enough capacitance and/or low enough AC frequency, it does not affect the current-to-voltage relationship, which is set by other elements in the circuit. However, in non-steady state scenarios, it affects the circuit's response to any changes, e.g. in the input voltage amplitude (analogous to the situation described above), or in the resistance between the probe (which is what occurs in the use of the conductivity sensor). In response to a step change, the circuit behaves similarly to the RC circuit described above.

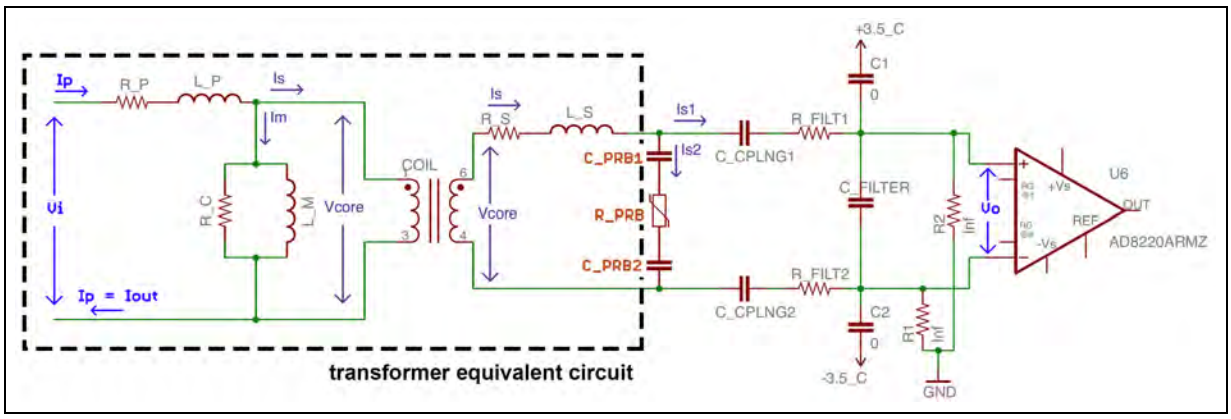

Figure C.1: Model of transformer including transformer unidealities. Reprint of Figure 3.8

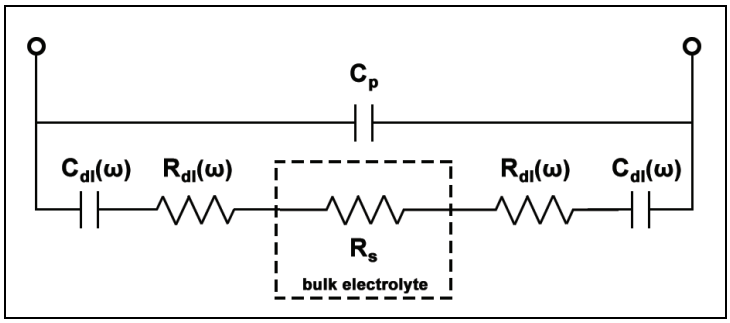

Figure C.2: Equivalent circuit of two electrodes in solution, including impedance (R and C) from double layer formation at electrode surface. Reprint of Figure 1.21.

For example, given a current $I_0 \sin(\omega t)$, the rate at which it changes under steady state is $\mathrm{d}I/\mathrm{d}t = I_0 \cos(\omega t)$, which means constant I_0. At $t = t_0 - \mathrm{d}t$, a step change in V_{in} occurs. Now at t_0, where the voltage would have been $V_0 \sin(\omega t_0)$, it is now $(V_0 + \Delta V_0) \sin(\omega t_0)$. Without a resistor, the instantaneous voltage across the capacitor would be $\Delta V_0 \sin(\omega t_0)$ higher than it would have been, and an extra current—on top of the original sinusoidal current flowing 90° out of phase with the voltage—would have rushed in nearly instantaneously to supply the necessary charge, from there on permanently increasing the amplitude of the current. With a series resistor, however, the rate of this current rush is limited, causing a capacitive response for $\mathrm{d}I_0/\mathrm{d}t$ in the same way as for $\mathrm{d}I/\mathrm{d}t$ in the DC circuit. The same RC time constant still applies.

C.1.2 Circuit analysis of electrode polarization

For the C-R-C model of the conductivity cell probes in Figure C.1, a smaller C_{probes} (or C_{dl} in Figure C.2) is desired so that the circuit's response to a change in R_{probes} is faster. This is accomplished by increasing the AC frequency, as in Figure C.3a, which limits the formation of the double layer. The smaller series capacitance would theoretically 'act more like a short circuit' in accordance to the discussion above, but this is only relevant to as far as the accurate 'transfer' of the AC signal (without degradation) is concerned. With a high enough frequency, this is not an issue. Put another way, since $Z = 1/j\omega C$, an increase in ω and an increase in C accomplish the same thing.

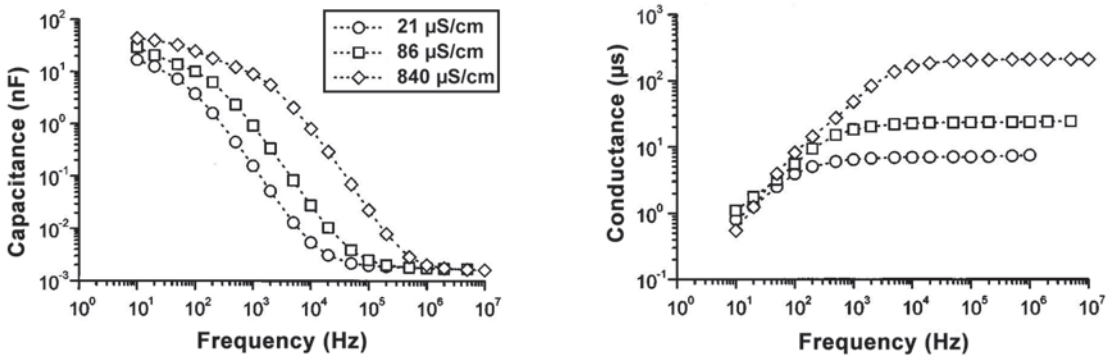

a) Capacitance. **b)** Conductance.

Figure C.3: Capacitances and conductances measured (using an impedance analyzer) for a coplanar plate microelectrode array immersed in three different KCl solutions, as a function of frequency. Source: Green et al. [114] Reprint of Figure 1.22.

An expansion of the MATLAB model of Figure C.1 given in Section 3.2.1 (p. 135) was implemented to model the results for a range of C_{probe} values. The primary purpose of this analysis was to try to explain some of the differences between the model results and the observed curves of I_{p}, V_{o}, and $I_{\text{p}}/V_{\text{o}}$. The results, given in Figure C.4, did not in fact shed light on the observed values. It was subsequently accepted that the deviation of the actual results from the results of Figure 3.9 (p. 138) could arise from other neglected and difficult-to-quantify sources of non-idealities, including R_{dl} and C_{p} in Figure C.2. However, the results in Figure C.4 are still interesting in that they corroborate some of the discussion above. Namely, as the capacitance decreases, the integrity of the AC signals are affected if the frequency is too low (Figure C.4a). At higher frequencies, the results are much more robust to the value of C_{probe} (Figure C.4b).

By comparing the actual measurements (Figure 3.12, p. 142 and Figure C.5 provided here) to the model results of Figure C.4, it was determined that the actual probe capacitance in either case was not low enough to affect the signals. The capacitance for the 1 kHz situation was, however, high enough to cause problems with the time response (Section 3.2.3, p. 144), which is not captured by these graphs. Thus, a 72 kHz excitation was ultimately used.

C.1.3 Characterization of 1 kHz conductivity cell

As discussed extensively here and in Chapter 3, the conductivity cells were initially excited with a 1 kHz AC signal, but ultimately used an excitation frequency of 72 kHz. Thus, the results given in Section 3.2.2 (p. 140) primarily correspond to the final 72 kHz system. However, the original system was also similarly characterized, as presented in Figures C.5 and C.6. The calibration curve and cell constant of the system are all reasonable, but cannot capture the timing issues that ultimately resulted in the switch to higher frequencies.

a) 1 kHz

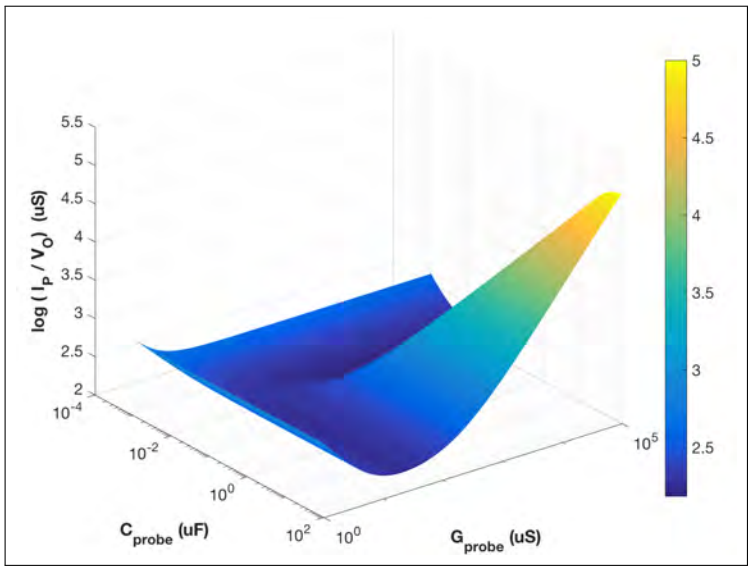

b) 72 kHz

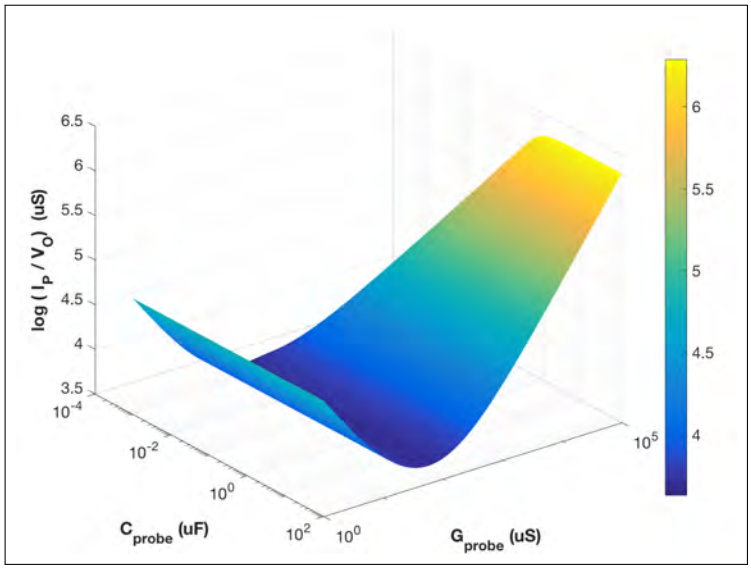

Figure C.4: Model of conductivity circuitry output for a range of conductances and probe capacitances, for two excitation frequencies.

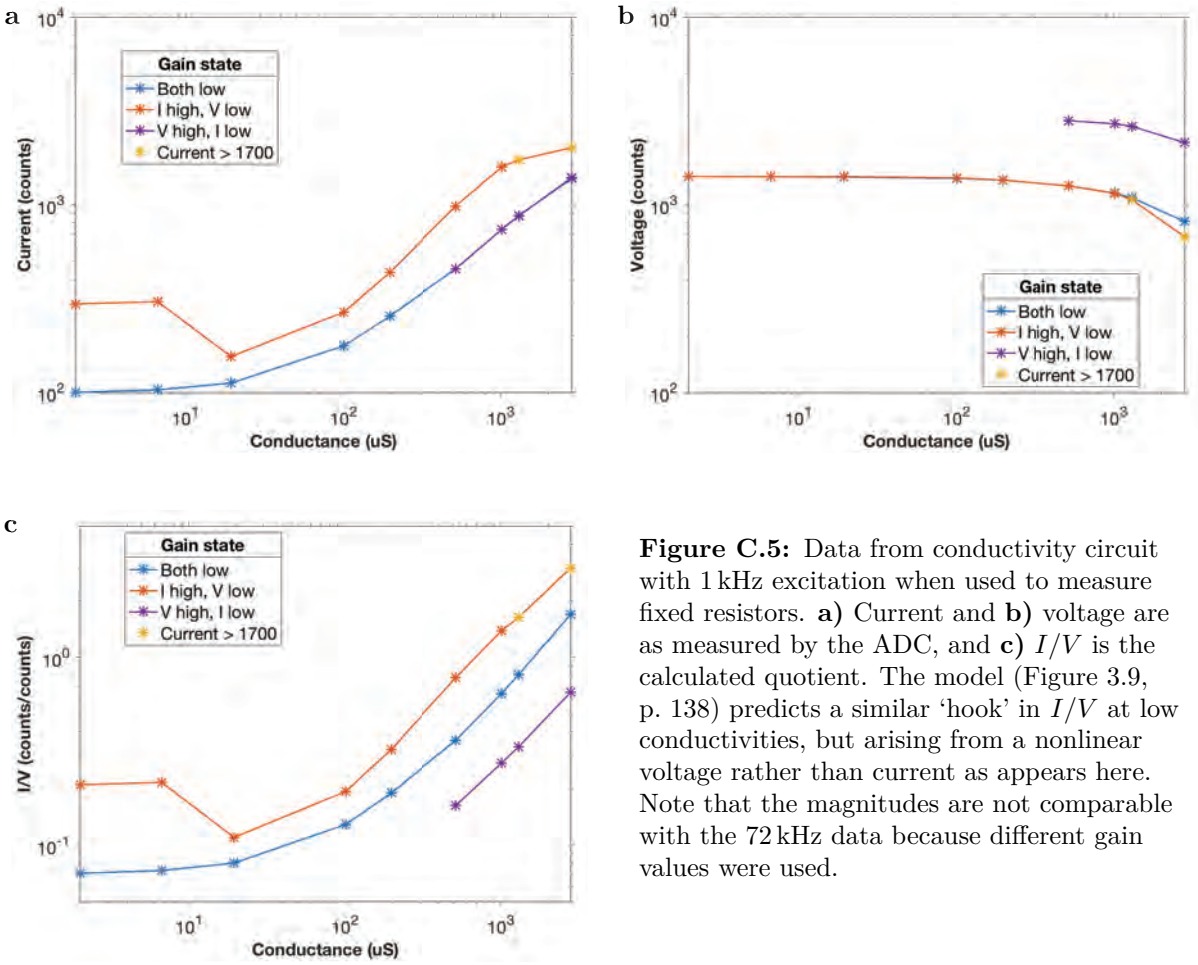

Figure C.5: Data from conductivity circuit with 1 kHz excitation when used to measure fixed resistors. **a)** Current and **b)** voltage are as measured by the ADC, and **c)** I/V is the calculated quotient. The model (Figure 3.9, p. 138) predicts a similar 'hook' in I/V at low conductivities, but arising from a nonlinear voltage rather than current as appears here. Note that the magnitudes are not comparable with the 72 kHz data because different gain values were used.

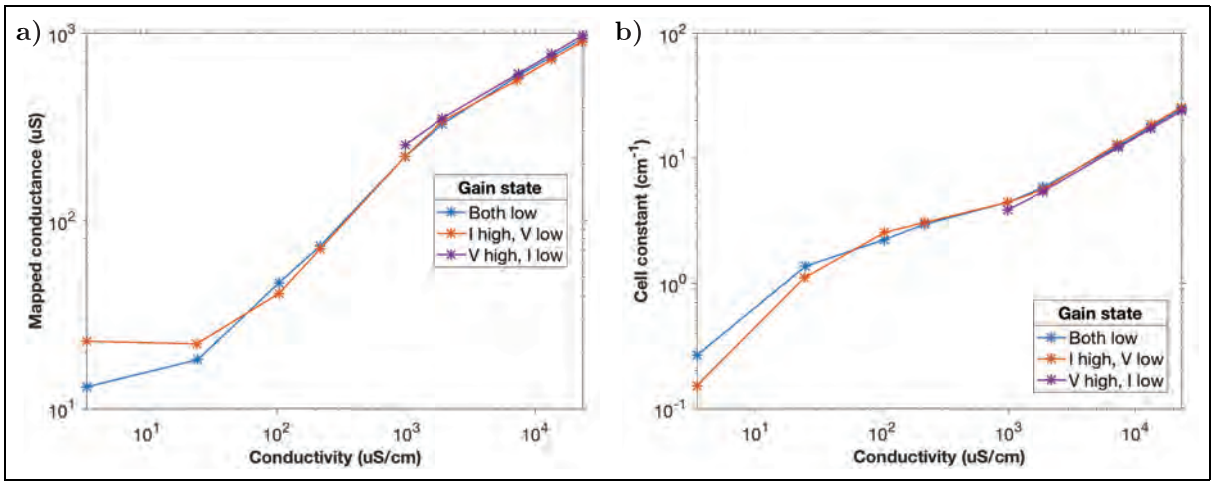

Figure C.6: Mapped conductivity and cell constant for 1 kHz excitation, using similar analysis as Figure 3.13 (p. 143). Probe data not shown.

C.2 Trimodal sensing in the flume: comparison between sensors

The results of the flume experiments, presented in Section 3.4.3 (p. 157), provided order-of-magnitude estimates for differences in time responses between the sensors by determining the extent of filtering required for a 'better match' between the time series. In that section, results were presented for a running mean filter (0.2 s for fluorescence, 0.1 s for conductivity). In Figures C.7 and C.8, results are presented for a low-pass Butterworth filter. Similar to the running mean filters described in Section 3.4.3, the parameters for the Butterworth filter—fourth-order, 3 Hz ctuoff for fluorescence, and second-order, 4 Hz cutoff for conductivity—were chosen by testing filters and evaluating the resulting qualitative similarity. The parameters for the two types of filters were chosen independently, but were found to represent similar time scales, thus corroborating the estimated scale of response time differences.

Section 3.4.3 also discussed time shifts, which were necessary due to different locations of the sensing volumes. To determine the 'best guess' time shifts, the time series were shifted by varying amounts and their qualitative similarity was compared. A 'good match' was determined based both on time series (as shown in Figure C.9) and the cloud plots. The time shifts applied for this particular series, based on all eddies in the ∼3 min run, were 0.1 s back in time for fluorescence and 0.07 s forward for temperature.

In looking at the cloud plots, we aim to eliminate 'large circles', which show only that one sensor started and stopped detecting the eddy before another, and instead create features with diagonal lines, which can show the rate at which two sensors rise or fall together. An example of unshifted cloud plots fo the running mean-filtered series are shown in Figure C.10, which can be compared to the shifted versions in Figure 3.26, p. 162). Although the difference may appear slight, the time shift replaces some of the big circles with slight diagonals, enabling analysis of the relative rise and fall time between the sensors.

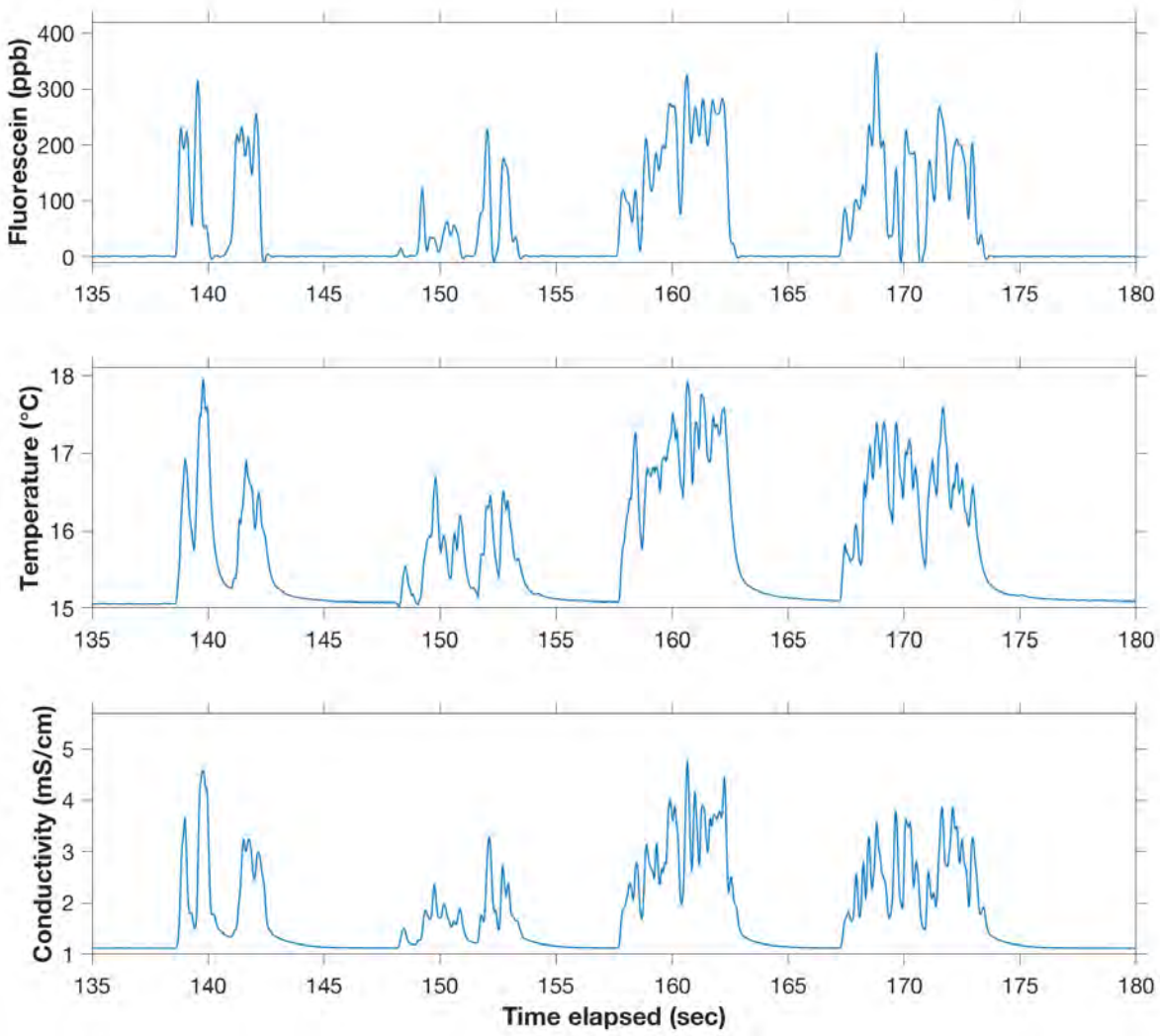

Figure C.7: Same time series as Figure 3.24 (p. 160) corresponding to dye injections in flume tests, but with low-pass Butterworth filters applied to the fluorescence (fourth-order, 3 Hz ctuoff) and conductivity (second-order, 4 Hz cutoff) time series. Similar to the running mean filter applied to the same time series for Figure 3.25, the Butterworth filters improve qualitative similarity between series and provide order-of-magnitude estimates for differences in time response.

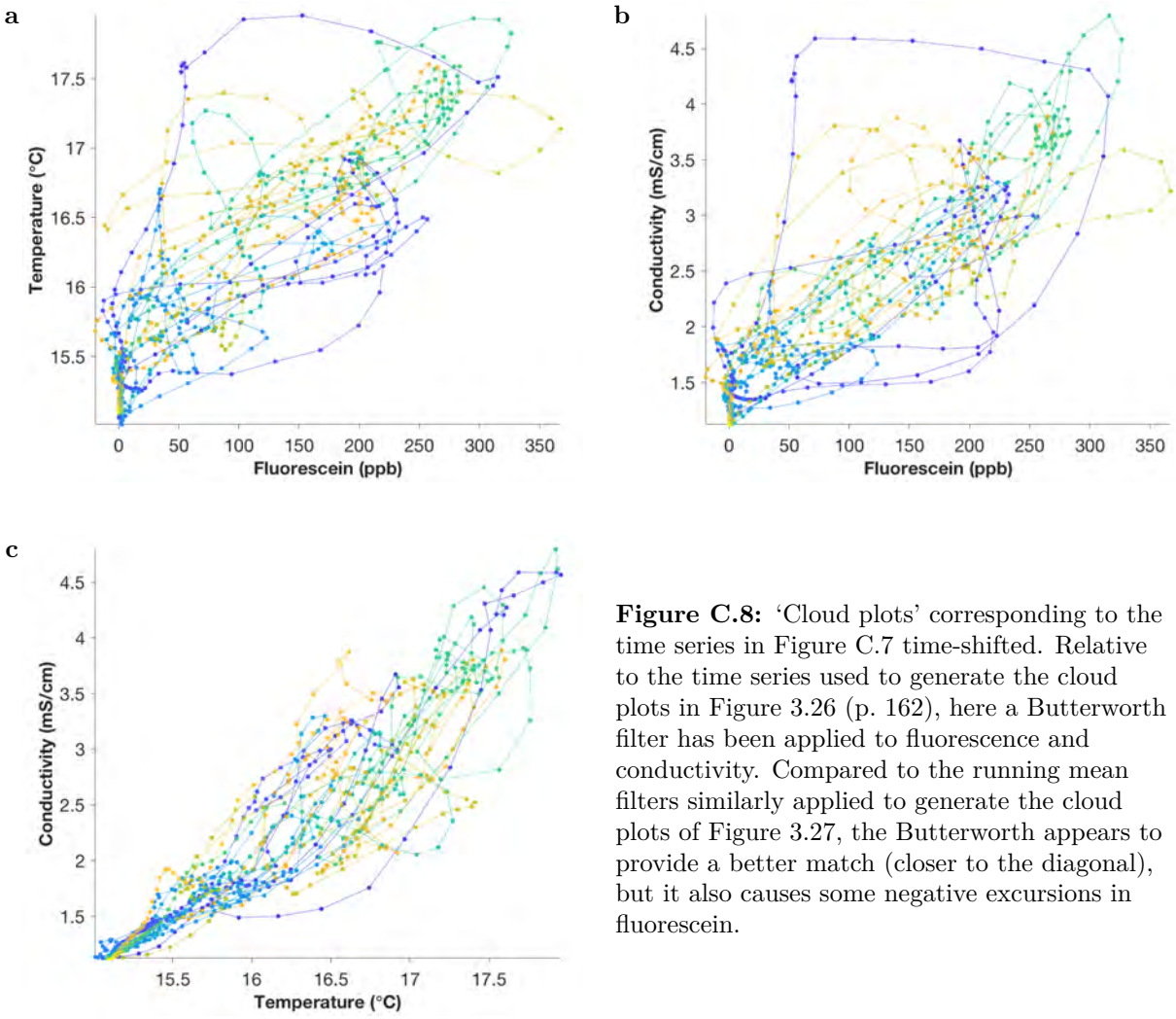

Figure C.8: 'Cloud plots' corresponding to the time series in Figure C.7 time-shifted. Relative to the time series used to generate the cloud plots in Figure 3.26 (p. 162), here a Butterworth filter has been applied to fluorescence and conductivity. Compared to the running mean filters similarly applied to generate the cloud plots of Figure 3.27, the Butterworth appears to provide a better match (closer to the diagonal), but it also causes some negative excursions in fluorescein.

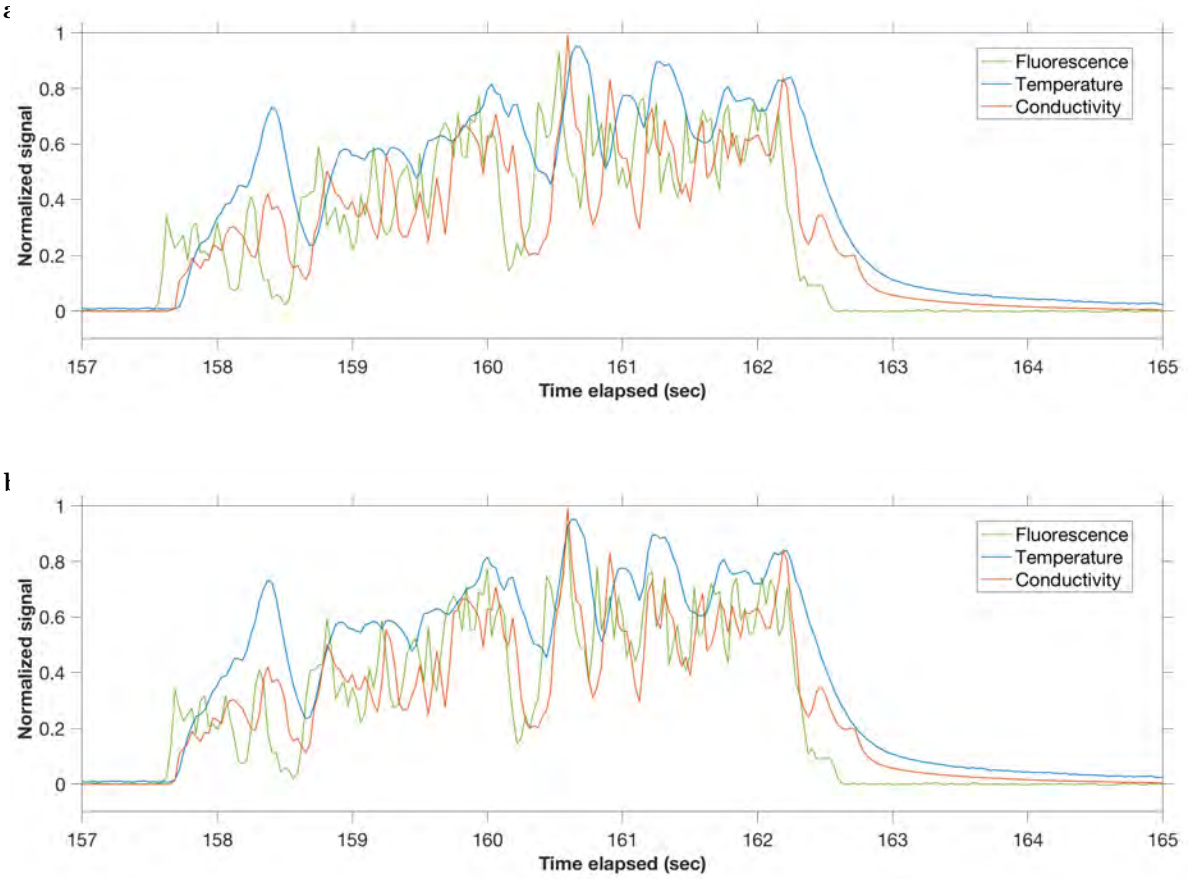

Figure C.9: Overlaid time series for the three sensors for a single turbulent dye injection during flume tests, shown **a)** before; and **b)** after a small time shift to account for differences in sensing volume locations. The time shifts applied here were 0.1 s back in time for fluorescence and 0.07 s forward for temperature. The eddy shown corresponds to the third eddy in Figure 3.24 and has no filters applied.

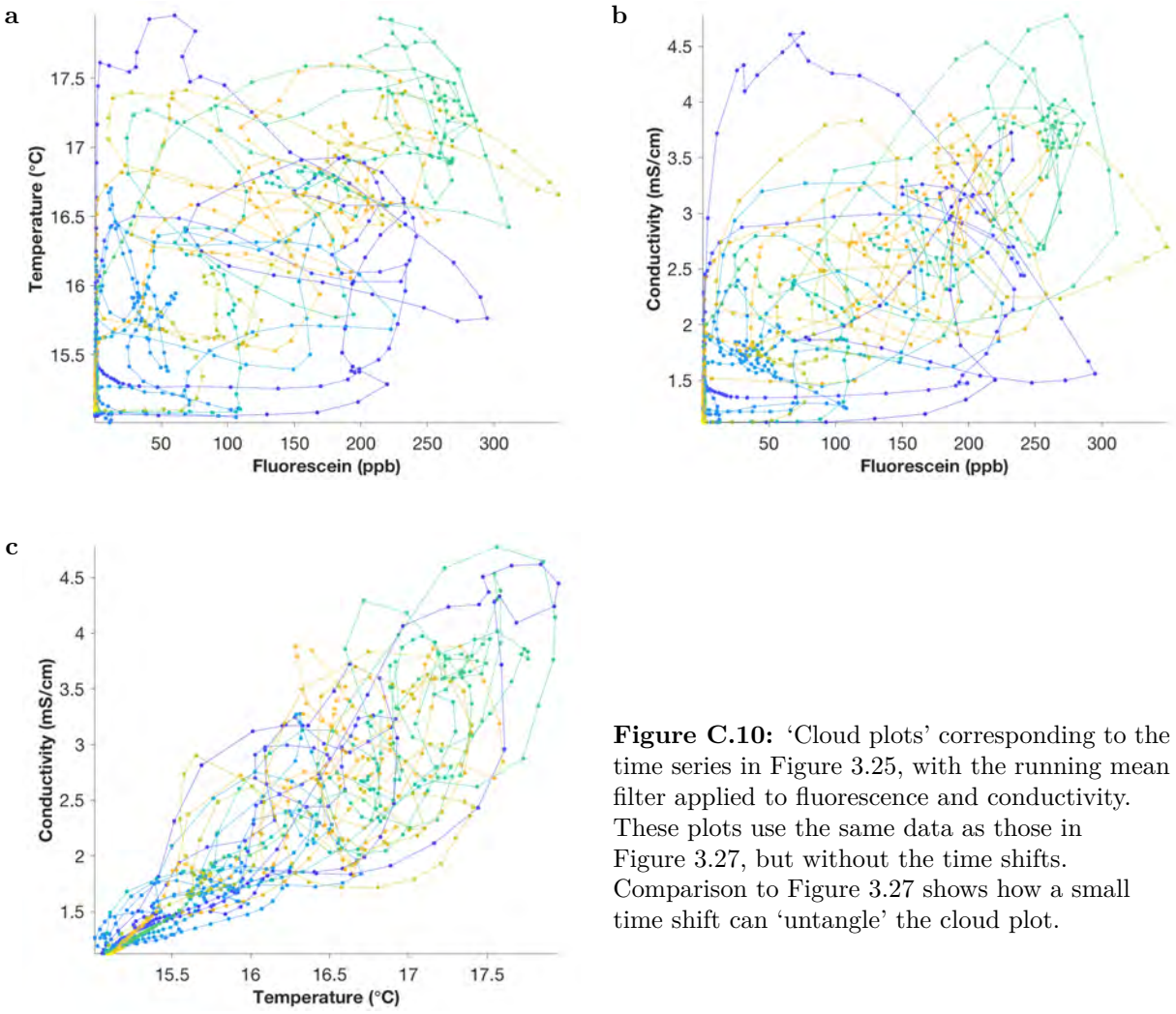

Figure C.10: 'Cloud plots' corresponding to the time series in Figure 3.25, with the running mean filter applied to fluorescence and conductivity. These plots use the same data as those in Figure 3.27, but without the time shifts. Comparison to Figure 3.27 shows how a small time shift can 'untangle' the cloud plot.

a) Test 1 **b)** Test 2 **c)** Test 3

Figure C.11: Setup for three different tests of sensor interference with velocity measurements, using **a)** first generation optical fiber holder; **b)** second generation holder with optical fibers aligned between Beams 1 and 2 of the ADV; and **c)** second generation holder with optical fibers aligned directly under Beam 2. Test 2 (**b**) is discussed in Section 4.4.3 (p. 183).

C.3 Sensing volume interference

As discussed in Section 4.4.3 (p. 183), the minimum distance between the optical fibers and the ADV sensing volume was tested by mounting the optical fibers at difference distances from the ADV's sensing volume in stagnant, unseeded water, and recording the ADV's signal for at least 5 min at each distance. Interference was identified as high signals in the ADV's amplitude and correlation outputs.

The degree of interference with ADV measurements by the optical fibers and their holders was actually sensitive to more than just distance. This is apparent by comparing tests conducted with three different configurations of optical fibers, shown in Figure C.11. The initial optical fiber holder (Figure C.11a, 'Test 1') was made of solid PVC with foam padding, but resulted in more interference than was desirable. It was hypothesized that the signal was due to backscatter of the sound waves from the physical bulk of the holder, so a second generation holder was constructed (Figure C.11b, 'Test 2') with special attention to reducing the solid bulk. In running Test 2, the degree of interference appeared to be sensitive to the rotational degrees of freedom of the optical fiber holder, as well as to its rotation around the axis of the ADV's transducer. Special attention was required to maintain the rotational position as the fibers were displaced. A subsequent test (Figure C.11c, 'Test 3') was run in which the optical fibers were positioned directly underneath Beam 2, rather than between two beams as in Tests 1 and 2, to see if the interference would be reduced.

Results are shown in Figures C.12 and C.13 (amplitude and correlations, respectively). The absolute magnitude of amplitudes is not comparable between tests (especially Test 1 vs Tests 2 and 3) because it depends on the scattering environment in the tank, which is not constant because of things growing in it, falling in it, getting stirred up, etc.

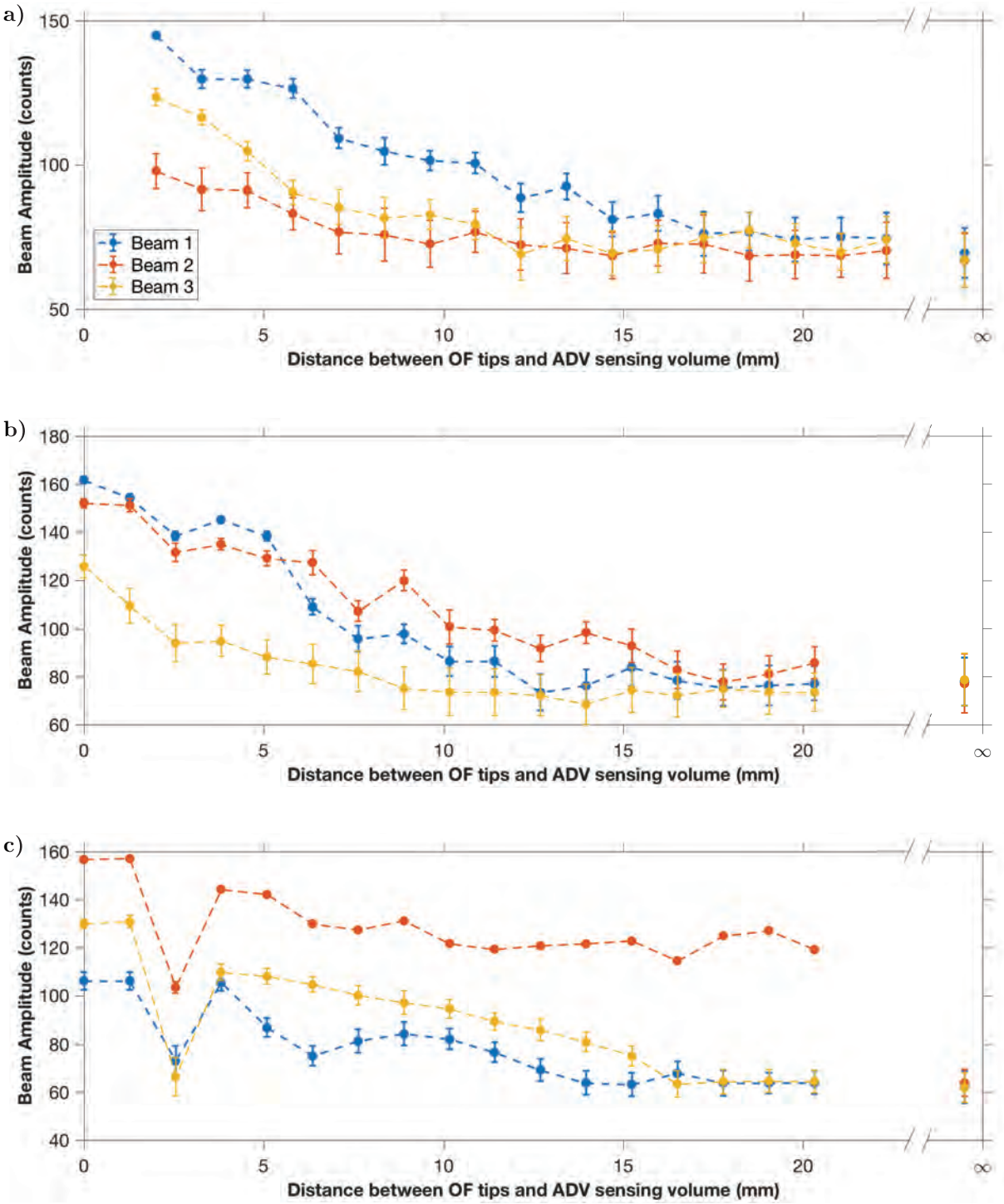

Figure C.12: Amplitude of ADV measurements as a function of distance between optical fiber tips for three different configurations (shown in Figure C.11). **a)** Test 1; **b)** Test 2; **c)** Test 3. The dip in amplitude for Test 3 at ∼2.5 cm separation is likely due to the rotation of the optical fibers; in cases where the amplitude was substantially lower due to rotation, it was generally observed that the optical fibers were no longer pointing toward the ADV's sensing volume.

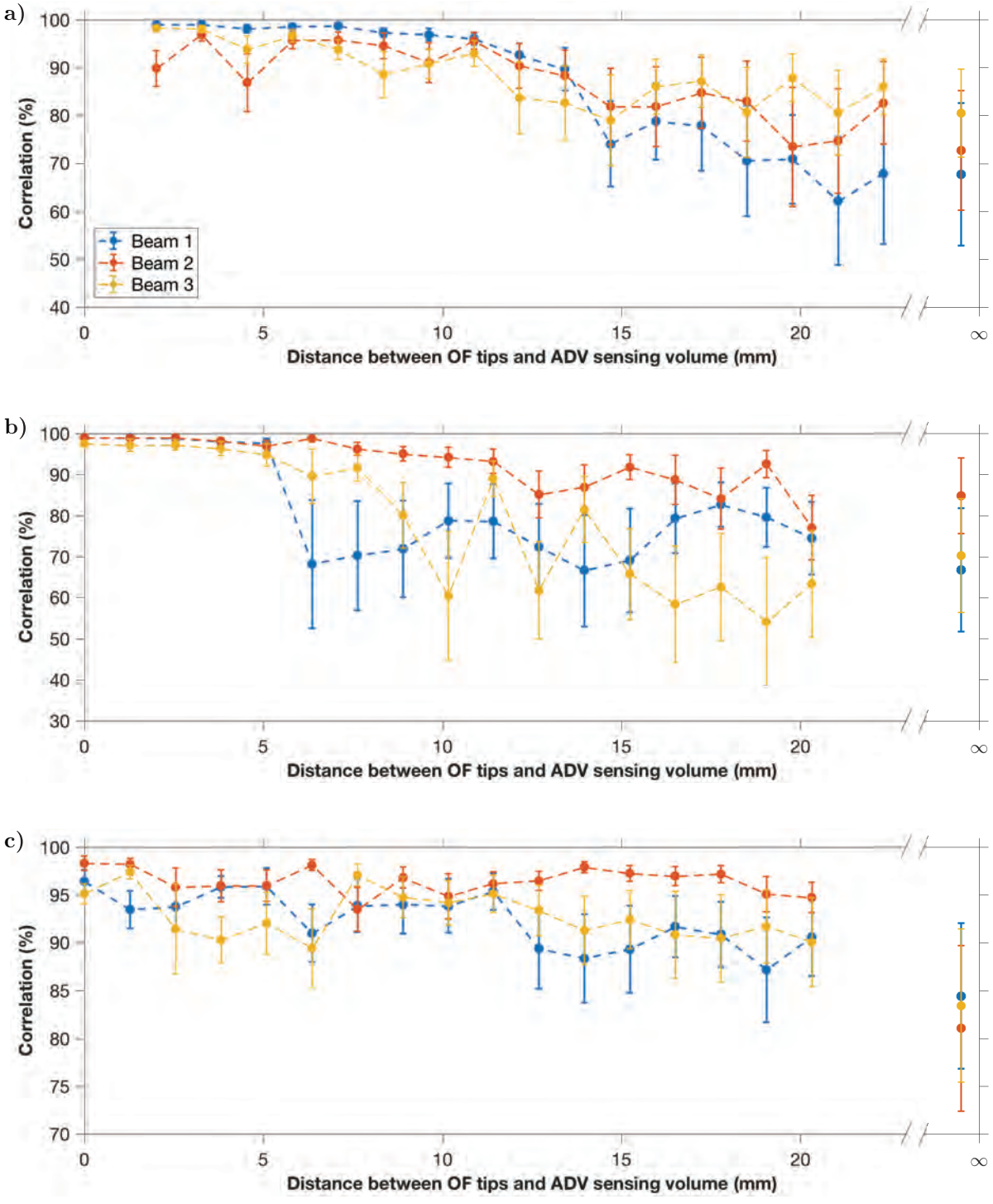

Figure C.13: Correlations for ADV measurements as a function of distance between optical fiber tips for three different configurations (shown in Figure C.11). **a)** Test 1; **b)** Test 2; **c)** Test 3.

The second generation holder did appear to help with the interference slightly, as judged by the flatter slope for Test 2 vs Test 1, which also allows a closer distance to be used. For Test 3, not surprisingly Beams 1 and 3 showed less interference than in Test 2. However, Beam 2 never reached an acceptable level of interference, so ultimately this configuration is not usable.

For completeness, probe checks at representative distances are also given for all three tests (Figures C.14 to C.16). The ADV's sensing volume is a Gaussian pulse around 15 cm, as discussed in Section 1.8.2 (p. 81), but in an environment with low scatterers the amplitudes are not expected to be high. Probe checks—at least under the 'poor' conditions of the tank—appeared to be somewhat stochastic, and the graphs given are only instant snapshots, so they are not fully representative. However, the optical fibers can generally be seen as spikes in the sensing volume or between the sensing volume and the transducer. Interference outside of the sensing volume is not an issue because these areas represent a different sensing volume and a different geometry of receive beams.

The probe checks provide a different visualization of the interference and confirm the results given in Figures C.12 and C.13. Note, however, that much of the spikiness of the probe checks, especially Test 1 (Figure C.14), is related to reflections off the glass wall of the tank and not the optical fibers. This issue was subsequently reduced with proper dampening materials on the floor and walls of the tank.

For use in EC experiments, we generally aligned the optical fibers beforehand using the alignment piece, with a separation distance of 5 mm $\sim$ 8 mm. Then, before the run, the ADV was tested using the manufacturer-supplied PC software to check for interference in the amplitude values, with adjustments made as necessary. The holder could also be tilted to reduce interference, as long as the fibers remain pointed at the ADV's sensing volume

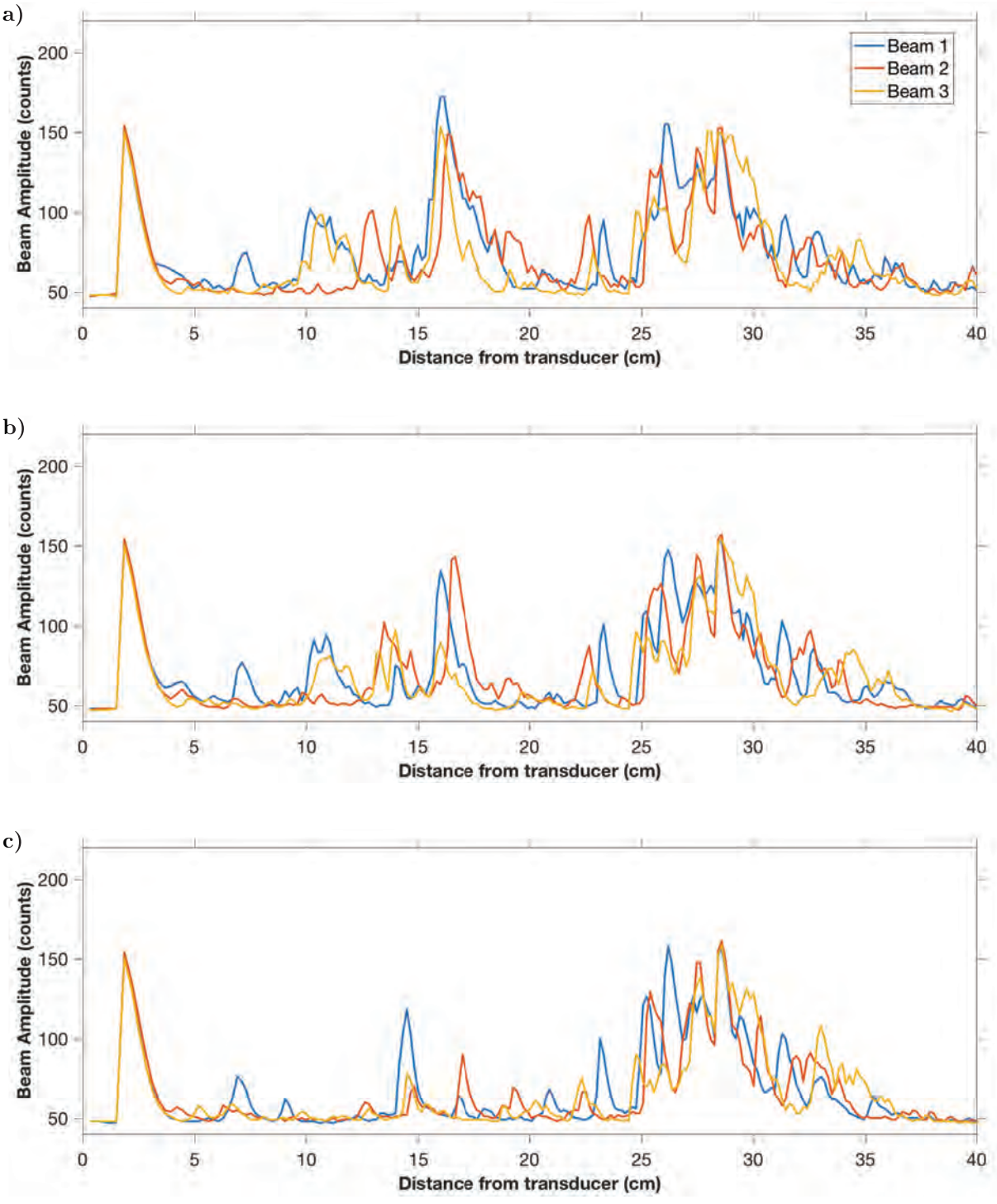

Figure C.14: Probe checks taken in Test 1 with the optical fiber tips at **a)** 0 mm, **b)** 7 mm ∼ 8 mm, and **c)** infinite offset from the holder.

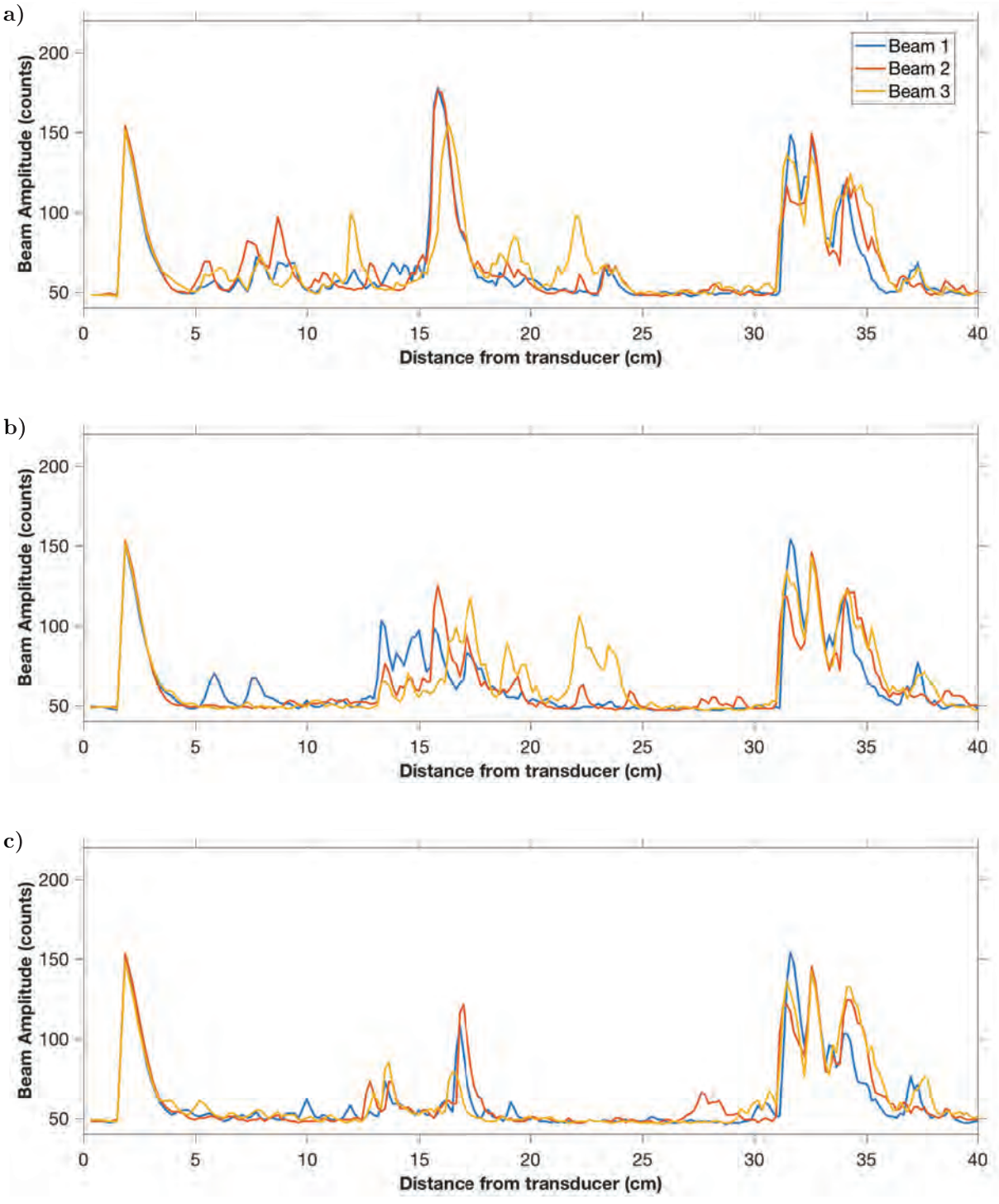

Figure C.15: Probe checks taken in Test 2 with the optical fiber tips at **a)** 0 mm, **b)** 7 mm ∼ 8 mm, and **c)** infinite offset from the holder.

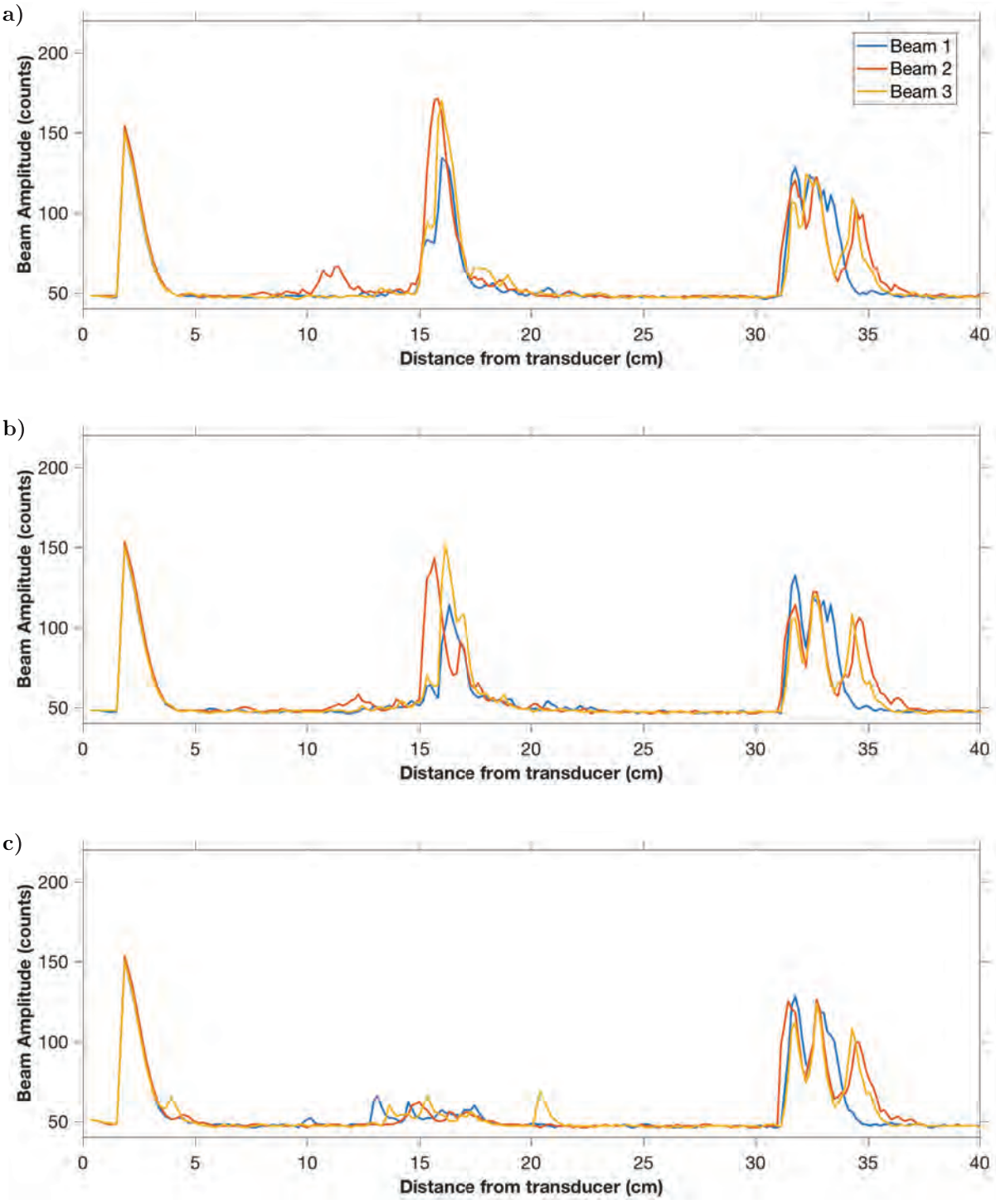

Figure C.16: Probe checks taken in Test 3 with the optical fiber tips at **a)** 0 mm, **b)** 7 mm ∼ 8 mm, and **c)** infinite offset from the holder.

C.4 Data from tank tests

This section presents supplemental data from the tank test analyzed in Chapter 4.

The full time series of vertical velocity and the three concentrations are presented in Figures C.17 to C.22 in 40 min sections. The time series were detrended with a 40 min linear detrend to aid in visualization; the conductivity's thermal drift, on the order of 10 min, is thus not removed and can be seen in the data.

With a 40 min time scale, features in the fluorescence measurements, which are fast and sharp, are difficult to see. The spikes may sometimes look like noise. They do, however, correspond to real features, as revealed by a closer zoom such as that given in Figure C.23. Another example is given in Figure 3.34 (p. 171), where it is compared to the features detected by the conductivity sensor.

The calculated fluxes can be better understood by examining the c' and w' series together. By overlaying the two time series, coinciding features that lead to flux can be identified. Such plots are presented for the $t = [80, 120]$min period in Figure 4.28 (p. 213). In Figures C.24 and C.25, they are presented for the other two flux periods.

Figures 4.27 and 4.37 (p. 211 and 224) present an analysis in which fluxes measured by one sensor are plotted against fluxes measured by another, for different degrees of low pass filtering (done with a running mean). The comparable analysis for fluxes calculated on time series with excursions removed and using a 10 min linear detrend for the mean removal is given in Figure C.26.

Similar plots can be made with different varying parameters, to examine the effect of other data processing choices. Data presented in Section 4.6 was calculated using 48 Hz measurements averaged down to 16 Hz, but the choice of averaging time can also be examined using the scatter plots. Results are given in Figure C.27 for data otherwise processed as described in Section 4.5.4 (i.e. no filtering of time series, no removal of excursions, 10 min linear detrend for mean removal). Across the board, averaging time appeared to have little effect on calculated fluxes, except when averaged to extremely low frequencies such as 0.1 and 0.05 Hz.

The effect of different flux window sizes can also be explored. Smaller window sizes should have more scatter, while cospectral analysis in Section 4.6.4 (p. 215) predicted that periods larger than $\sim$20 min should be stationary (fluxes converge). The results are shown in Figure C.28. The predicted trends are, in general, observed; with longer flux periods, the points are closer to the 1 : 1 line. In addition, it can be seen that, even with substantial scatter due to small flux windows, the fluxes measured by the different sensors generally track each other.

Power spectra of fluorescein, temperature, and conductivity are given in Figure C.29, which were shown in variance-preserving form in Figure 4.30 (p. 216). Note that, for the conductivity, the stagnant water test was done in tap water (as opposed to salted water) and thus could be expected to have lower components across the board, to the extent that fluctuations and/or noise scale to the mean value.

Normalized variance-preserving spectra are shown in Figure C.30 that correspond to the fluctuations used to calculate the fluxes presented in Figures 4.34 to 4.36. These spectra are presented similarly as those in Figure 4.32 (p. 217), which represented the time series (before and after

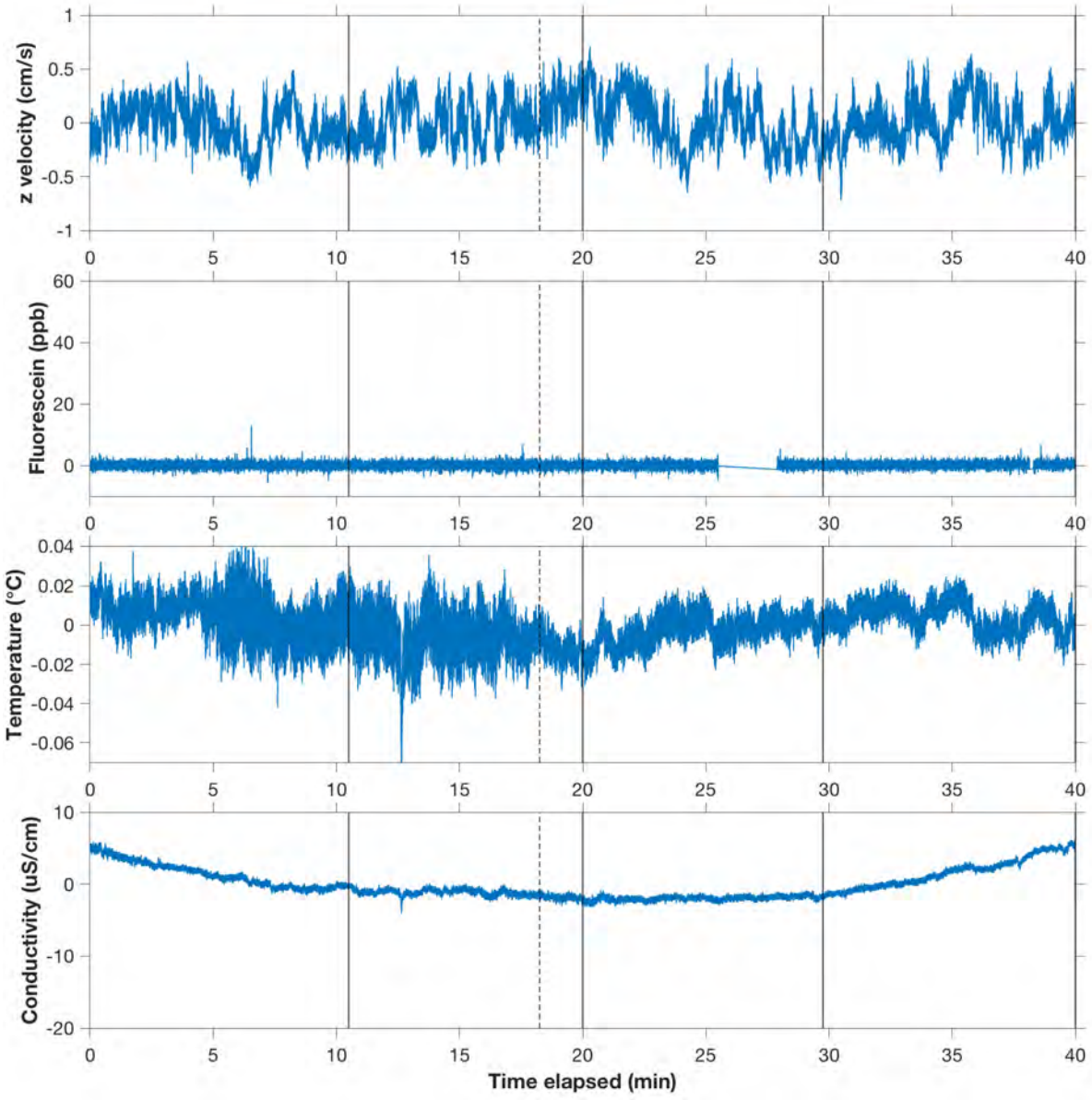

Figure C.17: Time series for EDDI and w measurements taken during EC run, corresponding to Period 1 (no flux).

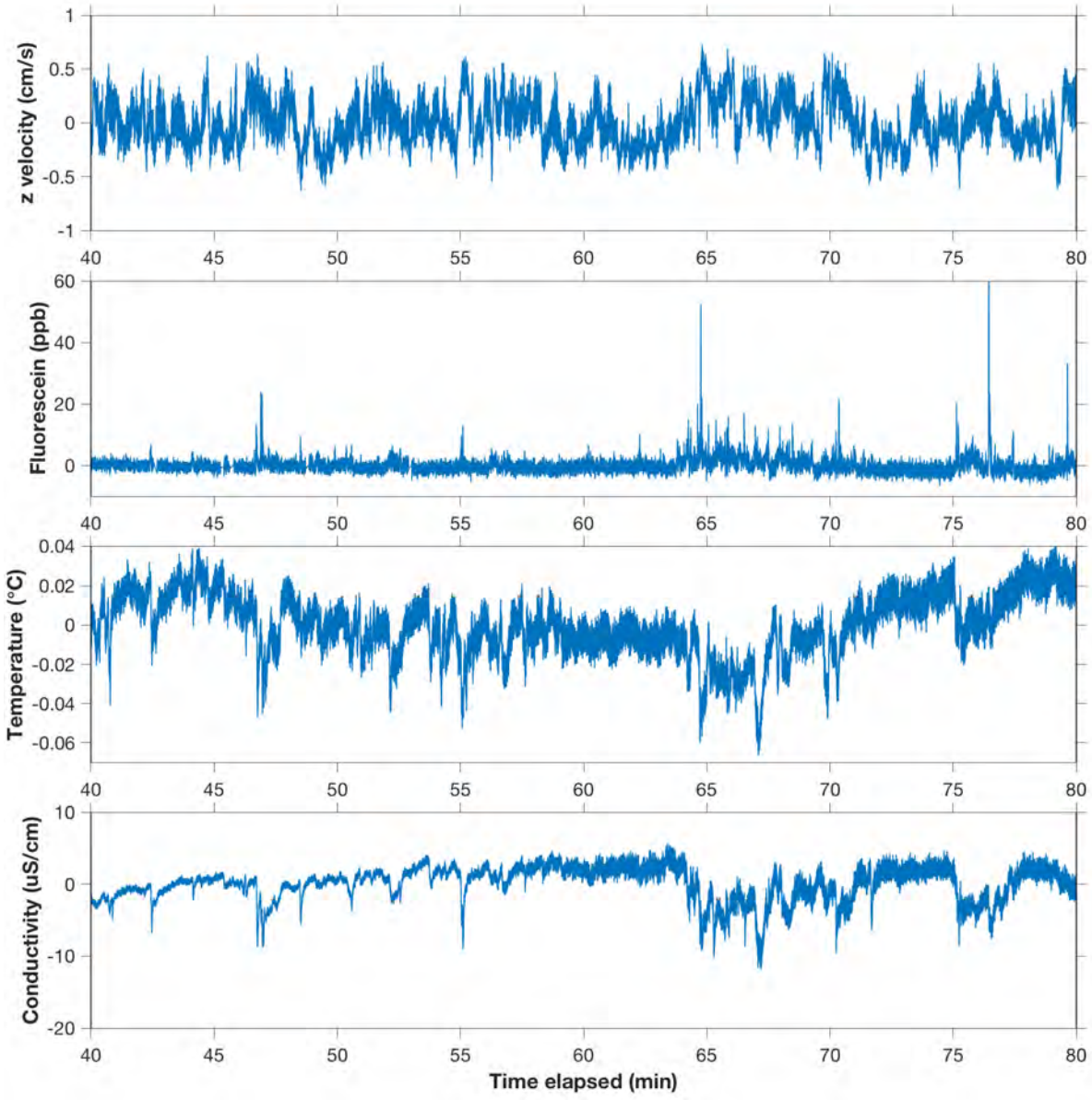

Figure C.18: Time series for EDDI and w measurements taken during EC run, corresponding to Period 1 (35 mL/min dye release).

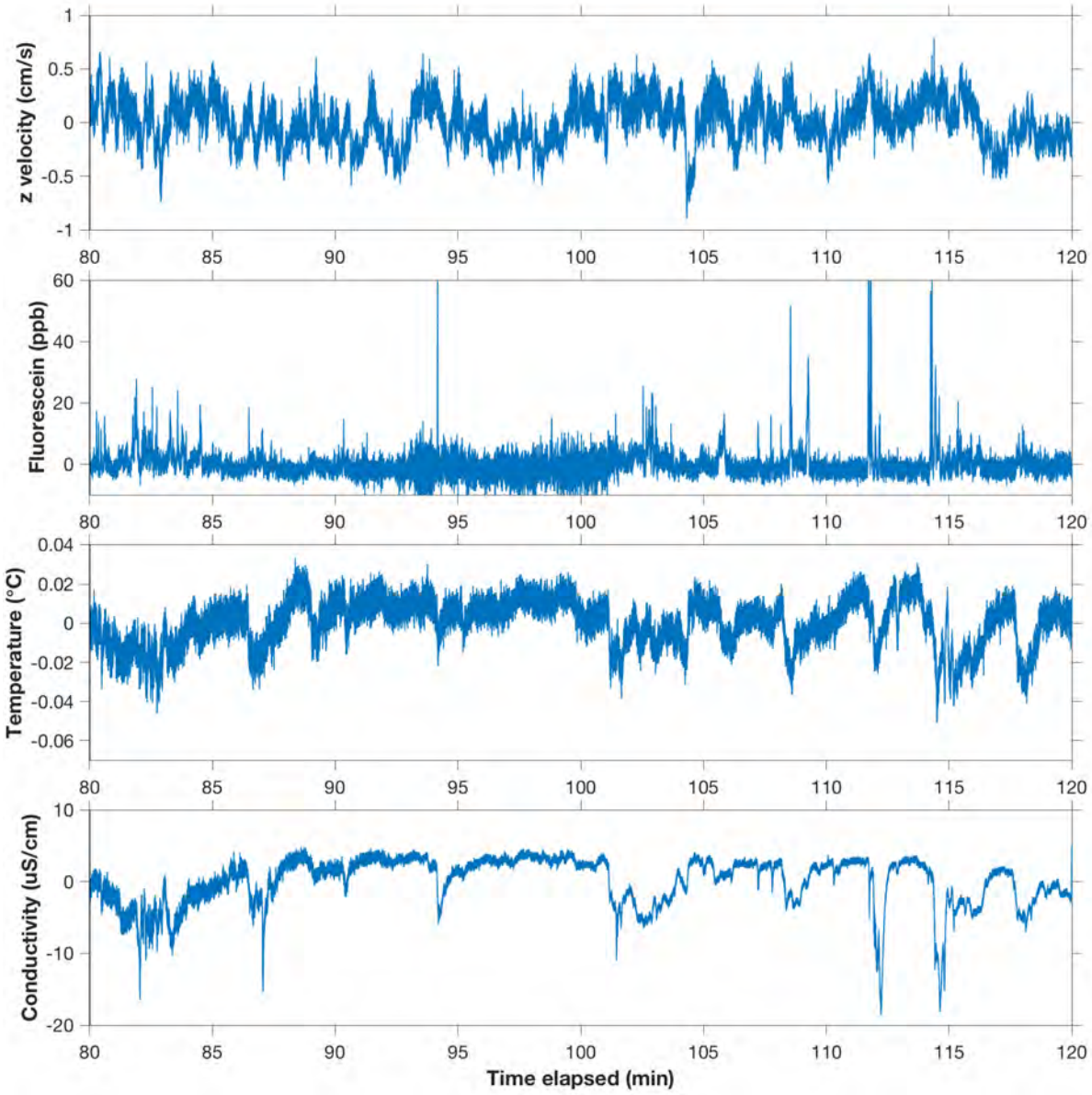

Figure C.19: Time series for EDDI and w measurements taken during EC run, corresponding to Period 3 (57 mL/min dye release).

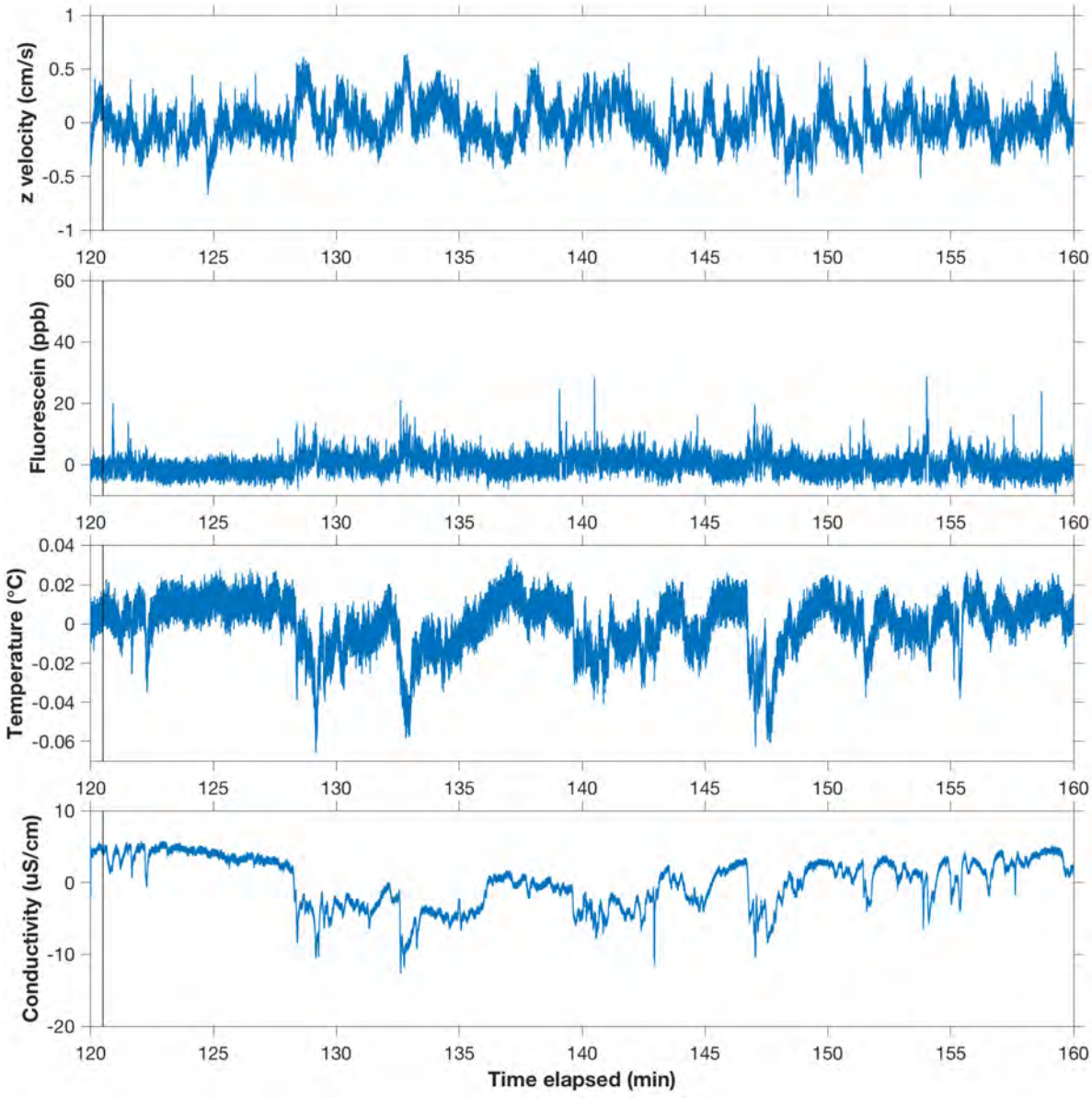

Figure C.20: Time series for EDDI and w measurements taken during EC run, corresponding to Period 4 (35 mL/min dye release).

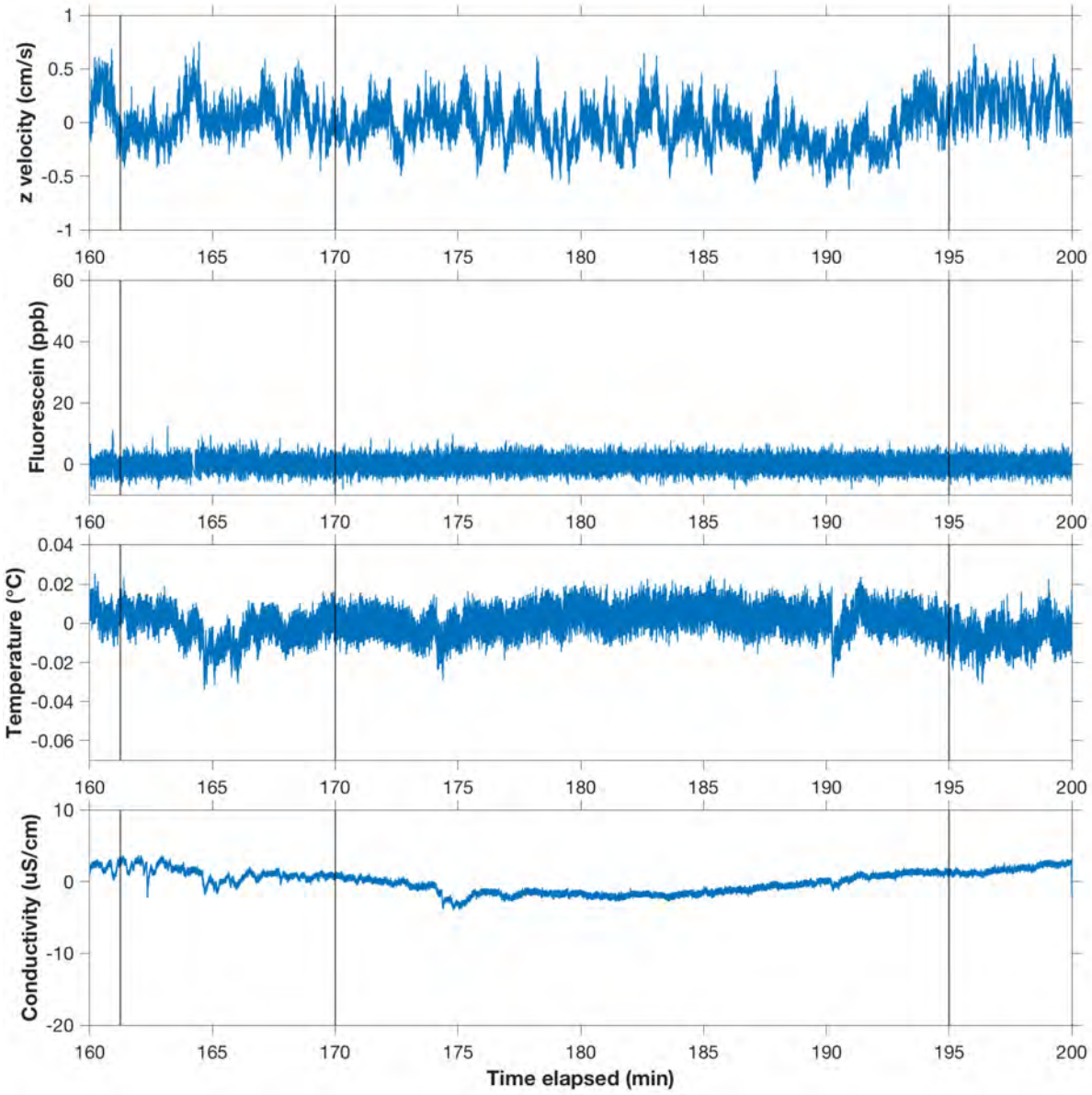

Figure C.21: Time series for EDDI and w measurements taken during EC run, corresponding to Period 5 (no flux, but likely release of plume near beginning).

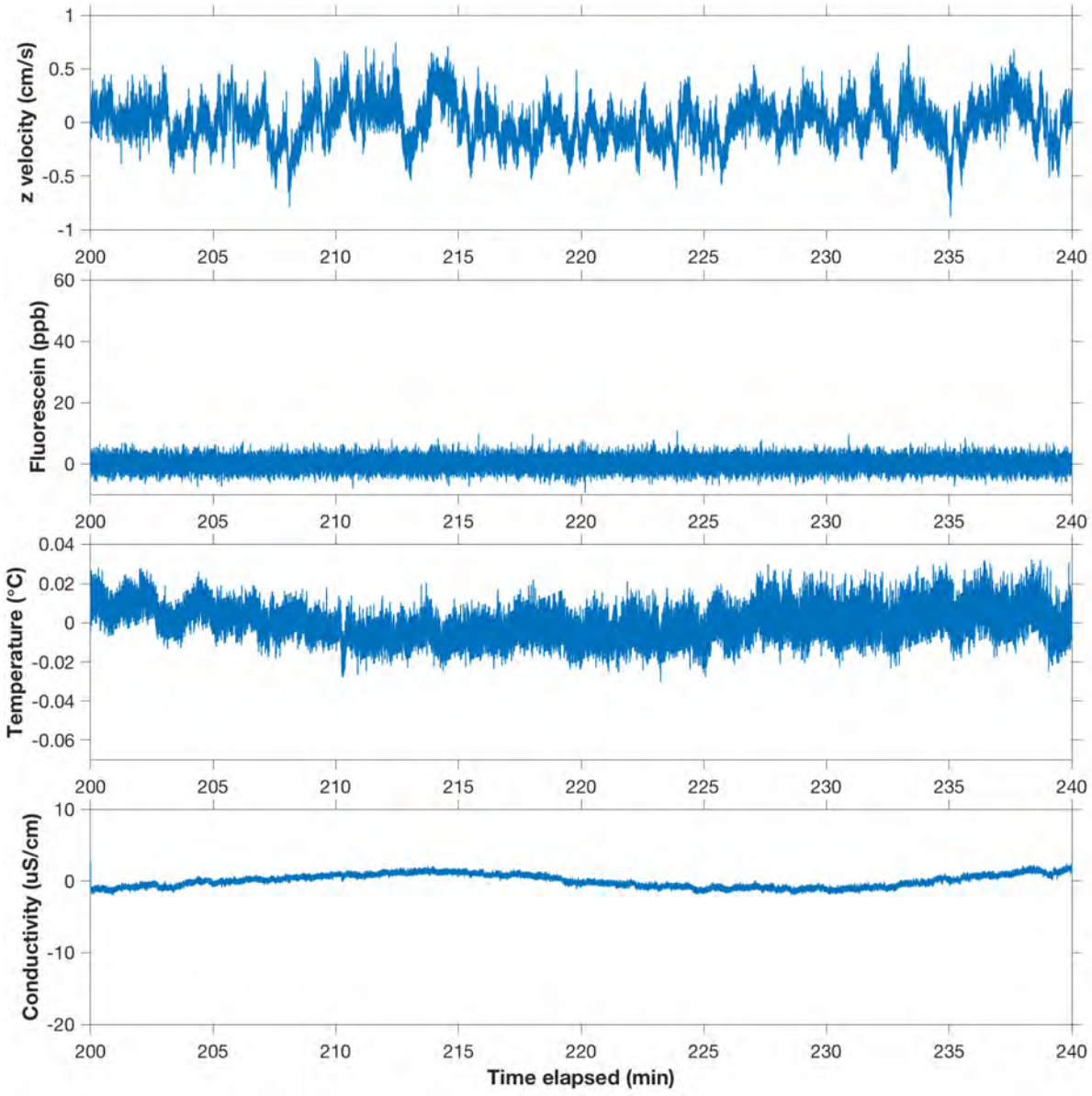

Figure C.22: Time series for EDDI and w measurements taken during EC run, corresponding to Period 6 (no flux).

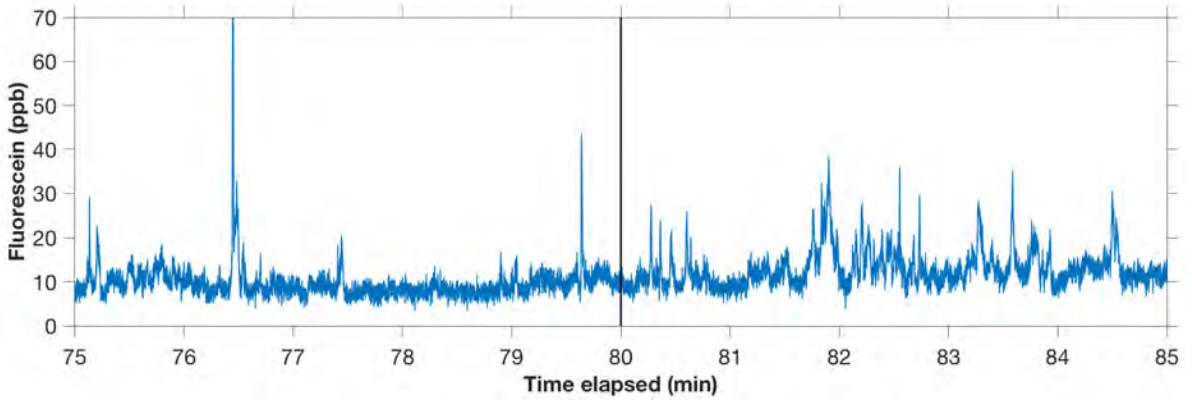

Figure C.23: Zoom in of fluorescence signal showing fine features that are difficult to see with a longer time scale. Time series is not detrended.

removal of excursions) after subtracting a 40 min linear trend. In this case, however, the appropriate 'mean' has been subtracted that corresponds to the Reynolds' decomposition used for calculating fluxes, which was either a 10 min linear trend or 30 s running mean. Thus, the spectra in Figure C.30 represent the frequency components of the fluctuations used to calculate fluxes.

Figure C.31 shows cumulative cospectra corresponding to 'turbulent' fluctuations only, i.e. calculated as described in Section 4.6.6 (p. 221) from fluctuations in velocity and concentration after subtracting a 30 s running mean from time series with excursions removed. They reflect the fluxes shown in Figure 4.35 (p. 222). The cospectra in Figure C.31 all converge below ∼0.015 Hz (∼67 s), showing that the Reynolds' decomposition did in fact remove lower frequency components as intended. One might expect that subtracting a 30 s running mean would remove components slower than *30* seconds, rather than 67. Further consideration of these frequency domain behaviors is left for future work, although the power spectra of the individual components as they pass through the mean removal process, shown in Figures B.24 and B.25 in Appendix B (Section B.10.1), may provide some insights.

Figure C.31 can be compared to the cospectra shown in Figure 4.33 (p. 219) for the original series after a 10 min linear detrend. As discussed in Chapter 4, fluxes calculated using the latter are thought to reflect mass transport by all fluid motions within the tank, including the larger, slower features discussed in Sections 4.6.5 and 4.7. Fluxes calculated from the higher-frequency 'turbulent' fluctuations were found to be much smaller, which is confirmed by a comparison of the cospectra.

The cospectra calculated from the 'turbulent' components also show some interesting features, such as some spectral components of the opposite sign than expected, particularly during the second time period ($t = [40, 80]$min). Figure C.32 shows zoomed versions of the original cospectra in Figure 4.33; by comparing Figures C.31 and C.32, it can be seen these features were in fact also present in the original flux calculation.

Finally, turbulence profiles are presented in Figure C.33, which were used to better understand the fluid dynamics of the tank. The profiles were found by taking ∼30 min measurements with the ADV at different heights above the sensing volume.

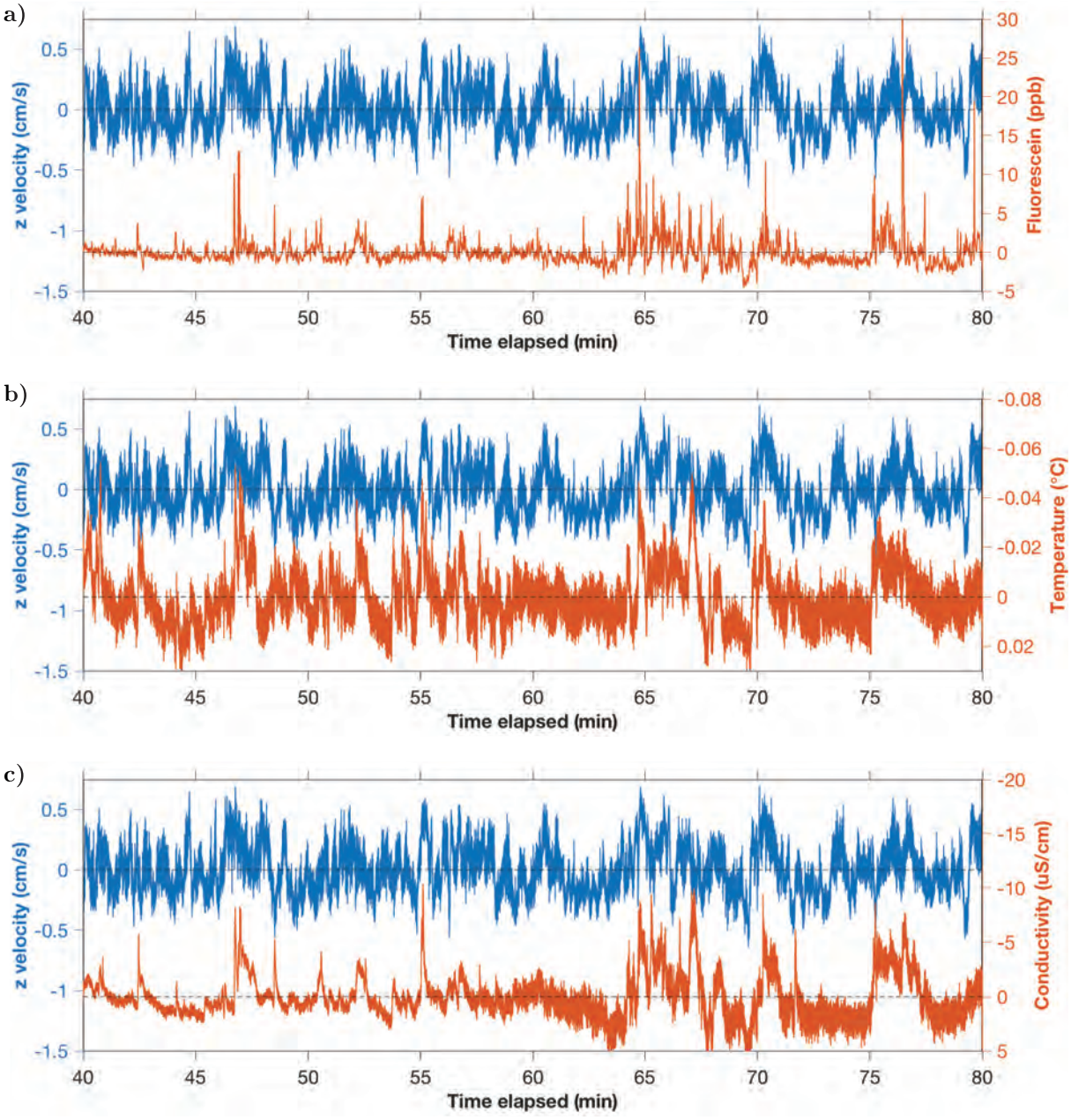

Figure C.24: Time series of fluctuations in **a)** fluorescein, **b)** temperature, and **c)** conductivity, overlaid with concurrently measured w fluctuations, for Period 2 of the EC run. Temperature and conductivity axes are reversed.

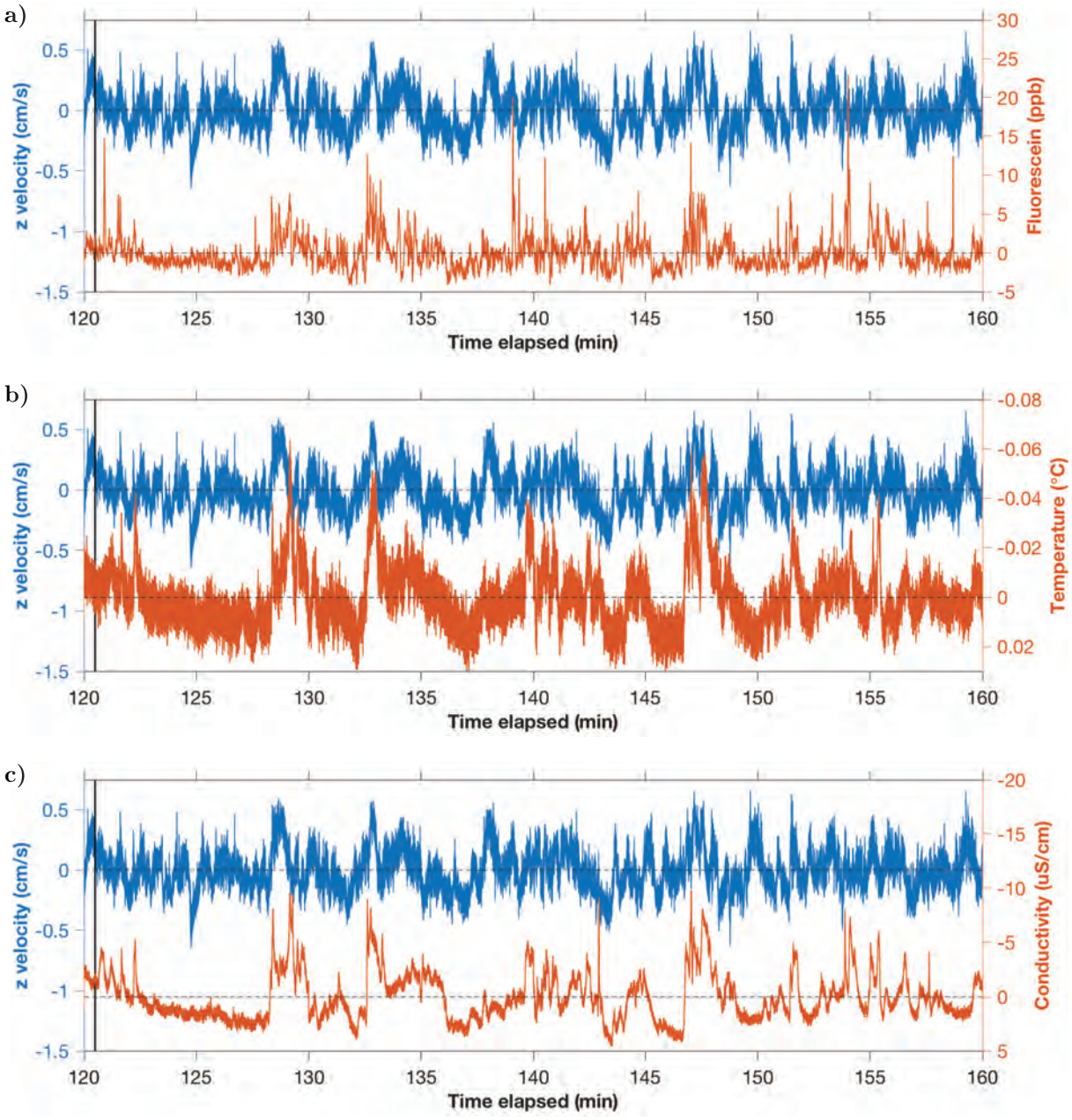

Figure C.25: Time series of fluctuations in **a)** fluorescein, **b)** temperature, and **c)** conductivity, overlaid with concurrently measured w fluctuations, for Period 4 of the EC run. Temperature and conductivity axes are reversed.

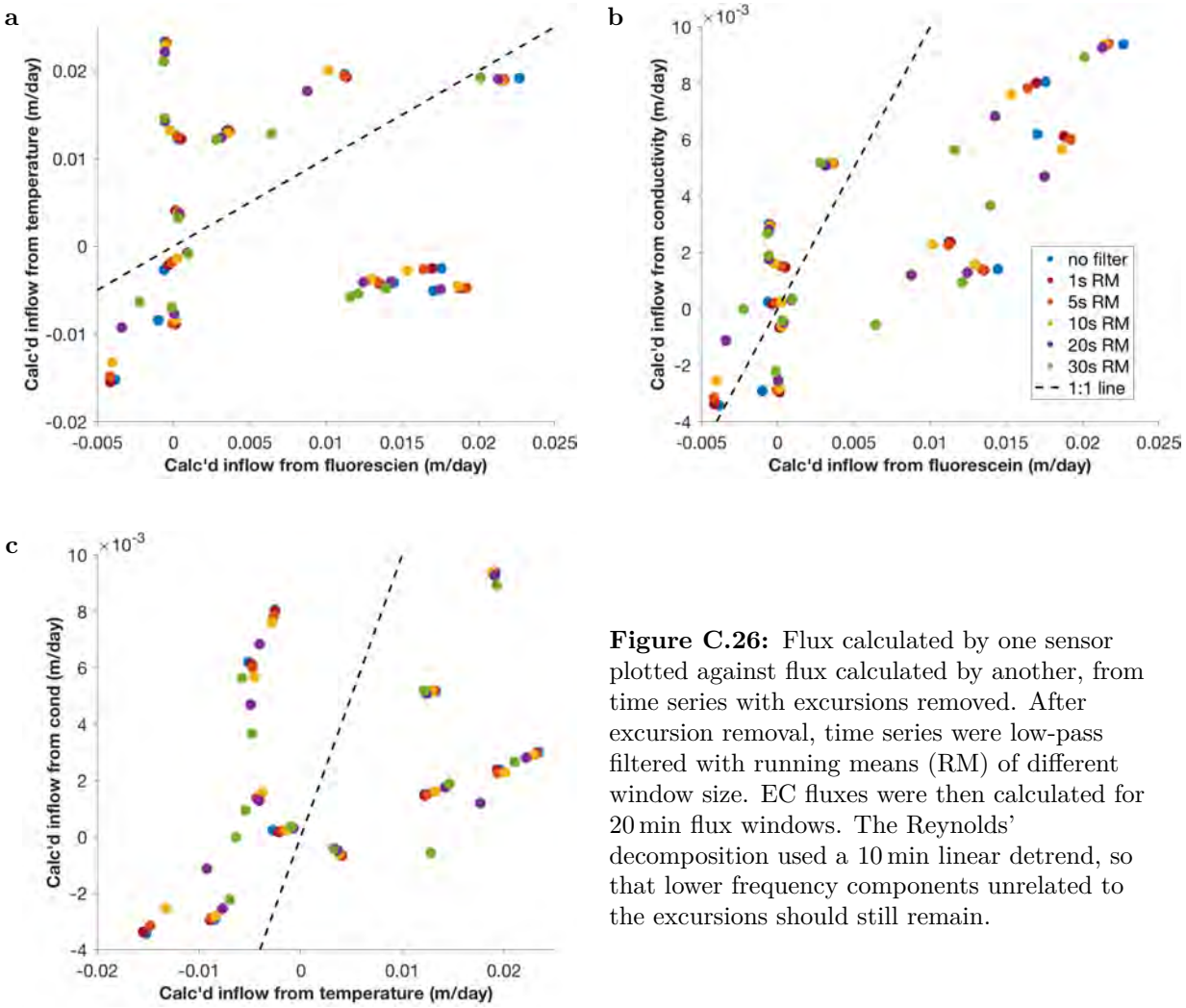

Figure C.26: Flux calculated by one sensor plotted against flux calculated by another, from time series with excursions removed. After excursion removal, time series were low-pass filtered with running means (RM) of different window size. EC fluxes were then calculated for 20 min flux windows. The Reynolds' decomposition used a 10 min linear detrend, so that lower frequency components unrelated to the excursions should still remain.

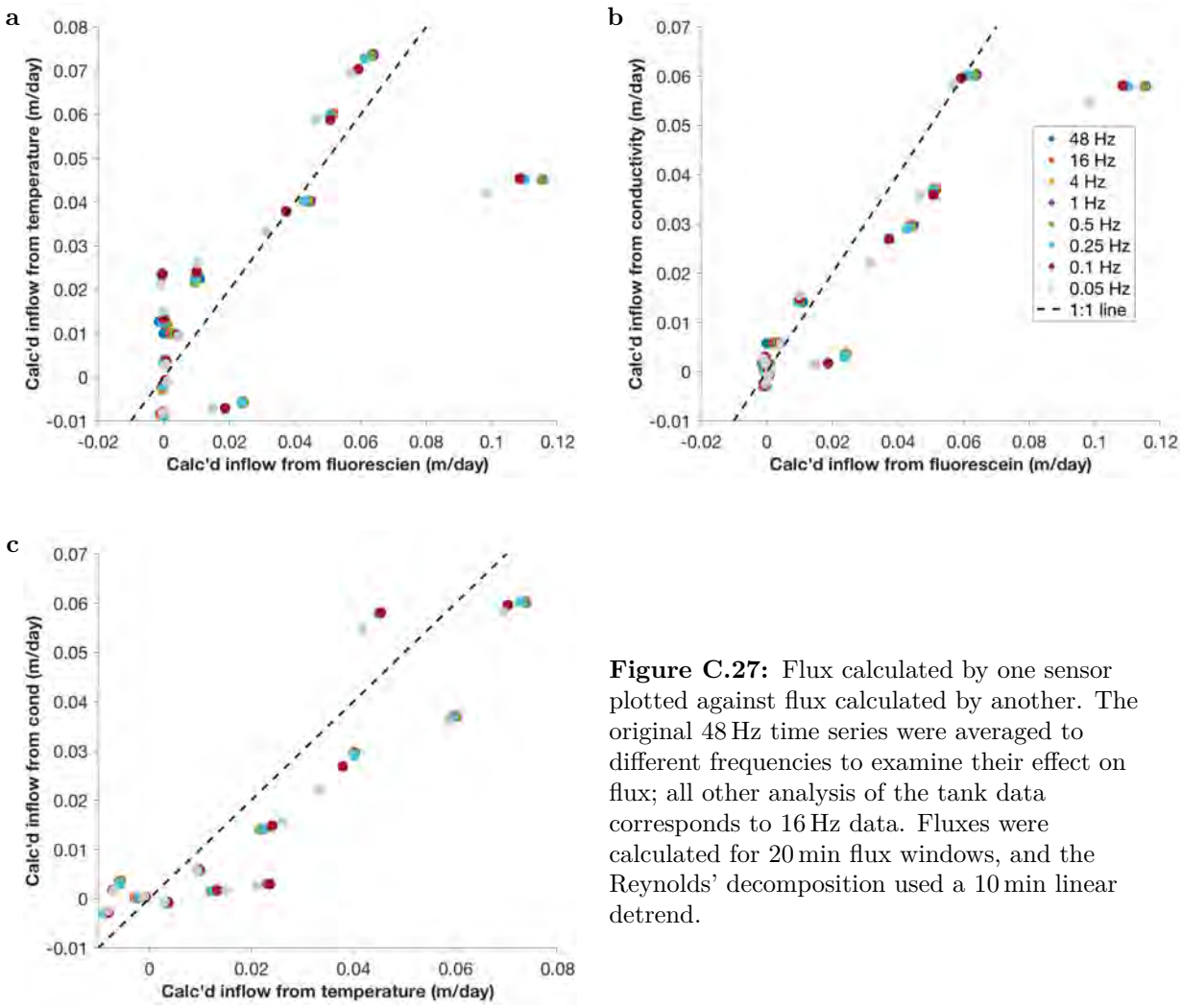

Figure C.27: Flux calculated by one sensor plotted against flux calculated by another. The original 48 Hz time series were averaged to different frequencies to examine their effect on flux; all other analysis of the tank data corresponds to 16 Hz data. Fluxes were calculated for 20 min flux windows, and the Reynolds' decomposition used a 10 min linear detrend.

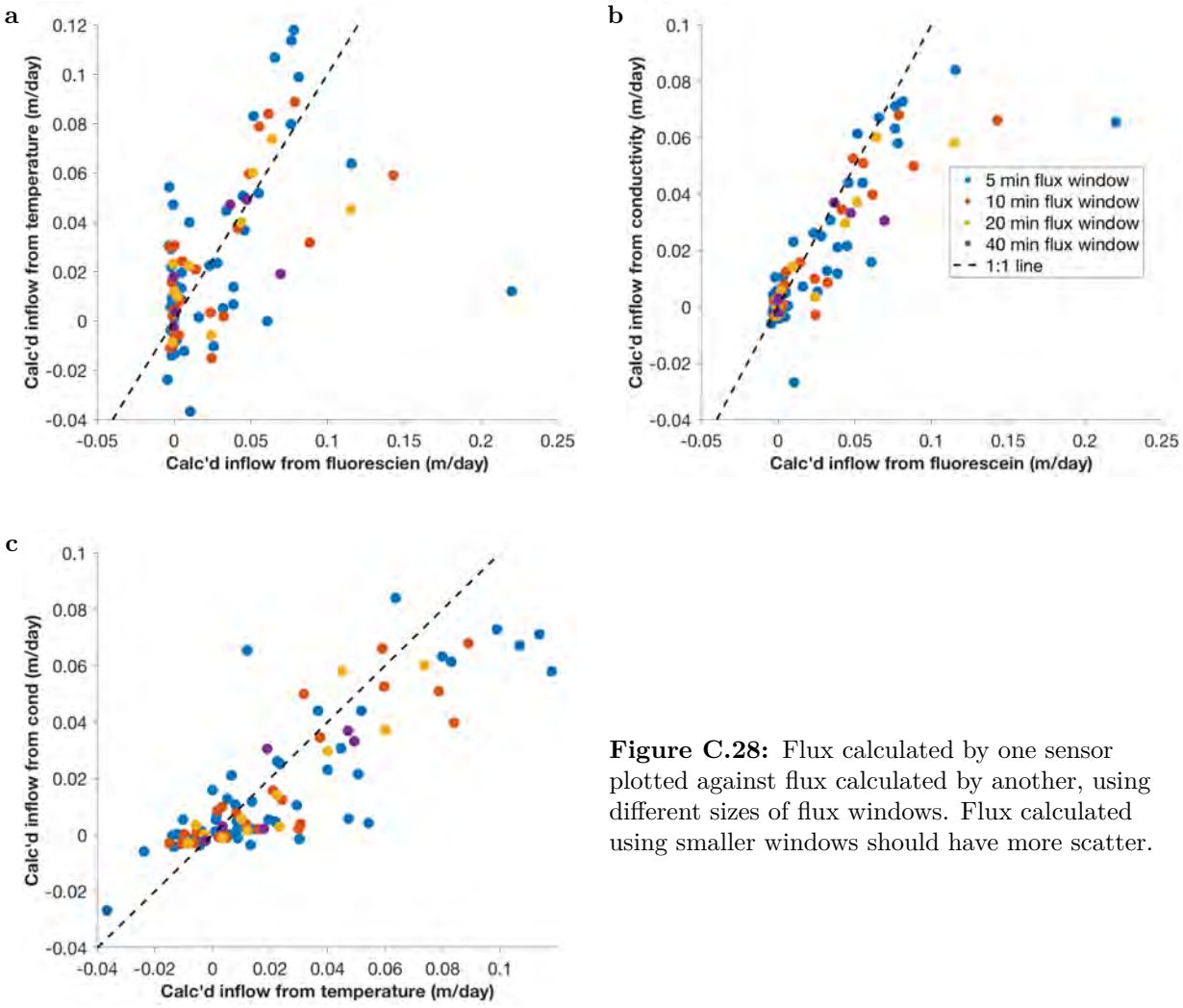

Figure C.28: Flux calculated by one sensor plotted against flux calculated by another, using different sizes of flux windows. Flux calculated using smaller windows should have more scatter.

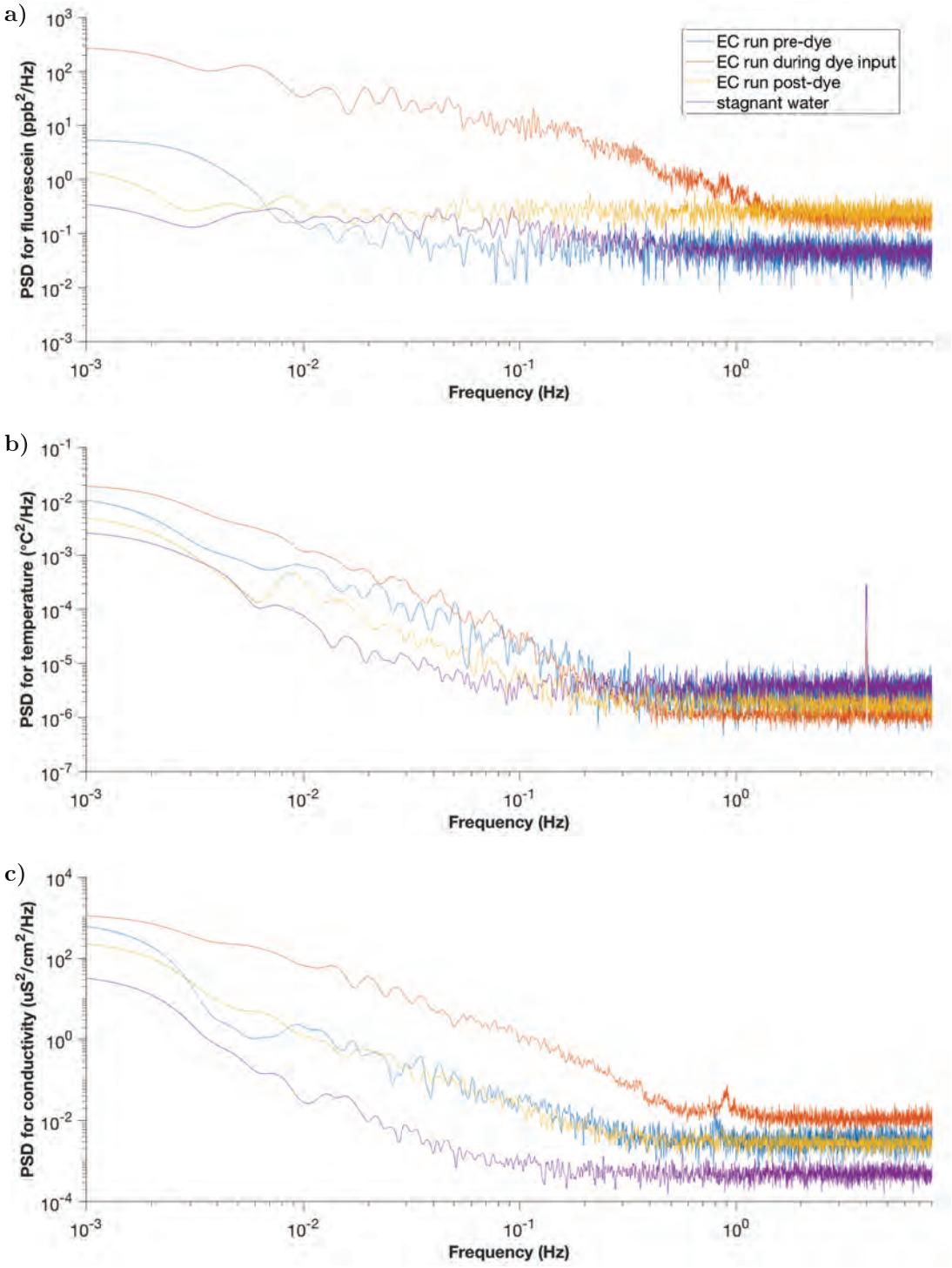

Figure C.29: Power spectra of **a)** fluorescein, **b)** temperature, and **c)** conductivity

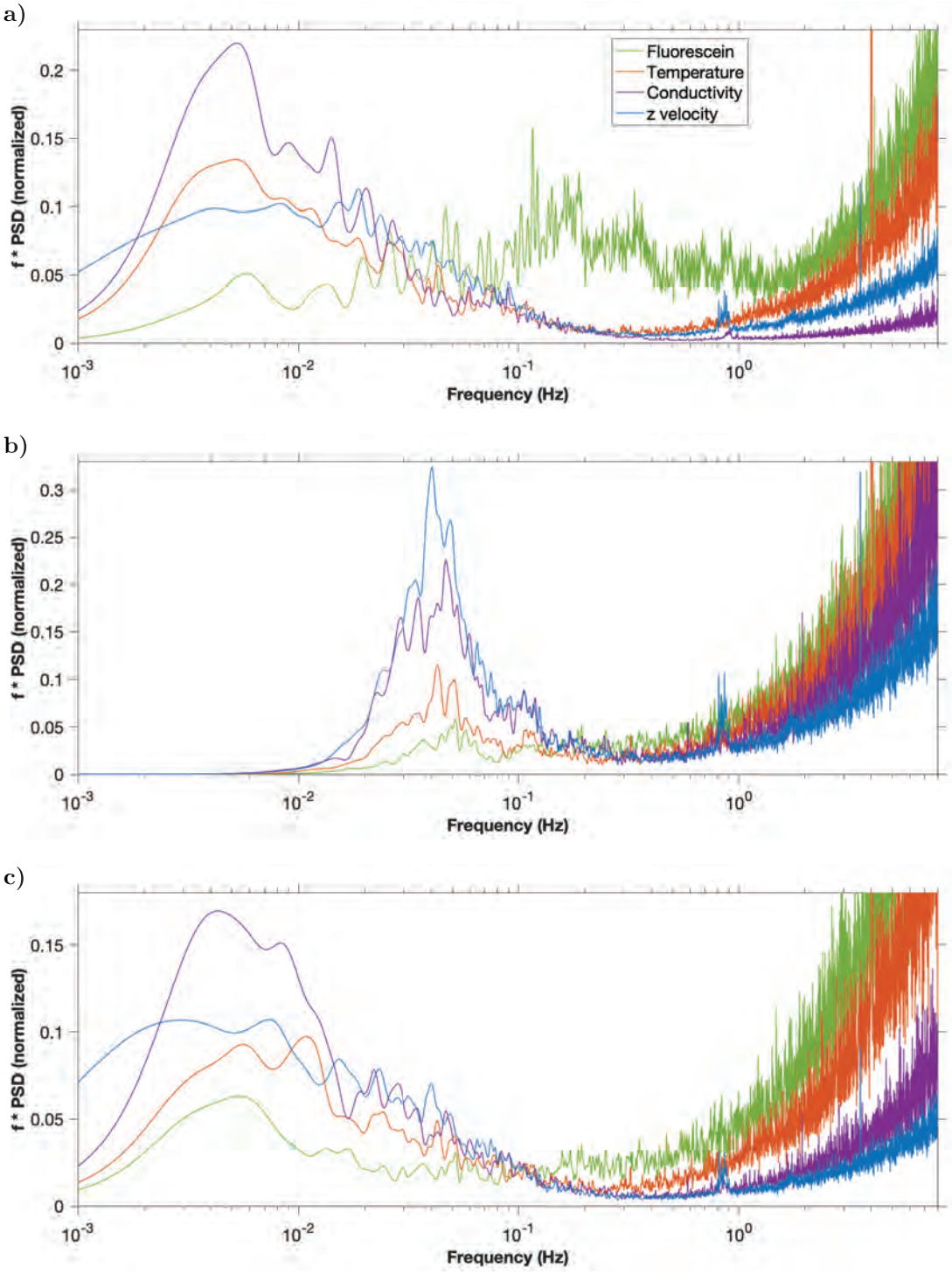

Figure C.30: Normalized variance-preserving spectra for entire EC run corresponding to fluctuations used in flux calculations: **a)** data with 10 min linear trend subtracted (fluxes in Figure 4.34); **b)** data with excursions removed and 30 min running mean subtracted (fluxes in Figure 4.35); and **c)** data with excursions removed and 10 min linear trend subtracted (fluxes in Figure 4.36). All spectra were normalized to total variance for each graph individually, so that peak heights represent relative distribution of power across frequency spectrum. Note that **b)** is similar to Figure B.25c (p. 309) but with different normalization.

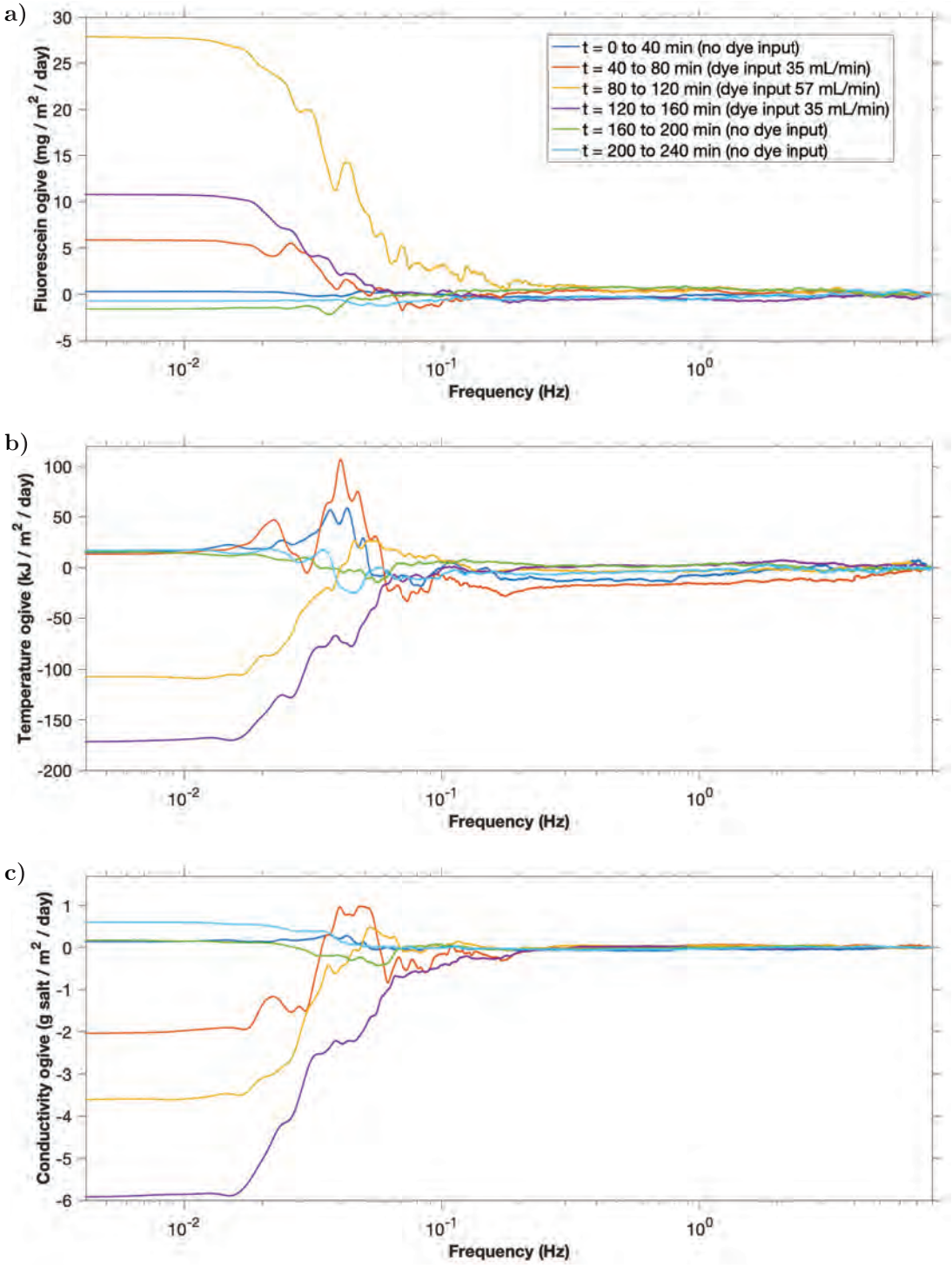

Figure C.31: Cumulative cospectra (ogive plots) for **a)** fluorescein, **b)** temperature, and **c)** conductivity, corresponding to 'turbulent' fluctuations only (i.e. calculated from data with excursions removed and after subtracting a 30 s running mean, as described in Section 4.6.6.

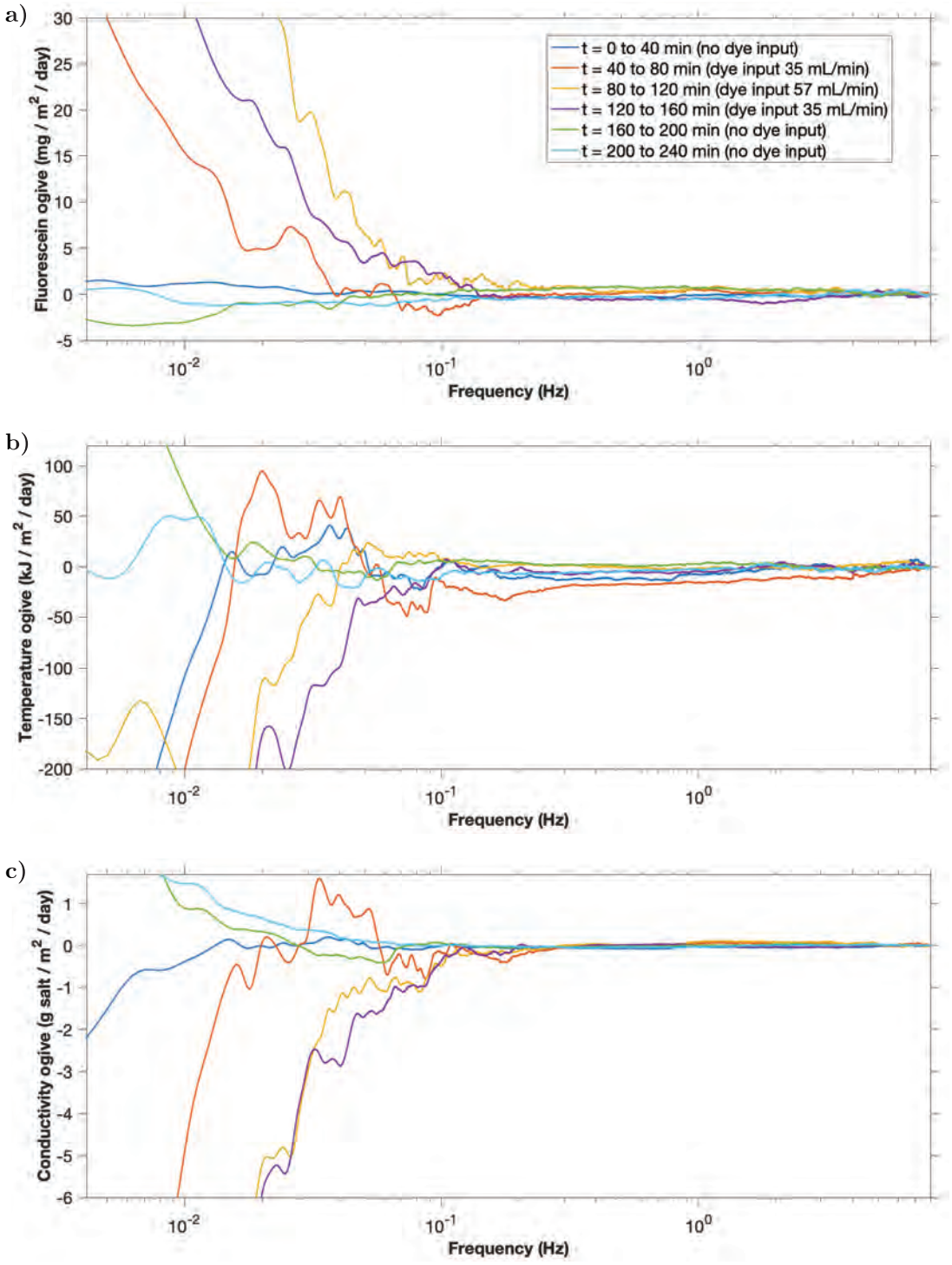

Figure C.32: Cumulative cospectra (ogive plots) for **a)** fluorescein, **b)** temperature, and **c)** conductivity for original time series, zoomed to match axes of Figure C.31 for easier comparison. Data are the same as in Figure 4.33.

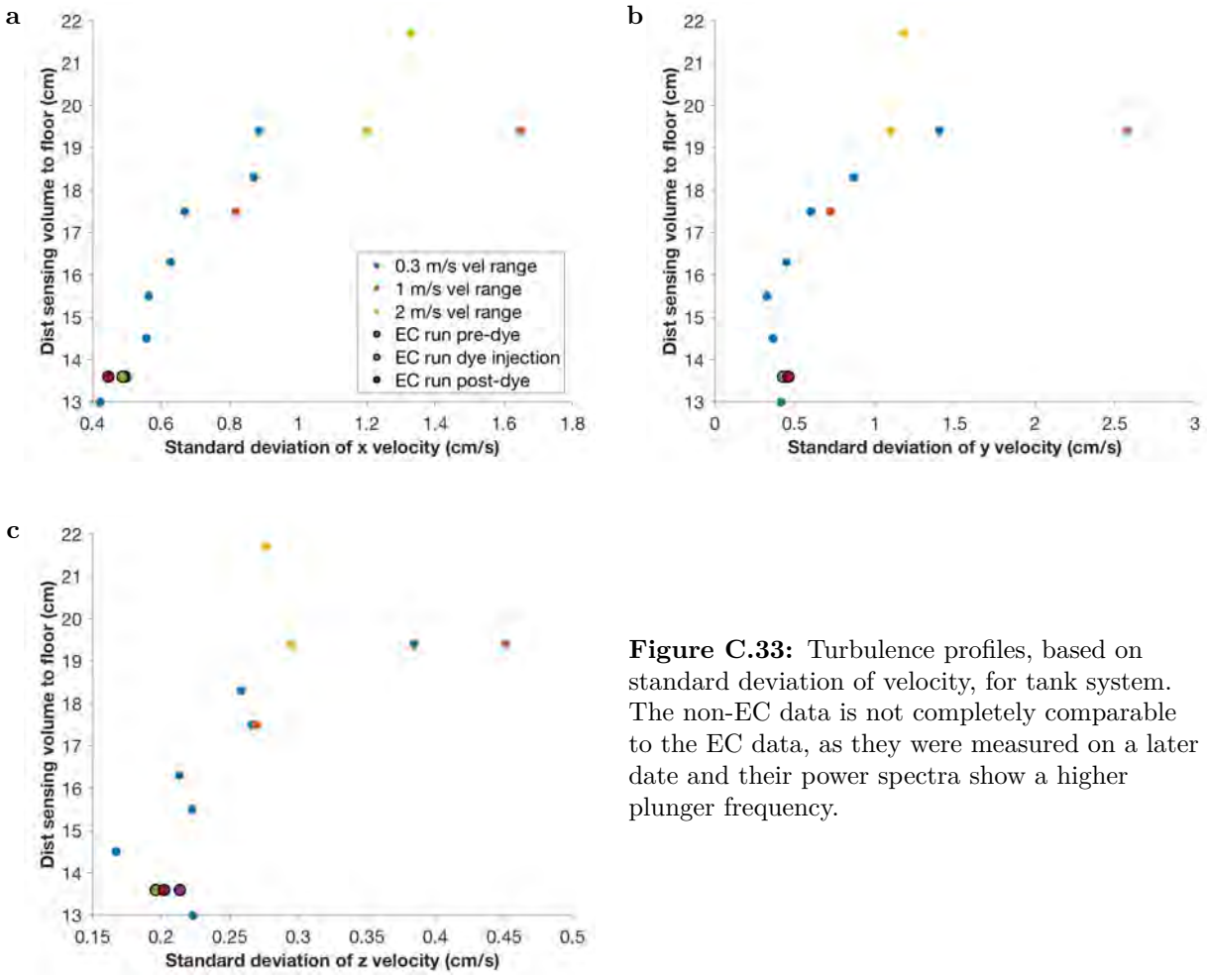

Figure C.33: Turbulence profiles, based on standard deviation of velocity, for tank system. The non-EC data is not completely comparable to the EC data, as they were measured on a later date and their power spectra show a higher plunger frequency.

Appendix D

Fieldwork checklists and gallery

Pack list 10/16/17

Lander with buoys tied on
Optical fibers in holder, in the cake carrier
Housing w/ electronics
PVC wedges for housing to prevent it from rolling
Ethernet cable
Blackout film with plastic clamps and small buoys attached at corners
4 bricks
Plastic sheet for light backdrop, with three elastic cable ties in the holes
Freezable bag with prelabelled, washed amber jars for collecting water
Waders
Sheet for blocking light from my computer

ADV case
- ADV
- OF alignment piece
- OF holder
- Shorter ADV cable
- Longer ADV cable
- 7/64" hex drive screwdriver (ADV housing – this is also the one to use for shaft collars on cables)

Plastic Box – High-use items (near top)
McMaster bag: Molykote 111 for O-ring; Molykote 44 for Ethernet connector; gloves to put on grease; paper towels; Sharpie
Loctite for ADV connector
Hose clamps
Reusable zip ties + others
Large screwdriver (hose clamp for housing)
Conductivity / temperature cable
Little red toolbox:
- 3/16" hex head screwdriver (ADV holder)
- 7/16" socket wrench and combo wrench (1/4" nuts)
- 9/16" combo wrench (3/8" nuts for OF holder)
- 3/32" hex drive screwdriver (shaft collars on OF holder - both ones holding OFs and ones at top)
- 5/32" hex drive screwdriver (cross bars)
- Pocket ruler
- Magnet wrapped in bubble wrap or paper towels

Conductivity & temperature meters
Blackout cloth
Write in the Rain notebook and pen

Plastic Box – Low use items (near bottom)
Multimeter with probes
Measuring tape
Masking tape
Optical tape
Extra rope
Little clear box with extras:
- ¼" washers and nuts (connections to lander)
- 3/8" nuts (OF holder)
- #8 thumb screws (OF holder)
- #12 thumb screws (ADV alignment piece)
- Caps for OFs- small free end, large free end, SMA905
- Parafilm
- Magnet in bubble wrap or paper towels
- Small, flexible cable ties I use to tie cables to OFs
- Cord ties for big cables
- Elastic cable ties for the light backdrop thing

Personal stuff / plastic bag
Computer
Water
Food
Change of clothes
Towels
Dive boots
Mask and snorkel
Sunscreen
Hat
Cell phone and small wallet in a Ziploc bag

Field order of operations
1016/17
Sub-bullets = need to bring into water on that trip

- Set up lander frame
- Spray Loctite on ADV to computer cable
- Mount ADV
    - ADV
    - ADV cable
    - Screwdriver or hex wrench for ¼”
- Check ADV on computer, make sure settings are ok. Take a recording while prepping housing
- Housing: open up, insert OFs, close
- Stop ADV recording
- Attach sensing volume alignment piece and OF holder vertical bar to ADV
    - Sensing volume alignment piece
    - OF holder’s vertical bar
- Housing onto the lander. May make sense to stick OFs onto their bar next. Then screw in the hose clamps to hold down the housing.
    - Housing with OFs
    - Hose clamps
    - Giant screwdriver
- Put the black plastic backdrop on, also drape a dark cloth over housing
    - Black plastic thing with cable ties in
    - Dark cloth
- Go back to align OFs to sensing volume, angling acceptance fiber towards backdrop; screw tight. Measure and record distances, then take off the sensing volume alignment piece
    - Combo wrench for 3/8” nuts
    - Pocket ruler
- Grease temperature/conductivity plugs while on land, then take cable to setup and plug in. Zip tie in OFs and/or cables
    - Temperature/conductivity cable
    - Zip ties
- Check ADV again, make sure probe check is ok and OFs aren’t in the way. Take a recording for a few minutes
- While waiting, can spray Loctite on both ends of the second ADV cable, and pre-grease the Ethernet cable
- Take water sample
- Check conductivity and temperature
- Change ADV to sample on synch, make sure the recorder has a file name
- Switch ADV cables. Stick on magnet. Plug in Ethernet and string it to land.
    - Second ADV cable
    - Ethernet cable
    - Magnet
- Put the giant tarp over the whole thing
- Connect to computer, ssh in

```
tmux
```
C-b ^P
```
sudo ./mainprogr
```
** make sure everything ok **
```
fnb
tnb
ts 3
mg 7000
```
`ft 1` → wait until counts settle
`fsm 3000 7000 10 20 20 << startscan` → hope to see minimal sunlight interference…
```
mg 4750
```
`cdd 100 300 << counts` → metric: `start`
** check that values are ok, esp for Teensy **
```
emt 30 32 180 mystic
```
C-b alt-shift-P
C-b d
```
logout
```

To return, ssh back in
```
tmux –a
```
** check on progress, cancel or clean up whatever **

`cdd 100 300 << couts` → metric: `end`
```
fsm 3000 7000 10 20 20 << endscan
x

scp
pi@raspberrypi.local:~/PhotonCounter/*.tx
t ~/Research/Data/---

mkdir ./Data/2017----
cd ..
mv *.txt ./Data/2017----

```
C-b alt-shift-P
C-b d

```
scp pi@raspberrypi.local:/home/pi/*.log
~/Research/Data/---

cd ~/pi
mkdir OldLogs
mv *.log OldLogs
```

Also be sure to measure conductivity and temperature and take a grab sample

Photo gallery

This section contains photos from the field deployment on 15 September 2017, showing onshore assembly followed by final connections at the measuring site. Subsequent photos show the teardown from the deployment of 26 September 2017, where the equipment was assembled and dissembled in the water. Also visible in the second deployment are the buoys added to help with deployment, and the light shield to block light to the measuring volume.

Appendix E

Schematics

The following schematics and board layouts are included:

- Schematic for "Board 1" (PMT / amplifiers for photon counter)
- Schematics for "Board 2" (counter circuitry and power circuitry) - 2 pages
- Schematic for temperature / conductivity board - does not include 1 µF capacitor on thermistor input and new ADC for temperature
- Schematic and board layout for reed switch board (installed on lid)
- Board layout for "Board 1" - 3 pages (top and bottom together, top only, bottom only)
- Board layout for "Board 2" - 5 pages (top and bottom together, then 4 layers separately)
- Board layout for temperature / conductivity board

The bill of materials for the main circuitry and (separately) temperature and conductivity circuitries is also included.

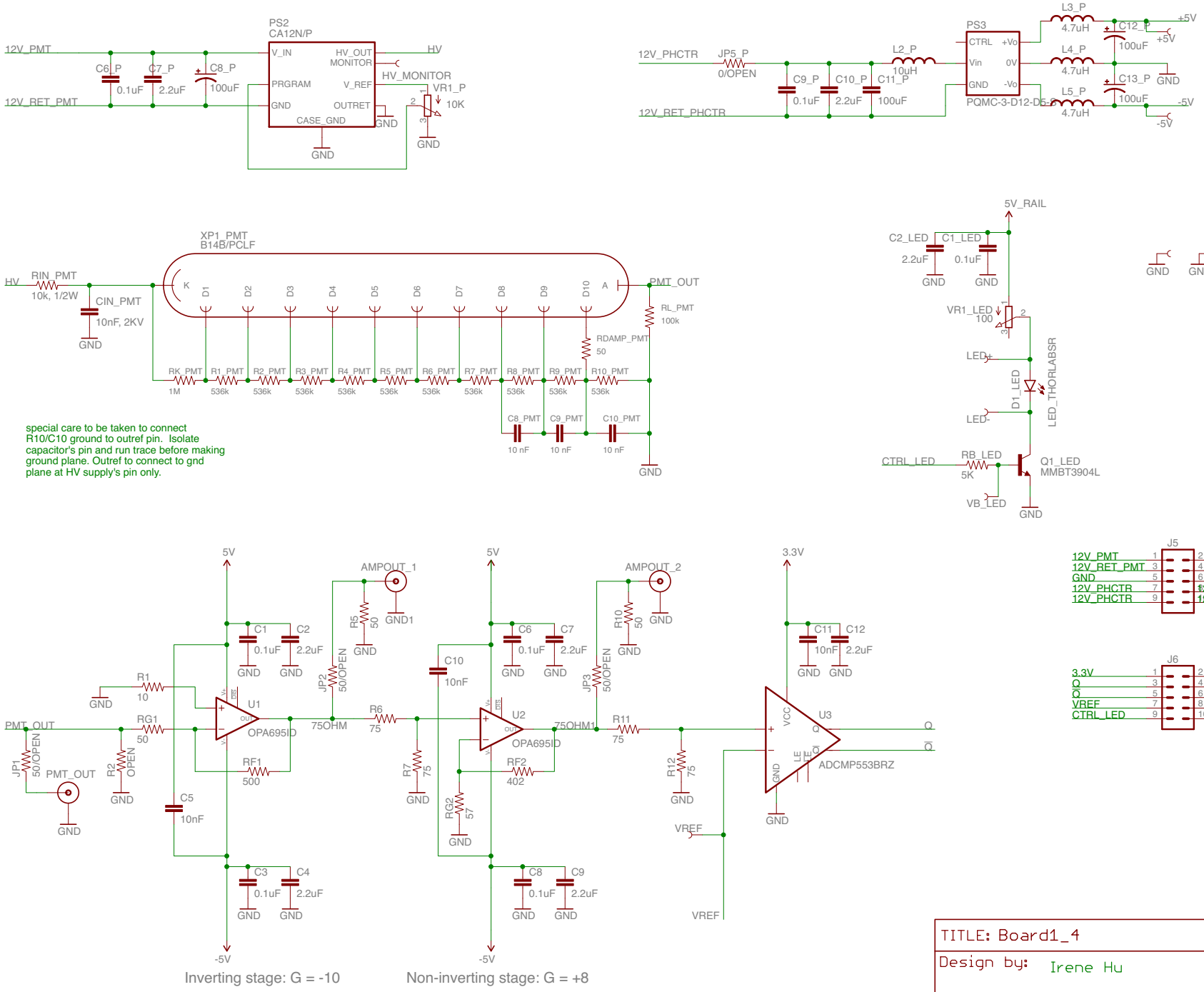

special care to be taken to connect R10/C10 ground to outref pin. Isolate capacitor's pin and run trace before making ground plane. Outref to connect to gnd plane at HV supply's pin only.

Inverting stage: G = -10

Non-inverting stage: G = +8

TITLE: Board1_4	
Design by: Irene Hu	REV:
Date: 8/16/16 12:56 PM	Sheet: 1/1

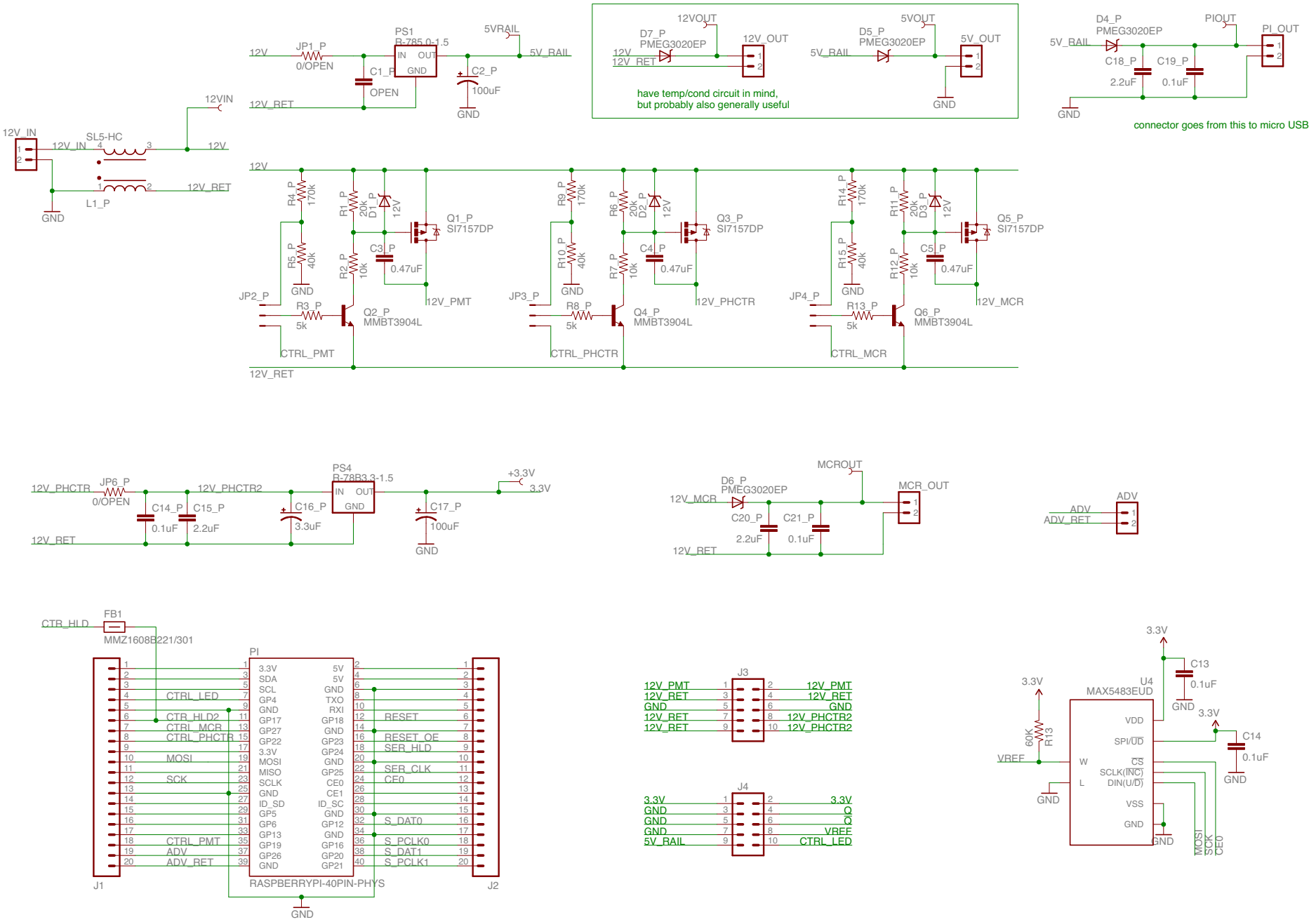

TITLE: Board2_5		
Design by: Irene Hu		REV:
Date: 12/19/16 2:48 PM	Sheet: 1/2	

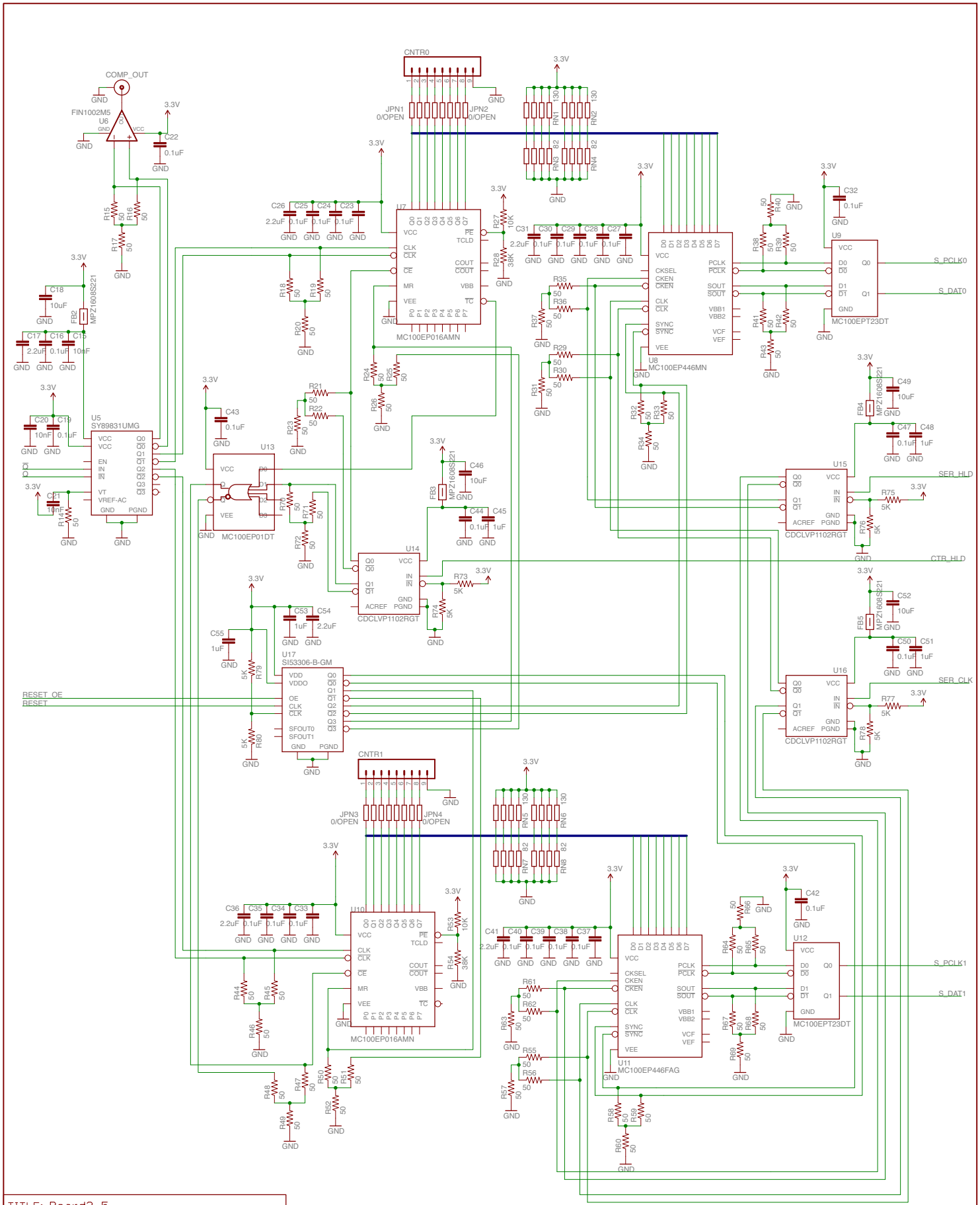

TITLE: Board2_5		
Design by: Irene Hu		REV:
Date: 12/19/16 2:48 PM	Sheet: 2/2	

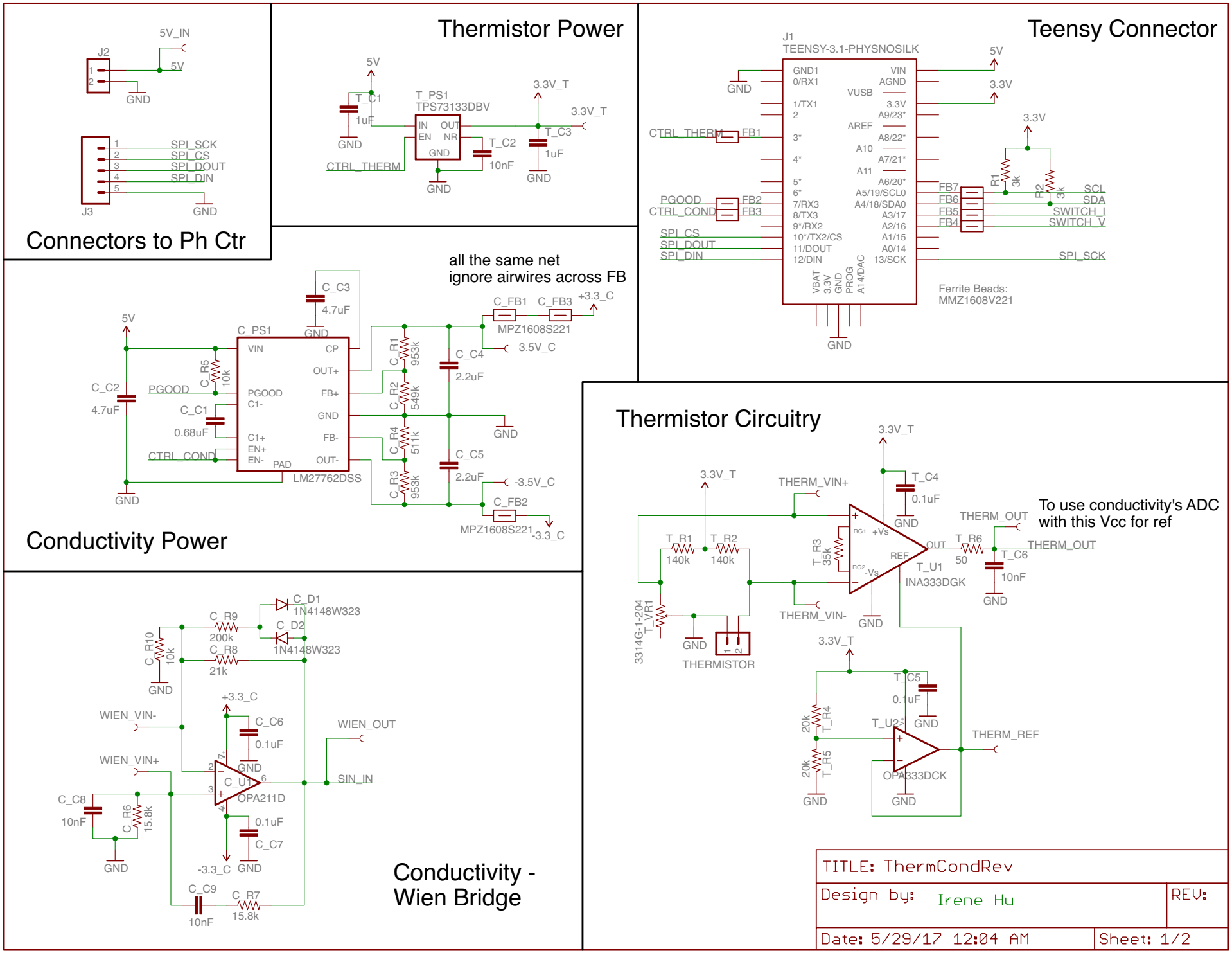
Connectors to Ph Ctr
5V_IN
J2
5V
GND
SPI_SCK
SPI_CS
SPI_DOUT
SPI_DIN
J3
Thermistor Power
5V
T_C1
1uF
T_PS1
TPS73133DBV
IN
OUT
EN
NR
GND
3.3V_T
T_C2
10nF
T_C3
1uF
CTRL_THERM
Teensy Connector
J1
TEENSY-3.1-PHYSNOSILK
GND1
0/RX1
1/TX1
2
3*
4*
5*
6*
7/RX3
8/TX3
9*/RX2
10*/TX2/CS
11/DOUT
12/DIN
VIN
AGND
VUSB
3.3V
A9/23*
AREF
A8/22*
A10
A7/21*
A11
A6/20*
A5/19/SCL0
A4/18/SDA0
A3/17
A2/16
A1/15
A0/14
13/SCK
VBAT
3.3V
GND
PROG
A14/DAC
FB1
FB2
FB3
FB4
FB5
FB6
FB7
PGOOD
CTRL_COND
SPI_CS
SPI_DOUT
SPI_DIN
R1
3k
R2
3k
SCL
SDA
SWITCH_I
SWITCH_V
SPI_SCK
Ferrite Beads:
MMZ1608V221
all the same net
ignore airwires across FB
C_C3
4.7uF
C_PS1
VIN
CP
OUT+
FB+
GND
FB-
OUT-
PAD
PGOOD
C1-
C1+
EN+
EN-
LM27762DSS
C_R5
10k
C_C2
4.7uF
C_C1
0.68uF
CTRL_COND
C_R1
953k
C_R2
549k
C_R4
511k
C_R3
953k
C_C4
2.2uF
C_C5
2.2uF
C_FB1
C_FB3
+3.3_C
MPZ1608S221
3.5V_C
-3.5V_C
C_FB2
MPZ1608S221
-3.3_C
Conductivity Power
Thermistor Circuitry
3.3V_T
THERM_VIN+
T_C4
0.1uF
T_R1
140k
T_R2
140k
T_R3
35k
RG1
+Vs
OUT
REF
RG2
-Vs
T_U1
INA333DGK
THERM_OUT
T_R6
50
T_C6
10nF
To use conductivity's ADC
with this Vcc for ref
3314G-1-204
T_VR1
THERM_VIN-
THERMISTOR
T_C5
0.1uF
T_R4
20k
T_R5
20k
T_U2
OPA333DCK
THERM_REF
C_D1
1N4148W323
C_D2
1N4148W323
C_R9
200k
C_R8
21k
C_R10
10k
WIEN_VIN-
WIEN_VIN+
C_C6
0.1uF
C_U1
OPA211D
WIEN_OUT
SIN_IN
C_C8
10nF
C_R6
15.8k
C_C7
0.1uF
-3.3_C
C_C9
10nF
C_R7
15.8k
Conductivity -
Wien Bridge
TITLE: ThermCondRev
Design by: Irene Hu
REV:
Date: 5/29/17 12:04 AM
Sheet: 1/2

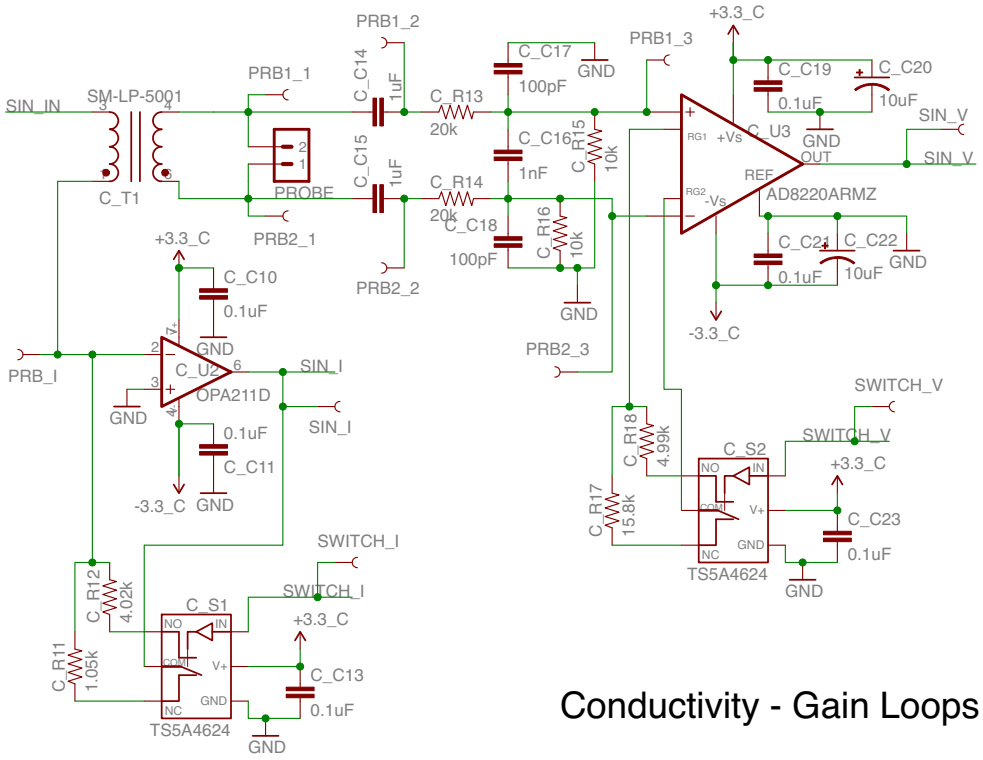

Conductivity - Gain Loops

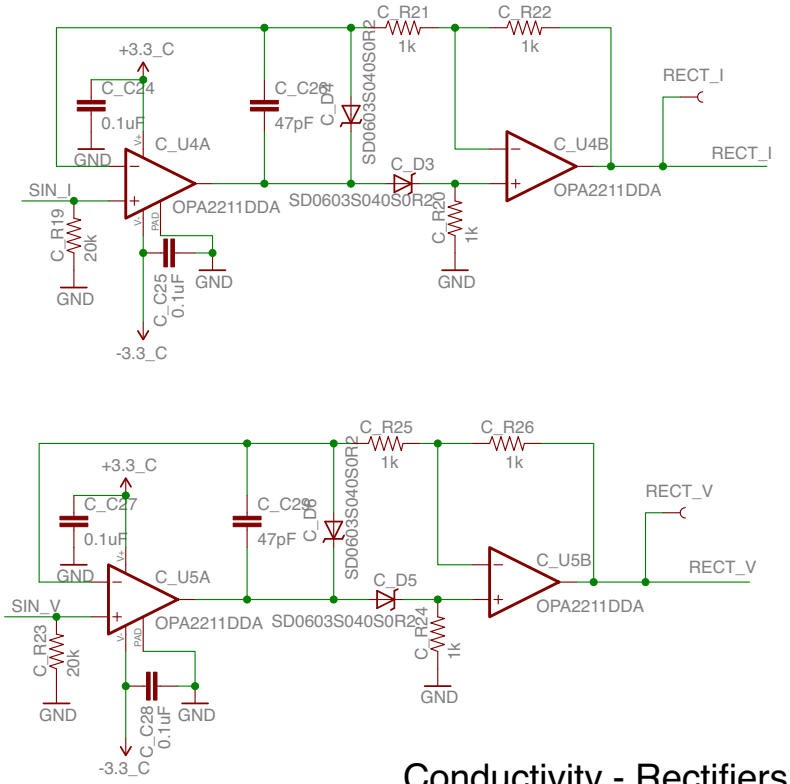

Conductivity - Rectifiers

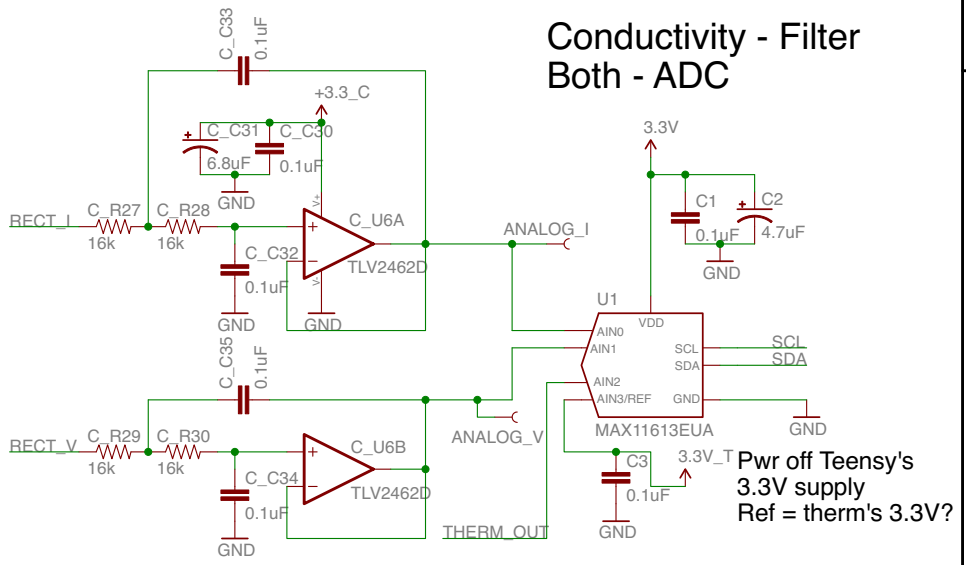

Conductivity - Filter
Both - ADC

Pwr off Teensy's
3.3V supply
Ref = therm's 3.3V?

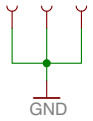

TITLE: ThermCondRev		
Design by: Irene Hu		REV:
Date: 5/29/17 12:04 AM	Sheet: 2/2	

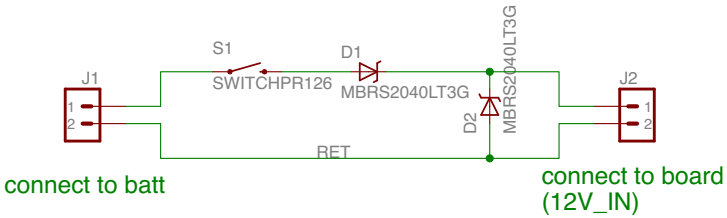

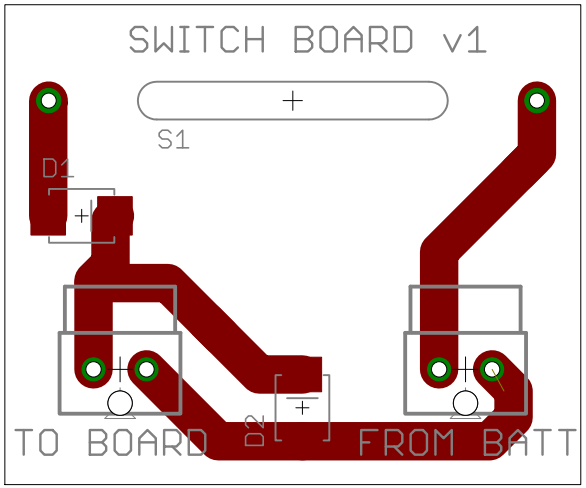

Switch_1_3
8/17/16 3:22 PM
Designed by: Irene Hu

TITLE: Switch_1_3	
Design by: Irene Hu	REV:
Date: 8/17/16 3:10 PM	Sheet: 1/1

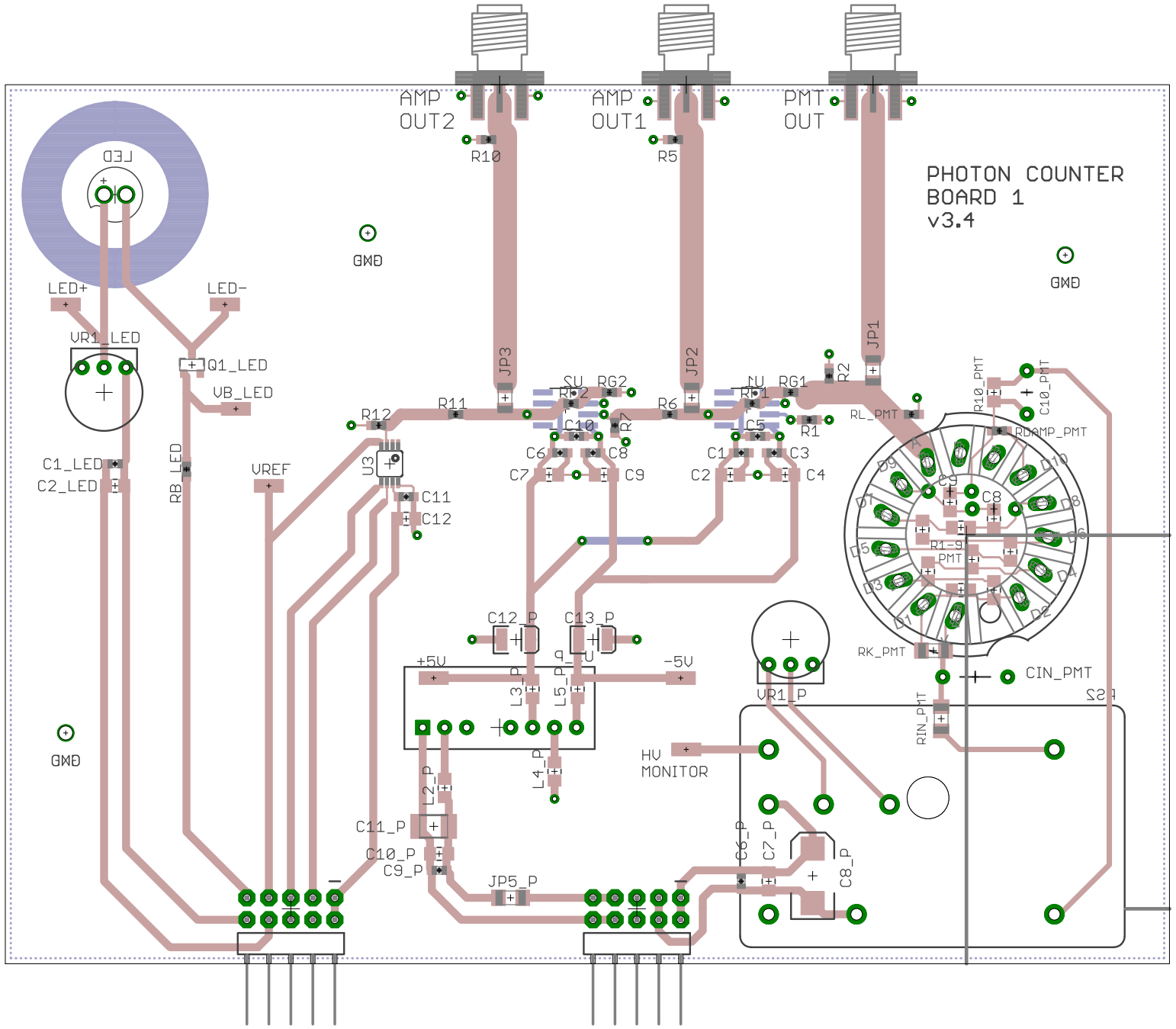

Board1_4
8/18/16 3:24 PM
Designed by: Irene Hu

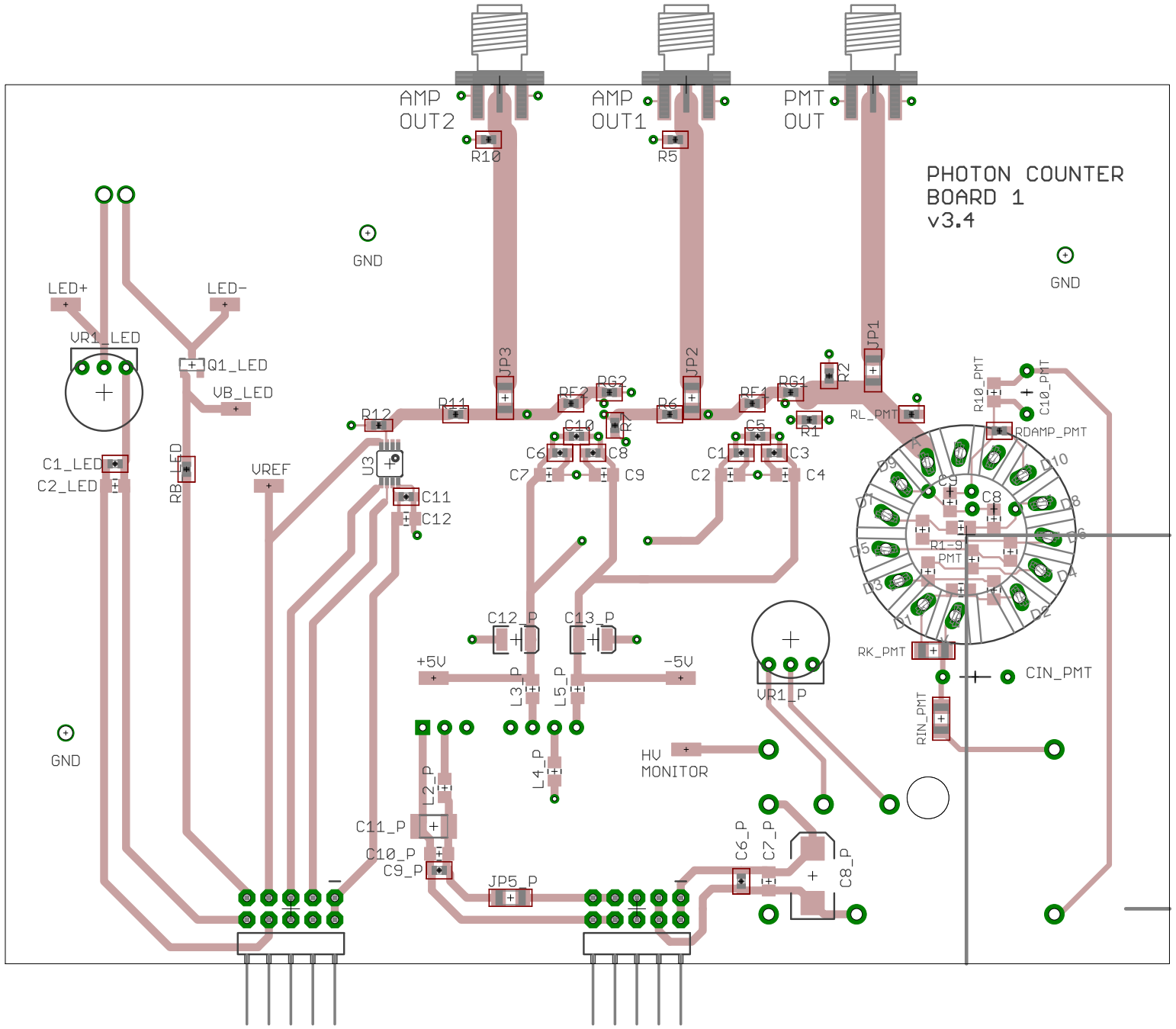

Board1_4
8/18/16 3:24 PM
Designed by: Irene Hu

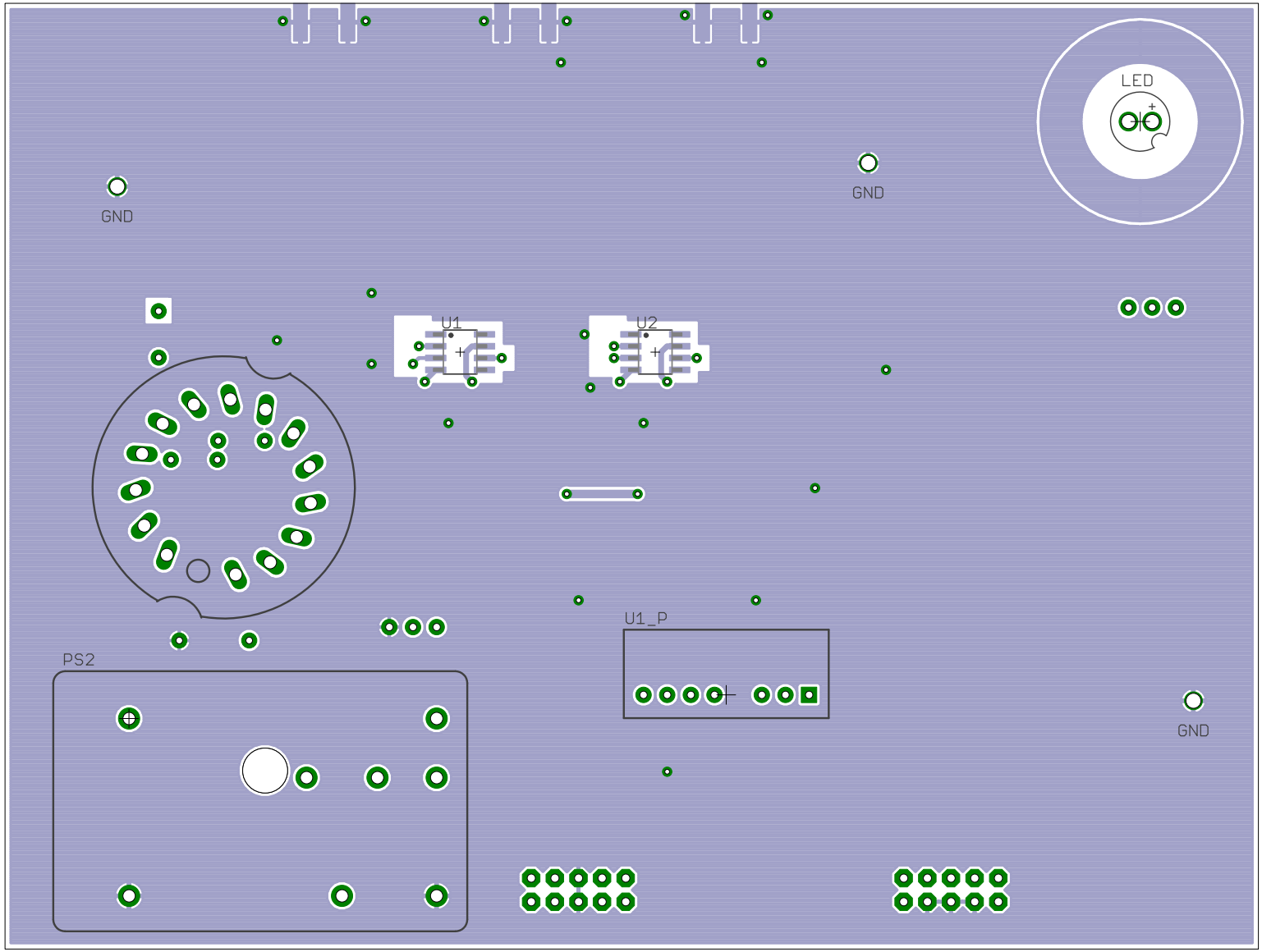
LED
GND
GND
U1
U2
U1_P
PS2
GND

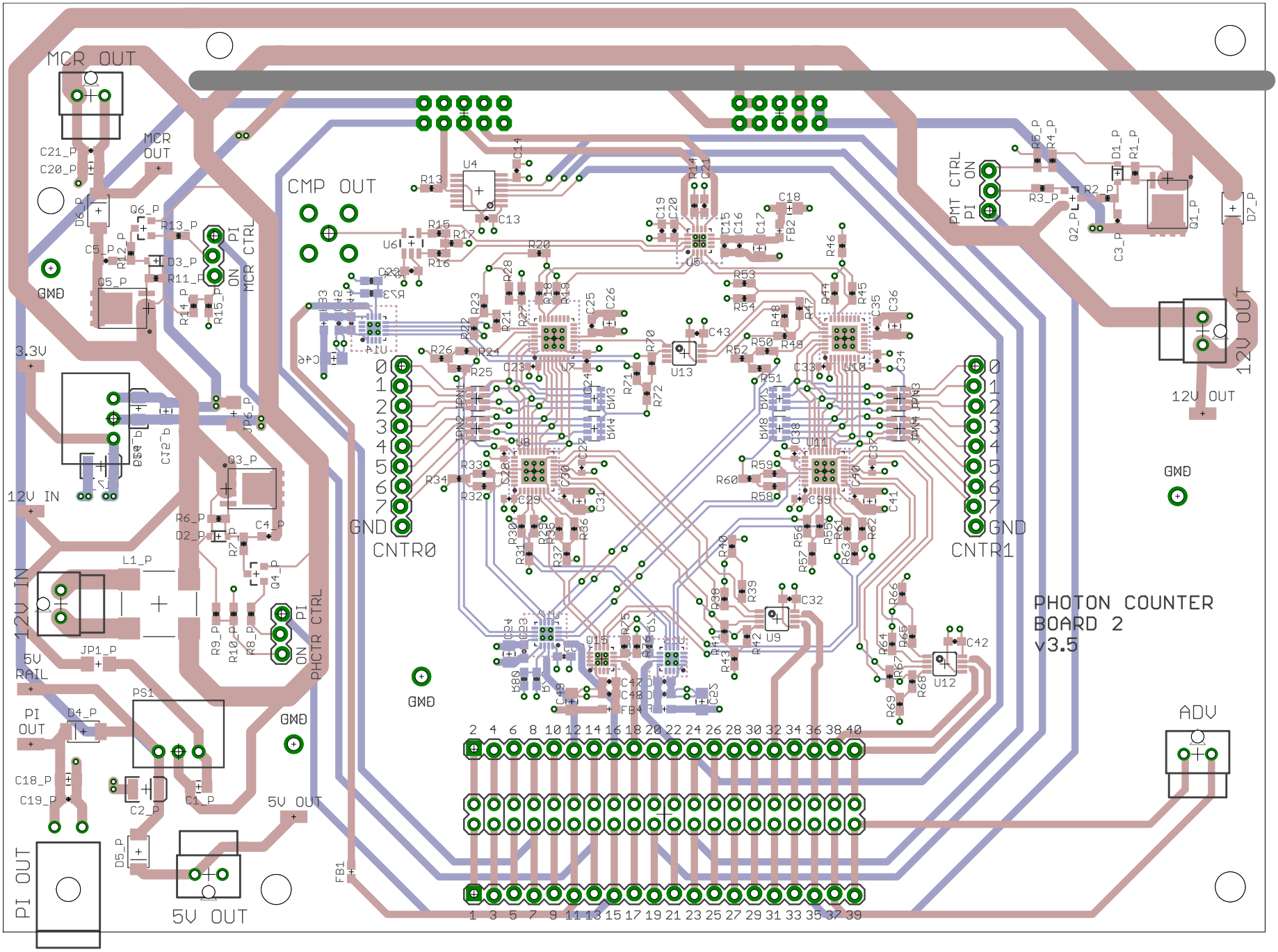
MCR OUT
MCR OUT
CMP OUT
PMT CTRL
ON
PI
PI CTRL
ON
MCR CTRL
GND
3.3V
12V IN
12V IN
5V RAIL
PI OUT
PI OUT
5V OUT
5V OUT
PHCTR CTRL
ON
PI
GND
GND
CNTR0
GND
CNTR1
12V OUT
12V OUT
GND
ADV
PHOTON COUNTER
BOARD 2
v3.5

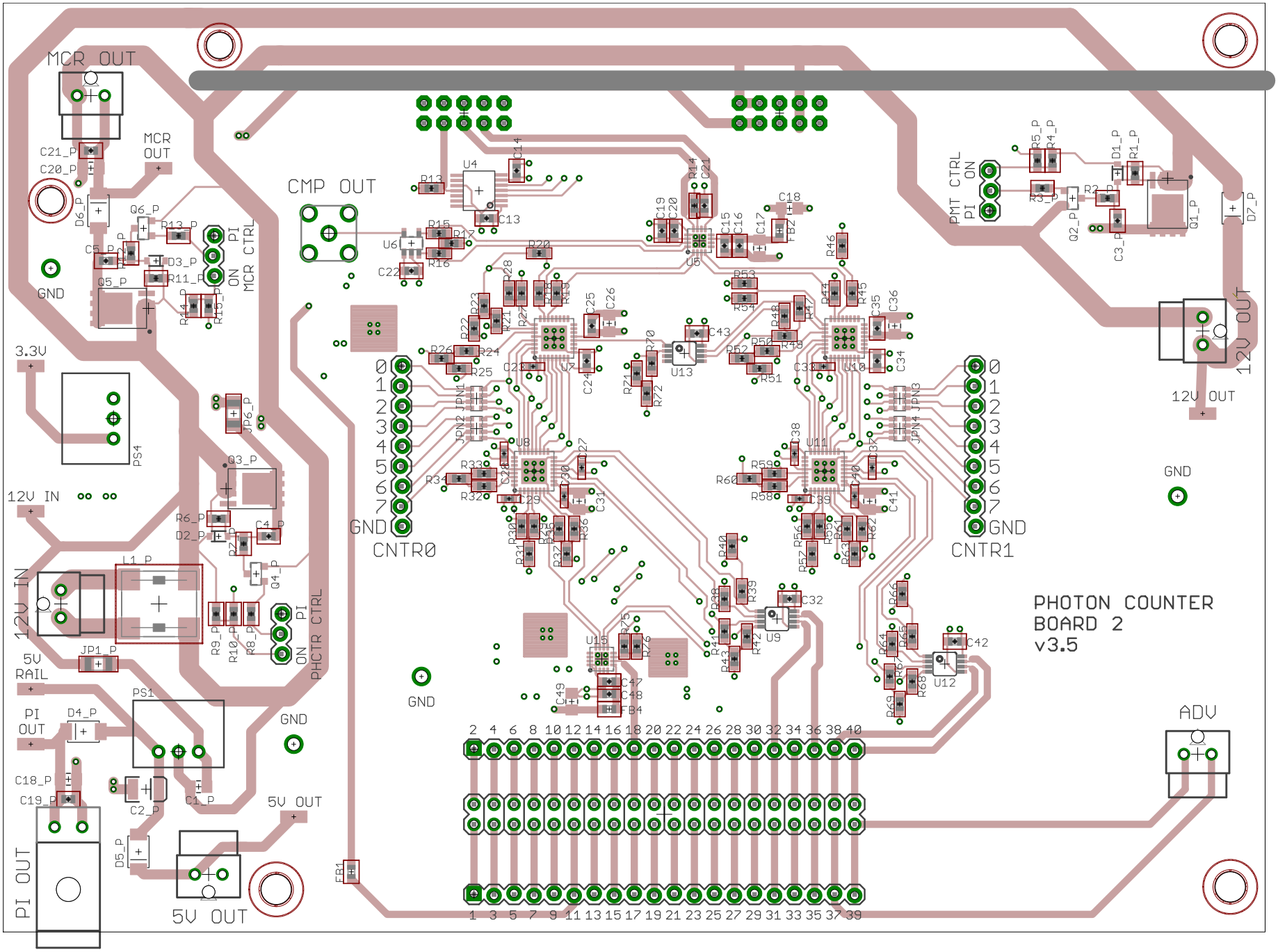

Board2_5
12/19/16 3:54 PM
Designed by: Irene Hu

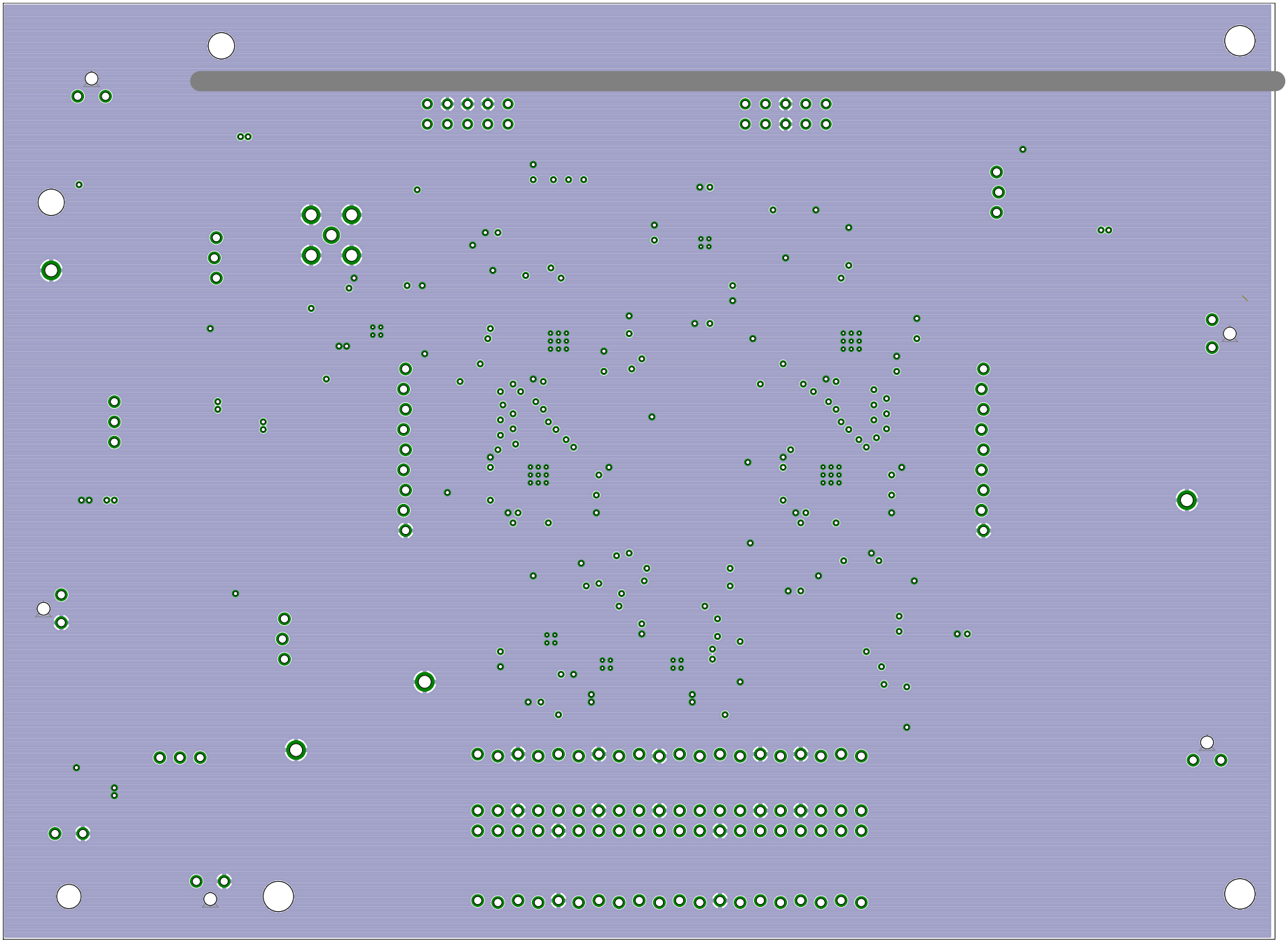

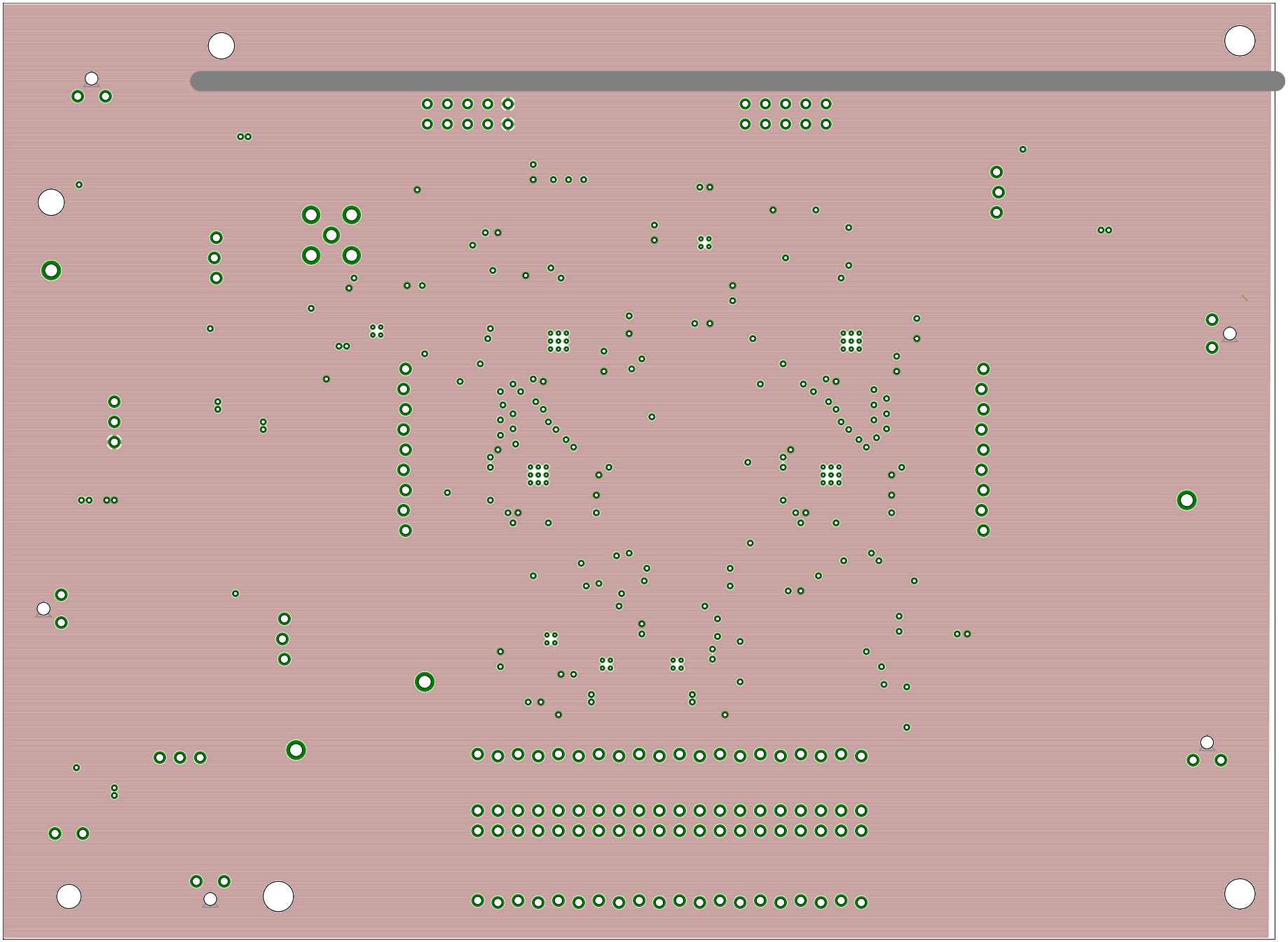

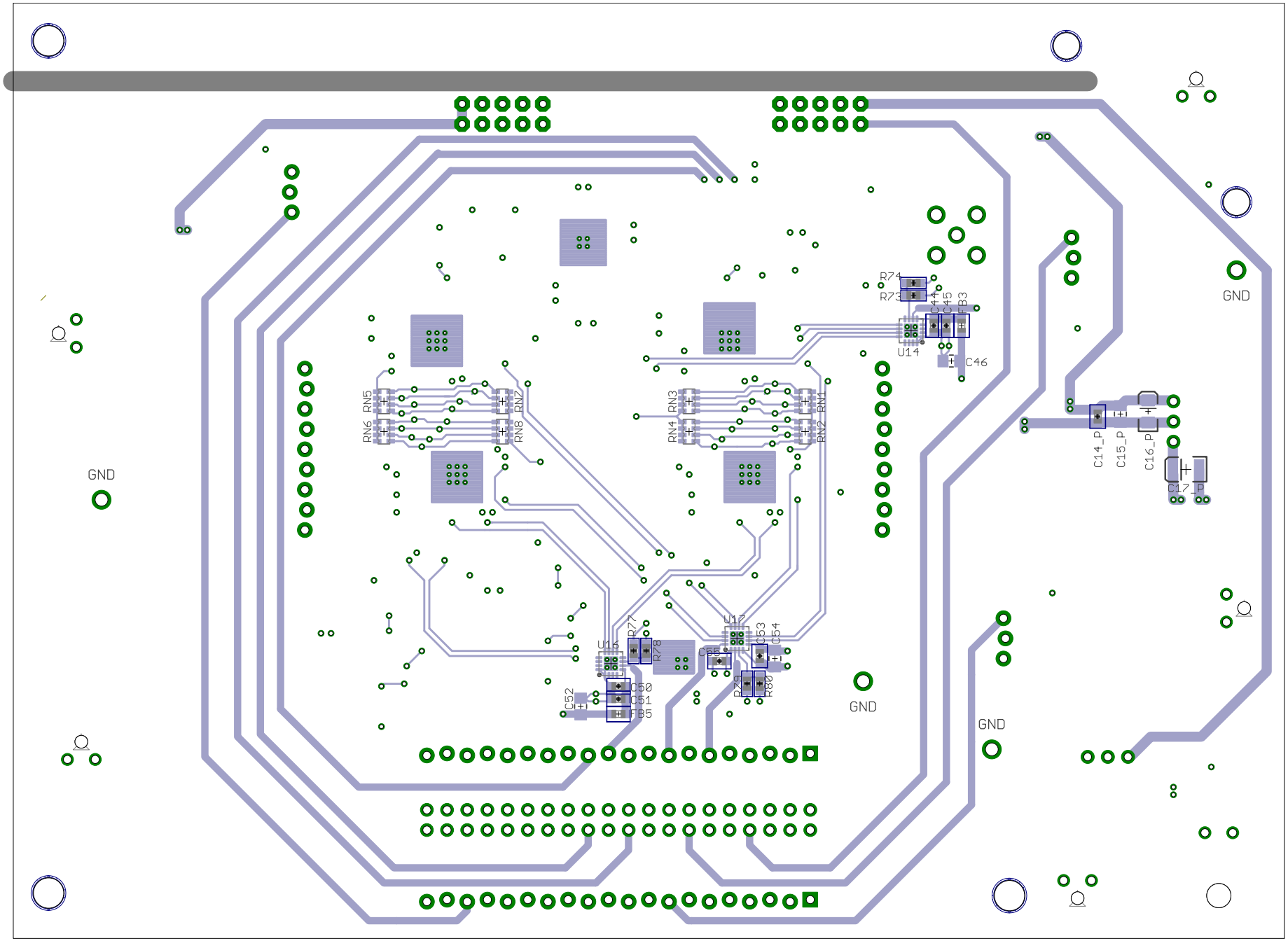
GND
GND
GND
GND
R74
R73
C44
C45
FB3
U14
C46
RN5
RN6
RN8
RN7
RN3
RN4
RN2
RN1
C14_P
C15_P
C16_P
C17
U16
R77
R78
C52
C50
C51
FB5
U12
C53
C54
R79
R80

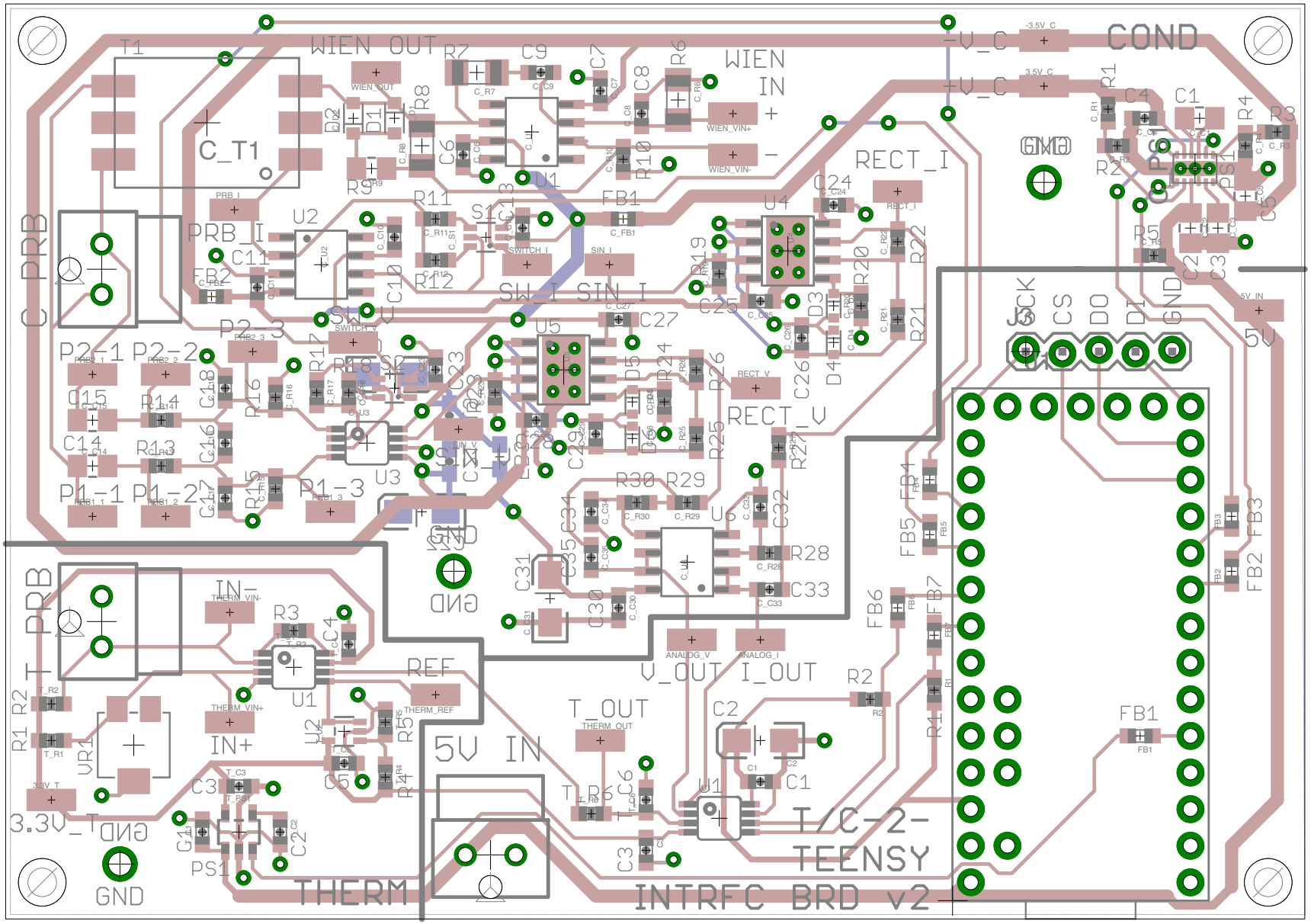

ThermCondRev
5/30/17 3:06 PM
Designed by: Irene Hu

Instrument v3.5

Type	Circuit	Part	Description	Part#	Need	Cost per - other	Link	Cost per - Digikey	Link	Total Cost
Capacitor	PhCtr B2	0402 0.1uF 6V ceramic X7R		C23/27-30/33/	10			0.09	https://www	0.9
Capacitor	Pwr B2	0603 0.1uF 25V ceramic X7R		C14/21_P	2			0.09	https://www	0.18
Capacitor	Pwr B1	0603 0.1uF 25V ceramic X7R		C6/9_P	2			0.09		0.18
Capacitor	PhCtr B2	0603 0.1uF 6V ceramic X7R			15			0.09	https://www	1.35
Capacitor	Pwr B2	0603 0.1uF 6V ceramic X7R		C19_P	1			0.09		0.09
Capacitor	LED B1	0603 0.1uF 6V ceramic X7R		C1_LED	1			0.09		0.09
Capacitor	PhCtr B1	0603 0.1uF 6V ceramic X7R		C1/3/6/8	4			0.09		0.36
Capacitor	Pwr B2	0603 0.47uF 16V ceramic X7R		C3-5_P	3			0.1	https://www	0.3
Capacitor	PhCtr B2	0603 10nF 16V ceramic X7R	[only needed to be 6V]	C15/20/21	3			0.13	https://www	0.39
Capacitor	PhCtr B1	0603 10nF1 6V ceramic X7R	[only needed to be 6V]	C5/10/11	3			0.13		0.39
Capacitor	PhCtr B2	0603 1uF 6V ceramic X7R		C45/48/51/53/	5			0.19	https://www	0.95
Capacitor	PhCtr B2	0805 10uF 6V ceramic X7R		C18/46/49/52	4			0.23	https://www	0.92
Capacitor	Pwr B2	0805 2.2uF 25V ceramic X7R		C15/20_P	2			0.18	https://www	0.36
Capacitor	Pwr B1	0805 2.2uF 25V ceramic X7R		C7/10_P	2			0.18		0.36
Capacitor	PhCtr B2	0805 2.2uF 6V ceramic X7R		C17/26/31/36/	6			0.14	https://www	0.84
Capacitor	Pwr B2	0805 2.2uF 6V ceramic X7R		C18_P	1			0.14		0.14
Capacitor	LED B1	0805 2.2uF 6V ceramic X7R		C2_LED	1			0.14		0.14
Capacitor	PhCtr B1	0805 2.2uF 6V ceramic X7R		C2/4/7/9/12	5			0.14		0.7
Capacitor	Pwr B2	1206 3.3uF 20V tantalum		C16_P	1			0.3	https://www	0.3
Capacitor	Pwr B1	1210 100uF 16V ceramic X5R		C11_P	1			1.71	https://www	1.71
Capacitor	Pwr B2	1411 100uF 6V tantalum		C2/17_P	2			0.86	https://www	1.72
Capacitor	Pwr B1	1411 100uF 6V tantalum		C12/13_P	4			0.86		3.44
Capacitor	Pwr B1	2917 100uF 25V tantalum		C8_P	1			2.25	https://www	2.25
Capacitor	PMT B1	5mm spacing 10 nF 450V ceramic disc		C8-10_PMT	3			0.74	https://www	2.22
Capacitor	PMT B1	7.5mm spacing 10 nF 2kV ceramic disc		CIN_PMT	1			0.56	https://www	0.56
Choke	Pwr B2	Wurth SL5 HC 744273501	high-current choke	L_IN	1			3.83	https://www	3.83
Connector	PMT B1	B14B/PCLF	et PMT socket for 9112B	XP1_PMT	1	40	http://www.e			40
Connector	PhCtr B2	header (F) 20x1		J1/2	2			1.36	https://www	2.72
Connector	PhCtr B2	header (F) AMPMODU 5-534206-5	straight 5x2, 30uin Au	J3/4	2			2.47	https://www	4.94
Connector	Pwr B2	header (M) 3x1		JP2-4_P	3					0
Connector	PhCtr B1	header (M) AMPMODU 86479-3	rt angle 5x2, 30uin Au	J5/6	2			3.74	https://www	7.48
Connector	PhCtr B2	header (M) Molex 0901310780	straight 20x2 unshrounded	Pi	1			4.21	http://www.c	4.21
Connector	Pwr B2	Molex Ultrafit 1722861302	Straight, 2-pos, 30 Au		1			1.19	https://www	1.19
Connector	Switch	Molex Ultrafit 1722861302	Straight, 2-pos, 30 Au	J1/2	2			1.19		2.38
Connector	Pwr B2	Molex Ultrafit 1723101302	Rt angle, 2-pos, 30 Au	PI_OUT	5			1.46	https://www	7.3
Connector	Pwr B2	shunt jumper		JP2-4_P	3			0.09	https://www	0.27
Connector	PhCtr B1	SMA edge launch 0.062" board			3			2.87	https://www	8.61
Connector	PhCtr B2	SMA straight		COMP_OUT	1			2.22	https://www	2.22
Connector	LED B1	Thorlabs LED socket		D1_LED	1	9.5	https://www			9.5
Diode	Pwr B2	NXP PMEG3020EP	Schottky 30V 2A low Vf	D4-7_P	4			0.41	https://www	1.64
Diode	Switch	ON MBRS2040LT3G	Schottky diode 40V 2A	D1/2	2			0.43	https://www	0.86

Instrument v3.5

Type	Circuit	Part	Description	Part#	Need	Cost per - other	Link	Cost per - Digikey	Link	Total Cost
Diode	Pwr B2	ON MM3Z12VT1G	12V Zener diode	D1-3_P	3			0.12	https://www	0.36
Ferrite Bead	PhCtr B2	TDK MMZ1608B221/301	0603 MMZ series	FB1	1			0.09	https://www	0.09
Ferrite Bead	PhCtr B2	TDK MPZ1608S221	0603 MPZ series	FB2/3/4/5	4			0.09	https://www	0.36
IC	PhCtr B1	AD ADCMP553BRMZ	Comparator	U3	1			4	https://www	4
IC	PhCtr B2	Fairchild FIN1002M5	Differential translator	U6	1			0.5	https://www	0.5
IC	PhCtr B2	Maxim MAX5483EUD	10k digital pot (varistor)	U4	1	0	https://www	2.46	https://www	0
IC	PhCtr B2	Micrel SY89831UMG	1:4 differential buffer	U5	1			5.97	https://www	5.97
IC	PhCtr B2	ON MC100EP016AMN	counter	U7, U10	2	1	https://www	15.9	https://www	2
IC	PhCtr B2	ON MC100EP01DT	LVPECL OR gate	U13	1	1	https://www	6.58	https://www	1
IC	PhCtr B2	ON MC100EP446MN	serializer	U8, U11	2	1	https://www	16.62	https://www	2
IC	PhCtr B2	ON MC100EPT23DT	dual LVPECL to LVTTL	U9, U12	2	1	https://www	7.49	https://www	2
IC	PhCtr B2	Silicon Labs SI53306-B-GM	1:4 translating buffer	U17	1			3.17	https://www	3.17
IC	PhCtr B2	TI CDCLVP1102RGT	translating 1:2 buffer	U14, 15, 16	3			5.22	https://www	15.66
IC	PhCtr B1	TI OPA695ID	Op Amp	U1, U2	2			3.72	https://www	7.44
Inductor	Pwr B1	0805 10uH 500mA		L2_P	1			0.12	https://www	0.12
Inductor	Pwr B1	0805 4.7uH 600mA		L3/4/5_P	3			0.29	https://www	0.87
Potentiometer	LED B1	Bournes 3352T-1-101LF	100 ohm pot wheel	VR1_LED	1			1.31	https://www	1.31
Potentiometer	Pwr B1	Bournes 3352T-1-103LF	10k pot wheel	VR1_P	1			1.31	https://www	1.31
Power	Pwr B1	Cui PQMC3-D12-D5-S	9-18V to +/-5V, 300mA	PS3	1			11.7	https://www	11.7
Power	Pwr B2	Recom R-78B3.3-1.5	5-18V to 3.3V, 1.5A	PS4	1			8.7	https://www	8.7
Power	Pwr B2	Recom R-78B5.0-1.5	5-18V to 5V, 1.5A	PS1	1			8.7	https://www	8.7
Power	Pwr B1	XP CA12N	HV supply -1250V	PS2	1			205	https://www	205
R Array	PhCtr B2	1206 0		JPN1/2/3/4	4			0.09	https://www	0.36
R Array	PhCtr B2	1206 130		RN1/2/5/6	4			0.09	https://www	0.36
R Array	PhCtr B2	1206 82		RN3/4/7/8	4			0.11	https://www	0.44
Resistor	PhCtr B1	0603 10		R1	1			0.09	https://www	0.09
Resistor	PMT B1	0603 100k 0.15W 0.1%		RL_PMT	1			0.72	https://www	0.72
Resistor	PhCtr B2	0603 10k		R27/53	2			0.15	https://www	0.3
Resistor	Pwr B2	0603 10k		R2/7/12_P	3			0.15		0.45
Resistor	Pwr B2	0603 170k		R4/9/14_P	3			0.09	https://www	0.27
Resistor	Pwr B2	0603 20k		R1/6/11_P	3			0.09	x	0.27
Resistor	PhCtr B2	0603 38k		R28/54	2			0.09	https://www	0.18
Resistor	PhCtr B1	0603 402		RF2	1			0.54	https://www	0.54
Resistor	Pwr B2	0603 40k		R5/10/15_P	3			0.09	https://www	0.27
Resistor	PhCtr B2	0603 50			55			0.09	https://www	4.95
Resistor	PhCtr B1	0603 50		R5/10/G1	3			0.09		0.27
Resistor	PMT B1	0603 50 1/8W 0.1%		RDAMP_PMT	1			2.04	https://www	2.04
Resistor	PhCtr B1	0603 500		RF1	1			0.09	x	0.09
Resistor	PhCtr B1	0603 57		RG2	1			0.3	https://www	0.3
Resistor	PhCtr B2	0603 5k		R73-80	8			0.09	https://www	0.72
Resistor	Pwr B2	0603 5k		R3/8/13_P	3			0.09		0.27

Instrument v3.5

Type	Circuit	Part	Description	Part#	Need	Cost per - other	Link	Cost per - Digikey	Link	Total Cost
Resistor	LED B1	0603 5k		RB_LED	1			0.09		0.09
Resistor	PhCtr B2	0603 60k		R13	1			0.09	https://www	0.09
Resistor	PhCtr B1	0603 75		R6/7/11/12	4			0.09	https://www	0.36
Resistor	PMT B1	0805 536k 1/8W 0.1%		R1-10_PMT	10			0.54	https://www	5.4
Resistor	Pwr B2	1206 0		JP/61_P	2			0.33	https://www	0.66
Resistor	Pwr B1	1206 0		JP5/6_P	2			0.33		0.66
Resistor	PMT B1	1206 10k 1/2W 5%		RIN_PMT	1			0.34	https://www	0.34
Resistor	PMT B1	1206 1M 1/4W 0.1%		RK_PMT	1			0.68	https://www	0.68
Resistor	PhCtr B1	1206 50		JP1-3	3			0.09	https://www	0.27
Switch	Switch	Standex-Meder PR126253001	reed switch 2.5A 25~30AT	S1	1			0.87	https://www	0.87
Test Point	Pwr B2	0805 SMD probe pad			7			0.23	https://www	1.61
Test Point	LED B1	0805 SMD probe pad		LED+, LED-, V	3			0.23		0.69
Test Point	PhCtr B1	0805 SMD probe pad		VREF	1			0.23		0.23
Test Point	Pwr B1	0805 SMD probe pad			3			0.23		0.69
Test Point	Pwr B2	Keystone compact 1.6mm black		GND	4			0.32	https://www	1.28
Test Point	Pwr B1	Keystone compact 1.6mm black		GND	3			0.32		0.96
Transistor	Pwr B2	ON MMBT3904L	BJT	Q2/4/6_P	3			0.09	https://www	0.27
Transistor	LED B1	ON MMBT3904L	BJT	Q1_LED	1			0.09		0.09
Transistor	Pwr B2	Vishay SI7157DP	P-Channel 20V MOSFET	Q1/3/5_P	3			1.3	https://www	3.9
										432.28

Cost of Components

			less HV converter, PMT socket
Board 1	Pwr B1	229.25	24.25
	PMT B1	51.96	11.96
	PhCtr B1	31.13	31.13
	LED B1	11.91	11.91
	Total	324.25	79.25
Board 2	Pwr B2	44.33	44.33
	PhCtr B2	59.59	59.59
	Total	103.92	103.92
Switch	Switch	4.11	4.11
Total sum		432.28	187.28

Excludes savings from bulk buying resistors and capacitors (--> ~1/8 or 1/9 of cost)

Conductivity / Temp

Type	Circuit	Part	Description	Part#	Need	Have	Order	Cost per - Digikey	Link	Total Cost
Capacitor	Temperature	0603 1uF 16V ceramic X7R		T_C1/3	2			0.09	https://www	0.18
Capacitor	Temperature	0603 10nF 16V ceramic X7R		T_C2/6	2			0.13	https://www	0.26
Capacitor	Temperature	0603 0.1uF 6.3V ceramic X7R		T_C4/5	2			0.09	https://www	0.18
Capacitor	Conductivity	0805 0.68uF 16V ceramic X7R		C_C1	1			0.17	http://www.c	0.17
Capacitor	Conductivity	0805 4.7uF 16V ceramic X7R		C_C2/3	5			0.22	http://www.c	1.1
Capacitor	Conductivity	0603 2.2uF 6.3V ceramic X7R		C_C4/5	2			0.22	https://www	0.44
Capacitor	Conductivity	0603 10nF 25V ceramic C0G/NP0 1%		C_C8/9	2			1.02	http://www.c	2.04
Capacitor	Conductivity	0805 1uF 10V X8L 5%		C_C14/15	2			0.32	http://www.c	0.64
Capacitor	Conductivity	0603 1nF 25V ceramic C0G/NP0 1%		C_C16	1			0.24	http://www.c	0.24
Capacitor	Conductivity	0603 100pF		C_C17/18	2			0.2		0.4
Capacitor	Conductivity	1206 10uF 10V 6.3V tantalum		C_C20/22	2			0.34	http://www.c	0.68
Capacitor	Conductivity	0603 47pF 10V ceramic C0G/NP0 5%		C_C26/29	2			0.1	http://www.c	0.2
Capacitor	Conductivity	1206 6.8uF 10V tantalum		C_C31	1			0.27	http://www.c	0.27
Capacitor	Conductivity	0603 0.1uF 6.3V ceramic X7R			16			0.09	https://www	1.44
Capacitor	General	0603 0.1uF 6.3V ceramic X7R		C1/3	2			0.09	https://www	0.18
Capacitor	General	1206 4.7uF 10V tantalum		C2	3			0.33	http://www.c	0.99
Connector	General	Molex Ultrafit 1722861302	Straight, 2-pos, 30 Au	J2	1			1.19	https://www	1.19
Connector	General	header (F) 5x1		J3	1					0
Connector	General	header (F) 14x1		J1	2			1.01	https://www	2.02
Connector	Temperature	Molex Ultrafit 1722861302	Straight, 2-pos, 30 Au	thermistor	1			1.19	https://www	1.19
Connector	Conductivity	Molex Ultrafit 1722861302	Straight, 2-pos, 30 Au	probe	1			1.19	https://www	1.19
Diode	Conductivity	1N4148W323	75V 150mA SOD323	D1/2	2			0.12	http://www.c	0.24
Diode	Conductivity	AVX SD0603S040S0R2	0603 40V 200mA Schottky	C_D3-6	4			0.4	http://www.c	1.6
IC	Temperature	TI INA333DGK	in amp	T_U1	1			3.76	http://www.c	3.76
IC	Temperature	TI OPA333DCK	op amp (buffer)	T_U2	1			2.21	https://www	2.21
IC	Conductivity	TI OPA211D	dual-supply op amp	C_U1/2	2			7.61	https://www	15.22
IC	Conductivity	TI TS5A4624	SPDT digital switch	C_S1/2	2			0.51	http://www.c	1.02
IC	Conductivity	AD AD8220ARMZ	in amp	C_U3	1			6.62	https://www	6.62
IC	Conductivity	TI OPA2211DDA	dual dual-supply op amp	C_U4/5	2			10.04	https://www	20.08
IC	Conductivity	TI TLV2462AID	dual single-supply op amp	C_U6	1			2.8	http://www.c	2.8
IC	General	Maxim MAX11135EUA	12-bit 4-ch I2C ADC 3.3V	C_U7	1			1.61	http://www.c	1.61
Potentiometer	Temperature	Bournes 3314G-1-204	200k 4mm trim pot	T_VR1	1			1.86	http://www.c	1.86
Power	Temperature	TI TPS73133DBV	3.3V LDO	T_PS1	1			0.86	https://www	0.86
Power	Conductivity	TI LM27762DSST	Dual regulated DC/DC	C_PS1	1			2.22	https://www	2.22
Resistor	General	0603 3k		R1/2	2			0.09		0.18
Resistor	Temperature	0603 150k 0.05%		T_R1/2	2			0.79	http://www.c	1.58
Resistor	Temperature	0603 34k 0.1%		T_R3	1			0.3	https://www	0.3
Resistor	Temperature	0603 20k		T_R4/5	2			0.09		0.18
Resistor	Temperature	0603 50		T_R6	1			0.09	https://www	0.09
Resistor	Conductivity	0603 549k 1%		C_R2	1			0.09	https://www	0.09
Resistor	Conductivity	0603 953k 1%		C_R1/3	2			0.09	https://www	0.18
Resistor	Conductivity	0603 511k 1%		C_R4	1			0.09	https://www	0.09
Resistor	Conductivity	0603 10k 0.05%		C_R10	1			0.67	http://www.c	0.67

Conductivity / Temp

Type	Circuit	Part	Description	Part#	Need	Have	Order	Cost per - Digikey	Link	Total Cost
Resistor	Conductivity	0603 10k		C_R5/15/16	3			0.09		0.27
Resistor	Conductivity	1206 15.8k 0.05%		C_R6/7	2			1.51	http://www.c	3.02
Resistor	Conductivity	1206 21k 0.05%		C_R8	1			1.51	http://www.c	1.51
Resistor	Conductivity	0805 200k 0.05%		C_R9	1			0.8	http://www.c	0.8
Resistor	Conductivity	0603 1.05k 0.1%		C_R11	1			0.3	https://www	0.3
Resistor	Conductivity	0603 4.02k 0.1%		C_R12	1			0.3	https://www	0.3
Resistor	Conductivity	0603 20k		C_R13/14/19/	4			0.09		0.36
Resistor	Conductivity	0603 15.8k 0.1%		C_R17	4			0.3	https://www	1.2
Resistor	Conductivity	0603 4.99k 0.1%		C_R18	1			0.3	https://www	0.3
Resistor	Conductivity	0603 1k 0.1%		C_R20-22,24-	6			0.3	https://www	1.8
Resistor	Conductivity	0603 16k 0.1%		C_R27-30	4			0.3	https://www	1.2
Test Point	General	0805 SMD probe pad		5V_IN	1			0.23	https://www	0.23
Test Point	Temperature	0805 SMD probe pad			5			0.23	https://www	1.15
Test Point	Conductivity	0805 SMD probe pad			20			0.23	https://www	4.6
Test Point	General	Keystone compact 1.6mm black		GND	7			0.32	https://www	2.24
Ferrite Bead	General	TDK MMZ1608B221/301	0603 MMZ series	FB1-7	6			0.09	https://www	0.54
Ferrite Bead	Conductivity	TDK MPZ1608S221	0603 MPZ series	C_FB1-3	3			0.09	https://www	0.27
Transformer	Conductivity	LM-NP-1001	Bournes line matching	C_T1	1			1.92	https://www	1.92
										100.47

Cost of Components

	Conductivity	77.49	
	Temperature	13.8	
	General	9.18	
	Total	100.47	

Excludes savings from bulk buying resistors and capacitors (--> ~1/8 or 1/9 of cost)

Appendix F

Summary of code

Code For RPi

LIBRARY

timehelp.c
a few timer helper functions
10/15/15 copied over functions from other files

GPIO.c
use for fast access to GPIO
sources: http://elinux.org/RPi_GPIO_Code_Samples#C, http://www.pieter-jan.com/node/15
9/3/15

interrupthandler.cpp
Handles takeover of ctrl-c to stop photon counter measurement
4/26/17

VRefPot.cpp
Library for interface with digital potentiometer controlling comparator reference for photon counter
Assumes a 10-bit pot (e.g. MAX5481 or MAX5483)
Calibration model is for varistor (MAX5483)
5/23/16 first draft
wiringPiSPI

teensy2pi.cpp
Raspberry Pi library to control thermistor and conductivity board via communication with Teensy
6/1/17 adapted from Teensy_spitest, Thermistor.cpp, and FlSensor.cpp
timehelp, wiringPiSPI, interrupthandler

PhCtr2.cpp
Library for interface with photon counter
For use with 16-bit counter (two chained counters, two serializers)
8/21/15 first adaptation for use on Raspberry Pi; 8/19/16 modified for 2 counters
GPIO

MCR.cpp
Library for interface with CM110 MCR for photon counting
This version uses USB-RS232 on Pi (not serial interface)
8/20/15 original MCR code adapted for pi; 9/30/15 for USB version; 8/22/16 for new boards
wiringSerial, GPIO

LED.cpp
Library for interface with LED for photon counting
8/18/15 first adaptation for use on Raspberry Pi
GPIO

FlSensor.cpp
Wrapper object that pulls together MCR, LED and PhCtr to take fluor measurements
11/3/15 first draft based on mainprogr.cpp
MCR, LED, PhCtr, timehelp, interrupthandler

EC.cpp
Puts together fluorescence sensor, Teensy and ADV objects for functions they do together
11/13/15 basic first draft; 7/8/17 major modification to add Teensy
MCR, LED, PhCtr, FlSensor, teensy2pi, ADV, timehelp, interrupthandler

ADV.cpp
Library for interface with ADV
9/29/15 basic first draft
wiringSerial, GPIO, timehelp, interrupthandler

THIRD PARTY LIBRARY

wiringSerial.c
Handle a serial port

wiringPiSPI.c
Simplified SPI access routines
EDITED BY IRENE 7/4/17

RUNNING CODE

mainprogr.cpp
Main program for running fluorescence sensor, Teensy (temperature/ conductivity), ADV, eddy correlation
Communication with user is via terminal
8/31/15: first conversion from Arduino code (version from 4/16/15) to C++. based on testLED (8/18), testMCR (8/24), testPhCtr (9/1); 11/9/15: combine with testADV4; 8/19/16: start modifying for 2 counters; 7/8/17: added Teensy code
MCR, LED, PhCtr, VRefPot, FlSensor, teensy2pi, ADV, EC, GPIO, timehelp, interrupthandler

Code for Teensy

LIBRARY

brd2teensy.cpp
Teensy library for interface with ADC121C027 for thermistor and MAX11613 ADC for conductivity circuits (ch 0 = I, ch 1 and 2 = V, ch 3 = T pwr/ref)
AIN0 conductivity current; AIN1 and AIN2 conductivity voltage; AIN3 temperature power for checking
Temperature is single channel of ADC121C027
Channel 18/19 i2c also hard coded
8/7/18 updated from brd2teensy_old for 2 ADCs
8/13/18 updated for rewired MAX11613
i2c_t3

THIRD PARTY LIBRARY

i2c_t3.cpp v9.2
Enhanced I2C library for Teensy 3.x & LC devices

t3spi.cpp
Teensy SPI library with slave mode support
EDITED BY IRENE 5/30/17

RUNNING CODE

tcBrdHandler.ino
Combines old tcBrdHandler, which handles SPI comm, with TestTCBoard
To Pi: uses t3spi library SPI_Slave_RXTX_1_0, interaces w/ Pi's teensy2pi object
To board: uses brd2teensy object
7/2/17
t3spi, brd2teensy

OLDER CODE NOT IN ACTIVE USE - RPi

LIBRARY

Thermistor.cpp
Library for interface with MAX6682 to read temperature from an NTC thermistor
4/20/17 first draft
wiringPiSPI, timehelp

Thermistor_p.cpp
Raspberry Pi library to talk to Teensy, which takes temperature measurements
Pi will do the calibration - only reads D value (as uint16) from Teensy
Both Pi and Teensy are Little Endian
Note: Pi's I2C speed at 1 MHz works. 100 KHz for some reason gives transmission errors
4/27/17
wiringPiSPI, GPIO, timehelp, pi2c, interrupthandler

Teensy_spitest.cpp
Raspberry Pi library to talk to Teensy
This version is just a test of SPI communication with Teensy
Meant to interface with Teensy's SPISlaveTest
5/26/17 adapted from VRefPot
GPIO, timehelp, wiringPiSPI

THIRD PARTY LIBRARY

pi2c.cpp
allows for easy communication to an Arduino from the Raspberry Pi over the I2C bus.
The default usage is for a Raspberry Pi Rev 1 - using the I2C "/dev/i2c-1". Rev0 and the "/dev/i2c-0" bus can be specfied though if needed.

RUNNING CODE

MCR_serial.cpp
Library for interface with CM110 MCR for photon counting
8/20/15 first adaptation for use on Raspberry Pi
wiringSerial, GPIO

testMCR_USB.cpp
based on testMCR.cpp from 8/24/15 (testing RS232-USB communications)
9/30/15
MCR_USB

testADV4.cpp
tests ADV controller communication
10/15/15 first draft
ADV, GPIO, timehelp

digitalPot.cpp
Quick program for sending digital pot some signals to determine "calibration" coefficients
For use with MAX5481 or 5483 (10 bit R divider)
5/16/16
wiringPiSPI

testThermistorCirc.cpp
Test out the thermistor circuitry and thermistor-to-digital convertor
For use with MAX6682
12/30/16
wiringPiSPI,timehelp
mainprogr_therm.cpp

Copy of my other "mainprogr" but only commands for the new thermistor
Communication with user is via terminal
4/20/17
Thermistor, timehelp

testi2c.cpp
Test i2c comm with Teensy. Pairs with TestI2C.ino written today
based on testThermistorCirc.cpp
RPi has 1.8k pull up resistors built into its I2C lines - no pullups nec
4/24/17
pi2c, timehelp

mainprogr_therm2.cpp
Copy of my other "mainprogr" but only commands for the new thermistor
This one uses the Thermistor_p class, which talks to the Teensy to get temperature measurements
Communication with user is via terminal
4/27/17
Thermistor_p, timehelp

testTeensySPI.cpp
test out the SPI comm with Teensy as slave
5/26/17
wiringPiSPI, Teensy_spitest, timehelp, GPIO

mainprogr_tc.cpp
Based on mainprogr_therm, which is also a copy of my other "mainprogr"
Only commands for thermistor/conductivity through Teensy
Uses the teensy2pi object to talk to Teensy; communication with user is via terminal
6/3/17
teensy2pi, timehelp, interrupthandler

OLDER CODE NOT IN ACTIVE USE - TEENSY

LIBRARY

Thermistor_t.cpp
Teensy library for interface with MAX6682 to read temperature from an NTC thermistor
Teensy's object will return only D. Calibration to be done by Pi
4/20/17 first draft; 4/23/17 modify for Teensy
spi4teensy3

Thermistor_t2.cpp
Teensy library for interface with ADS7042 ADC for thermistor circuit
Teensy's object will return only D. Calibration to be done by Pi
5/3/17 adapted from Thermistor_t
spi4teensy3

brd2teensy_old.cpp
Teensy library for interface with MAX11613 ADC for thermistor and conductivity circuits
AIN0 conductivity current; AIN1 conductivity voltage; AIN2 temperature -- hard coded
Channel 18/19 i2c also hard coded
5/28/17 adapted from Thermistor_t2
i2c_t3

THIRD PARTY LIBRARY

spi4teensy3.cpp
Faster SPI library optimized for the teensy 3.0 from pjrc.com

RUNNING CODE

TestThermistor.ino
Test out comunication with MAX6682 thermistor via Thermistor object
4/23/17
Thermistor_t
TestI2C.ino
Test I2C communications as slave to RPi
4/24/17
i2c_t3

ThermistorHandler.ino
Teensy as interface between thermistor and RPi
Communicates to thermistor over SPI and Pi over I2C
4/26/17
Thermistor_t, i2c_t3

TestThermistor2.ino
Test out comunication with ADS7042 and thermistor circuit via Thermistor object
5/2/17
Thermistor_t2

TestTCBoard.ino
Test out communication with temperature and conductivity board or via brd2teensy object
5/30/17

tcBrdHandler_nobrd.ino
based on the SPI test, which is modified from sample code
for t3spi library SPI_Slave_RXTX_1_0
made to interface with Rasperry Pi's teensy2pi object
6/2/17
t3spi

SUMMARY OF MATlAB FUNCTIONS AND SELECTION OF MATLAB SCRIPTS

LOAD FUNCTIONS

loadDPOdata
function to load data from DPO given filename
7/2/13

getAsThousandths
For processing the timestamps from DPO autosave
converts the text string (time part only) into thousandths of seconds
10/17/13

processFFtimestamp
function to process a single line from FastFrame timestamp file
8/6/13

procFastFrame
function to load and process FastFrame timestamp data from DPO
uses procTimestamp function to read and process individual lines
8/6/13

procFFMultFiles
DPO FastFrame timestamp processing to calc photon rate from multiple files
Number of events in files do not need to match; num events is output in array
8/6/13, mod 8/22/13

loadSFdata
function to load data from PE spectrofluorometer (converted to csv by spekwin) (single file with multiple series)
4/29/13 modified 9/12/13

loadSSdata
function to load data from spectrasuite (multiple files)
4/16/13

loadSS_HSacq
function to load "High speed acquisition" data from spectrasuite (multiple files with timestamps)
9/1/14

loadPhScan
function to load scan data from fluorescence sensor for unmodulated data
goes with 'fsn' command
based on Arduino code written as of 7/31/14
7/31/14

loadPhScan_wMod
function to load scan data from fluorescence sensor for modulated data
goes with 'fsm' command
based on Arduino code written as of 9/29/14
9/29/14

loadSeries
function to load time series from EC sensor
this is a more flexible version of loadPhSeries and loadPhSeries_wMod that optionally allows either fluorescence or Teensy data
goes with 'r' command
should also be compatible with fr, tr, etc
7/10/17

loadMeas
function to load "measure in place" measurements from Pi, alongside some variable entered through the Pi interface
goes with 'c' command, based on Pi code as of 8/10/17
8/10/17

loadDMM
function to load arbitrary number of time series from Keithley DMM as output by the KickStart program
3/7/18

loadECdat
function to load velocity and concentration data, filter out velocity outliers, and combine into one structure / data file
goes with 'e' command, based on RPi code written as of 7/10/17
7/11/17

loadADVdat2
function to load velocity and associated data, and filter out outliers
input file structure corresponds to Nortek software output
input file name and name-value pairs; can handle bursts
1/31/17 adapted from 1, modified 4/13/17

loadADVpchk
function to load ADV's probe check data as it comes from Nortek software
input file structure corresponds to Nortek software output
can handle burst mode
2/1/17, mod 4/13/17

loadADVsys
function to load ADV's system data (.sen) as it comes from Nortek software
input file structure corresponds to Nortek software output
3/27/17

ANALLYZE FUNCTIONS

countPeaks
function to count number of peaks ("photons") in DPO trace
scans linearly through data and counts # pulses w/ magn > |threshhold|
7/16/13

countPeaksMultFiles2
DPO processing to count photon peaks in multiple files
Also checks if record length and sample interval are same for all files; if not, prints an error to the screen
Output includes 3D array with all loaded trace data
9/19/13 adapted from other version

findMax
function to find the peak value (presumably a photon) in DPO data
7/2/13

findNoise
function to determine noise in DPO trace
noise is defined as standard deviation of the signal in the second half of the first div + entire second div. trace cannot have a photon in this region
7/2/13. Mod 7/10/13 and 7/1/16 for noise efinitions

findPulseDur
function to determine duration of a pulse in DPO trace
scans to both sides of specified peak to find when voltage crosses threshhold
7/2/13, mod 4/8/14

charPhotons
DPO processing to characterize photons using other functions
7/10/13

binData
function to bin data from spectrasuite
4/18/13

charUSBpeaks
processes USB4000 data to get stats on a single peak
makes lots of assumptions. Wrote this to get info on what USB4000 sees of MCR output
10/10/16

calcStats
function to calculate relevant stats from fluorescence data
stats: 1) sig peak; 2) wavelength of sig peak; 3) integrated sig; 4) exc peak; 5) wavelength of exc peak; 6) dark avg; 7) dark noise; 8) SNR; 9) exc to em ratio; (optional) 10) normalized sig peak; 11) normalized integrated sig
4/19/13, mod 4/29/13

mapSpectrums
creates a wavelength spectrum of ratios of data 2 to data 1
use to compare data from 2 instruments with different spectral responses, mapping runs from startWL to endWL in wavelength steps of stepsize
if data do not have datapoints for specified target wavelengths, uses AVERAGE of surrounding datapoints (a range of stepsize size, centerednaround target %wavelength).
no option right now to not average out datapoints, so pick sufficiently small stepsize to avoid schmearing
2/2/15

calc_t90
Function to calculate 90% response time from a time series
Input data structure should contain one transition only
2/4/18

avgDown
function to average down velocity and concentration data
1/10/16, 3/23/16, 7/16/17

interpOutNaNs
function to replace bad values in ADV data (NaNs) with linearly interpolated values
if first or last datapoints are NaN, make them equal to the first or last non-NaN value (not ideal, but keeps arrays same size)
only interps out bad data for the beam specified (to allow, as per Goring and Nikora 2002, each component to be despiked separately)
can be used for data replacement stage of despiking (detect and replace)
1/19/16, updated 4/6/17, 5/11/18

replaceBadDat
function to replace NaNs in ADV data (likely removed for bad SNR/corr)
values are replaced with linear interpolation
warning vector lists stretches with too many bad datapoints in a row
1/19/16?, updated 3/27/17

replaceBadDat_oneCol
similar to replaceBadDat but for an arbitrary siingle column only
basically it's interpOutNaNs but with extra warning functionality
values are replaced with linear interpolation
warning vector lists stretches with too many bad datapoints in a row
5/11/18

despike
function to despike ADV data using acceleration threshold method as described in Goring & Nikora 2002
values are replaced with linear interpolation
IH 1/20/16

doubleRot
function to do a double rotation
first identifies angles to make mean y and z velocities 0 (in that order)m=, then rotates all ADV data by these angles
based on Wilczak 2001
1/29/16

pfRot
function to do a planar fit rotation
first averages down into runs, then do planar fit to identify rotation, then rotate all ADV data by these angles
based on Wilczak 2001
1/31/16

rotByAngle
function to rotate by given pitch and roll angles (measured by ADV)
pitch is rotation around y axis; roll is around x axis
based on Wilczak 2001
3/27/17

calcFluxAll
calculate concentration, heat and/or salinity flux for each flux window
also outputs covariance and cumulative flux for each data point
7/22/17, updated 4/19/18, 9/6/18

calcFluxAll_NaNsOK
calculate concentration, heat and/or salinity flux for each flux window
also outputs covariance and cumulative flux for each data point
NaNs must be in the z / measurand columns - then they're excluded in flux and detrending calcs for only that measurand. no NaNs in time, they cause issues with the timestamp
10/2/18

calcCoSpectraAll_RM
calculate cospectra and cumulative cospectra for each flux window
uses running mean detrending
calculates for fluorescence, temperature and/or conductivity data, depending on what is present
8/1/17, modified 4/19/18

calcCoSpectraAll_LD
calculate cospectra and cumulative cospectra for each flux window
uses linear detrending
calculates for fluorescence, temperature and/or conductivity data, depending on what is present
9/27/18

PLOT FUNCTIONS

plotData
function to plot spectroscopic data
4/16/13, mod4/29/13

plotData_ErrorBars
function to plot spectroscopic data
this one includes error bars
8/1/14

plotDualData2
function to plot spectral scan data from different instruments (in different arrays) on 2 subplots
order that data arrays are given must match order that titles are given
data arrays must have same data runs in same order
series names will prefix data runs in legend
keep to <7 runs to maintain same color coding
4/30/13, modified periodically (code for colors and adjusting to changing matlab color schematics, last update 9/9/15)

plotCorrCloud
function to plot two data series against each other (check correlation), eg fluorescence vs conductivity
accepts name-value pairs for various options
8/22/17

plotSeries
function to plot a single data component of a time series (timestamp and data in same array)
eg one of the measurands or one of the velocities in an EC series
also has option to plot 2 components on two axes
accepts name-value pairs for various options
7/23/17, 5/12/18 add bar graph functionality, periodic updates for graph sizes

plotSeries_Subplots
function to plot multiple series together as subplots
accepts name-value pairs for various options
8/2/17, 5/12/18 add bar graph functionality, periodic updates for graph sizes

plotSeriesRatios
function to plot all series in yarrays, shifted to 0 base (default shift is min) and scaled to their range (max - min)
accepts name-value pairs for various options
7/29/17, 2/4/18 can print unscaled (original), periodic updates for graph sizes

SCRIPT-LEVEL FUNCTIONS AND SCRIPT EXAMPLES

script_20160705_twoChs
script to analyze pulses to test new PMT
this one analyzes various runs from PMT and 1 amp
7/5/16

script_20160707_pulseChar
script to analyze pulses to test new PMT
this one analyzes various runs from PMT and 2 amps
7/5/16

script_20180312_threeCals
script to compare calibrations from ph ctr, USB4000, and PE LS50B, EMISSION ONLY
3/12/18

script_20180313_threespectra
script to plot humic acid spectrums from different instruments
THEY ALL HAVE TO BE IN ORDER
3/13/18

script_20180715_scans
plot modulated scans before and after ec run
4/15/18: have a folder with many scans and want to look at them all
filename format: yyyymmdd_*scan.txt where * is start or end (there are some startscan2's, also)

script_20180323_conductivities
general script to analyze conductivity curves with different gains
must have a set of files for each 'run': conductance-conductivity relationships done with resistors, and measurements done with the probes at separately measured conductivities - named 'filename_resistors' and 'filename_probes'
file is "alternate" output of c command where fields are I/V avg, I/V stdev, I avg, V avg
if it has a '11' setting, that's ignored
menu at the top to specify which parts of code to run, but will need to set outliers further down
some sections MUST be run before others

```
loadData_Rs ___ calcFits_Rs, plotCurrent_Rs, plotVoltage_Rs, plotGs_Rs
                      \___ plotFits_Rs
                 _____\___ calcFits_CC ___ plotMappedC_Ps, plotCC
            /
loadData_Ps ___ calcFits_Ps, plotCurrent_Ps, plotVoltage_Ps, plotGs_Ps
                      \___ plotFits_Ps
```

'exclusions' will 'kick out' current and voltage values that exceed the threshold (assumption that they're not reliable because I maxed some chip or another out). They're called exclusions for historical reasons; actually I decided to fit to them and process separately, mostly because I'm so desperate to try to get a good cell constant curve
10/20/17

script_20180201_makevid
make a movie out of scrolling through time series
2/1/18

script_20180912_calibr
linear calibration using data points measured with 'c' command
F, T and C - all metrics in file must be numeric
gets curve fit and prints it in legend
9/12/18

script_20180320_DMM
look at DMM data for power meas
ch 1: V. ch 2: current.
3/20/18

script_20180812_teensyTiming
% read and plot T/C timing data from Teensy
% IH 8/12/18

script_20180719_noiseAnal_2
look at and compare the noise in C/T series (plot, output to file)
7/10/18 to 7/19
7/14 file prints out C and T stats; 7/19 prints only T, looks at FFTs, plots a high-freq time series

script_20180912_timeseries
plot some time series from EC runs and do some analysis, some sections simlar to EC scripts
e.g. mean removal and plotting different zooms with different mean removals and filters
includes psds
8/29/18
script_20180409_holderinterf
distance - interference test: loads/calcs/plots separation vs ADV amplitude/correlations
3/2/18

ADVDataStats
function to analyze ADV data - .dat and .pck files
loads, filters, return some key stats for multiple files; plots probe checks
input file structure corresponds to Nortek output
3/28/17

analyzeADVdat
function to analyze ADV data - .dat and .pck files
input file name and name-value pairs; can handle bursts
filters, analyzes, prints out data and plots various things
input file structure corresponds to Nortek software output
2/1/17, updated 4/13/17 4/18

script_20181011_ADV
make a graph of stats (e.g. stdv of velocity) vs pchk dist
10/11/18 - smushes the different velocity ranges together into their avg, EC is also just for the whole run
Previous 10/2 version also loads data differently, allows for despiking, and calcs and plots PSDs

script_20180928_triEC
Script for EC implementation of 1 run
use avg-removeNaNs-despike
This is the latest iteration of many EC scripts - includes several versions of PSDs (different detrends), filtering and time shift options, temperature compensation, file output

script_20181001_triEC
EC with excursion removal, i.e. first need to ID stationary regions bylooking at a RM
All EC data processing, including filtering and output to file
10/1/18, 10/7/18

script_20181007_fluxscatterplot
process and plot the flux data points i output into a csv file using the TriEC script
10/7/18
Previous 9/19/18 breaks it out by 2 parameters

script_20180930_allpsds
compare PSDs between different runs / sections of runs
based on tri EC scripts; but separates out into time regions
9/30/18

script_20181011_psds
compare PSDs for one run, 3 concs + z velocity normalized and on the same graph
several mean removal / detrend options
10/11/18

script_20181012_excursionpsds
psds of excursion-removed stuff
all three concs + z velocity on same graph, normalized
several mean removal / detrend options
10/12/18

script_20181012_plotRM
plot frequency response for my moving average filters
this took a lot of googling!
10/12/18

TRANSFORMER SIMULATION

gainLoopSim4
conductivity circuit simulation: transformer unidealities + coupling capacitors and voltage amp input filters
plot I_primary / V_probe vs G_thermistor (linearity of result)
also plot V_probe / V_primary vs G_thermistor (voltage range)
also plot I_primary / V_primary vs G_thermistor (current range)
5/15/17

gainLoopSim4_R2
conductivity circuit simulation: transformer unidealities + coupling capacitors and voltage amp input filters

plot I_primary / V_probe vs R_thermistor (expected output vs RESISTANCE - will be nonlinear)
also plot V_probe / V_primary vs R_thermistor (voltage range)
also plot I_primary / V_primary vs R_thermistor (current range)
7/14/17

gainLoopSim5
conductivity circuit simulation: transformer unidealities + coupling capacitors and voltage amp input filters + amplifier behavior for both current and voltage
so this is looking at actual expected, amplified outputs (before filter)
plot V_current / V_voltage vs G_thermistor (linearity of result)
also plot V_voltage / V_primary vs G_thermistor (voltage range)
also plot V_current / V_primary vs G_thermistor (current range)
6/29/17

gainLoopSim6
conductivity circuit simulation: transformer unidealities + coupling capacitors and voltage amp input filters + amplifier behavior for both current and voltage, with inclusion of small circuit elements around voltage circuitry amplifier
so this is looking at actual expected, amplified outputs (before filter)
plot V_current / V_voltage vs G_thermistor (linearity of result)
also plot V_voltage / V_primary vs G_thermistor (voltage range)
also plot I_current / V_primary vs G_thermistor (current range)
6/30/17

DEPRECATED FUNCTIONS – KEPT FOR BACKWARD COMPATIBILITY

loadPhData
function to load data from photon counter w/ counts (avg, stdev, max, min) vs some variable - eg time since turnon (testDrift), datapt time (dpTimes)
based on Arduino code written as of 8/7/14
8/8/14

loadPhSeries
function to load time series from fluorescence sensor for unmodulated data
goes with 'frn' command
based on Arduino code written as of 8/25/14
8/26/14

loadPhSeries_wMod
function to load time series from fluorescence sensor for modulated data
goes with 'frm' command
based on Arduino code written as of 10/1/14
10/1/14

loadECdat_noMod
function to load velocity and photon counter data, filter out velocity outliers, and combine into one structure / data file
this is for non-modulated photon counter data
goes with 'en' command
based on RPi code written as of 1/10/16
1/10/16, 3/23/16, 3/29/17

loadECdat_wMod
function to load velocity and photon counter data, filter out velocity outliers, and combine into one structure / data file
this is for modulated photon counter data
goes with 'em' command
based on RPi code written as of 1/10/16
1/10/16, 3/24/16, 3/29/17

loadADVdat
function to load velocity data only and filter out outliers
input file structure corresponds to Nortek software output
IH 5/7/16

countPeaksMultFiles
DPO processing to count photon peaks in multiple files
Also checks if record length and sample interval are same for all files; if not, prints an error to the screen
7/16/13, updated 7/30/13

interpOutNaNs_cir
function to replace bad values in ADV data (NaNs) with linearly interpolated
differs from non_circ version in that, if first or last datapoints are NaN, uses a circular boundary condition to wrap around
only interps out bad data for the beam specified (to allow, as per Goring and Nikora 2002, each component to be despiked separately)
can be used for data replacement stage of despiking (detect and replace)
1/19/16, updated 3/27/17

doubleRot_dan
function to do a double rotation
this one does it the way Dan McGinnis does- his use of x/y plane magnitude is equivalent to the first rotation, but for the second, use the average, magnitude (x after first rotation) instead of the x for each data point
1/29/16

doubleRot2
function to do a double rotation
first identifies angles to make mean z and y velocities 0 (in that order), then rotates all ADV data by these angles
based on Wilczak 2001
1/29/16

pfRot_exclLast
function to do a planar fit rotation
first averages down into runs, then do planar fit to identify rotation, then rotate all ADV data by these angles
based on Wilczak 2001
this one excludes the last run - to see if that's the source of nonzero
2/1/16

calcFlux
calculate flux for each flux window given EC data table with both concentration and velocity
also outputs covariance and cumulative flux for each data point
IH 2/4/16

calcFlux_blockMean [BLOCK MEAN VERSION]
calculate flux for each flux window given EC data table with both concentration and velocity
also outputs covariance and cumulative flux for each data point
for this version, running mean is actually a block mean
2/4/16, 2/7 renamed and deprecated

calcCoSpectra
calculate cospectra and cumulative cospectra for each flux window, given EC data table with both concentration and velocity
uses running mean detrending
3/9/16

plotDualData
function to plot spectral scan data from different instruments (in different arrays) on 2 subplots
order that data arrays is given must match order that titles are given
data arrays must have same data runs in same order
design choices to reduce clutter when many runs:
same runs in same order req allows same legend to be used
plot on SUBPLOTS, as opposed to same graph
7/29/13

plotECADVDat
function to plot ADV data component of an EC data time series
plots one beam only, as specified
1/14/16

plotECFluorDat
function to plot fluorescent data component of an EC data time series
1/14/16

plotADVDat
function to plot ADV velocity data - 3 axes together via subplots
input data format corresponds to loaded data from either EC sensor or Nortek file
1/14/16; mod 4/18/17

plotCorrelations
function to plot ADV correlation data - 3 axes together via subplots
input data format corresponds to Nortek data as loaded by loadADVdat2
2/4/17, mod 4/18/1

plotSNRs
function to plot ADV SNR data - 3 axes together via subplots
input data format corresponds to Nortek data as loaded by loadADVdat2
2/4/17, mod 4/18/17

script_EXAMPLE_1file
Example script for EC implementation of 1 run
use avg-removeNaNs-despike
this particular script combines two files to create 1 run
last updated 4/7/17

script_EXAMPLE_2files
Example script for EC implementation of 2 runs that are compared together
use avg-removeNaNs-despike
last updated 4/6/17

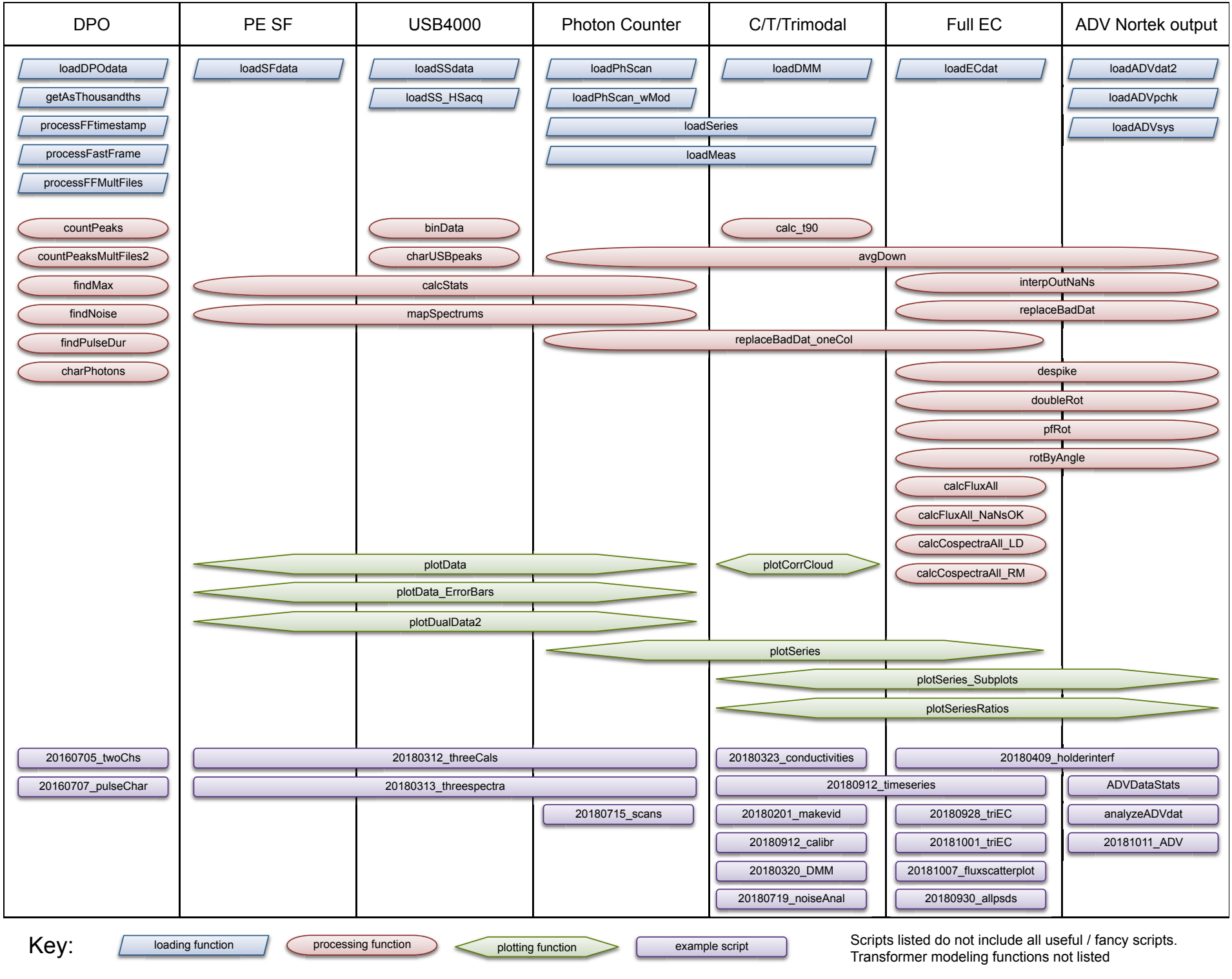
DPO
PE SF
USB4000
Photon Counter
C/T/Trimodal
Full EC
ADV Nortek output
loadDPOdata
getAsThousandths
processFFtimestamp
processFastFrame
processFFMultFiles
loadSFdata
loadSSdata
loadSS_HSacq
loadPhScan
loadPhScan_wMod
loadSeries
loadMeas
loadDMM
loadECdat
loadADVdat2
loadADVpchk
loadADVsys
countPeaks
countPeaksMultFiles2
findMax
findNoise
findPulseDur
charPhotons
binData
charUSBpeaks
calc_t90
avgDown
calcStats
mapSpectrums
replaceBadDat_oneCol
interpOutNaNs
replaceBadDat
despike
doubleRot
pfRot
rotByAngle
calcFluxAll
calcFluxAll_NaNsOK
calcCospectraAll_LD
calcCospectraAll_RM
plotData
plotData_ErrorBars
plotDualData2
plotCorrCloud
plotSeries
plotSeries_Subplots
plotSeriesRatios
20160705_twoChs
20160707_pulseChar
20180312_threeCals
20180313_threespectra
20180715_scans
20180323_conductivities
20180912_timeseries
20180201_makevid
20180912_calibr
20180320_DMM
20180719_noiseAnal
20180409_holderinterf
20180928_triEC
20181001_triEC
20181007_fluxscatterplot
20180930_allpsds
ADVDataStats
analyzeADVdat
20181011_ADV
Key:
loading function
processing function
plotting function
example script
Scripts listed do not include all useful / fancy scripts.
Transformer modeling functions not listed

Appendix G

Diagrams

The following diagrams are included:

- Block diagram and layout of lid and interior of housing (does not include temperature / conductivity)
- AutoCAD rendering for optical fiber holder
- AutoCAD rendering for benthic lander
- Drawn specifications for monochromator-to-PMT connector, optical-fiber-to-ADV connector, ADV holder, ADV sensing volume alignment piece, and chemical release plate and lid
- Flow net drafts for different designs of chemical release plate

Power estimates (ballpark):

- Photon counting board, PMT: spec sheet-based estimates 7/20/16, measurements 7/21/16; converter efficiency included in HV and +/-5V
- Relays: (5V relays) estimates 7/21/16
- LED: measurements 1/1/14 with DC/DC powered at ~12V
- MCR: measurements 6/12/16
- Pi: from website

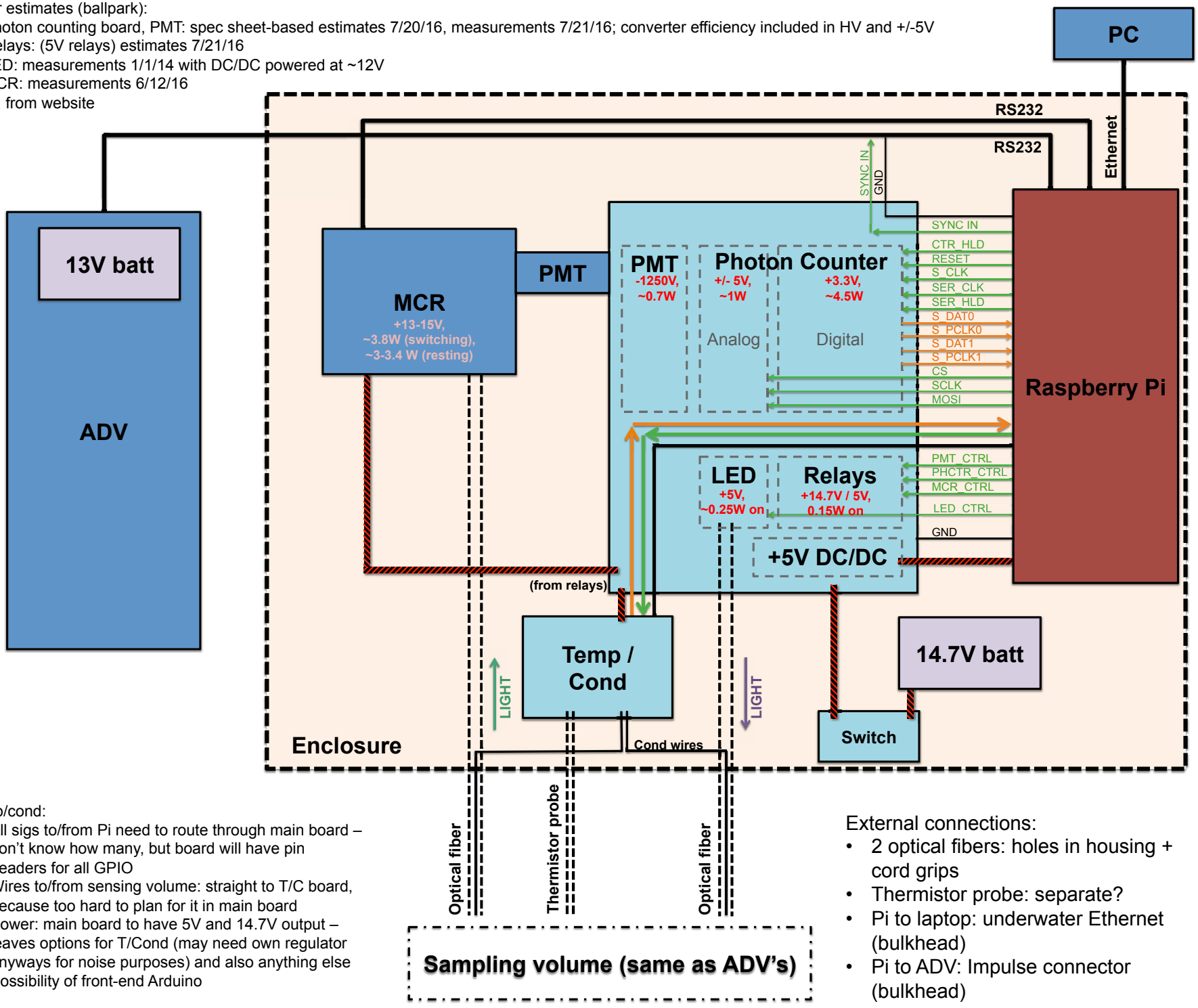

Temp/cond:

- All sigs to/from Pi need to route through main board – don't know how many, but board will have pin headers for all GPIO
- Wires to/from sensing volume: straight to T/C board, because too hard to plan for it in main board
- Power: main board to have 5V and 14.7V output – leaves options for T/Cond (may need own regulator anyways for noise purposes) and also anything else
- Possibility of front-end Arduino

External connections:

- 2 optical fibers: holes in housing + cord grips
- Thermistor probe: separate?
- Pi to laptop: underwater Ethernet (bulkhead)
- Pi to ADV: Impulse connector (bulkhead)

Top view

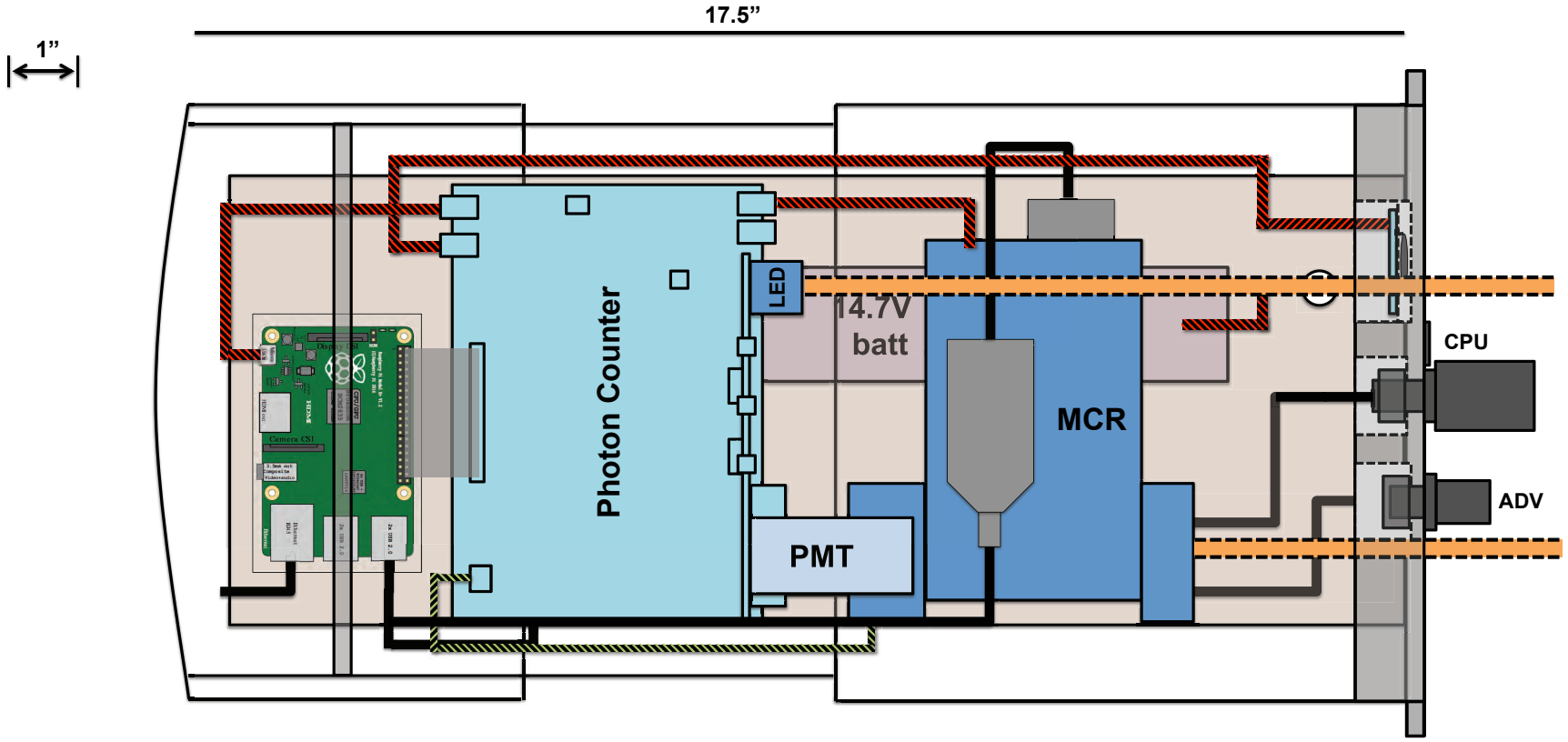

Design notes:

- All lines shown are inner diameters (8.625” for couplings, ~7.98” for pipe)
- Cord grips (external connection for optical fibers) not shown
- Housing is based on an 8” plug (= pipe + cap) cemented to an 8” coupling
- ¼” thick PVC disc to hold components in place, diam is ID of pipe
- Custom cap from 1” PVC
    - “Indent” into cap for all external connections
    - 3/16” or ¼” O-ring

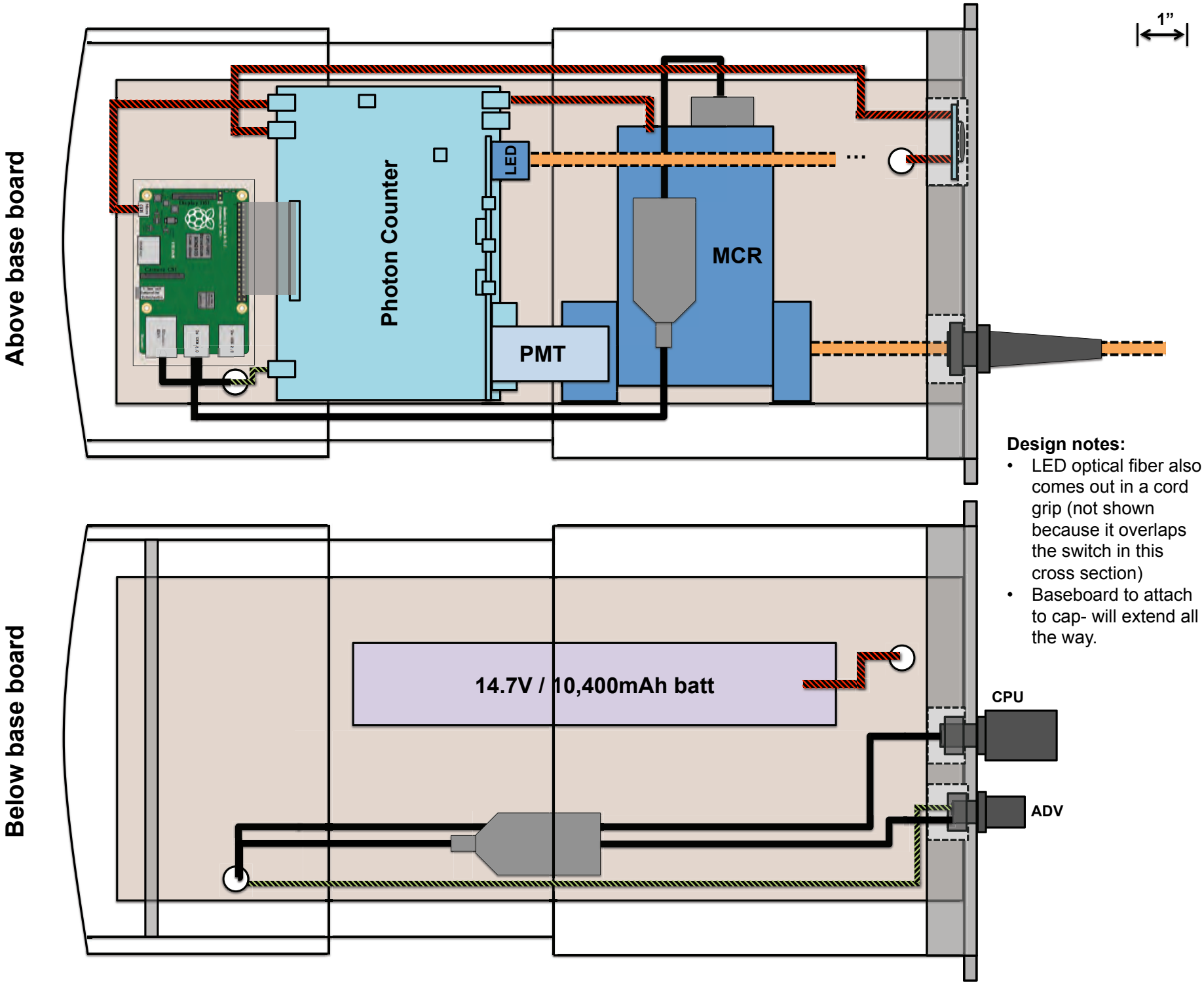
Above base board
Below base board
1”
Photon Counter
LED
MCR
PMT
14.7V / 10,400mAh batt
CPU
ADV
Design notes:
• LED optical fiber also comes out in a cord grip (not shown because it overlaps the switch in this cross section)
• Baseboard to attach to cap- will extend all the way.

Front view

1”

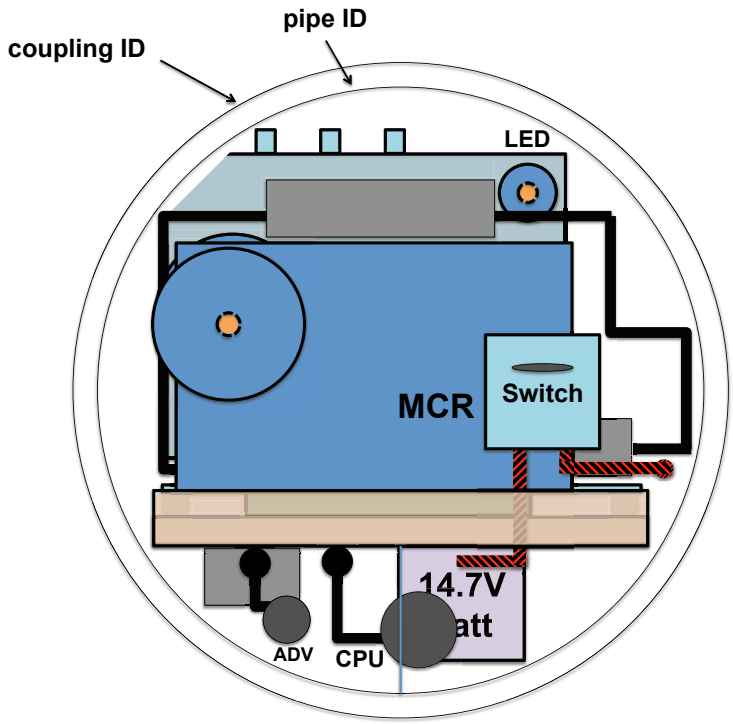

Past the MCR…

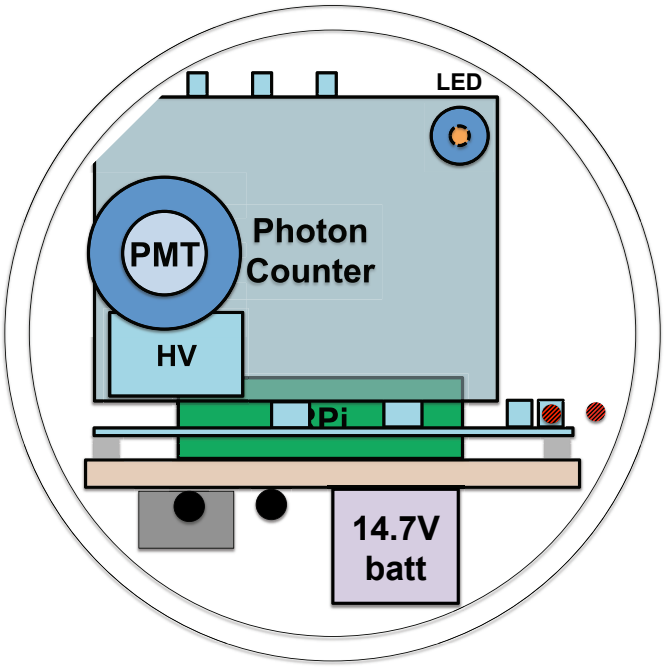

Design notes:

- Base: ¾” PVC, depressed 3/8” second half so MCR is elevated
- ¼” standoffs for PCB
- Photon counter board is clipped by 0.75” x 0.75” triangle on corner
- Measured height of baseboard from pipe ID: 1.95”

Side view

1”

Design notes:

- MCR optical fiber also comes out in a cord grip (not shown because it overlaps the switch in this cross section)
- ¼” thick PVC disc to hold components in place, at narrower section of housing

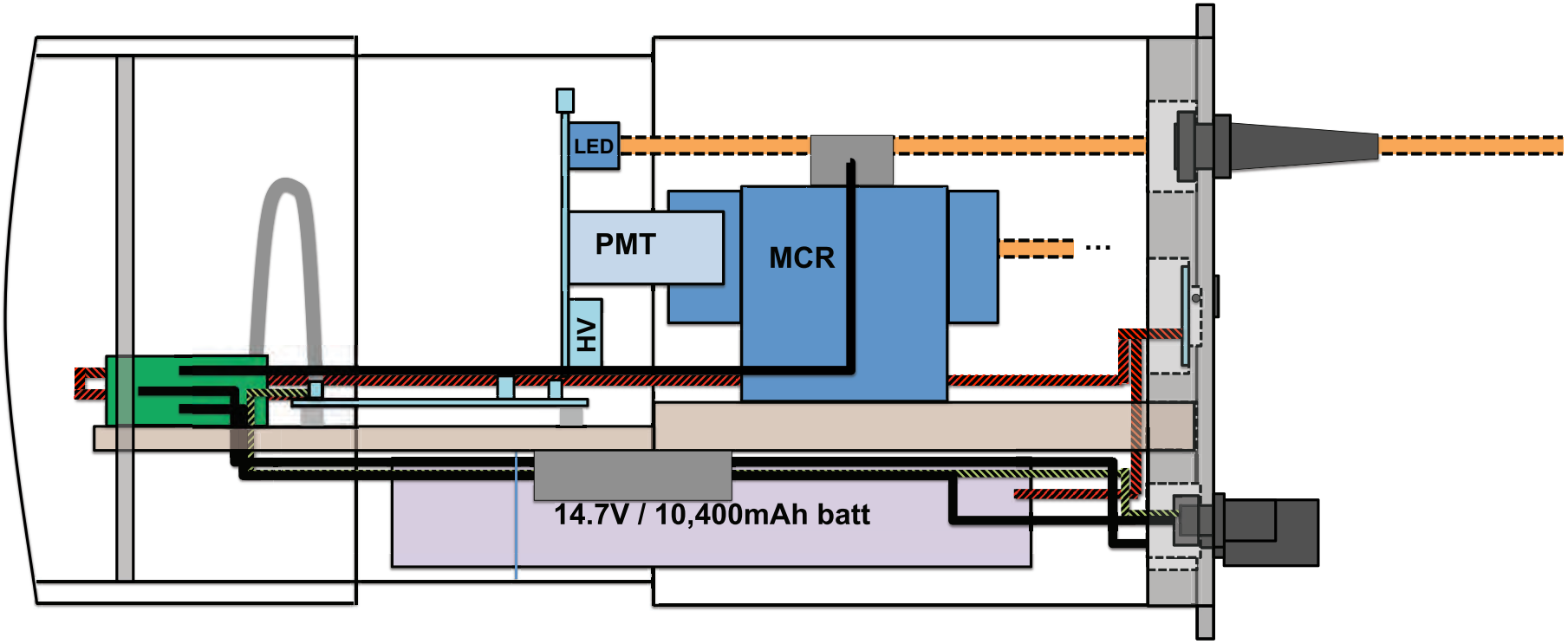

17.5”

Front face, viewed from outside

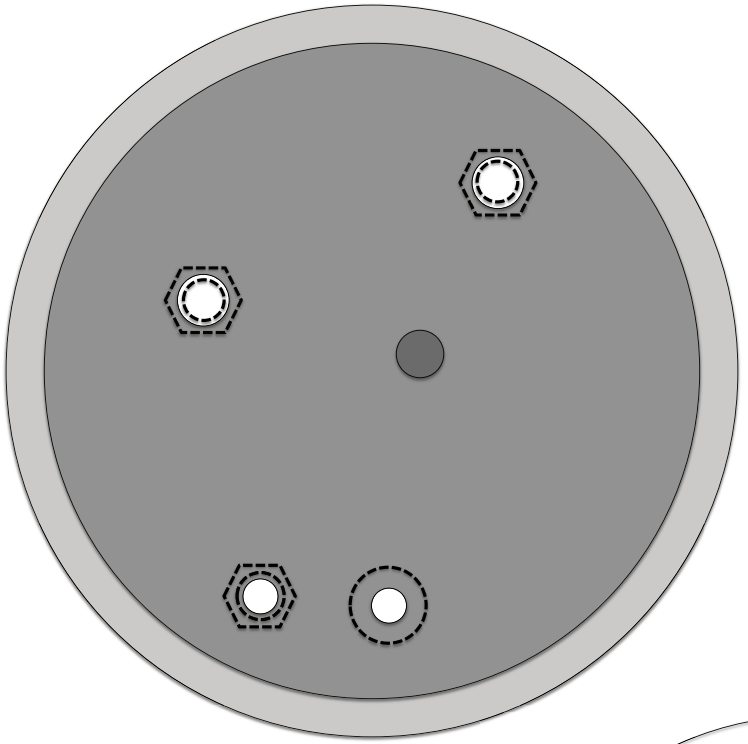

Front face, viewed from inside

1”

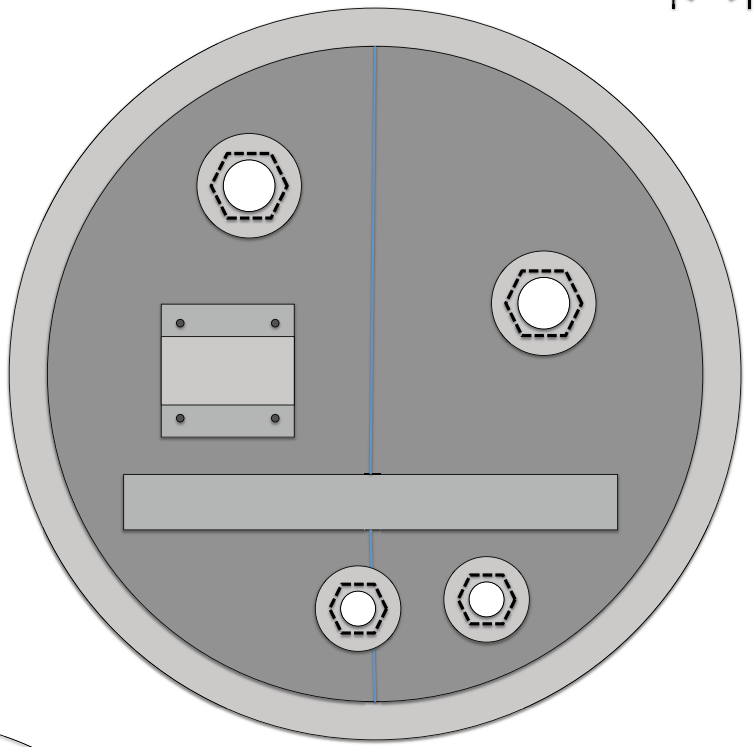

Approx layout of what’s inside

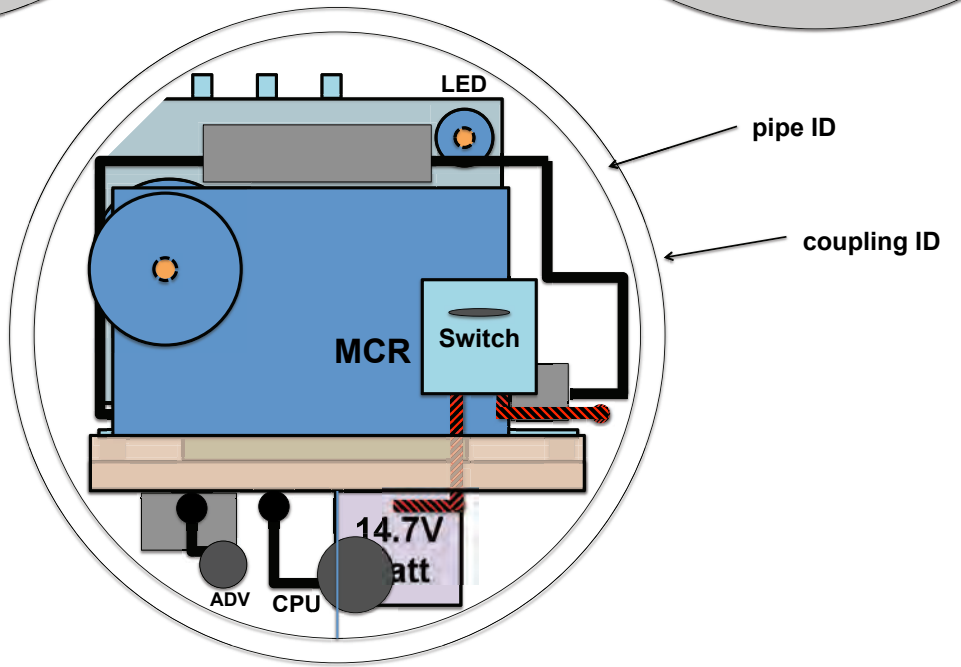

Viewed from outside, but showing all indents that are on the inside

1”

Overall dimension
- Full circle Ø9.625”: allows 0.5” “rim”
- Indent around rim
  - Create smaller inner circle Ø8.625” (OD of 8” pipe, should fit in coupling)
  - Depth 0.75”: gives rim depth 0.25”
- O-ring groove: around the smaller circle
  - For 3/16” thick O-ring (ID 8.475”, OD 8.895”), or ¼” O-ring (ID 8.475”, OD 9.025”)

Cord grips:
- Through-hole: Ø0.68”, or drill 9/16” and tap for 3/8”-18 NPT
- Indent:
  - Ø1.375” to accommodate 15/16” socket wrench (OD Ø1.25”) to tighten 0.94”-across hex nut (1” corner-to-corner)
  - Depth 0.75”: 0.25” lid thickness + 0.26” thick hex nut to take up 0.59” thread length

Slit for baseboard
- Rectangle 0.73” x 6.5” (for 0.73” x 6.5” board; can sand down board if it doesn’t fit)
- Position ~2.27” from bottom of INNER (Ø8.625”) circle (1.95” measured from other diagrams + 0.3225” from ID of pipe to ID of coupling,– measures 5.64” from top of inner circle
- Depth: ¾”

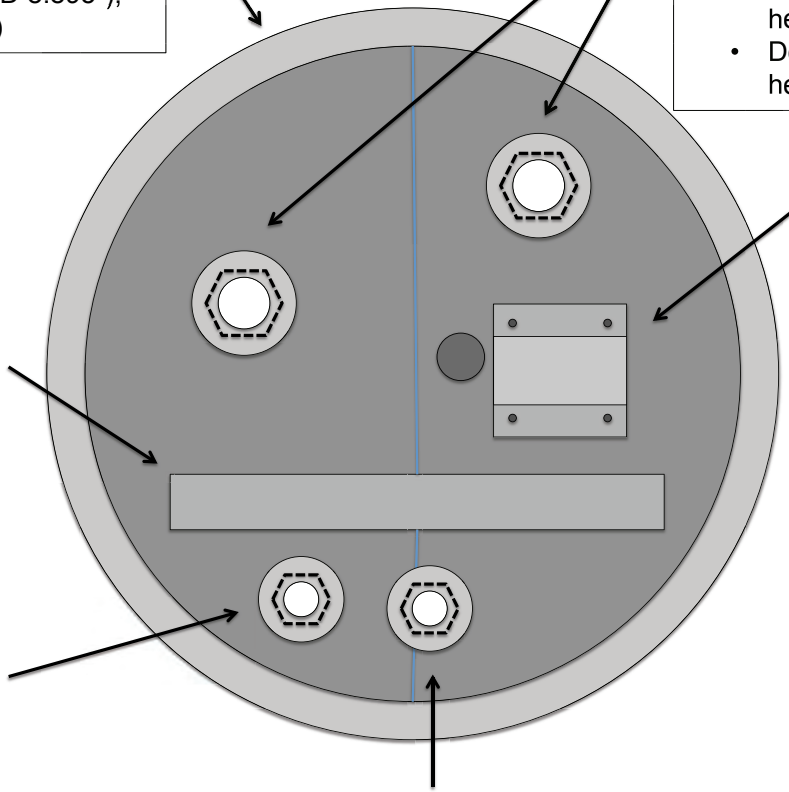

Switch
- Magnet velcro (outside):
  - Ø0.625” to match magnet
  - Position to be offset from reed switch on inside
- Indent for switch board:
  - Rectangle 1.75” wide x 1.75” tall (for 1.5” x 1.5” board – 1/8” clearance on all sides)
  - Depth 5/8”: gives 3/16” for reed switch (whose indent is 13/16”) to stick out above the board
  - Drill Ø0.089” and tap #4 at four corners, 0.25” from each edge of indent (0.125” from edge of board)
- Indent for switch:
  - Band 0.425” to 1.325” from top of switch board indent (0.3” to 1.2” from top of switch board)
  - Depth 13/16”: gives wall of 3/16” (actual distance from reed switch to magnet would also include air and velcro thickness; switch sticks out from board ~0.127”)

ADV Impulse connector
- Through-hole: Ø29/64” (close fit for 7/16-20)
- Indent:
  - Ø1.125” to accommodate 11/16” socket + extender of pass-through socket wrench, to tighten same-size hex nut (0.75” corner-to-corner)
  - Depth 13/16”: 3/16” lid thickness + 3/8” hex nut thickness take up 0.5625” of 0.5” thread length (nut will stick out)

Subconn ethernet connector
- Through-hole: Ø29/64” (close fit for 7/16-20)
- Indent:
  - Ø1.125” to accommodate 11/16” socket + extender of pass-through socket wrench, to tighten same-size hex nut (0.75” corner-to-corner)
  - Depth 0.75”: 0.25” lid thickness + 3/8” hex nut thickness take up 0.625” of 0.75” thread length (nut will stick out)

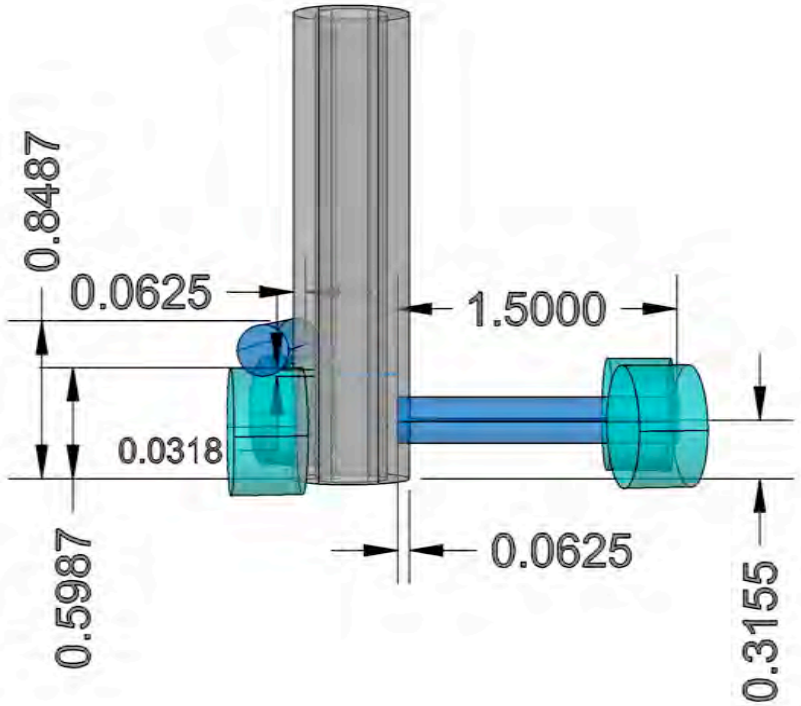
0.8487
0.0625
1.5000
0.0318
0.5987
0.0625
0.3155

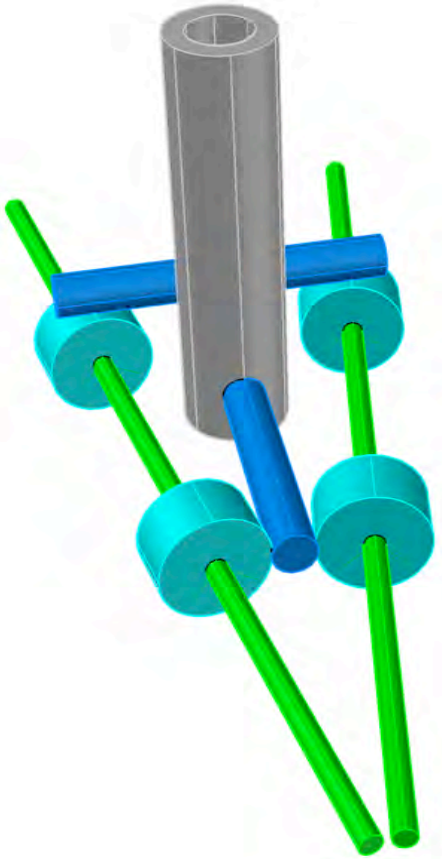

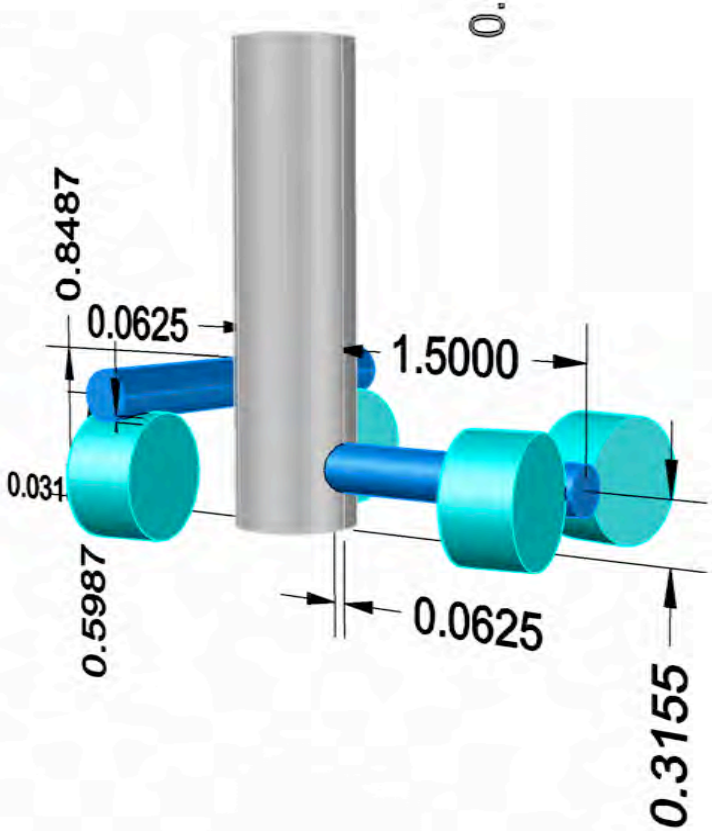
0.8487
0.0625
1.5000
0.031
0.5987
0.0625
0.3155

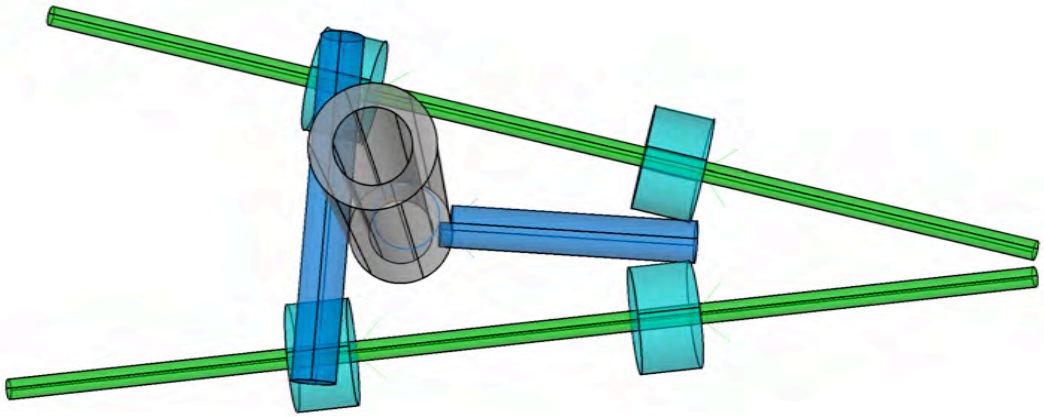

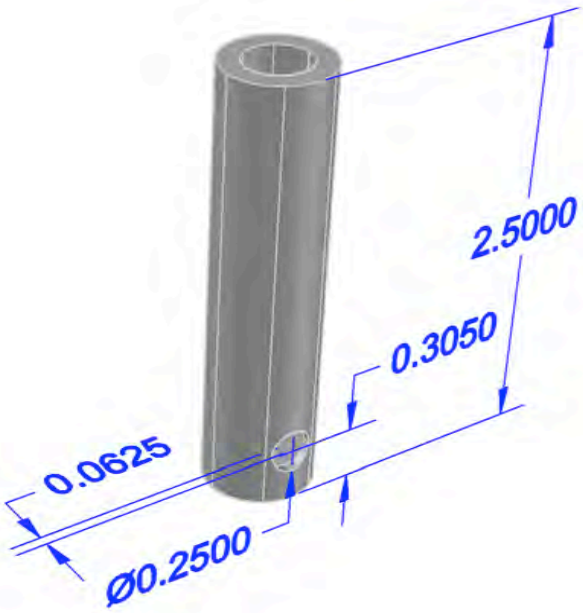

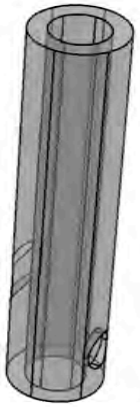

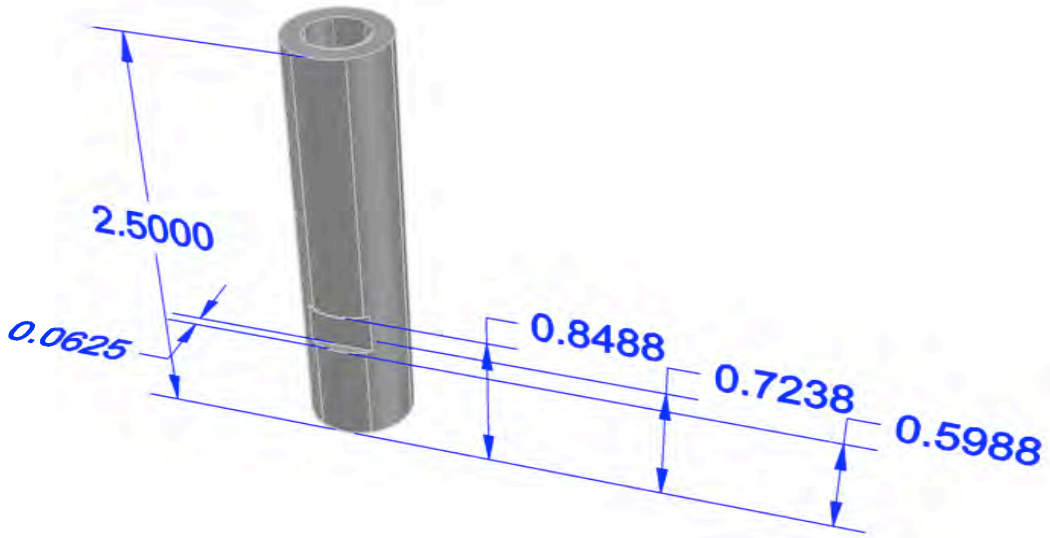

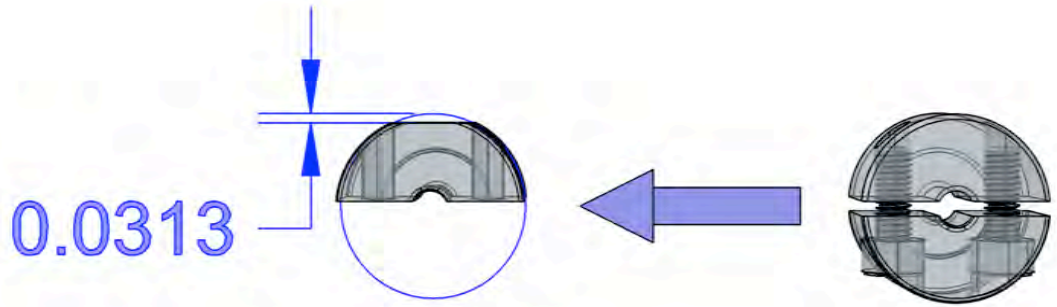

x 2

keep collar, mill a flat $\frac{1}{32}$"

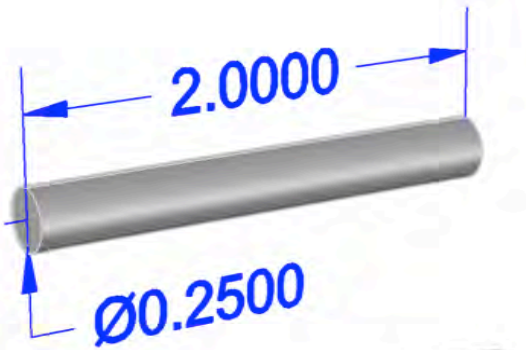

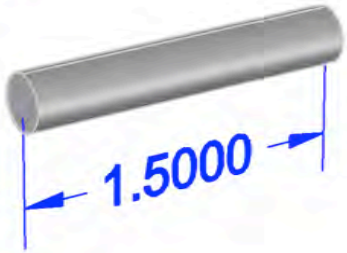

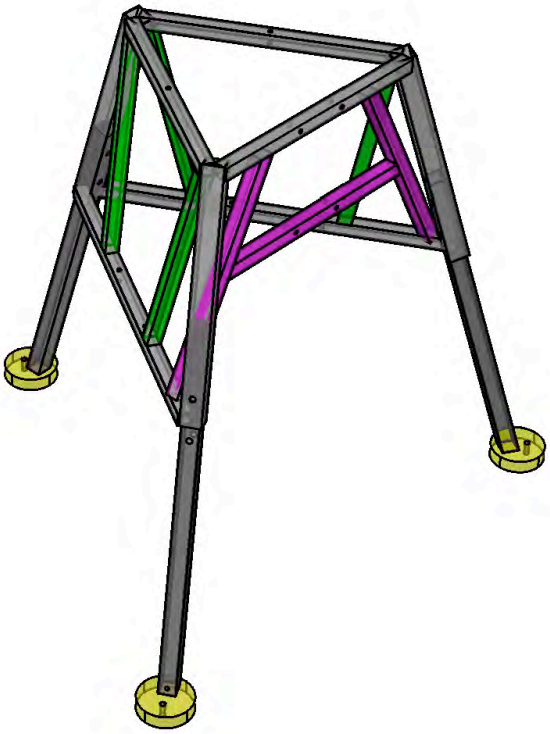

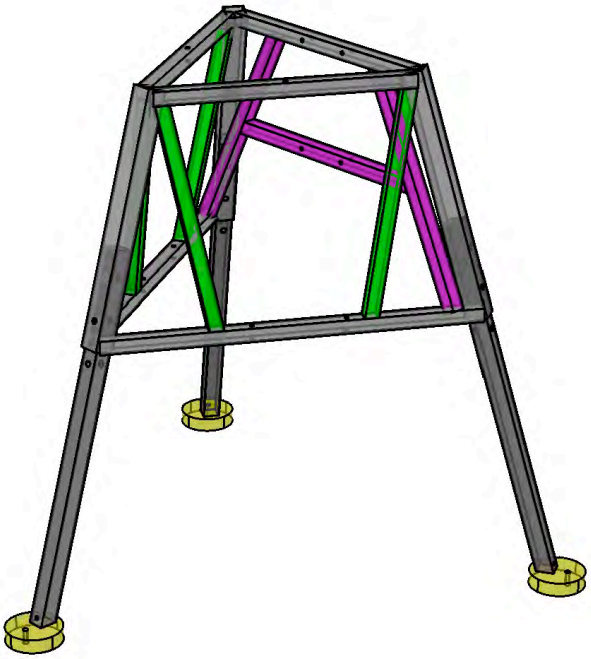

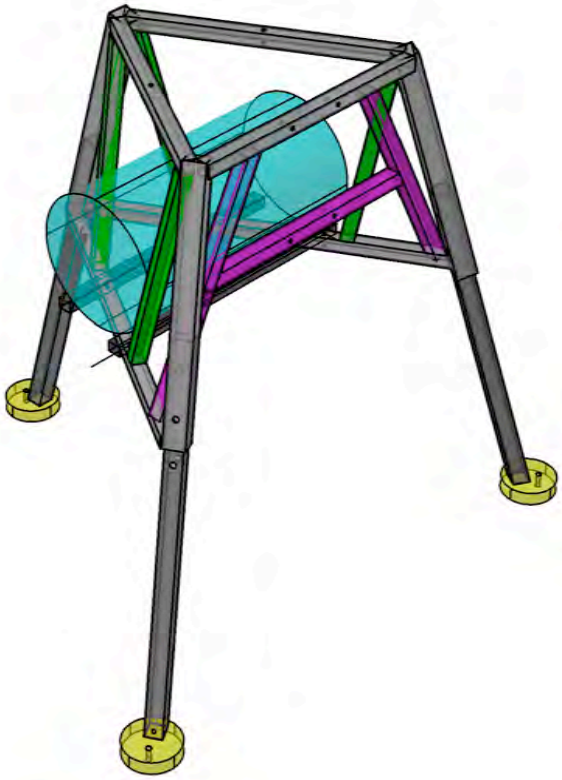

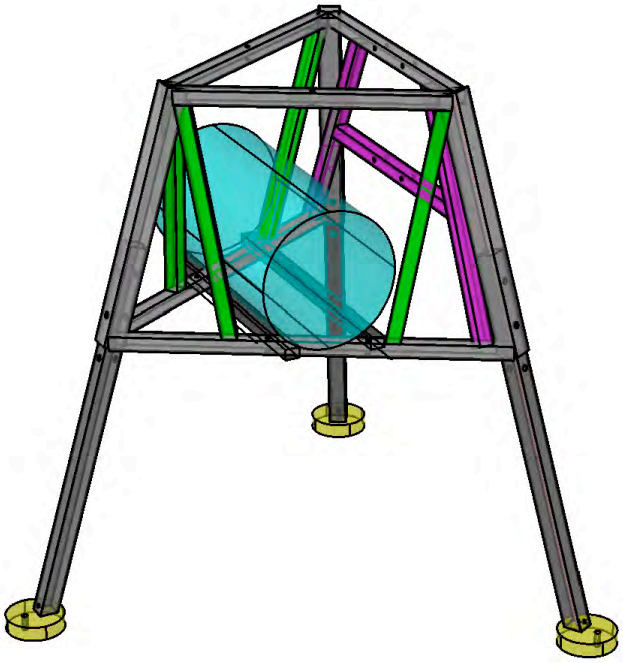

Monday 6/27/16

MCR connector — to PMT ref Notebook 2 p. 115 (connector dimensions before I modified; MCR's flange's dimensions)
p. 127 (design)
(p. 150-ish: making in machine shop)

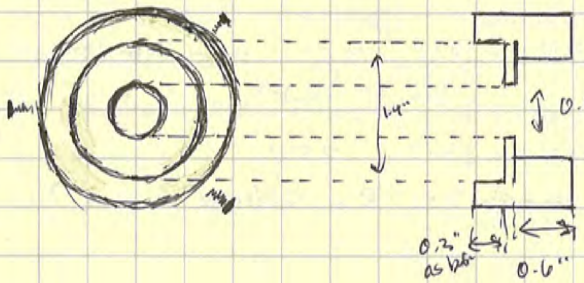

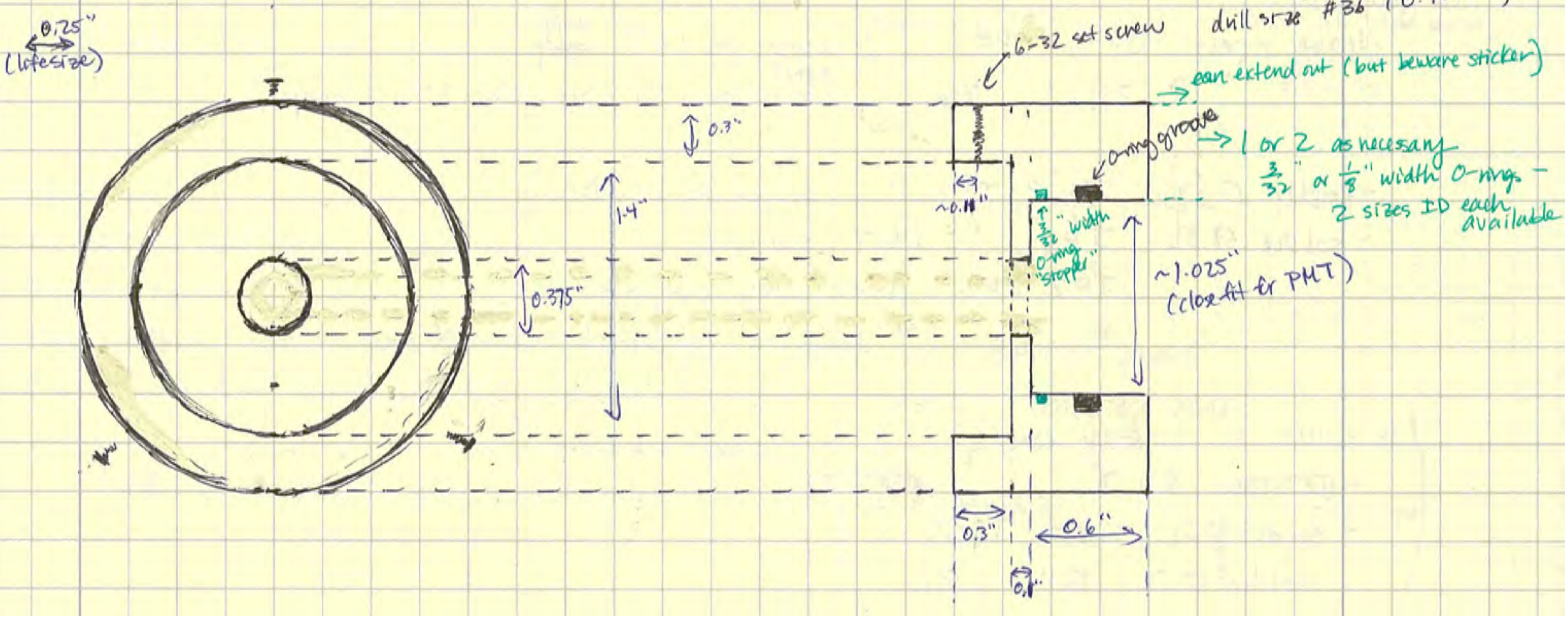

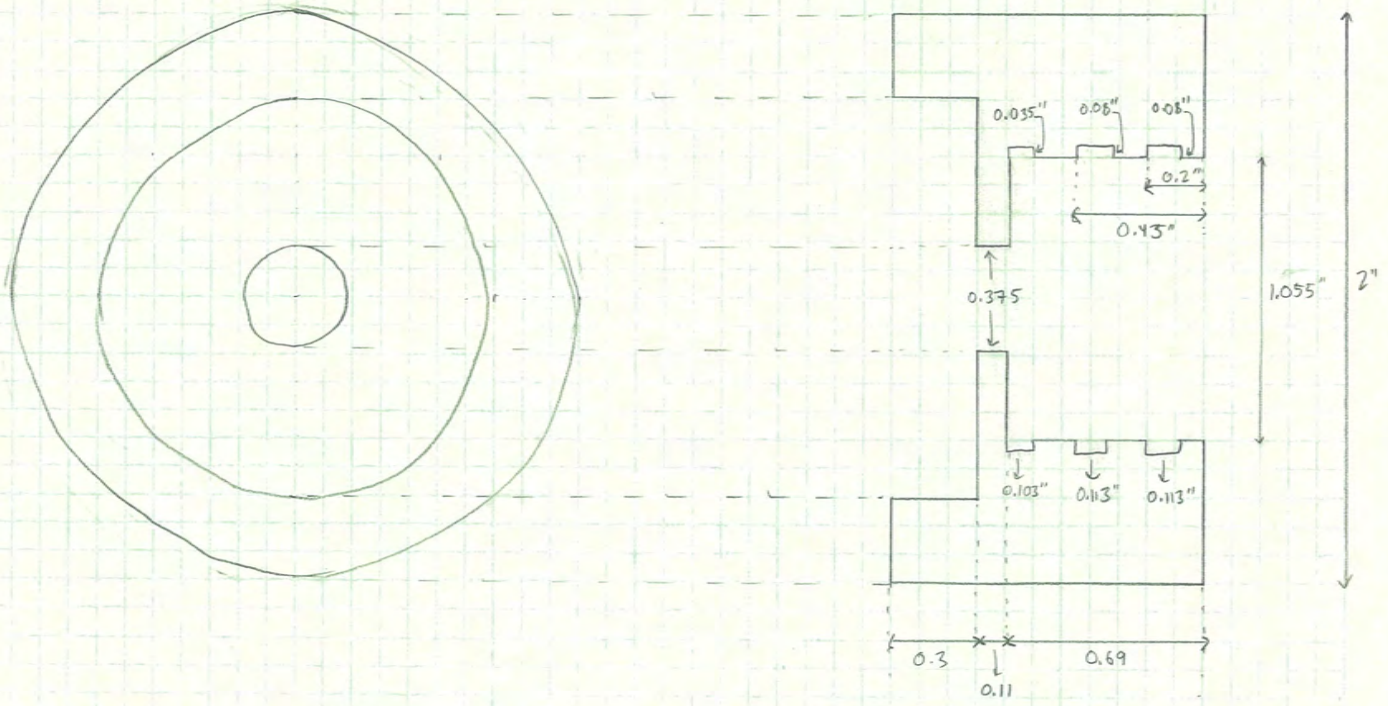
0.035"
0.08"
0.08"
0.2"
0.43"
0.375
1.055"
2"
0.103"
0.113"
0.113"
0.3
0.11
0.69

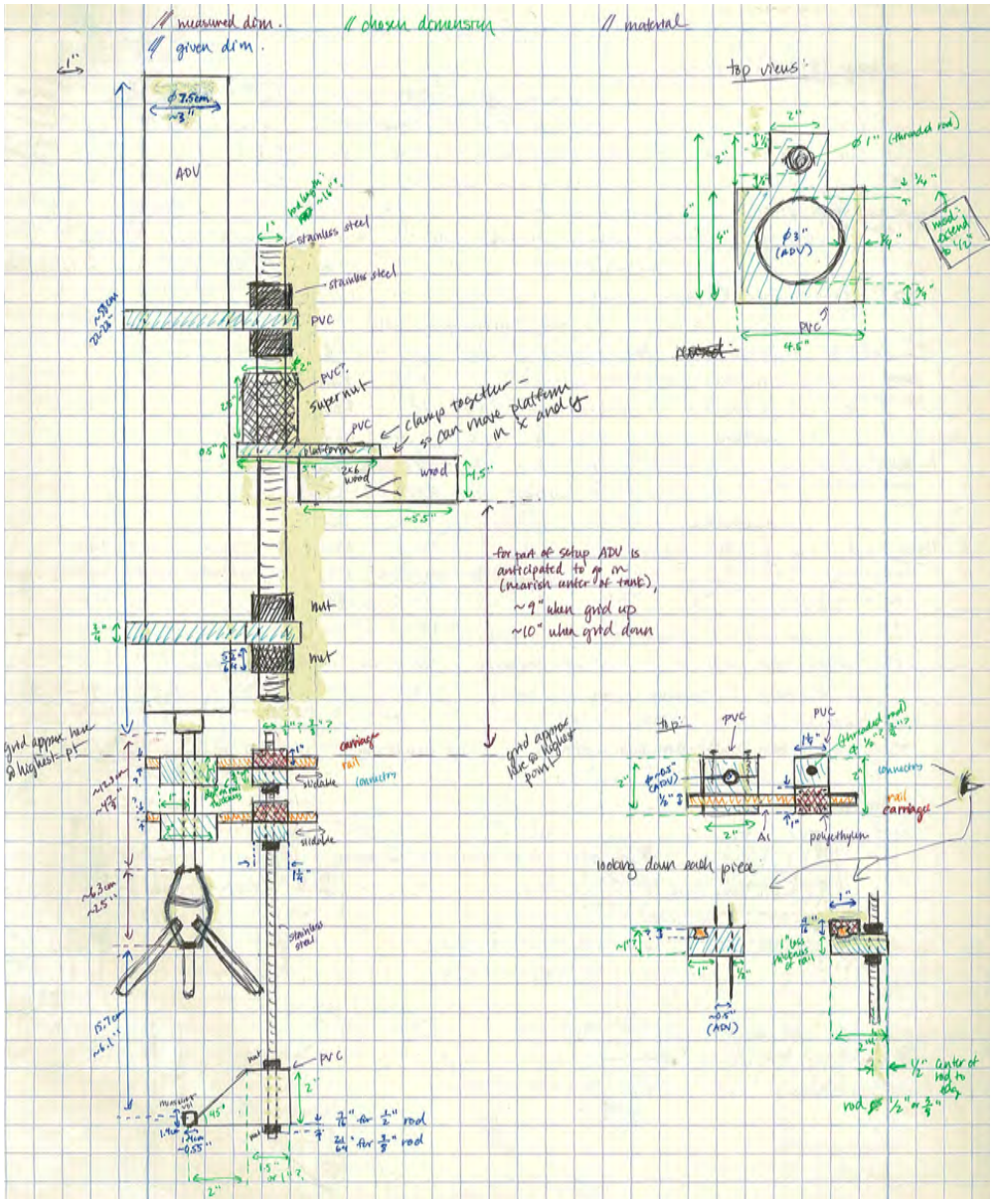
// measured dim.
// given dim.
// chosen dimension
// material
top views:
ADV
stainless steel
PVC
super nut
clamps together — so can move platform in x and y
platform
2x6 wood
nut
for part of setup ADV is anticipated to go in (nearish water surface of tank),
~9" when grid up
~10" when grid down
grid approx here @ highest pt
grid approx here @ highest point
carriage
rail
saddle
middle
polyethylene
locking down each piece
(ADV)
rod
PVC

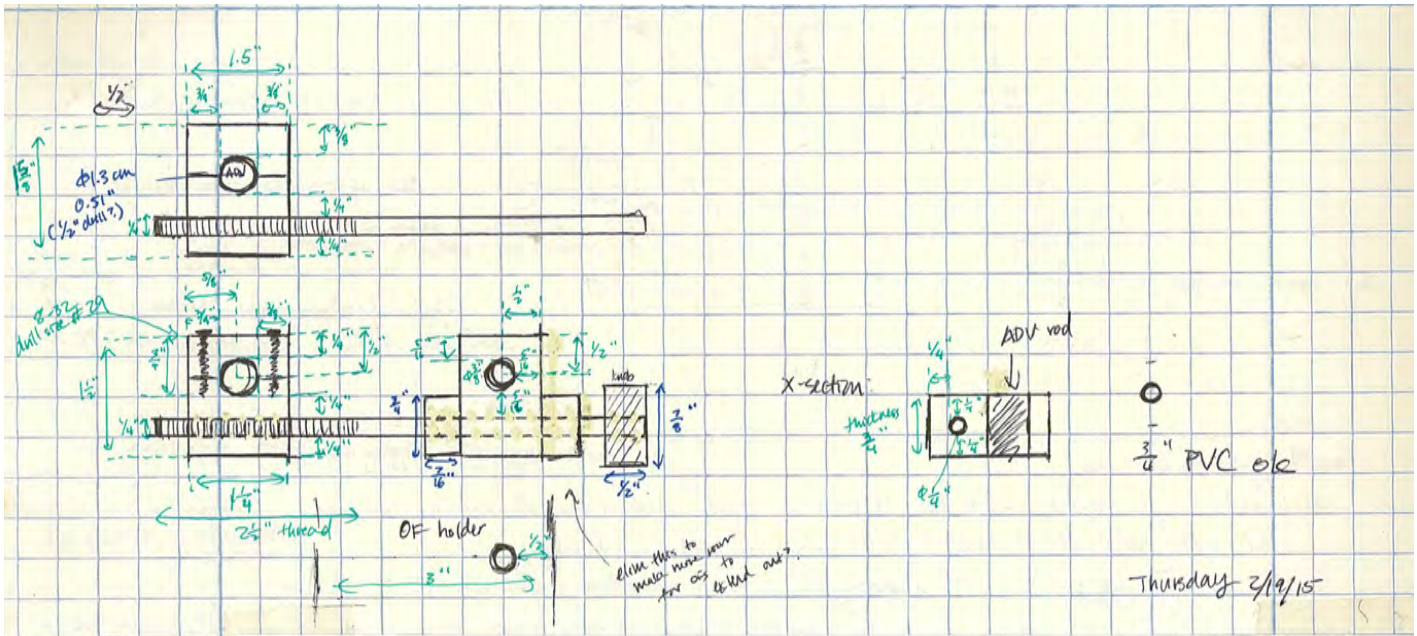

Line	Quantity	Product		Ships	Unit price	Total
1	1 pack	92185A230	Type 316 Stainless Steel Socket Head Cap Screw, 10-32 Thread, 2-1/2" Long, Fully Threaded, packs of 5	today	$7.30 pack	7.30
2	1 each	9521T25	Plastic Handle Paint Brush with 2-1/2" Wide Natural Bristle	today	$6.19 each	6.19
3	1 each	8517A59	Stainless Steel Protractor with Half-Round Head	today	$17.39 each	17.39
4	4 each	60475K66	Set Screw Shaft Collar for 1/4" Diameter, Nylon	today	$3.68 each	14.72
5	2 each	6479K67	Phenolic Fluted-Rim Knob, 1/4" Unthreaded Hole, 7/8" Diameter, Set Screw	today	$2.08 each	4.16
6	1 pack	90107A038	Type 316 Stainless Steel Flat Washer, 1" Screw Size, 1.062" ID, 2.000" OD, packs of 5	today	$9.35 pack	9.35
7	2 packs	93852A110	USS Flat Washer, 18-8 Stainless Steel, 1" Screw Size, 1.062" ID, 2.500" OD	today	$4.20 pack	8.40
8	1 each	8740K25	Chemical Resistant Type I PVC Rectangular Bar, 3/4" Thick, 1-1/2" Width, 1 ft. Length	today	$6.57 each	6.57

to screw ADV into its holder — 1
to paint wood — 2
to make OF grooves — 3
for OF holder apparatus — 4
for ADV holder — 6
for ADV holder (support platform) — 7
for OF holder apparatus — 8

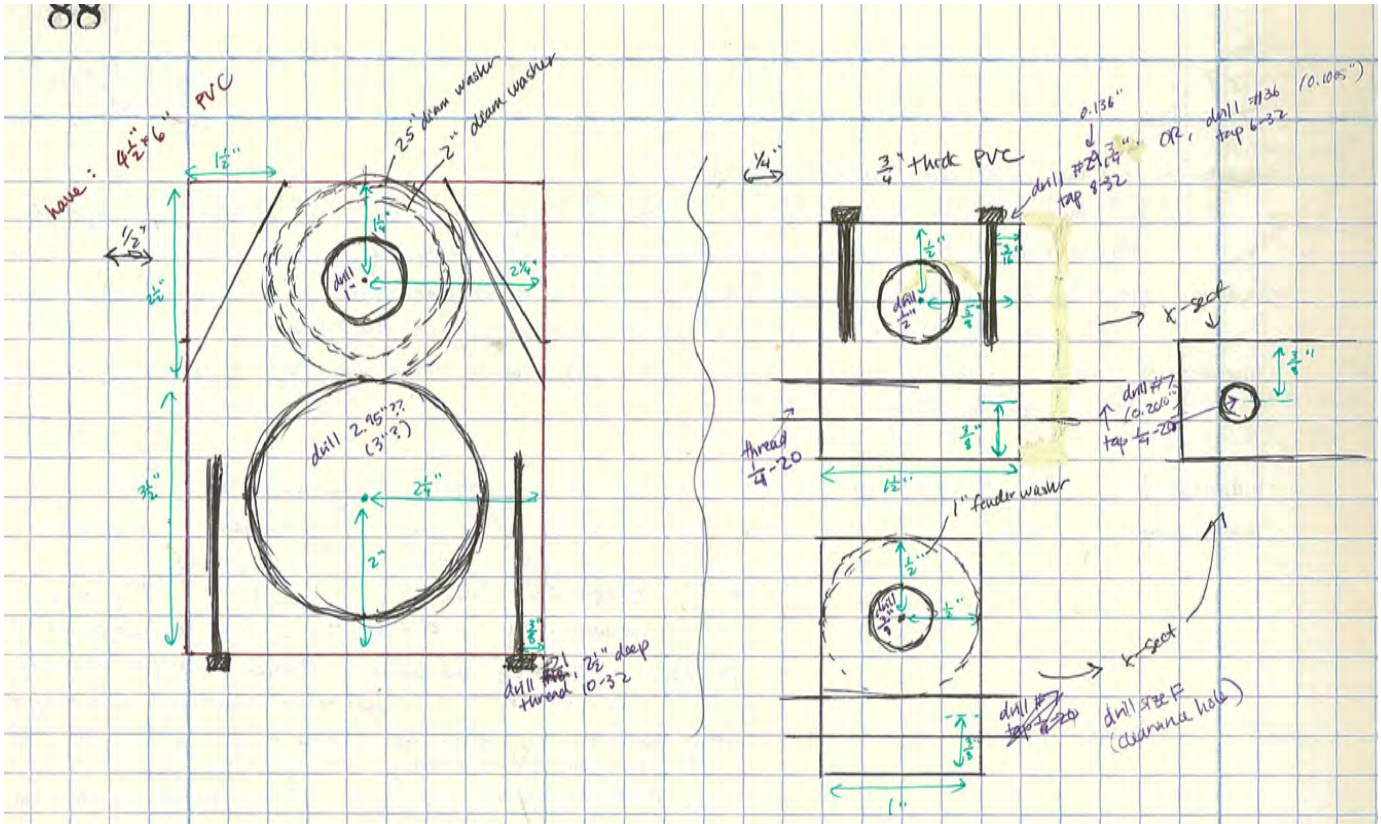

Line	Quantity	Product		Ships	Unit price	Total
1	1 pack	92185A151	Type 316 Stainless Steel Socket Head Cap Screw, 6-32 Thread, 3/4" Length, packs of 25	in the morning	$3.20 pack	3.20
2	1 pack	91525A136	Type 316 Stainless Steel Flat Washer, Oversized, 3/8" Screw Size, 1.000" OD, 0.056"-0.071" Thick, packs of 10	in the morning	$5.15 pack	5.15
3	6 packs	93852A139	USS Flat Washer, 316 Stainless Steel, 1" Screw Size, 1.062" ID, 2.500" OD	3 days	$4.71 pack	28.26

ADV holder assembled, but - - -

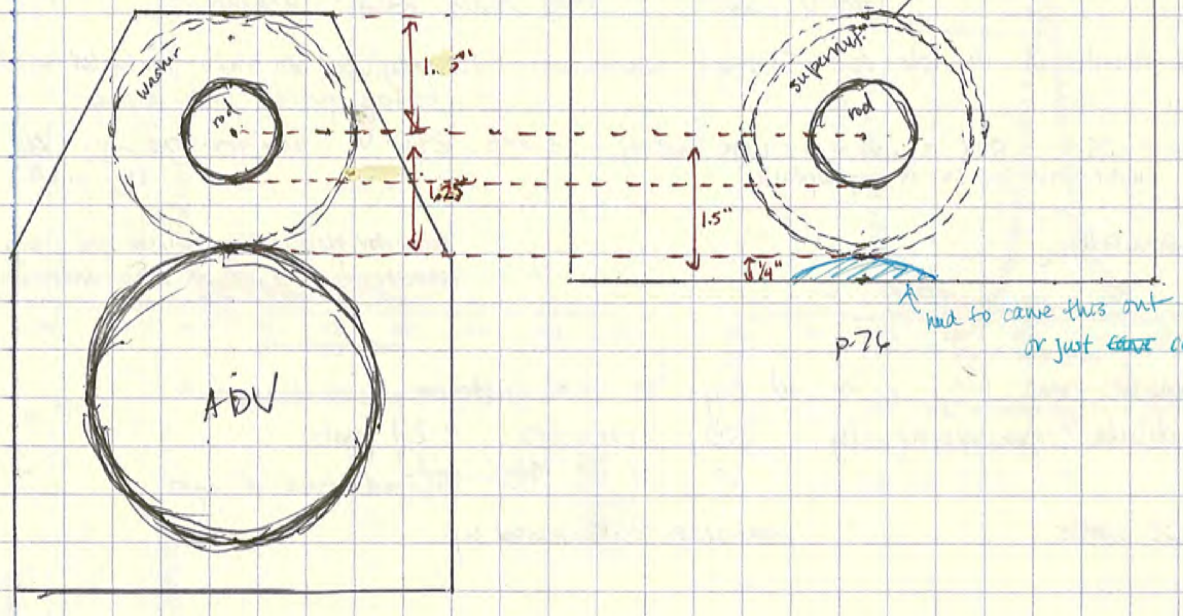

p.74

p.88

[10/Feb/2014:12:28:22 -0500]

Irene

18.84.7.151
Workbook1

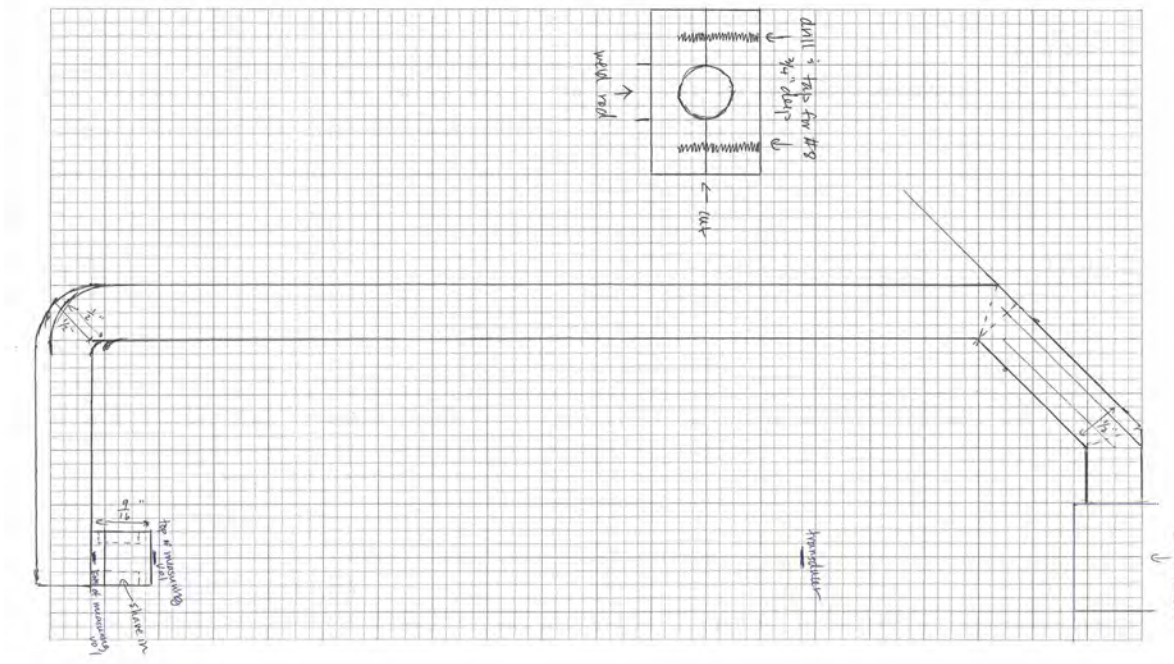

Monday 3/14/16

Chem release plate – ref Notebook IV p. 132 also p. 110

Currently have:

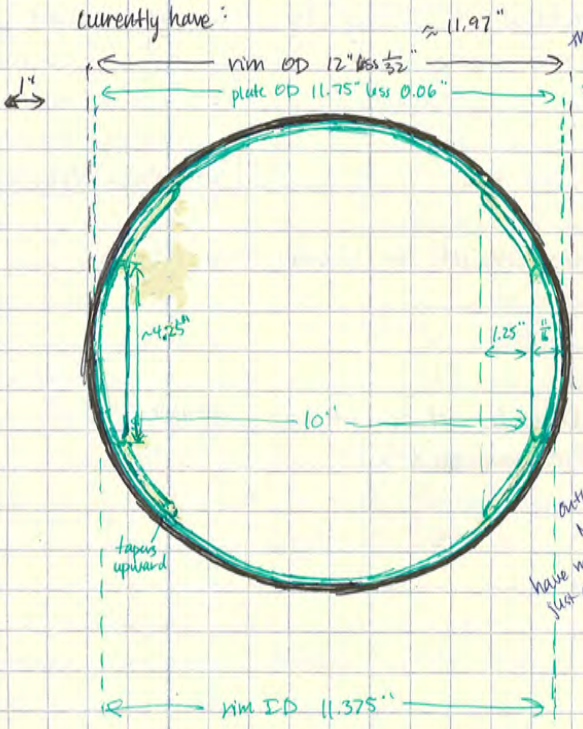

outline on p. 132 of Notebook IV – have more overhang than just above lip of the plate ~0.25" instead of 3/16" ⇒ diam 11.75" less 1/2" = 11.25"

lid: give ~1/8" rim around edge for gluing on OD ~12.25"

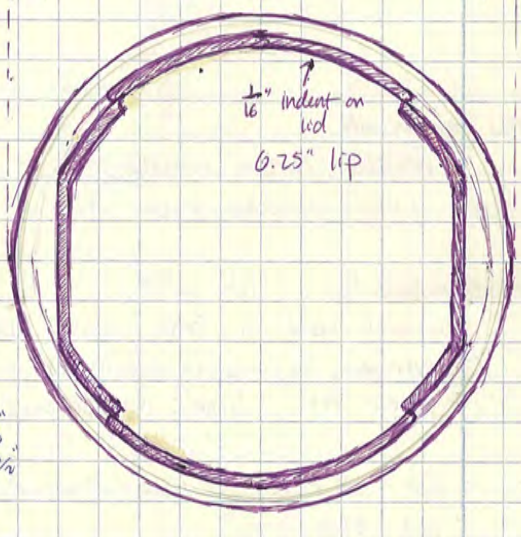

- OD 12.25"
- another rim 11.25"
- above reservoirs – match plate underneath (smooth out & round edge)
- another circle 10.75"
  - this works for both above reservoir wings & for the 1/16" indented lip
- another circle 10.25" for lip above reservoir rings
- vertical lines for reservoir – 1/4" in – for lip

lip is indented by 1/16"

from 0.25" thick

12/13/15

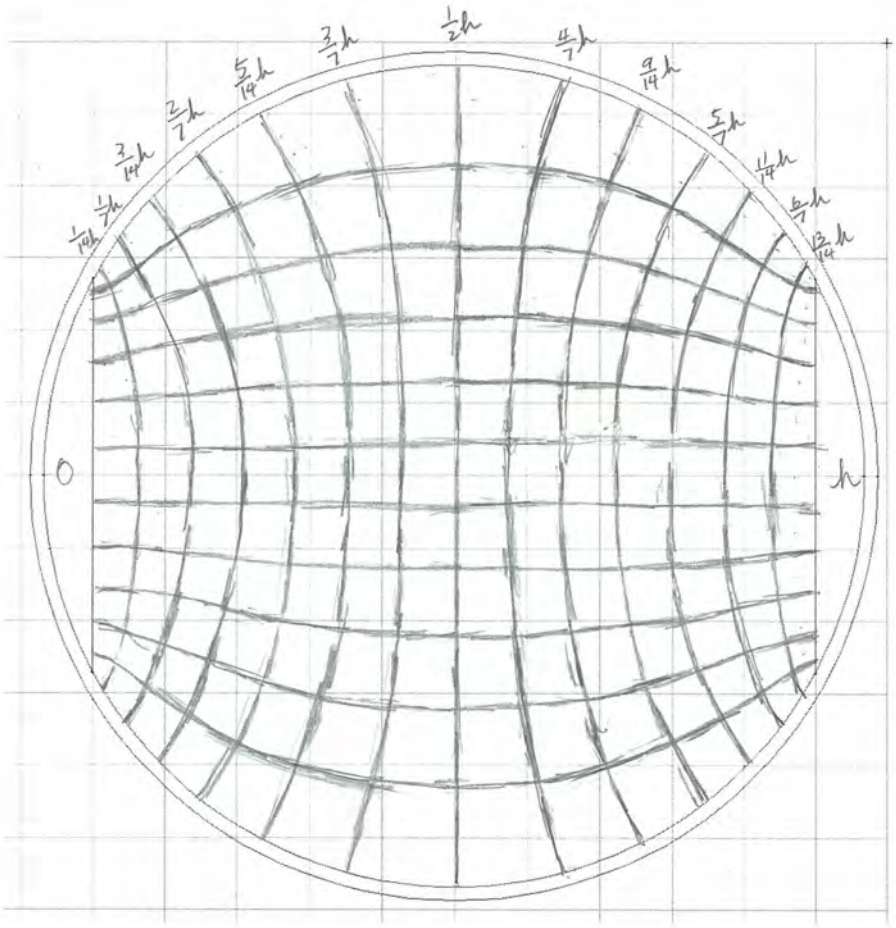

11 sts.

14 pot "tubs"

$\frac{11}{14} = 0.79$

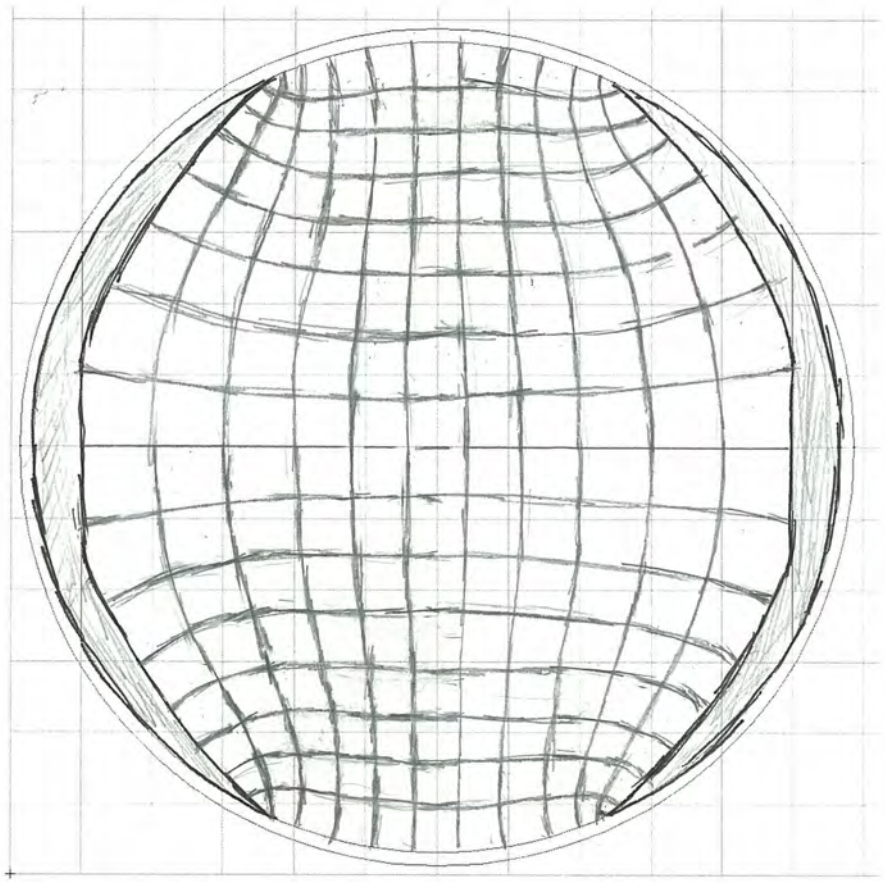

16 sfs

11 pot "tubas"

$\frac{16}{11} = 1.45$

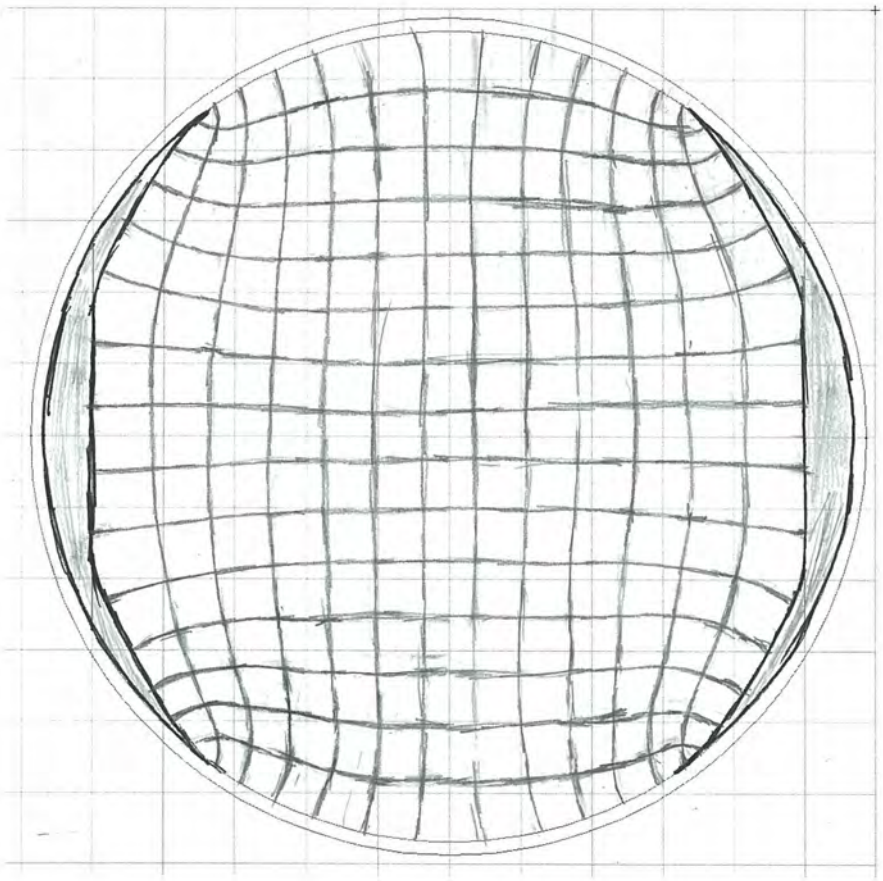

7.5 sts
6.3 pat rnds

1.2

15 sts
13 pat rnds

$\frac{15}{13} = 1.15$